

**TRIDENTATE PHOSPHINE LINKERS FOR IMMOBILIZED CATALYSTS:
DEVELOPMENT AND CHARACTERIZATION OF IMMOBILIZED RHODIUM
COMPLEXES AND SOLID-STATE NMR STUDIES OF POLYMERS**

A Dissertation

by

JOHANNES SEBASTIAN GUENTHER

Submitted to the Office of Graduate Studies of
Texas A&M University
in partial fulfillment of the requirements for the degree of

DOCTOR OF PHILOSOPHY

Approved by:

Chair of Committee,	Janet Blümel
Committee Members,	François Gabbai
	Christian Hilty
	Hae-Kwon Jeong
Head of Department,	David Russell

December 2012

Major Subject: Chemistry

Copyright 2012 Johannes Guenther

ABSTRACT

The major directions of this thesis involve (1) the synthesis, immobilization, and characterization of tridentate phosphine linkers on silica, (2) the study of unprecedented Si-C bond cleavage in Rh and Ir phosphine complexes, and (3) the study of performance polymers with solid-state NMR techniques.

First a brief overview of solid-state NMR and its relevance to the various areas of chemistry covered in this thesis is given.

Following the synthesis, immobilization, and characterization of tridentate phosphine ligands, $\text{EtOSi}[(\text{CH}_2)_n\text{PPh}_2]_3$ ($n = 4, 7, 11$) and $[\text{MeP}((\text{CH}_2)_n\text{PPh}_2)_3]^+\text{I}^-$ ($n = 4, 7, 11$) on silica is detailed. Both, immobilization by electrostatic interactions and by a covalent siloxane bond to the support, is studied and compared. Ligand exchange with Wilkinson's catalyst affords immobilized Rh complexes. These materials are applied to catalytic olefin hydrogenation. In either case active hydrogenation catalysts are obtained that can easily and efficiently be recycled up to 30 times. Detailed investigations reveal that irrespective of the linkage to the support the catalysts consist initially of well-defined molecular species that form supported Rh nanoparticles with a narrow size distribution in the course of the catalytic reaction. The nanoparticles are active hydrogenation catalysts as well, and no metal leaching into solution is detected.

The reaction of the tridentate phosphine ligands $\text{EtOSi}[(\text{CH}_2)_2\text{PPh}_2]_3$ and $\text{MeSi}[(\text{CH}_2)_2\text{PPh}_2]_3$ with Rh and Ir complexes is investigated. This reaction does not lead to the anticipated Wilkinson-type complexes with the metal in the +I oxidation state, but instead to oxidative addition of the $\text{C}(\text{sp}^3)\text{-Si}$ bond to Rh or Ir centers to yield octahedral complexes with the metal in the +III oxidation state. These complexes are fully characterized by multinuclear NMR in solution and in the solid state. Preliminary

density functional theory (DFT) calculations corroborate the preference for oxidative addition.

Subsequently the study of performance thermoplastics which are important materials for the oil and gas industry is presented. The polymer morphology is studied by solid-state NMR techniques. Special attention is devoted to potential decomposition pathways at elevated temperatures for polyetheretherketone (PEEK) and polyphenylene sulfide (PPS) polymers. ^{13}C CP/MAS (cross polarization with magic angle spinning) NMR and IR spectroscopy reveal that PEEK polymers show no detectable chemical change on the molecular level, while PPS polymers display signs of oxidation of the thioether group and branching via formation of ether, thioether, and biphenyl linkages. Furthermore, the water absorption of polybenzimidazole (PBI), polyetherketoneketone (PEKK), and their blend PEKK-PBI is studied. It is demonstrated that steam-treatment even at high temperatures and pressures does not cause chemical decomposition and that the changes, which are morphological in nature, are fully reversible.

TABLE OF CONTENTS

	Page
ABSTRACT	ii
TABLE OF CONTENTS	iv
LIST OF FIGURES.....	vi
LIST OF SCHEMES	xvii
LIST OF TABLES	xxi
NOMENCLATURE.....	xxiii
 CHAPTER	
I INTRODUCTION.....	1
II TRIDENTATE PHOSPHINE LINKERS FOR IMMOBILIZED CATALYSTS – IMMOBILIZATION OF PHOSPHONIUM SALTS	3
Introduction	3
Results and Discussion.....	17
Conclusion.....	73
Experimental	73
III TRIDENTATE PHOSPHINE LINKERS FOR IMMOBILIZED CATALYSTS – IMMOBILIZATION VIA COVALENT BONDS....	91
Introduction	91
Results and Discussion.....	94
Conclusion.....	119
Experimental	120
IV INTRAMOLECULAR CARBON-SILICON BOND ACTIVATION IN TRIDENTATE PHOSPHINE COMPLEXES OF RHODIUM AND IRIIDIUM	134
Introduction	134
Results and Discussion.....	137

	Conclusion.....	177
	Experimental	177
V	SOLID-STATE NMR AND IR STUDIES OF PERFORMANCE POLYMERS FOR THE OIL AND GAS INDUSTRY	189
	Introduction	189
	Results and Discussion.....	197
	Conclusion.....	254
	Experimental	255
VI	CONCLUSION	257
	REFERENCES.....	260
	APPENDIX A	276
	APPENDIX B	317
	APPENDIX C	330
	APPENDIX D	393

LIST OF FIGURES

FIGURE	Page
2.1 ^{29}Si CP/MAS spectrum of ethoxysilanes immobilized on silica.....	14
2.2 Single crystal X-ray structure of chelate ligand 18	25
2.3 Single crystal X-ray structure of the Rh norbornadiene complex 21	29
2.4 ^{31}P NMR spectrum (CD_2Cl_2) of Rh complex 25	31
2.5 ^{31}P NMR spectrum (CDCl_3) of Rh complex 26	33
2.6 Molecular models of 14 and 15 and estimated radii of their footprints.	35
2.7 Visualization of the experimental surface coverages for 14i (<i>top</i>) and 15i (<i>bottom</i>).	36
2.8 ^{31}P NMR of 14 (solution in C_6D_6 , bottom), ^{31}P HRMAS of a slurry of 14i with C_6D_6 (middle, spinning frequency 2 kHz), and ^{31}P MAS NMR of dry 14i (top, rotational frequency 4 kHz).	39
2.9 ^{31}P HRMAS spectra (C_6D_6 slurry, spinning frequency 2 kHz) of 13i , 14i , 15i , and 18i from top to bottom.	40
2.10 Possible modes of motion of immobilized phosphine ligands.	41
2.11 ^{31}P HRMAS lineshapes with indicated halfwidths (<i>left</i>) for 15i in the corresponding solvents.	43

2.12	Graphic display of the leaching studies for the model phosphonium salts 27-29	46
2.13	³¹ P MAS (spinning speed 4 kHz) spectra of 14i ·BH ₃ (TMS-capped) (<i>top</i>) and 14i (TMS-capped) after deprotection with DABCO (<i>bottom</i>).	49
2.14	²⁹ Si CP/MAS NMR (spinning speed 4 kHz) of 14i (TMS-capped).	50
2.15	Depiction of the surface environment of 13i (triphenylsilyl-capped).	51
2.16	Visualization of the silica surface of triphenylsilyl-capped 14i and 15i	51
2.17	³¹ P MAS spectrum of catalyst 24i (spinning speed 10 kHz).	53
2.18	Reaction apparatus, catalysts 22i – 24i (n = 1, 4, 8) and conditions for the catalytic hydrogenation of 1-dodecene.....	54
2.19	Activities of the indicated homogeneous and immobilized catalysts for the hydrogenation of 1-dodecene in the first run.	56
2.20	³¹ P MAS spectra of catalyst 24i before catalysis (<i>bottom</i>) and after (<i>top</i>).	57
2.21	Activity of 23i immobilized on 40 Å and 150 Å silica, respectively, for the hydrogenation of 1-dodecene.	58
2.22	Hydrogen consumption during 14 batchwise catalytic runs using 21i	59
2.23	Hydrogen consumption using catalyst 23i immobilized on end-capped and unmodified silica.	60
2.24	Hydrogen consumption over 30 batchwise catalytic runs using 23i	62
2.25	Split test to prove the absence of any Rh species in solution.....	63

2.26	Three-phase test using immobilized allyltriethoxysilane and 23i on different support batches.	64
2.27	Hydrogen consumption of the shown catalysts with and without the poisoning agent DBCOT.	66
2.28	Hydrogen consumption of the TMS-capped catalyst 23i in the first run with and without the poisoning agent DBCOT.	67
2.29	Olefin region of the ^1H NMR spectra (CDCl_3) of the reaction mixtures after the conversion indicated.	69
2.30	Reaction flask containing pristine 23i in toluene (<i>left</i>) and 23i after exposure to H_2 at 70°C (<i>right</i>).	70
2.31	TEM images of Rh nanoparticles that formed during catalysis with 22i (top), 23i (middle), and 24i (bottom), and their corresponding size distributions.	72
3.1	Possible pathways leading to the formation of Rh nanoparticles from a single-site catalyst.	93
3.2	^{29}Si CP/MAS NMR of 33bi (4 kHz spinning speed).	99
3.3	^{31}P CP/MAS NMR of 35i · BH_3 (<i>top</i>), 35i (<i>middle</i>) and 38i (<i>bottom</i>) (10 kHz spinning speed).	100
3.4	^{31}P NMR of 35 (solution in CDCl_3 , <i>bottom</i>), ^{31}P HRMAS of a slurry of 35i in toluene (<i>middle</i> , 2 kHz spinning speed), ^{31}P CP/MAS of dry 35i (<i>top</i> , 10 kHz spinning speed).	101
3.5	Tridentate phosphine linkers 35i and 15i , which have been immobilized by electrostatic interactions with the silica surface.	103

3.6	ORTEP representation of RhClpyCOD 39 showing 50% thermal ellipsoid probability.	105
3.7	³¹ P HRMAS NMR spectrum of 35i after the reaction with three equivalents of RhClpyCOD 39 (slurry in acetone, <i>bottom</i>), ³¹ P CP/MAS of 35i after the reaction with three equivalents of RhClpyCOD 39 (<i>middle</i>), and one equivalent of RhClpyCOD (<i>top</i>).	108
3.8	³¹ P HRMAS NMR of 43i (slurry in acetone, <i>top</i>), and ³¹ P NMR of 43 (solution in CDCl ₃ , <i>bottom</i>).	109
3.9	Activities of the indicated immobilized catalysts for the hydrogenation of 1-dodecene in the first run.	111
3.10	Activities of the indicated immobilized catalysts for the hydrogenation of 1-dodecene in the first run.	112
3.11	Activities of the indicated immobilized catalysts for the hydrogenation of 1-dodecene in the first run.	113
3.12	Three-phase test with 38i using immobilized allyltriethoxysilane (details see text and Experimental Section).	114
3.13	Hydrogen consumption of the catalyst 38i for the hydrogenation of 1-dodecene with and without the poisoning agent DBCOT (dibenzo[<i>a,e</i>]cyclooctatetraene).	115
3.14	Hydrogen consumption during 12 batchwise catalytic runs using 37i	116
3.15	Hydrogen consumption during 15 batchwise catalytic runs using 41i	117
3.16	TEM images of Rh nanoparticles that formed during catalysis with 37i (<i>top left</i>), 36i (<i>bottom left</i> , after exposure to air), RhClpyCOD (<i>top right</i>) in toluene and their corresponding size distribution (<i>bottom right</i>).	119

4.1	Tridentate phosphine ligands with C ₁ or C ₂ spacer lengths.	134
4.2	Single crystal X-ray structure of the siloxane compound 44b	138
4.3	³¹ P Wideline (<i>bottom</i>) and CP/MAS (<i>top</i> , 4 kHz spinning speed) NMR spectra of 44	140
4.4	³¹ P CP/MAS spectra of 44 (<i>top</i> , 4 kHz spinning speed) and 45 (<i>bottom</i> , 4.5 kHz spinning speed).	141
4.5	²⁹ Si CP/MAS spectra of 44 (<i>top</i> , 0 kHz spinning speed; middle: 1.5 kHz spinning speed; bottom, 10 kHz spinning speed).	142
4.6	²⁹ Si CP/MAS spectra of 44 (<i>top</i> , 1.5 kHz spinning speed) and 45 (<i>bottom</i> , 5 kHz spinning speed).	143
4.7	³¹ P NMR spectrum of 47 in CDCl ₃	145
4.8	³¹ P VT-NMR spectra of 47 in toluene at the indicated temperatures.	147
4.9	³¹ P CP/MAS NMR spectrum of 47 (13 kHz spinning speed).	148
4.10	²⁹ Si CP/MAS NMR spectrum of 47 (13 kHz spinning speed).	149
4.11	³¹ P NMR spectrum of a mixture of 48 and 49 in C ₆ D ₆	151
4.12	²⁹ Si NMR spectrum of a mixture of 48 and 49 in C ₆ D ₆	152
4.13	Alkyl region of the ¹³ C NMR spectrum of a mixture of 48 and 49 in C ₆ D ₆	154
4.14	Isomer ratio of 48 to 49 obtained at different reaction temperatures in the indicated solvents.	155

4.15	^{31}P NMR spectrum of 51 in CDCl_3 .	157
4.16	^{31}P NMR spectrum of 52 in CDCl_3 .	158
4.17	^{29}Si NMR spectra of 51 (<i>top</i>) and 52 (<i>bottom</i>) in CDCl_3 .	159
4.18	^{31}P NMR spectrum of a mixture of 51 (<i>blue</i>) and 55 (<i>green</i>) in CDCl_3	161
4.19	^{31}P NMR spectrum of 55 in CDCl_3 .	162
4.20	^{29}Si NMR spectrum of 55 in CDCl_3 .	163
4.21	Possible molecular structures of 55 .	164
4.22	^{31}P NMR spectra of 52 (Scheme 4.8) in CDCl_3 (<i>bottom</i>) and in the solid state (<i>top</i> , 10 kHz spinning speed).	165
4.23	^{29}Si CP/MAS NMR spectra of 45 (<i>bottom</i>) and 52 (<i>top</i>) (10 kHz spinning speed).	166
4.24	^{31}P NMR spectra of 51 in CDCl_3 (<i>bottom</i>) and in the solid state (<i>top</i> , 12 kHz spinning speed).	167
4.25	^{29}Si CP/MAS NMR spectra of 44 (<i>bottom</i> , 1.5 kHz spinning speed) and 51 (<i>top</i> , 5 kHz spinning speed).	168
4.26	Isomers considered in DFT geometry optimization.	169
4.27	Relative free energies of 48 , 49 , and 50 .	170
4.28	Relative free energies of 52 , 54 , and 56 .	171
4.29	Optimized geometry for 50 , side view (<i>left</i>) and top view (<i>right</i>).	172

4.30	Optimized geometry for 49 ; side view (<i>left</i>) and top view (<i>right</i>).	173
4.31	Optimized geometry for 48 ; side view (<i>left</i>) and top view (<i>right</i>).	174
5.1	Classification of thermoplastic polymers.	190
5.2	Nomenclature of PAEK polymers.	191
5.3	Motion-sensitive NMR parameters.	193
5.4	Dependence of the T_1 and T_2 relaxation times on the correlation time τ_c . ..	194
5.5	Semicrystalline polymer with crystalline and amorphous domains.	195
5.6	Torchia's pulse sequence to measure ^{13}C T_1 relaxation times.	196
5.7	Torchia's method to measure ^{13}C T_1 relaxation times, demonstrated with a PEEK polymer.	197
5.8	^{13}C CP/MAS NMR spectrum of PEEK (Victrex 450P).	198
5.9	Cross-polarization kinetics of the signal at 120 ppm.	199
5.10	Cross-polarization kinetics of the signal at 150 ppm.	199
5.11	(a) ^{13}C CP/MAS and (b) ^{13}C Dipolar Dephasing (40 μs dephasing delay) NMR spectra of Victrex 450P.	201
5.12	^{13}C CP/MAS NMR spectra of Victrex 450P (a), Evonik 4000PF (b), and Evonik 5000G (c). ..	202
5.13	^{13}C T_1 relaxation of PEEK Victrex 450P for the signal at 120.1 ppm.	204

5.14	^{13}C T_1 relaxation of PEEK Evonik 4000PF for the signal at 120.1 ppm. ..	204
5.15	^{13}C T_1 relaxation of PEEK Evonik 5000G for the signal at 120.1 ppm.	205
5.16	Possible structures of cross-linked PEEK.	207
5.17	^{13}C CP/MAS NMR of Victrex PEEK 450 (a) as received, (b) after heating to 300 °C for 4 h, and (c) heating to 420 °C for 1.5 h.	209
5.18	^{13}C T_1 relaxation of a PEEK sample after the indicated thermal treatments.	210
5.19	IR spectra of PEEK: original sample (<i>top</i>), and after thermal treatment at 300 °C (<i>bottom</i>).	212
5.20	Structure of PPS (polyphenylene sulfide).	213
5.21	^{13}C CP/MAS NMR spectrum of PPS. Asterisks denote spinning sidebands.	214
5.22	^{13}C CP/MAS NMR spectra of PPS (10 kHz) obtained with dipolar dephasing delays of (a) 0 μs , (b) 10 μs , and (c) 40 μs	215
5.23	^{13}C CP/MAS NMR spectra of PPS (10 kHz) obtained with variable contact times of (a) 0.2 ms, (b) 1.5 ms, and (c) 6.0 ms.	216
5.24	^{13}C CP/MAS NMR spectra of PPS obtained from vendors Fortron (a) and ChevronPhillips, grades R475 (b) and R470 (c).	217
5.25	Possible oxidation products of the sulfide group of PPS with the expected ^{13}C chemical shifts.	218
5.26	Possible branching of PPS with the expected ^{13}C chemical shifts.	219

5.27	^{13}C CP/MAS NMR spectra of PPS, (a) original sample, (b) heated to 250 °C for 4 h, (c) heated to 350 °C for 4 h, and (d) heated to 350 °C for 52 h.	220
5.28	^{13}C CP/MAS NMR spectra of PPS heated to 250 °C for 4 h (a) under a nitrogen atmosphere and (b) in air.	220
5.29	^{13}C CP/MAS NMR spectrum of PPS heated to 350 °C for 4 h (a) and simulated spectrum (b).	222
5.30	PPS heated to 350 °C for 4 h in air: (a) ^{13}C CP/MAS NMR with a contact time of 0.2 ms, (b) ^{13}C CP/MAS NMR with a 50 μs dipolar dephasing delay, and (c) routine ^{13}C CP/MAS NMR.	223
5.31	IR spectra of original PPS sample (<i>bottom</i>), and after heating it to 350 °C for 52 h (<i>top</i>).	224
5.32	IR spectral region from 1500 to 1050 cm^{-1} of the original PPS sample (<i>bottom</i>), and after heating it to 350 °C for 52 h (<i>top</i>).	225
5.33	^{13}C CP/MAS NMR spectra of the PEKK-PBI blend (<i>bottom</i> , $\nu_{\text{rot}} = 13$ kHz), neat PBI (<i>middle</i> , 10 kHz), and neat PEKK (<i>top</i> , 10 kHz).	228
5.34	^{13}C CP/MAS NMR spectra of (a) PBI ($\nu_{\text{rot}} = 10$ kHz), (b) PBI exposed to water at RT (10 kHz), (c) PBI steam-treated at 300 F for 48 h (10 kHz), and (d) PBI steam-treated at 600 F for 72 h (13 kHz).	229
5.35	Expansion of the aryl signal region of the ^{13}C CP/MAS NMR spectra of (a) PBI ($\nu_{\text{rot}} = 10$ kHz), (b) PBI exposed to water at RT (10 kHz), (c) PBI steam-treated at 300 F for 48 h (10 kHz), and (d) PBI steam-treated at 600 F for 72 h (13 kHz).	230

5.36	^{13}C CP/MAS NMR spectra of (a) PBI ($\nu_{\text{rot}} = 10$ kHz), (b) PBI treated with water at RT (10 kHz), and (c) PBI after re-drying the wet sample <i>in vacuo</i> (10 kHz).	231
5.37	^1H Wideline NMR spectra of (a) PBI that has been rigorously dried at 100 °C <i>in vacuo</i> for 24 h, (b) PBI that has been steam-treated at 300 F for 48 h, and then left exposed to the atmosphere for two months, and (c) PBI after steam-treatment at 300 F for for 48 h.	233
5.38	^1H Wideline NMR spectra of (a) PBI after treatment with water at RT, (b) PBI after steam-treatment at 300 F for 48 h, (c) PBI after steam-treatment at 600 F for 72 h, (d) simulation of the spectrum (c). The spectra are normalized to the height of the broad signal of the polymer protons.	234
5.39	IR spectra of original PBI (<i>bottom</i>), and PBI after steam-treatment at 300 F for 48 h (<i>middle</i>) and 600 F for 72 h (<i>top</i>).	237
5.40	IR spectra of PBI after steam-treatment at 300 F for 48 h (<i>bottom</i>), and subsequent redrying <i>in vacuo</i> at 120 °C (<i>top</i>).	238
5.41	^{13}C CP/MAS NMR spectra of (a) original PEKK ($\nu_{\text{rot}} = 10$ kHz), (b) PEKK treated with water at RT (10 kHz), (c) PEKK steam-treated at 300 F for 48 h (10 kHz), and (d) PEKK steam-treated at 600 F for 72 h (13 kHz).	239
5.42	IR spectra of PEKK (<i>bottom</i>), PEKK after steam-treatment at 300 F for 48 h (<i>middle</i>) and at 600 F for 72 h (<i>top</i>).	240
5.43	DSC curves of the indicated original and steam-treated PBI samples. Curves are offset vertically for clarity.	242
5.44	DSC curves of the indicated original and steam-treated PEKK samples. Curves are offset vertically for clarity.	243

5.45	DSC curves of the indicated original and steam-treated PEKK-PBI blend samples. Curves are offset vertically for clarity.....	244
5.46	^{13}C CP/MAS NMR spectra of (a) original PEKK-PBI blend ($v_{\text{rot}} = 13$ kHz), (b) PEKK-PBI blend steam-treated at 300 F for 48 h (12 kHz), and (c) PEKK-PBI blend steam-treated at 600 F for 72 h (12 kHz).	246
5.47	^1H Wideline NMR spectra of PEKK-PBI blend after (a) treatment with water at RT, (b) steam-treatment at 300 F for 48 h, and (c) steam-treatment at 600 F for 72 h.	247
5.48	IR spectra of original PEKK-PBI blend (<i>bottom</i>), and after being exposed to water at RT for 48 h (<i>top</i>).	248
5.49	^{13}C T_1 relaxation time characteristics of PEKK samples, treated as indicated.	249
5.50	^{13}C T_1 relaxation time characteristics of the indicated PBI samples.	251
5.51	^{13}C T_1 relaxation time characteristics of the indicated PEKK-PBI blend samples obtained from the ^{13}C NMR signal at 128 ppm.	252
5.52	Overview of the ^{13}C T_1 relaxation time characteristics of water-treated and original pure components PEKK and PBI and PEKK-PBI blends.	253

LIST OF SCHEMES

SCHEME	Page
2.1 Classification of catalysts	3
2.2 Rhodium complex immobilized via hydrogen bonding	6
2.3 Model of a supported aqueous phase catalyst (SAPC).	7
2.4 Phosphine ligands commonly used for SAPC.....	8
2.5 Immobilization of a Pd(0) catalyst (<i>left</i>) and a Mn(III) salen complex (<i>right</i>) via encapsulation.	9
2.6 Immobilization of Rh and Pd complexes on a polystyrene support.....	11
2.7 Nucleophilic addition of ethoxysilanes to surface siloxane groups (<i>top</i>) and condensation with surface silanol groups (<i>bottom</i>).	13
2.8 Rh complex immobilized on silica via an ionic tether.	15
2.9 Immobilization via electrostatic interactions.	16
2.10 Immobilization of tridentate phosphine ligands via electrostatic interactions (n = 1, 4, 9).	16
2.11 Outline of the general ligand synthesis and immobilization.	18
2.12 Synthesis of phosphine 1	19
2.13 Synthesis of phosphines 2 and 3	19

2.14 Synthesis of phosphonium salts 4-6 .	20
2.15 Synthesis of phosphonium salt 10 .	20
2.16 Attempted synthesis of 12 .	21
2.17 Synthesis of compounds 13-15 .	22
2.18 Synthesis of compound 16 .	23
2.19 Synthesis of tetraphosphine 17 .	23
2.20 Synthesis of compound 18 .	24
2.21 Synthesis of ligand 20 .	26
2.22 Attempted alternative synthesis of 20 .	27
2.23 Synthesis of complex 21 .	28
2.24 Attempted synthesis of the Rh complexes 22-24 .	30
2.25 Synthesis of Rh complex 25 .	31
2.26 Synthesis of Rh complex 26 .	32
2.27 Immobilization and synthesis of 22i-24i .	34
2.28 End-capping of silanol groups and phosphonium salt formation.	47
2.29 Silanol end-capping after protecting the phosphine groups.	48
2.30 Synthesis of immobilized Rh catalysts 22i-24i .	52

2.31	Catalytic hydrogenation of 1-dodecene.....	54
2.32	Catalytic hydrogenation of nitrobenzene.	69
3.1	Synthesis of the phosphine ligands 33 , 34 , and 35	95
3.2	Synthesis of 30 , 31 , and 32 and the corresponding byproducts 30b , 31b , and 32b	95
3.3	Synthesis of the phosphine ligands 33 , 34 , and 35 , their immobilization on SiO ₂ , and formation of the immobilized Rh complexes 36i , 37i , and 38i	96
3.4	Synthesis of the immobilized Rh complexes 40i , 41i , and 42i	106
3.5	Catalytic hydrogenation of 1-dodecene; pressure 1.1 atm, substrate to catalyst ratio 100 : 1, reaction temperature: 60 °C.....	110
4.1	Selective hydrogenation of cinnamaldehyde with catalyst A containing a COD ligand.	135
4.2	Si-C(sp ³) and Si-C(sp ²) activation via a Pd(0) intermediate.	136
4.3	Si-C(sp ³) activation.	136
4.4	Synthesis of the phosphine ligands 44 and 45	137
4.5	Synthesis of the phosphine ligand 44 with the side-products 44c and 44d	139
4.6	Selective formation of Rh complex 47 . Rh(I) stands for [(COD)RhCl] ₂ and ClRh(PPh ₃) ₃	144

4.7	Synthesis of Rh complexes 48 and 49 . Rh(I) stands for [(COD)RhCl] ₂ and ClRh(PPh ₃) ₃	150
4.8	Selective formation of the Ir complexes 51 and 52	156
4.9	Reaction of 45 with [(COD)IrCl] ₂ to form 52 and 55	160
4.10	Equilibrium between 51 (52) in solution and 53 (54) in the solid state.	164

LIST OF TABLES

TABLE	Page
2.1 Surface coverages of the modified silica 13i-15i , 18i , 21i-24i , and 27i-29i .	37
2.2 ^{31}P MAS and HRMAS NMR chemical shifts δ and signal halfwidths $\Delta\nu_{1/2}$ for the phosphonium and phosphine signals (P^+/P) of the linker-modified silica 13i-15i and 18i with maximal surface coverages (values for 25% coverage see Table 2.1).	42
3.1 Surface coverages of the modified silica 33i to 35i with the corresponding molecular species X (33 to 35 , and 33b to 35b).	98
3.2 ^{31}P MAS and HRMAS NMR chemical shifts δ and signal halfwidths $\Delta\nu_{1/2}$ for the phosphine signals of the ligand-modified silica 33i to 35i .	102
3.3 Signal halfwidths $\Delta\nu_{1/2}$ in the HRMAS spectra of 35i and 15i as slurries in the respective solvents.	103
3.4 Selected bond lengths and angles of RhClpyCOD 39 .	105
4.1 CSA parameters of 44 and 45 .	141
4.2 Calculated and experimental chemical shifts for 48 , 49 , 50 , 52 , and Ph_2PMe .	175
4.3 Calculated and experimental chemical shifts for 52 using different functionals.	176
5.1 ^{13}C T_1 relaxation times of the mobile domain A and the rigid domain B of the indicated samples.	206

5.2	^{13}C T_1 relaxation times of the mobile domain A and the rigid domain B of the indicated samples.	211
5.3	^1H chemical shifts δ , signal halfwidths $\Delta\nu_{1/2}$, and integrals of the two signals after deconvolution of the wideline NMR spectra of the respective materials.	235
5.4	DSC data of the indicated original and steam-treated samples.	245
5.5	^{13}C T_1 relaxation times of the mobile domain A and the rigid domain B of the indicated water-containing and dry samples.	250

NOMENCLATURE

δ	chemical shift in ppm
λ	wavelength
$\{^1\text{H}\}$	proton decoupled
$\{^{31}\text{P}\}$	phosphorus decoupled
Å	Ångstrom
AIBN	azabisisobutyronitrile
B3LYP	Becke, three parameter, Lee-Yang-Parr
BET	Brunauer Emmett Teller
br	broad
COD	cyclooctadiene
CP	cross-polarization
CSA	chemical shift anisotropy
d	doublet (NMR), days
DABCO	1,4-diazabicyclo[2.2.2]octane
DBCOT	dibenzo[<i>a,e</i>]octatetraene
DBU	1,8-diazabicyclo[5.4.0]undec-7-ene
DD	dipolar dephasing
DFT	density functional theory
DMSO	dimethylsulfoxide
DSC	dynamic scanning calorimetry
ESI	electrospray ionization
FID	free induction decay (NMR), flame ionization detector
FRPSG	fluorous reversed phase silica gel

GC	gas chromatography
h	hour
HRMAS	high-resolution magic angle spinning
HR-MS	high-resolution mass spectrometry
Hz	Hertz
<i>i</i>	iso
<i>J</i>	scalar coupling constant
IR	infrared
m	multiplet (NMR), medium (IR)
<i>m</i>	meta
MAS	magic angle spinning
Me	methyl
nbd	norbornadiene
NMR	nuclear magnetic resonance
<i>o</i>	ortho
<i>p</i>	para
PAEK	polyaryletherketone
PBI	polybenzimidazole
PEEK	polyetheretherketone
PEKK	polyetherketoneketone
ppm	parts per million
PPS	poly(<i>p</i> -phenylene) sulfide
PS	polystyrene
py	pyridine
R	alkyl group

s	singlet (NMR), strong (IR)
SAPC	supported aqueous phase catalyst
sdd	Stuttgart/Dresden effective core potential
sept	septet (NMR)
SLPC	supported liquid phase catalyst
t	triplet (NMR)
<i>t</i>	tertiary
TEM	transmission electron microscopy
THF	tetrahydrofuran
Tf	triflate
TMEDA	tetramethylethylenediamine
TMS	tetramethylsilane
T _g	glass transition temperature
TPPTS	triphenylphosphine trisulfonate
UV	ultraviolet
$\Delta\nu_{1/2}$	signal width at half height
Vis	visible
vs	very strong (IR)
VT	variable temperature
w	weak (IR)

CHAPTER I

INTRODUCTION

The problems chemists are concerned with at the beginning of the 21st century require, due to their complexity, an increasingly comprehensive approach involving synthesis, spectroscopic methods, as well as theoretical approaches. This is true for many if not all areas of chemistry such as, for example, catalysis, life sciences, or materials sciences. The uniting topic of this thesis is the application of solid-state NMR techniques in different areas of chemical research. NMR provides information of the molecular nature of crystalline or amorphous, insoluble materials that are not easily accessible by other methods. Certain NMR parameters are sensitive to molecular motion over a wide frequency range making solid-state NMR a popular tool in polymer and materials sciences.

The chapters of this dissertation span a wide range from research in catalysis in the chapters II and III, to organometallic chemistry in chapter IV, and to polymer characterization in chapter V.

The chapters II and III focus on the design and the characterization of immobilized catalysts. For this purpose, phosphine ligands were tethered to an inorganic support via electrostatic interactions and covalent bonds. The ligands and their corresponding Rh complexes were studied by ³¹P solid-state NMR. The immobilized Rh complexes were applied to catalytic olefin hydrogenation and their performance was studied with an emphasis on the nature of the active species and catalyst recycling.

Chapter IV addresses the intramolecular Si-C(sp³) bond activation in Rh and Ir complexes. Both spectroscopic and theoretical methods have been used to study the reactivity and selectivity of this reaction.

Chapter V describes the study of several performance polymers that are of interest in the energy sector, especially in high-temperature and high-pressure applications. Solid-state NMR investigations of PAEK polymers have been carried out to gain a better understanding with respect to the decomposition and failure mechanisms. A detailed knowledge of the morphology and structure should pave the way for a more reliable structure-property correlation for this class of materials.

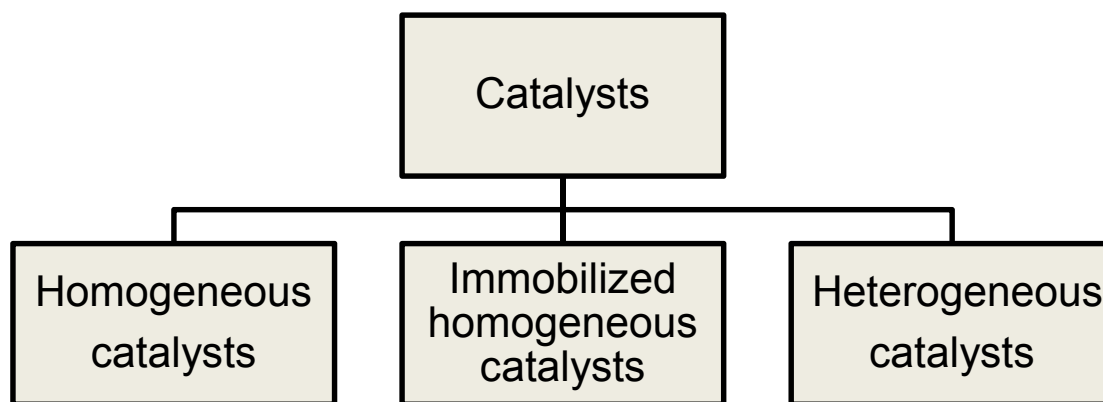
CHAPTER II

TRIDENTATE PHOSPHINE LINKERS FOR IMMOBILIZED CATALYSTS – IMMOBILIZATION OF PHOSPHONIUM SALTS*

INTRODUCTION

Classification of Catalysts

Catalysts have fascinated researchers in academia for more than a century and have contributed immensely to the development of the chemical industry. The numerous catalysts known today can be categorized in various ways. According to the state of aggregation in which they occur during reaction, and disregarding biocatalysts, catalysts can be divided into three main groups: homogeneous catalysts, heterogeneous catalysts, and bridging the two, homogeneous immobilized catalysts (Scheme 2.1).¹



Scheme 2.1. Classification of catalysts.

*Reproduced in part with permission from Guenther, J.; Reibenspies, J.; Blümel, J. "Synthesis, Immobilization, CP- and HR-MAS NMR of a New Chelate Phosphine Linker System, and Catalysis by Rhodium Adducts thereof" *Adv. Synth. Catal.* **2011**, 353, 443-460, DOI: 10.1002/adsc.201000585, <http://onlinelibrary.wiley.com/doi/10.1002/adsc.201000585>. © 2011 Wiley-VCH Verlag GmbH & Co. KGaA, Weinheim.

Homogeneous catalysts are usually small organic molecules or transition metal complexes, which are dissolved in the liquid reaction medium. Generally they exhibit a single, well-defined active species leading to high and reproducible selectivities.

Furthermore, using the spectroscopic toolbox that is available to study species in solution, such as NMR, IR, UV-VIS, and many other methods, great strides have been made regarding the understanding of these systems on a molecular level. One such example is the mechanistic work of Halpern and Brown elucidating the mechanism of the Rh-catalyzed asymmetric hydrogenation of olefins.²

Countless homogeneous catalysts have been designed to facilitate C-C, C-N, C-H and C-O bond formation and functionalization. Selected significant achievements, like the Ziegler-Natta catalysts for polymerization,³ Wilkinson's catalyst for hydrogenation,⁴ and Grubbs'⁵ and Schrock's⁶ catalysts for olefin metathesis were each recognized by the award of the Nobel Prize. Yet some problems remain. It can be very difficult to separate the catalyst from the reaction mixtures and since the process of separating the catalyst almost inevitably leads to its decomposition, they are practically not recoverable or reusable after the reaction.

In contrast to this, heterogeneous catalysts often contain precious metals or oxides thereof, supported on high surface area, porous supports. The reaction takes place at the surface of the material which represents a solid-gas or solid-liquid interface, depending on the reaction. The solid nature of the catalyst makes handling and product separation facile and this explains the tremendous range of applications in industrial settings.⁷ However, again major drawbacks exist. First, not all metal sites are necessarily surface sites and might therefore not be accessible to a substrate. Furthermore, many different sites can coexist, each of which might display its own activity and selectivity. Although great insights were gained in recent years regarding the mechanisms involved,

e.g. by Ertl *et al.*⁸ and Somorjai *et al.*,⁹ the study of heterogeneous systems is hampered by the amorphous nature of the support and the difficulty to discriminate the effect of the interfacial surface area from the participation of interior support domains.

As a consequence the immobilization of homogeneous catalysts on a solid support has become an attractive method to overcome the problems inherent with heterogeneous catalysts. In principle, immobilized homogeneous catalysts combine the advantages of homogeneous catalysts (e.g. high activity and selectivity, good reproducibility) with those of heterogeneous catalysts (e.g. long lifetime, ease of separation and recyclability).

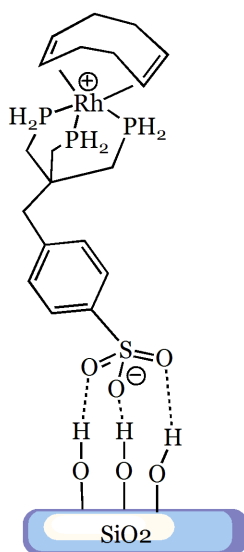
Immobilization Strategies

Supported catalysts proved to be valuable tools in regard to simplified separation and recovery of catalysts from reaction mixtures. Since the late 1960s, many approaches to 'heterogenize', 'immobilize', or 'anchor' a homogeneous catalyst on a solid support have been published by researchers both in academia and industry. Three main categories can be applied to the various methodologies: a) adsorption, b) encapsulation, and c) covalent tethering.¹⁰ The concepts will be briefly introduced with recent examples.

Adsorption via Van der Waals Interactions and Hydrogen Bonding

Catalysts immobilized by adsorption rely on van der Waals interactions or hydrogen bonding between the catalyst and the support. Since the former are comparatively weak interactions, the catalyst might leach into solution either due to interactions with the solvent and the substrates, or with the products formed during the reaction. The resilience of adsorbed catalysts can be improved by modifying the catalyst

and support to allow hydrogen bonding to occur. For example, Bianchini and coworkers have immobilized Rh and Ru complexes on silica via hydrogen bonding (Scheme 2.2).¹¹ The supported metal complexes have been employed in the hydrogenation of olefins, nitriles, and α,β -unsaturated ketones. In the reduction of benzylideneacetone, the catalyst showed higher selectivity as compared to a homogeneous analog. While the olefin moiety was reduced successfully, the carbonyl group remained intact. On the other hand the conversion of 61% was significantly lower as compared to 100% with the homogeneous catalyst.

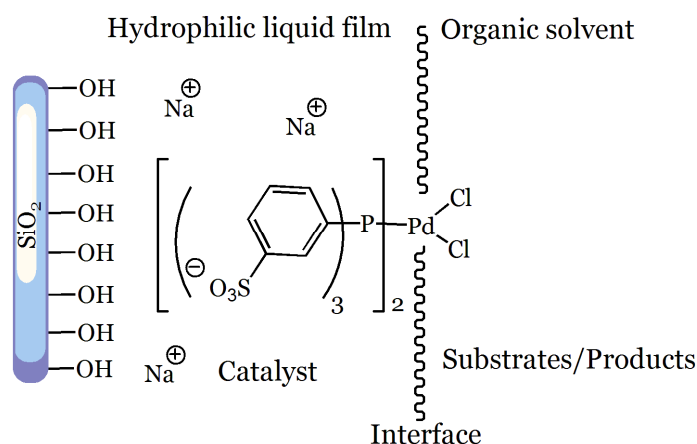


Scheme 2.2. Rh complex immobilized via hydrogen bonding.^{10c}

Supported Aqueous Phase Catalysts

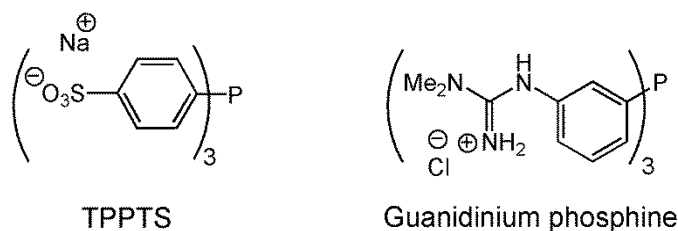
Supported aqueous phase catalysts (SAPC) were introduced by Davis and coworkers in 1989 as a new type of heterogeneous catalyst.¹² The key feature of this concept is to immobilize a water-soluble catalyst in a thin layer of hydrophilic liquid that

is supported on a solid hydrophilic material (Scheme 2.3). The reaction is carried out at the interface of the aqueous layer containing the catalyst and an organic solvent that is immiscible with water containing the substrates and products. Silica and glasses with controlled pore sizes are typically chosen as supports. Water and ethylene glycol are used as hydrophilic liquid phase. Na and Li salts of triphenylphosphine trisulfonate (TPPTS), or guanidinium phosphine (Scheme 2.4) are commonly used as water-soluble ligands for coordinating to suitable metal precursors.



Scheme 2.3. Model of a supported aqueous phase catalyst (SAPC).^{10c}

The SAPC system has been successfully applied to the Heck¹³ and Sonogashira reactions,¹⁴ hydrogenation,¹⁵ and hydroformylation.¹⁶ The initial activities of the immobilized catalysts were comparable to those of their homogeneous counterparts. But recycling experiments showed that the activity decreased significantly after the first run. TPPTS was oxidized during the reaction and this ultimately rendered the catalyst inactive.¹⁷



Scheme 2.4. Phosphine ligands commonly used for SAPC.

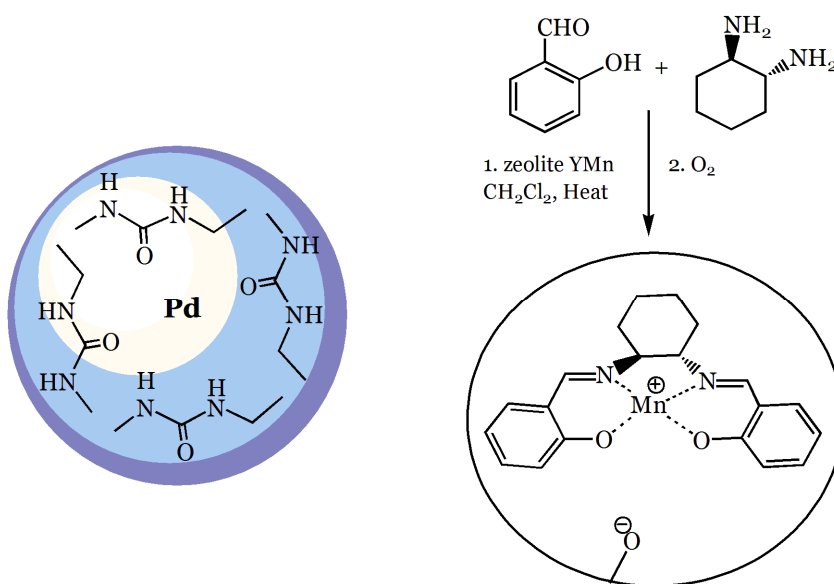
In the case of supported liquid phase catalysts (SLPC), the water film on the inner surface is replaced by a solvent of low vapor pressure (e.g. phthalic esters or ionic liquids).¹⁸ The use of SLPC is generally restricted to the synthesis of low-boiling compounds. This area has recently flourished with the advent of ionic liquids as the supported phase.

Biphasic Fluorous Catalysis

Fluorous reversed-phase silica gel (FRPSG) has been used as the support for perfluoro-tagged catalysts.¹⁹ The perfluoroalkyl tags are practically insoluble in organic or aqueous solvents at room temperature. This results in a selective strong adsorption on the fluorous support, while untagged components possess no affinity to the fluorous phase. As a consequence, polar as well as non-polar reaction media can be used, which makes this strategy applicable to a broader range of reactions and work-up conditions. It is possible to further adjust the reactivity by release from the support at elevated temperatures during the reaction and re-adsorption after full conversion. Tzschucke *et al.* utilized FRPSG as a solid support and immobilized a perfluoro-tagged Pd complex.²⁰ This catalyst has been applied to C-C coupling reactions and high reactivity was observed.

Encapsulation

Ley *et al.* developed a method to encapsulate Pd(0) in a polyurea framework (Scheme 2.5) and generate an immobilized catalyst, which has been successfully applied to hydrogenation²¹ and cross-coupling reactions.²² With this encapsulation strategy the need for stabilizing ligands becomes obsolete. Leaching of the metal was extremely low and the catalyst could easily be removed by filtration. Jamis and coworkers studied the immobilization of a Rh-BPPM (BPPM = (2S,4S)-*N*-(*tert*-butoxycarbonyl)-4-(diphenylphosphino)-2-[(diphenylphosphino)methyl] pyrrolidine) complex by entrapment within a silica matrix using a sol-gel process.²³ The resulting catalyst has been applied to the hydrogenation of sodium α -acetamidocinnamate, but the activity decreased significantly when the catalyst was re-used for several runs.



Scheme 2.5. Immobilization of a Pd(0) catalyst (*left*) and a Mn(III) salen complex (*right*) via encapsulation.

Another method to encapsulate a catalyst is to synthesize the catalyst within well-defined cages of a porous support, most often zeolites (Scheme 2.5, *right*). This approach is referred to in the literature as ‘ship in a bottle’.²⁴

Encapsulation is the only catalyst immobilization strategy that does not require any interaction between catalyst and support. Therefore, altering the ligands to attach tethers or polar groups is not needed. This avoids lengthy syntheses and possible changes to the electronic and steric nature of the ligands.

Covalent Tethering

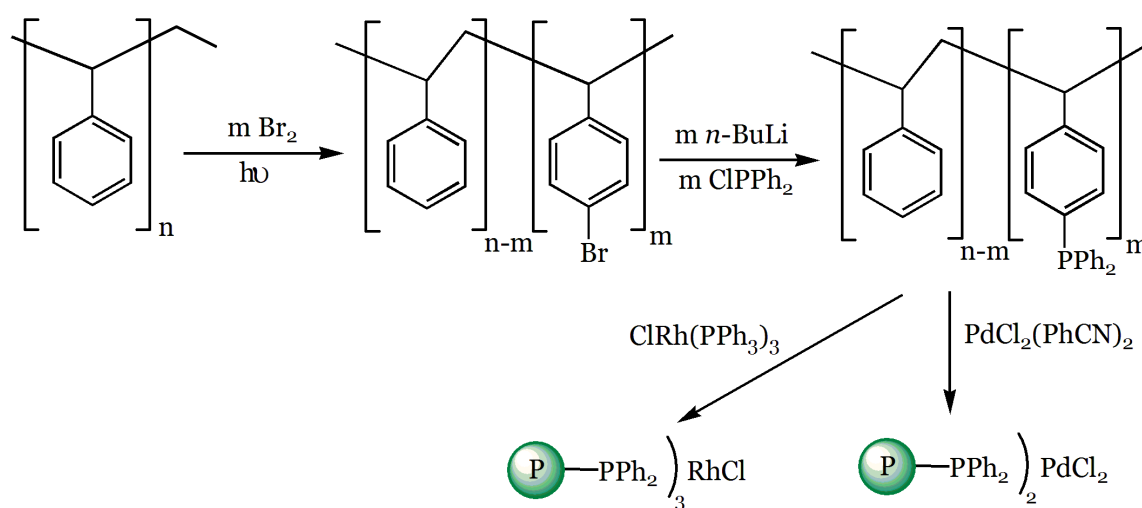
Binding of a ligand to a solid support via covalent bonds has become the most frequently employed strategy to immobilize a homogeneous catalyst. Depending on the nature of the support different strategies are utilized. Copolymerization of a functionalized ligand with a suitable monomer allows the immobilization in a wide range of polymers or organic/inorganic hybrid materials, whereas grafting a functionalized ligand or metal complex on a reactive surface is often preferred when using inorganic supports.²⁵

In general, the support material should be thermally, chemically, and mechanically stable under the reaction conditions. The active sites should be highly dispersed on the surface and easily accessible. Organic polymers and porous inorganic oxides have been used most extensively in this context.

Polymer Supports

Since the development of Merrifield resins²⁶ polymer supports tremendously impacted organic synthesis and catalysis, especially in the second half of the twentieth century. Numerous polymer supports, cross-linked (insoluble) and not cross-linked

(soluble) polymers have been synthesized and applied to solid-phase synthesis in areas spanning from biochemistry to materials science. Functionalized polystyrenes are available as linear, soluble, and as cross-linked polymers. The latter, generally referred to as PS resins, are among the most commonly used solid supports, partially owing to their commercial availability (Scheme 2.6).²⁷



Scheme 2.6. Immobilization of Rh and Pd complexes on a polystyrene support.

The use of soluble polymers²⁸ as supports has the advantage that during the reaction the metal complexes behave like homogeneous catalysts, ideally with only minimal interference from the polymer backbone. After the reaction the catalyst can be separated easily by precipitation. The first example was reported in the 1970s when Rh-containing soluble polymers were successfully applied as hydrogenation catalysts.²⁹ Since then, functionalized soluble polystyrenes,²⁷ polyethylene glycol,³⁰ polymethyl methacrylates,³¹ hyperbranched polymers,³² and polyelectrolytes³³ have been applied as soluble polymer supports for transition metal complexes.

Voegtler *et al.* were the first who introduced dendrimers as soluble supports.³⁴ As compared to soluble polymers, dendrimers are more uniform regarding their structure and molecular weight. Catalysts tethered to dendrimers have been applied to Ru-catalyzed olefin metathesis,³⁵ Pd-catalyzed cross-coupling reactions,³⁶ and many others. One drawback is the often lengthy and tedious synthesis of the dendrimers and therefore commercial applications of dendrimers are scarce. Furthermore, their separation from the reaction mixture typically requires membrane filtration.

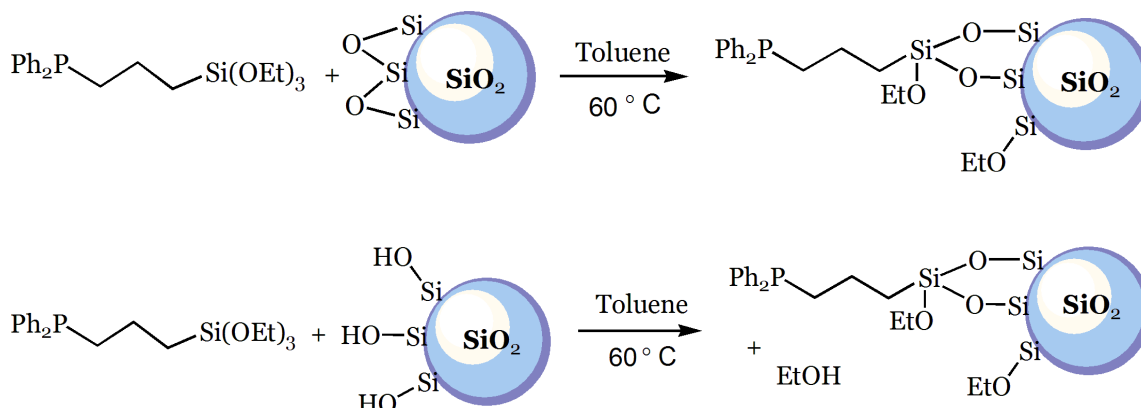
Inorganic Supports

The most commonly used inorganic supports are SiO₂, Al₂O₃, ZrO₂, ZnO, TiO₂, zeolites, and various clays. For each support there is a tremendous variety in their properties, for example, regarding their structural order, porosity, surface acidity and basicity, that influence the chemistry of these materials.³⁷ Not all materials are benign to the catalyst or linker to be immobilized or even inert to the substrates used in catalysis. Furthermore, the functional groups on the surface determine which method can be used to attach a tether to the surface.

Binding an organic functional group to the surface silanol groups of silica via a covalent bond is one of the most reliable methods for modifying silica surfaces. An early example of a Rh complex immobilized on silica having different tether lengths was reported by Čapka *et al.* in 1985.³⁸ The immobilized catalyst showed greater stability and selectivity than their homogeneous counterparts, presumably due to site isolation.³⁹

In our group extensive research has been conducted over the years to elucidate the surface chemistry of silica and alumina with bifunctional phosphine ligands incorporating ethoxysilanes.⁴⁰ These ligands bind to an oxide surface in a covalent manner via Si-O-Si bonds. The siloxane bond can form either via a condensation

reaction with a surface silanol group or by nucleophilic addition to a surface siloxane group (Scheme 2.7).



Scheme 2.7. Nucleophilic addition of ethoxysilanes to surface siloxane groups (*top*) and condensation with surface silanol groups (*bottom*).

An intimate knowledge of the nature of the immobilized ligand and its binding to the surface is paramount to interpret the performance of the immobilized metal catalysts and pursue rational improvements of the ligand design. ^{31}P and ^{29}Si solid-state NMR are excellent tools in this regard.⁴¹ The integrity of the phosphine ligand can conveniently and efficiently be probed by ^{31}P solid-state NMR. This is crucial to rule out possible side reactions such as oxidation or quaternization of the phosphine. ^{29}Si solid-state NMR yields valuable insight into the number of bonds the ethoxysilanes form with the support. Figure 2.1 shows the ^{29}Si CP/MAS spectrum of the bifunctional phosphine $\text{Ph}_2\text{P}(\text{CH}_2)_3\text{Si}(\text{OEt})_3$ immobilized on silica via covalent bonds. A distribution of species bound via one, two, or three siloxane bridges to the silica surface is usually obtained (Figure 2.1).^{37,40}

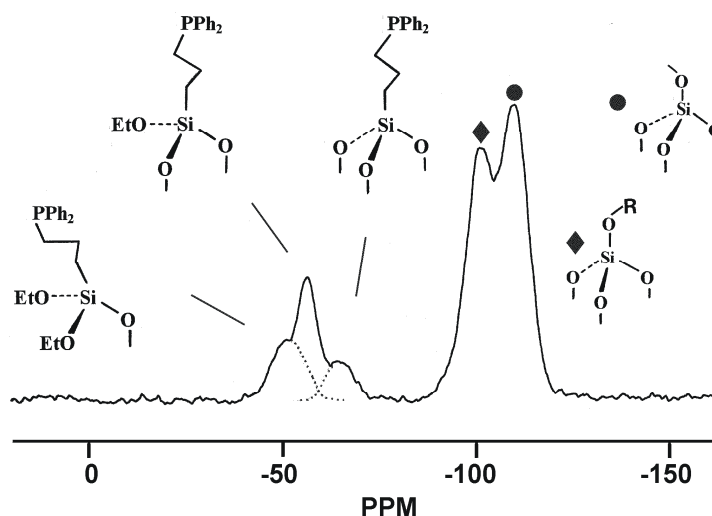


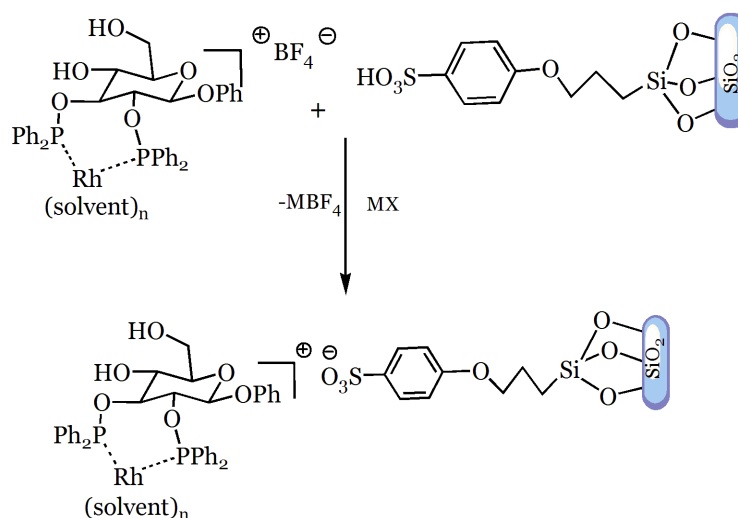
Figure 2.1. ^{29}Si CP/MAS spectrum of ethoxysilanes immobilized on silica.⁴⁰

Starting from this rather simple monophosphine incorporating a propyl tether a library of phosphine ligands varying in basicity, steric demand, conformational flexibility, and denticity has been developed in the Blümel group.⁴⁰

Immobilization via Ionic Tethers

More recently we and others have immobilized phosphine ligands via ionic moieties on oxide surfaces.^{42,43} This is achieved by ion-pairing with a charged support. The charge can either be part of the support as in zeolites and other inorganic ion exchange materials, or it can be introduced by surface grafting methods. Mazzei *et al.* were the first to use electrostatic interactions to immobilize a Rh complex with a PNNP ligand into the interlayers of clays.⁴³ Mineral clays have a layer structure composed of alternate layers of cations and anionic silicate sheets. The bulky cationic Rh complex can be exchanged into the intercrystal space of clays by increasing the clays' interlayer distances. Subsequently, Čapka *et al.* immobilized a carbohydrate-based catalyst by ion

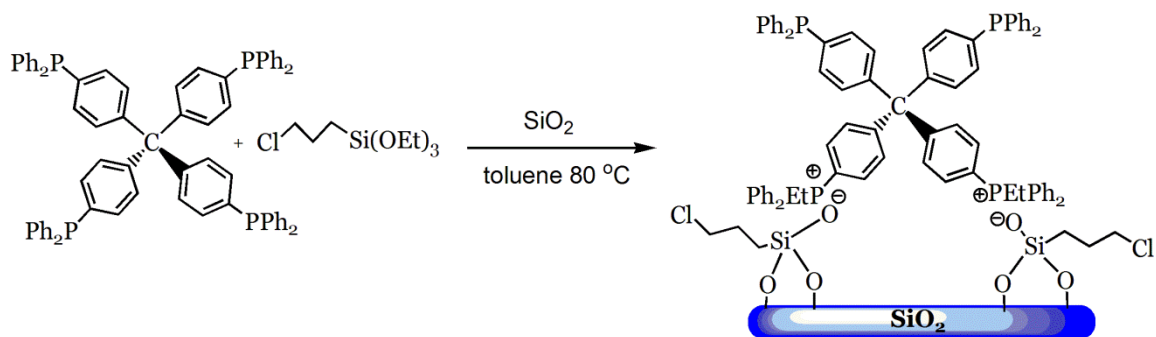
exchange.⁴⁴ The cationic Rh complex of 2,3-bis(*O*-diphenylphosphino)- β -D-glucopyranoside was immobilized on silica via ionic interactions (Scheme 2.8). The immobilized catalyst was applied to the hydrogenation of α -acetamidoacrylic acid ester. The enantioselectivity of the immobilized catalyst was even higher than the one of the homogeneous catalyst. The catalyst could be recycled up to 20 times, although appreciable amounts of the Rh complex leached.



Scheme 2.8. Rh complex immobilized on silica via an ionic tether.

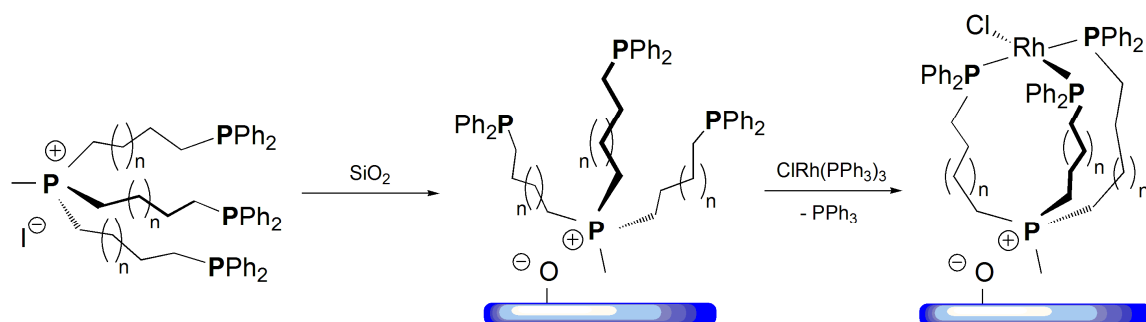
Recently, the Blümel group developed another technique to immobilize phosphine ligands with a rigid backbone via electrostatic interactions (Scheme 2.9).⁴² This technique is rather easy and controllable. A tetraphosphine ligand is reacted with silica in the presence of an alkoxy silane reagent. Depending on the reaction conditions, one, two, or three phosphines of one molecule form phosphonium salts on the silica surface, while the anions are immobilized in a covalent manner on the surface. The

remaining phosphines remain available for metal coordination. The ionic bonding has been proven to be very strong, as no leaching has been detected in any organic solvent.



Scheme 2.9. Immobilization via electrostatic interactions.⁴²

The goal of this study was to extend this methodology and bind tridentate phosphine ligands with flexible alkyl chain linkers to silica via a phosphonium ion. After coordination to Rh this ligand class should yield immobilized metal complexes that are conformationally highly flexible and should thus mimic ideally homogeneous catalysts (Scheme 2.10).



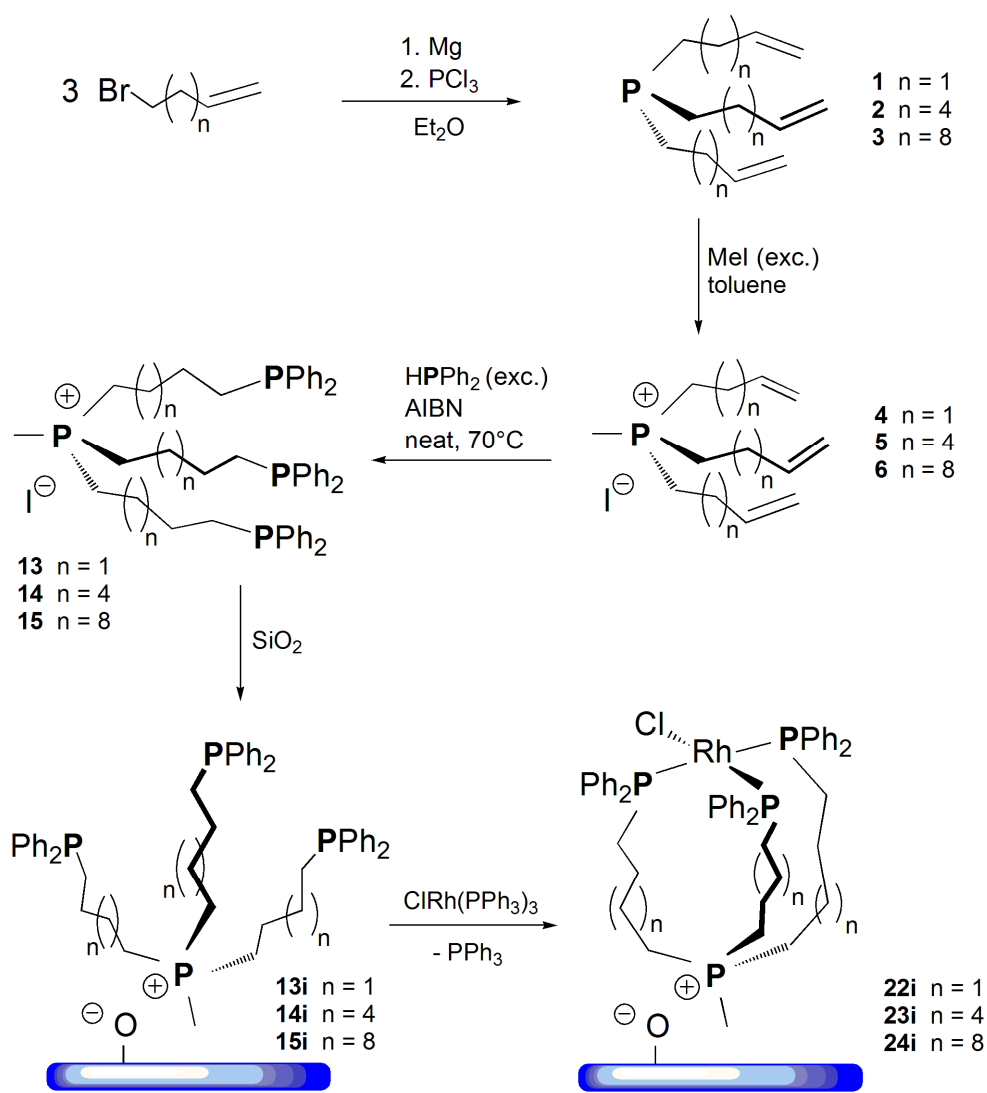
Scheme 2.10. Immobilization of tridentate phosphine ligands via electrostatic interactions ($n = 1, 4, 9$).

RESULTS AND DISCUSSION⁴⁵

Ligand Synthesis

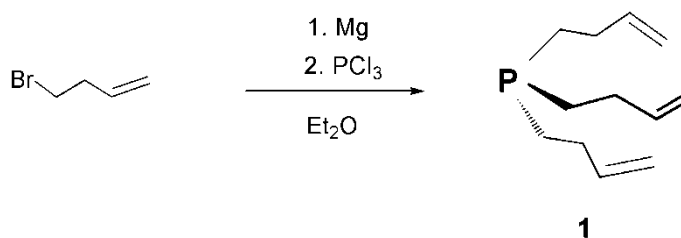
The desired tridentate phosphine ligands were synthesized according to Scheme 2.11. The coupling of commercially available bromoalkenes with PCl_3 via a Grignard reaction yields phosphines that incorporate terminal olefins in their substituents which are amenable to further functionalization.⁴⁶ It is easiest to introduce the desired phosphonium moiety at this stage since no discrimination between different phosphines is necessary. The phosphonium salts are robust and easy to handle and can be hydrophosphinated to yield the desired tridentate phosphine ligands incorporating a phosphonium group that serves as an ionic tether.

Immobilization and subsequent coordination of Rh allows the preparation of immobilized metal complexes that can serve as hydrogenation catalysts.



Scheme 2.11. Outline of the general ligand synthesis and immobilization.

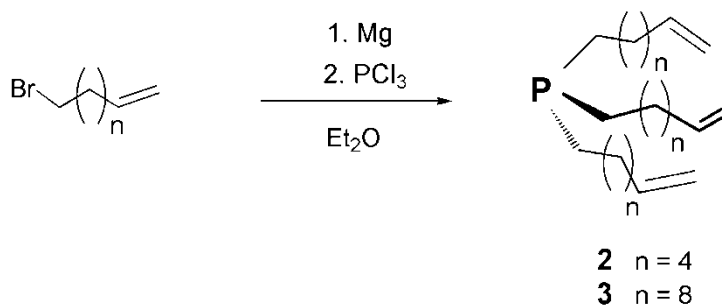
The phosphine ligand **1** has been synthesized starting from the corresponding commercially available bromo compound $\text{Br}(\text{CH}_2)_2\text{CH}=\text{CH}_2$ according to the procedure by Clark and Hartwell^{47a} (Scheme 2.12). The ^1H ,^{47a,b} ^{31}P ,^{47a} and ^{13}C ^{47c} NMR data are in accordance with the literature values.



Scheme 2.12. Synthesis of phosphine **1**.

It should be noted that it was not possible to isolate triallylphosphine $\text{P}(\text{CH}_2\text{CH}=\text{CH}_2)_3$ in high yields in an analogous manner, most probably because the allyl substituents are vulnerable to polymerization or formation of five-membered rings via radicals.⁴⁸

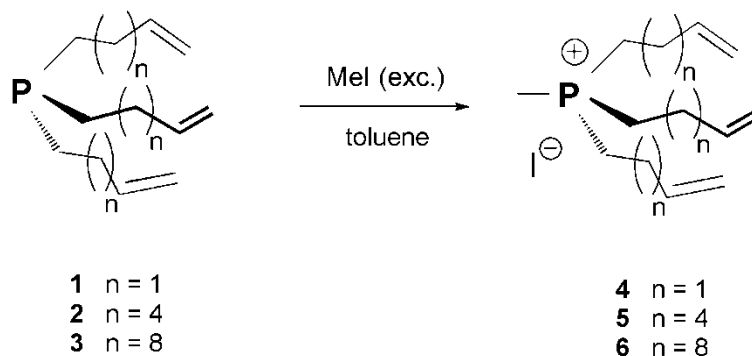
The phosphines **2** and **3** have been synthesized from the corresponding bromoalkenes as described by the Gladysz group (Scheme 2.13).⁴⁶



Scheme 2.13. Synthesis of phosphines **2** and **3**.

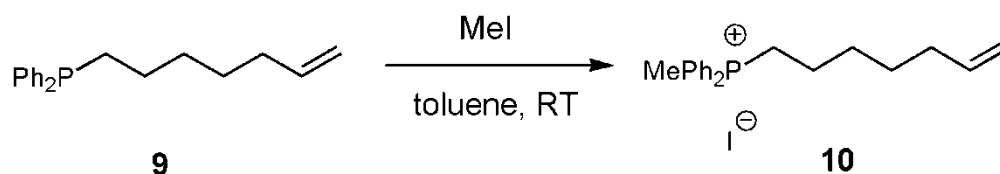
The phosphonium salts **4-6** (Scheme 2.14) have been synthesized in quantitative yields by stirring the corresponding phosphines **1-3** with an excess of CH_3I in toluene overnight. In principle, it is possible to introduce different anions either by anion

exchange or by using a different alkylating agent such as Meerwein's salt. However, this could not be pursued in a systematic manner within the given time frame of this work.



Scheme 2.14. Synthesis of phosphonium salts **4-6**.

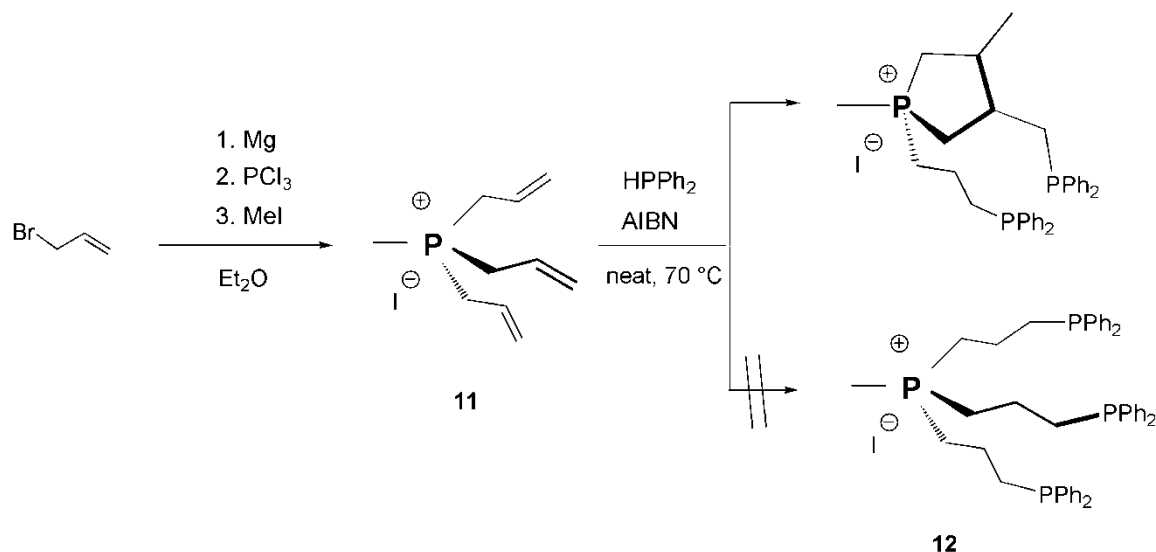
In analogy, phosphonium salt **10** (Scheme 2.15), incorporating only one unsaturated alkyl substituent, has been prepared by coupling bromohept-6-ene and Ph_2PCl , followed by alkylation with CH_3I .



Scheme 2.15. Synthesis of phosphonium salt **10**.

The methyl phosphonium salt $[\text{CH}_3\text{P}(\text{CH}_2\text{CH}=\text{CH}_2)_3]^+\text{I}^-$ (**11**) has been obtained by a one-pot reaction, alkylating triallylphosphine *in situ* without prior isolation. However, during the subsequent hydrophosphination with AIBN, polymerization or a

ring formation via radicals⁴⁸ takes place again, and therefore the linker $[\text{CH}_3\text{P}((\text{CH}_2)_3\text{PPh}_2)_3]^+\text{I}^-$ with C_3 chains (**12**) has no longer been pursued (Scheme 2.16).

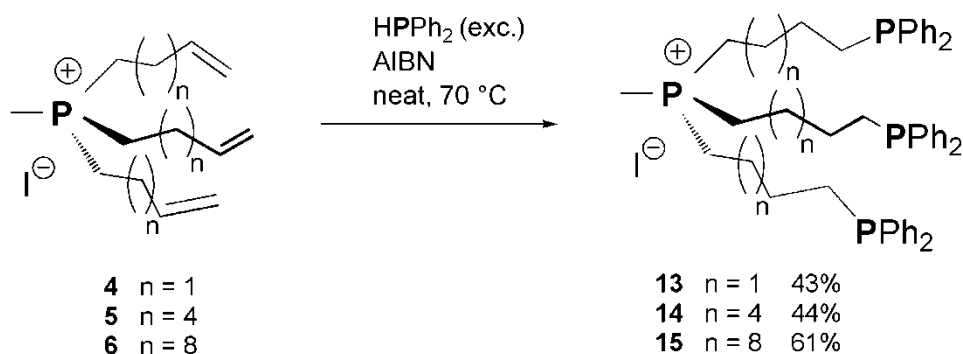


Scheme 2.16. Attempted synthesis of **12**.

There are several hydrophosphination methodologies reported in the literature. Knochel *et al.* used KO^tBu as a very basic catalyst to add HPPH_2 across activated olefins.⁴⁹ The catalytic hydrophosphination of styrene using Ni or Pd catalysts has been described by Beletskaya *et al.*⁵⁰ Examples for hydrophosphination of non-activated double bonds are much more scarce. Gaumont *et al.* performed the hydrophosphination of 1-octene with $\text{Ph}_2\text{HP}\cdot\text{BH}_3$ at $50\text{ }^\circ\text{C}$ under microwave irradiation, obtaining 58% of the desired product.⁵¹ In my hands hydrophosphination with $\text{Ph}_2\text{HP}\cdot\text{BH}_3$ at elevated temperatures was very sluggish and gave low or no yields. Also, photochemical hydrophosphination, as successfully applied previously,⁵² is possible, but the reaction is

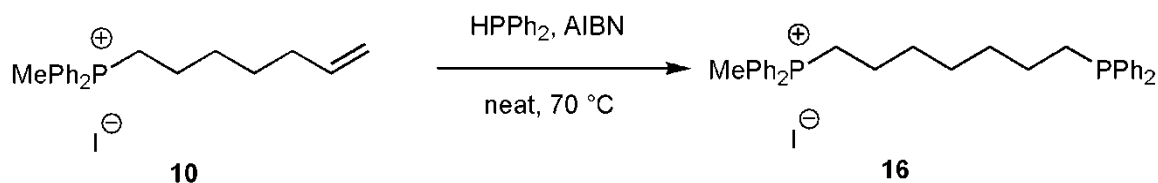
slow. Therefore, the hydrophosphination was performed under radical conditions using AIBN as initiator, as reported by Stelzer *et al.*⁵³

The triphosphines **13-15** (Scheme 2.17) have been obtained from **4-6** by applying an excess of HPh₂ and AIBN as the radical source, under solvent-free conditions at 70 °C.⁵² Overall, the general synthesis route for this ligand class, as outlined in Scheme 2.11, is very versatile, as the chain lengths, the substituents at phosphorus, and the counteranions can be varied easily. For example, a variety of secondary phosphines (R₂PH with R = Me, Et, ⁱPr, ^tBu, Cy, Ph) is commercially available, which in principle allows facile introduction of different substituents at the phosphorus atom and therewith finetuning of the steric and electronic properties.



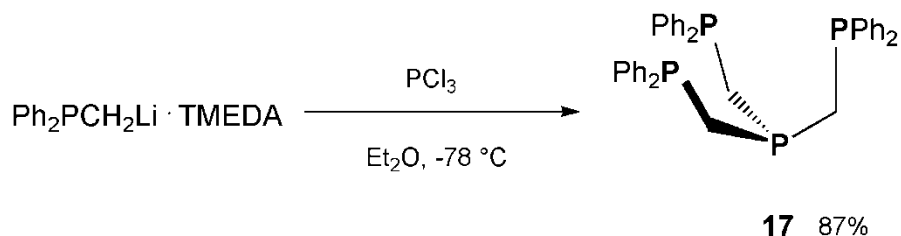
Scheme 2.17. Synthesis of compounds **13-15**.

The same hydrophosphination methodology could be applied to synthesize the monodentate analog **16** (Scheme 2.18).



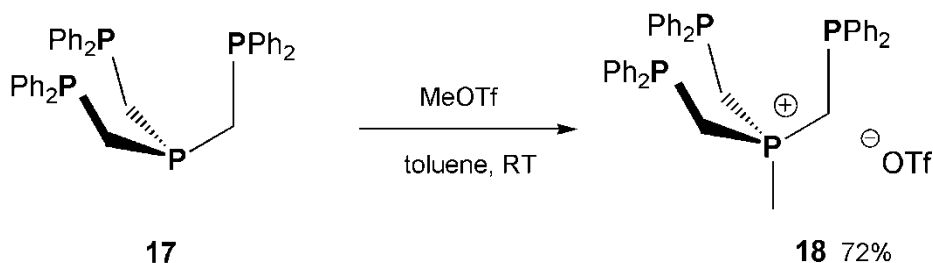
Scheme 2.18. Synthesis of compound **16**.

The tetraphosphine **17** with the shortest possible alkyl chain (Scheme 2.19) could be obtained in a very good yield of 87% by reacting $\text{Ph}_2\text{PCH}_2\text{Li} \cdot \text{TMEDA}$ ⁵⁴ with PCl_3 .



Scheme 2.19. Synthesis of tetraphosphine **17**.

The data of **17** are in accordance with the data obtained for **17**, synthesized from $\text{P}(\text{CH}_2\text{SiMe}_3)_3$ and ClPPh_2 .⁵⁵ CH_3I as the quaternizing reagent for **17** led to a mixture of different phosphonium salts. Therefore, MeOTf has been applied as quaternizing agent. Under very well controlled alkylating conditions only the most basic, the trialkyl phosphine moiety of **17**, is alkylated (Scheme 2.20). The resulting triflate salt **18** is also more crystalline than the iodide, facilitating the purification, and therefore clean **18** has been obtained in a good overall yield of 72%.



Scheme 2.20. Synthesis of compound **18**.

Crystals suitable for X-ray structure determination (Figure 2.2, Appendix A) could be grown from an acetonitrile solution. All bond lengths and angles are in the expected range. As with the X-ray structure of the analogous compound $\text{EtOSi}(\text{CH}_2\text{PPh}_2)_3$ ⁵⁶ the orientation of the phosphine groups is not preorganized for coordination, but dominated by the crystal packing. As expected, the triflate counteranion occupies the sterically least crowded space within the lattice close to the methyl group of the phosphonium moiety. This constellation indicates that the linker **18** might indeed "stand upright" on the surface, when the phosphonium group is bound to the silica via electrostatic interactions (see below).

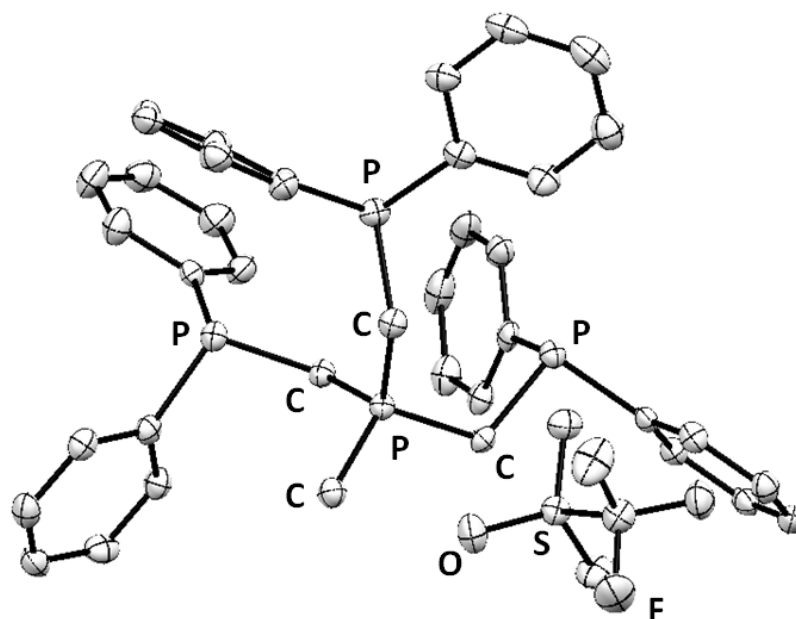
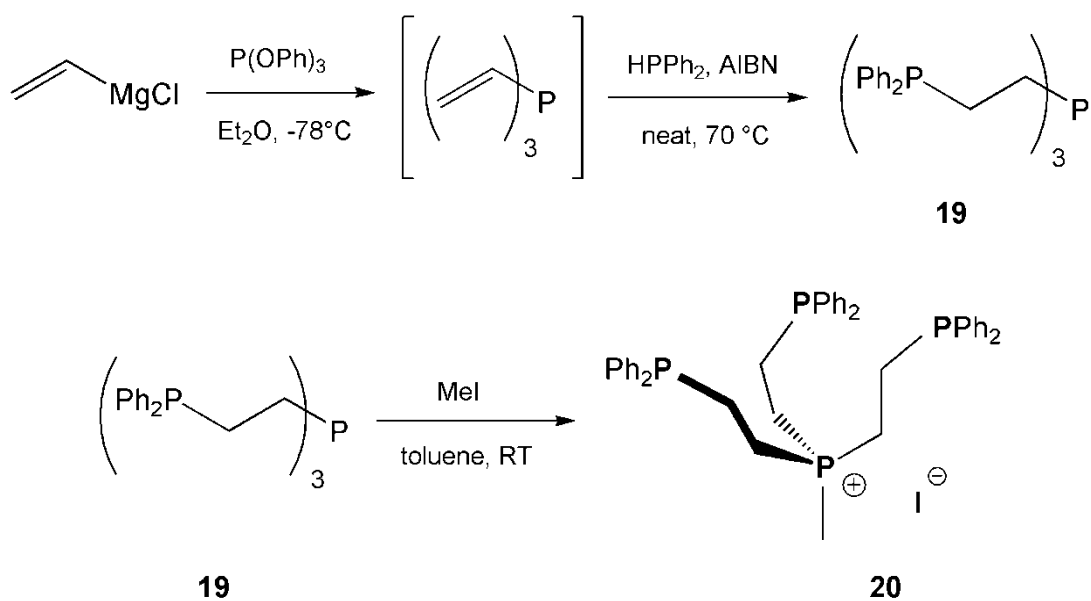


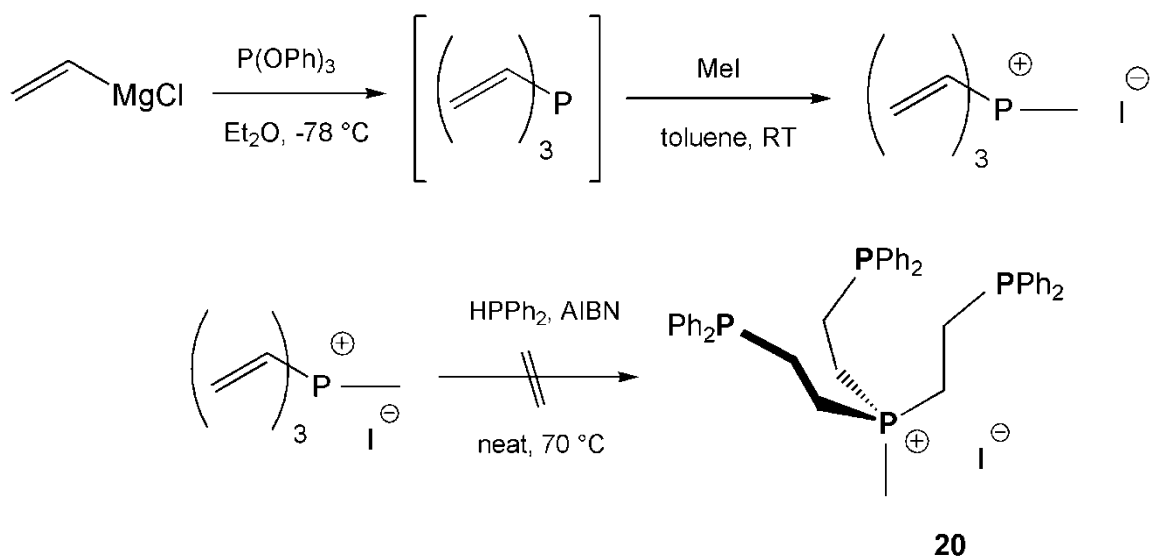
Figure 2.2. Single crystal X-ray structure of chelate ligand **18**.

The triphosphine **20**⁵⁷ with a C2 spacer between phosphonium salt and donor phosphine has been obtained analogously to **18** by alkylation of the corresponding tetraphosphine **19** with MeOTf. First $\text{P}(\text{OPh})_3$ was reacted with vinylmagnesiumchloride to yield trivinylphosphine,⁵⁸ which was not isolated but hydrophosphinated *in situ* to yield the tetraphosphine **19**. Careful alkylation with a slightly substoichiometric amount of MeI gave **20** in 44% yield (Scheme 2.21).



Scheme 2.21. Synthesis of ligand **20**.

An alternative route forming methyltrivinylphosphonium iodide⁵⁸ first and then carrying out the hydrophosphination was also evaluated. The solubility of methyl trivinylphosphonium iodide in HPPH₂ is very low and no conversion was observed after two days. Therefore this route was not explored further (Scheme 2.22).

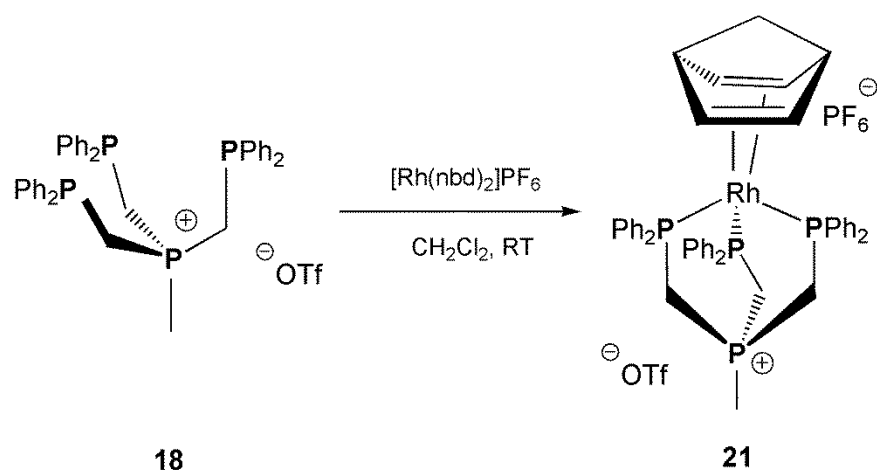


Scheme 2.22. Attempted alternative synthesis of **20**.

Rhodium Complexes

Rh complexes of the ligands **13-15**, **18**, and **20** have been synthesized to serve as reference compounds for the investigation of the spectroscopic and catalytic characteristics of the immobilized catalysts **22i-24i**, and **21i** (see below).

The ligand **18** which is related to the literature-known triphos ligand reacts cleanly with $[\text{Rh}(\text{nbd})_2]\text{PF}_6$ to give **21** in quantitative yield as an orange powder (Scheme 2.23).



Scheme 2.23. Synthesis of complex **21**.

The presence of the phosphonium group does not disturb the coordination of the phosphines to metal centers. The Rh complex has been fully characterized in solution by multinuclear NMR, and a single crystal X-ray structure has been obtained (Figure 2.3). The cation incorporating the Rh center is well defined, and overall the structure of **21** resembles the analogous Si-triphos^{59a} and triphos^{59b} Rh structures. The coordination of all three phosphine groups of **18** is obvious, as it is the case in an analogous methoxy-norbornadienyl Rh complex,⁶⁰ as well as for example in various other tripod Rh^{61a} and Cu^{61b} complexes, and Sn,^{61c} Ir,^{61d} and Rh^{61e} complexes with borate tripod ligands. In contrast to these systems, **21** needs two counteranions to satisfy the positive charges of the Rh(I) center and the phosphonium ligand. Although the counteranions are more disordered, it is obvious from the structure that OTf[−] and PF₆[−] each have their specific place in the lattice and are not interchangeable. Interestingly, the closest counteranions in the lattice are both located at the same side of the complex, a fact that should facilitate the later well-defined binding of **21** to the silica surface. Furthermore, the phenyl rings

are fanning out of the ligand, and thus might form a protecting "umbrella" that prevents the interaction of the Rh center with the reactive surface.

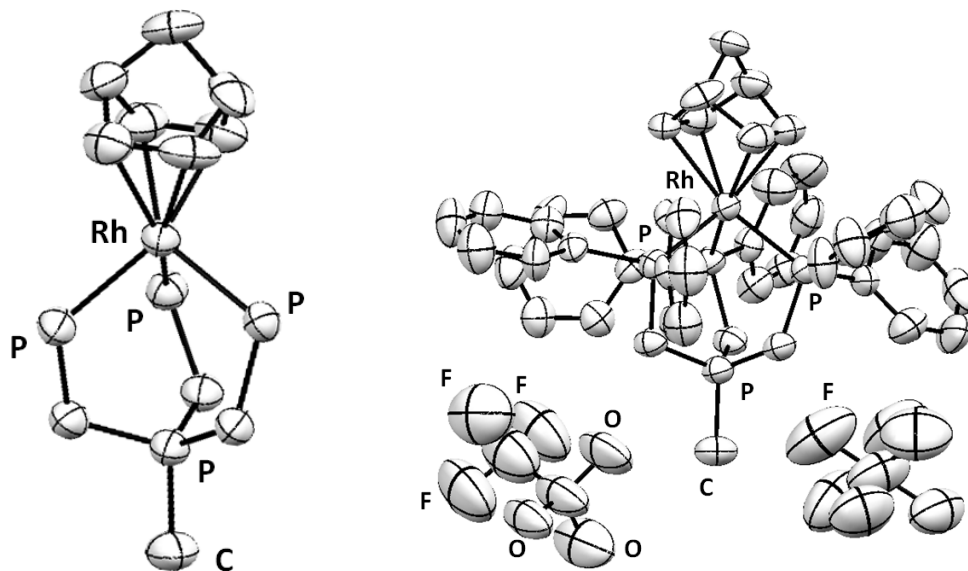
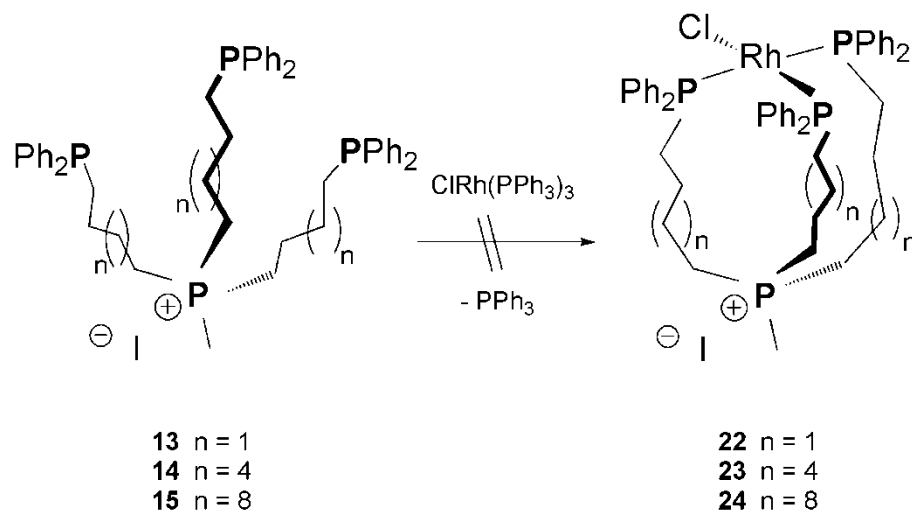


Figure 2.3. Single crystal X-ray structure of the Rh norbornadiene complex **21**. In the left presentation the counteranions TfO^- and $[\text{PF}_6]^-$, and the phenyl rings have been removed for clarity.

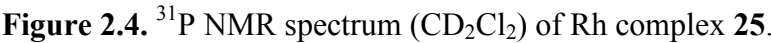
Attempts to isolate and characterize well-defined Rh complexes of the ligands **13-15** have not been successful so far (Scheme 2.24). Using Wilkinson's complex as Rh precursor led to insoluble precipitates that could not be analyzed by NMR irrespective of the phosphine ligand, **13-15**, used. This could be due to the formation of oligomers and polymers with Rh centers serving as nodes and crosslinks between ligand molecules. Broad resonances could be observed when $\text{RhCl}(\text{COD})\text{py}$ was employed in ^{31}P and ^1H

NMR over the temperature range from -80 °C to 90 °C with VT-NMR. This indicates that there might be rapid ligand exchange.



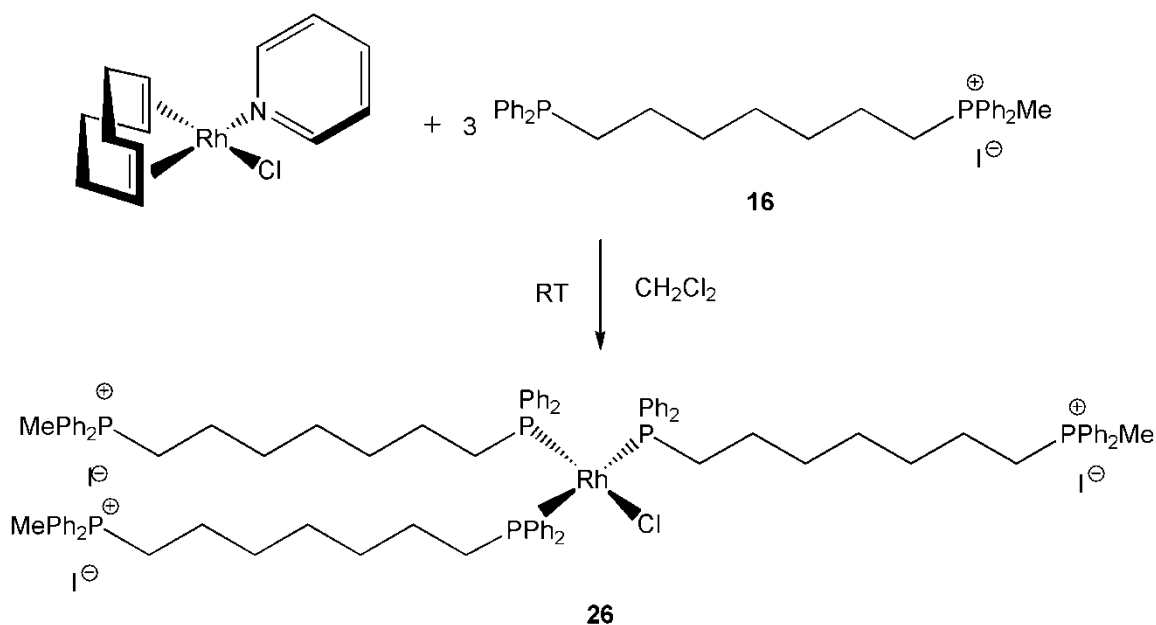
Scheme 2.24. Attempted synthesis of the Rh complexes **22-24**.

A likely scenario includes the formation of oligomers and polymers, probably accompanied by dynamic ligand exchange phenomena. This assumption is corroborated by the formation of well-defined **25** when using **16** (Scheme 2.25) as a monodentate analog for **13-15**. Reaction of RhClpyCOD with one or three equivalents of the monodentate phosphine **16** cleanly affords **25** or **26** (Scheme 2.26), as determined by ^{31}P NMR.



The formation of **25** is evident from ^{31}P NMR by the doublet at 25 ppm with a coupling constant $^1J(^{103}\text{Rh}-^{31}\text{P})$ of 147 Hz and the disappearance of the signal at -16.71 ppm for the free phosphine (Figure 2.4).

The ^{31}P NMR spectrum of **26** displays a doublet of triplets at 38.43 ppm and a doublet of doublets at 23.85 ppm in a 1:2 ratio which is highly suggestive of a square-planar coordination at Rh with one phosphorus donor coordinating *trans* to a chlorine ligand in analogy to Wilkinson's complex (Figure 2.5).



Scheme 2.26. Synthesis of Rh complex **26**.

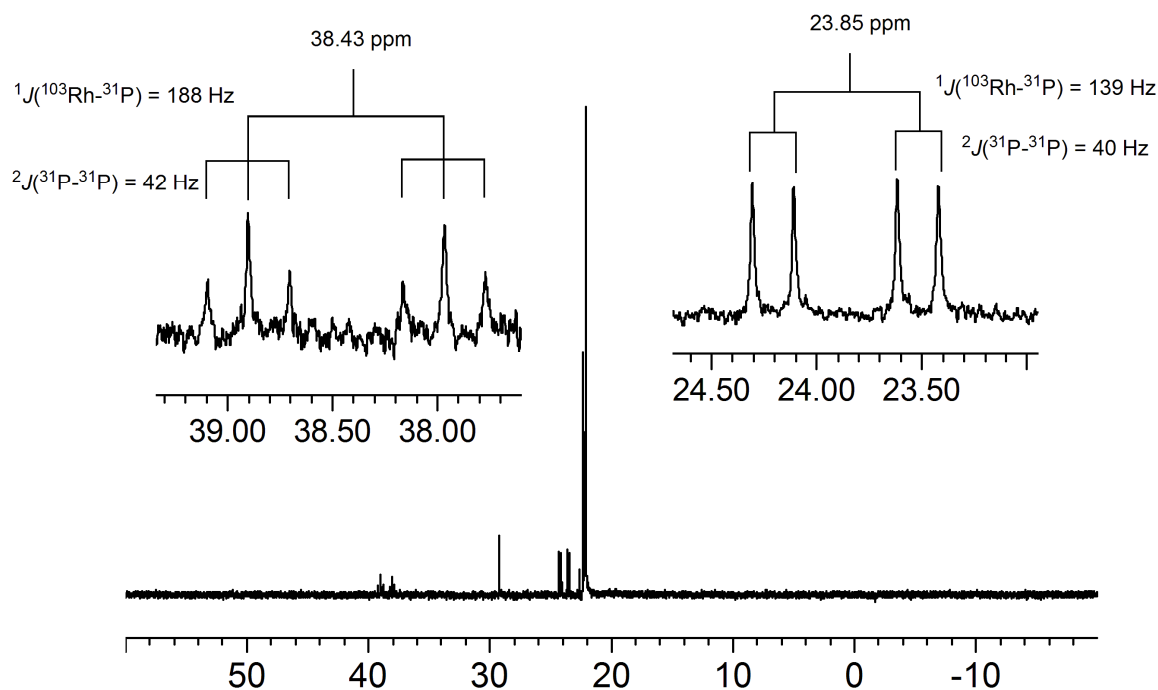
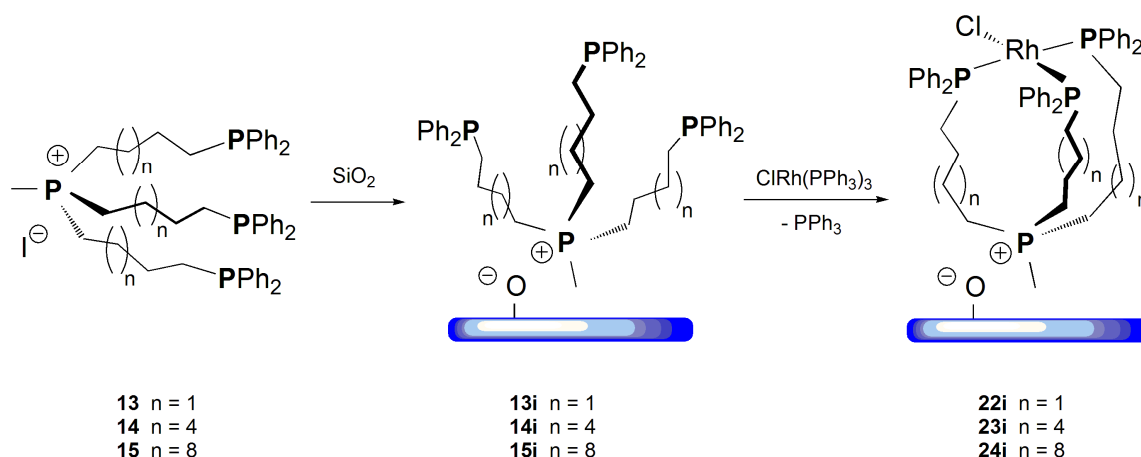


Figure 2.5. ^{31}P NMR spectrum (CDCl_3) of Rh complex **26**.

Immobilization and NMR Spectroscopic Characterization of the Phosphine Linkers and Rh Complexes

The conventional way of binding metal complexes to oxide surfaces uses ethoxysilane-containing linkers,^{37b,c, 52b, 56, 63} such as $(\text{EtO})_3\text{Si}(\text{CH}_2)_3\text{PPh}_2$,^{62a} which form covalent Si-O-Si bonds with silica. On acidic oxides such as alumina, however, the ethoxysilane linkers can leach from the surface,^{62a} and furthermore the ethoxysilanes can lead to the quaternization of the phosphine groups.⁶³ The Blümel group has applied this reaction recently to bind rigid tetraphenylelement phosphine linkers without intramolecular ethoxysilane groups to silica supports.⁴² In the course of these studies it was found that phosphonium salts are also bound strongly via electrostatic interactions to the oxide support,^{42,63} and that preformed phosphonium salts can be strongly adsorbed directly on oxide supports, without addition of alkoxysilanes.⁶³

The linkers **13-15** and **18** have been immobilized on silica to give **13i-15i** and **18i** according to the straightforward standard procedure of stirring the mixture in toluene overnight at 50 °C. The materials are washed with copious amounts of solvents afterwards to ensure that no merely adsorbed species remain. The resulting surface coverages are given in Table 2.1, together with the data for the corresponding immobilized Rh complexes. **22i** to **24i** have been obtained by ligand exchange at RT (Scheme 2.27), and **21i** by reaction of **21** with silica. Although this work focuses on silica as the support, it should be mentioned that other oxide supports like alumina are also amenable to phosphonium immobilization.



Scheme 2.27. Immobilization and synthesis of **22i-24i**.

The experimental maximal surface coverages for a monolayer of linker or Rh complex on the silica surface always remained below the theoretically possible surface coverages. A rough estimate of the calculated maximal surface coverage can be obtained by using the linker chain length, including the phenyl groups, as the radius of a circle

that would describe the footprint of the molecule if it was planar. For example, the chain lengths for **14** and **15** can be estimated to be 11.3 and 14.9 Å, respectively, and their (flat) footprint would be about 401 and 698 Å² (Figure 2.6).

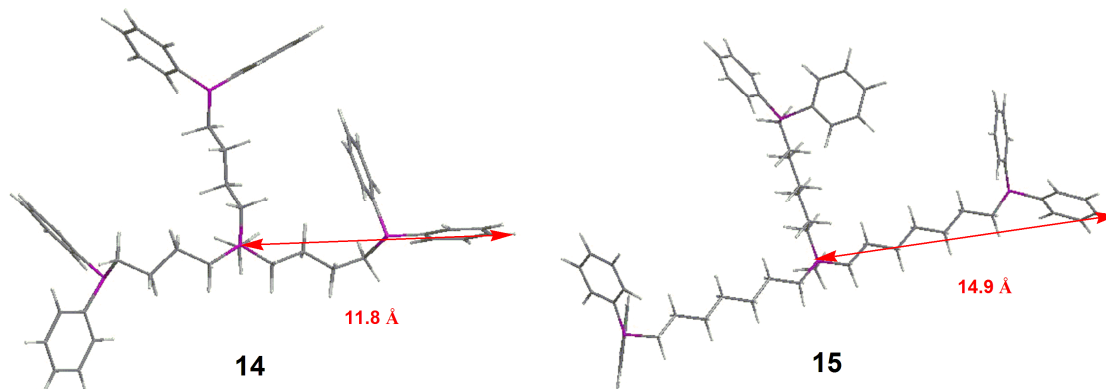


Figure 2.6. Molecular models of **14** and **15** and estimated radii of their footprints.

Taking into account that only 78.5% of a flat surface can be filled with circles, this would translate into surface coverages of about 20 molecules per 100 nm² surface for **14i** and about 11 per 100 nm² for **15i**.

The experimentally determined maximal surface coverages of about 14 and 8 molecules of **14i** and **15i** on 100 nm² of silica surface are lower, most probably due to the fact that favorable binding sites are not homogeneously distributed on the surface. Additionally, the narrow ends of the irregular pores, which count for the silica surface area when determined by BET isotherm measurements, might not be accessible for the rather large linker systems **13i-15i**. Figure 2.7 visualizes the experimental surface coverages. Although this is a crude simplification it gives nonetheless an estimate of the intermolecular distances of the immobilized species.

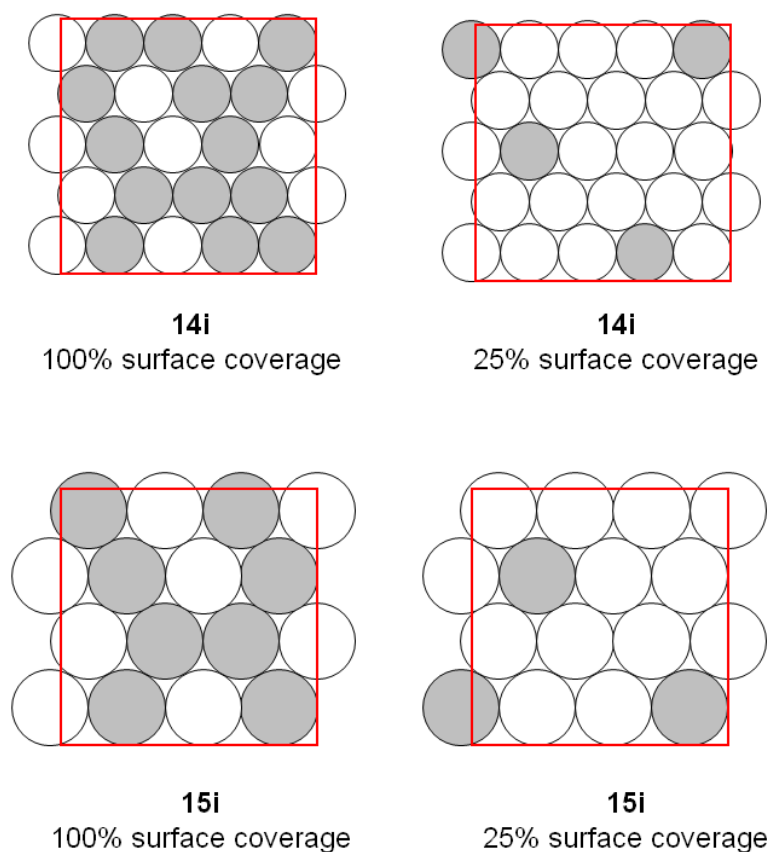


Figure 2.7. Visualization of the experimental surface coverages for **14i** (*top*) and **15i** (*bottom*). Grey circles depict occupied, white circles unoccupied surface sites. Left sketches: maximal surface coverages; right sketches: one fourth of the maximal surface coverages.

Most importantly, while statistically many linkers are still in contact with each other on the surface, when they are immobilized with maximal coverage, at 25% of the maximal loading the linkers are well separated from each other. This means that the Rh complexes immobilized with 25% of the maximal coverage should not be able to dimerize and therewith lose their catalytic activity prematurely.⁶⁴ The surface coverages

with model phosphonium salts $[\text{MePBu}_3]^+\text{I}^-$ **27**, $[\text{MePOct}_3]^+\text{I}^-$ **28**, and $[\text{MePOct}_3]^+\text{BF}_4^-$ **29** are much higher (Table 2.1 gives the maximal experimental coverages), because the chains are shorter without the extending diphenylphosphine groups, and this leads to smaller footprints.

Table 2.1. Surface coverages^{a)} of the modified silica **13i-15i**, **18i**, **21i-24i**, and **27i-29i**.

Material	molecules per 100 nm ² SiO ₂	mg of X per g SiO ₂	mmol of X per g SiO ₂
18i	3.25	36	0.041
13i	2.14	28	0.027
14i	1.57	24	0.020
15i	2.88	28	0.036
21i	3.25	42	0.041
22i	2.14	31	0.027
23i	1.57	27	0.020
24i	2.88	36	0.036
27i	34.3	147	0.427
28i	47.7	304	0.593
29i	39.3	238	0.489

^{a)} All surface coverages correspond to 25% of the maximal coverage of the surface with a monolayer of the molecular species **X**, with the exception of where the surface coverage is 100%.

The most powerful method for characterizing all surface-bound species is solid-state NMR spectroscopy.⁴¹ For the chemistry presented here, ³¹P is the analytically most valuable nucleus, because of its high sensitivity and the diagnostic chemical shift range of common phosphorus containing chemical species. Whenever the materials or

molecules are rigid by nature, the classical way of measurement, which involves filling the dry material into a rotor and spinning with the magic angle (MAS) while cross-polarizing (CP) the proton magnetization, is the only option.^{42a} Possible drawbacks of CP/MAS are that the signals cannot always be integrated reliably, and that at higher rotational frequencies the Hartmann-Hahn matching pattern splits into separate bands and signal intensity might be lost.^{41d}

However, in cases where the species possess some degree of motional freedom in the presence of a solvent, spinning a slurry of the material reduces the linewidths substantially in an HRMAS (high-resolution MAS)^{62l,m} spectrum. Problems associated with CP are avoided, because HRMAS spectra are best recorded with high-power decoupling only.^{62l} The surface-bound linkers **18i** and **13i-15i** with their long flexible alkyl chains are sufficiently mobile in the presence of a solvent such as benzene to be amenable to HRMAS. Figure 2.8 shows for **14i** as an example that due to the mobilizing effect of the solvent, combined with MAS, very narrow lines can be obtained with HRMAS. The halfwidths of the HRMAS signals (middle) for both the phosphonium and phosphine moieties of **14i** are, with 92 and 73 Hz, nearly as small as those in the solution spectrum (bottom). In contrast to this, the corresponding signals of the classical MAS spectra of the dry material **14i** are much broader with 421 and 635 Hz. All chemical shifts and halfwidths of the ³¹P MAS signals of the dry materials **13i-15i** and **18i**, and for their HRMAS resonances are given in Table 2.1. As expected, the longer the alkyl chains, the higher the mobility is in the presence of the solvent, in accordance with the results of a study with monodentate, covalently bound linkers with long alkyl chains (Figure 2.9).^{52b} But even for the linker **18i** with the shortest possible alkyl chain, the HRMAS signals show substantially narrower lines.⁵⁶ When the surface coverage is lowered to 25% of the maximal coverage, typically the signal halfwidths increase. For

example, the halfwidth for the phosphonium (phosphine) moiety of **14i** increases from 92 (73) to 278 (189) Hz. This again corroborates former results that have been obtained without spinning.^{62a} The lower surface coverage leads to reduced mobility of the phosphine group, because now there are enough surface sites left for the phosphine to adsorb. This in turn also reduces the rotational and overall mobility of the phosphonium group.

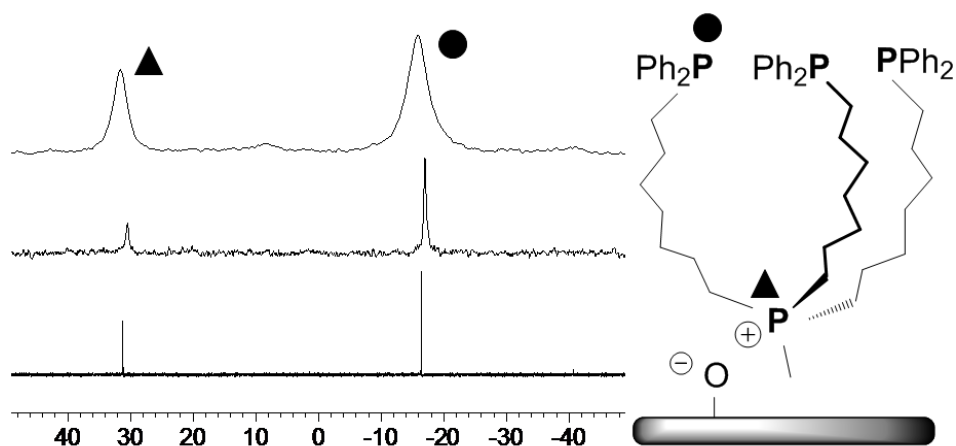


Figure 2.8. ^{31}P NMR of **14** (solution in C_6D_6 , *bottom*), ^{31}P HRMAS of a slurry of **14i** with C_6D_6 (*middle*, spinning frequency 2 kHz), and ^{31}P MAS NMR of dry **14i** (*top*, rotational frequency 4 kHz).

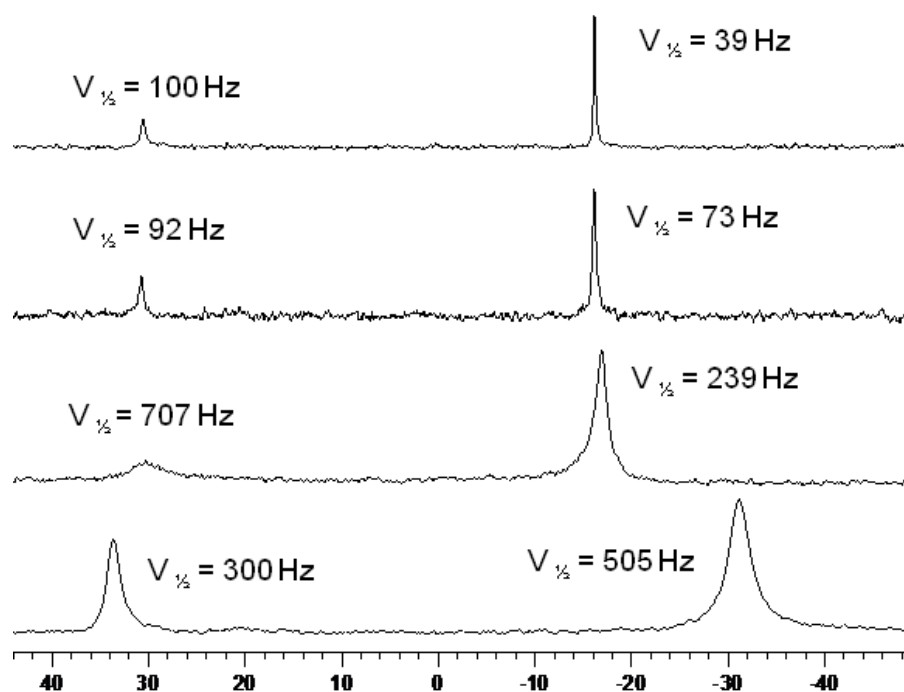


Figure 2.9. ^{31}P HRMAS spectra (C_6D_6 slurry, spinning frequency 2 kHz) of **13i**, **14i**, **15i**, and **18i** from top to bottom.

Interestingly, although the effect is not as pronounced as with the phosphine groups, even for the phosphonium ^{31}P HRMAS signals of all surface-bound linkers the linewidths become smaller (Figure 2.9, Table 2.2). This indicates that in spite of the strong electrostatic interactions with the surface some mobility of the phosphonium moiety must be possible.

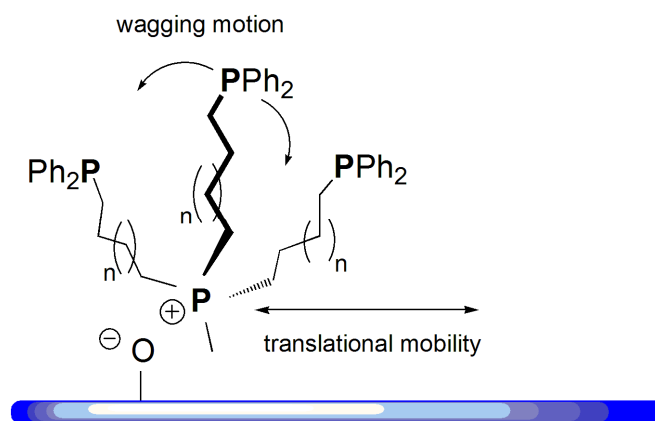


Figure 2.10. Possible modes of motion of immobilized phosphine ligands.

Preliminary studies using the deuterated phosphonium salt $[\text{Ph}_3\text{PCD}_3]\text{I}$ bound to the silica surface via electrostatic interactions prove that there is no translational motion of the salt on the surface in the absence of a solvent.^{45,65} The mobility of linkers tethered to oxide surfaces in the presence of a solvent is more intricate and a matter of ongoing research. Early ^2H NMR experiments suggest that immobilized phosphonium salts such as $[\text{Ph}_3\text{PCD}_3]\text{I}$ are mobile on the surface, leading to a collapse of the ^2H Pake Pattern to give only the isotropic line.⁶⁵ Whether the mobility of the linkers presented here is of a translational or wagging type (Figure 2.10), will be the subject of a future, more detailed study. Most important with respect to catalysis is that the phosphine groups, and therewith the linker chains, are sufficiently mobile in a solvent to mimic homogeneous catalysis.

Table 2.2. ^{31}P MAS and HRMAS NMR chemical shifts δ and signal halfwidths $\Delta\nu_{1/2}$ for the phosphonium and phosphine signals (P^+/P) of the linker-modified silica **13i-15i** and **18i** with maximal surface coverages (values for 25% coverage see Table 2.1). Rotational frequencies were 4 kHz for MAS measurements of dry materials, and 2 kHz for HRMAS of slurries with C_6D_6 .

Material (P^+/P)	$\delta(^{31}\text{P})$ (MAS) [ppm]	$\delta(^{31}\text{P})$ (HRMAS) [ppm]	$\Delta\nu_{1/2}$ (MAS) [Hz]	$\Delta\nu_{1/2}$ (HRMAS) [Hz]
18i	35.0/-29.2	33.7/-31.2	835/1780	300/505
13i	31.8/-15.9	30.0/-17.8	666/1448	604/239
14i	31.5/-15.9	30.4/-17.0	421/635	92/73
15i	31.6/-16.0	30.4/-16.9	352/416	100/39

One key question in the quest for the optimal immobilized catalyst is whether the catalytic activity and selectivity depend on the chain length and therewith the mobility of the linker and the catalyst. The more mobile the immobilized catalyst, the better it should be able to simulate the performance of a homogeneous catalyst. As it is already known from earlier studies without sample rotation^{62a} the ^{31}P NMR linewidths obtained from slurries of immobilized linkers are dependent on the solvent. In general, the less viscous and more polar the solvent is, the narrower are the signals. This is in accordance with the ^{31}P HRMAS signals of the linkers presented here, so even with spinning at 2 kHz the solvent plays a major role for the spectrum quality. As an example, **15i** has also been measured in the presence of a variety of organic solvents other than benzene, and the resulting phosphine signals are displayed in Figure 2.11. The chemical shifts change over a range of maximally 0.4 ppm in the different solvents, which does not exceed the

chemical shift changes one would find in solution. The linewidths are smallest with 20-24 Hz for the least viscous and most polar solvents, such as dichloromethane, acetonitrile and methanol, while the unpolar hexane leads to a comparatively broad line with a halfwidth of 134 Hz. However, while the linkers **13i-15i** and **18i** are rather robust, taking the coordinated metal complexes into account, non-protic and non-coordinating solvents are preferred for catalysis. Fortunately, the linewidths of **15i** in toluene (26 Hz) and benzene (43 Hz) imply that the linkers are still very mobile under the conditions of catalysis (Figure 2.11, Table 2.2). Therefore, toluene as the solvent for the Rh catalysts **22i-24i** and **21i** should provide conditions as close as possible to homogeneous catalysis with respect to catalyst mobility.

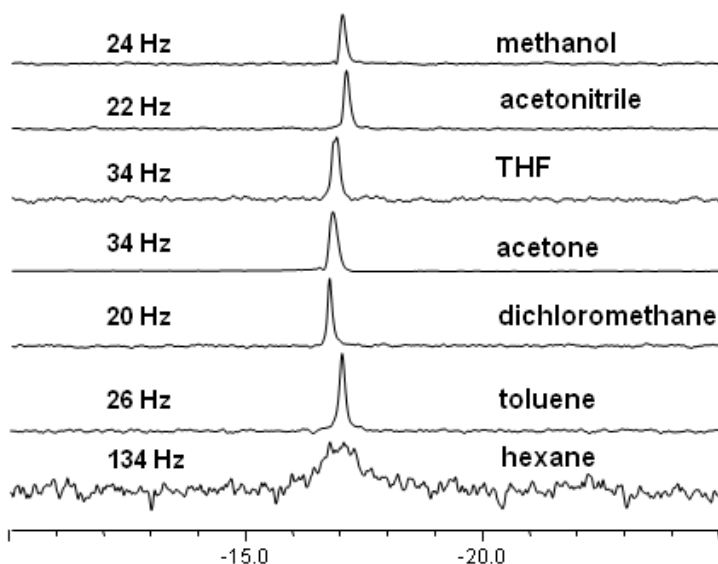


Figure 2.11. ^{31}P HRMAS lineshapes with indicated halfwidths (*left*) for **15i** in the corresponding solvents. Rotational frequency 2 kHz.

The linkers **13i-15i** and **18i** are bound to the support via electrostatic interactions of the phosphonium groups with the silica surface. While covalently bound linkers such as ethoxysilanes show some detachment from the surface under harsh conditions,^{62a} for surface-bound phosphonium salts the database is rather slim. Preliminary experiments in the Blümel group show that the bonding of tetraarylphosphonium salts on a silica surface is rather strong, and arylphosphonium salts proved impossible to remove from the support in substantial amounts by ion exchange or other reagents without dissolving the oxide support.^{42a} However, the solubility of the molecular phosphonium salts in the given solvents might play a role, and it should be higher for alkyl phosphonium salts. Naturally, leaching due to linker detachment is a major issue for immobilized catalysts, and therefore the leaching of alkyl phosphonium salts was probed quantitatively and in detail. In order to be able to work with large quantities and determine the leaching gravimetrically, while avoiding the expensive bromo alkene starting materials, we synthesized the phosphonium salts **27-29** (Figure 2.12) as model compounds and immobilized them in maximal surface coverage as **27i-29i** (Table 2.1). The leaching test revealed that practically no leaching occurs in nonpolar solvents. Most importantly, the solvent used for the catalysis, toluene, does not detach measurable amounts of the phosphonium salts from the surface (Figure 2.12). However, polar and protic solvents, such as THF and methanol should be avoided as reaction medium for catalysis, since they lead to major detachment of the linker system from the SiO₂ surface. Hereby, the phosphonium salt with the shortest alkyl chains, **27i**, is most vulnerable to leaching. Interestingly, the binding is practically independent of the nature of the counteranion.

This indicates that for the tested salts, the electrostatic interactions are not substantially augmented by additional F...H hydrogen bonds between the F atoms of the BF₄⁻ counteranion and protons of the surface silanol groups,⁶⁶ or the formation of new boron-containing species on the surface.⁶⁷ Rather, the solubility of the phosphonium salts in the corresponding solvents and the ability of the solvent to replace the salts from the surface seem to play major roles. This is reflected in the fact that THF and methanol lead to the largest amounts of detached phosphonium salts from the surface. Toluene is the most favorable solvent for catalysis, as it hardly leads to any leaching (Figure 2.12). As compared to the surface-bound model phosphonium salts **27i-29i**, the linkers **13i-15i** and **18i** should be somewhat more robust towards leaching, or else one would have detected the signals of free phosphines in solution in the HRMAS spectra of Figure 1.11. Probably, the diphenyl phosphine groups reduce the solubility and additionally function as a shield against detachment by the solvents. The single crystal X-ray structure of **21** with its "umbrella" of phenyl groups (Figure 2.3) supports this assumption.

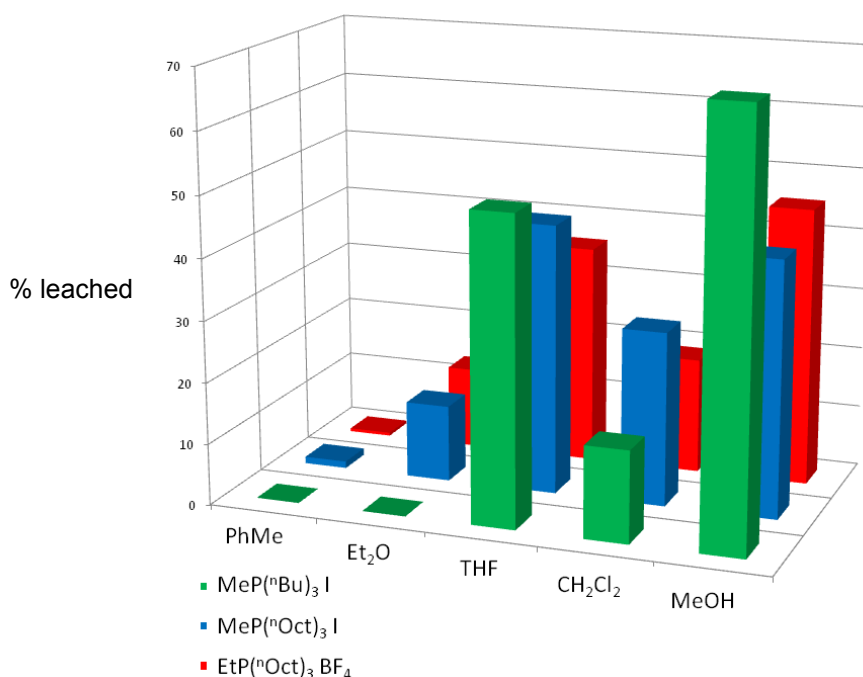
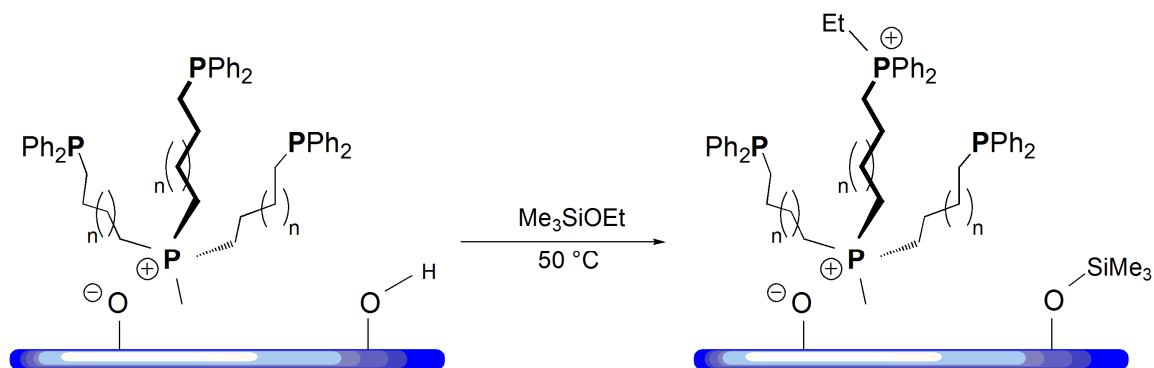


Figure 2.12. Graphic display of the leaching studies for the model phosphonium salts **27-29**. Leaching test: 400 mg of functionalized SiO₂ was suspended in the respective solvent (5 ml) and stirred for 24h at RT. The amount of leached phosphonium salt in the supernatant was determined gravimetrically.

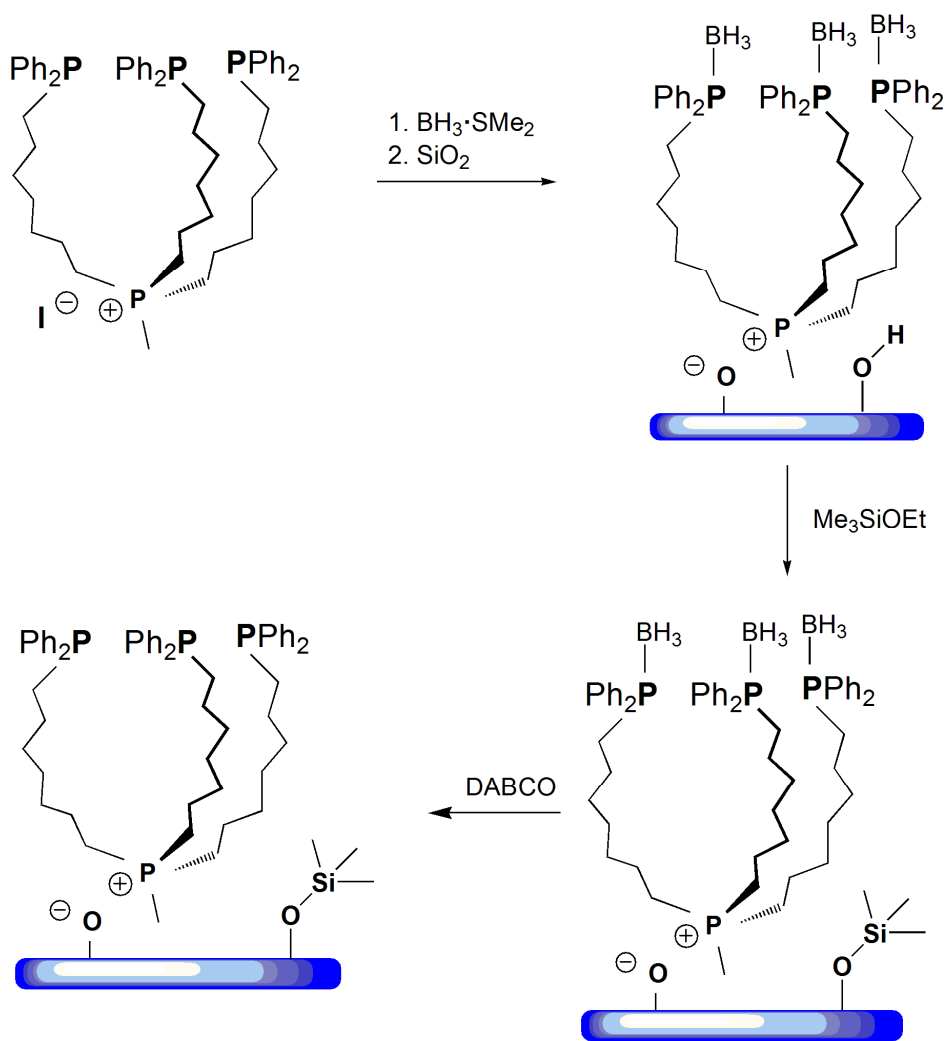
The surface of silica is devoid of any strongly acidic or basic sites compared to other oxidic surfaces such as zeolites or alumina and is therefore rather inactive with robust organometallic complexes.³⁷ However, isolated surface silanol groups do remain under the drying conditions used for this study and their oxygen atoms can act as ligands that bind to metals. Thus the immobilization of phosphine ligands was also performed on silica with end-capped silanol groups. This can, for example, be done by reacting the surface silanol groups with trimethylchlorosilane or trimethylethoxysilane.^{37b}

An early attempt to carry out the end-capping after ligand immobilization also led to partial alkylation of the phosphine groups (Scheme 2.28).^{63b}



Scheme 2.28. End-capping of silanol groups and phosphonium salt formation.

This side-reaction could be avoided by protecting the phosphine ligands as borane adducts prior to end-capping the surface silanol groups (Scheme 2.29).



Scheme 2.29. Silanol end-capping after protecting the phosphine groups.

The phosphine ligands **13-15** were protected as borane adducts *in situ* prior to the immobilization via the procedure described earlier.⁶⁸ Then the material was reacted with an excess of trimethylethoxysilane at 50 °C in toluene for 24 h. ^{31}P NMR shows signals at 31.2 ppm for the phosphonium moiety and a broad signal at 17.9 ppm for the borane protected phosphines (Figure 2.13). Deprotection of the phosphines is facile. Stirring the functionalized silica with an excess DABCO (1,4-diazabicyclo[2.2.2]octane) in toluene

at RT quantitatively deprotected the phosphine donors.^{63b,69} This results in the disappearance of the signal at 17.9 ppm (Figure 2.13).

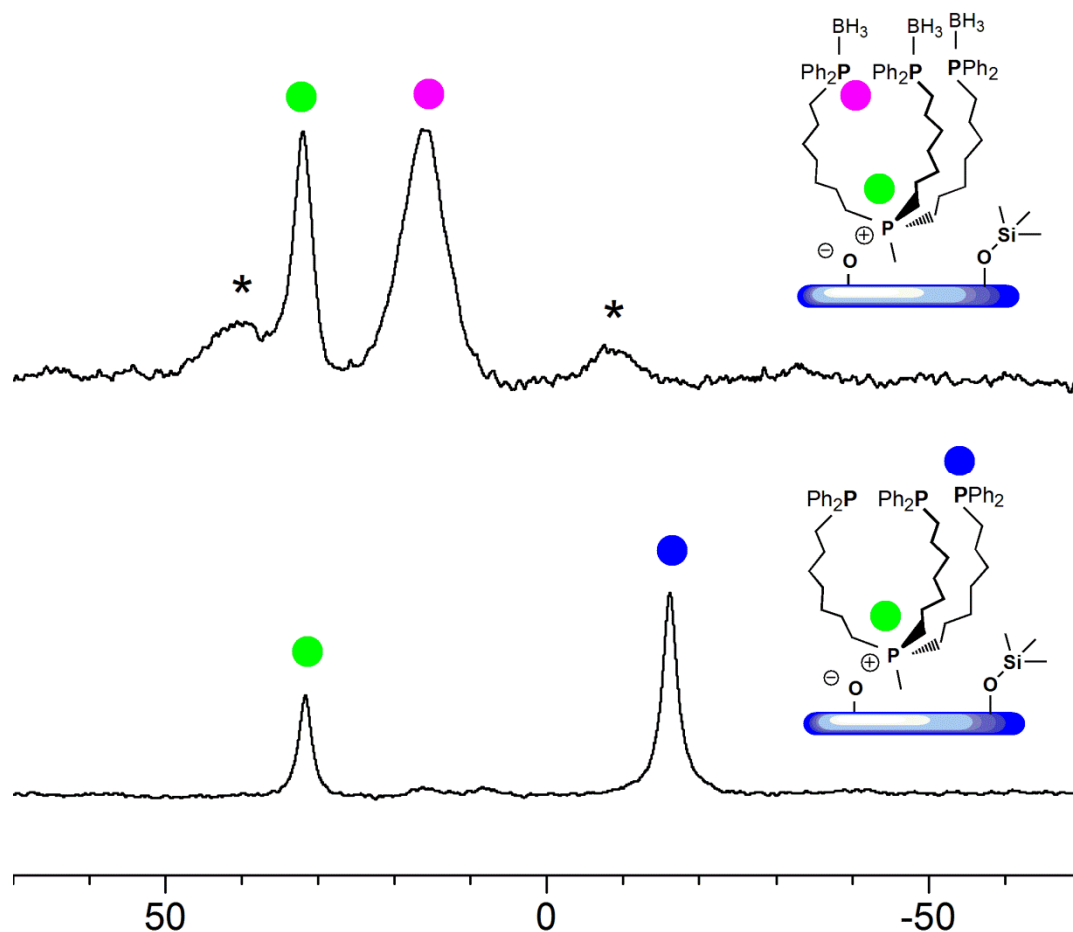


Figure 2.13. ^{31}P MAS (spinning speed 4 kHz) spectra of **14i**·BH₃ (TMS-capped) (*top*) and **14i** (TMS-capped) after deprotection with DABCO (*bottom*). The asterisks denote spinning sidebands.

The successful end-capping of the surface silanol groups was proven by ^{29}Si CP/MAS. The trimethylsilyl groups lead to a resonance at 13.5 ppm in a chemical shift

range typical for surface-bound trialkylsiloxanes.⁷⁰ The silica surface sites, $(\text{SiO})_3\text{SiOR}$, with $\text{R} = \text{H}$, alkyl, and bulk silica, $(\text{SiO})_4\text{Si}$, lead to the resonances at -100 and -110 ppm (Figure 2.14).

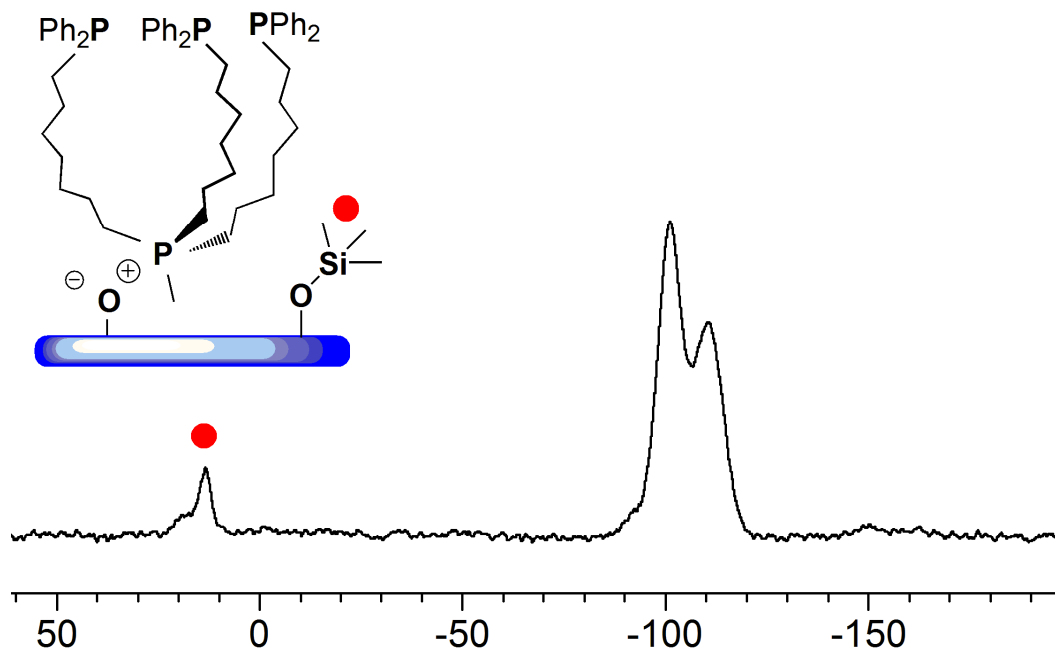


Figure 2.14. ^{29}Si CP/MAS NMR (spinning speed 4 kHz) of **14i** (TMS-capped).

It is assumed that the silyl groups on the surface serve a dual purpose. They mask surface silanol groups that might lead to unwanted reactions with organometallic species, but they also create an obstacle for possible translational movement of the immobilized species. The latter effect should be more pronounced with bulkier protecting groups as depicted in Figure 2.15. Therefore, a material with bulky triphenylsilyl protecting groups on the surface was employed using the same synthetic route as for the trimethylsilyl groups.

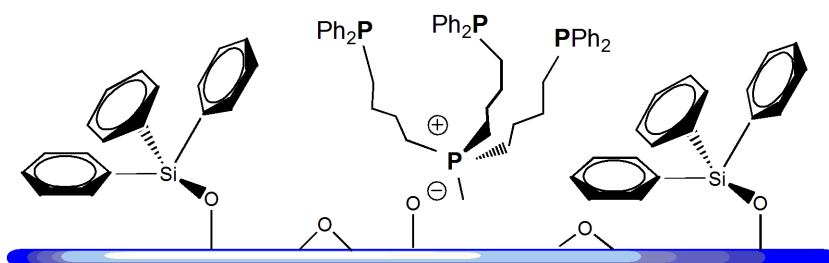


Figure 2.15. Depiction of the surface environment of **13i** (triphenylsilyl-capped).

As in the case of trimethylethoxysilane as endcapping agent, the immobilized phosphine linkers were obtained cleanly, as demonstrated by ^{31}P solid-state NMR (not shown). In this case the loading of triphenylsilyl protecting groups was estimated by measuring the weight increase of the sample. Figure 2.16 visualizes the surface coverage of immobilized phosphine linkers and surrounding triphenylsilyl groups for triphenylsilyl-capped **14i** and **15i** assuming random dispersion for both species.

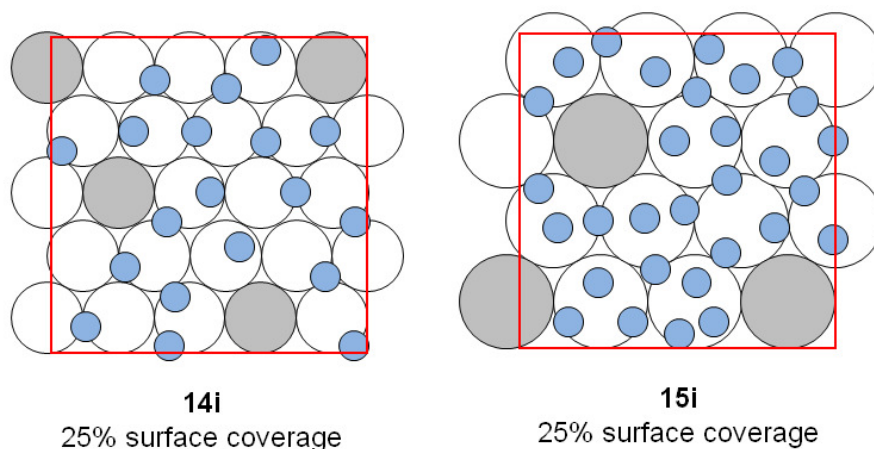
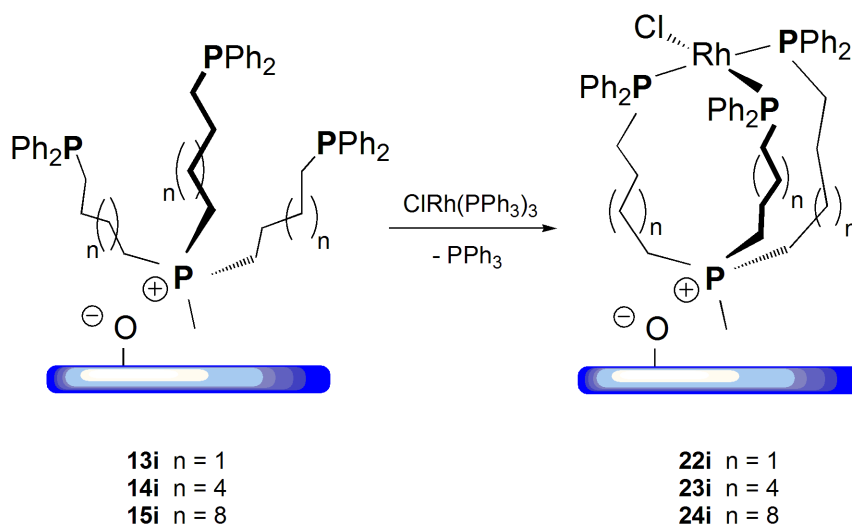


Figure 2.16. Visualization of the silica surface of triphenylsilyl-capped **14i** and **15i**. Grey circles depict occupied surface sites, white circles surface sites not occupied by a linker, and blue circles stand for the triphenylsilyl groups.

The effect of end-capping on the catalytic performance of the immobilized Rh complexes will be discussed in the following chapter.

Immobilized Rh Complexes and Catalysis

The immobilized Rh complexes **22i-24i** have been obtained from **13i-15i** by ligand exchange with Wilkinson's catalyst $\text{ClRh}(\text{PPh}_3)_3$ at room temperature (Scheme 2.30).



Scheme 2.30. Synthesis of immobilized Rh catalysts **22i-24i**.

With a 25% surface coverage of the linkers on the surface only one Rh center should be bound per immobilized linker molecule, as discussed in the previous chapter. The immobilized complex **21i** has been obtained by directly attaching **21** on the silica surface. The catalyst obtained after immobilizing **18** to give **18i**, and then treating it with Wilkinson's catalyst displayed catalysis characteristics identical to those of **21i**. The ^{31}P

MAS spectra prove that, after washing the materials thoroughly, there is no adsorbed PPh_3 left. Furthermore, no uncoordinated linker phosphines are present, and most importantly, there are no phosphine oxide signals with their characteristic chemical shift anisotropy (CSA) pattern.^{41,63,71} This is, for example, demonstrated by the spectrum of **24i** in Figure 2.17. The phosphonium signal and the signal of the phosphines in *trans* position to each other overlap at about 30 ppm, while the resonance of the phosphorus nucleus *trans* to Cl appears at about 41 ppm. Overall, the ^{31}P MAS spectrum resembles the ones of various immobilized Wilkinson-type Rh complexes studied earlier.^{61g-i} We could prove that in toluene, as anticipated from the linker leaching studies described above, all catalysts are firmly tethered to the support and that no noticeable leaching of the ligand or the metal center into solution occurs, even after stirring the material for a prolonged period of time in toluene.

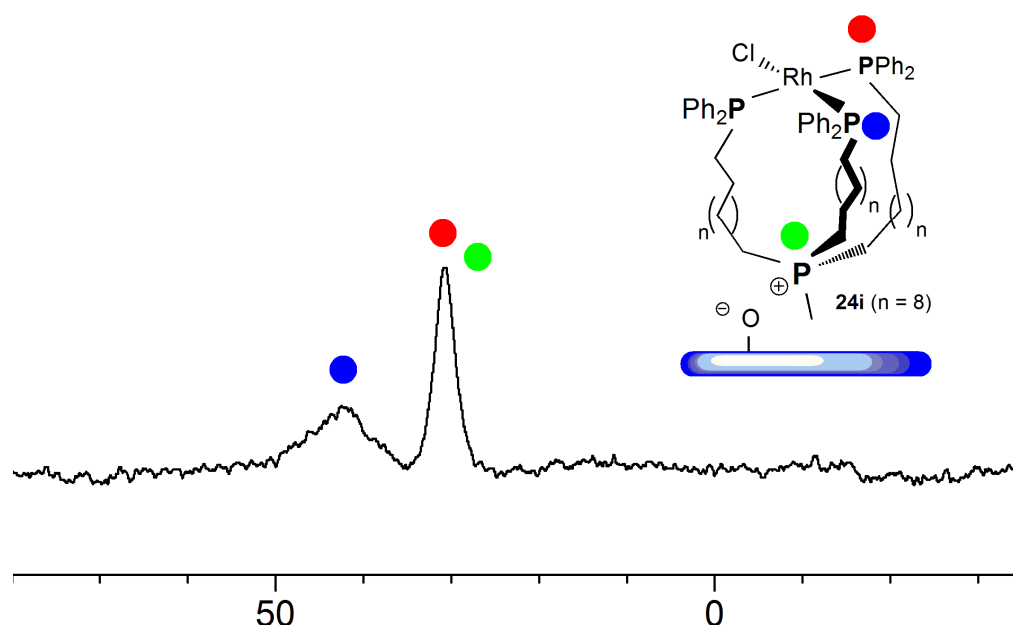
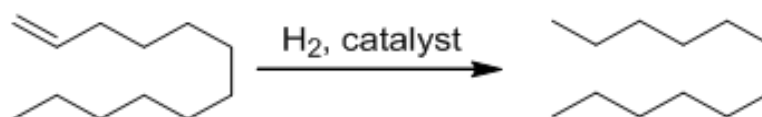


Figure 2.17. ^{31}P MAS spectrum of catalyst **24i** (spinning speed 10 kHz).

Application of Rh Complexes in Catalytic Olefin Hydrogenation

Olefin hydrogenation is one of the best developed and most important catalytic reactions in academia and industry.⁷² Therefore, the catalytic hydrogenation of 1-dodecene as a model reaction (Scheme 2.30) has been pursued. This also allowed the comparison with earlier results of the Blümel group^{62g-i} and others,^{19b} especially since the standard reaction conditions have been applied (Figure 2.18).



Scheme 2.31. Catalytic hydrogenation of 1-dodecene.

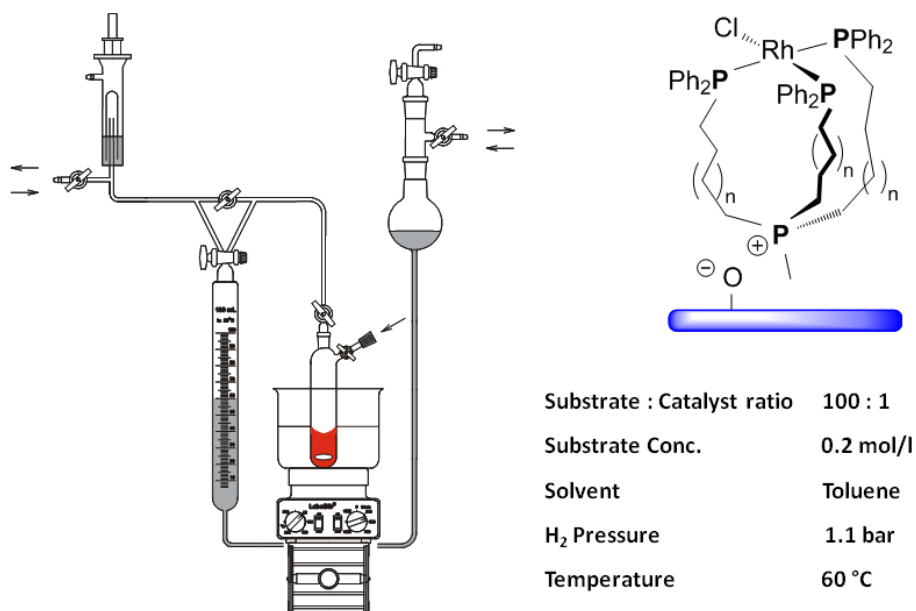


Figure 2.18. Reaction apparatus,⁶²ⁱ catalysts **22i** – **24i** ($n = 1, 4, 8$) and conditions for the catalytic hydrogenation of 1-dodecene.

The only difference here is that the catalysts bound by the new alkyldiarylphosphine ligands required a slightly higher temperature of 60 °C to perform the hydrogenation reactions within reasonable time frames. Guided by earlier work on hydrogenation catalysts within the group,^{62g,h} a reduced surface coverage of 25% of the maximal coverage has been used to prevent the dimerization of the Rh catalysts. For example, when **24i** with maximal surface coverage (100%, 6.28 molecules per 100 nm² SiO₂ surface, 108 mg of **24** per g of SiO₂, 0.08 mmol of **24** per g of SiO₂) is used for catalysis, only about 50% H₂ conversion is obtained after 20 h of reaction time. With 25% surface coverage (data in Table 2.1), quantitative hydrogenation of 1-dodecene is achieved within 10 h. Therefore, if not mentioned otherwise, in the following all catalysts studied have been immobilized with 25% surface coverage.

Systems designed earlier using an ethoxysilane linker could be recycled up to 13 times.^{62g-i} As the record so far, a Wilkinson-type Rh catalyst immobilized recently via a phosphonium-bound rigid tetraphenyltin scaffold can be recycled 30 times until the H₂ consumption drops below 100% within 100 h.^{42b} Following the usual test protocol for new linker systems, the first run of the catalysts **22i-24i** has been probed in comparison with Wilkinson's catalyst in solution. Encouraged by the catalytic activity of other Rh norbornadienyl complexes with chelate ligands,⁷³ **21i** with the shortest possible alkyl chains was included in this study. The graphic representation of the results in Figure 2.19 shows that, according to expectation, the homogeneous catalyst ClRh(PPh₃)₃ is the fastest, because the substrate does not have to diffuse into the pores of a support material and contains the less basic triaryl- instead of diarylalkyl phosphine ligands. Regarding the chain lengths of the linkers, the catalyst with the longest alkyl chain, **24i**, is the most active in the hydrogenation of 1-dodecene (Figure 2.19), probably due to its maximal mobility. It is followed by the C₇ species **23i**, and finally **22i**. In contrast to our

anticipation, however, the catalyst **21i** that is bound to the surface via a tripod-type linker is only in the beginning the least active. After an induction period of about two hours, it catalyzes the hydrogenation even faster than **24i**, and reaches 100% substrate conversion at about the same overall reaction time (Figure 2.19).

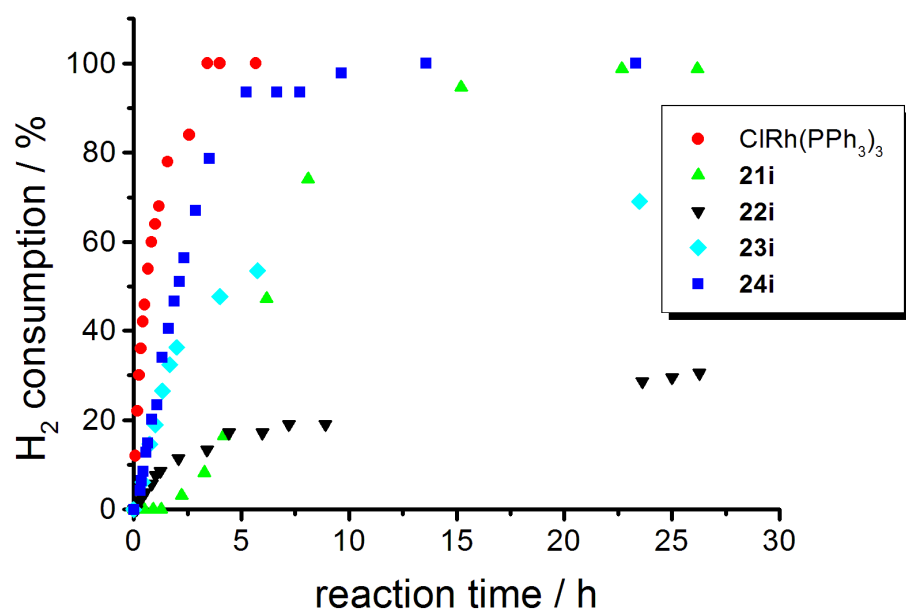


Figure 2.19. Activities of the indicated homogeneous and immobilized catalysts for the hydrogenation of 1-dodecene in the first run.

The ^{31}P MAS spectrum of **24i** after catalysis (Figure 2.20, top) shows basically the same signals as the spectrum recorded of the material prior to catalysis. Only the relative signal intensities are changed, a phenomenon observed previously.^{62f,h} Most importantly, no signals of dimeric species of the type $[(\text{R}_3\text{P})_2\text{RhCl}]_2$ are visible.

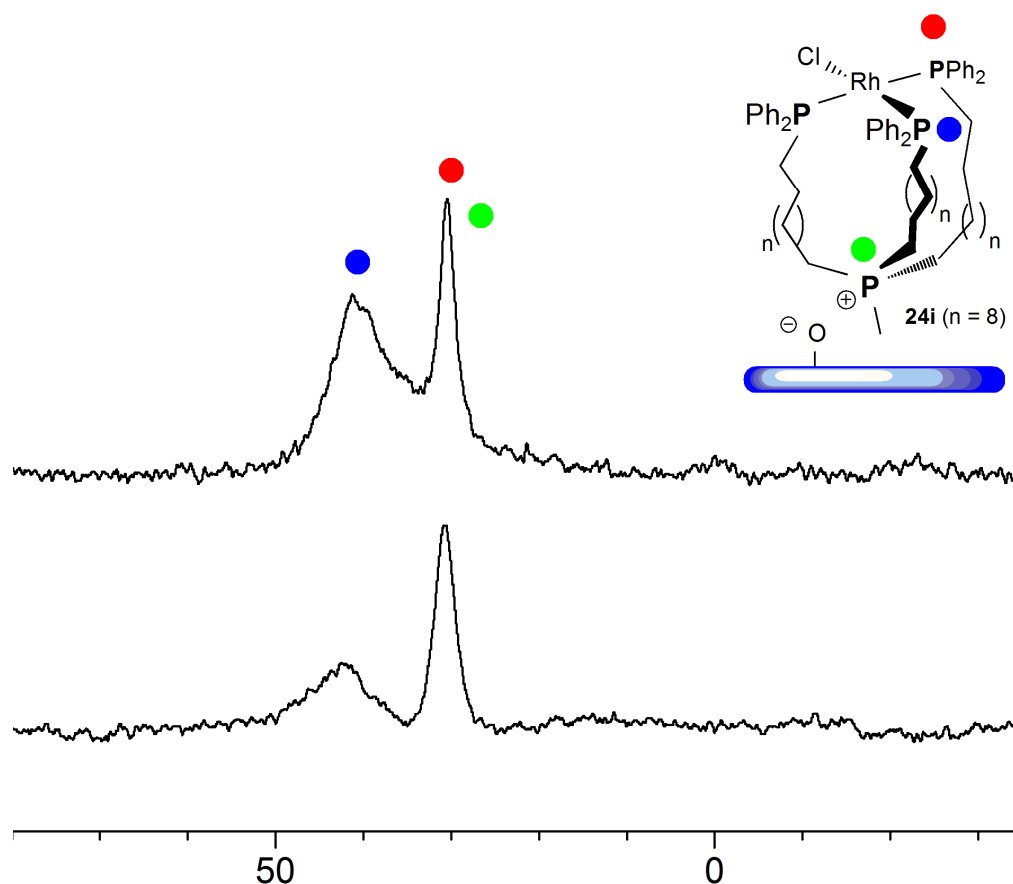


Figure 2.20. ^{31}P MAS spectra of catalyst **24i** before catalysis (*bottom*) and after (*top*).

In order to investigate the effect of the average pore size on the substrate diffusion within the silica support, catalyst **23i** on silica with an average pore size of 150 Å has been obtained. Its catalytic activity has been compared to analogs on 40 Å silica. As anticipated, the material showed a faster catalytic reaction in the first run, even approaching the activity of Wilkinson's catalyst in solution. This again emphasizes that the initial catalytically active species is a highly active hydrogenation catalyst mimicking in principle the active species in solution, and only being impeded by the diffusion of the substrates into the pores. Due to the diminished mechanical stability of this support

material, however, the studies have been continued with the mechanically more robust 40 Å silica (Figure 2.21).

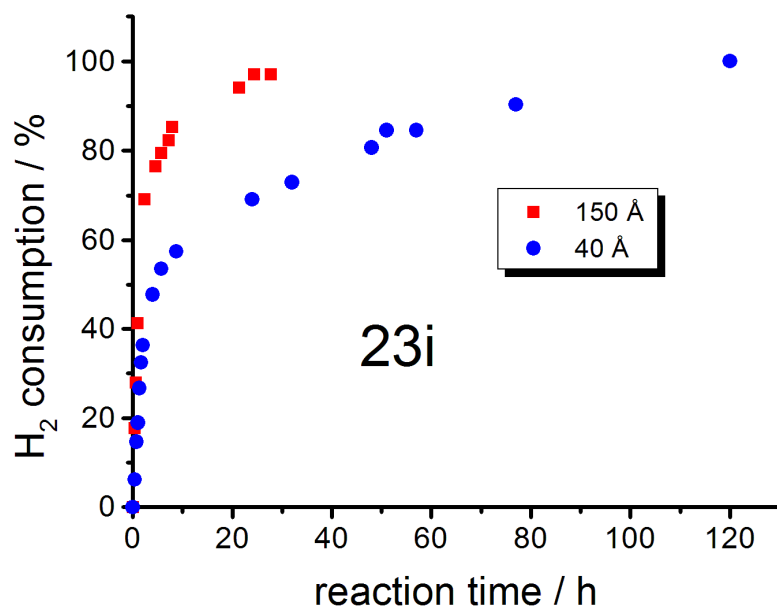


Figure 2.21. Activity of the **23i** immobilized on 40 Å and 150 Å silica, respectively, for the hydrogenation of 1-dodecene.

Next, the recycling characteristics of all immobilized catalysts have been tested. In earlier findings for immobilized Wilkinson-type catalysts at room temperature,^{62g-i} the first run had always shown the fastest conversion, and the activity slowly decreased with every subsequent batch-wise recycling step. The catalysts **22i-24i** and **21i**, however, display a different scenario, as the first run is often comparatively slow (Figure 2.19). Then, the activity increases with every recycling step and reaches a maximum at the third or fourth run, before the activity finally consolidates at about 100% conversion

within 30 to 40 h. For **21i** there is even an induction period of about two hours. These phenomena can be explained based on the catalysis results discussed below.

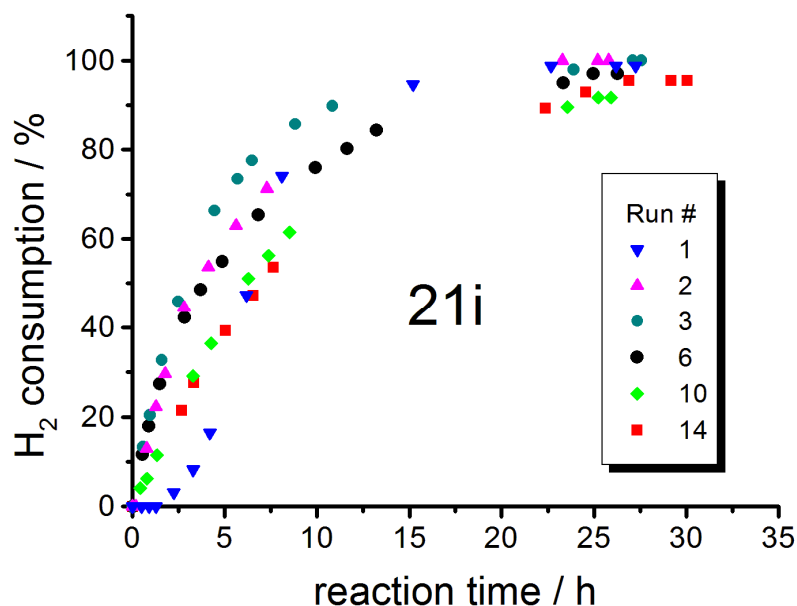


Figure 2.22. Hydrogen consumption during 14 batchwise catalytic runs using **21i**.

Interestingly, **21i** shows better recycling characteristics than **22i**, although the alkyl chains of the linker are shorter. Catalyst **21i** can be recycled for a respectable 14 times, before the conversion no longer reaches 100% within 35 h (Figure 2.22). The catalyst **22i** can only be recycled three times, before the conversion drops below 85% within 120 h. End-capping of residual surface silanol groups after the linker tethering and prior to the catalyst immobilization with trimethylsilyl (TMS) groups (see above) had a positive effect on the recycling characteristics of **22i**. Now, **22i** can be recycled seven times with 100% conversion of 1-dodecene within 35 h. Therefore, it can be concluded that with short linkers and in the absence of "shielding" counteranions (see X-

ray structure in Figure 2.3), the decomposition of the catalytically active species by contact with the reactive silica surface is a major problem that can be ameliorated with TMS-capping. However, the increase in catalytic activity from the first run with only 70% conversion within 30 h to the third, fourth and consecutive runs with 100% indicates the formation of a second catalytically active species even after end-capping (see below).

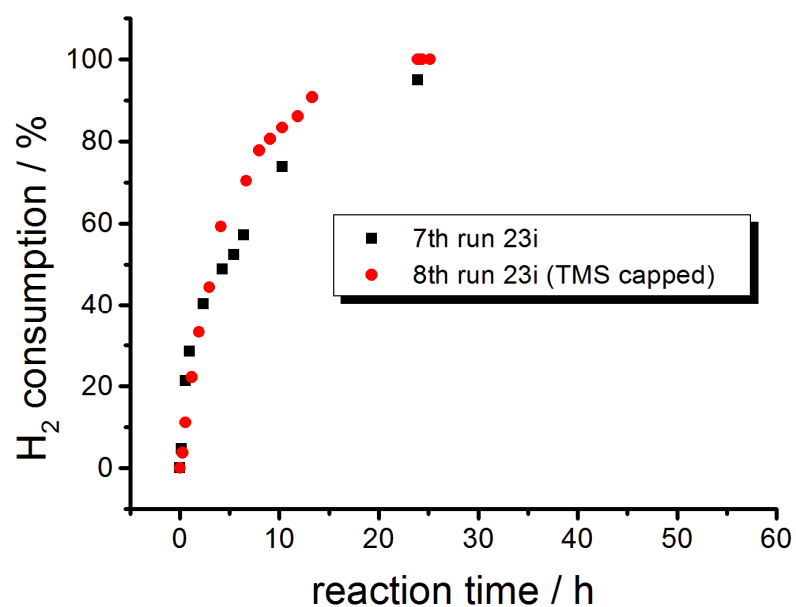


Figure 2.23. Hydrogen consumption using catalyst **23i** immobilized on end-capped and unmodified silica.

Although these initial results are encouraging in the case of **22i**, end-capping with either TMS or triphenylsilyl-groups had negligible effects on the catalytic performance of **23i** (Figure 2.23). Overall it appears that there is a slight benefit to end-

capping the silanol groups on the surface, but after multiple runs the catalytic activity of the end-capped materials approaches that of the unmodified catalysts.

In contrast to expectation, based on the activity in the first run (Figure 2.19) and the fact that the catalyst **24i** incorporates the longest linker alkyl chains that are supposed to keep the catalyst at a distance from the surface, the recycling characteristics of **24i** are disappointing. In the second and third recycling run, **24i** needs about 100 h to reach 80% conversion. This scenario can be interpreted as an optimally mimicked homogeneous catalyst in the first run, while subsequently another, catalytically less active species is formed (see below), or the catalyst decomposes gradually by the interaction with the silica surface. This behavior can be rationalized by the increased conformational flexibility of **24i** which allows interactions with reactive surface sites. Metal complexes of this nature have been recently described by Chang *et al.*⁷⁴

The most impressive recycling performance has been found for **23i**, which can be recycled for 30 times in a batchwise manner, before the conversion of 1-dodecene to dodecane drops below 100% within 50 h (Figure 2.24). Interestingly, between the batchwise recycling runs, the washed and dried immobilized catalyst can be stored under inert gas atmosphere for months without losing activity. Wilkinson-type Rh catalysts immobilized with other linker types are less robust in this respect.^{62h}

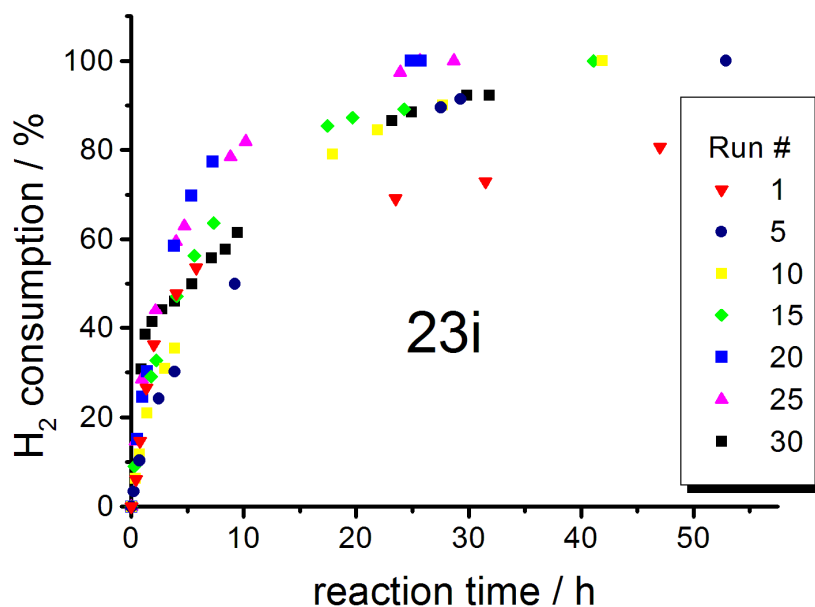


Figure 2.24. Hydrogen consumption over 30 batchwise catalytic runs using **23i**. Only every fifth run is shown for clarity.

From the above results it is obvious that there is at least one additional species besides **22i-24i** and **21i**, which is formed during catalysis. The most basic question in order to narrow in the nature of the new species is, whether the catalytic activity remains with the support, or whether it is found in solution. In order to clarify this issue, a split test has been performed on **23i** (Figure 2.25).⁷⁵ After about 8 h of the third catalytic run with **23i** and 40% conversion, an aliquot of the supernatant was removed from the reaction mixture. Then, the supported catalyst with the remaining supernatant, and also the aliquot of the supernatant, were subjected again to the hydrogenation conditions. While the solid remains catalytically active and consumes all residual 1-dodecene, the supernatant does not show any substrate conversion (Figure 2.24). Therefore, all catalytically active species involved stay firmly attached to the support.

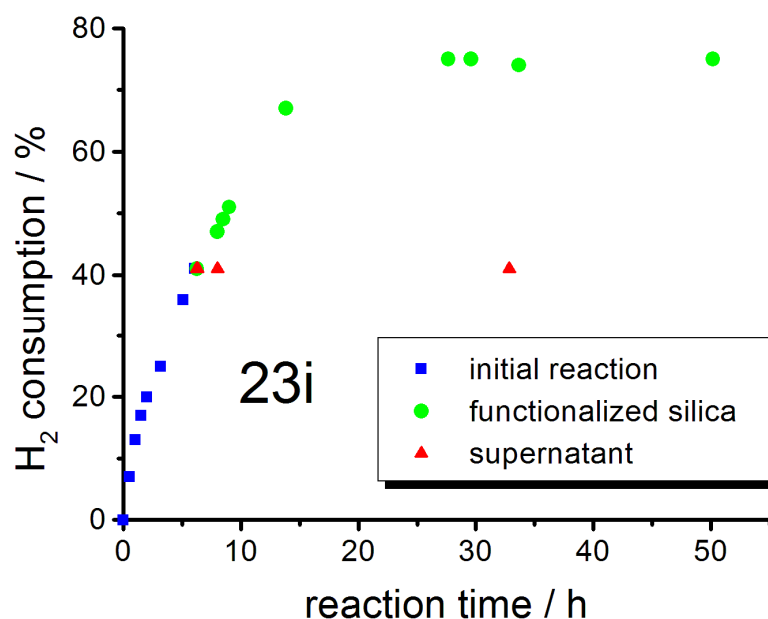


Figure 2.25. Split test to prove the absence of any Rh species in solution. Only the surface-bound catalyst **23i** keeps hydrogenating the substrate 1-dodecene (details see Experimental Section).

Another test that confirms that the catalytically active species stays on the support involves covalently binding an olefin to a different batch of support material and analyzing whether it is hydrogenated by the immobilized catalyst.⁷⁶ For this three-phase test, allyltriethoxysilane was covalently bound to a different batch of silica via Si-O-Si linkages according to a literature procedure.^{62b,c} Then, the batch with allyltriethoxysilane-modified silica was combined with a batch of **23i** and subjected to the hydrogenation conditions. The immobilized catalyst **23i** did not hydrogenate any of the tethered olefin, as checked by monitoring the hydrogen consumption and ¹³C HRMAS^{62l,m} (Figure 2.26) of the tethered olefin. When the homogeneous catalyst ClRh(PPh₃)₃ was added as a control experiment, however, all surface-bound allyl groups

were hydrogenated. Therefore, it can be concluded that no catalytically active species leaches from **23i** into solution.

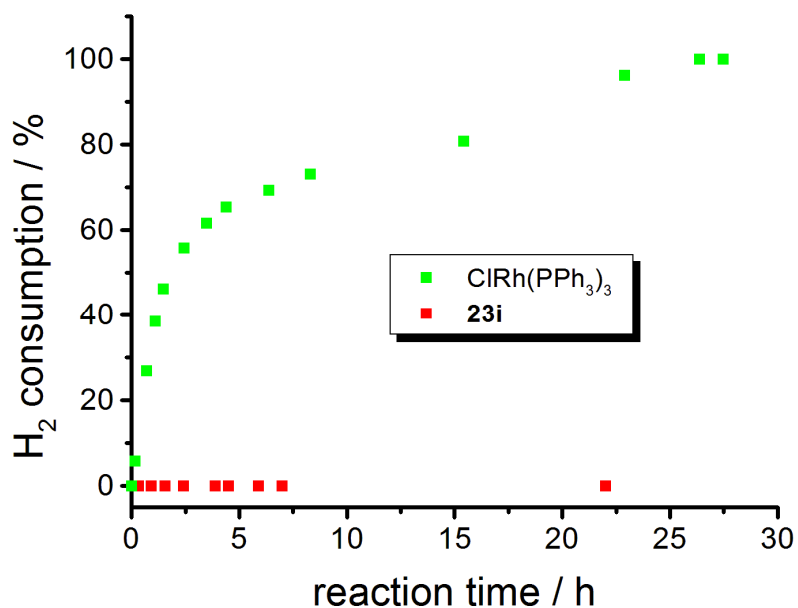


Figure 2.26. Three-phase test using immobilized allyltriethoxysilane and **23i** on different support batches.

In order to better describe the new surface-bound catalyst that forms during the reaction, the following observation was taken into account: The silica-bound catalyst changed its color from orange to black within 5 h during the first run. This indicates the formation of metal particles in addition to the molecular catalyst, and based on the pioneering work of Angelici *et al.*,⁷⁷ this would explain the initial increase of the hydrogenation activity due to the spill-over effect of the metal particles.

In an effort to corroborate whether indeed metal particles form with the linkers **13i-15i** during catalysis, a test developed by the Crabtree group was performed.⁷⁸

Homogeneous, molecular Rh catalysts can be poisoned by adding DBCOT (dibenzo[a,e]cyclooctatetraene) to the reaction mixture. DBCOT is a strong ligand, but it is not hydrogenated. Therefore, once DBCOT binds to the Rh center, it prevents further hydrogenation of other substrates. However, DBCOT does not strongly bind to metal surfaces due to steric constraints. Therefore, it cannot inhibit the catalytic activity of metal particles.

Figure 2.27 shows the DBCOT poisoning results and the validity of the test. When two equivalents of DBCOT are added to the homogeneous Wilkinson's catalyst in solution, the conversion of dodecene decreases from originally 100% within 4 h to about 43% in 25 h. For the test with the immobilized catalyst **23i**, one batch of TMS-capped **23i** at the 8th run has been studied. In comparison, **23i** at the 9th run has been tested in the presence of two equivalents of DBCOT. Both substrate consumption curves are nearly identical. Therefore, it is concluded that at the 8th catalytic run at the latest the catalyst consists mainly of metal particles that are not affected by the DBCOT, and not of molecular single-site species.

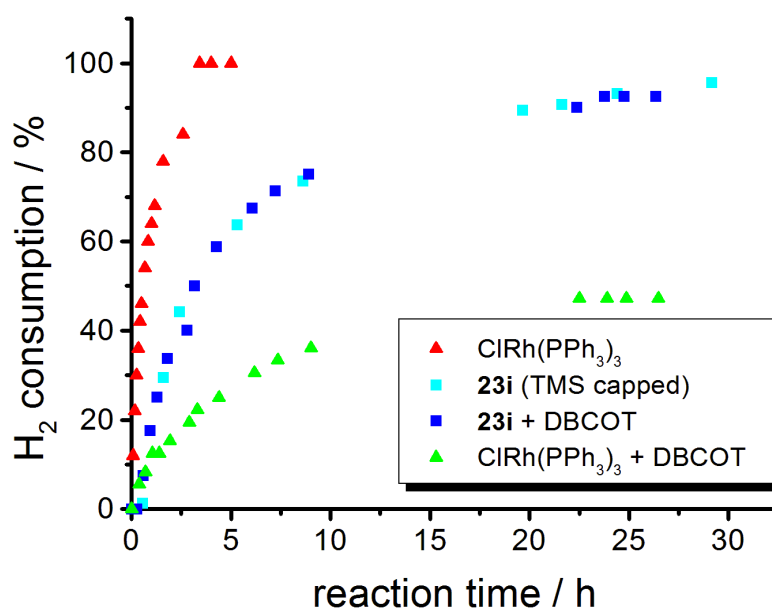


Figure 2.27. Hydrogen consumption of the shown catalysts with and without the poisoning agent DBCOT.

Next it was studied whether the metal particle formation coincides with the color change of the material in the first run. For this purpose, pristine TMS-capped **23i** has been split into two batches, and one has been allowed to hydrogenate 1-dodecene under the standard conditions, while the other has been additionally poisoned with 2 equivalents of DBCOT. In the first 5 h both batches showed orange color, and while the poisoned batch only reached about 30%, the pristine batch gave about 44% conversion (Figure 2.28). After 5 h, the poisoned catalyst turned black and its catalytic activity soon matched the one of the pristine batch. Therefore, the formation of metal particles correlates with the color change of the catalyst and its performance, and this takes place within the first 5 to 10 h of hydrogenation. So, in the beginning of the first catalytic run, both surface-bound molecular complexes, as well as metal particles take part in the catalytic hydrogenation.

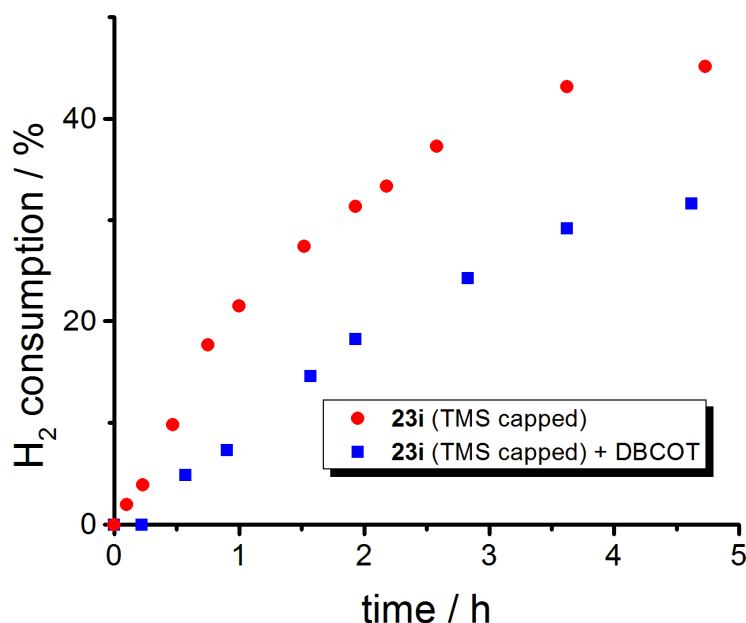


Figure 2.28. Hydrogen consumption of the TMS capped catalyst **23i** in the first run with and without the poisoning agent DBCOT.

For **21i** the extended induction period is most probably not due to the norbornadiene dissociation, because the molecular complex **21** in solution is not catalytically active. The catalytic activity of **21i** seems to be solely based on the formation of metal particles, which coincides with the color change occurring at the onset of the hydrogen consumption.

Further evidence for this assumption is based on the selectivity of the hydrogenation reaction. It is known that heterogeneous catalysts that consist of metal particles can shift double bonds in linear 1-alkenes,^{79a} as well as cyclic olefins.^{79b} This double bond shift only takes place in the presence of H₂. For example, material containing Rh(0) on silica, obtained by depositing [(COD)RhCl]₂ on silica according to the literature procedure⁸⁰ (see Experimental Section), did not isomerize 1-dodecene in

the absence of H₂, as proven by ¹H NMR. The same result was obtained for **21i** after the 14th run, when it was stirred with 1-dodecene in the absence of H₂. Since this isomerization will not be obvious for 1-dodecene after quantitative hydrogenation, we investigated the reaction mixture of the third catalytic run by GC and ¹H NMR at about 40% conversion with catalyst **23i**. Indeed, not only resonances for the terminal olefin ¹H signals of residual 1-dodecene with a relative intensity of about 2%, but also ca. 98% of signal intensity for protons at different internal double bonds have been found. The reason for 1-dodecene being present in only 1% is most probably because it is more easily transformed into dodecane than the dodecene isomers with internal double bonds, and therefore continually removed from the equilibrium. As a comparison, we analyzed the reaction mixture after 52% substrate conversion by Wilkinson's catalyst, and found less than 20% of ¹H signal intensity stemming from dodecene isomers with internal double bonds (Figure 2.29).

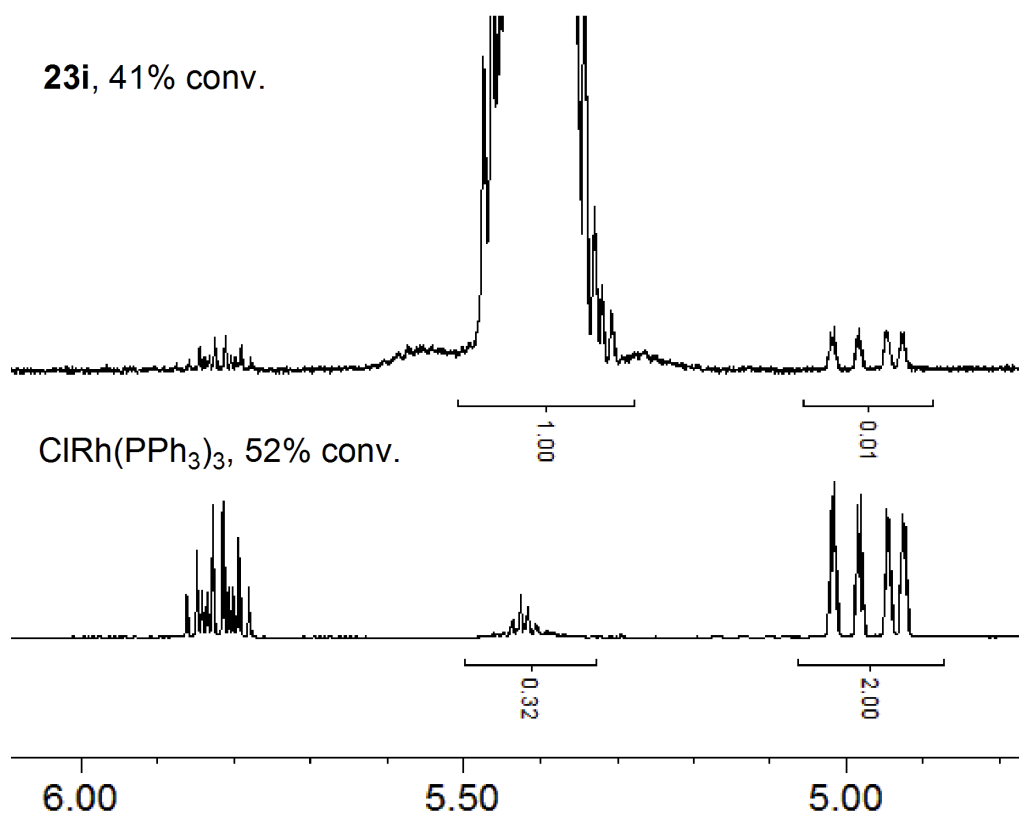
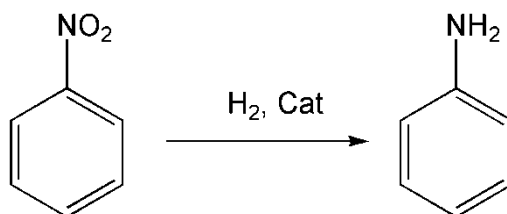


Figure 2.29. Olefin region of the ¹H NMR spectra (CDCl₃) of the reaction mixtures after the conversions indicated.

Finally, the nitrobenzene test⁷⁸ has been applied to prove the presence of metal particles on the silica surface of catalyst **22i**.



Scheme 2.32. Catalytic hydrogenation of nitrobenzene.

In this test, it is known that only heterogeneous metal particles catalyze the reduction of nitrobenzene to aniline (Scheme 2.32). Indeed, Wilkinson's catalyst in solution does not consume hydrogen in the presence of nitrobenzene within the first 10 h of reaction. Hydrogen consumption only starts when the solution turns black and cloudy, indicating decomposition of the homogeneous catalyst under formation of metal particles. Catalyst **22i**, after an induction period of about 10 h, starts to transform nitrobenzene into aniline, and achieves about 85% conversion after 200 h of reaction time.

Next, catalytically active metal particles have been generated to prove this hypothesis. The immobilized catalyst **23i** can be stirred at 70 °C under a nitrogen atmosphere overnight without a visible change of its orange color taking place. However, with admission of hydrogen, the color darkens slightly even at room temperature. At 70 °C, exposure of **23i** to a hydrogen atmosphere leads to the blackening of the material within one hour (Figure 2.30).

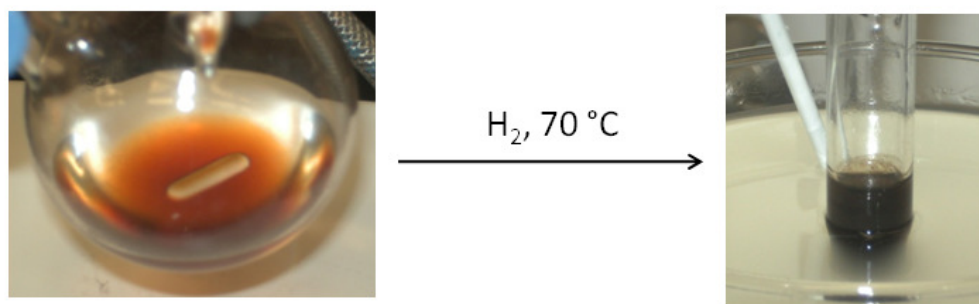


Figure 2.30. Reaction flask containing pristine **23i** in toluene (*left*) and **23i** after exposure to H₂ at 70 °C (*right*).

Therefore, it is concluded that hydrogen is the reducing agent, while the temperature is only a minor issue, and the olefin does not play a significant role in this process. Based on this insight, $[(\text{COD})\text{RhCl}]_2$ was deposited on silica according to the literature procedure⁸⁰ (see Experimental Section), and the dry material was reduced in a stream of hydrogen, while increasing the temperature from 60 to 120 °C for 4 h. During this time, the color of the powder changed from yellow to black. The resulting material contains 0.04 weight-% of Rh. The heterogeneous catalyst obtained in this way is rather slow with respect to hydrogenation. For about 85% substrate conversion it needs 80 h. However, the recycling characteristics are reasonable, as the activity does not change substantially between the second and the third run. Interestingly, comparing the obtained hydrogen consumption curves with those of **24i**, they are nearly identical. Therefore, one can conclude that due to the long linker alkyl chains that allow maximal mobility, the interactions with the surface, and hydrogen access, **24i** is reduced rapidly and forms metal particles.

In order to confirm these assumptions and probe the size of the generated metal particles, TEM measurements of **22i-24i** were recorded. The pictures in Figure 2.31 show clearly that Rh nanoparticles⁸¹ form within the silica. Their size distribution is similar and rather narrow, with an average diameter of 3 to 4 nm. The diameter is most probably dominated by the average pore size of the support material (4 nm, 40 Å), that prevents the particles from growing any larger. Therefore, the size distribution suggests that the nanoparticles reside within the pores of the support material. The inclusion of the nanoparticles within the pores explains the optimal recyclability of the catalysts, and the absence of leaching. Unfortunately, the TEM measurements do not allow precise quantification of the catalytically active Rh centers. However, clearly only a fraction of the metal centers is exposed on the surface and accessible for the substrate. But on the

other hand, the longevity of the nanoparticle catalysts is yet another proof that the pores of the silica are not clogged by the substrate or products, or any decomposed catalyst.

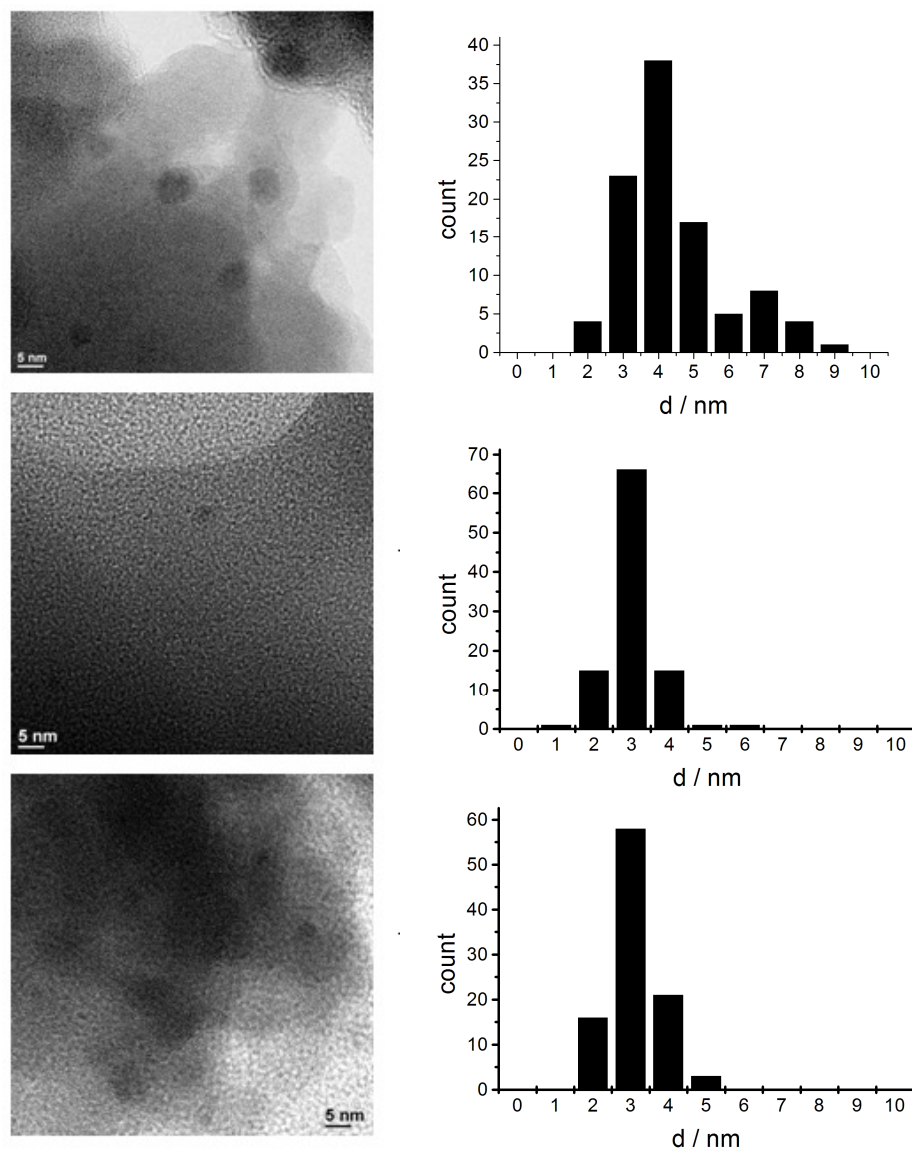


Figure 2.31. TEM images of Rh nanoparticles that formed during catalysis with **22i** (*top*), **23i** (*middle*), and **24i** (*bottom*), and their corresponding size distributions.

CONCLUSION

A new class of tridentate phosphine ligands incorporating long alkyl chains has successfully been synthesized and immobilized via electrostatic interactions. The immobilized Rh catalysts, obtained by ligand exchange, can be recycled more than 30 times without major loss of activity. In contrast to Rh catalysts previously immobilized via rigid tetraphenylelement linker scaffolds that prevent interactions with the silica surface,^{42b} here, under reducing conditions and at the elevated temperature of 60 °C needed for these catalysts with alkyldiphenylphosphine ligands to function, a second catalytically active species forms. It could be proven by catalytic test reactions, catalyst poisoning experiments, and TEM measurements that the new active species consist of Rh nanoparticles.⁸¹ All linkers lead, albeit on a different timescale, basically to the same nanoparticles, which explains their very similar catalytic characteristics. The next chapter will discuss efforts to slow down the decomposition of the original metal complexes.

EXPERIMENTAL

General Remarks

The ¹H, ¹³C, ¹⁹F, and ³¹P NMR spectra of liquids were recorded at 499.70, 125.66, 202.28, and 470.17 MHz on a 500 MHz Varian spectrometer and referenced as follows: ¹H: residual internal CHCl₃ (δ, 7.26 ppm), CDHCl₂ (δ, 5.32 ppm) or benzene-d₅ (δ, 7.16 ppm); ¹³C: internal CDCl₃ (δ, 77.23 ppm) or benzene-d₆ (δ, 128.06 ppm). ³¹P NMR spectra were referenced to neat Ph₂PCl (δ, 81.92 ppm) which was placed in a capillary centered in the NMR sample tube. ¹⁹F NMR spectra were referenced to trifluorotoluene (δ, -63.72 ppm) as external standard. The ¹³C, ¹⁹F, and ³¹P spectra were recorded with ¹H decoupling if not stated otherwise. The solid-state NMR spectra were

measured with a Bruker Avance 400 widebore NMR spectrometer with 4 or 7 mm MAS probeheads. For the ^{31}P HRMAS and MAS measurements ^1H high-power decoupling was applied. The recycle delays were 5 s for HRMAS and 10 s for MAS spectra. ^{29}Si CP/MAS spectra were recorded with a 5 ms contact time and a 3 s recycle delay. For more measurement details, see ref. [62]. GC analyses were carried out on a Shimadzu GC 2010 gas chromatograph equipped with a SHRXI-5MS column ($15\text{m} \times 0.25\text{mm} \times 0.25\mu\text{m}$) and a flame ionization detector (GC:FID). TEM images were obtained on an FEI Tecnai G2 F20 microscope and ImageJ software was used to determine the particle size distribution. Melting points were recorded with a Stanford Research Systems (SRS) MPA100 (Opti-Melt) automated melting point system. All reactions were carried out using standard Schlenk techniques and a purified N_2 atmosphere, if not stated otherwise. Reagents purchased from Sigma Aldrich or VWR were used without further purification. Solvents were dried by boiling them over Na, distilled, and stored under N_2 . CH_2Cl_2 was obtained from a solvent purification system. The silica (Merck, 40 Å average pore diameter, 0.063 to 0.2 mm average particle size, specific surface area $750\text{ m}^2/\text{g}$) was rigorously dried in vacuo at $400\text{ }^\circ\text{C}$ for 4 days to remove adsorbed water and condense surface silanol groups).

General procedure for the immobilization of phosphine linkers 13-15 and 18, and Rh complex 21 via the phosphonium group

Phosphine linker **14** (67 mg, 0.065 mmol) was dissolved in toluene (15 ml) and added to a suspension of 2.434 g of SiO_2 in toluene (40 ml). The mixture was stirred overnight at $50\text{ }^\circ\text{C}$. The silica was allowed to settle down and the supernatant was removed. The functionalized silica **14i** was then washed with toluene ($2 \times 10\text{ ml}$) and with Et_2O ($2 \times 10\text{ ml}$). Subsequently the silica was dried *in vacuo* for several hours. The

supernatant and the solvents from the washing process were combined and all volatile matter was removed *in vacuo*. The residue showed no ^{31}P NMR resonance, so all the linker **14** was immobilized on the support, resulting in **14i** with about 2 molecules per 100 nm^2 of silica surface (data for all immobilized species are given in Table 2.1).

General procedure for the catalyst preparation

$\text{ClRh}(\text{PPh}_3)_3$ (23 mg, 0.025 mmol), dissolved in 10 ml of toluene, was added to a slurry of the functionalized silica **14i** (1.006 g, 0.026 mmol ligand) in 10 ml of toluene. The mixture was stirred overnight at RT, then the silica was allowed to settle down and the supernatant was removed. The catalyst-containing silica **23i** was washed with toluene ($3 \times 10\text{ ml}$) and dried *in vacuo* for 4 h. The supernatant and the washing portions were combined and the solvent was removed *in vacuo*. The residue was analyzed by NMR and showed only the ^{31}P resonance of PPh_3 .

General procedure for TMS-capped catalysts

To prepare catalyst **23i-TMS** with end-capped SiOH groups ligand **14** was protected as the BH_3 adduct by adding $\text{BH}_3 \cdot \text{SMe}_2$ (0.5 ml, 400 mg, 5.265 mmol) to a solution of **14** (240 mg 0.235 mmol) in toluene (20 ml). The reaction mixture was stirred for 5 h at RT and the quantitative conversion to **14·BH₃** was checked by ^{31}P NMR (broad signal, $\delta = 15.5\text{ ppm}$). Then the solvent was removed *in vacuo* and the precipitate washed with pentane ($2 \times 5\text{ ml}$). **14·BH₃** was then immobilized according to general procedure described above. 4 ml of Me_3SiOEt was added to **14i·BH₃** (2.999 g, 0.080 mmol ligand) and the mixture was stirred at $60\text{ }^\circ\text{C}$ for 40 h. Then the supernatant was removed and the functionalized silica was washed with toluene ($3 \times 10\text{ ml}$) and dried *in vacuo*. Then **14i·BH₃-TMS** was added to 139 mg (1.239 mmol) of DABCO (1,4-

diazabicyclo[2.2.2]octane), dissolved in 30 ml of toluene, and stirred overnight. Finally, the supernatant was removed, and **14i-TMS** was washed two times with 10 ml aliquots of toluene. Then **23i-TMS** was prepared from **23i-TMS** according to the general procedure for the catalyst preparation described above.

General procedure for the catalytic hydrogenation

The immobilized catalyst **23i** (386 mg, 0.010 mmol Rh) was added to 4 ml of toluene in a Schlenk flask. Then the Schlenk flask was attached to the standardized hydrogenation apparatus⁶²ⁱ and warmed up to 60 °C. The apparatus was allowed to stand under H₂ prior to catalysis in order to make sure that H₂ is not lost due to a leakage. Additionally, any loss of H₂ after 100% conversion of the substrate was monitored and excluded. To start the catalysis, 1 mmol of 1-dodecene, dissolved in 1 ml of toluene, was added to the suspension through the stopcock via syringe. Then the suspension was stirred vigorously with a magnetic stir bar and the hydrogen uptake was monitored. After complete consumption of the hydrogen the silica was allowed to settle down, the supernatant was removed and the silica was washed with toluene (2×4 ml). The supernatant was analyzed by GC and ¹H NMR to confirm quantitative conversion of the olefin to dodecane. The H₂ consumption always matched the substrate formation within the error margins of the analytical methods. For example, after the consumption of 54% H₂ in the 15th catalytic run with **23i**, the GC and ¹H NMR analyses indicated 57 and 55% dodecane formation.

Procedure for the three-phase test

Immobilized catalyst **23i-TMS** (375 mg, 0.01 mmol Rh) and allyltriethoxysilyl-functionalized silica^{62b} (890 mg, 0.5 mmol allyl groups) were added to a Schlenk flask

with 5 ml of toluene and warmed to 60 °C. Then the Schlenk flask was purged with H₂, connected to the standardized hydrogenation apparatus,⁶²ⁱ and the H₂ consumption was monitored. As a control experiment the same procedure was carried out with Wilkinson's catalyst (8 mg, 0.01 mmol) instead of immobilized catalyst **23i-TMS**.

Procedure for the split test

Immobilized catalyst **23i** (386 mg, 0.010 mmol Rh) was added to 4 ml of toluene in a Schlenk flask. Then the Schlenk flask was attached to the standardized hydrogenation apparatus⁶²ⁱ and warmed to 60 °C. To start the catalysis 1-dodecene (1 mmol, dissolved in 1 ml of toluene) was added. The hydrogen consumption was monitored and after ca. 40% conversion the hydrogen reservoir was disconnected and the silica support was allowed to settle down. Then 2 ml of the hot supernatant were removed with a syringe and filtered through a frit. Both the remaining reaction mixture with the silica support and the filtered supernatant were reconnected to separate hydrogenation apparatuses, and the hydrogen consumption was monitored for both samples. After the hydrogen uptake had stopped, for both cases the reaction mixtures were analyzed by GC and ¹H NMR.

General procedure for the Rh(0) catalyst preparation⁸⁰

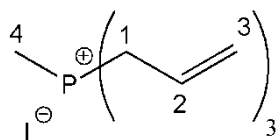
Silica (1.029 g) was suspended in 15 ml of toluene. [(COD)RhCl]₂ (10 mg, 0.020 mmol) was dissolved in 10 ml of toluene, added to the silica slurry, and the mixture was stirred for 3 h at RT. Then the solvent was removed *in vacuo* to give a yellow powder. This material was then heated from 60 °C to 120 °C over 4 h in an H₂ gas stream. The material darkened gradually until it became black.

Catalyst poisoning experiment with DBCOT

The immobilized catalyst **23i-TMS** (375 mg, 0.010 mmol Rh) was stirred in 4 ml of toluene in a Schlenk flask. Then dibenzo[*a,e*]cyclooctatetraene DBCOT (4 mg, 0.020 mmol) was added and the mixture was stirred for 2 h at RT. The Schlenk flask was attached to the standardized hydrogenation apparatus⁶²ⁱ and warmed to 60 °C. Then 1 mmol of 1-dodecene, dissolved in 1 ml of toluene, was added to the slurry through the stopcock via syringe. While the mixture was stirred, the hydrogen uptake was monitored. After complete conversion the silica was allowed to settle down. Then the supernatant was removed and the silica was washed with toluene (2×4 ml). The supernatant was analyzed by GC and ¹H NMR to confirm 100% conversion.

Methyltris(prop-2-enyl)phosphonium iodide **11**

PCl₃ (254 mg, 1.849 mmol) was dissolved in Et₂O (10 ml) and added dropwise to a 1M ether solution of allylmagnesium bromide (5.5 ml, 5.500 mmol), diluted with 40 ml in Et₂O, over 1 h at 0 °C. Then the reaction mixture was allowed to warm up to RT and stirred overnight. After the reaction mixture was cooled to 0°C and quenched with 20 ml of H₂O, the mixture was stirred at RT for 2h. The organic layer was filtered through Na₂SO₄ and the aqueous layer was washed twice with 30 ml portions of Et₂O. The organic layers were combined, 947 mg (6.672 mmol) of methyl iodide was added, and the reaction mixture was stirred overnight at RT. Then the solvent was removed *in vacuo*. The crude product was washed with pentane (6×15 ml) to give triallyl-methyl phosphonium iodide **11** (263 mg, 0.977 mmol) as a colorless waxy solid in 53% yield.

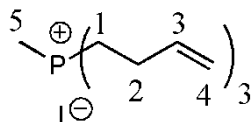


$\text{C}_{10}\text{H}_{18}\text{IP}$
Mol. Wt.: 269.130

^1H NMR (CDCl_3 , 499.70 MHz): δ (ppm) = 5.70-5.87 (m, 3H, H2), 5.58 (ddq, $^3J_{\text{trans}}(^1\text{H}-^1\text{H}) = 16.9$ Hz, $^3J(^1\text{H}-^1\text{H}) = 5.3$ Hz, $^2J(^1\text{H}-^1\text{H}) = 1.0$ Hz, 3H, H3_Z), 5.49 (ddd, $^3J_{\text{cis}}(^1\text{H}-^1\text{H}) = 9.9$ Hz, $^3J(^1\text{H}-^1\text{H}) = 4.8$ Hz, $^2J_{\text{cis}}(^1\text{H}-^1\text{H}) = 0.8$ Hz, 3H, H3_E), 3.52 (dd, $^2J(^{31}\text{P}-^1\text{H}) = 15.8$ Hz, $^3J(^1\text{H}-^1\text{H}) = 7.4$ Hz, 6H, H1), 2.08 (d, $^2J(^{31}\text{P}-^1\text{H}) = 13.2$ Hz, 3H, H4); **^{13}C NMR** (CDCl_3 , 125.66 MHz): δ (ppm) = 125.32 (d, $^3J(^{31}\text{P}-^{13}\text{C}) = 12.2$ Hz, C2), 123.17 (d, $^2J(^{31}\text{P}-^{13}\text{C}) = 10.3$ Hz, C3), 25.72 (d, $^1J(^{31}\text{P}-^{13}\text{C}) = 47.7$ Hz, C1), 4.14 (d, $^1J(^{31}\text{P}-^{13}\text{C}) = 53.3$ Hz, C4); **^{31}P NMR** (CDCl_3 , 202.28 MHz): δ (ppm) = 27.47.

Methyltris(but-3-enyl)phosphonium iodide 4

Phosphine **1** (311 mg, 1.584 mmol) was dissolved in 20 ml of toluene and 0.43 ml of CH_3I (800 mg, 5.654 mmol) was added. The reaction mixture was stirred at RT for 48 h. Then the solvent was removed *in vacuo* and the remaining residue was washed with pentane to give **4** (401 mg, 1.185 mmol) as a colorless solid in 75% yield.



$\text{C}_{13}\text{H}_{24}\text{IP}$
Mol. Wt.: 328.207

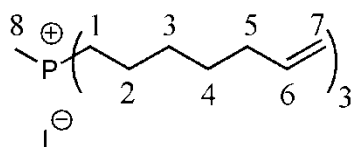
^1H NMR (CDCl_3 , 499.70 MHz): δ (ppm) = 5.88 (ddt, $^3J_{\text{trans}}(^1\text{H}-^1\text{H}) = 16.6$ Hz, $^3J_{\text{cis}}(^1\text{H}-^1\text{H}) = 10.2$ Hz, $^3J(^1\text{H}-^1\text{H}) = 6.4$ Hz, 3H, H3), 5.23 (ddt, $^3J_{\text{trans}}(^1\text{H}-^1\text{H}) = 17.1$ Hz,

$^2J(^1\text{H}-^1\text{H}) = 2.1 \text{ Hz}$, $^4J(^1\text{H}-^1\text{H}) = 1.5 \text{ Hz}$, 3H, H4_{cis}), 5.16 (ddt, $^3J_{\text{cis}}(^1\text{H}-^1\text{H}) = 10.2 \text{ Hz}$, $^2J(^1\text{H}-^1\text{H}) = 2.3 \text{ Hz}$, $^4J(^1\text{H}-^1\text{H}) = 1.2 \text{ Hz}$, 3H, H4_{trans}), 2.67 (m, 6H, H1), 2.46 (m, 6H, H2), 2.02 (d, $^2J(^{31}\text{P}-^1\text{H}) = 13.5 \text{ Hz}$, 3H, H5); $^{13}\text{C NMR}$ (CDCl₃, 125.66 MHz): δ (ppm) = 134.75 (d, $^3J(^{31}\text{P}-^{13}\text{C}) = 12.3 \text{ Hz}$, C3), 117.97 (s, C4), 25.82 (d, $^2J(^{31}\text{P}-^{13}\text{C}) = 4.1 \text{ Hz}$, C2), 20.53 (d, $^1J(^{31}\text{P}-^{13}\text{C}) = 47.8 \text{ Hz}$, C1), 6.43 (d, $^1J(^{31}\text{P}-^{13}\text{C}) = 50.9 \text{ Hz}$, C5); $^{31}\text{P NMR}$ (CDCl₃, 202.28 MHz): δ (ppm) = 33.28 (s).

mp 170-173°C.

Methyltris(hept-6-enyl)phosphonium iodide **5**

Phosphine **2** (362 mg, 1.123 mmol) was dissolved in 30 ml of toluene and 0.3 ml of CH₃I (684 mg, 4.819 mmol) was added. The reaction mixture was stirred at RT for 36 h. Then the solvent was removed *in vacuo* and the remaining residue was washed with pentane to give **5** (356 mg, 0.766 mmol) as a colorless oil in 68% yield.



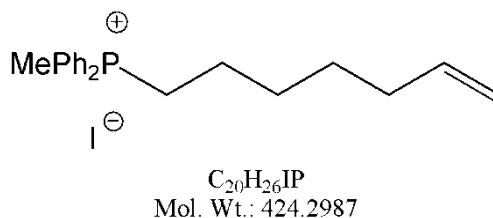
C₂₂H₄₂IP
Mol. Wt.: 464.467

$^1\text{H NMR}$ (C₆D₆, 499.70 MHz): δ (ppm) = 5.89 (tdd, $^3J_{\text{trans}}(^1\text{H}-^1\text{H}) = 16.9$, 3 Hz, $^3J_{\text{cis}}(^1\text{H}-^1\text{H}) = 10.1 \text{ Hz}$, $^3J(^1\text{H}-^1\text{H}) = 6.7$, 3 Hz, 3H, H6), 5.17 (ddt, $^3J_{\text{trans}}(^1\text{H}-^1\text{H}) = 17.1 \text{ Hz}$, $^2J(^1\text{H}-^1\text{H}) = 2.1 \text{ Hz}$, $^4J(^1\text{H}-^1\text{H}) = 1.5 \text{ Hz}$, 3H, H7_{cis}), 5.07 (tdd, $^3J_{\text{cis}}(^1\text{H}-^1\text{H}) = 10.2 \text{ Hz}$, $^2J(^1\text{H}-^1\text{H}) = 2.3 \text{ Hz}$, $^4J(^1\text{H}-^1\text{H}) = 1.2$, 3H, H7_{trans}), 2.39-2.56 (m, 6H, H1), 2.19 (d, $^2J(^{31}\text{P}-^1\text{H}) = 13.8 \text{ Hz}$, 3H, H8), 2.04-2.16 (m, 6H, H5), 1.41 (b, 18H, H2-H4); $^{13}\text{C NMR}$

(C₆D₆, 125.66 MHz): δ (ppm) = 139.05 (s, C6), 114.98 (s, C7), 33.94 (s, C5), 30.89 (d, $^3J(^{31}\text{P}-^{13}\text{C}) = 15.4$ Hz, C3), 28.61 (s, C4), 21.90 (d, $^2J(^{31}\text{P}-^{13}\text{C}) = 4.5$ Hz, C2), 20.83, (d, $^1J(^{31}\text{P}-^{13}\text{C}) = 48.2$ Hz, C1), 5.87 (d, $^1J(^{31}\text{P}-^{13}\text{C}) = 51.5$ Hz, C8); **^{31}P NMR** (C₆D₆, 202.28 MHz): δ (ppm) = 29.69 (s).

Diphenylmethyl(hept-6-enyl)phosphonium iodide **10**

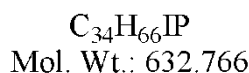
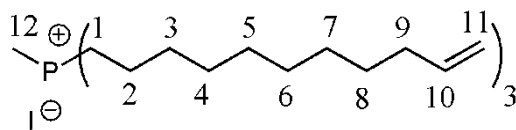
Phosphine **9** (761 mg, 2.695 mmol) was dissolved in 20 ml of toluene and MeI (2.052 g, 14.502 mmol) was added. The solvent was removed in vacuo and the remaining residue was washed with pentane to yield **10** (923 mg, 2.175 mmol) as a white solid in 80 % yield.



^1H NMR (CDCl₃, 499.70 MHz): δ (ppm) = 7.86 (dd, $^3J(^{31}\text{P}-^1\text{H}) = 12.7$ Hz, $^3J(^1\text{H}-^1\text{H}) = 7.7$ Hz, 4H, H_{ortho}), 7.77 (t, $^3J(^1\text{H}-^1\text{H}) = 7.5$ Hz, 2H, H_{para}), 7.68 (t, $^3J(^1\text{H}-^1\text{H}) = 6.9$ Hz, 4H, H_{meta}), 5.72 (m, 1H, CH=CH₂), 4.87-4.95 (m, 2H, CH=CH₂), 3.72 (m, 2H, P⁺CH₂), 2.84 (d, $^2J(^{31}\text{P}-^1\text{H}) = 13.5$ Hz, 3H, PCH₃), 1.89 (q, $J(^1\text{H}-^1\text{H}) = 6.7$ Hz, 2H), 1.52-1.59 (m, 4H), 1.38 (m, 2H); **^{13}C NMR** (CDCl₃, 125.66 MHz): δ (ppm) = 138.29 (s, C6), 129.37 (d, $^4J(^{31}\text{P}-^{13}\text{C}) = 2.9$ Hz, C_{para}), 132.56 (d, $^2J(^{31}\text{P}-^{13}\text{C}) = 10.1$ Hz, C_{ortho}), 130.32 (d, $^3J(^{31}\text{P}-^{13}\text{C}) = 12.4$ Hz, C_{meta}), 119.19 (d, $^1J(^{31}\text{P}-^{13}\text{C}) = 84.8$ Hz, C_{ipso}), 114.72 (s, C7), 33.23 (s, C5), 29.61 (d, $^3J(^{31}\text{P}-^{13}\text{C}) = 16.2$ Hz, C3), 28.11 (d, $^4J(^{31}\text{P}-^{13}\text{C}) = 0.9$ Hz, C4), 23.24 (d, $^1J(^{31}\text{P}-^{13}\text{C}) = 50.8$ Hz, C1), 21.98 (d, $^2J(^{31}\text{P}-^{13}\text{C}) = 4.0$ Hz, C2), 8.97 (d, $^1J(^{31}\text{P}-^{13}\text{C}) = 55.1$ Hz, CH₃); **^{31}P NMR** (CDCl₃, 202.28 MHz): δ (ppm) = 24.14 (s).

Methyltris(undec-10-enyl)phosphonium iodide 6

Phosphine **3** (431 mg, 0.878 mmol) was dissolved in 20 ml of toluene and 463 mg of CH₃I (0.203 ml, 3.272 mmol) was added. The reaction mixture was stirred at RT for 24 h. Then the solvent was removed *in vacuo* and the remaining residue was washed with pentane to give **6** (490 mg, 0.774 mmol) as a colorless oil in 88% yield.

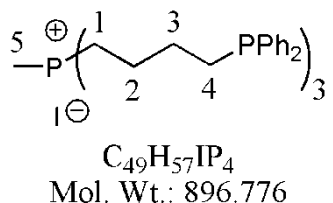


¹H NMR (C₆D₆, 499.70 MHz): δ (ppm) = 5.82 (ddt, ³J_{trans}(¹H-¹H) = 15.0 Hz, ³J_{cis}(¹H-¹H) = 10.2 Hz, ³J(¹H-¹H) = 6.7 Hz, 3H, H10), 4.96-5.14 (m, 6H, overlapping H11_{cis} and H11_{trans}), 2.45-2.60 (m broad, 6H, H1), 2.33 (d, ¹J(³¹P-¹H) = 13.8 Hz, 3H, H12), 2.07 (q, J = 7.3 Hz, 6H, H2*), 1.94-2.05 (m, 6H, H9*), 1.20-1.51 (b, 36H, H3-H8); **¹³C NMR** (C₆D₆, 125.66 MHz): δ (ppm) = 139.26 (s, C10), 114.58 (s, C11), 34.29 (s, C9), 31.11 (d, ³J(³¹P-¹³C) = 15.1 Hz, C3), 29.99[#] (s), 29.93[#] (s), 29.64[#] (s), 29.56[#] (s), 29.43[#] (s), 22.17 (d, ²J(³¹P-¹³C) = 4.6 Hz, C2), 20.96 (d, ¹J(³¹P-¹³C) = 48.5 Hz, C1), 6.09 (d, ¹J(³¹P-¹³C) = 51.4 Hz, C12); **³¹P NMR** (C₆D₆, 202.28 MHz): δ (ppm) = 31.11 (s).
*assignments interchangeable. [#]no assignments of C4-C8 possible.

Methyltris(4-diphenylphosphinobutyl)phosphonium iodide 13

Phosphonium salt **4** (246 mg, 0.727 mmol), AIBN (119 mg, 0.724 mmol), and 0.9 ml of Ph₂PH (963 mg, 5.172 mmol) were combined in a Schlenk flask, heated under a N₂ atmosphere to 70 °C and stirred for 3.5 days. The conversion was monitored by ³¹P NMR of the reaction mixture. After completion of the reaction, 2 ml of toluene was

added to remove excess Ph_2PH , and the product precipitated after adding 3 ml of pentane. The supernatant was discarded and the solid was again treated with 2 ml of toluene and precipitated with 3 ml of pentane. The precipitate was dried *in vacuo* at 70°C to give **13** (640 mg, 0.725 mmol) in quantitative yield as a colorless powder.

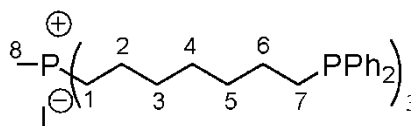


^1H NMR (CDCl_3 , 499.70 MHz): δ (ppm) = 7.42-7.37 (m, 12H, H_o), 7.34-7.28 (m, 18H, H_p , H_m), 2.31 (m, 6H, H_1), 2.09 (m, 6H, H_3), 1.95 (d, $^2J(^{31}\text{P}-^1\text{H}) = 13.3$, 3H, H_5), 1.65-1.55 (m, 12H, overlapping H_2 , H_4); **^{13}C NMR** (CDCl_3 , 125.66 MHz): δ (ppm) = 137.99 (d, $^1J(^{31}\text{P}-^{13}\text{C}) = 12.4$ Hz, C_i), 132.72 (d, $^2J(^{31}\text{P}-^{13}\text{C}) = 18.65$ Hz, C_o), 128.81 (s, C_p), 128.58 (d, $^3J(^{31}\text{P}-^{13}\text{C}) = 6.79$ Hz, C_m), 27.06 (d, $^1J(^{31}\text{P}-^{13}\text{C}) = 12.6$ Hz, C_4), 26.85 (dd, $^2J(^{31}\text{P}-^{13}\text{C}) = 16.8$ Hz, $^3J(^{31}\text{P}-^{13}\text{C}) = 15.6$ Hz, C_3), 22.59 (dd, $^3J(^{31}\text{P}-^{13}\text{C}) = 13.0$ Hz, $^2J(^{31}\text{P}-^{13}\text{C}) = 4.3$ Hz, C_2), 20.45 (d, $^1J(^{31}\text{P}-^{13}\text{C}) = 48.3$ Hz, C_1), 5.49 (d, $^1J(^{31}\text{P}-^{13}\text{C}) = 51.9$ Hz, C_5); **^{31}P NMR** (C_6D_6 , 202.28 MHz): δ (ppm) = 31.56 (s, R_3MeP^+), -16.49 (s, RPh_2P). The material is softening over the temperature range of 50 - 70°C .

HR-MS (MALDI $^+$): $[\text{M}^+] = \text{C}_{49}\text{H}_{57}\text{P}_4$ 769.3411(calcd.), 769.4390 (found); $[\text{MO}^+] = \text{C}_{49}\text{H}_{57}\text{P}_4\text{O}$ 785.3360 (calcd.), 785.4048 (found); $[\text{MO}_2^+] = \text{C}_{49}\text{H}_{57}\text{P}_4\text{O}_2$ 801.3309 (calcd.), 801.4435 (found); $[\text{MO}_3^+] = \text{C}_{49}\text{H}_{57}\text{P}_4\text{O}_3$ 817.3258 (calcd.), 817.4487 (found).

Methyltris(7-diphenylphosphinoheptyl)phosphonium iodide **14**

Phosphonium salt **5** (442 mg, 0.952 mmol), AIBN (155 mg, 0.944 mmol), and 1.0 ml of Ph₂PH (1007 mg, 5.323 mmol) were combined in a Schlenk flask, heated under a N₂ atmosphere to 70 °C and stirred for 3.5 days. The conversion was monitored by ³¹P NMR of the reaction mixture. After completion of the reaction 2 ml of toluene was added to remove excess Ph₂PH, and the product precipitated after adding 3 ml of pentane. The supernatant was discarded and the solid was again treated with 2 ml of toluene and precipitated with 3 ml of pentane. The precipitate was dried *in vacuo* at 70°C to give **14** (971 mg, 0.950 mmol) in quantitative yield as a colorless oil.



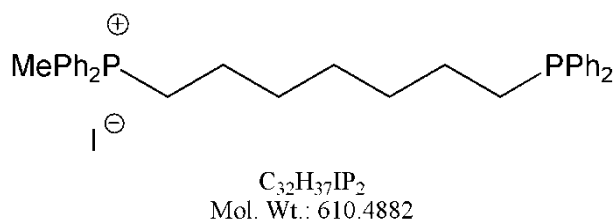
C₅₈H₇₅IP₄
Mol. Wt.: 1023.015

¹H NMR (C₆D₆, 499.70 MHz): δ (ppm) = 7.52 (dd, ³*J*(³¹P-¹H) = 7.6 Hz, ³*J*(¹H-¹H) = 7.6 Hz, 12H, H_o), 7.14 (t, ³*J*(¹H-¹H) = 7.3 Hz, 12H, H_m), 7.07 (t, ³*J*(¹H-¹H) = 7.4 Hz, 6H, H_p), 2.47 (m, 6H, H₁), 2.32 (d, ²*J*(³¹P-¹H) = 13.9 Hz, 3H, H₈), 2.09 (m, 6H, H₆), 1.53 (m, 6H, H₇), 1.48-1.20 (m, 24H, H₂-H₅); **¹³C NMR** (C₆D₆, 125.66 MHz): δ (ppm) = 139.98 (d, ¹*J*(³¹P-¹³C) = 14.5 Hz, C_i), 133.24 (d, ²*J*(³¹P-¹³C) = 18.5 Hz, C_o), 128.79 (d, ³*J*(³¹P-¹³C) = 6.5 Hz, C_m), 128.65 (s, C_p), 31.26 (d, *J*(³¹P-¹³C) = 12.7 Hz, C3*), 30.89 (d, *J*(³¹P-¹³C) = 15.1 Hz, C5*), 29.05 (s, C₄), 28.59 (d, *J*(³¹P-¹³C) = 12.5 Hz, C6*), 26.47 (d, *J*(³¹P-¹³C) = 16.3 Hz, C7*), 22.10 (d, ²*J*(³¹P-¹³C) = 4.6 Hz, C₂), 20.86 (d, ¹*J*(³¹P-¹³C) = 47.9 Hz, C₁), 6.01 (d, ¹*J*(³¹P-¹³C) = 51.56 Hz, C₈); **³¹P NMR** (C₆D₆, 202.28 MHz): δ (ppm) = 31.34 (s, R₃MeP⁺), -16.34 (s, RPh₂P). *assignments interchangeable.

HR-MS (MALDI⁺): [M⁺] = C₅₈H₇₅P₄ 895.4819 (calcd.), 895.5497 (found); [MO⁺] = C₅₈H₇₅P₄O 911.4768 (calcd.), 911.5306 (found); [MO₂⁺] = C₅₈H₇₅P₄O₂ 927.4718 (calcd.), 927.5779 (found).

(Diphenylphosphinoheptyl)diphenylmethylphosphonium iodide 16

10 (684 mg, 1.612 mmol), AIBN (83 mg, 0.505 mmol) and Ph₂PH (1070 mg, 5.746 mmol) were combined in a Schlenk flask and heated under a N₂ atmosphere to 70 °C and stirred for 5 d. The conversion was monitored by ³¹P NMR of the reaction mixture. Volatiles were removed *in vacuo* and the residue washed with pentane to yield **16** (950 mg, 1.556 mmol) as a white foam in 96 % yield.

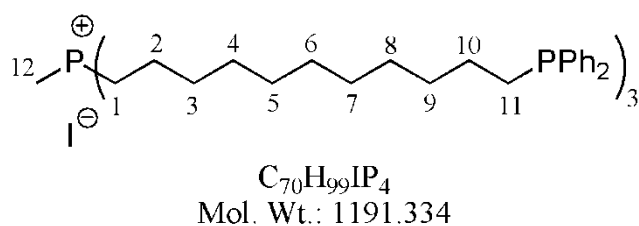


¹H NMR (CD₂Cl₂, 499.70 MHz): δ (ppm) = 7.82-7.88 (m, 4H, H^{P+}_{ortho}), 7.81 (t, ³J(¹H-¹H) = 7.8 Hz, 2H, H^{P+}_{para}), 7.69 (dt, ³J(¹H-¹H) = 7.1 Hz, ³J(³¹P-¹H) = 2.4 Hz, 4H, H^{P+}_{meta}), 7.40 (dd, ³J(³¹P-¹H) = 7.1 Hz, ³J(¹H-¹H) = 7.7 Hz, 4H, H^P_{ortho}), 7.29-7.35 (m, 6H, H^P_{para}/H^P_{meta}), 3.14 (dd, ²J(³¹P-¹H) = 13.4 Hz, ³J(¹H-¹H) = 8.1 Hz, 2H, H1), 2.74 (d, ²J(³¹P-¹H) = 13.5 Hz, 3H, CH₃), 2.02 (t, ³J(¹H-¹H) = 7.1 Hz, 2H, H4)*, 1.47-1.60 (m, 4H, H2, H3), 1.36-1.42 (m, 4H, H6,H7), 1.26-1.34 (m, 2H, H5)*, *assignments interchangeable; **¹³C NMR** (CD₂Cl₂, 125.66 MHz): δ (ppm) = 134.84 (s, d, ⁴J(³¹P-¹³C) = 2.9 Hz, C^{P+}_{para}), 132.57 (d, ²J(³¹P-¹³C) = 18.5 Hz, C^P_{ortho}), 132.45 (d, ²J(³¹P-¹³C) = 10.9 Hz, C^{P+}_{ortho}), 130.21 (d, ³J(³¹P-¹³C) = 12.4 Hz, C^{P+}_{meta}), 128.38 (s, C^P_{para}), 128.31 (d, ³J(³¹P-¹³C) = 6.5 Hz, C^P_{meta}), 30.65 (d, J(³¹P-¹³C) = 12.9 Hz), 30.11 (d, J(³¹P-¹³C) = 16.2

Hz), 28.50 (d, $^4J(^{31}\text{P}-^{13}\text{C}) = 0.9$ Hz, C4), 27.64 (d, $J(^{31}\text{P}-^{13}\text{C}) = 11.4$ Hz), 25.81 (d, $J(^{31}\text{P}-^{13}\text{C}) = 16.5$ Hz), 23.16 (d, $^1J(^{31}\text{P}-^{13}\text{C}) = 50.2$ Hz, C1), 21.96 (d, $^2J(^{31}\text{P}-^{13}\text{C}) = 4.1$ Hz, C2), 8.53 (d, $^1J(^{31}\text{P}-^{13}\text{C}) = 54.9$ Hz, CH₃), C^P_{ipso} and C^{P+}_{ipso} are missing due to low intensity; ^{31}P NMR (CD₂Cl₂, 202.28 MHz): δ (ppm) = 24.83 (s, P⁺), -16.71 (s, P).

Methyltris(11-diphenylphosphinoundecyl)phosphonium iodide **15**

Phosphonium salt **6** (507 mg, 0.801 mmol), AIBN (130 mg, 0.792 mmol), and Ph₂PH (0.9 ml, 963 mg, 5.172 mmol) were combined in a Schlenk flask, heated under a N₂ atmosphere to 70 °C and stirred for 4 d. The conversion was monitored by ^{31}P NMR of the reaction mixture. After completion of the reaction 2 ml of toluene was added to remove excess Ph₂PH, and the product precipitated after adding 3 ml of pentane. The supernatant was discarded and the solid was again treated with 2 ml of toluene and precipitated with 3 ml of pentane. The precipitate was dried *in vacuo* at 70 °C to give **15** (940 mg, 0.789 mmol) as a colorless oil in quantitative yield.



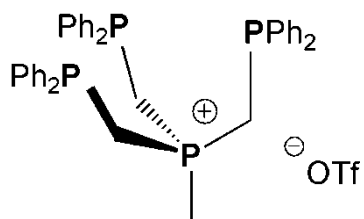
^1H NMR (C₆D₆, 499.70 MHz): δ (ppm) = 7.48 (dd, $^3J(^{31}\text{P}-^1\text{H}) = 7.7$ Hz, $^3J(^1\text{H}-^1\text{H}) = 7.6$ Hz, 12H, H_o), 7.16-7.05 (m, 18H, H_m, H_p), 2.53 (m, 6H, H1), 2.33 (d, $^2J(^{31}\text{P}-^1\text{H}) = 13.8$ Hz, 3H, H12), 2.02 (m, 6H, H10), 1.54 (m, 6H, H11), 1.49-1.21 (m, 48H, H2-H9); ^{13}C NMR (C₆D₆, 125.66 MHz): δ (ppm) = 140.03 (d, $^1J(^{31}\text{P}-^{13}\text{C}) = 14.7$ Hz, C_i), 133.16 (d, $^2J(^{31}\text{P}-^{13}\text{C}) = 18.6$ Hz, C_o), 128.71 (d, $^3J(^{31}\text{P}-^{13}\text{C}) = 6.4$ Hz, C_m), 128.63 (s,

C_p), 31.69 (d, $^3J(^{31}\text{P}-^{13}\text{C}) = 12.7$ Hz, C9*), 31.14 (d, $^3J(^{31}\text{P}-^{13}\text{C}) = 15.0$ Hz, C3), 30.11 (s, C4[#]), 30.07 (s, C5[#]), 29.98 (s, C6[#]), 29.79 (s, C7[#]), 29.61 (s, C8[#]), 28.67 (d, $^2J(^{31}\text{P}-^{13}\text{C}) = 12.5$ Hz, C10*), 26.56 (d, $^1J(^{31}\text{P}-^{13}\text{C}) = 16.4$ Hz, C11*), 22.19 (d, $^2J(^{31}\text{P}-^{13}\text{C}) = 4.7$ Hz, C2), 20.93 (d, $^1J(^{31}\text{P}-^{13}\text{C}) = 48.2$ Hz, C1), C12 signal not localized; **³¹P NMR** (C₆D₆, 202.28 MHz): δ (ppm) = 31.37 (s, R₃MeP⁺), -16.32 (s, RPh₂P). *,[#]assignments interchangeable.

HR-MS (MALDI⁺): [M⁺] = C₇₀H₉₉P₄ 1063.6697 (calcd.), 1063.6920 (found); [MO⁺] = C₇₀H₉₉P₄O 1079.6646 (calcd.), 1079.6873 (found); [MO₂⁺] = C₇₀H₉₉P₄O₂ 1095.6596 (calcd.), 1095.7205 (found).

Methyltris(diphenylphosphinomethyl)phosphonium triflate 18

Phosphine **17** (868 mg, 1.382 mmol) was dissolved in 50 ml of toluene and MeOTf (227 mg, 1.383 mmol), dissolved in 10 ml of toluene, was added dropwise over a period of 3 h. Then the reaction mixture was stirred overnight at RT. The product precipitated after adding 30 ml of pentane to the reaction mixture. The supernatant was removed and the precipitate was washed with pentane (2×10 ml), and subsequently with 50 ml of degassed H₂O. The residue was dried *in vacuo* to give **18** (709 mg, 0.894 mmol) as a colorless powder in 65% yield. Single crystals suitable for X-ray structure determination were grown from a solution in MeCN by slow evaporation of the solvent.



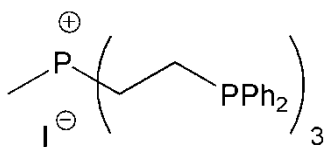
$C_{41}H_{39}F_3O_3P_4S$
Mol. Wt.: 792.702

1H NMR (C_6D_6 , 499.70 MHz): δ (ppm) = 7.45–7.40 (m, 12H, H_{ortho}), 7.38–7.35 (m, 18H, H_{meta} , H_{para}), 2.99 (d, $^2J(^{31}P-^1H) = 14.4$ Hz, 6H, CH_2), 1.33 (d, $^2J(^{31}P-^1H) = 14.4$ Hz, 3H, CH_3).; **$^{13}C\{^{31}P\}$ NMR** (C_6D_6 , 125.66 MHz): δ (ppm) = 134.85 (C_i), 133.00 (C_o), 130.37 (C_p), 129.32 (C_m), 21.73 (CH_2), 8.48 (CH_3); **^{31}P NMR** (C_6D_6 , 202.28 MHz): δ (ppm) = 35.16 (q, $^2J(^{31}P-^{31}P) = 54.3$ Hz, R_3MeP^+), -29.41 (d, $^2J(^{31}P-^{31}P) = 54.5$ Hz, RPh_2P); **^{19}F NMR** ($CDCl_3$, 470.17 MHz): δ (ppm) = -78.13 (CF_3).

Melting range 161–165 °C.

Methyltris(diphenylphosphinoethyl)phosphonium iodide **20**

Phosphine **19** (631 mg, 0.941 mmol) was dissolved in 40 ml of toluene and MeI (127.2 mg, 0.897 mmol) dissolved in 20 ml toluene was added dropwise whereupon a white precipitate formed. The supernatant, containing the product, was removed and the solvent was removed *in vacuo* to yield **20** (318 mg, 0.391 mmol) as a white solid in 44 % yield.

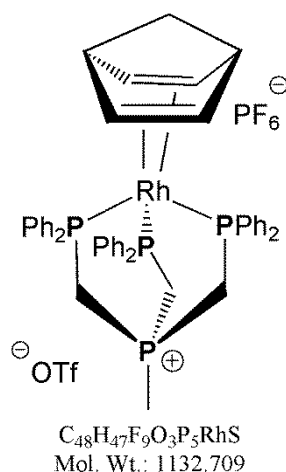


$C_{43}H_{45}IP_4$
Mol. Wt.: 812.617

¹H NMR (C₆D₆, 499.70 MHz): δ (ppm) = 7.64 (t, ³J (¹H-¹H) = 6.9 Hz, 12H, H_{meta})*, 7.18 (t, ³J (¹H-¹H) = 8.6 Hz, 12H, H_{ortho})*, 6.99-7.05 (m, 6H, H_{para}), 2.47 (d, ²J(¹³P-¹H) = 13.7 Hz, 3H, CH₃), 2.35-2.46 (m, 6H, PCH₂)[#], 2.23-2.32 (m, 6H, P⁺CH₂)[#], *,[#] assignment interchangeable; **¹³C NMR** (C₆D₆, 125.66 MHz): δ (ppm) = 137.54 (d, ¹J(³¹P-¹³C) = 13.7 Hz, C_{ipso}), 133.76 (d, ²J(³¹P-¹³C) = 19.1 Hz, C_{ortho}), 129.37 (s, C_{para}), 129.18 (d, ³J(³¹P-¹³C) = 6.8 Hz, C_{meta}), 20.12 (dd, ¹J(³¹P-¹³C) = 18.0 Hz, ²J(³¹P-¹³C) = 5.3 Hz, C), 17.91 (dd, ¹J(³¹P-¹³C) = 46.7 Hz, ²J(³¹P-¹³C) = 21.4 Hz, P⁺CH₂), 6.02 (d, ¹J(³¹P-¹³C) = 50.0 Hz, CH₃); **³¹P NMR** (C₆D₆, 202.28 MHz): δ (ppm) = 37.60 (q, ³J(³¹P-³¹P) = 40.1 Hz, P⁺), -12.41 (d, ³J(³¹P-³¹P) = 40.1 Hz, PPh₂).

Rhodium complex **21**

Ligand **18** (36 mg, 0.045 mmol) was dissolved in 4 ml of CH₂Cl₂ under a N₂ atmosphere. Then [Rh(nbd)₂]PF₆ (20 mg, 0.046 mmol), dissolved in 2 ml of CH₂Cl₂, was added. The reaction mixture was stirred for 30 min at RT, before the solvent was removed *in vacuo* and an orange powder was obtained. The residue was washed with pentane (2×5 ml) and dried *in vacuo* to give **21** (52 mg, 0.54 mmol) as an orange powder in quantitative yield. Single crystals suitable for X-ray structure determination were obtained by applying a pentane layer over a saturated solution of **21** in CH₂Cl₂.



^1H NMR (C_6D_6 , 499.70 MHz): δ (ppm) = 7.37 (t, $^3J(^1\text{H}-^1\text{H}) = 7.4$ Hz, 6H, H_p), 7.17 (t, $^3J(^1\text{H}-^1\text{H}) = 7.4$ Hz, 12H, H_m), 7.05 (broad t, $^3J(^{31}\text{P}-^1\text{H}) = 8.3$ Hz, $^3J(^1\text{H}-^1\text{H}) = 7.7$ Hz, 12H, H_o), 3.84 (s, 2H, CH), 3.64 (s, 4H, =CH), 3.48 (d, $^2J(^{31}\text{P}-^1\text{H}) = 11.4$ Hz, 6H, PCH_2), 2.69 (d, $^2J(^{31}\text{P}-^1\text{H}) = 14.3$ Hz, 3H, CH_3), 1.46 (s, 2H, CH_2); **$^{13}\text{C}\{^{31}\text{P}\}$ NMR** (C_6D_6 , 125.66 MHz): δ (ppm) = 143.67 (=CH), 133.25 (C_i), 132.03 (C_o), 131.61 (C_p), 129.82 (C_m), 75.60 (CH_2), 63.00 (d, $^1J(^{103}\text{Rh}-^{13}\text{C}) = 3.3$ Hz, =CH*), 50.45 (d, $^2J(^{103}\text{Rh}-^{13}\text{C}) = 5.8$ Hz, PCH_2^*), 46.6 (CH), 19.36 (CH_3); **^{31}P NMR** (C_6D_6 , 202.28 MHz): δ (ppm) = 38.88 (dq, $^2J(^{31}\text{P}-^{31}\text{P}) = 21.3$ Hz, $^3J(^{103}\text{Rh}-^{31}\text{P}) = 7.8$ Hz, R_3MeP^+), 7.19 (d, $^1J(^{103}\text{Rh}-^{31}\text{P}) = 118.3$ Hz, $^2J(^{31}\text{P}-^{31}\text{P}) = 21.2$ Hz, RPh_2P), -145.00 (sept, $^1J(^{31}\text{P}-^{19}\text{F}) = 712.5$ Hz, PF_6); **^{19}F NMR** (CDCl_3 , 470.17 MHz): δ (ppm) = -71.38 (d, $^1J(^{31}\text{P}-^{19}\text{F}) = 712.5$ Hz, PF_6), -78.71 (CF_3). *assignments interchangeable.

CHAPTER III

TRIDENTATE PHOSPHINE LINKERS FOR IMMOBILIZED CATALYSTS – IMMOBILIZATION VIA COVALENT BONDS

INTRODUCTION

The shortage of resources and the implementation of a sustainable energy economy highlight the pivotal role of catalysis in chemistry. The necessity to use energy more efficiently and generate commodity chemicals from emerging feedstocks increases the demand for improved catalysts. Immobilized catalysts are especially promising as they aim to combine the advantages of homogeneous and heterogeneous catalysts.^{1,7,40} Their molecular nature should assure high activity and make them amenable to rational catalyst design by fine-tuning the ligand environment. Immobilization on a suitable support facilitates handling, product separation, and recycling. Furthermore, site isolation on the surface can prevent certain deactivation pathways, such as dimerization, compared to catalysts in solution. In favorable cases the spatial confinement of immobilized catalysts can even lead to higher selectivities compared to their homogeneous analogs.⁸² In this way improved catalysts can make a significant impact towards a more sustainable production and conversion of chemicals. Yet there is a striking imbalance between extensive work published in academia and the very few large scale industrial processes employing immobilized catalysts.⁸³ To be relevant for industrial applications the immobilized catalyst has to be stable under the reaction conditions over extended periods of time, but the fate of the catalytic species is neglected in many studies. Only a thorough understanding of the failure mechanisms allows rational and timely improvement in the way catalysts are immobilized and recycled.

To achieve the objectives mentioned above a detailed knowledge of the surface chemistry is paramount. One key aspect is the nature of the active catalyst site for a given system and whether it is molecular in nature or consists of metal aggregates or nanoparticles.⁸⁴ Related to this, many aspects of the mechanism of nanoparticle formation on solid supports remain elusive despite tremendous progress in this field.⁸⁵ The study of these interactions is often hampered by the amorphous nature of many supports and the difficulty to discriminate the interfacial surface area from the bulk support.

Even though surface atoms can act as donors for metal coordination, e. g. oxygen atoms on silica or alumina surfaces,^{74,86} it is advantageous to introduce conventional ligands, and thus prevent potential decomposition of sensitive metal complexes on reactive support surfaces. This also allows tuning the electronic and steric properties of the donor. Phosphines are one of the most widely used classes of ligands in catalysis, and they can be easily immobilized on an oxide support like silica^{37b,c} by ethoxysilane groups.^{62b,c,g} This strategy has led to many successful transition metal catalysts, such as Rh,^{62g-i,42} Ni,^{62d,f} and Pd^{62m,n} complexes for a variety of reactions, most notably hydrogenations.^{62g-i,h}

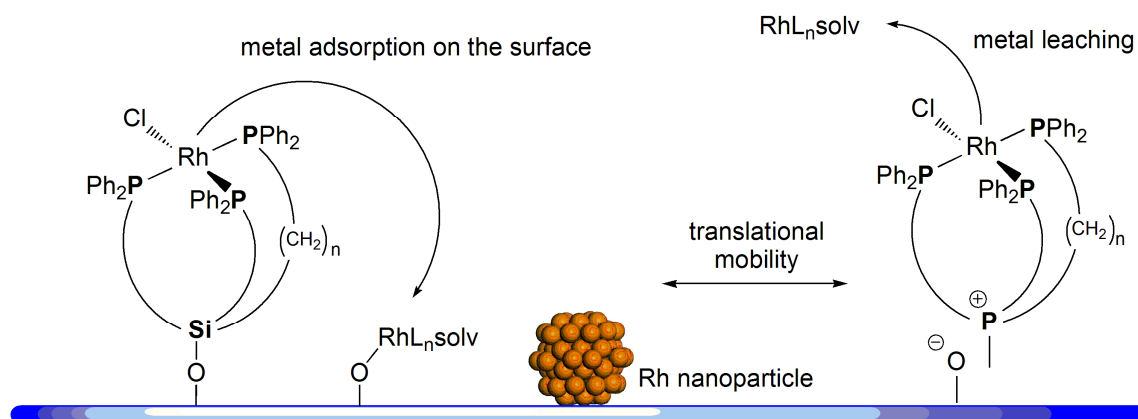


Figure 3.1. Possible pathways leading to the formation of Rh nanoparticles from single-site catalyst.

Blümel *et al.* described the immobilization of tridentate phosphines with long alkyl chains via a phosphonium linker (chapter II) in a recent paper.⁴⁵ No ligand leaching was observed in non-polar solvents, such as toluene, and highly active hydrogenation catalysts were obtained after coordination of the immobilized phosphine ligands to Wilkinson-type Rh complexes. It has been shown that the monomolecular species were transformed within the first 5 hours of the reaction into Rh nanoparticles with a narrow size distribution. These nanoparticles are located in the pores of the support material, which explains their narrow size distribution. In the course of the reaction these nanoparticles contribute to the product formation as active hydrogenation catalysts, but the controlled ligand environment of a molecular species is lost. HRMAS NMR experiments suggest that, although the ligands do not leach from the surface, they are translationally mobile on the surface, which might facilitate the formation of Rh nanoparticles (Figure 3.1).^{45,65}

The aim of the work presented in this chapter is to test whether the translational mobility of the phosphine ligands on the surface propagates the formation of

nanoparticles by bringing the Rh centers in direct contact with each other. For this purpose, tridentate phosphine linkers of the analogous type are synthesized and immobilized on silica in a covalent manner via ethoxysilane groups. The covalent attachment renders translational mobility impossible, as proven, for example, by the dependence of the catalytic activity from the distance of the ligands on the surface.^{62g,h}

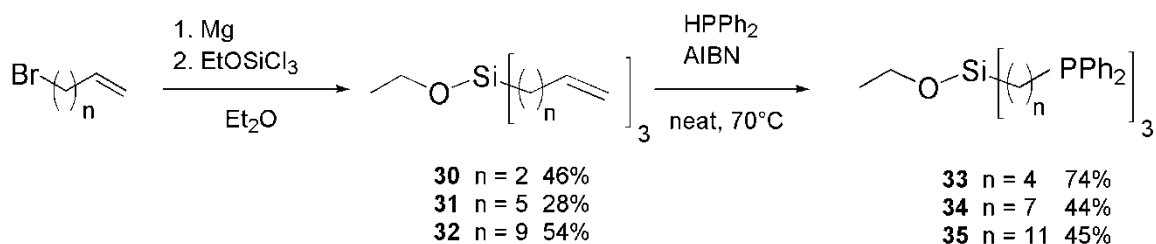
At this point it is worth noting that this methodology leads to highly dispersed linkers on the silica surface.^{42,62g-i,64a,b} This has also been demonstrated recently by Reek *et al.* using two-photon fluorescence spectroscopy.^{64b} The group used triethoxysilanes and observed that the reaction conditions influenced the distribution on the surface. Condensation of the precursors in solution prevents highly dispersed ligand sites on the support. Using monoethoxysilanes prevents condensation of the linkers prior to immobilization which would lead to cross-linking of the ligands and clustering of the metal complexes on the surface.

The ligands **33**, **34**, and **35** were synthesized and immobilized on silica. The immobilized ligands and their respective Rh complexes were characterized by solid-state NMR. Their activities with respect to the hydrogenation of 1-dodecene and the lifetimes of the catalysts were studied. Furthermore, the nature of the active species, especially regarding potential nanoparticle formation, was investigated.

RESULTS AND DISCUSSION

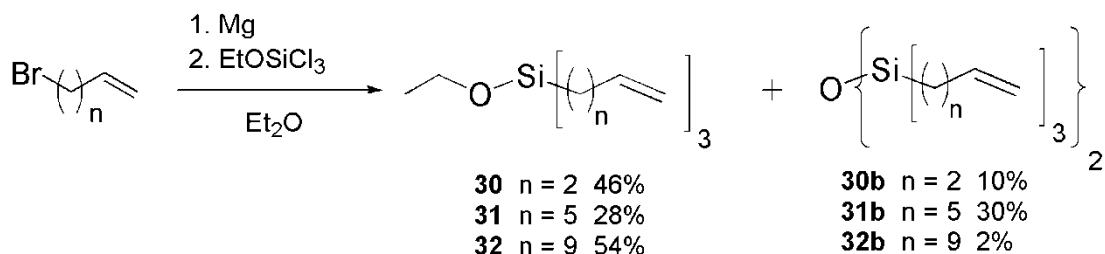
Ligand Synthesis

The new phosphine ligands **33**, **34**, and **35** were obtained by two standard synthetic procedures in good yields starting from the respective bromoalkenes $\text{Br}(\text{CH}_2)_n\text{CH}=\text{CH}_2$ ($n = 2, 5, 9$) (Scheme 3.1).^{52b}



Scheme 3.1. Synthesis of the unsaturated ethoxysilanes **30**, **31**, and **32**, and the phosphine ligands **33**, **34**, and **35**.

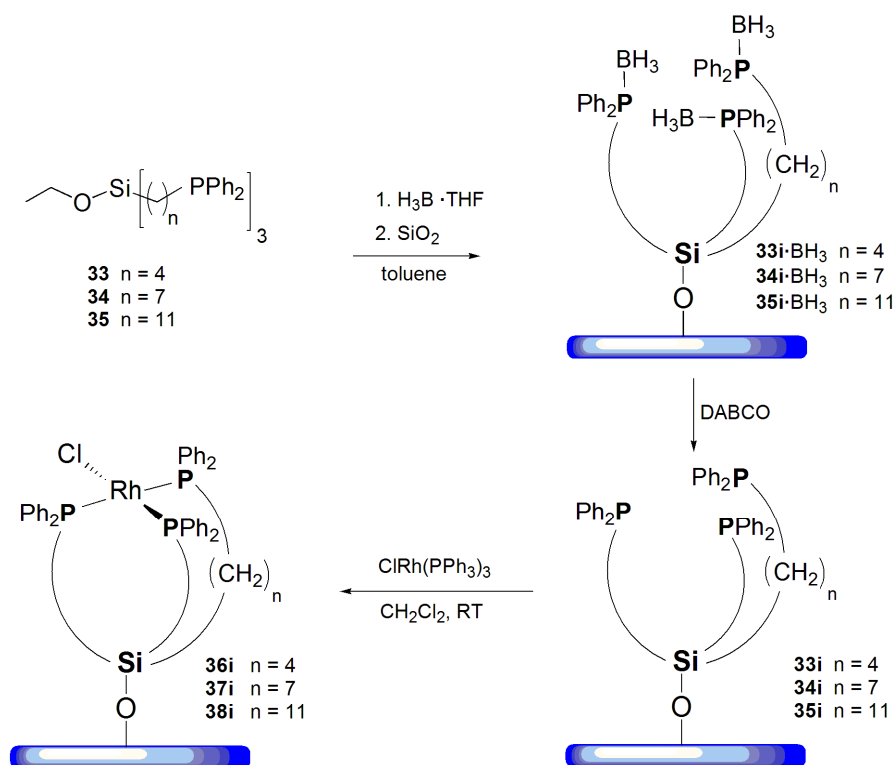
The bromoalkenes were treated with Mg to form the Grignard reagents and subsequently reacted with EtOSiCl₃ to give **30** to **32** as colorless liquids. Hydrolysis and condensation of the ethoxysilane groups due to traces of water in the reaction mixtures led to the formation of O[Si((CH₂)_nCH=CH₂)₃]₂ ($n = 2, 5, 9$) **30b** to **32b** as byproducts in varying amounts (Scheme 3.2).



Scheme 3.2. Synthesis of **30**, **31**, and **32** and the corresponding byproducts **30b**, **31b**, and **32b**.

The linkers **33** to **35** were obtained by hydrophosphination of **30** to **32** with a slight excess of Ph₂PH in the presence of AIBN as a radical starter as described by Stelzer *et*

*al.*⁵³ The hexaphosphines $\text{O}[\text{Si}((\text{CH}_2)_n\text{PPh}_2)_3]_2$ ($n = 4, 7, 11$), **33b** to **35b**, were synthesized in an analogous manner by hydrophosphination of **30b** to **32b**.



Scheme 3.3. Synthesis and immobilization of the borane-protected phosphine ligands **33i**· BH_3 , **34i**· BH_3 , and **35i**· BH_3 , on SiO_2 and formation of the immobilized Rh complexes **36i**, **37i**, and **38i**.

Immobilization and NMR Spectroscopic Characterization of the Phosphine Linkers and Rh Complexes

The linkers **33-35** were immobilized on silica via a covalent Si-O-Si bond as described in the literature (Scheme 3.3).^{52b,62b,c,g} To achieve appreciable surface loadings, the immobilization required elevated temperatures. Carrying out the immobilization of the unprotected phosphine linkers led to the covalently bound phosphine but it was accompanied by partial phosphine oxidation and quaternization (Table 3.1, Entry 1) as reported earlier by the Blümel group.^{63b} To prevent phosphine oxidation and alkylation during the immobilization step the ligands **33** to **35** were protected as the respective borane adducts *in situ* with H₃B·THF. After the immobilization step at elevated temperatures, the phosphines were deprotected with DABCO (1,4-diazabicyclo[2.2.2]octane) at room temperature to yield **33i** to **35i**. As an alternative to using the ethoxysilanes **33** to **35** the immobilization can also be carried out with the disiloxanes **33b** to **35b** which lead to comparable surface loadings. To the best of our knowledge, it has never been previously reported that molecular siloxanes can be bound directly to silica surfaces. The reaction temperatures and the corresponding surface coverages are summarized in Table 3.1.

Table 3.1. Surface coverages of the modified silica **33i** to **35i** with the corresponding molecular species **X** (**33** to **35**, and **33b** to **35b**).

Material	Reaction time [h]	T [°C]	Molecules per 100 nm ² SiO ₂	mmol of X per g SiO ₂
33i	24 ^[a]	70	11.5	0.143 ^[b]
33i	72	70	8.2	0.110
33i	72	60	3.2	0.040
34i	48	70	3.0	0.037
35i	72	80	2.7	0.034
33bi	72	90	14.6	0.183
34bi	48	90	5.4	0.068
35bi	24	90	10.2	0.127

^[a] SiO₂ and unprotected ligand were stirred in toluene overnight at 70 °C. ^[b] Partial oxidation and alkylation of phosphine.

The silica functionalized with phosphine ligands **33i** to **35i** and **33bi** to **35bi** were characterized by ²⁹Si CP/MAS, ³¹P CP/MAS, and ³¹P HRMAS NMR.⁴¹ The surface-bound trialkylsiloxane can be observed by ²⁹Si CP/MAS in the expected chemical shift range as a resonance at 6.0 ppm (Figure 3.2).^{45,70} The ²⁹Si signal corresponding to O₃Si-OH and O₃Si-OEt surface silicon species appears at -104 ppm, the resonance for internal O₄Si at -111 ppm.

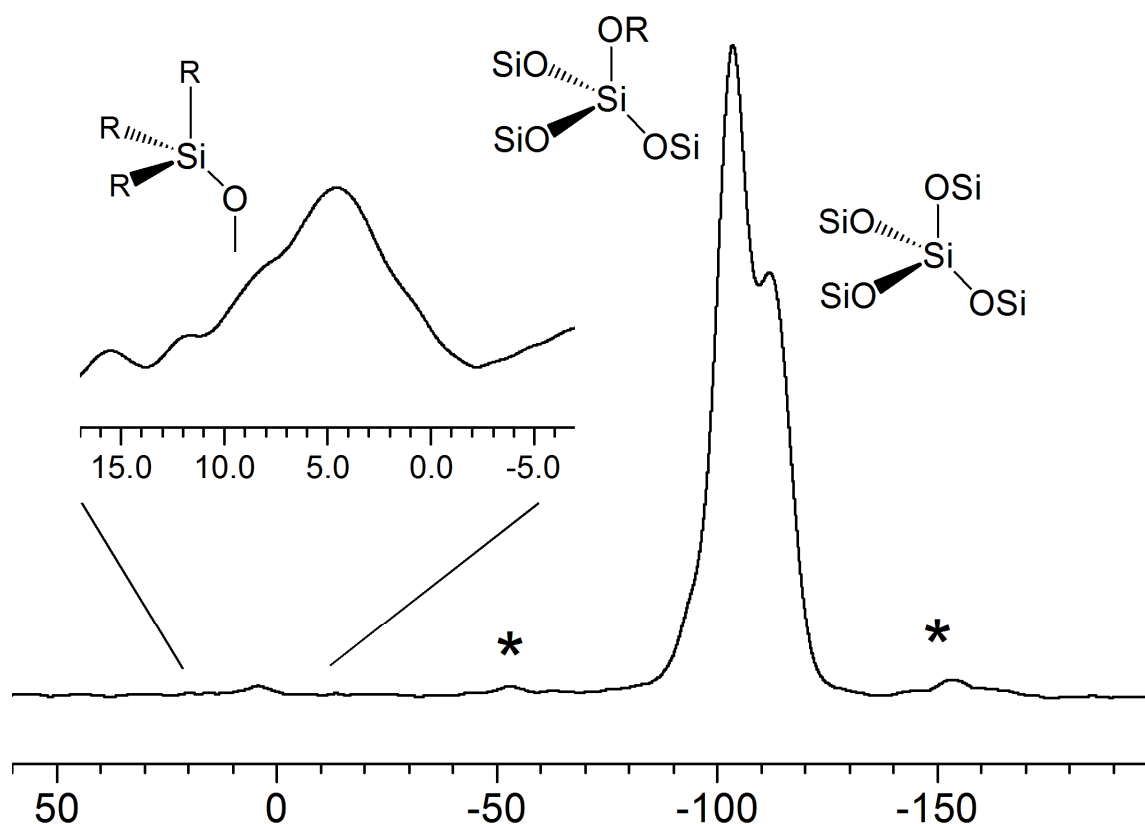


Figure 3.2. ^{29}Si CP/MAS NMR of **33bi** (4 kHz spinning speed). Asterisks denote rotational sidebands of the signal at -104 ppm.

The immobilized phosphine boranes **33**·BH₃ to **35**·BH₃ lead to resonances at ca. 15 ppm characteristic for borane adducts of phosphines. Deprotection with DABCO was quantitative, proven by the disappearance of the peak at 15 ppm and a new signal shifted upfield to about -16 ppm for the unprotected phosphines (Figure 3.3).

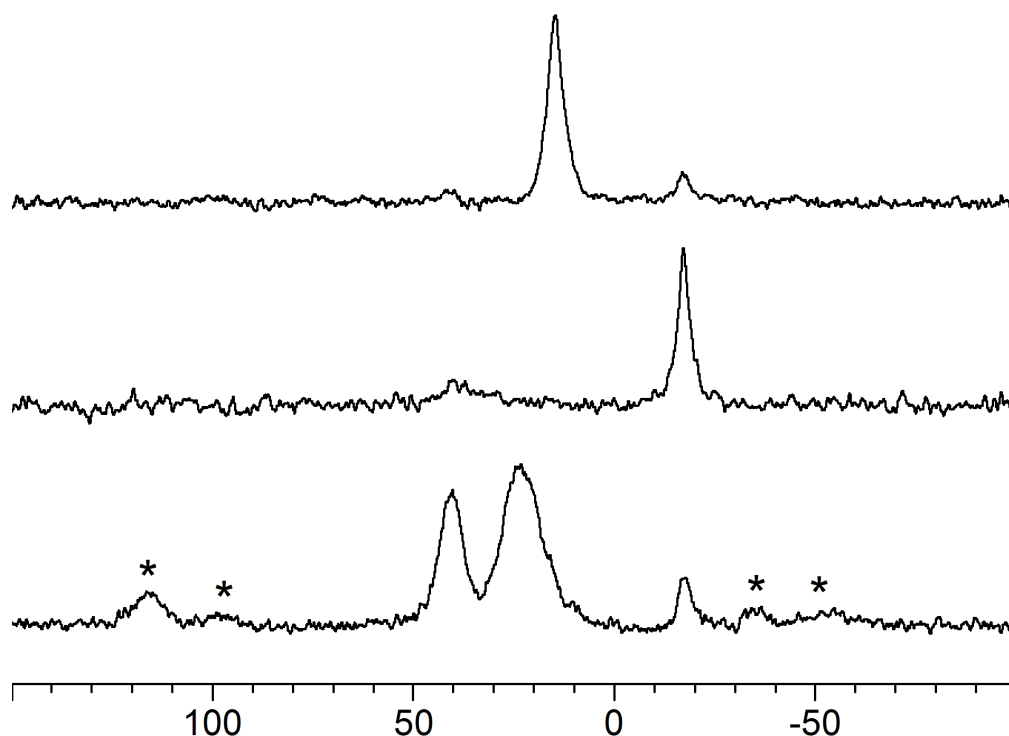


Figure 3.3. ^{31}P CP/MAS NMR of **35i**· BH_3 (*top*), **35i** (*middle*) and **38i** (*bottom*) (10 kHz spinning speed). Asterisks denote rotational sidebands.

The long alkyl chain linkers lead to increased mobility of the phosphine groups in the presence of an organic solvent making the functionalized silica materials **33i** to **35i** amenable to characterization by ^{31}P HRMAS NMR.^{56,62j,k,l} The linewidths in HRMAS NMR spectra qualitatively reflect the mobility of immobilized species, as fast motion leads to partial averaging of the CSA (chemical shift anisotropy) and dipolar interactions.^{62j,62l,87} Initial HRMAS measurements were carried out in toluene guided by earlier work in our group (chapter II).^{62m,n} Following expectations, the signal linewidths drastically decrease as compared to the linewidths in ^{31}P CP/MAS spectra of the same dry materials (Figure 3.4). This is advantageous with respect to the decreased measurement time, which is minutes instead of hours now. More importantly, the

spectral resolution is superior in HRMAS (see below). As expected, the linewidth decreases from 480 Hz for **33i** to 93 Hz for **35i** with increasing alkyl chain length (Table 3.2).

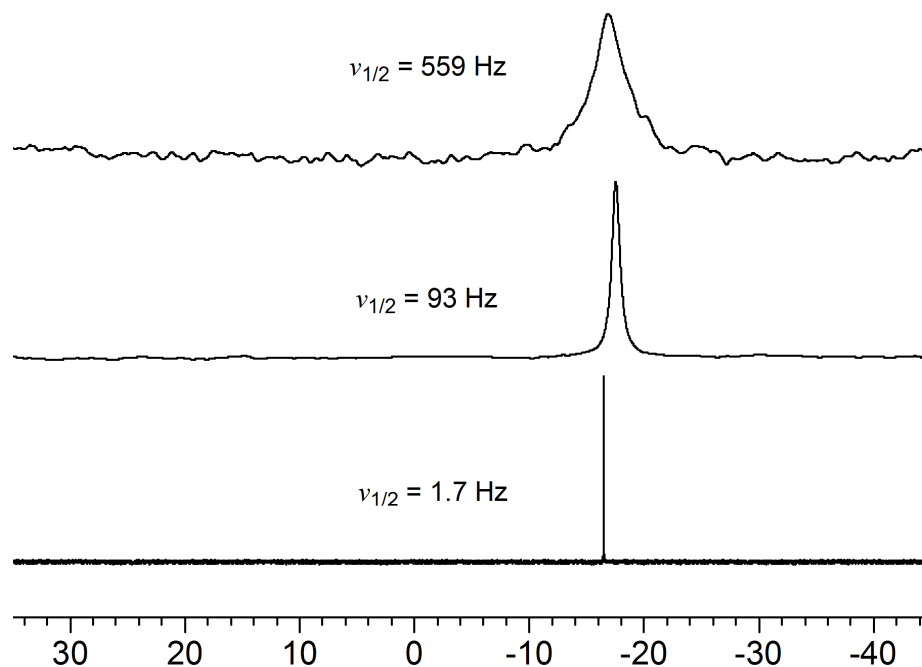


Figure 3.4. ^{31}P NMR of **35** (solution in CDCl_3 , *bottom*), ^{31}P HRMAS of a slurry of **35i** in toluene (*middle*, 2 kHz spinning speed), ^{31}P CP/MAS of dry **35i** (*top*, 10 kHz).

Table 3.2. ^{31}P MAS and HRMAS NMR chemical shifts δ and signal halfwidths $\Delta\nu_{1/2}$ for the phosphine signals of the ligand-modified silica **33i** to **35i**. Rotational frequencies were 10 kHz for MAS and 2 kHz for HRMAS measurements of slurries with toluene.

Material	MAS $\delta(^{31}\text{P})$ [ppm]	HRMAS $\delta(^{31}\text{P})$ [ppm]	MAS $\Delta\nu_{1/2}$ [Hz]	HRMAS $\Delta\nu_{1/2}$ [Hz]
33i	-16.78	-16.84	1351	480
34i	-17.16	-17.50	900	130
35i	-16.87	-17.53	559	93

^{31}P HRMAS spectra for **35i** were recorded in various organic solvents that are relevant for synthesis and catalysis in this work, and compared to the spectra of the analogous phosphine linker **15i** (Figure 3.5; chapter II) immobilized via a phosphonium group (Table 3.3). In all solvents studied the signals are broader in the case of the covalently bound phosphine, proving that the line-narrowing effect in the case of material **15i** is due to both, movement of the phosphine “arms” as well as the translational mobility of the entire linker on the surface. Detachment of **15i** from the surface was ruled out for non-polar solvents such as toluene and hydrocarbons. These measurements show that the linkers **33i** to **35i** still retain a high degree of motion and the respective catalysts should therefore mimic homogeneous catalysis optimally while the covalent attachment prevents potential dimer and cluster formation as pathways to catalyst decomposition (Figure 3.1).

Table 3.3. Signal halfwidths $\Delta\nu_{1/2}$ in the ^{31}P HRMAS spectra of **35i** and **15i** as slurries in the respective solvents.

solvent	35i $\Delta\nu_{1/2}$ [Hz]	15i $\Delta\nu_{1/2}$ [Hz]
MeOH	83	24
MeCN	83	22
THF	90	34
Acetone	142	34
CH_2Cl_2	90	20
Toluene	93	26
Hexane	205	134

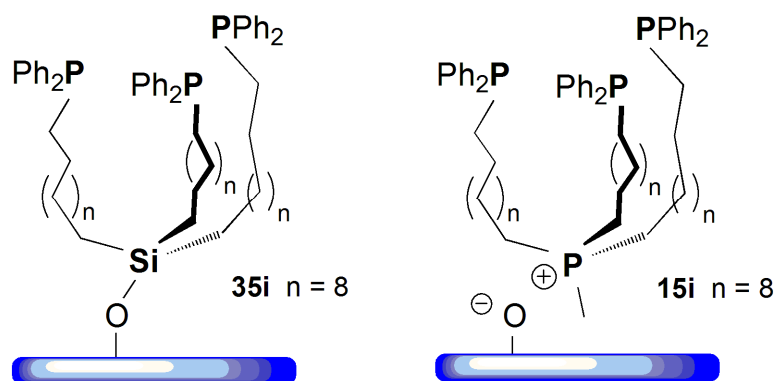


Figure 3.5. Tridentate phosphine linkers **35i** and **15i**, which has been immobilized by electrostatic interactions with the silica surface.⁴⁵

The immobilized Rh complexes **36i** to **38i** have been obtained from **33i** to **35i** by ligand exchange with Wilkinson's catalyst $\text{ClRh}(\text{PPh}_3)_3$ at room temperature (Scheme 3.3).^{42,62g-i} The ^{31}P CP/MAS NMR spectra show that none of the liberated PPh_3 remains adsorbed at the surface after washing the materials with toluene (Figure 3.3, bottom). The phosphine coordinated *trans* to the Cl ligand leads to a peak at 40.29 ppm and the signal of the two phosphines *cis* to Cl is found at 24.04 ppm.^{42,62g-i,88}

The use of soluble Rh precursors that lack triphenylphosphine ligands are of additional interest, since the immobilization of Wilkinson's catalyst can lead to the formation of $[(\text{PPh}_3)_2\text{RhCl}]_2$ at elevated temperatures, which is strongly adsorbed at the silica surface.⁸⁹ Therefore, RhClpyCOD **39** has been investigated as an alternative metal precursor. Although the complex was published as early as 1973, its X-ray crystal structure has not yet been reported.^{90a} Crystals suitable for single crystal X-ray diffraction were obtained by slow evaporation of the solvent from a MeCN solution of **39** (Appendix A). The structure shows a square planar geometry with respect to the coordinating N and Cl, and the centers of the C=C bonds. All bond lengths and angles

are in the expected range (Figure 3.6; Table 3.4). Rajput *et al.* reported the X-ray structure of a related compound incorporating a ferrocenyl substituent on the pyridine ligand.^{90b} In this compound, for example, the Rh-Cl distance is 2.358 Å and the bonds to the carbons *trans* to pyridine are lengthened as compared to the Rh-C bonds *trans* to Cl. That complex also displays a square planar geometry with a N-Rh-Cl bond angle of 88.26°.

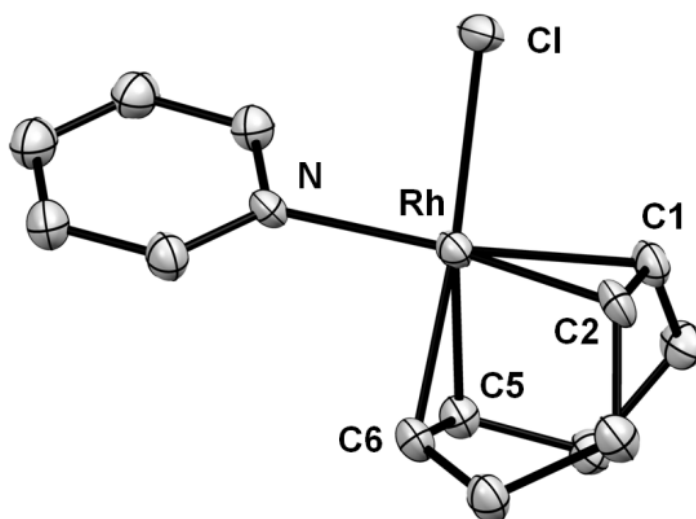
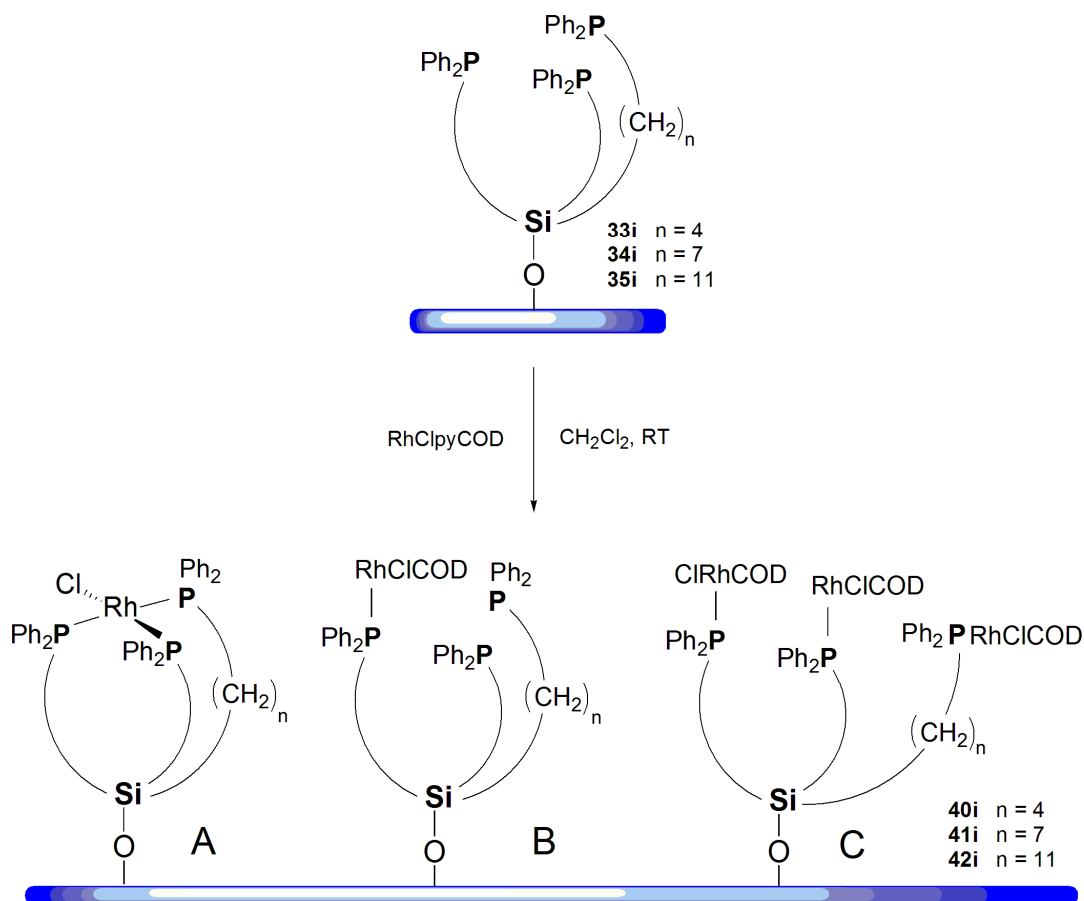


Figure 3.6. ORTEP representation of RhClpyCOD **39** showing 50% thermal ellipsoid probability. H atoms are omitted for clarity.

Table 3.4. Selected bond lengths and angles of RhClpyCOD **39**.

Bond lengths [Å]		Bond angles [°]	
Rh – N	2.125(8)	N – Rh – Cl	87.5(2)
Rh – Cl	2.377(2)	N – Rh – C2	157.8(4)
Rh – C1	2.137(10)	N – Rh – C1	163.7(3)
Rh – C2	2.133(9)	C6 – Rh – N	91.9(3)
Rh – C5	2.107(10)	C5 – Rh – N	93.8(3)
Rh – C6	2.102(9)	Cl – Rh – C5	157.7(3)
C1 – C2	1.409(5)	Cl – Rh – C6	163.5(3)
C5 – C6	1.397(2)	Torsion angles [°]	
		C1 – C2 – Rh - N	178.9(8)
		C5 – C6 – Rh - N	88.3(6)

The ligand exchange reactions were carried out in analogy to the procedure for Wilkinson's catalyst (Scheme 3.4). It is noteworthy that the materials obtained after thorough washing were yellow or slightly orange as compared to the bright orange silica obtained when using $\text{ClRh}(\text{PPh}_3)_3$ for the ligand exchange. The functionalized materials **40i** to **42i** were analyzed by ^{31}P CP/MAS and ^{31}P HRMAS NMR (Figures 3.7 and 3.8).



Scheme 3.4. Synthesis of the immobilized Rh complexes **40i**, **41i**, and **42i**.

When reacting **35i** with one equivalent of RhClpyCOD a spectrum similar to **38i** is observed, but showing a large signal corresponding to uncoordinated phosphine. When using three equivalents of RhClpyCOD **39** no more uncoordinated phosphine remains and the intensity of the peak at 25 ppm which corresponds to a phosphine *cis* to Cl increases (Figure 3.7). Most likely, in the latter case each phosphine is coordinated to a separate Rh center leading predominantly to structure C (Scheme 3.4). When using one equivalent of RhClpyCOD the majority of the species resemble structure A, resulting in

a 1 : 2 ratio of the resonances at 40 ppm and 24 ppm. The minor presence of species with the structure B cannot be ruled out.

To confirm this assumption, the coordination chemistry of **35** in solution was studied. **35** reacts with one equivalent of RhClpyCOD in CH₂Cl₂ under dilute conditions (1 mM) to form a Wilkinson-type complex with ³¹P resonances at 25.34 ppm (dd, ¹J(¹⁰³Rh-³¹P) = 138.7 Hz, ²J(³¹P-³¹P) = 39.8 Hz) and 37.54 ppm (dt, ¹J(¹⁰³Rh-³¹P) = 193.6 Hz, ²J(³¹P-³¹P) = 39.8 Hz). Upon concentration of the solution, an orange precipitate forms which is insoluble in organic solvents. This can be explained by the formation of a coordination polymer with the Rh center acting as a node. Potential condensation of the siloxane groups may also contribute to the poor solubility. Employing three equivalents of RhClpyCOD with respect to **35** in CH₂Cl₂ gives complex **43** cleanly. **43** displays only a single resonance in ³¹P NMR at 26.14 ppm with a large ¹J(¹⁰³Rh-³¹P) coupling (Figure 3.8, *bottom*). The preference to substitute the ligand *cis* to Cl prior to COD has also been observed for ligand **16** (Scheme 2.25, Chapter II) and this is in accord with a report by Gray *et al.*⁹¹ In support of this interpretation, the ³¹P HRMAS NMR spectrum of **43i** shows a clearly resolved doublet at 25.7 ppm with a ¹J coupling constant of 148.7 Hz between ¹⁰³Rh and ³¹P.

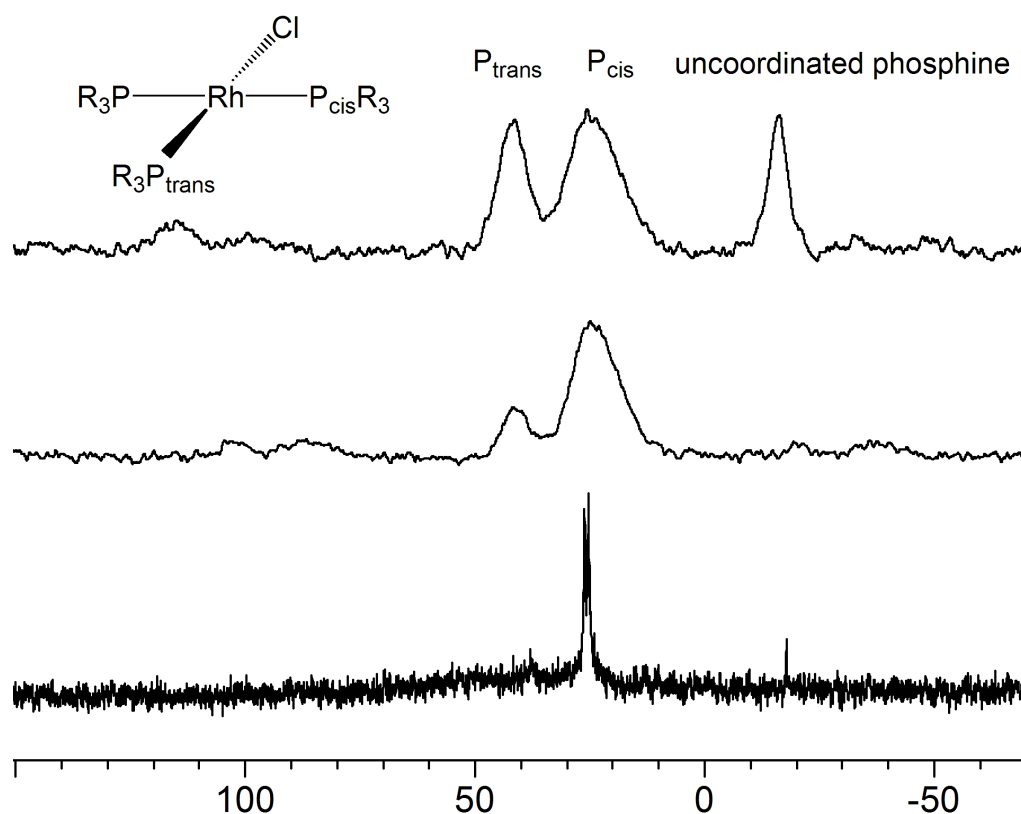


Figure 3.7. ^{31}P HRMAS NMR spectrum of **35i** after the reaction with three equivalents of RhClpyCOD **39** (slurry in acetone, *bottom*), ^{31}P CP/MAS of **35i** after the reaction with three equivalents of RhClpyCOD **39** (*middle*), and one equivalent of RhClpyCOD (*top*).

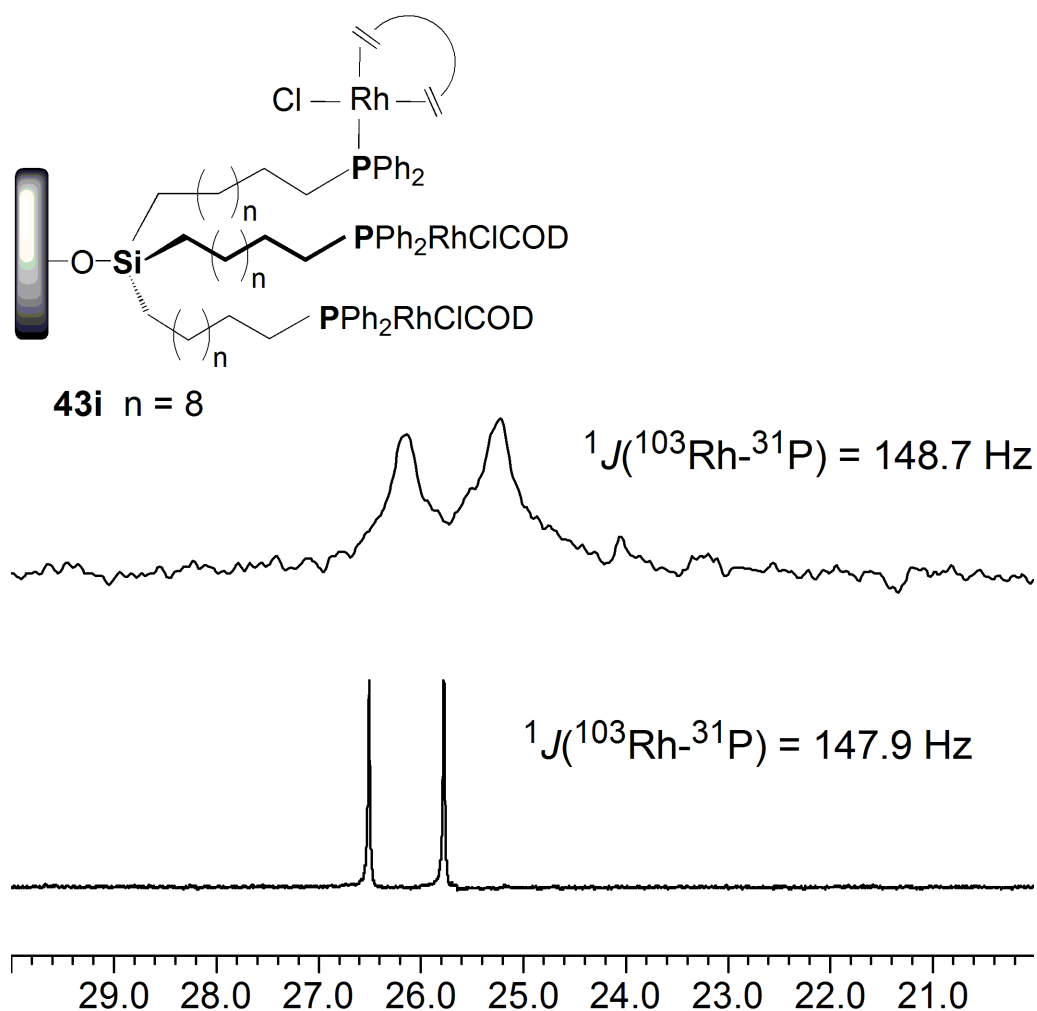
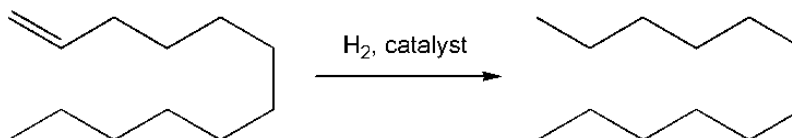


Figure 3.8. ^{31}P HRMAS NMR of **43i** (slurry in acetone, *top*), and ^{31}P NMR of **43** (solution in CDCl_3 , *bottom*).

Application of Rh Complexes in Catalytic Olefin Hydrogenation

Few reactions in transition metal catalysis have enjoyed a more detailed investigation than hydrogenation both in solution and on surfaces.^{62g-i,72} The hydrogenation of olefins in particular is of great importance for industrial applications and fundamental research. Therefore, the hydrogenation of 1-dodecene was chosen as a

model system to investigate the catalytic activity of the functionalized silica **36i** to **38i** and **40i** to **42i** (Scheme 3.5).^{19b,42,62g-i,88}



Scheme 3.5. Catalytic hydrogenation of 1-dodecene; pressure 1.1 atm, substrate to catalyst ratio 100 : 1, reaction temperature 60 °C.

Figures 3.9 and 3.10 show the hydrogen uptake of **36i** to **38i**, and **40i** to **42i**, respectively. The materials obtained using Wilkinson's catalyst as precursor show no induction period and lead to fast hydrogen uptake in the first few hours before slowing down somewhat after 2-3 h. The Rh complex **38i** with the longest alkyl chain is the most active catalyst, confirming the assumption that the higher degree of mobility of the catalyst results in higher activity. It is noteworthy to mention, however, that the materials darken gradually and turn brown overnight. The complexes with chain lengths of 7 and 4 CH₂ units show comparable catalytic activities.

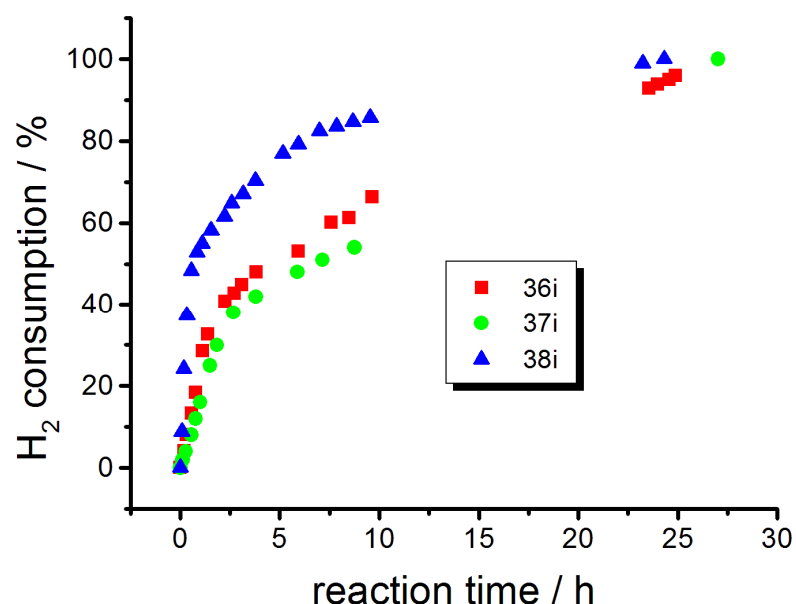


Figure 3.9. Activities of the indicated immobilized catalysts for the hydrogenation of 1-dodecene in the first run.

The activity of **40i** to **42i** in the first run is shown in Figure 3.10. There is a significant difference as compared to **36i** to **38i**, as all three materials show an induction period with no initial hydrogen uptake (Figure 3.11). An induction period is characteristic for systems in which the employed metal complex is not an active catalyst itself and needs to be transformed into an active species, which can be another molecular species, an aggregate, or a nanoparticle. Especially **41i** shows a sigmoidal hydrogen uptake which has been described by Finke *et al.* as a hallmark of nanoparticle formation.⁷⁵ Similar to the catalysts **36i** to **38i**, **40i** to **42i** also change color from yellow or slightly orange to black within the first run. Two scenarios can explain the experimental observation: (a) The induction period is due to the transformation of the molecular species into metal nanoparticles which constitute the catalytically active species. (b) Alternatively, the immobilized Rh complexes still bearing COD as a ligand

are not catalytically active and have to undergo ligand loss to become active species. It is also possible that both scenarios (a) and (b) occur simultaneously. The length of the induction period is in the order of minutes and does not correlate well with the color change of the materials within hours and which is most notable after full conversion of the substrate. To investigate the role of the COD ligand the hydrogen uptake with $\text{ClRh}(\text{PPh}_3)_3$ as the catalyst in the presence of two equivalents of COD was monitored. The solution was yellow in contrast to the orange solution in the absence of COD and no hydrogen uptake was observed within the first ten hours. This might be due to slow dissociation of the COD ligand or due to the slow hydrogenation of the internal double bonds of COD.⁹² These observations render scenario (b) highly likely as the reason of the induction period.

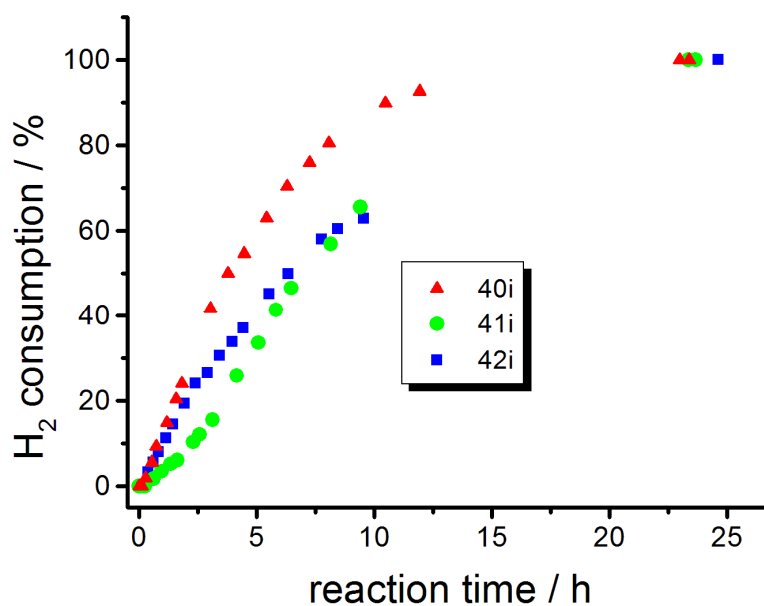


Figure 3.10. Activities of the indicated immobilized catalysts for the hydrogenation of 1-dodecene in the first run.

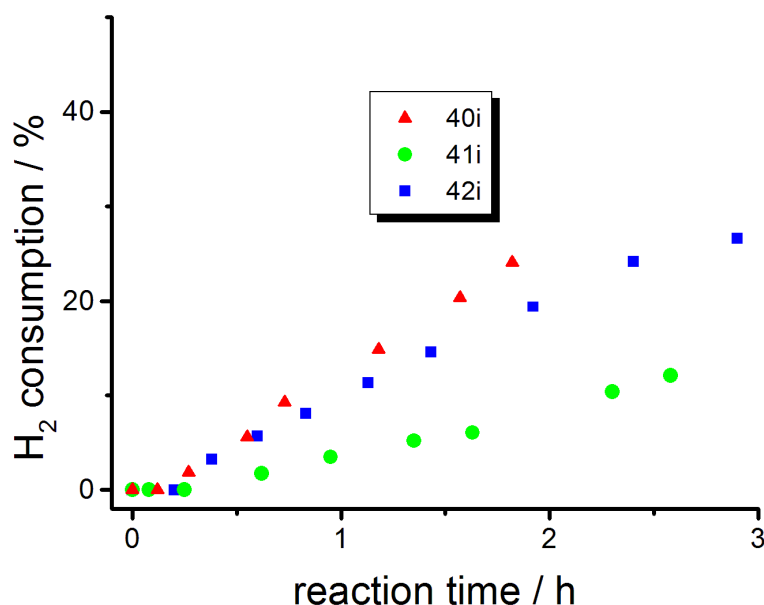


Figure 3.11. Activities of the indicated immobilized catalysts for the hydrogenation of 1-dodecene in the first run, showing only the beginning of the catalytic reaction with the induction period. For full run see Figure 3.10.

Next, the nature of the active species in the case of **36i** to **38i** was further investigated. A three-phase test similar to the one reported by Collman and coworkers was carried out using allyltriethoxysilane as the substrate, immobilized on a different silica batch (Table 3.1).⁷⁶ No hydrogen uptake is detected using **38i** as catalyst, proving that the catalytic activity is associated with the solid support and no active species leach into the solution (Figure 3.12). Wilkinson's catalyst showed full conversion within 24 h in a control experiment.

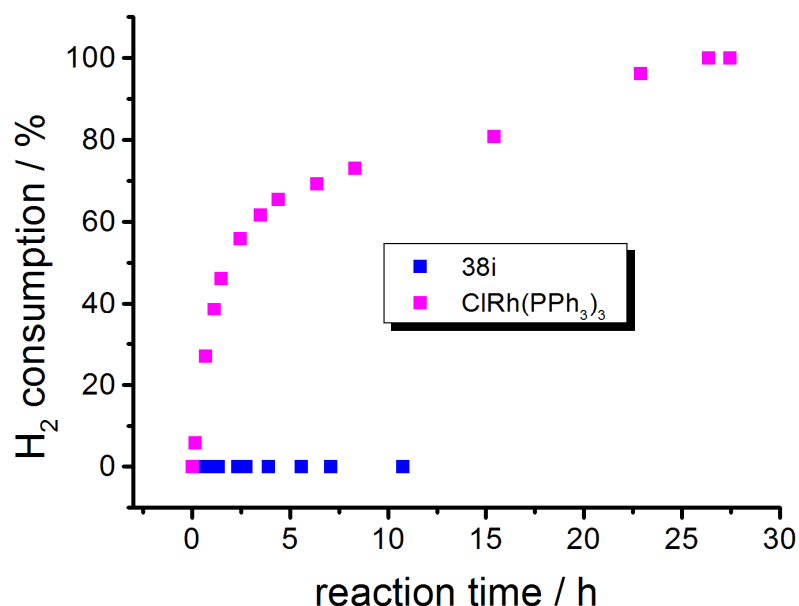


Figure 3.12. Three-phase test with **38i** using immobilized allyltriethoxysilane (details see text and Experimental Section).

The formation of metal aggregates or nanoparticles is a common complicating factor in the area of immobilized molecular transition metal catalysts. This topic has been reviewed in detail by Finke *et al.* and has also been observed in our group recently.^{45,75} The Crabtree group has developed an elegant test to distinguish molecular hydrogenation catalysts from colloidal metal particles.⁷⁸ Carrying out hydrogenation reactions in the presence of DBCOT (dibenzo[*a,e*]cyclooctatetraene) efficiently poisons homogeneous metal catalysts due to the strong binding of DBCOT to the metal center, which blocks open coordination sites for incoming substrate molecules. As discussed in chapter II we extended this test to distinguish between immobilized single-site catalysts of a molecular nature and metal nanoparticles on a silica surface. Analogously, we tested the hydrogenation of 1-dodecene with **38i** in the presence of 2 equivalents of DBCOT (Figure 3.13). No hydrogen uptake or color change is observed over the course of 10

hours. This result strengthens the assumption that initially the material consists of a single-site catalyst with the three phosphines coordinating to Rh in a chelating manner.

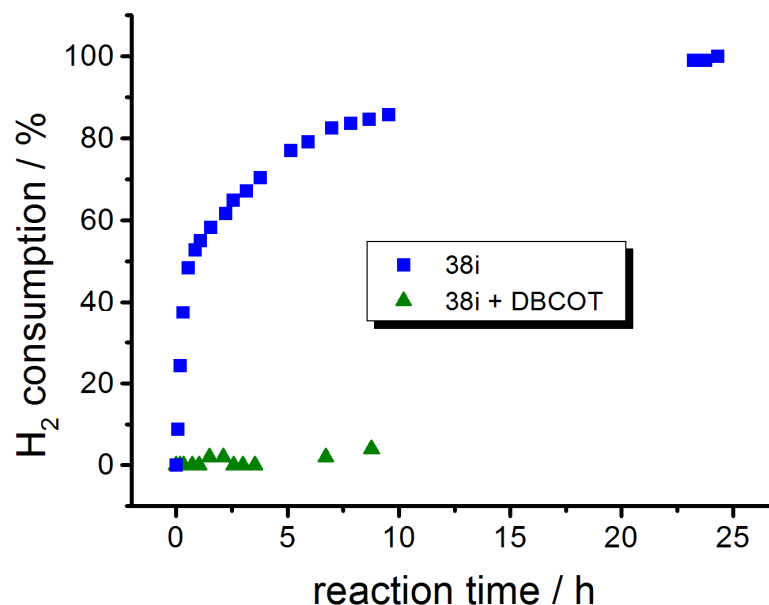


Figure 3.13. Hydrogen consumption of the catalyst **38i** for the hydrogenation of 1-dodecene with and without the poisoning agent DBCOT (dibenzo[*a,e*]cyclooctatetraene).

The recycling characteristics of the materials **37i** and **41i** were studied by carrying out the hydrogenation of 1-dodecene in a batchwise manner. After complete conversion, which usually takes about 24 hours, the functionalized material was allowed to settle and the supernatant was removed with a pipette. The supernatant was analyzed by GC and ¹H NMR to confirm full conversion. The functionalized silica was washed with toluene and employed in the subsequent catalytic run. In the case of **37i** the catalytic activity is high as compared to Wilkinson's catalyst under the same conditions

throughout the first 4 hours before a distinct drop in the activity takes place (Figure 3.14). In the subsequent runs the activity increases and reaches a maximum in the 5th run, after which the activity begins to decrease slightly.

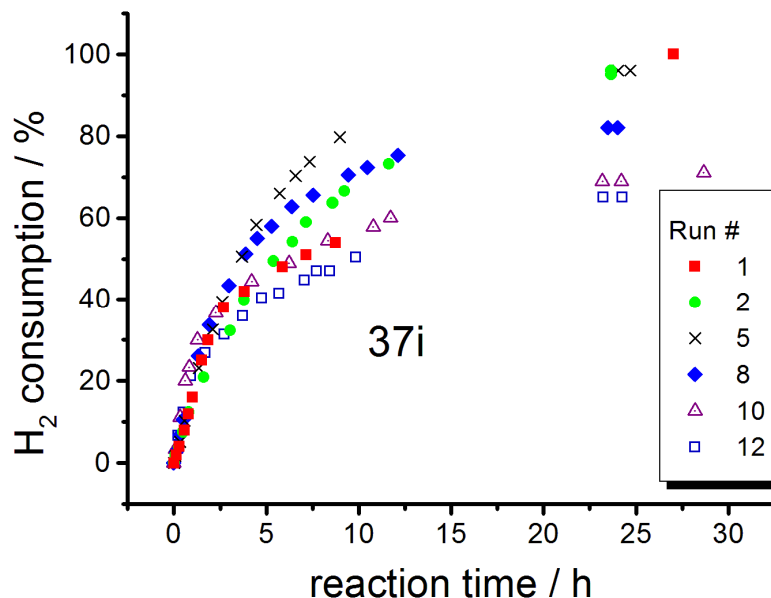


Figure 3.14. Hydrogen consumption during 12 batchwise catalytic runs using **37i**. Only selected runs are shown for clarity.

For **41i** the difference between the first and the following runs is even more drastic (Figure 3.15). The hydrogen uptake in the first run is sigmoidal and shows a distinct induction period which is not observed in the second and the following runs. Similarly to **37i**, the activity increases at first, reaching its maximum around the 8th run and then decreases to reach a plateau after the 11th run.

For practical purposes we exposed one of the catalysts, **36i**, to air (stirred as a slurry in toluene for 24 h) between the sixth and seventh catalytic run. No decrease of

the catalytic activity was noted. This is favorable with respect to catalyst handling and a potential industrial application. It also suggests, however, that the active species at that stage is not a single-site catalyst anymore, since phosphine complexes of Rh are highly air-sensitive in solution and prone to ligand oxidation.⁹³

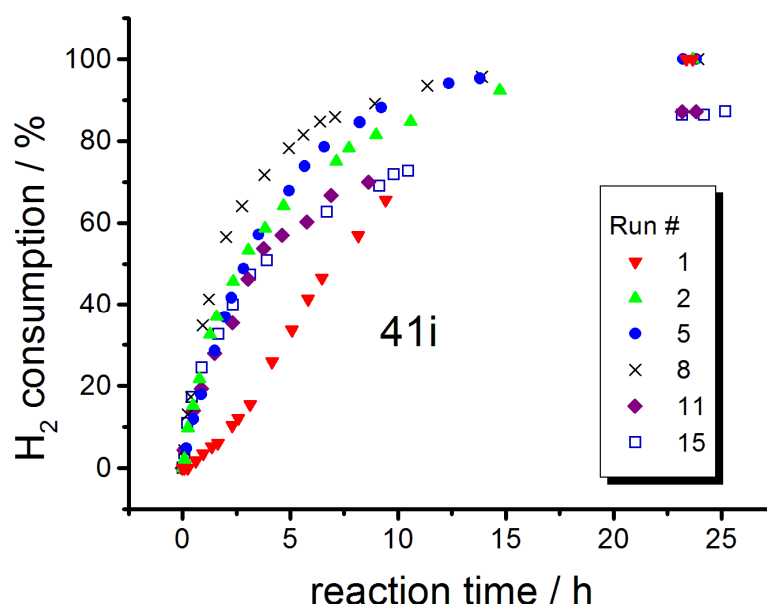


Figure 3.15. Hydrogen consumption during 15 batchwise catalytic runs using **41i**. Only selected runs are shown for clarity.

The catalysts **36i** and **37i** were therefore subjected to TEM analyses (Figure 3.16). **37i** was analyzed after 12 catalytic runs and **36i** after 7 runs, being exposed to air after the sixth run. In both cases Rh nanoparticles were detected on the surface or within the pores of the silica support.^{81,94} The average size is about 2.5 nm in the case of **37i** with a broad size distribution from 1.5 nm to 3.5 nm. For **36i** nanoparticles are observed as well, but not enough nanoparticles could be identified to estimate an average size or

size distribution. The reaction mixture using RhClpyCOD as a homogeneous metal precatalyst for comparison was also analyzed. Unexpectedly, using RhClpyCOD led to the formation of highly dispersed Rh nanoparticles with a narrow size distribution centered at 1.7 nm. The nanoparticles stay suspended in toluene for at least two weeks without noticeable aggregation.

For all immobilized catalysts, the results of the TEM analyses in combination with spectroscopic data and poisoning experiments suggest that the initial species is a well-defined single-site metal complex which is highly active in the hydrogenation of 1-dodecene. Over time the species gradually decompose to form surface-supported Rh nanoparticles which also constitute active hydrogenation catalysts.⁷⁷ A more systematic study of nanoparticle growth and size distribution was beyond the scope of the present work but will shed light on the changes in catalytic activity in a future project.

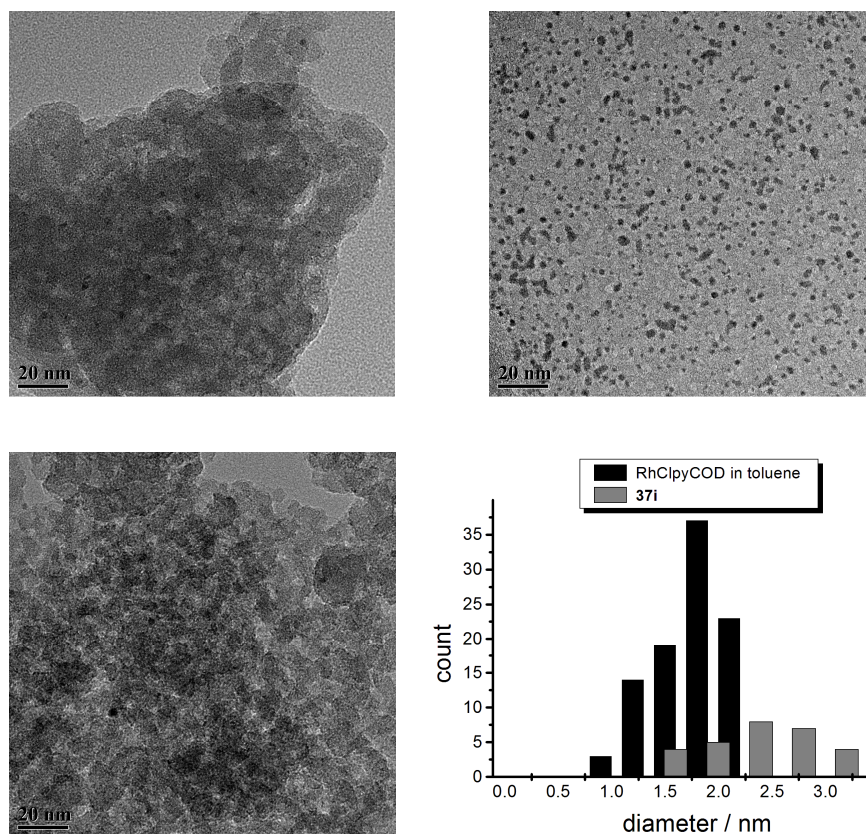


Figure 3.16. TEM images of Rh nanoparticles that formed during catalysis with **37i** (*top left*), **36i** (*bottom left*, after exposure to air), RhClpyCOD (*top right*) in toluene and their corresponding size distributions (*bottom right*).

CONCLUSION

In summary we have demonstrated that tridentate phosphine ligands covalently immobilized on silica coordinate Rh complexes in the usual way. The initial metal complex is a single-site species with a well-defined coordination environment. Under hydrogenation conditions the single-site species are transformed into nanoparticles on the time scale of several hours. This study therefore suggests that translational mobility of the entire linker/metal complex assembly is not a prerequisite for metal aggregation or nanoparticle formation. In other words, the metal atoms do not have to be delivered to

the nanoparticle directly by the metal complex. Therefore, they must either be stabilized by the solvent after leaving the linker and migrate in the solvent/support interface, since no substantial amount of metal has ever been detected in our group by AAS in the supernatant. Alternatively, the metal atoms, after being detached from the linkers, could possess the ability to migrate over the surface, where they finally assemble to form nanoparticles. Both scenarios would explain why all nanoparticles are found in the pores of the support, but never in the supernatant.

EXPERIMENTAL

General Remarks

The ^1H , ^{13}C , and ^{31}P NMR spectra of liquids were recorded at 499.7, 125.7, and 202.3 MHz on a 500 MHz Varian spectrometer and referenced as follows: ^1H : residual internal CHCl_3 (δ , 7.26 ppm), CDHCl_2 (δ , 5.32 ppm) or benzene- d_5 (δ , 7.16 ppm); ^{13}C : internal CDCl_3 (δ , 77.23 ppm) or benzene- d_6 (δ , 128.06 ppm). ^{31}P NMR spectra were referenced with respect to neat Ph_2PCl (δ , 81.92 ppm) which was centered in a capillary in the NMR sample tube. The ^{13}C and ^{31}P NMR spectra were recorded with ^1H decoupling if not stated otherwise. ^{29}Si NMR spectra of liquids were recorded at 79.37 MHz on a 400 MHz Inova spectrometer and referenced to external hexamethyldisiloxane ($\text{Me}_3\text{SiOSiMe}_3$) in CDCl_3 (δ , 6.53 ppm). The solid-state NMR spectra were measured with a Bruker Avance 400 widebore NMR spectrometer equipped with a 4 mm MAS probehead. For the ^{31}P HRMAS and MAS measurements ^1H high-power decoupling was applied. The recycle delays were 5 s for HRMAS and 10 s for MAS spectra. For more measurement details, see the ref.⁶²¹ GC analyses were carried out on a Shimadzu GC 2010 gas chromatograph equipped with a SHRXI-5MS column (15 m \times 0.25 mm \times 0.25 μm) and a flame ionization detector (GC-FID). TEM images were obtained on an FEI

Tecnai G2 F20 microscope and ImageJ software was used to determine the particle size distribution. Melting points were recorded with a Stanford Research Systems (SRS) MPA100 (Opti-Melt) automated melting point system. All reactions were carried out using standard Schlenk techniques and a purified N₂ atmosphere, if not stated otherwise. Reagents purchased from Sigma Aldrich or VWR were used without further purification. Solvents were dried by boiling them over Na, distilled, and stored under N₂. CH₂Cl₂ was obtained from a solvent purification system. The silica (Merck, 40 Å average pore diameter, 0.063 to 0.2 mm average particle size, specific surface area 750 m²/g) was rigorously dried in vacuo at 400 °C for 4 days to remove adsorbed water and condense surface silanol groups.

General Procedure A - Immobilization

Method A

Phosphine **33** (294 mg, 0.368 mmol) was dissolved in toluene (10 ml) and added to a suspension of SiO₂ (1.169 g) (specific surface area 750 m²g⁻¹, average pore diameter 40 Å, particle size 70 to 230 mesh) in toluene (40 ml). The mixture was stirred overnight at 70 °C. The silica was allowed to settle and the supernatant was removed. The functionalized silica was then washed twice with toluene (20 ml) and then twice with CH₂Cl₂ (20 ml). After this, the silica was dried *in vacuo* at room temperature for several hours. The supernatant and the washing phases were combined and the solvent was removed *in vacuo*. The residue was weighed and analyzed by ³¹P and ¹H NMR. The surface coverage was determined gravimetrically by measuring the weight increase of the silica support and the excess ligand in the supernatant.

Method B

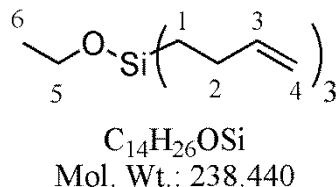
Phosphine **33** (436 mg, 0.547 mmol) was dissolved in toluene (15 ml), then 3 ml of a $\text{H}_3\text{B}\cdot\text{THF}$ solution (1 M) was added and the solution was stirred for 30 min. Then the solvent was removed *in vacuo*, the residue redissolved in toluene (10 ml), and added to a suspension of SiO_2 (3.449 g) (specific surface area $750\text{ m}^2\text{g}^{-1}$, average pore diameter 40 Å, particle size 70 to 230 mesh) in toluene (40 ml). The mixture was stirred for 48 h at 60°C . The silica was allowed to settle and the supernatant was removed. The functionalized silica was then washed twice with toluene (20 ml) and twice with CH_2Cl_2 (20 ml). Subsequently, the silica was dried *in vacuo* for several hours. The supernatant and the washing phases were combined and the solvent was removed *in vacuo*. The residue was analyzed by ^{31}P NMR and ^1H NMR. The surface coverage was determined gravimetrically by measuring the weight increase of the silica support and the excess ligand in the supernatant. Then a solution of DABCO (187 mg, 1.667 mmol) in toluene (10 ml) was added to a suspension of the functionalized silica and stirred at room temperature for 24 h. The supernatant was removed and the silica was washed twice with CH_2Cl_2 (20 ml). Then the silica was dried *in vacuo* at room temperature for several hours.

General Procedure B - Hydrogenation

Immobilized catalyst **38i** (347 mg, 0.010 mmol Rh) was suspended in 4 ml of toluene in a Schlenk flask. The Schlenk flask was attached to the hydrogenation apparatus and heated to 60°C . To start the catalytic reaction 1 mmol of 1-dodecene, dissolved in toluene (1 ml), was added to the suspension with a syringe through the stopcock. Then the suspension was stirred at 750 rpm and the hydrogen uptake was monitored. After complete conversion the silica was allowed to settle. The supernatant was removed and

the silica was washed twice with 4 ml of toluene. The supernatant was analyzed by GC and ^1H NMR to confirm 100% conversion of the substrate.

Tris(but-3-enyl)ethoxysilane **30**



Magnesium (670 mg, 26.56 mmol) was suspended in Et_2O (20 ml) and bromobut-3-ene (2.622 g, 19.4 mmol) was added dropwise. The reaction mixture was stirred at RT for 3 h. Then the Grignard reagent was added to EtOSiCl_3 (861 mg, 4.692 mmol) in Et_2O (20 ml) at 0 °C via a cannula. The reaction mixture was allowed to warm to RT and was stirred for 2 more hours. Then 20 ml of the solvent was removed *in vacuo* and hexanes were added. The reaction mixture was filtered through celite and the solvent was removed *in vacuo*. The crude product was purified by column chromatography (SiO_2 , hexanes : ethylacetate = 8 : 1) to yield **30** (514 mg, 2.158 mmol) as a colorless liquid in 46% yield. Hexa(but-3-enyl)disiloxane **30b** (94 mg, 0.233 mmol) was isolated as a minor product as a colorless liquid in 10% yield.

Tris(but-3-enyl)ethoxysilane **30**

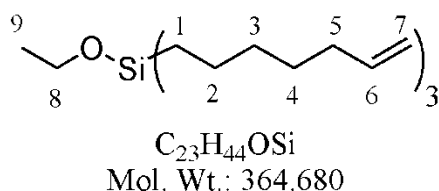
^1H NMR (CDCl_3 , 499.70 MHz): δ (ppm) = 5.88 (tdd, $^3J_{\text{trans}}(^1\text{H}-^1\text{H}) = 16.4$ Hz, $^3J_{\text{cis}}(^1\text{H}-^1\text{H}) = 10.1$ Hz, $^3J(^1\text{H}-^1\text{H}) = 6.3$ Hz, 3H, H3), 4.99 (tdd, $^3J_{\text{trans}}(^1\text{H}-^1\text{H}) = 17.0$ Hz, $^2J(^1\text{H}-^1\text{H}) = 3.5$ Hz, $^4J(^1\text{H}-^1\text{H}) = 1.7$ Hz, 3H, H4_Z), 4.87 (tdd, $^3J_{\text{cis}}(^1\text{H}-^1\text{H}) = 10.1$ Hz, $^2J(^1\text{H}-^1\text{H}) = 3.2$ Hz, $^4J(^1\text{H}-^1\text{H}) = 1.4$ Hz, 3H, H4_E), 3.68 (q, $^3J(^1\text{H}-^1\text{H}) = 6.9$ Hz, 2H, H5), 2.07-2.13

(m, 6H, H2), 1.18 (t, $^3J(^1\text{H}-^1\text{H}) = 6.9$ Hz, 3H, H6), 0.71-0.76 (m, 6H, H1); $^{13}\text{C}\{^1\text{H}\}$ NMR (CDCl₃, 125.66 MHz): δ (ppm) = 141.50 (s, C3), 111.10 (s, C4), 58.53 (s, C5), 27.64 (s, C2), 18.08 (s, C6), 13.18 (s, C1); $^{29}\text{Si}\{^1\text{H}\}$ NMR (CDCl₃, 79.37 MHz): δ (ppm) = 14.70 (s).

Hexa(but-3-enyl)disiloxane **30b**

^1H NMR (CDCl₃, 499.70 MHz): δ (ppm) = 5.89 (tdd, $^3J_{\text{trans}}(^1\text{H}-^1\text{H}) = 16.5$ Hz, $^3J_{\text{cis}}(^1\text{H}-^1\text{H}) = 10.1$ Hz, $^3J(^1\text{H}-^1\text{H}) = 6.3$ Hz, 6H, H3), 5.01 (tdd, $^3J_{\text{trans}}(^1\text{H}-^1\text{H}) = 17.1$ Hz, $^2J(^1\text{H}-^1\text{H}) = 3.5$ Hz, $^4J(^1\text{H}-^1\text{H}) = 1.7$ Hz, 6H, H4_Z), 4.91 (tdd, $^3J_{\text{cis}}(^1\text{H}-^1\text{H}) = 10.1$ Hz, $^2J(^1\text{H}-^1\text{H}) = 3.2$ Hz, $^4J(^1\text{H}-^1\text{H}) = 1.3$ Hz, 6H, H4_E), 2.10-2.16 (m, 12H, H2), 0.70-0.76 (m, 12H, H1); $^{13}\text{C}\{^1\text{H}\}$ NMR (CDCl₃, 125.66 MHz): δ (ppm) = 141.13 (s, C3), 113.08 (s, C4), 27.01 (s, C2), 14.01 (s, C1).

Tris(hept-6-enyl)ethoxysilane **31**



Magnesium (939 mg, 38.6 mmol) was suspended in Et₂O (20 ml) and bromohept-6-ene (3.385 g, 19.115 mmol) was added dropwise. The reaction mixture was stirred at RT for 3 h. The Grignard reagent was then added to EtOSiCl₃ (945 mg, 5.150 mmol) in Et₂O (20 ml) at 0 °C via a cannula. The reaction mixture was allowed to warm to RT and was stirred for 2 more hours. Then 20 ml of the solvent was removed *in vacuo* and hexanes were added. The reaction mixture was filtered through celite and the solvent was

removed *in vacuo*. The crude product was purified by column chromatography (SiO₂, hexanes : ethylacetate = 8 : 1) to yield **31** (523 mg, 1.434 mmol) as a colorless liquid in 28% yield. The colorless liquid hexa(hept-6-enyl)disiloxane **31b** (510 mg, 0.778 mmol) was isolated as the major product in 30% yield.

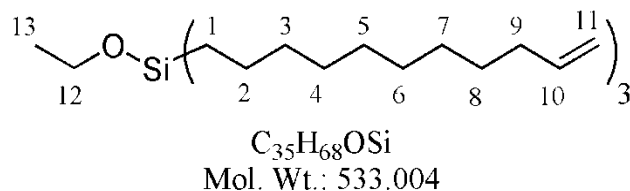
Tris(hept-6-enyl)ethoxysilane **31**

¹H NMR (CDCl₃, 499.70 MHz): δ (ppm) = 5.81 (tdd, $^3J_{\text{trans}}(^1\text{H}-^1\text{H}) = 16.9$, 3 Hz, $^3J_{\text{cis}}(^1\text{H}-^1\text{H}) = 10.2$ Hz, $^3J(^1\text{H}-^1\text{H}) = 6.7$ Hz, 3H, H₆), 4.99 (tdd, $^3J_{\text{trans}}(^1\text{H}-^1\text{H}) = 17.1$ Hz, $^2J(^1\text{H}-^1\text{H}) = 2.1$ Hz, $^4J(^1\text{H}-^1\text{H}) = 1.5$ Hz, 3H, H_{7Z}), 4.93 (tdd, $^3J_{\text{cis}}(^1\text{H}-^1\text{H}) = 10.2$ Hz, $^2J(^1\text{H}-^1\text{H}) = 2.3$ Hz, $^4J(^1\text{H}-^1\text{H}) = 1.1$ Hz, 3H, H_{7E}), 3.65 (q, $^3J(^1\text{H}-^1\text{H}) = 6.9$ Hz, 2H, H₈), 2.00-2.07 (m, 6H, H₅), 1.30-1.41 (m, 18H, H₂, H₃, H₄), 1.17 (t, $^3J(^1\text{H}-^1\text{H}) = 6.9$ Hz, 2H, H₉), 0.56-0.61 (m, 6H, H₁); **¹³C{¹H} NMR** (CDCl₃, 125.66 MHz): δ (ppm) = 139.21 (s, C₆), 114.11 (s, C₇), 58.37 (s, C₈), 33.73 (s), 33.11 (s), 28.57 (s), 23.02 (s), 18.65 (s, C₉), 13.59 (s, C₁); **²⁹Si{¹H} NMR** (CDCl₃, 79.37 MHz): δ (ppm) = 15.36 (s).

Hexa(hept-6-enyl)disiloxane **31b**

¹H NMR (CDCl₃, 499.70 MHz): δ (ppm) = 5.81 (tdd, $^3J_{\text{trans}}(^1\text{H}-^1\text{H}) = 16.9$, 3 Hz, $^3J_{\text{cis}}(^1\text{H}-^1\text{H}) = 10.2$ Hz, $^3J(^1\text{H}-^1\text{H}) = 6.7$ Hz, 6H, H₆), 4.99 (tdd, $^3J_{\text{trans}}(^1\text{H}-^1\text{H}) = 17.1$ Hz, $^2J(^1\text{H}-^1\text{H}) = 2.1$ Hz, $^4J(^1\text{H}-^1\text{H}) = 1.5$ Hz, 6H, H_{7Z}), 4.93 (tdd, $^3J_{\text{cis}}(^1\text{H}-^1\text{H}) = 10.2$ Hz, $^2J(^1\text{H}-^1\text{H}) = 2.2$ Hz, $^4J(^1\text{H}-^1\text{H}) = 1.2$ Hz, 6H, H_{7E}), 2.04 (dt, $^3J(^1\text{H}-^1\text{H}) = 6.7$ Hz, $^3J(^1\text{H}-^1\text{H}) = 6.6$ Hz, 12H, H₅), 1.30-1.43 (m, 368H, H₂, H₃, H₄), 0.56-0.61 (m, 12H, H₁); **¹³C{¹H} NMR** (CDCl₃, 125.66 MHz): δ (ppm) = 139.16 (s, C₆), 114.15 (s, C₇), 33.69 (s), 33.01 (s), 28.57 (s), 22.91 (s), 14.99 (s, C₁).

Tris(undec-10-enyl)ethoxysilane **32**



Magnesium (980 mg, 40.31 mmol) was suspended in THF (20 ml) and bromoundec-10-ene (3.757 g, 16.11 mmol) was added dropwise. The reaction mixture was stirred at RT for 3 h. Then the Grignard reagent was added to EtOSiCl₃ (738 mg, 4.022 mmol) in THF (20 ml) at 0 °C via a cannula. The reaction mixture was allowed to warm to RT and was stirred for 2 more hours. Then 20 ml of the solvent was removed *in vacuo* and hexanes were added. The reaction mixture was filtered through celite and the solvent was removed *in vacuo*. The crude product was purified by column chromatography (SiO₂, hexanes : ethylacetate = 19 : 1) to yield **32** (1.163 g, 2.181 mmol) as a colorless liquid in 54% yield. The colorless liquid hexa(undec-10-enyl)disiloxane **32b** (43 mg, 0.043 mmol) was isolated as a minor byproduct in 2% yield.

Tris(undec-10-enyl)ethoxysilane **32**

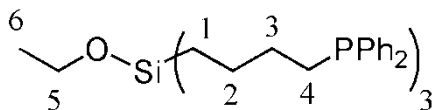
¹H NMR (CDCl₃, 499.70 MHz): δ (ppm) = 5.81 (tdd, ³*J*_{trans}(¹H-¹H) = 16.9 Hz, ³*J*_{cis}(¹H-¹H) = 10.2 Hz, ³*J*(¹H-¹H) = 6.7 Hz, 3H, H10), 4.99 (tdd, ³*J*_{trans}(¹H-¹H) = 17.1 Hz, ²*J*(¹H-¹H) = 3.7 Hz, ⁴*J*(¹H-¹H) = 1.6 Hz, 3H, H11_Z), 4.92 (tdd, ³*J*_{cis}(¹H-¹H) = 10.2 Hz, ²*J*(¹H-¹H) = 2.3 Hz, ⁴*J*(¹H-¹H) = 1.2 Hz, 3H, H11_E), 3.66 (q, ³*J*(¹H-¹H) = 6.9 Hz, 2H, H12), 2.04 (dt, ³*J*(¹H-¹H) = 7.7 Hz, ³*J*(¹H-¹H) = 6.8 Hz, ⁴*J*(¹H-¹H) = 1.3 Hz, 6H, H9), 1.24-1.41 (m, 42H), 1.17 (t, ³*J*(¹H-¹H) = 6.9 Hz, 3H, H13), 0.58-0.61 (m, 6H, H1): **¹³C{¹H}** **NMR** (CDCl₃, 125.66 MHz): δ (ppm) = 139.18 (s, C10), 114.06 (s, C11), 58.33 (s,

C12), 33.82 (s, C9)*, 33.66 (s, C8)*, 29.54 (s, C3)[#], 29.29 (s, C4)[#], 29.16 (s, C5)[#], 28.96 (s, C6)[#], 23.17 (s, C2), 18.65 (s, C13), 13.64 (s, C1); ²⁹Si{¹H} NMR (CDCl₃, 79.37 MHz): δ (ppm) = 15.47 (s); *,[#] assignments interchangeable.

Hexa(undec-10-enyl)disiloxane **32b**

¹H NMR (CDCl₃, 499.70 MHz): δ (ppm) = 5.81 (tdd, ³J_{trans}(¹H-¹H) = 16.9 Hz, ³J_{cis}(¹H-¹H) = 10.2 Hz, ³J(¹H-¹H) = 6.7 Hz, 6H, H10), 4.99 (tdd, ³J_{trans}(¹H-¹H) = 17.1 Hz, ²J(¹H-¹H) = 3.6 Hz, ⁴J(¹H-¹H) = 1.6 Hz, 6H, H11_Z), 4.91-4.95 (m, 6H, H11_E), 2.04 (dtt, ³J(¹H-¹H) = 7.7 Hz, ³J(¹H-¹H) = 6.9 Hz, ⁴J(¹H-¹H) = 1.2 Hz, 12H, H9), 1.23-1.41 (m, 84H), 0.55-0.60 (m, 12H, H1).

Tris(4-diphenylphosphinobutyl)ethoxysilane **33**



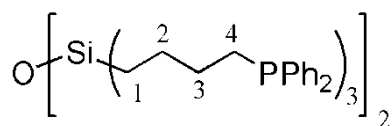
C₅₀H₅₉OP₃Si
Mol. Wt.: 797.013

The ethoxysilane **30** (239 mg, 1.002 mmol), AIBN (44 mg, 0.267 mmol), and Ph₂PH (748 mg, 4.211 mmol) were combined in a Schlenk flask, heated to 70 °C and stirred for 4 d. The conversion was monitored by ³¹P NMR of the reaction mixture. The crude product was purified by column chromatography (SiO₂, toluene) to yield **33** (588 mg, 0.737 mmol) as a colorless viscous oil in 74% yield.

¹H NMR (C₆D₆, 499.70 MHz): δ (ppm) = 7.44-7.49 (m, 12H, H_{ortho}), 7.02-7.12 (m, 18H, H_{para}, H_{meta}), 3.49 (q, ³J(¹H-¹H) = 6.9 Hz, 2H, H5), 2.00-2.05 (m, 6H, H4), 1.51-1.60 (m,

6H, H3), 1.42-1.51 (m, 6H, H2), 1.11 (t, $^3J(^1\text{H}-^1\text{H}) = 6.9$ Hz, 2H, H6), 0.49-0.54 (m, 6H, H1); $^{13}\text{C}\{^1\text{H}\}$ NMR (C_6D_6 , 125.66 MHz): δ (ppm) = 139.99 (d, $^1J(^{31}\text{P}-^{13}\text{C}) = 14.7$ Hz, C_{ipso}), 133.15 (d, $^2J(^{31}\text{P}-^{13}\text{C}) = 18.5$ Hz, C_{ortho}), 128.68 (d, $^3J(^{31}\text{P}-^{13}\text{C}) = 6.4$ Hz, C_{meta}), 128.61 (s, C_{para}), 58.49 (s, C5), 30.33 (d, $^3J(^{31}\text{P}-^{13}\text{C}) = 15.9$ Hz, C2), 28.33 (d, $^1J(^{31}\text{P}-^{13}\text{C}) = 12.7$ Hz, C4), 25.29 (d, $^3J(^{31}\text{P}-^{13}\text{C}) = 13.1$ Hz, C3), 18.97 (s, C6), 13.87 (s, C1); $^{31}\text{P}\{^1\text{H}\}$ NMR (C_6D_6 , 202.28 MHz): δ (ppm) = -16.39 (s); $^{29}\text{Si}\{^1\text{H}\}$ NMR (CDCl_3 , 79.37 MHz): δ (ppm) = 12.21 (s).

Hexa(4-diphenylphosphinobutyl)disiloxane **33b**



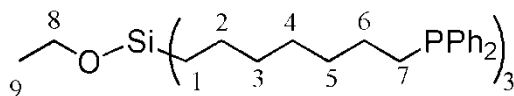
$\text{C}_{96}\text{H}_{108}\text{OP}_6\text{Si}_2$
Mol. Wt.: 1519.897

The disiloxane **30b** (389 mg, 0.965 mmol), AIBN (104 mg, 0.633 mmol), and Ph_2PH (1.157 g, 6.215 mmol) were combined in a Schlenk flask, heated to 70 °C, and stirred for 5 d. The conversion was monitored by ^{31}P NMR of the reaction mixture. The crude product was purified by column chromatography (SiO_2 , hexanes : ethylacetate = 4 : 1) to yield **33b** (1.095 g, 0.720 mmol) as a colorless viscous oil in 75% yield.

^1H NMR (C_6D_6 , 499.70 MHz): δ (ppm) = 7.45-7.49 (m, 24H, H_{ortho}), 7.03-7.12 (m, 36H, H_{para} , H_{meta}), 1.99-2.04 (m, 12H, H4), 1.48-1.58 (m, 12H, H3), 1.37-1.45 (m, 12H, H2), 0.40-0.45 (m, 12H, H1); $^{13}\text{C}\{^1\text{H}\}$ NMR (C_6D_6 , 125.66 MHz): δ (ppm) = 139.98 (d, $^1J(^{31}\text{P}-^{13}\text{C}) = 14.6$ Hz, C_{ipso}), 133.16 (d, $^2J(^{31}\text{P}-^{13}\text{C}) = 18.6$ Hz, C_{ortho}), 128.69 (d, $^3J(^{31}\text{P}-^{13}\text{C}) = 6.4$ Hz, C_{meta}), 128.63 (s, C_{para}), 30.23 (d, $^3J(^{31}\text{P}-^{13}\text{C}) = 15.8$ Hz, C2), 28.32 (d,

$^1J(^{31}\text{P}-^{13}\text{C}) = 12.8 \text{ Hz}$, C4), 25.09 (d, $^3J(^{31}\text{P}-^{13}\text{C}) = 13.0 \text{ Hz}$, C3), 15.16 (s, C1); $^{31}\text{P}\{^1\text{H}\}$ NMR (C_6D_6 , 202.28 MHz): δ (ppm) = -16.43 (s); $^{29}\text{Si}\{^1\text{H}\}$ NMR (CDCl_3 , 79.37 MHz): δ (ppm) = 15.73 (s).

Tris(7-diphenylphosphinoheptyl)ethoxysilane **34**



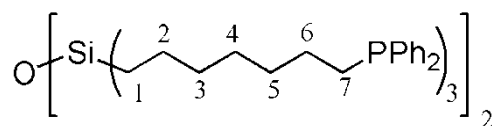
$\text{C}_{59}\text{H}_{77}\text{OP}_3\text{Si}$
Mol. Wt.: 923.251

The ethoxysilane **31** (480 mg, 1.316 mmol), AIBN (94 mg, 0.572 mmol), and Ph_2PH (942 mg, 5.060 mmol) were combined in a Schlenk flask, heated to 70 °C and stirred for 5 d. The conversion was monitored by ^{31}P NMR of the reaction mixture. The crude product was purified by column chromatography (SiO_2 , toluene) to yield **34** (538 mg, 0.582 mmol) as a colorless viscous oil in 44% yield.

^1H NMR (C_6D_6 , 499.70 MHz): δ (ppm) = 7.45 (dd, $^3J(^{31}\text{P}-^1\text{H}) = 6.9 \text{ Hz}$, $^3J(^1\text{H}-^1\text{H}) = 6.9 \text{ Hz}$, 12H, H_{ortho}), 7.03-7.12 (m, 18H, H_{meta} , H_{para}), 3.64 (q, $^3J(^1\text{H}-^1\text{H}) = 6.9 \text{ Hz}$, 2H, H8), 1.95-2.00 (m, 6H, H7), 1.42-1.51 (m, 6H, H6), 1.31-1.39 (m, 12H, H5, H2), 1.24-1.31 (m, 6H), 1.17-1.24 (m, 6H), 1.18 (t, $^3J(^1\text{H}-^1\text{H}) = 6.9 \text{ Hz}$, 3H, H9), 0.66-0.71 (m, 6H, H1); $^{13}\text{C}\{^1\text{H}\}$ NMR (C_6D_6 , 125.66 MHz): δ (ppm) = 140.02 (d, $^1J(^{31}\text{P}-^{13}\text{C}) = 14.7 \text{ Hz}$, C_{ipso}), 133.14 (d, $^2J(^{31}\text{P}-^{13}\text{C}) = 18.5 \text{ Hz}$, C_{ortho}), 128.67 (d, $^3J(^{31}\text{P}-^{13}\text{C}) = 6.4 \text{ Hz}$, C_{meta}), 128.59 (s, C_{para}), 58.52 (s, C8), 34.06 (s), 31.59 (d, $J(^{31}\text{P}-^{13}\text{C}) = 12.6 \text{ Hz}$, C5), 29.42 (s), 28.63 (d, $J(^{31}\text{P}-^{13}\text{C}) = 12.4 \text{ Hz}$, C7), 25.51 (d, $J(^{31}\text{P}-^{13}\text{C}) = 16.3 \text{ Hz}$, C6), 23.76 (s), 18.67 (s,

C9), 14.26 (s, C1); $^{31}\text{P}\{^1\text{H}\}$ NMR (C_6D_6 , 202.28 MHz): δ (ppm) = -16.38 (s); $^{29}\text{Si}\{^1\text{H}\}$ NMR (C_6D_6 , 79.37 MHz): δ (ppm) = 13.93 (s).

Hexa(7-diphenylphosphinoheptyl)disiloxane 34b

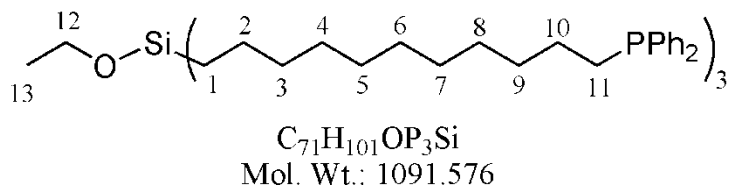


$\text{C}_{114}\text{H}_{144}\text{OP}_6\text{Si}_2$
Mol. Wt.: 1772.376

The disiloxane **31b** (465 mg, 0.709 mmol), AIBN (88 mg, 0.535 mmol), and Ph_2PH (1.187 g, 6.376 mmol) were combined in a Schlenk flask, heated to 70 °C and stirred for 5 d. The conversion was monitored by ^{31}P NMR of the reaction mixture. The crude product was purified by column chromatography (SiO_2 , toluene : ethylacetate = 9 : 1) to yield **34b** (855 mg, 0.502 mmol) as a colorless viscous oil in 70% yield.

^1H NMR (C_6D_6 , 499.70 MHz): δ (ppm) = 7.44-7.49 (m, 24H, H_{ortho}), 7.03-7.14 (m, 36H, H_{meta} , H_{para}), 1.96-2.01 (m, 12H, H7), 1.43-1.53 (m, 12H, H6), 1.34-1.42 (m, 24H, H5, H2), 1.27-1.34 (m, 12H), 1.20-1.27 (m, 12H), 0.56-0.61 (m, 12H, H1); $^{13}\text{C}\{^1\text{H}\}$ NMR (C_6D_6 , 125.66 MHz): δ (ppm) = 140.01 (d, $^1J(^{31}\text{P}-^{13}\text{C}) = 14.6$ Hz, C_{ipso}), 133.14 (d, $^2J(^{31}\text{P}-^{13}\text{C}) = 18.5$ Hz, C_{ortho}), 128.68 (d, $^3J(^{31}\text{P}-^{13}\text{C}) = 6.4$ Hz, C_{meta}), 128.60 (s, C_{para}), 33.95 (s), 31.55 (d, $J(^{31}\text{P}-^{13}\text{C}) = 12.5$ Hz, C5), 29.42 (s), 28.63 (d, $J(^{31}\text{P}-^{13}\text{C}) = 12.3$ Hz, C7), 25.51 (d, $J(^{31}\text{P}-^{13}\text{C}) = 16.2$ Hz, C6), 23.58 (s), 15.62 (s, C1); $^{31}\text{P}\{^1\text{H}\}$ NMR (C_6D_6 , 202.28 MHz): δ (ppm) = -16.38 (s).

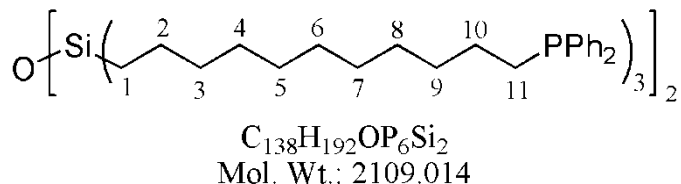
Tris(11-diphenylphosphinoundecenyl)ethoxysilane **35**



The ethoxysilane **32** (375 mg, 0.703 mmol), AIBN (104 mg, 0.634 mmol), and Ph_2PH (575 mg, 3.040 mmol) were combined in a Schlenk flask, heated to 70 °C and stirred for 4 d. The conversion was monitored by ^{31}P NMR of the reaction mixture. The crude product was purified by column chromatography (SiO_2 , toluene) to yield **35** (350 mg, 0.320 mmol) as a colorless viscous oil in 45% yield.

^1H NMR (CDCl_3 , 499.70 MHz): δ (ppm) = 7.39-7.44 (m, 12H, H_{ortho}), 7.30-7.35 (m, 18H, H_{meta} , H_{para}), 3.65 (q, $^3J(^1\text{H}-^1\text{H}) = 6.9$ Hz, 2H, H12), 2.01-2.06 (m, 6H, H11), 1.37-1.48 (m, 12H, H10), 1.20-1.35, 42H), 1.17 (t, $^3J(^1\text{H}-^1\text{H}) = 6.9$ Hz, 3H, H13), 0.55-0.61 (m, 6H, H1); $^{13}\text{C}\{^1\text{H}\}$ NMR (CDCl_3 , 125.66 MHz): δ (ppm) = 139.05 (d, $^1J(^{31}\text{P}-^{13}\text{C}) = 13.0$ Hz, C_{ipso}), 132.67 (d, $^2J(^{31}\text{P}-^{13}\text{C}) = 18.3$ Hz, C_{ortho}), 128.38 (s, C_{para}), 128.32 (d, $^3J(^{31}\text{P}-^{13}\text{C}) = 6.5$ Hz, C_{meta}), 58.34 (s, C12), 33.70 (s), 31.23 (d, $J(^{31}\text{P}-^{13}\text{C}) = 12.9$ Hz), 29.66 (s), 29.59 (s), 29.52 (s), 29.31 (s), 29.28 (s), 28.04 (d, $J(^{31}\text{P}-^{13}\text{C}) = 11.0$ Hz), 25.96 (d, $J(^{31}\text{P}-^{13}\text{C}) = 15.9$ Hz), 23.19 (s), 21.46 (s, C13), 13.65 (s, C1); $^{31}\text{P}\{^1\text{H}\}$ NMR (CDCl_3 , 202.28 MHz): δ (ppm) = -16.33 (s); $^{29}\text{Si}\{^1\text{H}\}$ NMR (CDCl_3 , 79.37 MHz): δ (ppm) = 15.53 (s).

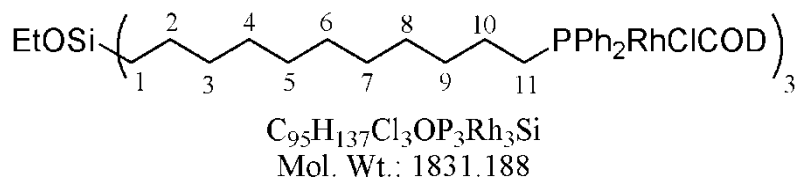
Hexa(11-diphenylphosphinoundecenyl)disiloxane **35b**



The disiloxane **32b** (628 mg, 0.633 mmol), AIBN (140 mg, 0.853 mmol), and Ph₂PH (1.151 g, 6.086 mmol) were combined in a Schlenk flask, heated to 70 °C and stirred for 4 d. The conversion was monitored by ³¹P NMR of the reaction mixture. The crude product was purified by column chromatography (SiO₂, toluene) to yield **35b** (950 mg, 0.450 mmol) as a colorless viscous oil in 71% yield.

¹H NMR (CDCl₃, 499.70 MHz): δ (ppm) = 7.44-7.52 (m, 24H, H_{ortho}), 7.28-7.41 (m, 36H, H_{meta}, H_{para}), 2.06-2.14 (m, 12H, H11), 1.26-1.58 (m, 108H), 0.61-0.69 (m, 12H, H1); ¹³C{¹H} NMR (CDCl₃, 125.66 MHz): δ (ppm) = 139.03 (d, ¹J(³¹P-¹³C) = 13.3 Hz, C_{ipso}), 132.65 (d, ²J(³¹P-¹³C) = 17.9 Hz, C_{ortho}), 128.29 (d, ³J(³¹P-¹³C) = 7.9 Hz, C_{meta}), 128.17 (s, C_{para}), 33.59 (s), 31.19 (d, J(³¹P-¹³C) = 12.2 Hz), 29.61 (s), 29.53 (s), 29.48 (s), 29.31 (s), 29.25 (s), 28.02 (d, J(³¹P-¹³C) = 11.6 Hz), 25.94 (d, J(³¹P-¹³C) = 14.8 Hz), 23.07 (s), 15.06 (s, C1); ³¹P{¹H} NMR (CDCl₃, 202.28 MHz): δ (ppm) = -16.34 (s).

Rhodium complex **43**



RhClpyCOD (**39**, 35 mg, 0.107 mmol) was dissolved in CH₂Cl₂ (10 ml). Ligand **35**, dissolved in CH₂Cl₂ (15 ml), was added dropwise and the reaction mixture was stirred at room temperature for 4h. The solvent was removed *in vacuo* and the residue was washed with copious amounts of pentane. After drying **43** (50 mg, 0.021 mmol) was obtained as an orange powder in 60% yield.

¹H NMR (CDCl₃, 499.70 MHz): δ (ppm) = 7.59-7.65 (m, 12H, H_{ortho}), 7.34-7.41 (m, 18H, H_{meta}, H_{para}), 5.46 (bs, 6H, H_{Olefin}), 3.65 (q, (³J(¹H-¹H) = 6.9 Hz, 2H, CH₂O), 2.99 (bs, 6H, H_{Olefin}), 2.43-2.50 (m, 6H, H₁₁), 2.23-2.41 (m, 12H, CH₂COD), 1.96-2.05 (m, 6H), 1.76-1.89 (m, 12H, CH₂COD), 1.37-1.45 (m, 6H), 1.19-1.33 (m, 42H), 1.15 (t, (³J(¹H-¹H) = 6.9 Hz, 3H, CH₃), 0.52-0.59 (m, 6H, H₁); **¹³C{¹H} NMR** (CDCl₃, 125.66 MHz): δ (ppm) = 133.51 (d, (²J(³¹P-¹³C) = 10.2 Hz, C_{ortho}), 132.35 (d, (¹J(³¹P-¹³C) = 39.5 Hz, C_{ipso}), 129.88 (d, (⁴J(³¹P-¹³C) = 2.1 Hz, C_{para}), 128.08 (d, (³J(³¹P-¹³C) = 9.4 Hz, C_{meta}), 104.35 (dd, (¹J(¹⁰³Rh-¹³C) = 12.6 Hz, (²J_{trans}(³¹P-¹³C) = 6.4 Hz, C_{Olefin}), 70.08 (d, (¹J(¹⁰³Rh-¹³C) = 13.1 Hz, C_{Olefin}), 58.29 (s, CH₂O), 33.68 (s), 32.91 (d, (⁴J(³¹P-¹³C) = 2.3 Hz, C₈), 31.44 (d, (³J(³¹P-¹³C) = 13.5 Hz, C₉), 29.58 (s), 29.56 (d, (²J(³¹P-¹³C) = 8.0 Hz, C₁₀), 29.29 (s), 28.91 (d, (¹J(³¹P-¹³C) = 57.5 Hz, C₁₁), 27.96 (s), 27.40 (s), 27.20 (s), 25.98 (s), 23.16 (s, C₂), 18.63 (s, CH₃), 13.63 (s, C₁); **³¹P{¹H} NMR** (CDCl₃, 202.28 MHz): δ (ppm) = 26.14 (d, (¹J(¹⁰³Rh-³¹P) = 147.9 Hz).

CHAPTER IV

INTRAMOLECULAR CARBON–SILICON BOND ACTIVATION IN TRIDENTATE PHOSPHINE COMPLEXES OF RHODIUM AND IRIIDIUM

INTRODUCTION

Transition metal complexes of tripodal phosphine ligands have been the subject of numerous studies over the years. Ligands of the general formula $E((CH_2)_n PPh_2)_3$ ($n = 1, 2$; $E = RC, RSi, N, RP^+, RB^-$; $R = \text{aryl, alkyl, alkoxy}$) and their respective transition metal complexes have been reported and have found a wide range of applications in catalysis (Figure 4.1).^{59,60,61,95}

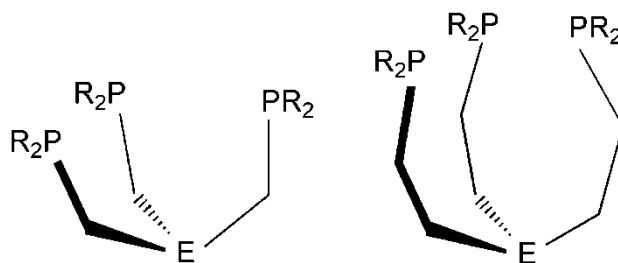
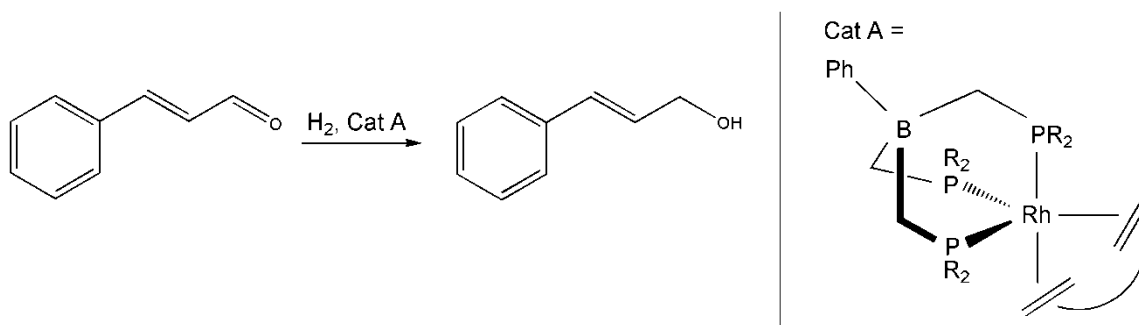


Figure 4.1. Tridentate phosphine ligands with C_1 and C_2 spacers.

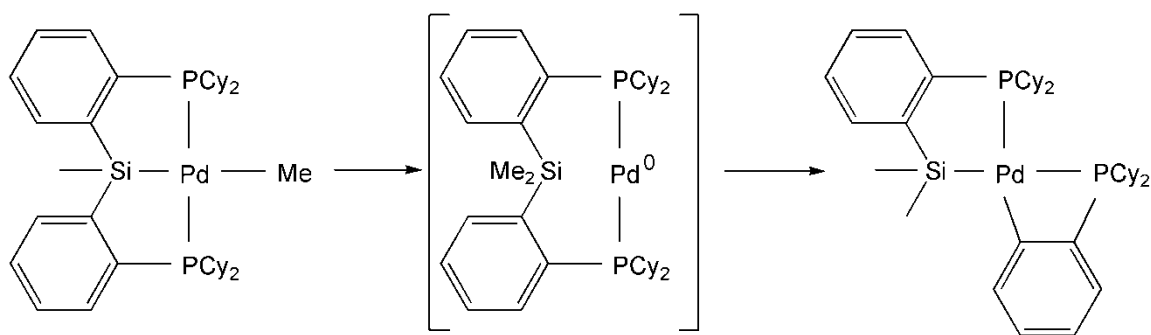
The C_3 symmetry of such ligands allows selective facial coordination in metal complexes.⁹⁵ This can lead to unusual coordination geometries and subsequently to unexpected reactivity. One particularly interesting example is the anionic tripod ligand $[PhB(CH_2PPh_2)_3]^-$ whose Rh complex is active in the selective hydrogenation of cinnamaldehyde reported by Tejel *et al.* (Scheme 4.1).^{61e,96}



Scheme 4.1. Selective hydrogenation of cinnamaldehyde with catalyst A containing a COD ligand.^{61e}

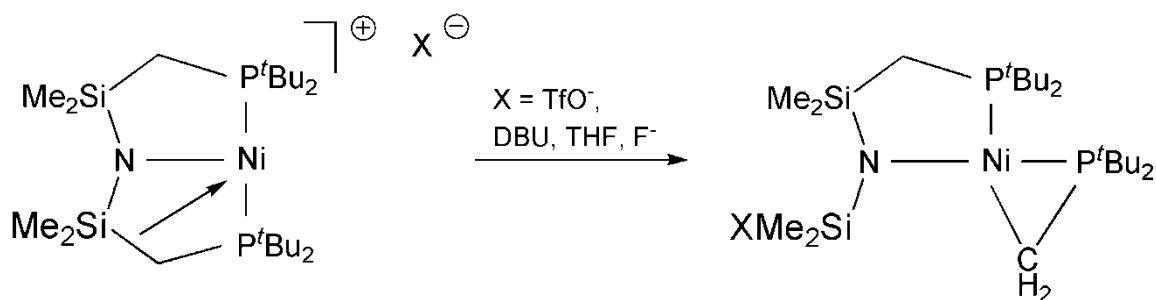
Previously tridentate phosphine ligands incorporating an ethoxysilane group had been synthesized in the Blümel group.⁵⁶ The intention was to utilize the ethoxysilane group in these ligands to allow tethering to an oxide support for catalyst immobilization. The immobilization of the ligands on SiO₂ and the coordination chemistry of the respective Pd, Ni, and W complexes had been studied and the intramolecular insertion of Rh into a Si-C(sp³) bond of one of the ligands has been observed.^{56,97}

In this chapter the reactivity of the ligand EtOSi((CH₂)₂PPh₂)₃ with [(COD)RhCl]₂ and [(COD)IrCl]₂ that involves a Si-C(sp³) bond cleavage is reported. While Si-C(sp) and Si-C(sp²) bond activation is well documented,⁹⁸ examples of cleavage of non-activated Si-C(sp³) bonds in transition metal complexes are scarce. Some early examples of Si-C bond activation utilizing Pt were reported in the 1990s and early 2000s.⁹⁹ Dinuclear Ru compounds are also able to cleave Si-C bonds as shown by Girolami *et al.*¹⁰⁰ More recently Turculet *et al.* reported reversible Si-C bond activation in Ni and Pd pincer complexes (Scheme 4.2).¹⁰¹



Scheme 4.2. Si-C(sp³) and Si-C(sp²) bond activation via a Pd(0) intermediate.¹⁰¹

Employing another pincer complex Caulton and coworkers described Si-C bond cleavage at Ni that does not involve an oxidative addition (Scheme 4.3).¹⁰²



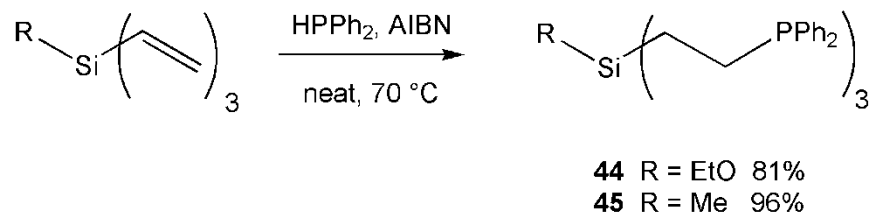
Scheme 4.3. Example for Si-C(sp³) bond activation.¹⁰²

In the examples described so far the Si-C bond was activated in a stoichiometric manner and the focus was on characterizing the organometallic species formed. Xi *et al.* on the other hand described the Pd-catalyzed synthesis of siloles that proceeds via Si-CH₃ bond cleavage.¹⁰³ A better understanding of the factors governing Si-C bond activation should pave the way for broader applications in the field of synthesis.

RESULTS AND DISCUSSION

Ligand Synthesis

The ligands **44** and **45** were synthesized in a single step from commercially available starting materials. Hydrophosphination of methyltrivinylsilane or ethoxytrivinylsilane with AIBN as initiator and a slight excess of diphenylphosphine led to the desired products in high yields (Scheme 4.4). The spectroscopic data for **44** and **45** are in agreement with the literature data.^{97,104}



Scheme 4.4. Synthesis of the phosphine ligands **44** and **45**.

During the purification process of **44**, crystals suitable for X-ray diffraction were obtained that consisted of condensed and partially oxidized ligand **44b** (Figure 4.2). The Si-O-Si angle is 180° in **44b**. The values of the Si-O-Si angles in disiloxanes (R₃Si-O-SiR₃) depend on the electronic and steric properties of the R group connected to silicon.^{105a} The angle in the sterically congested [(*p*-tol-O)₃Si]₂O is 180° as well, whereas it is only 148.8° in hexamethyldisiloxane.^{105a,b}

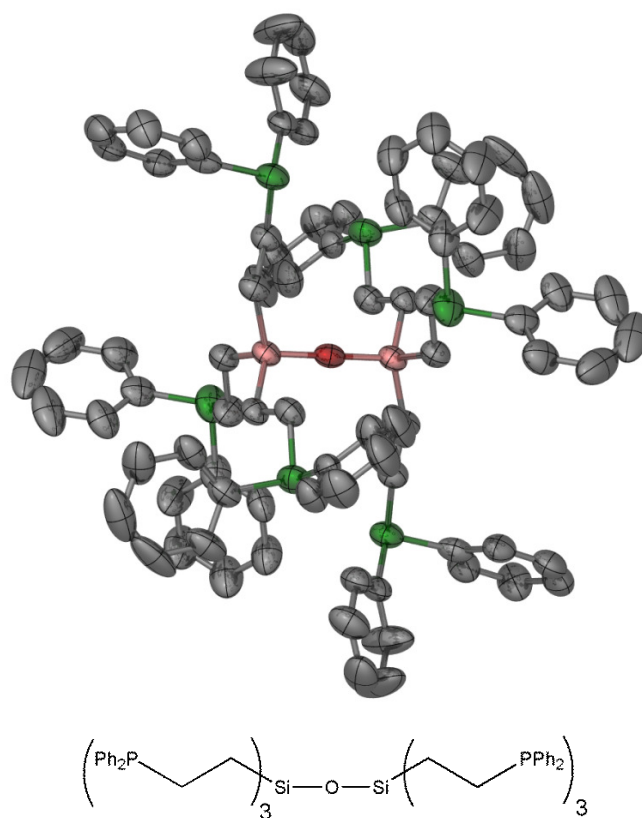
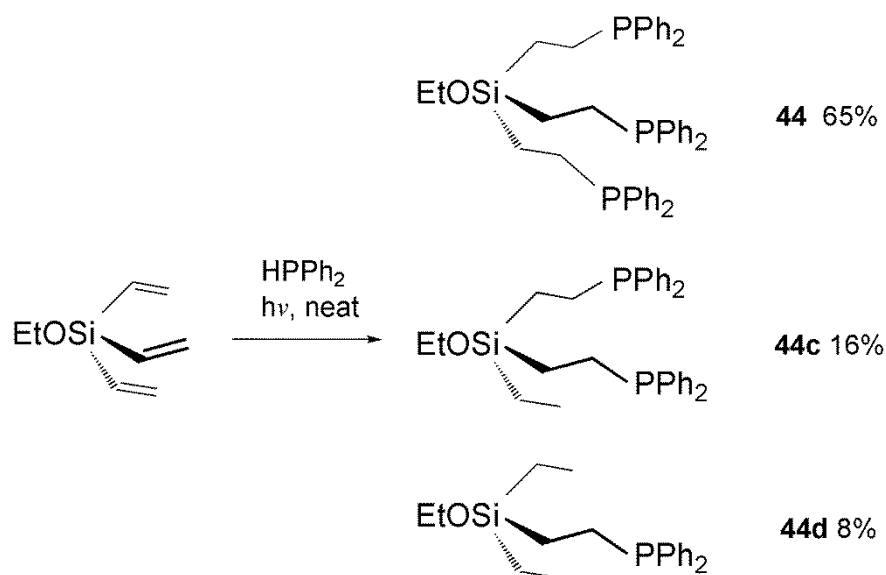


Figure 4.2. Single crystal X-ray structure of the siloxane compound **44b**. Hydrogen atoms are omitted for clarity.

Hydrophosphination of ethoxytrivinylsilane with diphenylphosphine under radical conditions via irradiation with UV light was also explored (Scheme 4.5), as described by Blümel and coworkers.^{52b} **44** was the major product, but significant amounts of partially hydrogenated phosphine ligands **44c** and **44d** were also observed. The hydrogen source is most likely Ph_2PH and its coupling product $\text{Ph}_2\text{P}-\text{PPh}_2$ has indeed been observed by ^{31}P NMR. Thus, this method proved to be less efficient and was not pursued further.



Scheme 4.5. Synthesis of the phosphine ligand **44** with the side-products **44c** and **44d**.

The ligands **44** and **45** were subjected to analysis by ^{31}P and ^{29}Si solid-state NMR. Ligand **44** shows three isotropic lines at -5.5, -8.9, and -11.6 ppm in its ^{31}P CP/MAS spectrum because the phosphorus nuclei are magnetically inequivalent in the unit cell (Figure 4.3). The CSAs of the three resonances are given in table 4.1 and are in agreement with literature data for similar diphenylalkyl phosphines.^{71,97}

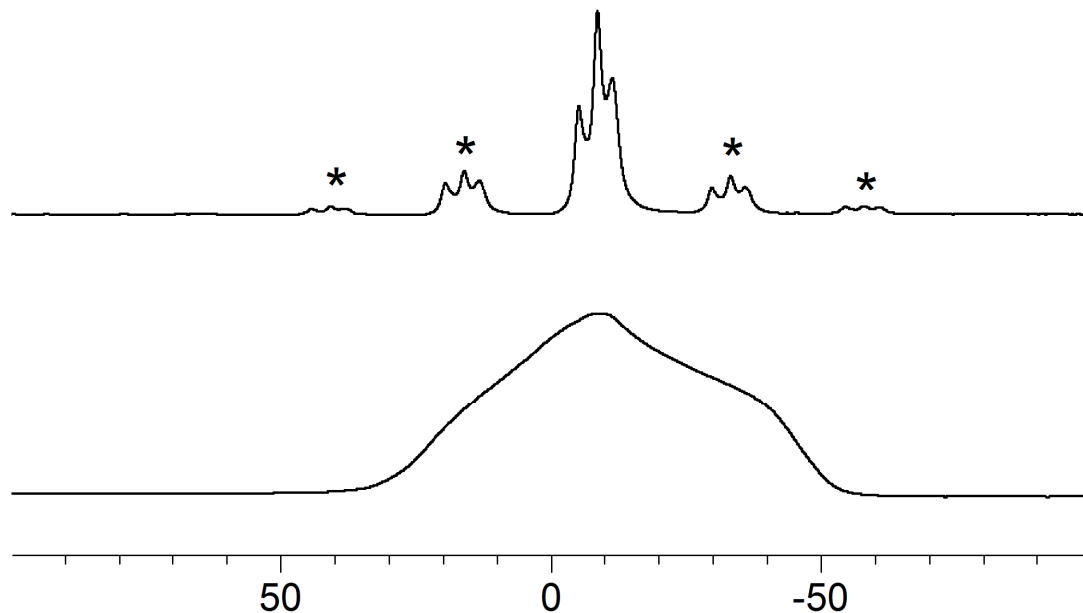


Figure 4.3. ^{31}P Wideline (*bottom*) and CP/MAS (*top*, 4 kHz spinning speed) NMR spectra of **44**. Asterisks denote rotational sidebands.

Figure 4.4 compares the ^{31}P CP/MAS spectra of polycrystalline **44** and **45**. **45** also exhibits three isotropic lines at -9.3, -10.8, and -12.9 ppm, with slightly smaller CSAs as compared to **44** (Table 4.1).

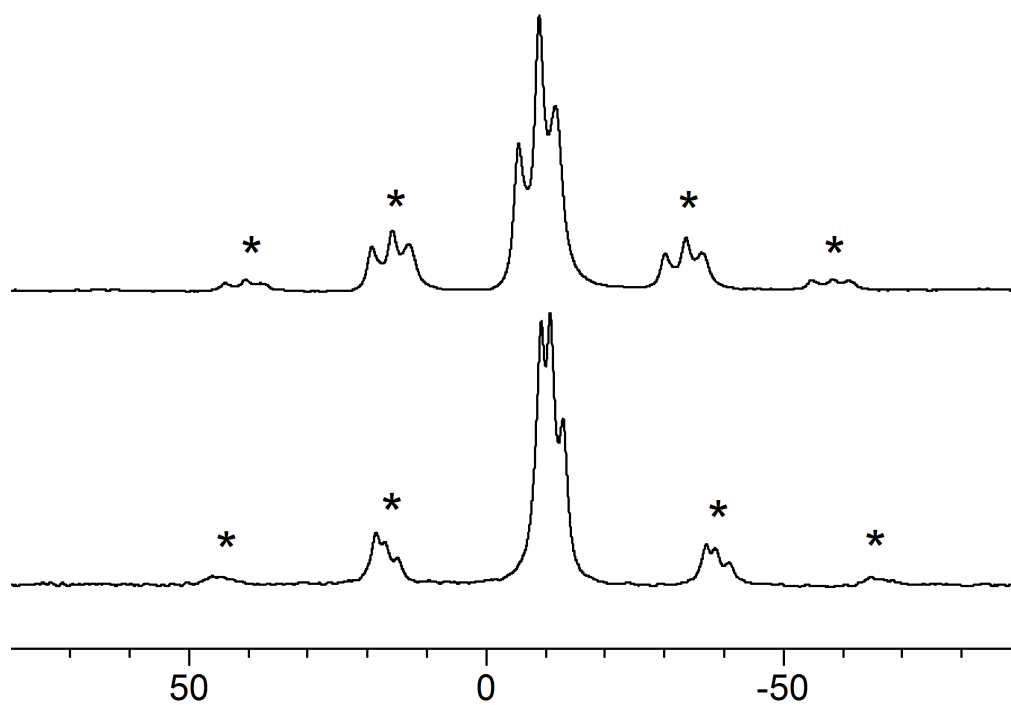


Figure 4.4. ^{31}P CP/MAS spectra of **44** (*top*, 4 kHz spinning speed) and **45** (*bottom*, 4.5 kHz spinning speed). Asterisks denote rotational sidebands.

Table 4.1. CSA parameters of **44** and **45**.

Compound	δ_{iso} [ppm]	δ_{11} [ppm]	δ_{22} [ppm]	δ_{33} [ppm]	$\delta_{11} - \delta_{33}$ [ppm]
44	-5.6	23.6	6.07	-46.4	70
	-9.0	26.1	-9.0	-44.7	70.8
	-11.7	17.5	-0.03	-52.2	69.7
45	-9.27	25.73	-9.27	-44.27	70
	-10.77	14.33	-0.77	-45.77	60.1
	-12.92	7.91	-4.58	-42.08	49.99

Both ligands were also investigated by ^{29}Si solid-state NMR (Figures 4.5 and 4.6). The spectrum of **44** shows an isotropic line at 13.1 ppm similar to the chemical shift observed in acetone- d_6 at 15.18 ppm. The primary CSA components are estimated to be $\delta_{11} = 28$ ppm, $\delta_{22} = 18$ ppm, and $\delta_{33} = -6$ ppm. The span ($\delta_{11} - \delta_{33}$) of the wideline pattern, 34 ppm, is slightly smaller than the value reported for trimethylmethoxysilane, 41 ppm, which has a similar electronic environment around Si.⁷¹

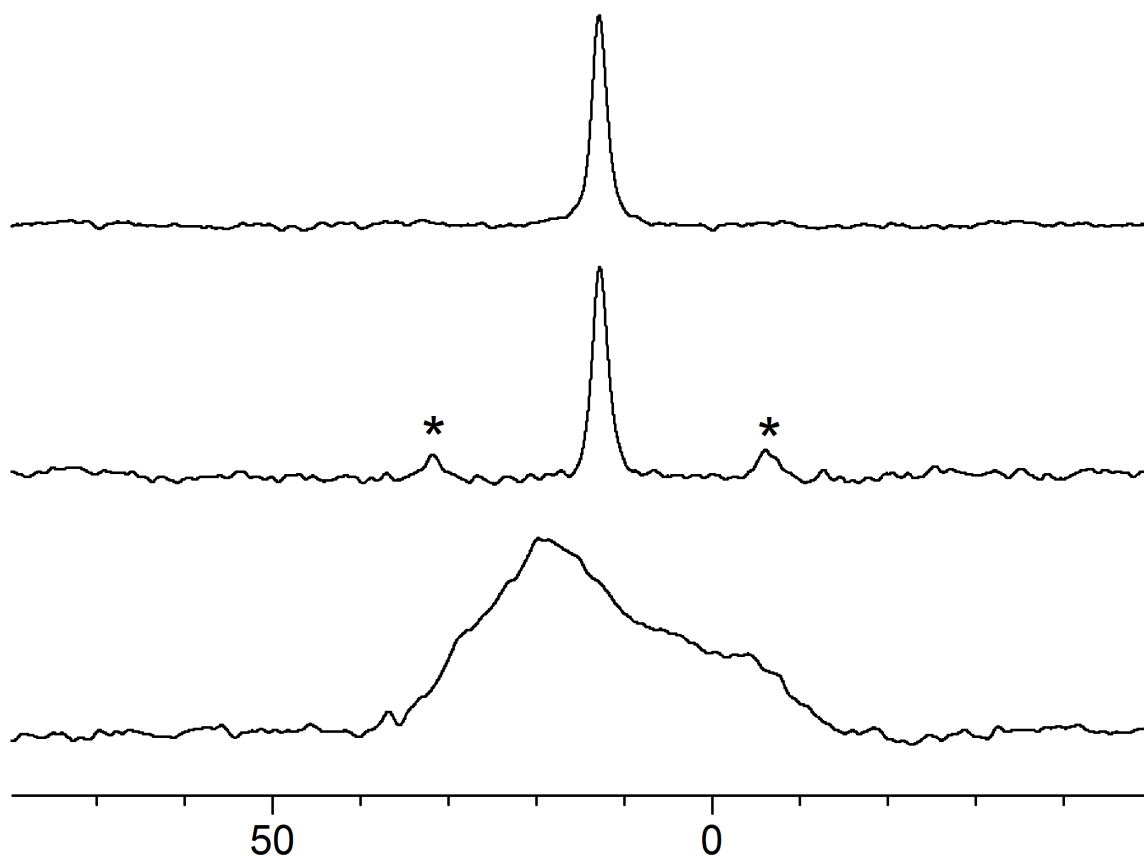


Figure 4.5. ^{29}Si CP/MAS spectra of **44** (*top*, 10 kHz spinning speed; *middle*, 1.5 kHz spinning speed; *bottom*, 0 kHz spinning speed). Asterisks denote rotational sidebands.

45 has an isotropic chemical shift of 6.7 ppm in the solid state, corresponding well to the value of 6.27 ppm in CDCl_3 . Its CSA is smaller as compared to **44** due to its more symmetric electronic environment around Si and therefore no rotational sidebands are visible.

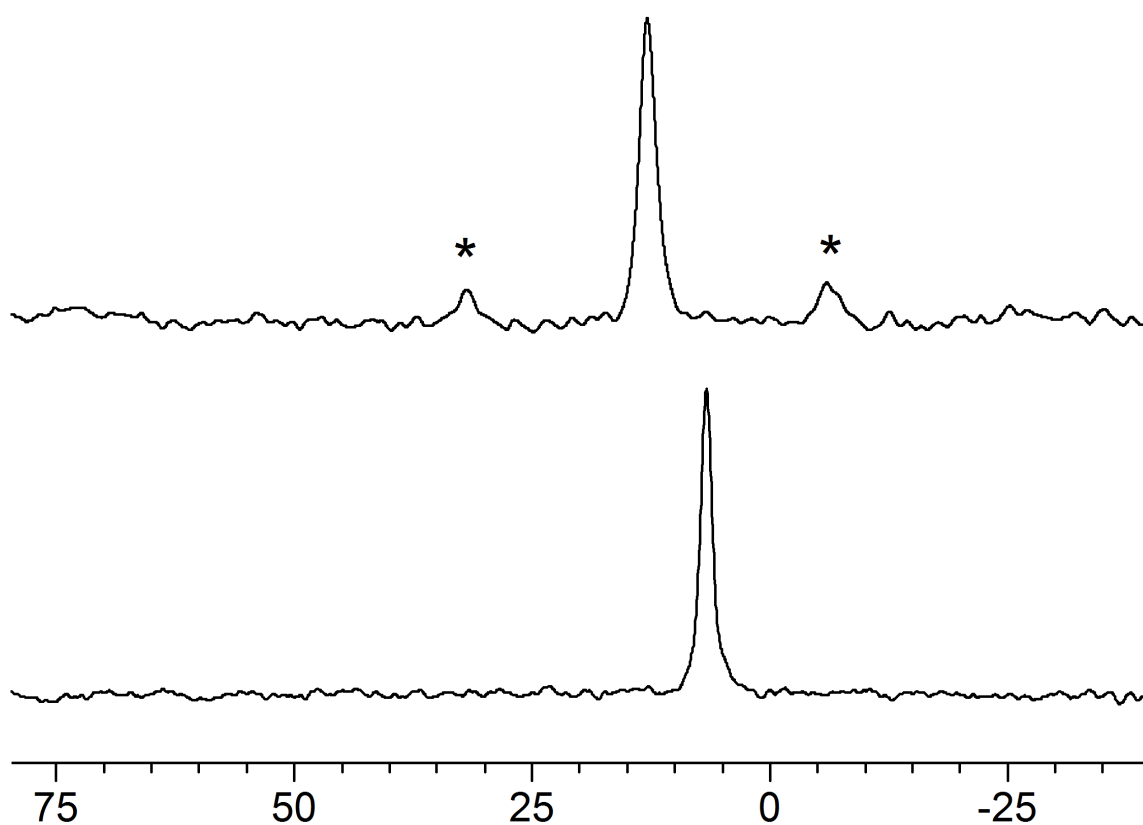
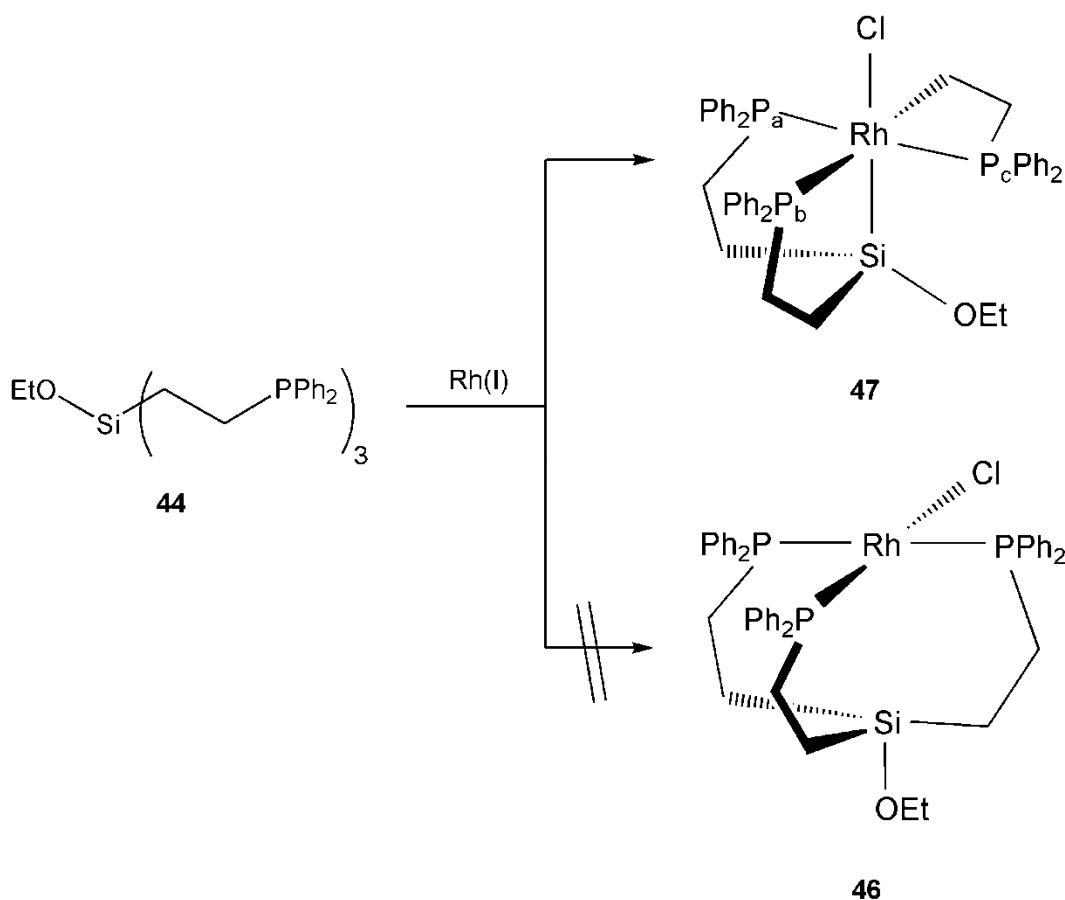


Figure 4.6. ^{29}Si CP/MAS spectra of **44** (*top*, 1.5 kHz spinning speed) and **45** (*bottom*, 5 kHz spinning speed). Asterisks denote rotational sidebands.

Rhodium and Iridium Complexes

Recently it was discovered in the Blümel group that ligand **44** reacts with Rh(I) precursors such as Wilkinson's complex or $[(\text{COD})\text{RhCl}]_2$ in an unexpected way, not leading to the anticipated square planar triphosphine complex **46**, but selectively to **47** (Scheme 4.6).⁹⁷



Scheme 4.6. Selective formation of Rh complex **47**. Rh(I) stands for $[(\text{COD})\text{RhCl}]_2$ and $\text{ClRh}(\text{PPh}_3)_3$.

The structure of **47** was deduced from its characteristic ^{31}P NMR spectrum showing a double doublet of doublets at 43.97 ppm, a double doublet at 21.36 ppm, and another double doublet at -66.66 ppm (Figure 4.7). The large coupling of 391 Hz is a $^2J(^{31}\text{P}\text{-}^{31}\text{P})$ coupling between the two phosphorus nuclei *trans* to each other.

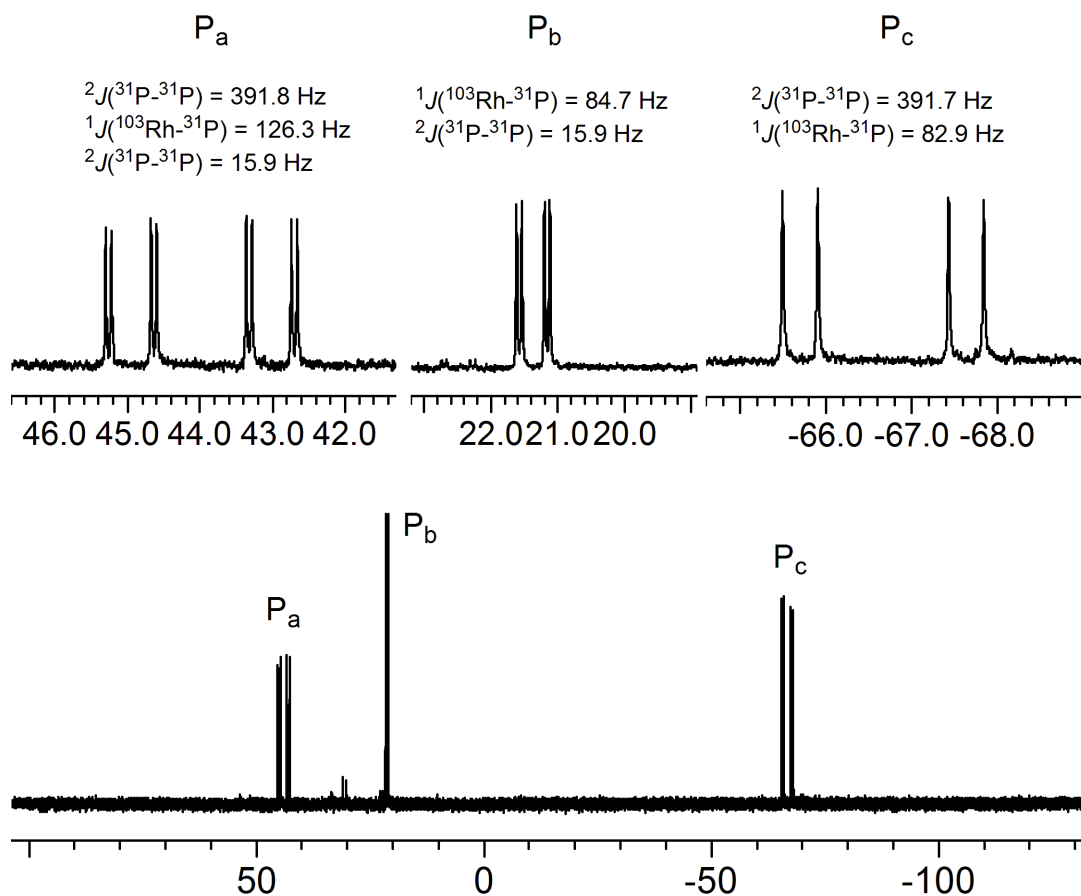


Figure 4.7. ^{31}P NMR spectrum of **47** in CDCl_3 . Assignments P_{a-c} see Scheme 4.6 above.

All phosphorus nuclei P_{a-c} display large $^1J(^{103}\text{Rh}-^{31}\text{P})$ coupling constants of 126.3, 84.7, and 82.9 Hz, respectively. Additionally, the two phosphorus nuclei P_a and P_b couple with each other, resulting in a coupling constant $^2J(^{31}\text{P}-^{31}\text{P}) = 15.9$ Hz.

47 was characterized previously in detail by multinuclear NMR, including two-dimensional ^1H - ^1H , ^{13}C - ^1H , ^{31}P - ^1H , ^{13}P - ^{13}C , and ^{29}Si - ^{31}P correlation experiments, as well as HR-MS.⁹⁷ These results have been reproduced and additionally, correct C and H elemental analysis values have been obtained that further corroborate the assigned structure.

Variable temperature NMR experiments have been undertaken to investigate whether **47** undergoes reductive elimination to yield **46** (Figure 4.8). Over the temperature range from +80 °C to -80 °C in toluene no species other than **47** could be identified. The signals around 30 ppm probably stem from decomposition and partial oxidation of the phosphine ligand. Interestingly, the chemical shift of P_c changes about 5 ppm, from -62.4 to -67.4 ppm, on going from -80 °C to +80 °C, while the shifts of the other signals remain practically unchanged.

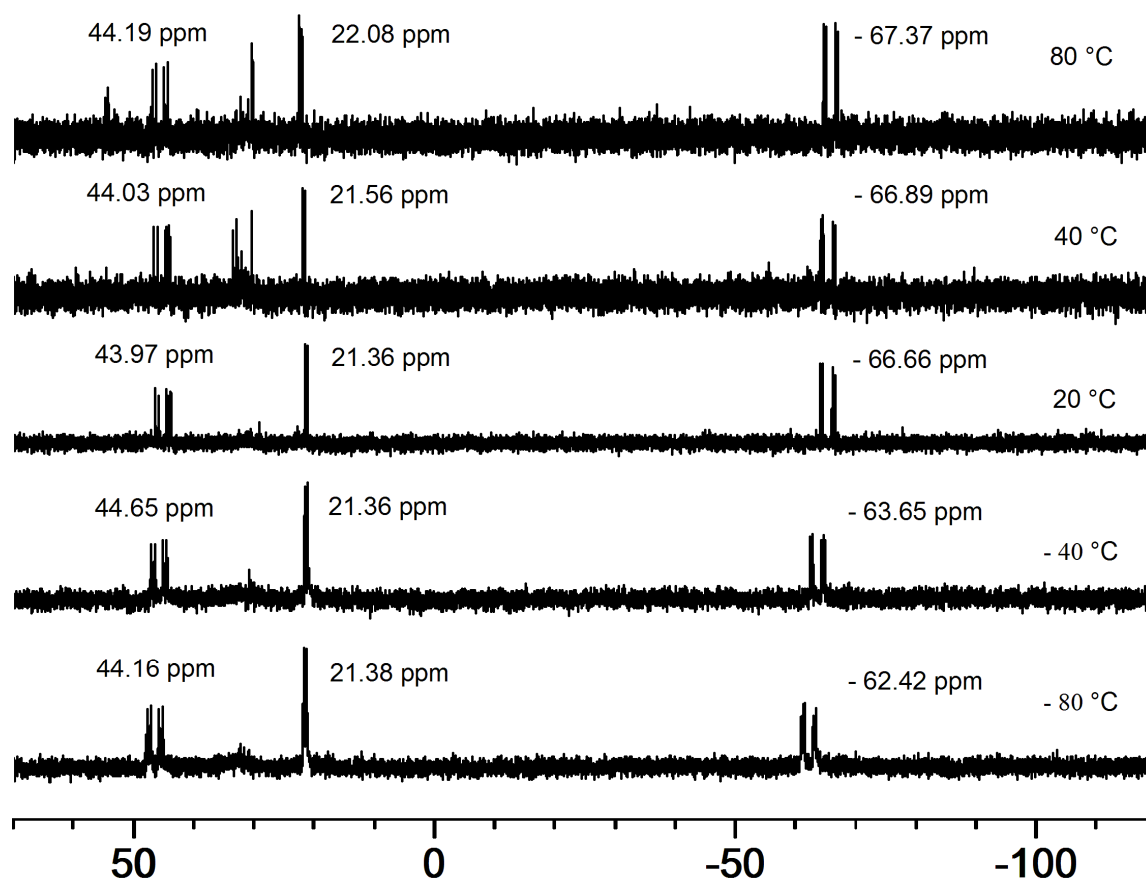


Figure 4.8. ^{31}P VT-NMR spectra of **47** in toluene at the indicated temperatures.

It can be concluded that no reductive elimination takes place once **47** is formed. A related experiment was carried out to probe whether **46** forms as an intermediate prior to the cleavage of the Si-C bond. Therefore, ligand **44** was added to a solution of $[(\text{COD})\text{RhCl}]_2$ in toluene at $-78\text{ }^{\circ}\text{C}$ and the reaction mixture was warmed up while being monitored by ^{31}P NMR. Yet again no species other than **47** was observed. The nature of the solvent does not appear to play a crucial role, as **47** was obtained as the sole product in organic solvents of various polarities such as toluene, benzene, THF, dichloromethane, and chloroform.

Single crystals suitable for X-ray diffraction remained elusive, but the structure of **47** in the solid state was investigated by ^{29}Si CP/MAS and ^{31}P CP/MAS NMR. In the ^{31}P CP/MAS NMR spectrum two isotropic lines at 42 and 30 ppm are clearly observed (Figure 4.9). A much smaller peak in the chemical shift range of the uncoordinated phosphine ligand, at -9 ppm, is also visible. A small hump can be observed at -65 ppm for the phosphorus nucleus P_c , but unfortunately, it is overlapping with the rotational sidebands of first order. The ^{31}P CP/MAS spectrum is therefore in accordance with the spectrum of **47** in solution. It is important to emphasize that signal intensities in spectra recorded with cross-polarization cannot be integrated due to differences in the kinetics of polarization transfer.^{41b-d} Due to less efficient cross-polarization in the case of the metal complexes it was necessary to record ^{31}P CP/MAS spectra with ca. 1000 scans compared to 128 scans for the free phosphine. ^{29}Si CP/MAS spectra required approximately 20.000 to 40.000 scans for a sufficient signal to noise ratio in the case of the metal complexes compared to 2000 scans for the free ligand.

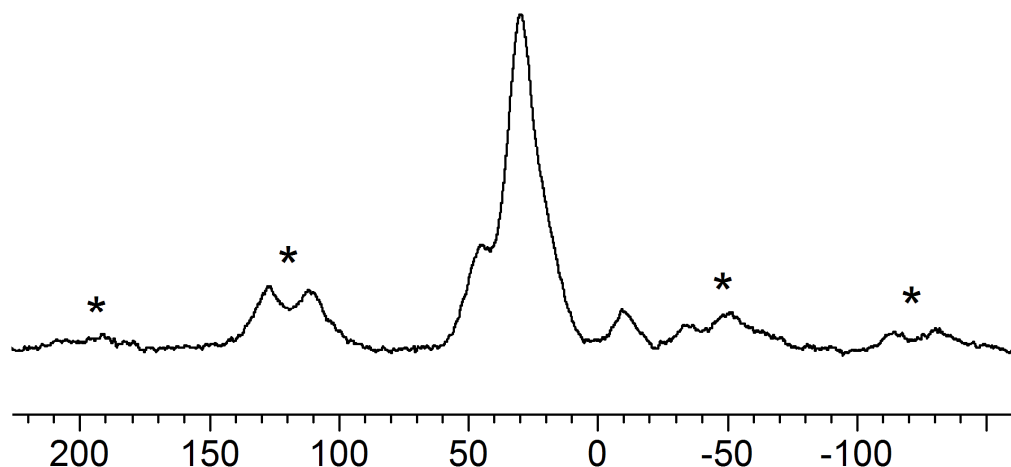


Figure 4.9. ^{31}P CP/MAS NMR spectrum of **47** (13 kHz spinning speed). Asterisks denote rotational sidebands.

In the ^{29}Si CP/MAS NMR of **47** two resonances at 75.4 ppm and 13.6 ppm are observed (Figure 4.10). The chemical shift of the signal at 75.4 ppm is in good agreement with the value of **47** in $\text{THF-}d_8$ with 76.70 ppm. The resonance at 13.6 ppm, is assigned to excess free ligand.

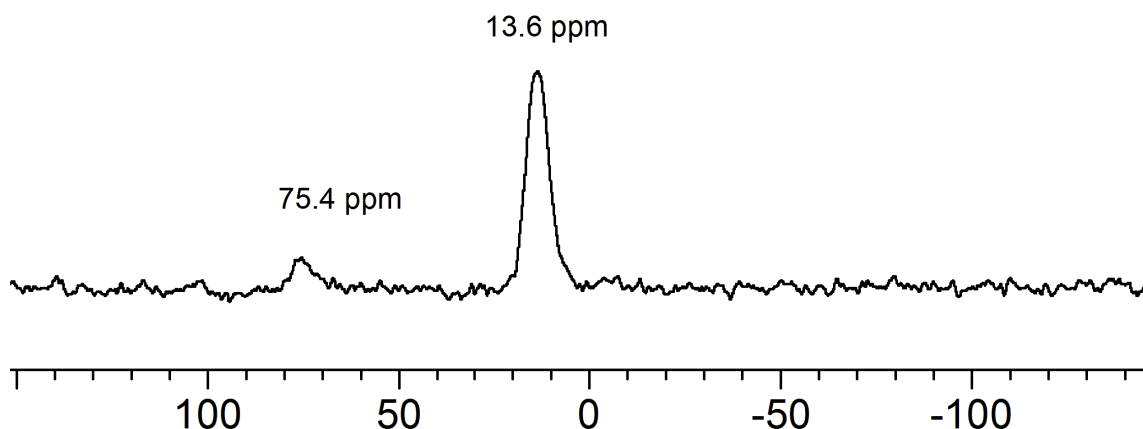
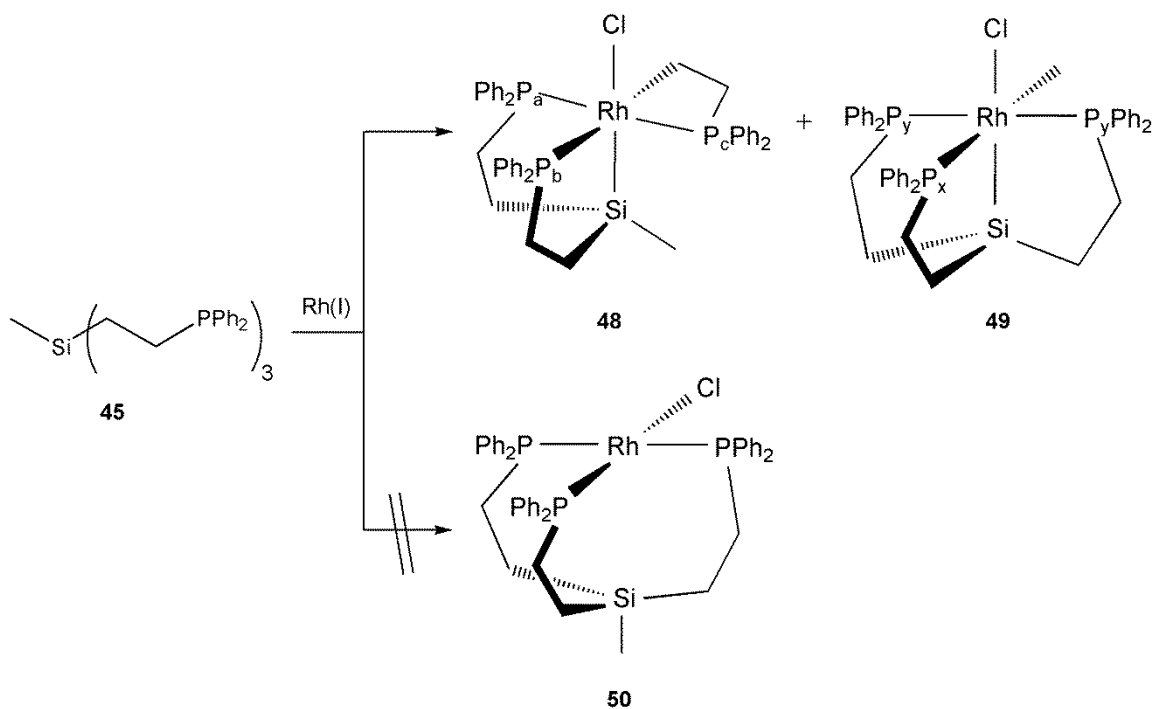


Figure 4.10. ^{29}Si CP/MAS NMR spectrum of **47** (13 kHz spinning speed).

Next, ligand **45** was employed for this study to probe the selectivity of the C-Si bond cleavage, and to explore whether the Si-CH₂ bond of one of the ligand phosphine groups or the Si-Me bond would react preferentially. Furthermore, exchanging the ethoxy group for a methyl group might change the solubility of the product which might aid crystallization efforts of the compounds.

When **45** was reacted with $[(\text{COD})\text{RhCl}]_2$ a mixture of the isomers **48** and **49** was obtained (Scheme 4.7). As in the case of the ligand **44** no Rh(I) species like **50** could be detected.



Scheme 4.7. Synthesis of Rh complexes **48** and **49**. Rh(I) stands for $[(\text{COD})\text{RhCl}]_2$ and $\text{ClRh}(\text{PPh}_3)_3$.

The ^{31}P NMR spectrum of **48** is very similar to the spectrum of **47**, showing three signals in a 1 : 1 : 1 ratio at 46.06, 22.36, and -68.32 ppm for P_a , P_b , and P_c (Figure 4.11). The remaining signals are assigned to **49**. The two equivalent phosphines P_y *trans* to each other give rise to a doublet of doublets at 37.94 ppm, with a $^1J(^{103}\text{Rh}-^{31}\text{P})$ coupling constant of 115.9 Hz, and a $^2J(^{31}\text{P}-^{31}\text{P})$ coupling constant of 21.2 Hz. The resonance of the phosphine P_x *trans* to the methyl group appears as a doublet of triplets at 28.97 ppm, with a $^1J(^{103}\text{Rh}-^{31}\text{P})$ coupling constant of 88.7 Hz, and a $^2J(^{31}\text{P}-^{31}\text{P})$ coupling constant of 21.2 Hz.

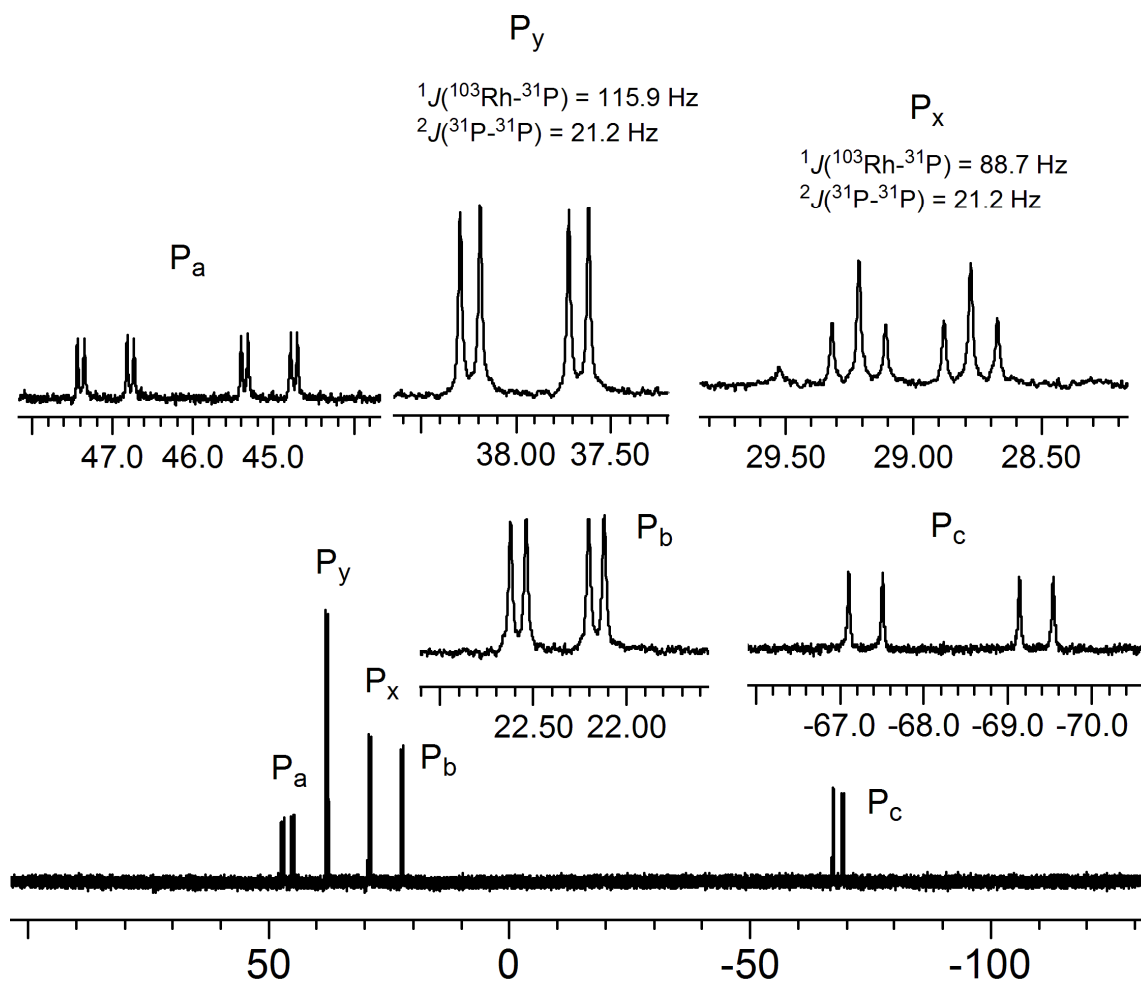


Figure 4.11. ^{31}P NMR spectrum of a mixture of **48** and **49** in C_6D_6 . For signal assignments P_{a-c} and $P_{x,y}$ see Scheme 4.7 above.

This assignment is corroborated by ^{29}Si NMR (Figure 4.12). The mixture of the two isomers, **48** and **49**, leads to two distinct multiplets at 97.05 ppm and 64.06 ppm. The multiplet at 64.06 ppm for **48** is split into a doublet four times with a large $^1J(^{103}\text{Rh}-^{29}\text{Si})$ coupling constant of 32.5 Hz and three smaller $^2J(^{31}\text{P}-^{29}\text{Si})$ coupling constants of 12.6, 7.4, and 4.7 Hz. This is in accord with the multiplet observed for **47**. The multiplet assigned to **49** at 97.05 ppm also shows a large 1J coupling of 28.2 Hz between ^{29}Si and

^{103}Rh . The two equivalent phosphines P_y give rise to a triplet with $^2J(^{31}\text{P}-^{29}\text{Si}) = 6.5$ Hz, and the phosphine *trans* to the methyl group leads to a doublet with $^2J(^{31}\text{P}-^{29}\text{Si}) = 2.7$ Hz. Therefore, overall a doublet of double triplets is observed.

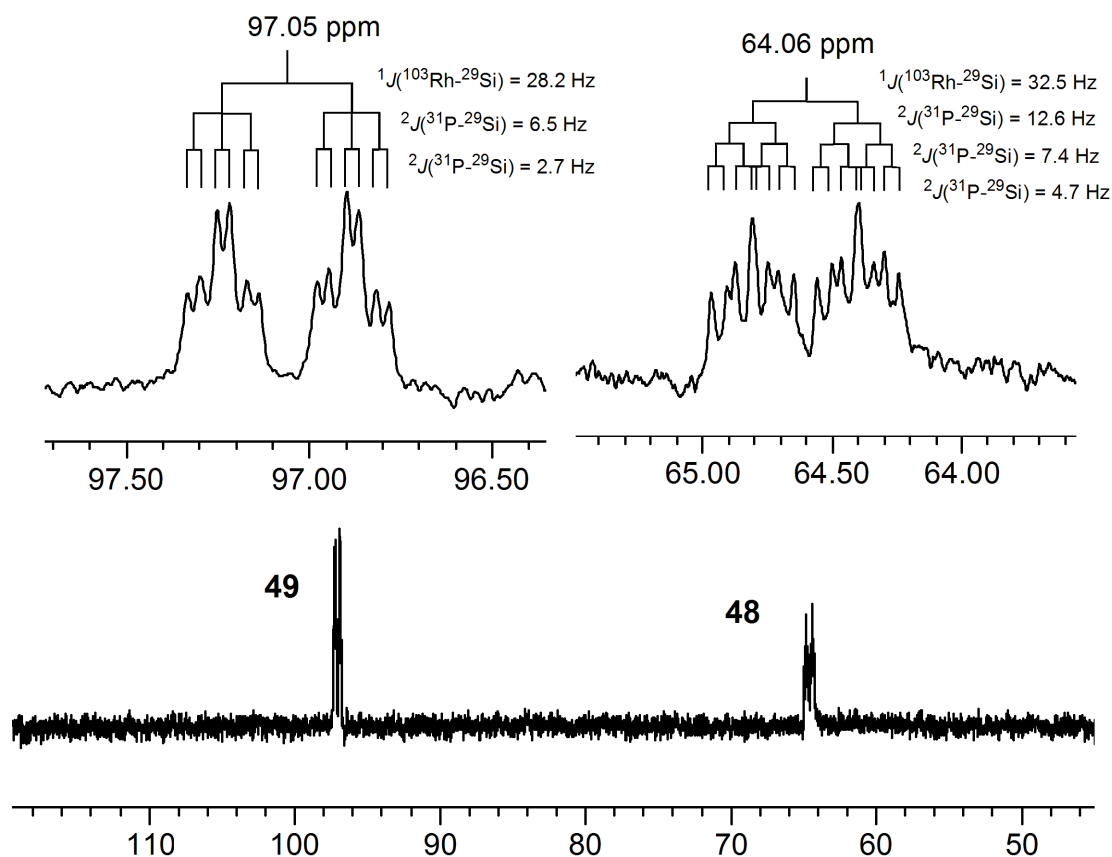


Figure 4.12. ^{29}Si NMR spectrum of a mixture of **48** and **49** in C_6D_6 .

The ^1H and ^{13}C NMR spectra are highly congested impeding firm interpretation. Yet, some information can be gained from the alkyl region of the ^{13}C NMR spectrum (Figure 4.13). The multiplet at 9.29 ppm is assigned to the methyl group C of **49** bound to Rh. The large J value of 73.9 Hz is due to coupling of the phosphine with P_x *trans* to

the methyl group. Coupling of the methyl C with ^{103}Rh gives rise to a doublet with a coupling constant of 17.1 Hz, and coupling with the two equivalent phosphines P_y *cis* to the methyl group leads to a triplet with $^2J(^{31}\text{P}-^{13}\text{C}) = 7.1$ Hz. The signal at -0.49 ppm is assigned to **48**. Its chemical shift and coupling constants are very similar to those of **47**. A double doublet of doublets is observed with the largest coupling of 47.9 Hz to the phosphine *trans* to the CH_2 group. Coupling to P_e leads to a doublet with $^2J(^{31}\text{P}-^{13}\text{C}) = 32.9$ Hz and the coupling with ^{103}Rh amounts to 13.9 Hz. All the chemical shifts and coupling constants are within the typical range reported for similar Rh complexes,¹⁰⁶ e.g. Osakada *et al.* observed $^1J(^{103}\text{Rh}-^{29}\text{Si})$ coupling constants ranging from 29.4 to 49.6 Hz in compounds of the general formula $\text{HRhX}(\text{Si}(\text{OEt})_{3-n}\text{Me}_n)(\text{PPh}_3)_2$ ($\text{X} = \text{I}, \text{Cl}; n = 1, 2$).¹⁰⁷ Tobita and co-workers also described a similar compound, $\text{HRhCl}[(\kappa^2\text{Si}, P)\text{-Me}_2\text{Si}(\text{CH}_2)_2\text{PPh}_2](\text{PMe}_3)_2$, which, in ^{29}Si NMR, displays a $^1J(^{103}\text{Rh}-^{29}\text{Si})$ coupling of 26.1 Hz and three $^2J_{\text{cis}}$ couplings between ^{31}P and ^{29}Si of 10.5, 8.2, and 6.9 Hz. In the ^{31}P NMR spectrum, a large $^2J_{\text{trans}}$ coupling of 364 Hz and a significantly smaller *cis* coupling of 26 Hz was observed.¹⁰⁸

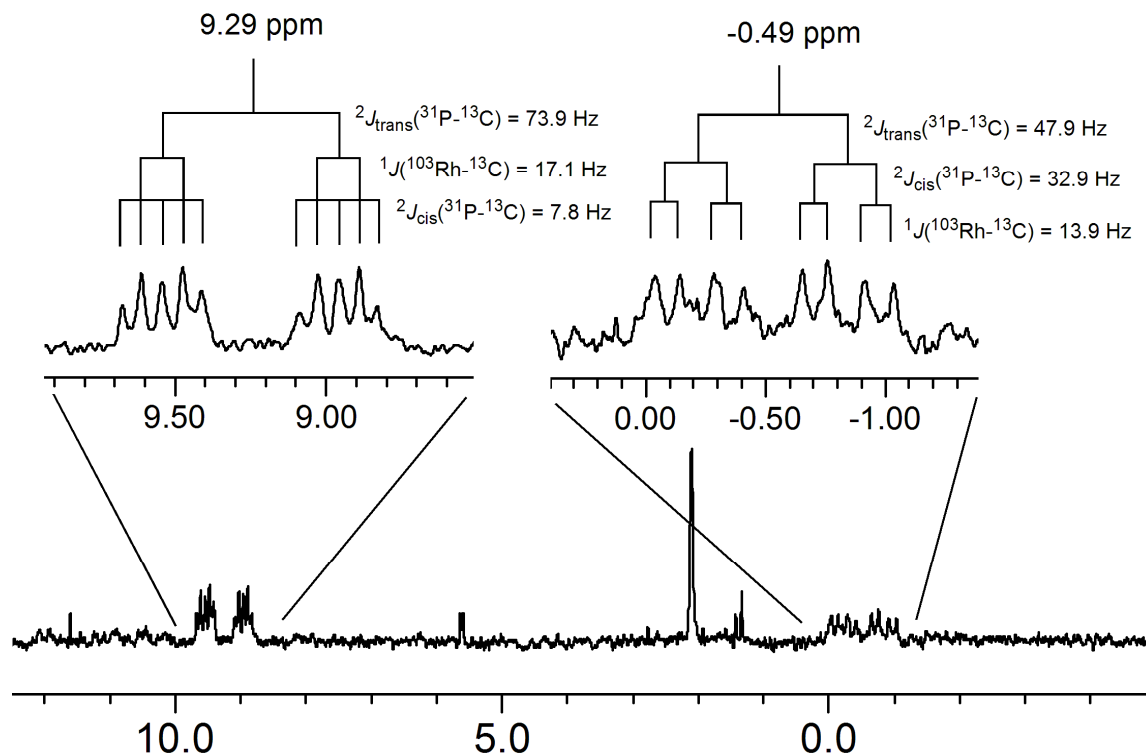


Figure 4.13. Alkyl region of the ^{13}C NMR spectrum of a mixture of **48** and **49** in C_6D_6 .

After removal of the solvent, a sample was subjected to analysis by HR-MS. A peak at $m/z = 785.1542$ was detected corresponding to $[\text{M}-\text{Cl}]^+$ (calculated = 785.1558).

Considerable effort was devoted to synthesize **48** and **49** selectively. A temperature dependence of the ratio of **48** to **49** was noted early on. A systematic study in THF and toluene revealed a preference for the formation of **49** at lower temperatures (Figure 4.14).

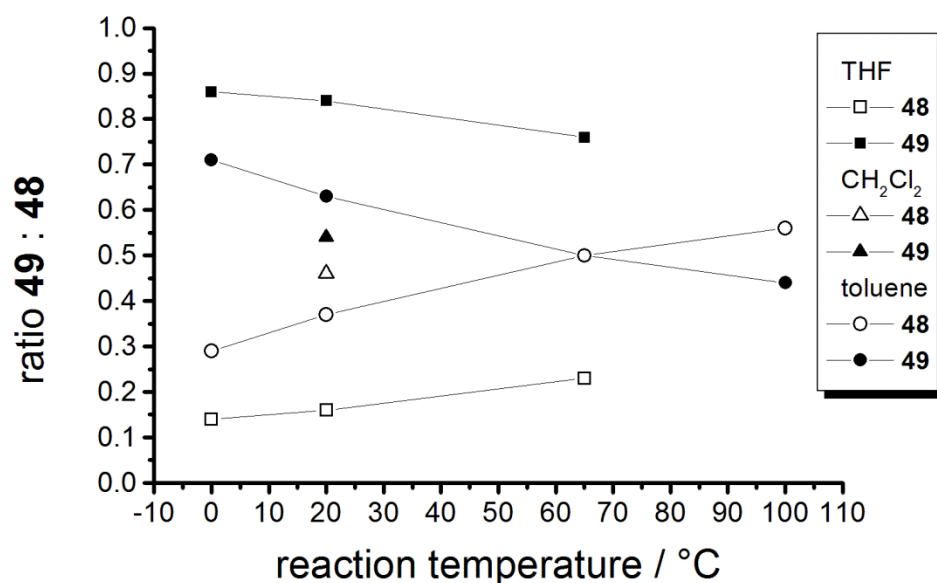
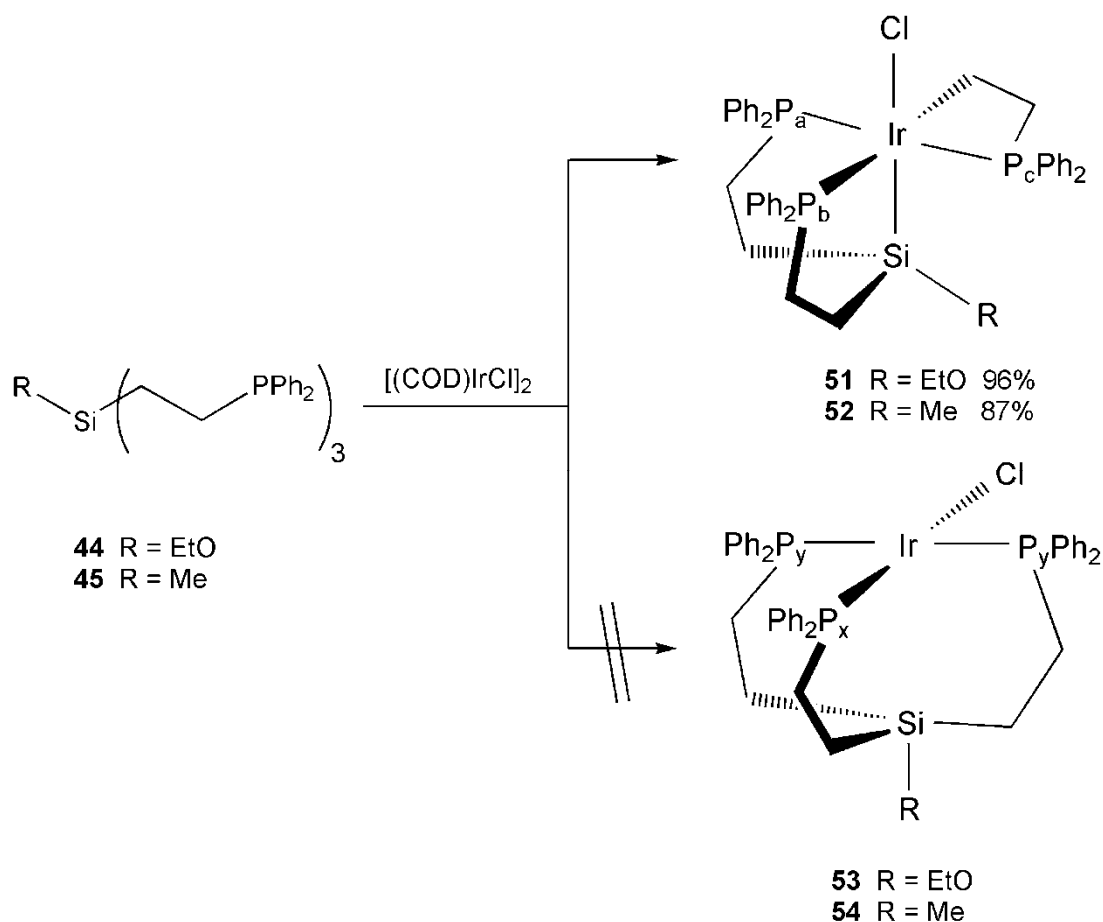


Figure 4.14. Isomer ratio of **48** to **49** obtained at different reaction temperatures in the indicated solvents. The ratios were determined by ^{31}P NMR spectroscopy.

While the reaction proceeds to completion within a few hours at elevated temperatures, at 0 °C the reaction time exceeds ten days. Furthermore, at low temperatures an orange precipitate was often encountered which proved to be insoluble in common organic solvents. Carrying out the reaction under dilute conditions (0.13 mM) prevented this precipitate. Due to the already slow reaction at 0 °C the reaction temperature was not lowered further. Attempts to isolate either isomer in pure form remained unsuccessful.

In order to probe the generality of the Si-C bond cleavage described above this study was extended to the reaction of the ligands **44** and **45** with $[(\text{COD})\text{IrCl}]_2$.



Scheme 4.8. Selective formation of the Ir complexes **51** and **52**.

Ligand **44** reacts with $[(\text{COD})\text{IrCl}]_2$ in toluene at elevated temperatures to give **51** selectively and in quantitative yield, as determined by ^{31}P NMR (Scheme 4.8). Apart from the absence of coupling with the metal, the ^{31}P NMR spectrum of **51** resembles the spectrum of the Rh complex **48** (Figure 4-15). The two phosphines *trans* to each other display a large coupling constant of 358.3 Hz. P_a resonates at 8.87 ppm as a doublet of doublets. The *cis*-coupling with the phosphine *trans* to the alkyl group is much smaller with $J = 3.5$ Hz. The signal at 2.19 ppm is assigned to P_b . The two coupling constants are

$J_{\text{cis}}(^{31}\text{P}_\text{b}-^{31}\text{P}_\text{a}) = 3.5 \text{ Hz}$ and $J_{\text{cis}}(^{31}\text{P}_\text{b}-^{31}\text{P}_\text{c}) = 5.3 \text{ Hz}$. The resonance of P_c is observed in the high-field region of the spectrum, at -90.91 ppm.

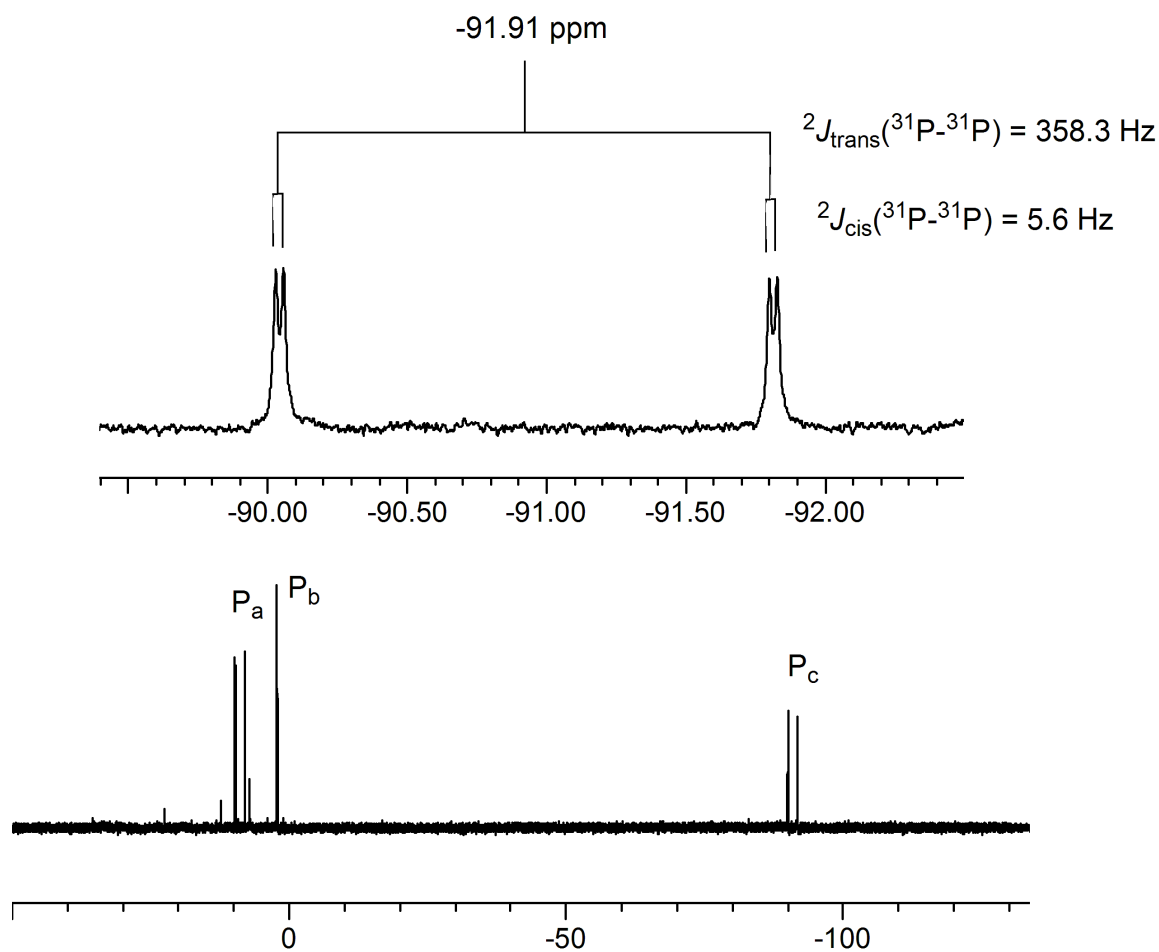


Figure 4.15. ^{31}P NMR spectrum of **51** in CDCl_3 . For signal assignments P_a , P_b , and P_c see Scheme 4.8 above.

45 reacts with $[(\text{COD})\text{IrCl}]_2$ in refluxing THF in the same manner to form **52** and its ^{31}P NMR spectrum is almost identical to the one of **51** (Figure 4.16). One difference

is that the values of the two *cis*-coupling constants, $^2J_{\text{cis}}(^{31}\text{P}_\text{b}-^{31}\text{P}_\text{a}) = 4.7 \text{ Hz}$, $^2J_{\text{cis}}(^{31}\text{P}_\text{b}-^{31}\text{P}_\text{c}) = 4.8 \text{ Hz}$ are very similar, thus leading to a *pseudo*-triplet for P_b at 3.79 ppm.

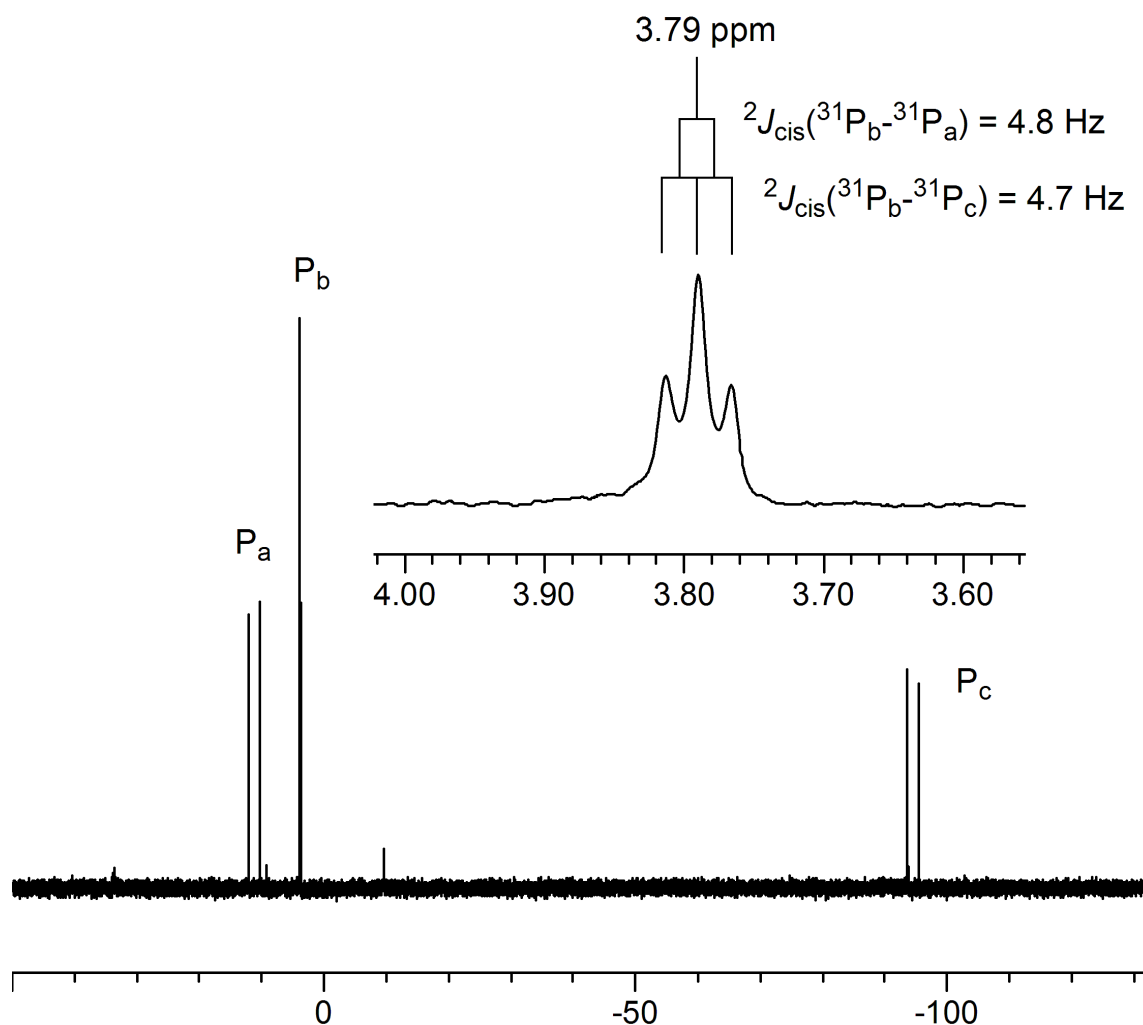


Figure 4.16. ^{31}P NMR spectrum of **52** in CDCl_3 . For signal assignments P_a , P_b , and P_c see Scheme 4.8 above.

The respective ^{29}Si NMR spectra are also similar. In the case of **51** a doublet of doublets is observed at 50.48 ppm (Figure 4.17). The two coupling constants of 10.4 Hz

and 5.1 Hz are due to couplings to two of the phosphines. The third coupling is probably too small to be resolved. The ^{29}Si nucleus in **52** resonates at 35.83 ppm. The upfield shift as compared to **51** is expected due to the higher electron donating ability of the methyl group as compared to the ethoxy group. Furthermore, two coupling constants of 8.4 Hz and 4.9 Hz due to coupling with ^{31}P nuclei can be extracted.

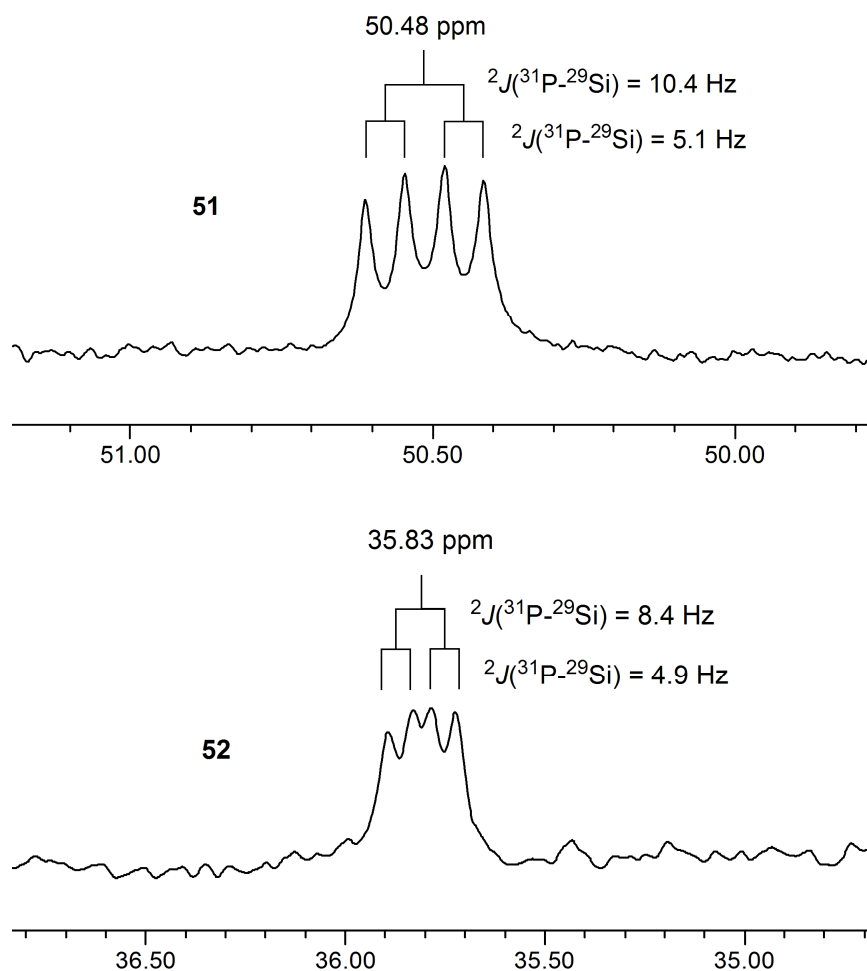
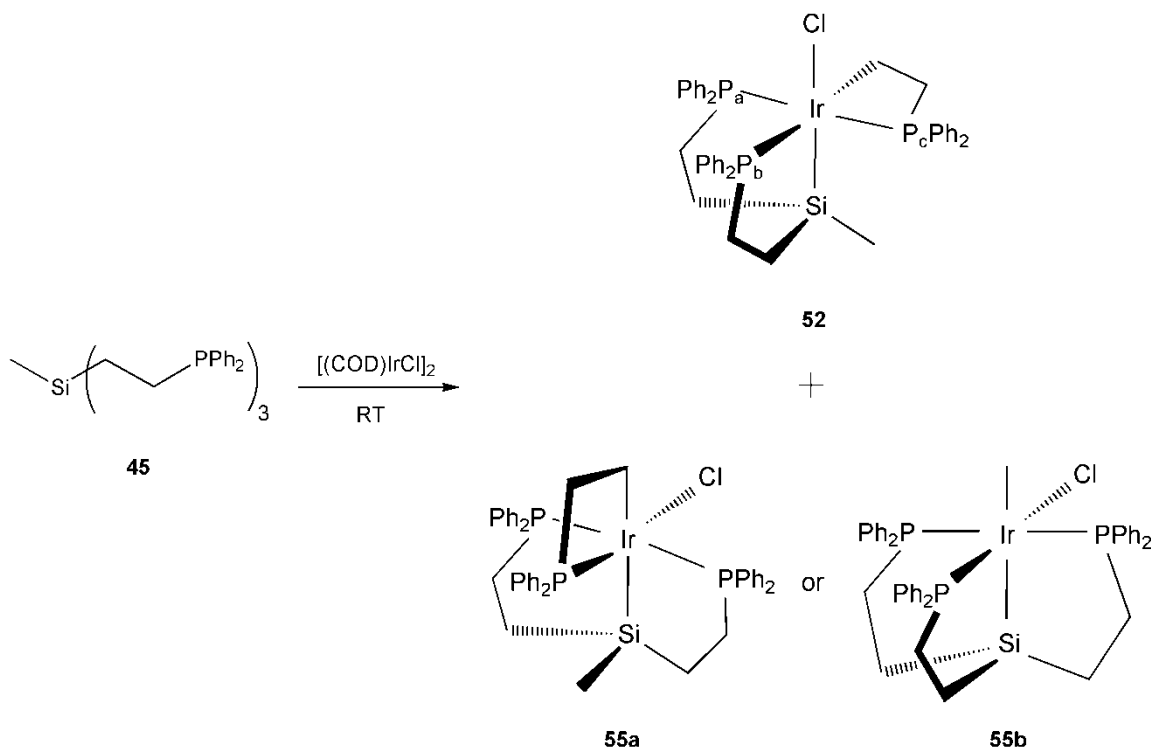


Figure 4.17. ^{29}Si NMR spectra of **51** (top) and **52** (bottom) in CDCl_3 .

The constitution of **51** and **52** was corroborated by HR-MS measurements and elemental analyses.

The reaction of **44** with $[(\text{COD})\text{IrCl}]_2$ yields exclusively **51** in THF as well as benzene, CH_2Cl_2 , CHCl_3 , and toluene, both under reflux and at room temperature. In contrast to this, the reaction of **45** with $[(\text{COD})\text{IrCl}]_2$ in THF, benzene, CH_2Cl_2 , CHCl_3 , and PhCl at room temperature leads to a mixture of products (Scheme 4.9).



Scheme 4.9. Reaction of **45** with $[(\text{COD})\text{IrCl}]_2$ to form **52** and **55a** or **55b**.

Figure 4.18 shows the ^{31}P NMR spectrum of the reaction mixture. One set of 3 signals can be assigned to **52**. The other species displays a triplet at 13.00 ppm with a

coupling constant of 14.7 Hz and a doublet at 9.27 ppm with a coupling constant of 14.6 Hz in a 1 : 2 ratio.

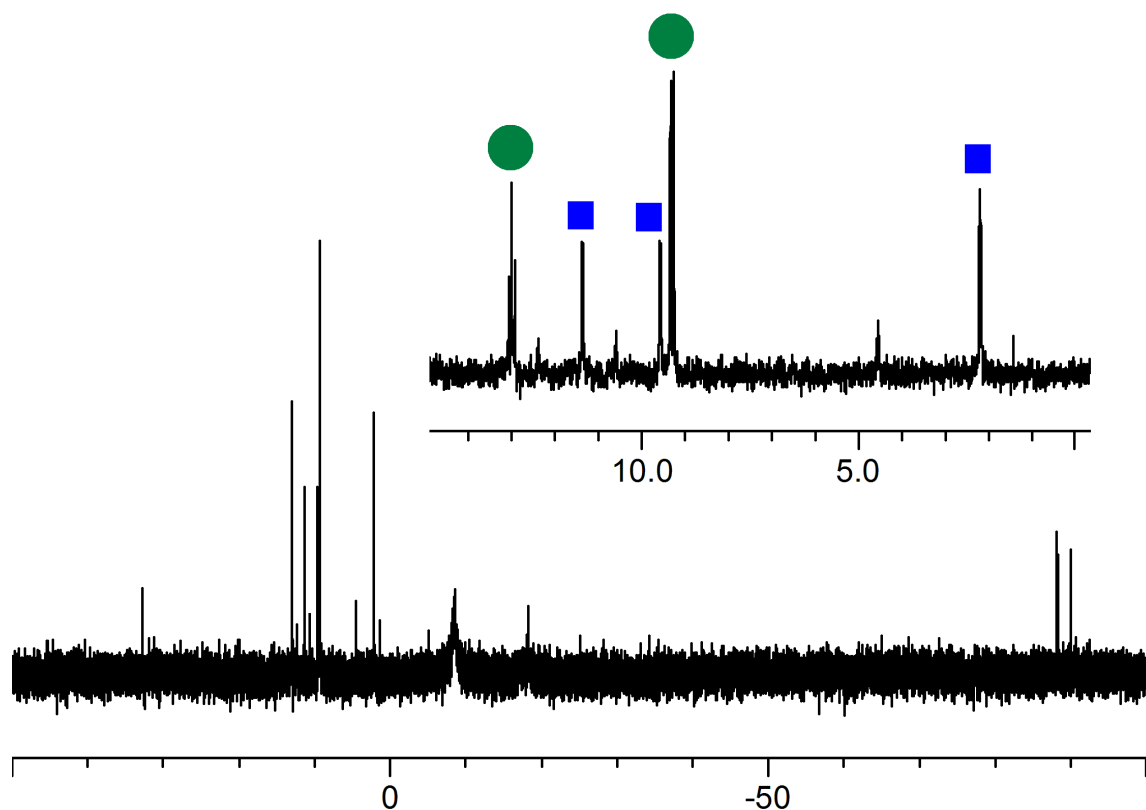


Figure 4.18. ^{31}P NMR spectrum of a mixture of **52** (*blue*) and **55** (*green*) in CDCl_3 .

Attempts to isolate the second species, **55**, in analytically pure form failed, but a sample of sufficient quality for NMR spectroscopic studies could be obtained by reacting **45** with $[(\text{COD})\text{IrCl}]_2$ in CH_2Cl_2 at room temperature for 3 days. The ^{31}P NMR spectrum (Figure 4.19) shows resonances for **55** as well as three singlets at 33.89, 32.72, and -18.11 ppm. The two singlets around 30 ppm possibly stem from phosphine oxides. The signal at -18.11 ppm does not correspond to uncoordinated ligand **45**, which

resonates at -9.88 ppm. The chemical shift of -18.11 ppm is close to the chemical shift of $\text{Ph}_2\text{PCH}_2\text{CH}_2\text{OH}$, which is reported to be at -23.0 ppm in CH_2Cl_2 ,¹⁰⁹ and could therefore stem from cleavage of the Ir-C bond. It is further noteworthy that there are broad signals around 32 and -8 ppm. The resonance at -8 ppm is in the region of uncoordinated ligand 45.

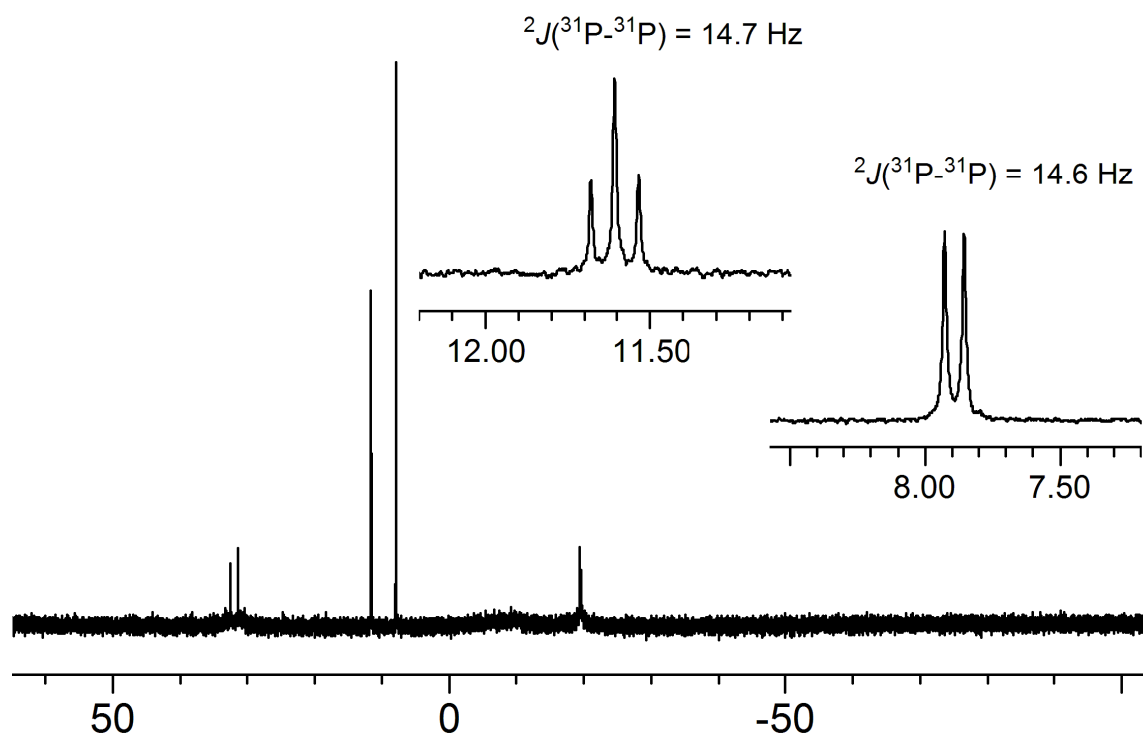


Figure 4.19. ^{31}P NMR spectrum of **55b** in CDCl_3 .

The chemical shifts, the multiplicities, and the integrals of the signals in the ^{31}P NMR spectrum suggest a square planar coordination with one phosphine coordinated *trans* to the Cl substituent and two equivalent phosphines *cis* to Cl. ^{29}Si NMR clearly shows that the silane underwent a chemical change as compared to the uncoordinated

ligand, since the resonance displayed a downfield coordination shift of 73.3 ppm and is now detected as a doublet at 79.57 ppm with a coupling constant of 2.0 Hz (Figure 4.20).

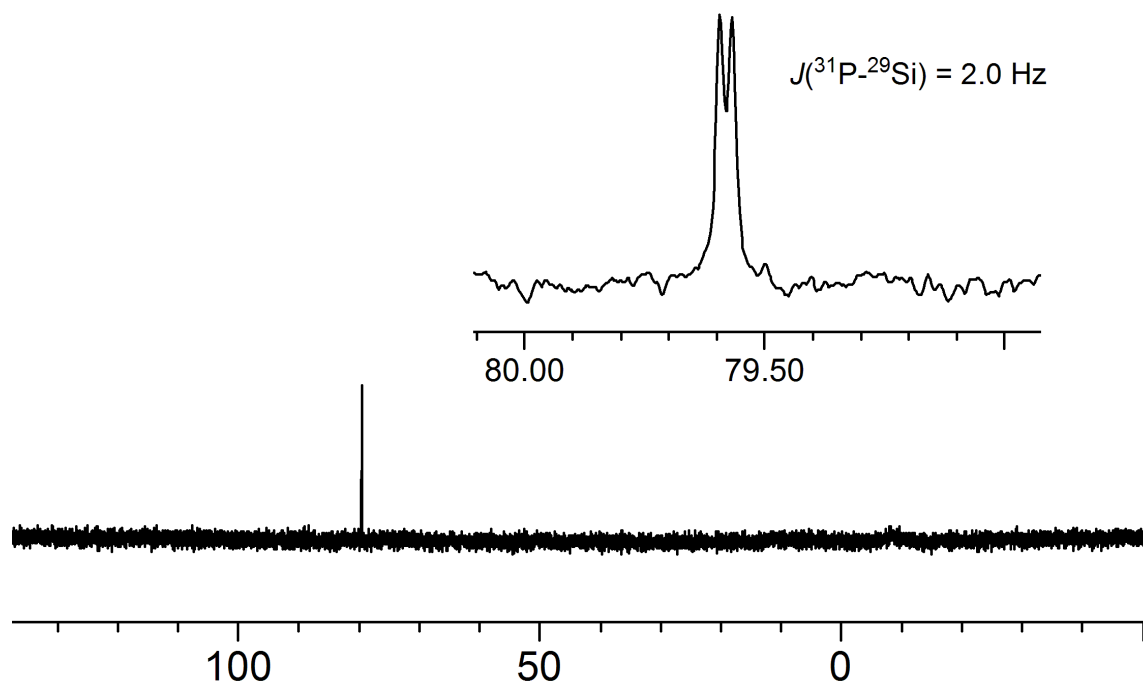


Figure 4.20. ^{29}Si NMR spectrum of **55b** in CDCl_3 .

Both structures, **55a** and **55b**, are in reasonable agreement with the data from ^{31}P and ^{29}Si NMR spectroscopy.

The ^1H NMR spectrum displays broad signals that lead to overlapping of key resonances. However, **55a** is expected to show characteristic multiplets between 3.5 ppm and 4.5 ppm for the methylene protons α to P_a in the ^1H NMR spectrum (Figure 4.21).

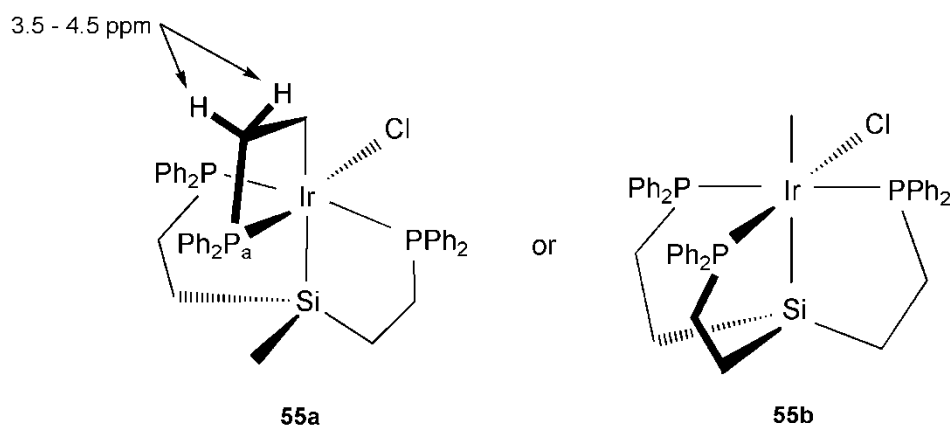


Figure 4.21. Isomers **55a** and **55b**.

The absence of any resonances between 3.5 ppm and 5 ppm suggests that **55b** is the structure of the second isomer.

The structure of **52** was investigated by ^{31}P and ^{29}Si solid-state NMR (Figures 4.22 and 4.23).

In the ^{31}P solid-state NMR spectrum the three isotropic lines corresponding to the resonances in solution are clearly visible at 10.4, 7.0, and -92.9 ppm. The high crystallinity of the sample and the resulting small linewidth allow the large ^{31}P - ^{31}P *trans* coupling of 350 Hz to be observed. In addition to the narrow resonances of **52** there is a very broad peak at -8 ppm. The chemical shift corresponds to free ligand, which is present in traces (Figure 4.10, *bottom*). As discussed above, the cross-polarization is much more efficient for the ligand than for the metal complex, hence the large signal intensity of the ^{31}P resonance at about -10 ppm (Figure 4.10, *top*).

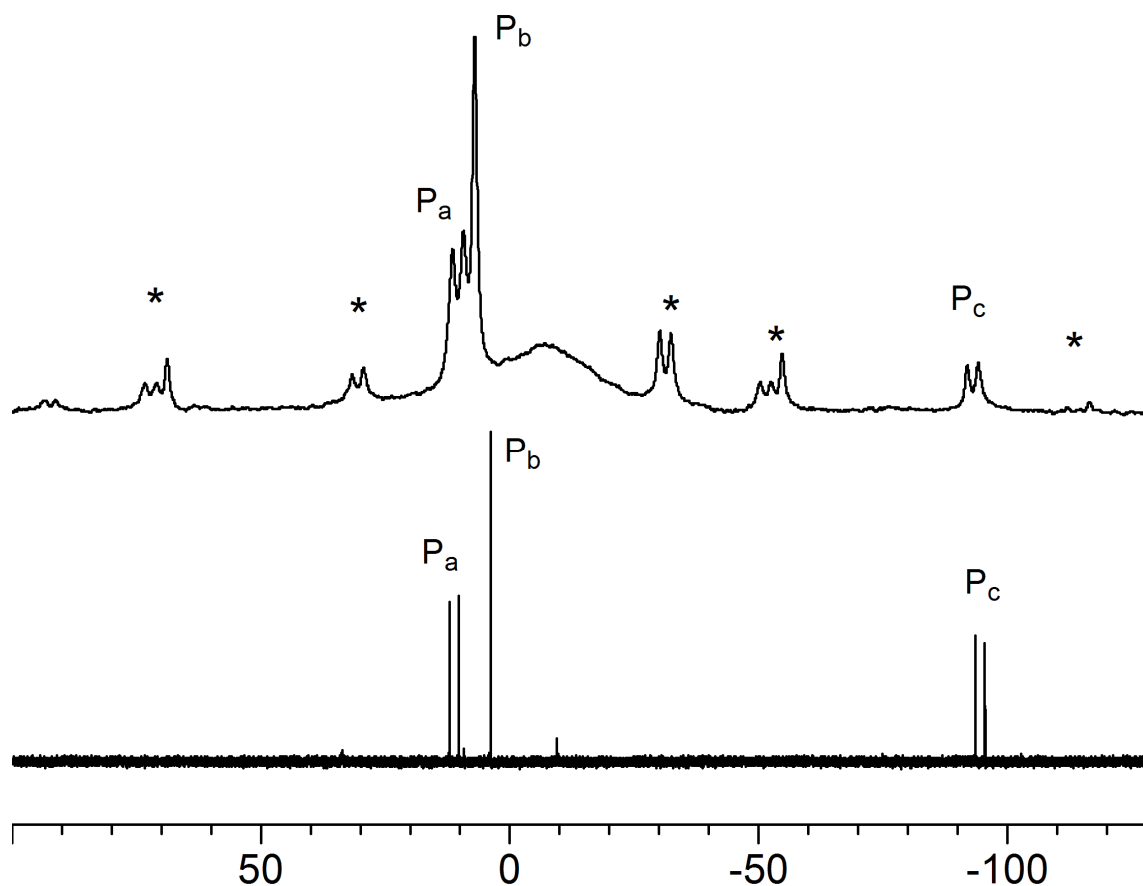


Figure 4.22. ^{31}P NMR spectrum of **52** (Scheme 4.8) in CDCl_3 (*bottom*) and ^{31}P CP/MAS spectrum of polycrystalline **52** (*top*, 10 kHz spinning speed). Asterisks denote rotational sidebands.

In the ^{29}Si CP/MAS spectrum two resonances are observed (Figure 4.23). A narrow resonance at 37.5 ppm with a large CSA is assigned to **52** based on its chemical shift. A second species with a much larger linewidth is observed at 6.9 ppm. The chemical shift of the latter is nearly identical to the chemical shift of the uncoordinated ligand **45**. As discussed in the case of the Rh complex **47**, in CP the magnetization transfer is much more efficient for the free ligand than for the metal complex, and therefore the large intensity of the ligand signal misrepresents its small amount.

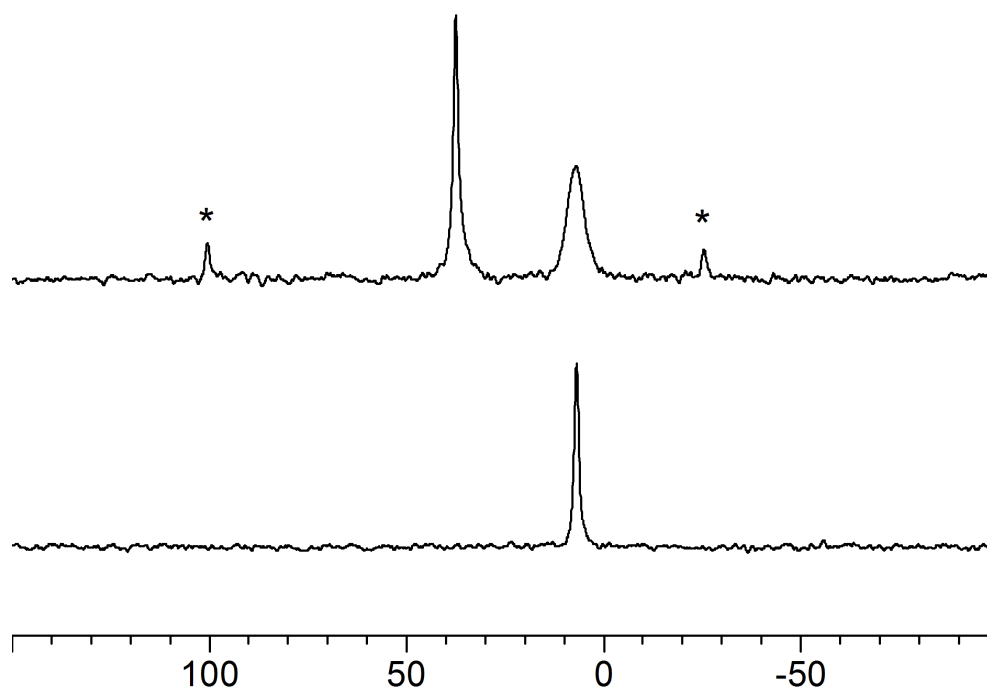


Figure 4.23. ^{29}Si CP/MAS NMR spectra of **45** (*bottom*) and **52** (*top*) (10 kHz spinning speed). Asterisks denote spinning sidebands.

The analogous scenario was observed in the case of **51**, although the lines are broader in the ^{31}P and ^{29}Si solid-state NMR spectra. Figure 4.24 shows the ^{31}P CP/MAS spectrum.

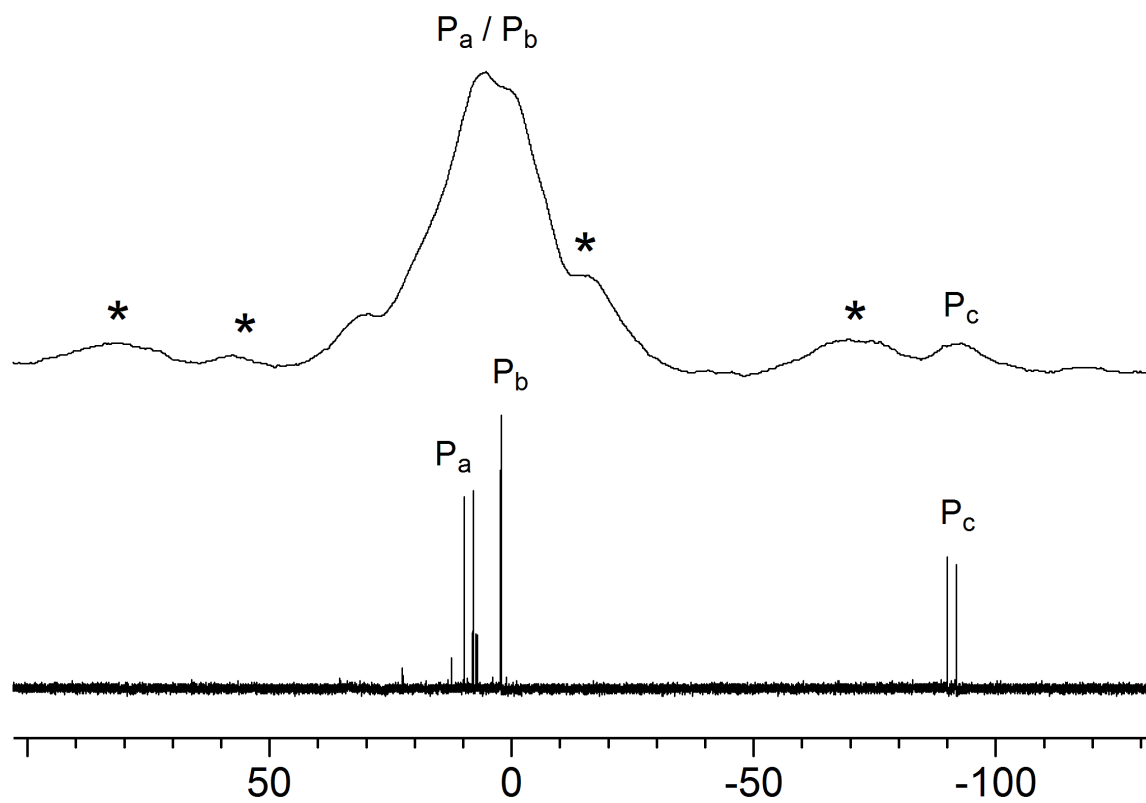


Figure 4.24. ^{31}P NMR spectra of **51** in CDCl_3 (*bottom*) and ^{31}P CP/MAS of polycrystalline **51** (*top*, 12 kHz spinning speed). Asterisks denote spinning sidebands.

Isotropic lines corresponding to **51** are observed at 8, 2, and -92 ppm. The broad lines prevent the detection of J -couplings between the phosphorus nuclei. An additional resonance is seen at 30 ppm which could be due to partial oxidation of the phosphine.

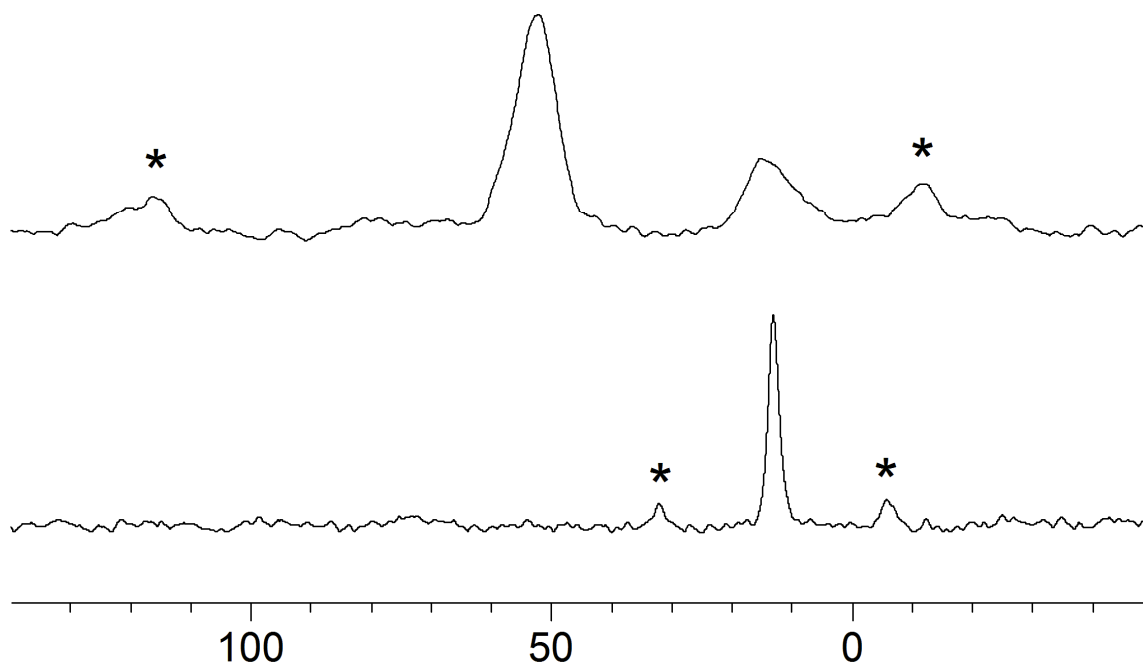


Figure 4.25. ^{29}Si CP/MAS NMR spectra of **44** (*bottom*, 1.5 kHz spinning speed) and **51** (*top*, 5 kHz spinning speed). Asterisks denote spinning sidebands.

As in the case of **52**, two resonances are observed in the ^{29}Si CP/MAS spectrum, one belonging to **51**, while the other one is assigned to free ligand **44** (Figure 4.25).

Computational Studies of Rh and Ir Complexes

To gain further insight into the oxidative addition of the C-Si bond to Rh and Ir and the energetics involved a preliminary computational study was carried out. The calculations were restricted to the complexes of ligand **45**. Geometry optimizations were carried out using the B3LYP¹¹⁰ functional with the quasi-relativistic Stuttgart-Dresden (sdd)¹¹¹ basis set for Rh and Ir and 6-31G(d)¹¹² for C, H, Si, Cl, and P. For further details see Experimental section.

For Ir and Rh three isomers each were evaluated: Two of the isomers, **50** and **54**, have a coordination environment similar to Wilkinson's complex with the metal in the + I oxidation state. The remaining isomers are in the + III oxidation state. **49** and **56** form by cleavage of the Si-Me bond, whereas **48** and **52** form by cleavage of one of the ligand phosphine "arms" (Figure 4.26).

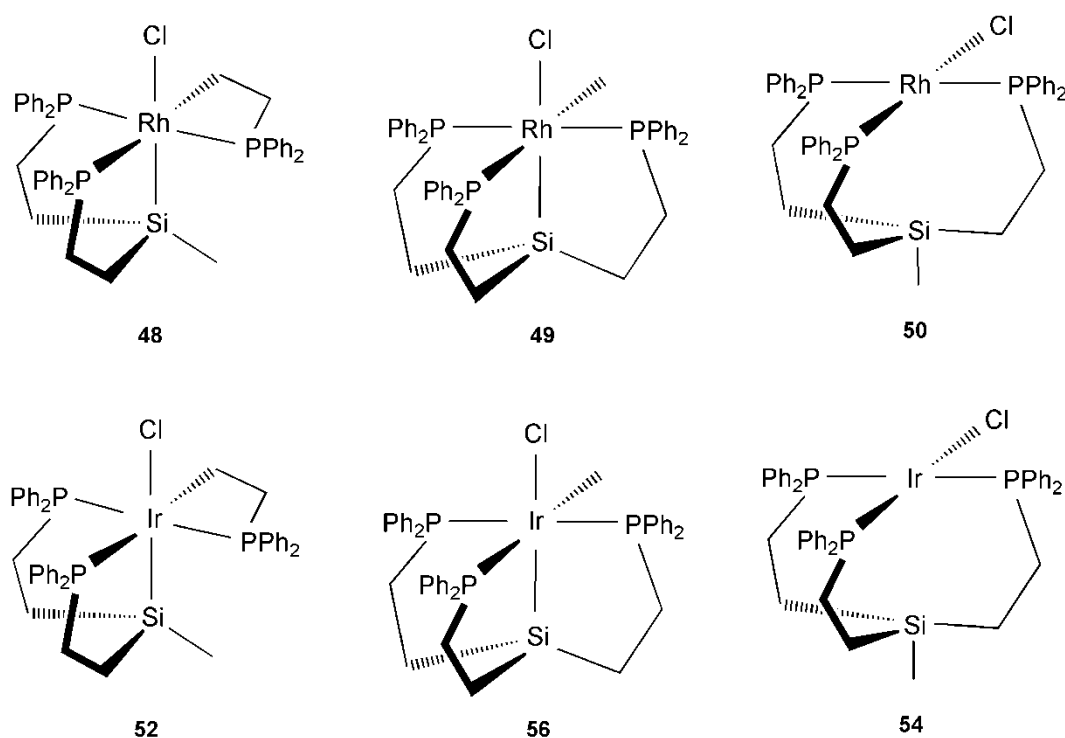


Figure 4.26. Isomers considered in DFT geometry optimization.

Free energies

All six structures represent local minima shown by frequency analysis. In the case of Rh the isomer **50** is 6.55 kcal/mol higher in energy as compared to **49** and 8.31 kcal/mol higher than **48** (Figure 4.27). The difference in free energy of 1.76 kcal/mol

between **49** and **48** is of minor significance, especially since solvent effects were not taken into account.

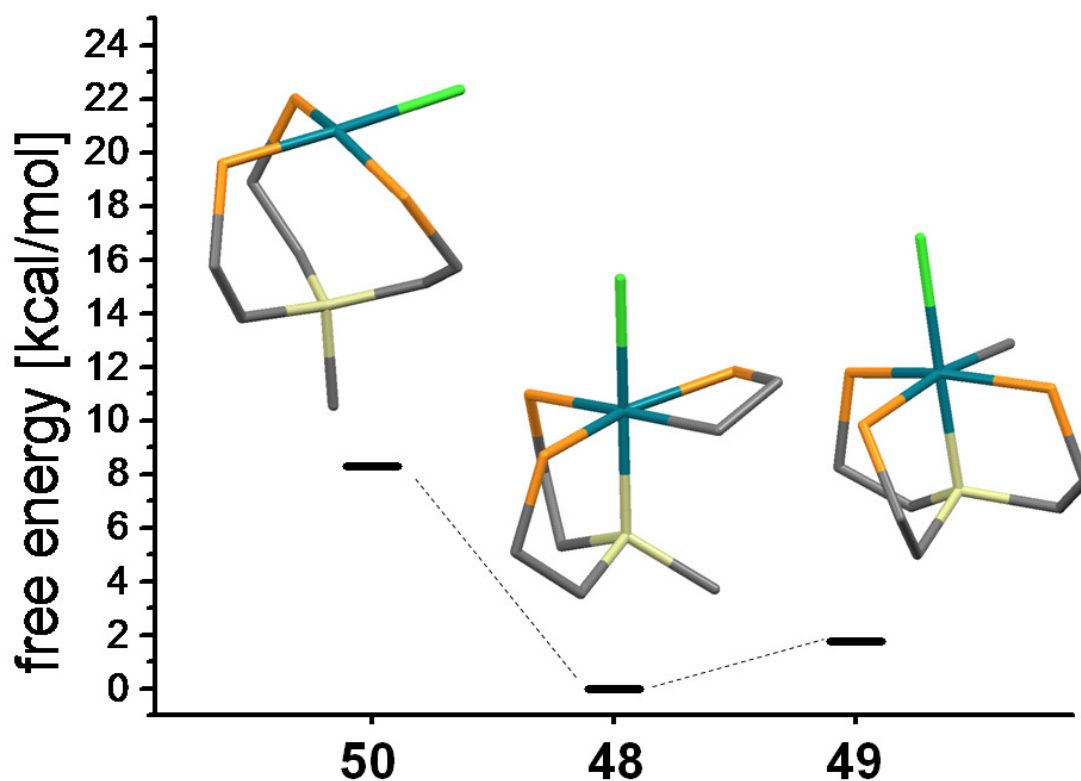


Figure 4.27. Relative free energies of **48**, **49**, and **50**.

In the case of Ir the isomer **54** is even more unfavored as its free energy is calculated to be 18.38 kcal/mol higher than **56** and 21.04 kcal/mol higher than **52** (Figure 4.28). The calculations further suggest that **52** is 2.66 kcal/mol lower in energy and thus more stable than **56**.

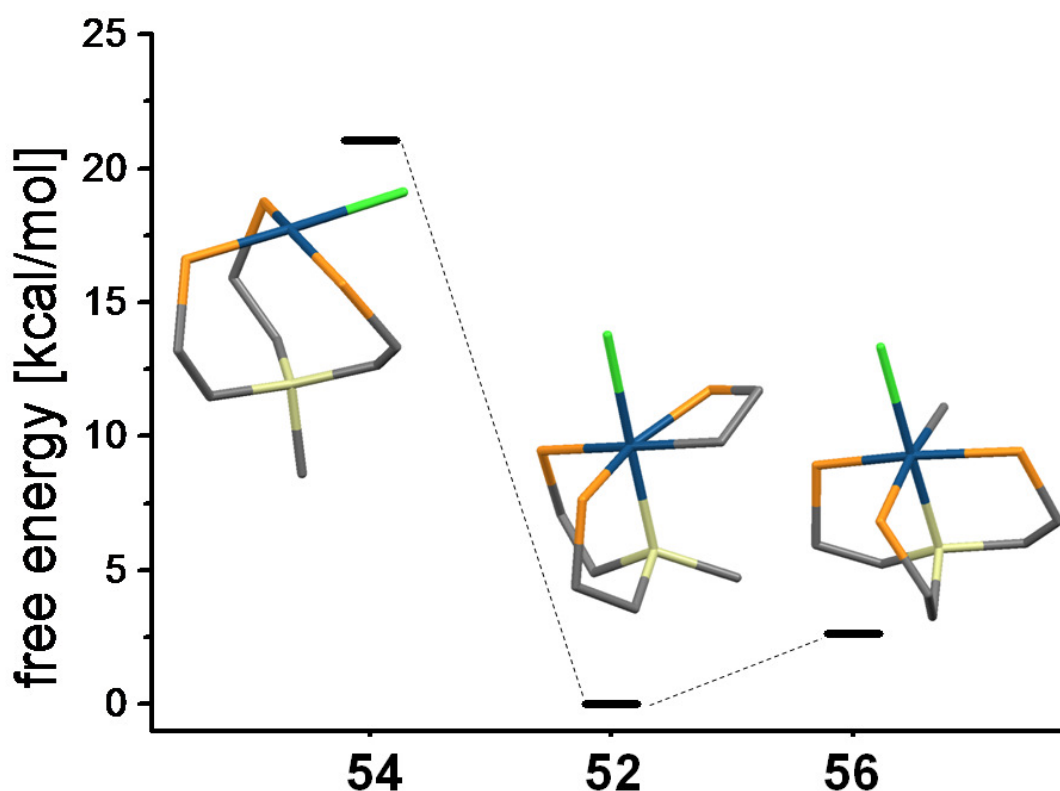


Figure 4.28. Relative free energies of **52**, **54**, and **56**.

The relative energies above are in agreement with the experimental observations as neither **4-7** nor **4-11** could be observed. It can also be inferred that the energy barrier for the interconversions of **4-5** and **4-6**, as well as **4-9** and **4-13**, must be quite high in solution since no equilibration is observed by VT-NMR experiments.

Optimized structures

The optimized structures for the Rh complexes **48** to **50** and the Ir complexes **52**, **54**, and **56**, are very similar, which is not surprising taking into account that their covalent radii differ by only 0.01 Å.¹¹³ Therefore, and for the sake of brevity only the geometry of the Rh complexes will be discussed.

50 has a slightly distorted square planar coordination sphere at Rh with no indication of any bonding interactions with Si, as the distance of 3.40 Å is much larger than the Rh-Si bond in a closely related compound reported by Tobita *et al.* (2.33 Å) (Figure 4.29).¹⁰⁸ All the bond lengths are within the range reported for similar complexes, for example the three Rh-P bonds are calculated to be 2.393 Å, 2.329 Å and 2.270 Å compared to 2.338 Å, 2.304 Å, and 2.225 Å determined for Wilkinson's complex by X-ray diffraction.¹¹⁴ Most notably the P-M-P angle of 157.3° is significantly smaller than 180°. This is probably due to the strain imposed by the ligand. The tetrahedral environment at Si is compressed substantially with all three C-Si-Me angles around 100° and one of the C-Si-C angles widened to 127.3°.

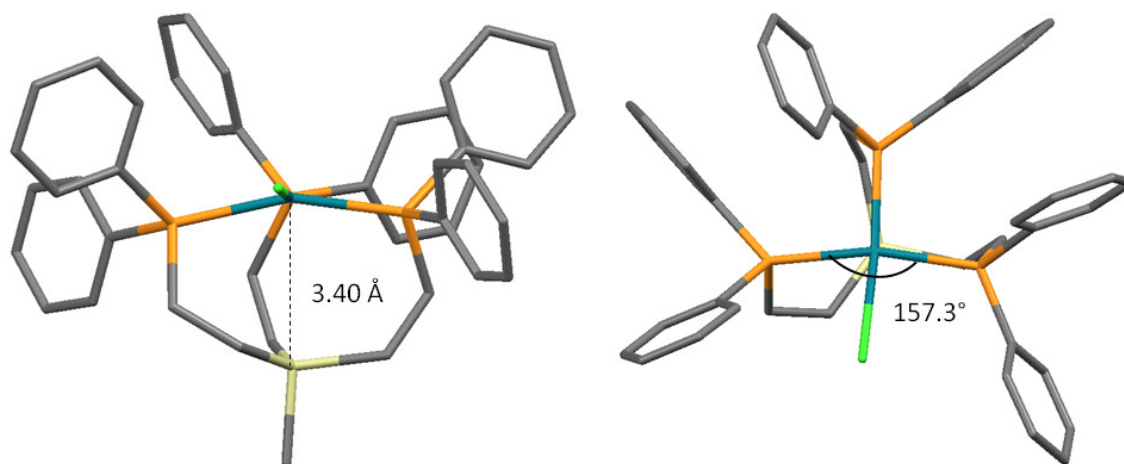


Figure 4.29. Optimized geometry for **50**, side view (*left*) and top view (*right*). Hydrogen atoms are omitted for clarity.

Both **48** and **49** show a distorted octahedral environment with a short Rh-Si distance of 2.367 Å and 2.311 Å, respectively, indicative of a Rh-Si single bond (Figures

4.30 and 4.31).¹⁰⁸ In **49** the Rh sits slightly above the PPP plane, the Si-Rh-Cl angle is 178.1°, and, as in **48**, the P-Rh-P_{trans} angle of 162.8° deviates from 180°. The geometry at Si is much closer to an ideal tetrahedron compared to **48**. Only one of the C-Si-C angles is widened to 116.9°, imposed by the coordination of the three phosphine groups to Rh.

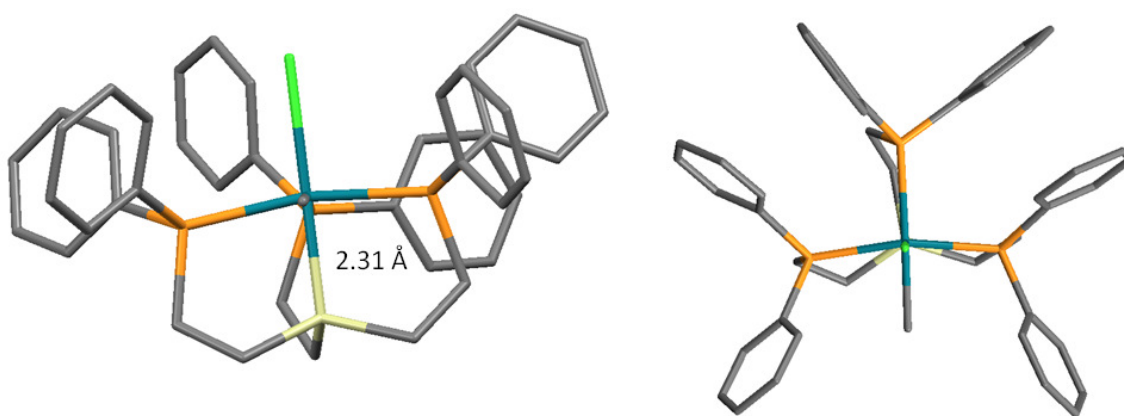


Figure 4.30. Optimized geometry for **49**; side view (*left*) and top view (*right*). Hydrogen atoms are omitted for clarity.

Compared to **49**, the geometry of **48** deviates more strongly from an ideal octahedron, due to the strain imposed by the 4-membered ring (Figure 4.31). The Rh-Si distance of 2.367 Å is slightly elongated compared to **49**. The two *trans* angles, Si-Rh-Cl (173.8°) and P-Rh-P_{trans} (160.2°) deviate more from 180° as compared to these angles in **49**. Most noticeable is the strain in the 4-membered ring with a C-Rh-P angle of 69.1°. The geometry at Si is also less symmetric with a large Rh-Si-Me angle of 124.0°. The other angles are compressed by 2° to 6° compared to the tetrahedral angle of 109.2°.

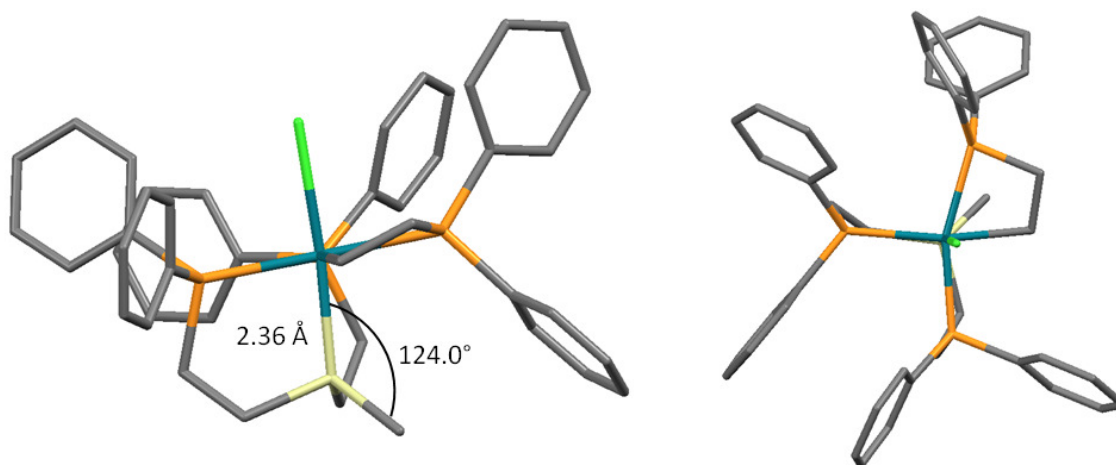


Figure 4.31. Optimized geometry for **48**; side view (*left*) and top view (*right*). Hydrogen atoms are omitted for clarity.

NMR chemical shift calculations

For the compounds **48**, **49**, **50**, and **52** that were isolated or characterized by NMR experimentally, NMR chemical shift calculations at the B3LYP/6-311+G(d) level of theory were carried out (Table 4.2). Initially the same functional and basis sets as for the geometry optimizations were used (B3LYP¹¹⁰; sdd¹¹¹ for Rh and Ir; 6-311+G(d)¹¹² for Si, Cl, P, C, H).

Table 4.2. Calculated and experimental chemical shifts for **48**, **49**, **50**, **52**, and Ph₂PMe.

Compound	$\delta(^{29}\text{Si})$ exp. ^b [ppm]	$\delta(^{29}\text{Si})^a$ calc. [ppm]	$\delta(^{31}\text{P})$ exp. ^b [ppm]	$\delta(^{31}\text{P})^a$ calc. [ppm]
48	--	1.9	--	93.79 / 66.16 / 64.98
49	64.06	110.23	46.07 / 22.37 / - 68.32	86.73 / 51.63 / - 29.07
50	97.05	130.104	37.95 / 28.99	70.545 / 47.02
52	35.83 (CDCl ₃)	96.646	10.89 / 2.66 / - 94.25	76.34 / 47.09 / - 16.89
PPh ₂ Me	--	--	-27	-16

^a) ²⁹Si chemical shifts were referenced to TMS; ³¹P chemical shifts were referenced to H₃PO₄ at the same level of theory. ^b) NMR spectra were recorded in C₆D₆ unless stated otherwise.

The relative chemical shifts are in good agreement with the experiment. Regarding ²⁹Si NMR, the calculations reproduce a downfield shift upon oxidative addition of the C-Si bond to Rh. Furthermore, the experimental chemical shift difference of 33 ppm between **48** and **49** is similar to the 20 ppm predicted by the DFT calculation. The computations also predict the correct relative chemical shifts in ³¹P NMR. For **48** and **52** P_c is shifted upfield, whereas P_a resonates furthest downfield. The differences of the chemical shifts of P_a and P_b for **48** and **52** are overestimated by 10 – 20 ppm by the calculation, whereas the chemical shift difference between P_b and P_c is underestimated by 10 to 30 ppm.

Next, different functionals were evaluated to probe whether significant improvement in the prediction of the absolute chemical shifts could be achieved.

Therefore, the chemical shifts of **52** with three functionals commonly used in organometallic chemistry were calculated (Table 4.3).

Table 4.3. Calculated and experimental chemical shifts for **52** using different functionals.

Functional	$\delta(^{29}\text{Si})^{\text{a}}$ [ppm]	$\delta(^{31}\text{P})^{\text{a}}$ [ppm]
Expt.	35.83	10.89 / 2.66 / -94.25
B972 ¹¹⁵	89.68	64.74 / 35.74 / -27.26
B3LYP ¹¹⁰	96.64	77.16 / 47.06 / -16.84
B3PW91 ^{110a,116}	91.53	66.41 / 37.42 / -27.59

^{a)} ²⁹Si chemical shifts were referenced to TMS at the same level of theory; ³¹P chemical shifts were referenced to H₃PO₄ at the same level of theory.

A slight but not significant improvement of about 10 ppm is achieved employing either the B972 or the B3PW91 functional compared to B3LYP.

The disagreement of the experimental and calculated absolute chemical shifts is not surprising for the level of theory used.¹¹⁷ It is necessary to include spin-orbit coupling associated with relativistic effects for quantitative agreement in systems containing heavy atoms such as Rh and Ir. This requires extensive computational resources and was outside the scope of this work.

CONCLUSION

It has been shown that the tridentate phosphine ligands $\text{RSi}((\text{CH}_2)_2\text{PPh}_2)_3$ (**44**, $\text{R} = \text{OEt}$; **45**, $\text{R} = \text{Me}$) react with Rh(I) and Ir(I) precursors undergoing oxidative addition of the Si-C bond to the metal center. In the case of **45** two isomers have been observed originating from cleavage of the C-Me or C- CH_2 bond. The reaction is irreversible in solution in the temperature range from $-80\text{ }^\circ\text{C}$ to $80\text{ }^\circ\text{C}$ according to ^{31}P NMR. The products have also been characterized in the solid state by ^{31}P CP/MAS and ^{29}Si CP/MAS NMR and further efforts will be directed towards structural characterization by X-ray diffraction.

Preliminary DFT calculations corroborate the preference to undergo oxidative addition.

EXPERIMENTAL

The ^1H , ^{13}C , and ^{31}P NMR spectra of liquids were recorded at 499.7, 125.7, and 202.3 MHz on a 500 MHz Varian spectrometer and referenced as follows: ^1H : residual internal CHCl_3 (δ , 7.26 ppm), CDHCl_2 (δ , 5.32 ppm) or benzene- d_5 (δ , 7.16 ppm); ^{13}C : internal CHCl_3 (δ , 77.23 ppm) or benzene- d_6 (δ , 128.06 ppm). ^{31}P NMR spectra were referenced to neat Ph_2PCl (δ , 81.92 ppm) which was centered in a capillary in the NMR sample tube. The ^{13}C , ^{19}F , and ^{31}P spectra were recorded with ^1H decoupling if not stated otherwise. ^{29}Si NMR spectra of liquids were recorded at 79.37 MHz on a 400 MHz Inova spectrometer and referenced to external hexamethyldisiloxane ($\text{Me}_3\text{SiOSiMe}_3$) in CDCl_3 (δ , 6.53 ppm). The solid-state NMR spectra were measured with a Bruker Avance 400 widebore NMR spectrometer with a 4 mm MAS probehead. The recycle delays were 3 s for ^{29}Si and ^{31}P CP/MAS spectra. The CSAs were determined by simulating the spectra with the software WSolids.¹¹⁸ Melting points were recorded with a Stanford

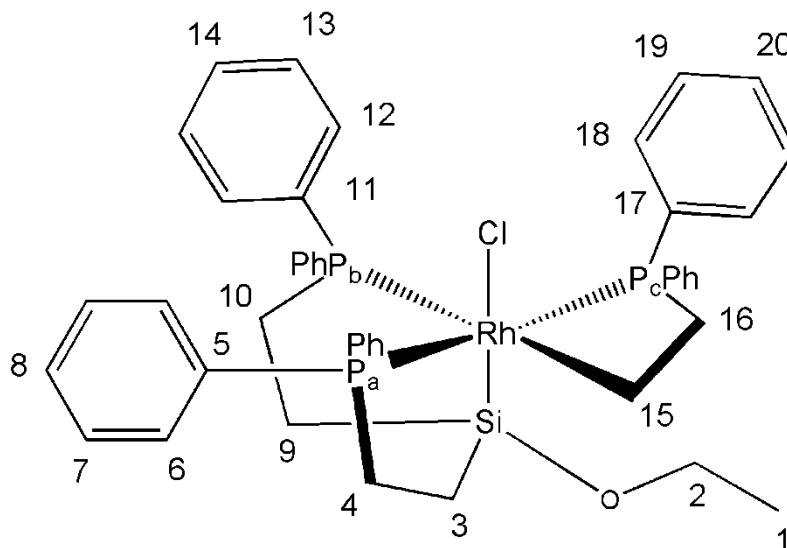
Research Systems (SRS) MPA100 (Opti-Melt) automated melting point system. Microanalyses were conducted by Atlantic Microlab. All reactions were carried out using standard Schlenk techniques and a purified N₂ atmosphere, if not stated otherwise. Reagents purchased from Sigma Aldrich or VWR were used without further purification. Solvents were dried by boiling them over Na, distilled, and stored under N₂. CH₂Cl₂ was obtained from a solvent purification system.

Ligand 45

A solution of methyltrivinylsilane (571 mg, 4.595 mmol) was combined with diphenylphosphine (2.732 g, 14.667 mmol) and AIBN (115 mg, 0.700 mmol) and stirred for 48 h at 70 °C. The crude product was purified by column chromatography (SiO₂, toluene) to yield **45** as a white powder in 96% yield (3.012 g, 4.412 mmol).

¹H NMR (CDCl₃, 500.13 MHz): δ (ppm) = 7.31-7.36 (m, 12H, H_{aryl}), 7.28-7.31 (m, 18H, H_{aryl}), 1.80-1.85 (m, 6H, PCH₂), 0.55-0.61 (m, 6H, SiCH₂), -0.02 (s, 3H, CH₃); ¹³C NMR (CDCl₃, 125.77 MHz): δ (ppm) = 136.65 (d, ¹J(³¹P-¹³C) = 14.2 Hz, C_{ipso}), 132.69 (d, ²J(³¹P-¹³C) = 17.9 Hz, C_{ortho}), 128.36 (s, C_{para}), 128.36 (d, ³J(³¹P-¹³C) = 6.4 Hz, C_{meta}), 21.45 (d, ¹J(³¹P-¹³C) = 14.2 Hz, PCH₂), 10.85 (d, ²J(³¹P-¹³C) = 10.8 Hz, SiCH₂), -5.69 (s, SiCH₃); ³¹P{¹H} NMR (CDCl₃, 202.28 MHz): δ (ppm) = -9.88 (s); ²⁹Si{¹H} NMR (CDCl₃, 79.37 MHz): δ (ppm) = 6.27 (q, ³J(³¹P-²⁹Si) = 21.2 Hz).

Complex 47



$[(\text{COD})\text{RhCl}]_2$ (28 mg, 0.056 mmol) in 5 ml toluene was added to a solution of ligand **44** (80 mg, 0.112 mmol) in 5 ml of toluene. The reaction mixture was stirred at room temperature for 5 h. The solvent was partially removed *in vacuo*. 20 ml of pentane were added and a yellow precipitate formed which was filtered off. After drying *in vacuo*, **47** was obtained as a dark-orange oil in 98% yield (94 mg, 0.110 mmol).

$^1\text{H}\{^3\text{P}\}$ NMR (THF- d_8 , 500.13 MHz): δ (ppm) = 8.06 (d, $^3J(^1\text{H}-^1\text{H}) = 7.4$ Hz, 2H, H6'), 8.87 (d, $^3J(^1\text{H}-^1\text{H}) = 7.3$ Hz, 2H, H12'), 7.75 (d, $^3J(^1\text{H}-^1\text{H}) = 7.7$ Hz, 2H, H6), 7.35 (d, $^3J(^1\text{H}-^1\text{H}) = 7.5$ Hz, 2H, H12), 7.35 (d, $^3J(^1\text{H}-^1\text{H}) = 7.5$ Hz, 2H, H18'), 7.25 (overlapping signals, 5H, H7', H19', H20'), 7.18 (overlapping signals, 3H, H8', H20, H14'), 7.12 (dd, $^3J(^1\text{H}-^1\text{H}) = 7.6$ Hz, 2H, H13), 7.01 (dd, $^3J(^1\text{H}-^1\text{H}) = 7.6$ Hz, 2H, H19), 6.85 (dd, $^3J(^1\text{H}-^1\text{H}) = 7.2$ Hz, 1H, H14), 6.78 (dd, $^3J(^1\text{H}-^1\text{H}) = 7.3$ Hz, 1H, H8), 6.74 (dd, $^3J(^1\text{H}-^1\text{H}) = 7.6$

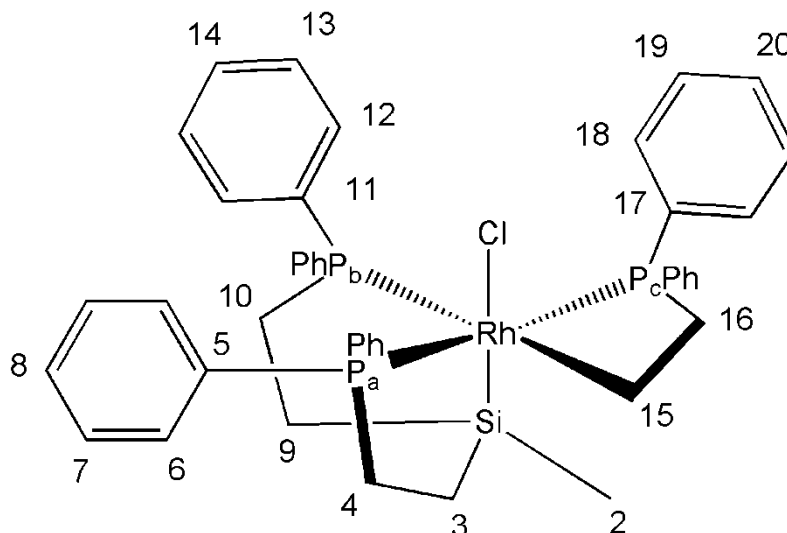
Hz, 2H, H13), 6.62 (dd, $^3J(^1\text{H}-^1\text{H}) = 7.7$ Hz, 2H, H7), 6.55 (bd, $^3J(^1\text{H}-^1\text{H}) = 5.5$ Hz, 2H, H18), 4.12 (ddd, $^2J(^1\text{H}-^1\text{H}) = 11.2$ Hz, $^3J(^1\text{H}-^1\text{H}) = 11.2$ Hz, $^3J(^1\text{H}-^1\text{H}) = 11.0$ Hz, 1H, H16_b), 3.45 (dd, $^2J(^1\text{H}-^1\text{H}) = 11.2$ Hz, $^3J(^1\text{H}-^1\text{H}) = 11.2$ Hz, 1H, H16_a), 3.28 (dq, $^2J(^1\text{H}-^1\text{H}) = 9.5$ Hz, $^3J(^1\text{H}-^1\text{H}) = 7.0$ Hz, 1H, H2), 2.75 (overlapping signals, 3H, H2, H10_b, H4_a), 2.25 (ddd, $^2J(^1\text{H}-^1\text{H}) = 13.9$ Hz, $^3J(^1\text{H}-^1\text{H}) = 13.9$ Hz, $^3J(^1\text{H}-^1\text{H}) = 6.0$ Hz, 1H, H4_b), 1.77 (ddd, $^2J(^1\text{H}-^1\text{H}) = 14.4$ Hz, $^3J(^1\text{H}-^1\text{H}) = 14.2$ Hz, $^3J(^1\text{H}-^1\text{H}) = 5.6$ Hz, 1H, H10_a), 1.41 (ddd, $^3J(^1\text{H}-^1\text{H}) = 13.8$ Hz, $^2J(^1\text{H}-^1\text{H}) = 6.4$ Hz, $^3J(^1\text{H}-^1\text{H}) = 6.0$ Hz, 1H, H3_b), 1.37 (ddd, $^3J(^1\text{H}-^1\text{H}) = 13.6$ Hz, $^2J(^1\text{H}-^1\text{H}) = 6.0$ Hz, $^3J(^1\text{H}-^1\text{H}) = 5.5$ Hz, 1H, H9_a), 1.26 – 1.32 (overlapping signals, 2H, H3_a, H15_a), 1.02 (ddd, $^3J(^1\text{H}-^1\text{H}) = 14.0$ Hz, $^3J(^1\text{H}-^1\text{H}) = 14.0$ Hz, $^2J(^1\text{H}-^1\text{H}) = 6.0$ Hz, 1H, H9_b), 0.65 (t, $^3J(^1\text{H}-^1\text{H}) = 7.0$ Hz, 3H, H1), 0.65 (overlapping signals, 1H, H15_b); **^{13}C NMR** (THF- d_8 , 125.77 MHz): δ (ppm) = 142.1 (ddd, $^1J(^{31}\text{Pb}-^{13}\text{C}) = 24.5$ Hz, $^3J(^{31}\text{P}-^{13}\text{C}) = 6.2$ Hz, $^3J(^{31}\text{P}-^{13}\text{C}) = 4.1$ Hz, C11 ϵ) 138.9 (d, $^1J(^{31}\text{Pb}-^{13}\text{C}) = 21.7$ Hz, C11), 136.2 (d, $^1J(^{31}\text{P}-^{13}\text{C}) = 28.3$ Hz, C17)*, 136.1 (d, $^1J(^{31}\text{P}-^{13}\text{C}) = 15.0$ Hz, C17 ϵ)*, 136.0 (d, $^1J(^{31}\text{P}-^{13}\text{C}) = 8.0$ Hz, C5)*, 135.9 (ddd, $^1J(^{31}\text{P}-^{13}\text{C}) = 8.2$ Hz, $^3J(^{31}\text{P}-^{13}\text{C}) = 4.2$ Hz, $^3J(^{31}\text{P}-^{13}\text{C}) = 4.2$ Hz, C5 ϵ)*, 133.7 (d, $^2J(^{31}\text{Pc}-^{13}\text{C}) = 9.5$ Hz, C18), 135.7 (d, $^2J(^{31}\text{Pc}-^{13}\text{C}) = 8.0$ Hz, C18 ϵ), 132.6 (d, $^2J(^{31}\text{Pb}-^{13}\text{C}) = 10.8$ Hz, C12 ϵ), 132.5 (d, $^2J(^{31}\text{Pa}-^{13}\text{C}) = 8.0$ Hz, C6 ϵ), 132.4 (d, $^2J(^{31}\text{Pa}-^{13}\text{C}) = 8.2$ Hz, C6), 131.6 (d, $^2J(^{31}\text{Pb}-^{13}\text{C}) = 8.1$ Hz, C12), 129.0 (d, $^4J(^{31}\text{Pb}-^{13}\text{C}) = 2.0$ Hz, C14 ϵ), 129.6 (d, $^3(^{31}\text{Pb}-^{13}\text{C}) = 8.3$ Hz, C-13 ϵ), 129.2 (d, $^4J(^{31}\text{P}-^{13}\text{C}) = 2.1$ Hz, C20)[#], 128.9 (d, $^4J(^{31}\text{P}-^{13}\text{C}) = 1.7$ Hz, C20 ϵ)[#], 129.6 (d, $^4J(^{31}\text{P}-^{13}\text{C}) = 1.6$ Hz, C8)[#], 129.7 (d, $^4J(^{31}\text{Pa}-^{13}\text{C}) = 1.7$ Hz, C8), 128.2 (d, $^4J(^{31}\text{Pb}-^{13}\text{C}) = 1.7$ Hz, C14), 128.1 (d, $^3J(^{31}\text{Pb}-^{13}\text{C}) = 9.3$ Hz, C7 ϵ), 128.1 (d, $^3J(^{31}\text{Pc}-^{13}\text{C}) = 9.0$ Hz, C19), 128.1 (d, $^3J(^{31}\text{Pb}-^{13}\text{C}) = 8.0$ Hz, C13), 127.9 (d, $^3J(^{31}\text{Pa}-^{13}\text{C}) = 8.8$

Hz, C7), 126.8 (d, $^3J(^{31}\text{P}_\text{c}-^{13}\text{C}) = 9.2$ Hz, C19'), 59.35 (s, C2), 40.98 (d, $^1J(^{31}\text{P}_\text{c}-^{13}\text{C}) = 37.3$ Hz, C16), 23.77 (dd, $^1J(^{31}\text{P}_\text{a}-^{13}\text{C}) = 33.8$ Hz, $J(^{31}\text{P}-^{13}\text{C}) = 2.4$ Hz, C4), 21.75 (d, $^1J(^{31}\text{P}_\text{b}-^{13}\text{C}) = 26.8$ Hz, C10), 18.61 (s, C1), 18.09 (dd, $^2J(^{31}\text{P}_\text{a}-^{13}\text{C}) = 25.4$ Hz, $J(^{31}\text{P}-^{13}\text{C}) = 3.0$ Hz, C3), 16.80 (d, $^2J(^{31}\text{P}_\text{b}-^{13}\text{C}) = 25.8$ Hz, C9), 0.88 (ddd, $^2J(^{31}\text{P}_\text{b}-^{13}\text{C}) = 76.6$ Hz, $^2J(^{31}\text{P}_\text{c}-^{13}\text{C}) = 33.9$ Hz, $^1J(^{103}\text{Rh}-^{13}\text{C}) = 14.1$ Hz, C15), *,[#] assignments interchangeable;

$^{31}\text{P}\{^1\text{H}\}$ NMR (THF- d_8 , 202.45 MHz): δ (ppm) = 44.9 (ddd, $^2J(^{31}\text{P}_\text{a}-^{31}\text{P}_\text{c}) = 400.2$ Hz, $^1J(^{103}\text{Rh}-^{31}\text{P}_\text{a}) = 126$ Hz, $^2J(^{31}\text{P}_\text{a}-^{31}\text{P}_\text{b}) = 15.7$ Hz, P_a), 20.8 (dd, $^1J(^{103}\text{Rh}-^{31}\text{P}_\text{b}) = 84.9$ Hz, $^2J(^{31}\text{P}_\text{b}-^{31}\text{P}_\text{a}) = 15.7$ Hz, P_b), -65.8 (dd, $^2J(^{31}\text{P}_\text{c}-^{31}\text{P}_\text{a}) = 400.2$ Hz, $^1J(^{103}\text{Rh}-^{31}\text{P}_\text{c}) = 82.3$ Hz, P_c);

$^{29}\text{Si}\{^1\text{H}\}$ NMR (THF- d_8 , 99.35 MHz): δ (ppm) = 76.70 (dddd, $^1J(^{103}\text{Rh}-^{29}\text{Si}) = 35.7$ Hz, $^2J(^{31}\text{P}-^{29}\text{Si}) = 13.2$ Hz, $^2J(^{31}\text{P}_\text{a}-^{29}\text{Si}) = 8.5$ Hz, $^2J(^{31}\text{P}_\text{b}-^{29}\text{Si}) = 4.9$ Hz. **HR-MS** (FAB⁺): $m/z = 815.1674$ calcd. for $[\text{M}-\text{Cl}]^+ = 815.1664$. **Elemental Analysis** ($\text{C}_{44}\text{H}_{47}\text{ClRhOP}_3\text{Si}$) calcd.: C 62.08, H 5.57, Cl 4.17; found: C 62.34, H 5.69, Cl 4.04.

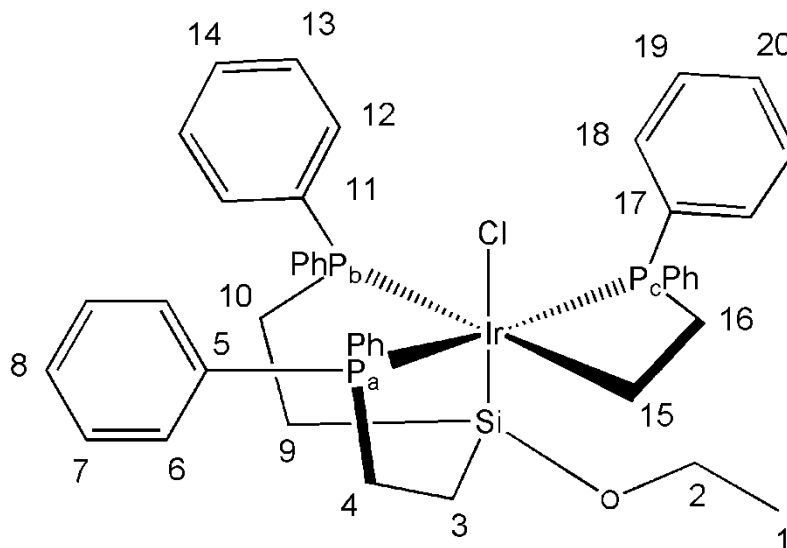
Complex 48



$[(\text{COD})\text{RhCl}]_2$ (22.8 mg, 0.046 mmol) in 10 ml THF was added to a solution of tripod ligand **45** (64.0 mg, 0.094 mmol) in 20 ml THF. The reaction mixture was stirred at 60 °C for 3 h. The solvent was partially removed *in vacuo*. 20 ml of pentane were added and a yellow precipitate formed which was filtered off. After drying *in vacuo*, a mixture of **48** and **49** was obtained in a 1.0 : 3.3 ratio.

$^{31}\text{P}\{^1\text{H}\}$ NMR (C_6D_6 , 202.28 MHz): δ (ppm) = 46.07 (ddd, $^2J(^{31}\text{P}_a-^{31}\text{P}_c) = 410.5$ Hz, $^1J(^{103}\text{Rh}-^{31}\text{P}_a) = 124.8$ Hz, $^2J(^{31}\text{P}_a-^{31}\text{P}_b) = 16.8$ Hz, P_a), 22.37 (dd, $^1J(^{103}\text{Rh}-^{31}\text{P}_b) = 84.8$ Hz, $^2J(^{31}\text{P}_b-^{31}\text{P}_a) = 17.0$ Hz, P_b), -68.32 (dd, $^2J(^{31}\text{P}_c-^{31}\text{P}_a) = 410.4$ Hz, $^2J(^{31}\text{P}_c-^{31}\text{P}_b) = 81.6$ Hz, P_c); $^{29}\text{Si}\{^1\text{H}\}$ NMR (C_6D_6 , 79.37 MHz): δ (ppm) = 64.06 (dddd, $^1J(^{103}\text{Rh}-^{29}\text{Si}) = 32.5$ Hz, $J(^{31}\text{P}-^{29}\text{Si}) = 12.6$ Hz, $J(^{31}\text{P}-^{29}\text{Si}) = 7.4$ Hz, $J(^{31}\text{P}-^{29}\text{Si}) = 4.7$ Hz, P_c). **HR-MS** (ESI^+): $m/z = 785.1542$ calcd. for $[\text{M}-\text{Cl}]^+ = 785.1558$.

Complex 51



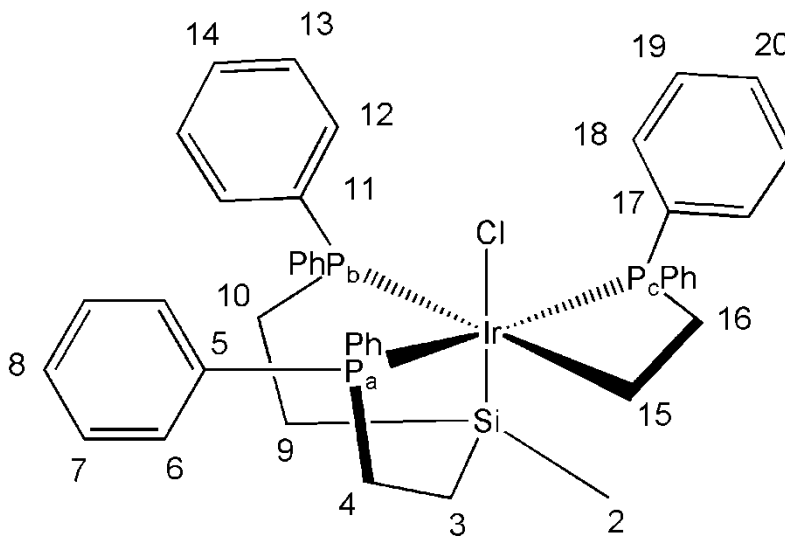
$[(\text{COD})\text{IrCl}]_2$ (74 mg, 0.119 mmol) in 20 ml toluene was added dropwise to a solution of tripod ligand **44** (171 mg, 0.239 mmol) in 20 ml toluene at 90 °C. The reaction mixture was stirred at 90 °C for 4 h. The solvent was removed *in vacuo* and the precipitate was washed with copious amounts of pentane. After drying *in vacuo* **51** was obtained as a yellow powder in 96% yield (218 mg, 0.231 mmol).

$^1\text{H}\{^{31}\text{P}\}$ NMR (CDCl_3 , 499.70 MHz): δ (ppm) = 7.82 (d, $^3J(^1\text{H}-^1\text{H}) = 7.6$ Hz, 2H, H6), 7.79 (d, $^3J(^1\text{H}-^1\text{H}) = 7.2$ Hz, 2H, H12), 7.69 (d, $^3J(^1\text{H}-^1\text{H}) = 8.2$ Hz, 2H, H6'), 7.31-7.37 (m, 7H, H7, H14, H12', H20), 7.15-7.24 (m, 7H, H13, H13', H20', H19*), 7.02 (t, $^3J(^1\text{H}-^1\text{H}) = 7.4$ Hz, 2H, H19'), 6.79-6.86 (m, 2H, H8), 6.70 (m, 4H, H7', H18*), 6.60 (bd, $^3J(^1\text{H}-^1\text{H}) = 7.1$ Hz, 2H, H18'), 4.34 (t, $^3J(^1\text{H}-^1\text{H}) = 10.0$ Hz, 1H, H16), 4.10 (t, $^3J(^1\text{H}-^1\text{H}) = 12.8$ Hz, 1H, H16'), 3.26 (dq, $^2J(^1\text{H}-^1\text{H}) = 9.9$ Hz, $^3J(^1\text{H}-^1\text{H}) = 6.9$ Hz, 1H, H2), 2.92 (dq, $^2J(^1\text{H}-^1\text{H}) = 9.9$ Hz, $^3J(^1\text{H}-^1\text{H}) = 6.9$ Hz, 1H, H2'), 2.87 (ddd, $J(^1\text{H}-^1\text{H}) =$

14.5 Hz, $J(^1\text{H}-^1\text{H}) = 3.9$ Hz, $J(^1\text{H}-^1\text{H}) = 2.3$ Hz, 1H, H4), 2.70 (dt, $J(^1\text{H}-^1\text{H}) = 14.2$ Hz, $J(^1\text{H}-^1\text{H}) = 5.9$ Hz, 1H, H10), 1.86-2.00 (m, 2H, H4', H10'), 1.24-1.32 (m, 1H, H15), 1.14-1.23 (m, 1H, H19), 1.07 (dt, $J(^1\text{H}-^1\text{H}) = 13.9$ Hz, $J(^1\text{H}-^1\text{H}) = 6.3$ Hz, 1H, H3), 0.82-0.91 (m, 2H, H9', H3'), 0.70-0.80 (m, 1H, H15), 0.67 (t, $^3J(^1\text{H}-^1\text{H}) = 6.9$ Hz, 3H, H1), *assignments interchangeable; **$^{13}\text{C}\{^1\text{H}\}$ NMR** (CDCl_3 , 125.66 MHz): δ (ppm) = 142.13 (dd, $^1J(^{31}\text{P}_\text{b}-^{13}\text{C}) = 38.8$ Hz, $^3J(^{31}\text{P}-^{13}\text{C}) = 4.8$ Hz, C11), 137.50 (d, $^1J(^{31}\text{P}_\text{b}-^{13}\text{C}) = 31.4$ Hz, C11'), 134.56 (d, $^3J(^{31}\text{P}_\text{a}-^{13}\text{C}) = 7.9$ Hz, C7), 133.70 (C5)*, 133.00 (C17)*, 132.26 (d, $^2J(^{31}\text{P}_\text{c}-^{13}\text{C}) = 8.7$ Hz, C18), 131.97 (d, $^2J(^{31}\text{P}_\text{b}-^{13}\text{C}) = 10.3$ Hz, C12), 131.52 (d, $^2J(^{31}\text{P}_\text{a}-^{13}\text{C}) = 7.8$ Hz, C6), 131.24 (d, $^2J(^{31}\text{P}_\text{a}-^{13}\text{C}) = 7.8$ Hz, C6'), 130.52 (d, $^3J(^{31}\text{P}_\text{b}-^{13}\text{C}) = 8.2$ Hz, C13), 129.28 (d, $^4J(^{31}\text{P}_\text{a}-^{13}\text{C}) = 1.8$ Hz, C8), 128.88 (d, $^4J(^{31}\text{P}_\text{c}-^{13}\text{C}) = 1.6$ Hz, C20), 128.85 (s, C14), 128.83 (d, $^3J(^{31}\text{P}_\text{b}-^{13}\text{C}) = 8.8$ Hz, C13'), 128.58 (d, $^4J(^{31}\text{P}_\text{c}-^{13}\text{C}) = 2.2$ Hz, C20'), 128.37 (d, $^4J(^{31}\text{P}_\text{a}-^{13}\text{C}) = 2.0$ Hz, C8'), 127.81 (d, $^4J(^{31}\text{P}_\text{b}-^{13}\text{C}) = 1.7$ Hz, C14'), 127.46 (d, $^3J(^{31}\text{P}_\text{a}-^{13}\text{C}) = 9.6$ Hz, C7')[#], 127.31 (d, $J(^{31}\text{P}-^{13}\text{C}) = 8.7$ Hz, C18, C19), 127.17 (d, $^3J(^{31}\text{P}_\text{c}-^{13}\text{C}) = 9.5$ Hz, C19'), 126.15 (d, $^2J(^{31}\text{P}_\text{b}-^{13}\text{C}) = 9.3$ Hz, C12')[#], 58.40 (s, C2), 41.08 (dd, $^1J(^{31}\text{P}_\text{c}-^{13}\text{C}) = 43.9$ Hz, $^3J(^{31}\text{P}-^{13}\text{C}) = 4.3$ Hz, C16), 24.66 (d, $^1J(^{31}\text{P}-^{13}\text{C}) = 34.6$ Hz, C10)[&], 24.58 (d, $^1J(^{31}\text{P}-^{13}\text{C}) = 38.5$ Hz, C4)[&], 18.80 (s, C1), 16.39 (d, $^2J(^{31}\text{P}_\text{b}-^{13}\text{C}) = 18.3$ Hz, C9), 15.69 (d, $^2J(^{31}\text{P}_\text{a}-^{13}\text{C}) = 21.0$ Hz, C3), C15, C5' and C17' are missing due to low intensity, *,[#],[&] assignments interchangeable; **$^{31}\text{P}\{^1\text{H}\}$ NMR** (CDCl_3 , 202.45 MHz): δ (ppm) = 8.87 (dd, $^2J(^{31}\text{P}_\text{a}-^{31}\text{P}_\text{c}) = 358.2$ Hz, $^2J(^{31}\text{P}_\text{a}-^{31}\text{P}_\text{b}) = 3.5$ Hz, P_a), 2.19 (dd, $^2J(^{31}\text{P}_\text{b}-^{31}\text{P}_\text{c}) = 5.3$ Hz, $^2J(^{31}\text{P}_\text{b}-^{31}\text{P}_\text{a}) = 3.6$ Hz, P_b), -90.90 (dd, $^2J(^{31}\text{P}_\text{c}-^{31}\text{P}_\text{a}) = 358.2$ Hz, $^2J(^{31}\text{P}_\text{c}-^{31}\text{P}_\text{b}) = 5.6$ Hz, P_c); **$^{29}\text{Si}\{^1\text{H}\}$ NMR** (CDCl_3 , 79.37 MHz): δ (ppm) = 50.48 (dd, $^2J(^{31}\text{P}-^{29}\text{Si}) = 10.4$ Hz, $^2J(^{31}\text{P}-^{29}\text{Si}) = 5.1$ Hz). **HR-MS** (ESI^+): $m/z = 905.2240$

calcd. for $[M-Cl]^+ = 905.2238$. **Elemental Analysis** ($C_{44}H_{47}ClIrOP_3Si$) calcd.: C 56.19, H 5.04, Cl 3.78; found: C 53.38, H 4.99, Cl 3.78.

Complex 52



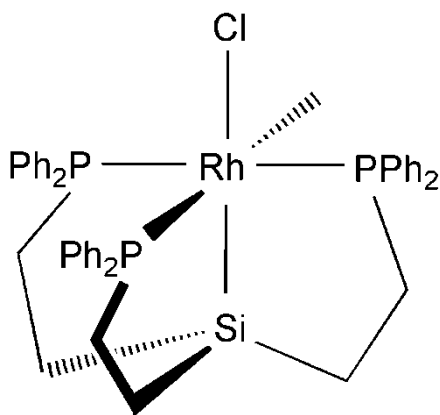
[(COD)IrCl]₂ (99 mg, 0.160 mmol) in 10 ml THF was added dropwise to a solution of tripod ligand **45** (220 mg, 0.322 mmol) in 10 ml THF at RT. The reaction mixture was stirred at 60°C for 24 h. The solvent was removed *in vacuo* and the precipitate was washed with copious amounts of pentane. After drying *in vacuo* **52** was obtained as a yellow powder in 87% yield (254 mg, 0.278 mmol).

¹H{³¹P} NMR (CDCl₃, 499.70 MHz): δ (ppm) = 7.75 (d, ³J(¹H-¹H) = 7.9 Hz, 4H, H6), 7.73 (d, ³J(¹H-¹H) = 8.3 Hz, 2H, H12), 7.36-7.30 (m, 7H, H7, H14, H14', H12', H20), 7.26-7.14 (m, 7H, H13, H13', H20', H19*), 7.06 (t, ³J(¹H-¹H) = 7.9 Hz, 2H, H19') 6.87-6.79 (m, 2H, H8), 6.71 (m, 4H, H7', H18*), 6.61 (bd, ³J(¹H-¹H) = 6.1 Hz, 2H, 18'), 4.45

(dd, $J(^1\text{H}-^1\text{H}) = 13.3$ Hz, $J(^1\text{H}-^1\text{H}) = 10.9$ Hz, 1H, H16), 3.62 (ddd, $J(^1\text{H}-^1\text{H}) = 11.7$ Hz, $J(^1\text{H}-^1\text{H}) = 10.3$ Hz, $J(^1\text{H}-^1\text{H}) = 9.4$ Hz, 1H, H16), 2.90-2.81 (m, 2H, H4, H10), 2.01 (ddd, $J(^1\text{H}-^1\text{H}) = 14.4$ Hz, $J(^1\text{H}-^1\text{H}) = 14.2$ Hz, $^3J(^1\text{H}-^1\text{H}) = 6.0$ Hz, 1H, H10)[#], 1.93 (ddd, $J(^1\text{H}-^1\text{H}) = 14.1$ Hz, $J(^1\text{H}-^1\text{H}) = 14.0$ Hz, $^3J(^1\text{H}-^1\text{H}) = 6.3$ Hz), 1H, H4)[#], 1.23-1.11 (m, 2H, H15, H9), 1.10-1.00 (m, 1H, H3), 0.89 (ddd, $^1J(^1\text{H}-^1\text{H}) = 13.7$ Hz, $^3J(^1\text{H}-^1\text{H}) = 13.5$ Hz, $^3J(^1\text{H}-^1\text{H}) = 5.7$ Hz), 1H, H9), 0.78 (ddd, $^1J(^1\text{H}-^1\text{H}) = 14.2$ Hz, $^3J(^1\text{H}-^1\text{H}) = 13.9$ Hz, $^3J(^1\text{H}-^1\text{H}) = 6.3$ Hz), 1H, H3), 0.56 (bddd, $J(^1\text{H}-^1\text{H}) = 10.6$ Hz, $J(^1\text{H}-^1\text{H}) = 9.6$ Hz, 1H, H15), -0.29 (s, 3H, H2), *,[#] assignments interchangeable; **$^{13}\text{C}\{^1\text{H}\}$ NMR** (CDCl_3 , 125.66 MHz): δ (ppm) = 142.51 (dd, $^1J(^{31}\text{P}_\text{b}-^{13}\text{C}) = 33.5$ Hz, $^3J(^{31}\text{P}-^{13}\text{C}) = 4.9$ Hz, C11), 137.56 (d, $^1J(^{31}\text{P}_\text{b}-^{13}\text{C}) = 31.1$ Hz, C11'), 134.96 (d, $^3J(^{31}\text{P}_\text{a}-^{13}\text{C}) = 8.1$ Hz, C7), 134.51 (dd, $^1J(^{31}\text{P}_\text{a}-^{13}\text{C}) = 41.5$ Hz, $^3J(^{31}\text{P}_\text{a}-^{13}\text{C}) = 5.6$ Hz, C5), 133.16 (ddd, ($^1J(^{31}\text{P}_\text{c}-^{13}\text{C}) = 49.6$ Hz, $^3J(^{31}\text{P}_\text{a}-^{13}\text{C}) = 36.9$ Hz, $^3J(^{31}\text{P}_\text{b}-^{13}\text{C}) = 5.8$ Hz, C17), 132.44 (d, $^2J(^{31}\text{P}_\text{c}-^{13}\text{C}) = 10.0$ Hz, C18), 132.15 (dd, $^1J(^{31}\text{P}_\text{a}-^{13}\text{C}) = 35.9$ Hz, $J(^{31}\text{P}-^{13}\text{C}) = 6.1$ Hz, C5), 131.85 (d, $^2J(^{31}\text{P}_\text{b}-^{13}\text{C}) = 7.6$ Hz, C12), 131.61 (d, $^2J(^{31}\text{P}_\text{a}-^{13}\text{C}) = 9.6$ Hz, C6), 131.20 (d, $^2J(^{31}\text{P}_\text{a}-^{13}\text{C}) = 7.7$ Hz, C6'), 130.98 (dd, $^1J(^{31}\text{P}_\text{c}-^{13}\text{C}) = 49.8$ Hz, $J(^{31}\text{P}-^{13}\text{C}) = 9.3$ Hz, C17'), 130.68 (d, $^3J(^{31}\text{P}_\text{b}-^{13}\text{C}) = 8.0$ Hz, C13), 129.67 (d, $^4J(^{31}\text{P}_\text{a}-^{13}\text{C}) = 1.6$ Hz, C8), 129.16 (d, $^4J(^{31}\text{P}_\text{c}-^{13}\text{C}) = 1.8$ Hz, C20), 128.94 (s, C14), 128.90 (d, $^2J(^{31}\text{P}_\text{b}-^{13}\text{C}) = 8.6$ Hz, C13'), 128.53 (d, $^4J(^{31}\text{P}_\text{c}-^{13}\text{C}) = 2.3$ Hz, C20'), 128.37 (d, $^4J(^{31}\text{P}_\text{a}-^{13}\text{C}) = 2.3$ Hz, C8'), 127.82 (d, $^4J(^{31}\text{P}_\text{b}-^{13}\text{C}) = 1.8$ Hz, C14'), 127.72 (d, $^3J(^{31}\text{P}_\text{a}-^{13}\text{C}) = 9.2$ Hz, C19'), 127.41 (d, $^3J(^{31}\text{P}_\text{a}-^{13}\text{C}) = 9.6$ Hz, C7'), 127.32 (d, $^2J(^{31}\text{P}_\text{c}-^{13}\text{C}) = 8.3$ Hz, C18'), 127.27 (d, $^3J(^{31}\text{P}_\text{c}-^{13}\text{C}) = 9.1$ Hz, C19), 126.12 (d, $^2J(^{31}\text{P}_\text{b}-^{13}\text{C}) = 9.4$ Hz, C12'), 42.13 (dd, $^1J(^{31}\text{P}_\text{c}-^{13}\text{C}) = 42.7$ Hz, $^3J(^{31}\text{P}-^{13}\text{C}) = 3.3$ Hz, C16), 26.13 (d, $J(^{31}\text{P}-^{13}\text{C}) = 38.8$ Hz, C10)[&], 25.61 (d, $J(^{31}\text{P}-^{13}\text{C}) = 34.9$

Hz, C4)[&], 16.85 (dd, $^2J(^{31}\text{P}_b-^{13}\text{C}) = 19.7$ Hz, $J(^{31}\text{P}-^{13}\text{C}) = 2.3$ Hz, C9), 16.04 (d, $^2J(^{31}\text{P}-^{13}\text{C}) = 22.2$ Hz, C3), -0.69 (s, C2), -14.73 (ddd, $^2J(^{31}\text{P}-^{13}\text{C}) = 69.6$ Hz, $^2J(^{31}\text{P}-^{13}\text{C}) = 29.6$ Hz, $^2J(^{31}\text{P}-^{13}\text{C}) = 3.5$ Hz, C15),[&] assignments interchangeable; $^{31}\text{P}\{^1\text{H}\}$ NMR (CDCl₃, 202.28 MHz): δ (ppm) = 11.12 (dd, $^2J(^{31}\text{P}_a-^{31}\text{P}_c) = 368$ Hz, $^2J(^{31}\text{P}_a-^{31}\text{P}_b) = 4.7$ Hz, P_a), 3.79 (dd, $^2J(^{31}\text{P}_b-^{31}\text{P}_c) = 4.8$ Hz, $^2J(^{31}\text{P}_b-^{31}\text{P}_a) = 4.7$ Hz, P_b), -94.61 (dd, $^2J(^{31}\text{P}_c-^{31}\text{P}_a) = 368.1$ Hz, $^2J(^{31}\text{P}_c-^{31}\text{P}_b) = 4.8$ Hz, P_c); $^{29}\text{Si}\{^1\text{H}\}$ NMR (CDCl₃, 79.37 MHz): δ (ppm) = 35.83 (dd, $J(^{31}\text{P}-^{29}\text{Si}) = 8.5$ Hz, $J(^{31}\text{P}-^{29}\text{Si}) = 4.9$ Hz). **HR-MS** (ESI⁺): $m/z = 875.1995$ calcd. for $[\text{M}-\text{Cl}]^+ = 875.2133$. **Elemental Analysis** (C₄₃H₄₅ClIrPSi) calcd.: C 56.72 H 4.98 Cl 3.89; found: C 57.30 H 5.11 Cl 3.50.

Complex 49



$[(\text{COD})\text{RhCl}]_2$ (22.8 mg, 0.046 mmol) in 10 ml THF was added to a solution of tripod ligand **45** (64.0 mg, 0.094 mmol) in 20 ml THF. The reaction mixture was stirred at 60 °C for 3 h. The solvent was partially removed *in vacuo*. 20 ml of pentane were added

and a yellow precipitate formed which was filtered off. After drying *in vacuo*, a mixture of **48** and **49** was obtained in a 1.0 : 3.3 ratio.

$^{31}\text{P}\{^1\text{H}\}$ NMR (C_6D_6 , 202.28 MHz): δ (ppm) = 37.95 (dd, ($^1J(^{103}\text{Rh}-^{31}\text{P}_{\text{cis}}) = 115.96$ Hz, $^2J(^{31}\text{P}_{\text{cis}}-^{31}\text{P}_{\text{trans}}) = 21.2$ Hz), P_{cis}), 28.99 (dt, ($^1J(^{103}\text{Rh}-^{31}\text{P}_{\text{trans}}) = 88.5$ Hz, $^2J(^{31}\text{P}_{\text{trans}}-^{31}\text{P}_{\text{cis}}) = 21.1$ Hz, P_{trans}); **$^{29}\text{Si}\{^1\text{H}\}$ NMR** (C_6D_6 , 79.37 MHz): δ (ppm) = 97.05 (dtd, ($^1J(^{103}\text{Rh}-^{29}\text{Si}) = 28.2$ Hz, $J(^{31}\text{P}-^{29}\text{Si}) = 6.5$ Hz, $J(^{31}\text{P}-^{29}\text{Si}) = 2.7$ Hz).

CHAPTER V
SOLID-STATE NMR AND IR STUDIES OF PERFORMANCE POLYMERS
FOR THE OIL AND GAS INDUSTRY

INTRODUCTION

Performance Polymers

Thermoplastic polymers are commonly classified according to Figure 5.1, differentiating between amorphous and semicrystalline polymers. In the case of semicrystalline polymers the material properties depend significantly on the morphology, e.g. the size and distribution of the crystallites, the chain entanglement in the amorphous phase and the crystallite interface. Direct measurements of the morphology are notoriously difficult and thus one relies heavily on indirect methods such as mechanical properties, DSC, or spectroscopic techniques such as IR and NMR.

Among the polymers that are suitable for high-temperature applications are PBI (polybenzimidazole, poly[2,2'-(*m*-phenylene)-5,5'-bibenzimidazole]) (polybenzimidazole), PPS (polyphenylene sulfide), as well as polymers of the PAEK (polyaryletherketone) family.¹²¹ The PAEK polymers differ from one another in the ratio of aryether to ketone function, which is reflected in their name as shown in Figure 5.2.

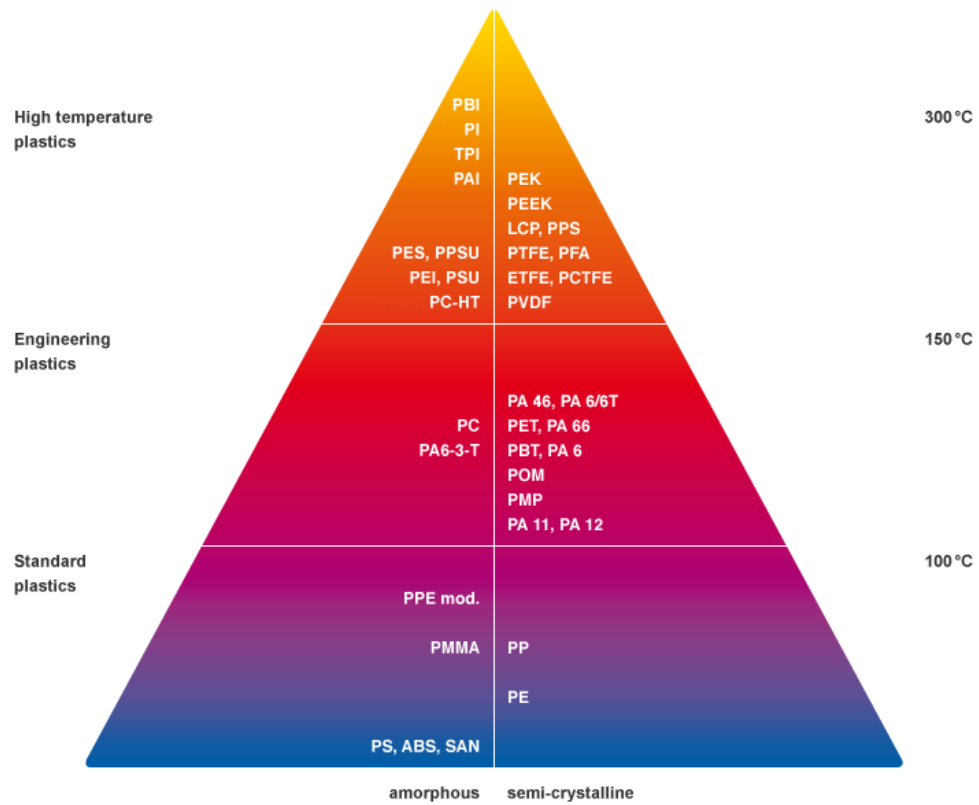


Figure 5.1. Classification of thermoplastic polymers. ¹²⁰

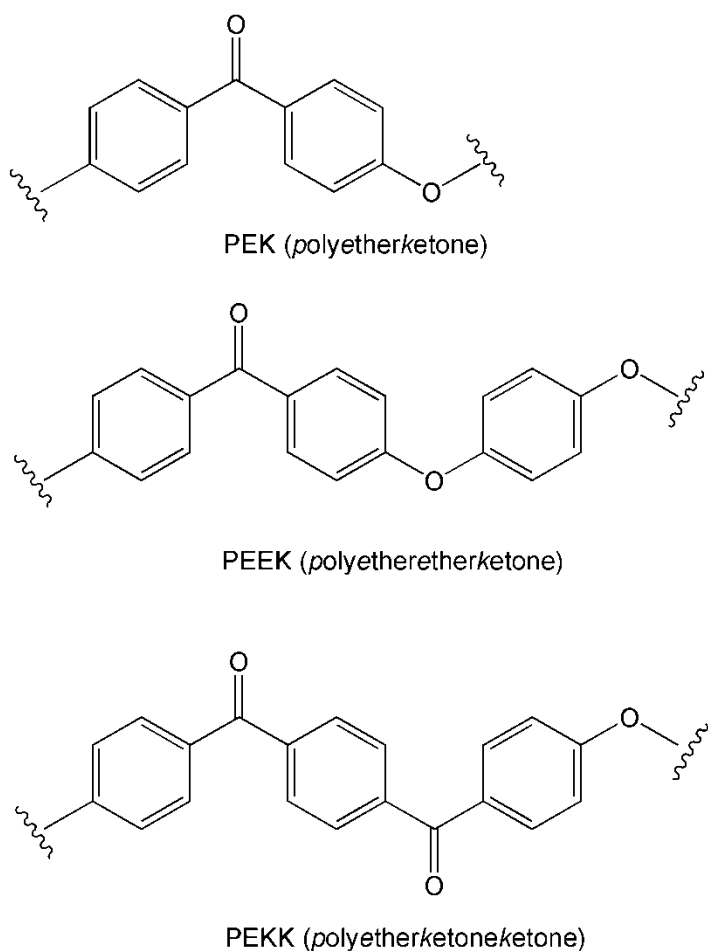


Figure 5.2. Nomenclature of PAEK polymers.

An increase of the ketone to ether ratio leads generally to higher crystallinity and thus increased glass transition temperature and melting point. These desirable attributes can be offset, however, by poor processability.

PAEK (polyaryletherketone) polymers, and PEEK (polyetheretherketone) polymers in particular, are of growing importance for the oil and gas industry. They display many advantageous properties for their use under extreme service environments, such as high pressures and temperatures. They have high melting points and glass transition temperatures, and are mechanically and chemically rather robust. In order to

further improve the performance of PAEK polymers and prolong their lifetimes, a better understanding of their composition down to the molecular level is necessary. Hereby, their ratio of rigid versus mobile, and crystalline versus amorphous domains are key characteristics. Furthermore, their change before and after application on a molecular level needs to be investigated in order to gain more insight into decomposition processes under realistic conditions.

Both PAEKs and PPS require high processing temperatures. The post-reactor processing is known to influence the material properties likely due to cross-linking, but the understanding is anecdotal and the underlying chemistry is poorly understood. The failure mechanisms of PAEKs and PPS due to oxidative stress at service temperature also warrant further investigations. PEEK polymers were introduced more than 20 years ago, but more recently new polymer grades of PEEK as well as new polymers of the PAEK family, e.g. PEKKEK, are being commercialized. Yet no reliable structure-performance relationship for these materials exists. This is especially troublesome as they are used in ever more demanding environments such as off-shore drilling.

PBI is one of the polymers with the highest temperature resistance. It is therefore widely used in extreme conditions for example the gown of firefighters. It is also blended with other polymers, such as PEKK, to extend its service range. Unlike PAEKs, PBI is known to be highly hydrophilic. It is necessary to better understand PBI's interactions with water and steam, which could lead to hydrolysis on the polymer and possibly material failure.

In this chapter solid-state NMR and IR studies of these polymers are presented which complement investigations of mechanical and tribological aspects carried out in the research groups of Dr. Schwartz and Dr. Sue within the APPEAL (Advancing Performance Polymers for Energy Applications) Industrial Consortium.

Solid-state NMR in Polymer Science

Solid-state NMR spectroscopy is a powerful method that allows a multitude of diverse measurements of crystalline and amorphous materials.¹²² Polymers represent the most prominent and the classic materials for solid-state NMR investigations. The most commonly observed parameter in NMR is the chemical shift which reveals information of the chemical constitution on a molecular level. Unlike in solution, in the solid state anisotropic interactions prevail, giving rise to broader lines and generally more complex spectra. Interpretation is therefore more complicated, but additional information can be gained as well. Several NMR parameters are sensitive to molecular motion and are therefore exploited in polymer science (Figure 5.3).¹²³

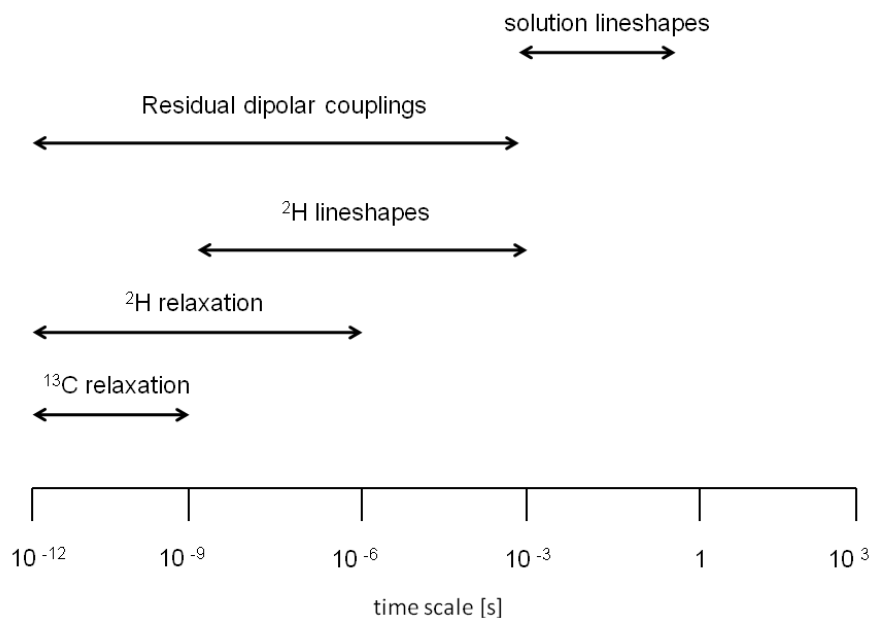


Figure 5.3. Motion-sensitive NMR parameters.^{122,123}

Very slow processes such as chain reptation can be studied by 2D exchange spectroscopy, which is especially effective using deuterated materials.^{124,125,126} Dynamic phenomena on intermediate timescales can best be studied by the observation of signal lineshapes. Especially the lineshapes of ^2H NMR signals are sensitive to molecular motion.¹²⁷ In the regime of fast motion relaxation times can serve as probes of molecular motion. Of the various relaxation times the longitudinal (or spin-lattice) relaxation time T_1 and the transverse (or spin-spin) relaxation time T_2 are most commonly measured and are interpreted in a straightforward manner (Figure 5.4)

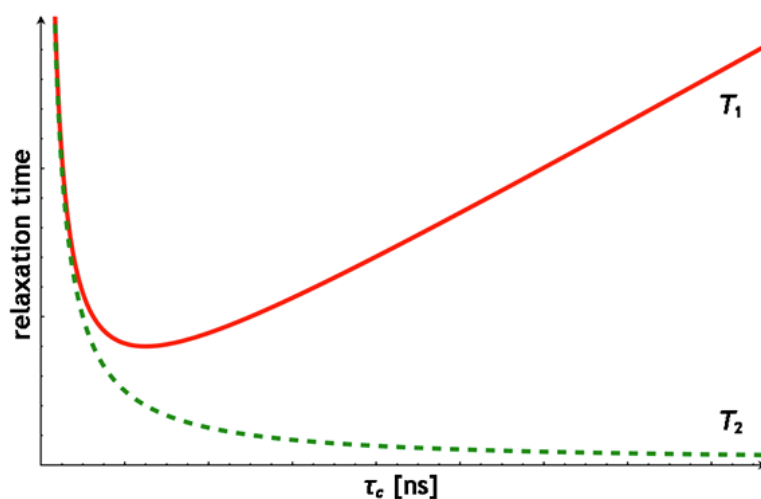


Figure 5.4. Dependence of the T_1 and T_2 relaxation time on the correlation time τ_c for the model of dipolar interactions of isolated spin pairs. The relaxation times additionally depend on the gyromagnetic ratio, the magnetic field strength, and the spin-spin distance.

In semicrystalline polymers the relaxation within the crystalline domains can be described with a single time constant (Figure 5.5). In the amorphous domains and especially at the interface between crystalline and amorphous regions many sites of various mobilities exist. However, if the mobility in the amorphous and crystalline domains differ largely the relaxation can approximately be described by two discrete time constants.

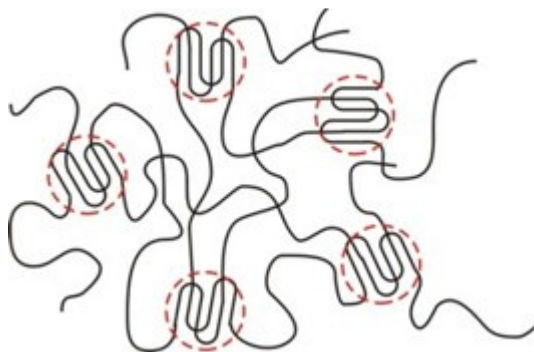


Figure 5.5. Semicrystalline polymer with crystalline and amorphous domains.

Other phenomena such as rotating frame relaxation, $T_{1\rho}$ ¹²⁸ or the kinetics of cross-polarization¹²⁹ are more convoluted by multiple spin-spin and spin-lattice effects acting simultaneously and can thus lead to erroneous interpretation.

In this chapter 1D ^{13}C CP/MAS NMR was used to investigate changes on the molecular level such as oxidation, chain scission, or hydrolysis. These results were complemented by IR measurements.

^{13}C T_1 relaxation times were measured to determine changes in polymer morphology. The measurements were carried out using a pulse sequence reported by Torchia (Figure 5.6).¹³⁰

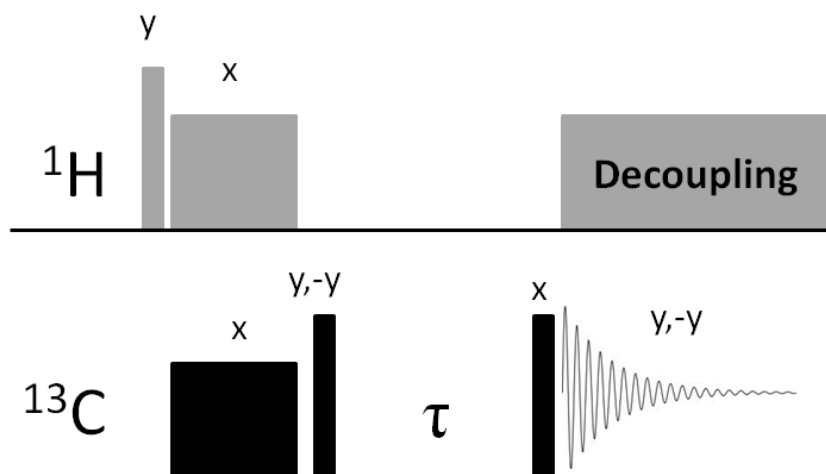


Figure 5.6. Torchia's pulse sequence to measure ^{13}C T_1 relaxation times.¹³⁰

The pulse sequence is based on a cross-polarization experiment. After polarization transfer from ^1H to ^{13}C a ^{13}C 90° pulse is applied to flip the magnetization onto the $-z$ axis. During the delay τ , the magnetization decays with the time constant T_1 . After that another 90° pulse is applied to flip the remaining magnetization in the xy plane for the acquisition of the FID. To determine T_1 , the delay τ is incremented and the respective spectra are recorded. Plotting the signal intensity versus the delay τ gives the relaxation curve (Figure 5.7). In order to obtain maximal S/N ratio for each spectrum, and thus well-defined relaxation curves, usually the most intensive signal in the spectrum is chosen (Figure 5.7, signal denoted by arrow).

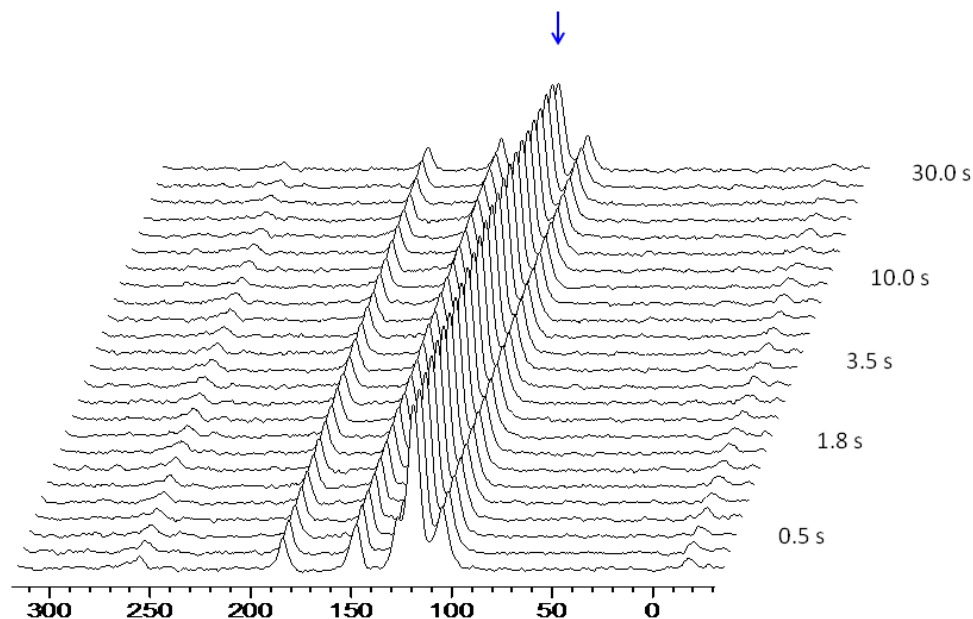


Figure 5.7. Torchia's method to measure ^{13}C T_1 relaxation times, demonstrated with a PEEK polymer.¹³⁰

RESULTS AND DISCUSSION

Polyetheretherketones PEEK

First, a selection of pure PEEK polymers has been studied by ^{13}C CP/MAS NMR spectroscopy. Figure 5.8 displays the spectrum obtained from Victrex 450P. All signals can be assigned unequivocally to the corresponding carbon positions in the structure, in accordance to the literature.¹³¹ Two signal groups overlap, the signals of the carbons in the *ipso*- and *ortho*-positions of the keto group at 132.3 ppm, and the carbon resonances in the *ortho* positions to the ether functionality of the diether and of the ketoether benzene rings at 120.1 ppm.

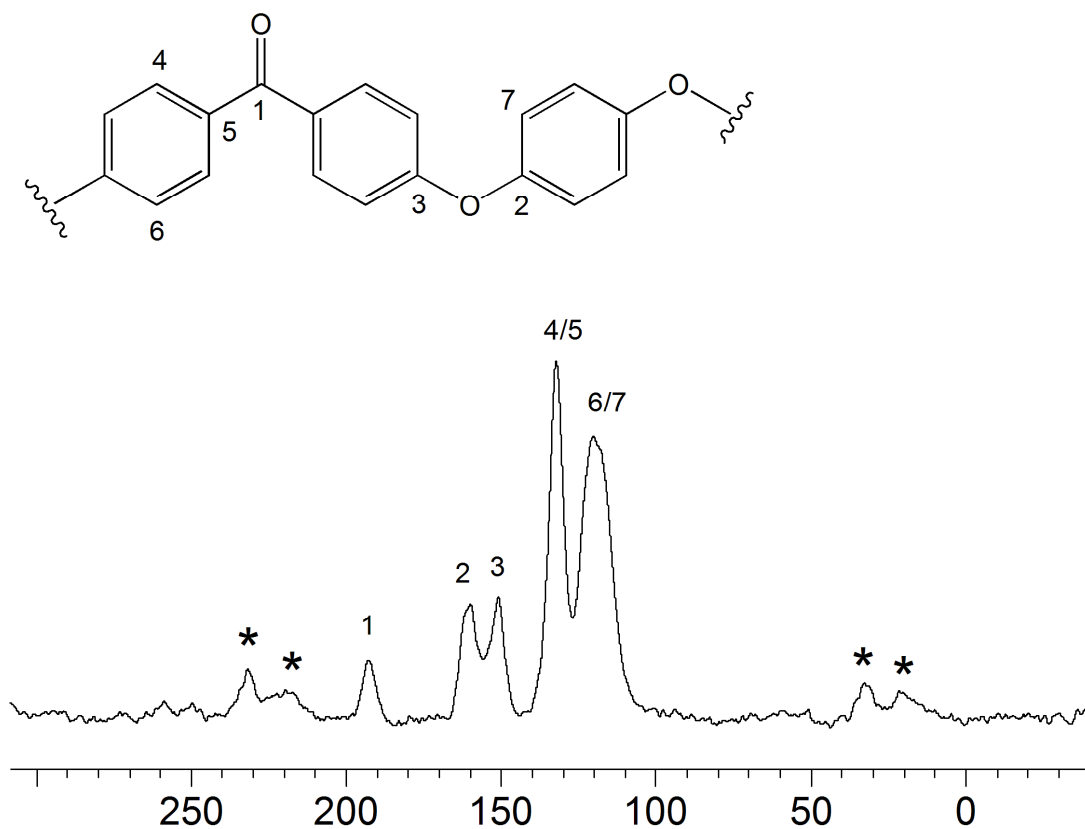


Figure 5.8. ^{13}C CP/MAS NMR spectrum of PEEK (Vicatex 450P). Asterisks denote rotational sidebands.

The efficiency of cross-polarization from ^1H to ^{13}C can differ significantly for different species in a sample and even for different moieties such as protonated and quaternary carbon atoms.¹²⁹ To ensure efficient measurement conditions the contact time of the CP pulse sequence was optimized. Figures 5.9 and 5.10 show the signal intensities of the peaks at 120 ppm and 150 ppm, respectively, as a function of contact time. Hereby, the pulse repetition time was 5 s.

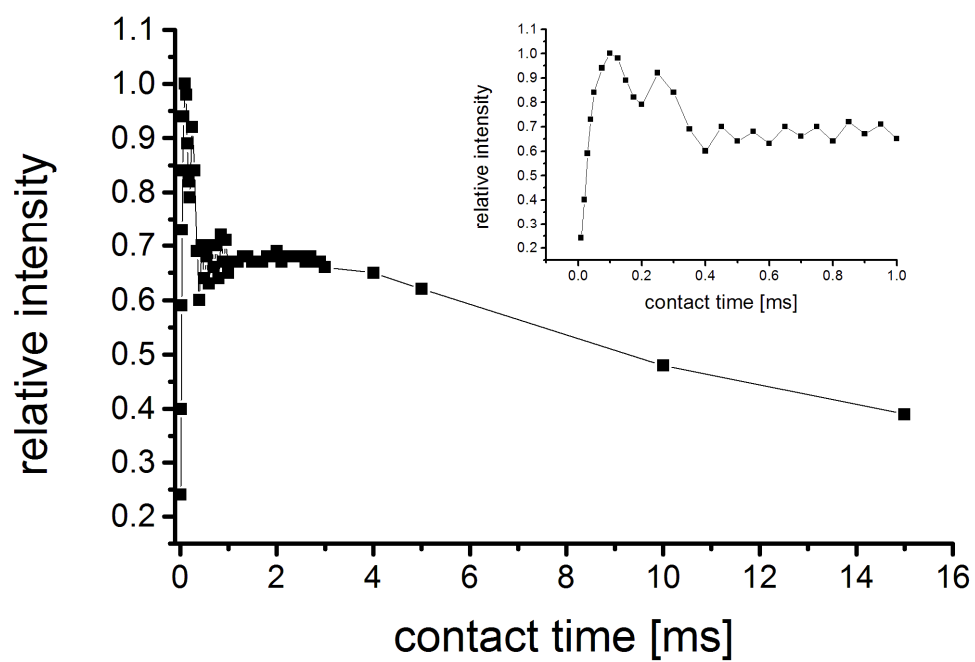


Figure 5.9. Cross-polarization kinetics of the signal at 120 ppm.

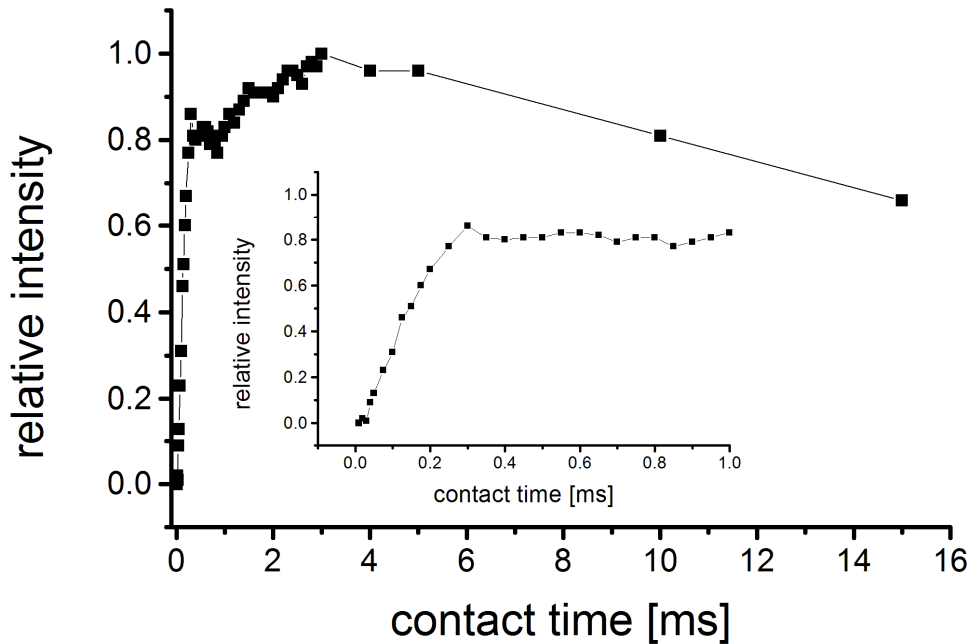


Figure 5.10. Cross-polarization kinetics of the signal at 150 ppm.

As expected the signal intensity rises quickly in the beginning and then slowly decreases for very long contact times due to spin-lattice relaxation in the rotating frame and cross-relaxation. A contact time of 1.5 ms was chosen which is on the plateau for both, quaternary carbons and those having hydrogen bound to them, thus ensures equally efficient cross-polarization.

In principle, plotting the signal intensity as a function of contact time allows the determination of various NMR parameters such as the time constant of cross-polarization T_{CP} and the time constant of spin-lattice relaxation in the rotating frame for ^{13}C , $T_{1\rho}$, which are also motion sensitive. The interpretation is often hampered by different physical processes occurring simultaneously. The initial curves show oscillations of the signal intensity. This has been described in the literature for similar systems, both for static measurements and measurements under MAS conditions.¹²⁹ This effect is due to dipolar oscillations as described by Klinowski in a recent review of cross-polarization.¹²⁹ However, fitting of the curves, extraction of $T_{1\rho}$, and interpretation in terms of molecular motion was beyond the scope of this work.

In order to confirm the signal assignments, a Dipolar Dephasing (DD) pulse sequence has been applied (Figure 5.11). Hereby, a delay is inserted after the CP pulse, so that non-quaternary carbon signals relax prior to the recording of the signal, which leads to their diminished signal intensities.¹³² In contrast to this, quaternary carbon signals, due to the absence of directly bound protons, are not prone to this signal intensity loss. The top spectrum in Figure 5.11 shows that the signals of all quaternary carbons at 193.0, 160.0, and 150.9 ppm retain their original signal intensities. However, the signal at 120.1 ppm is substantially diminished because it stems from non-quaternary carbons. With DD, the resonance at 132.3 ppm is about half its original intensity, in

accordance with its origin, being composed of the signals of one quaternary and one non-quaternary carbon site.

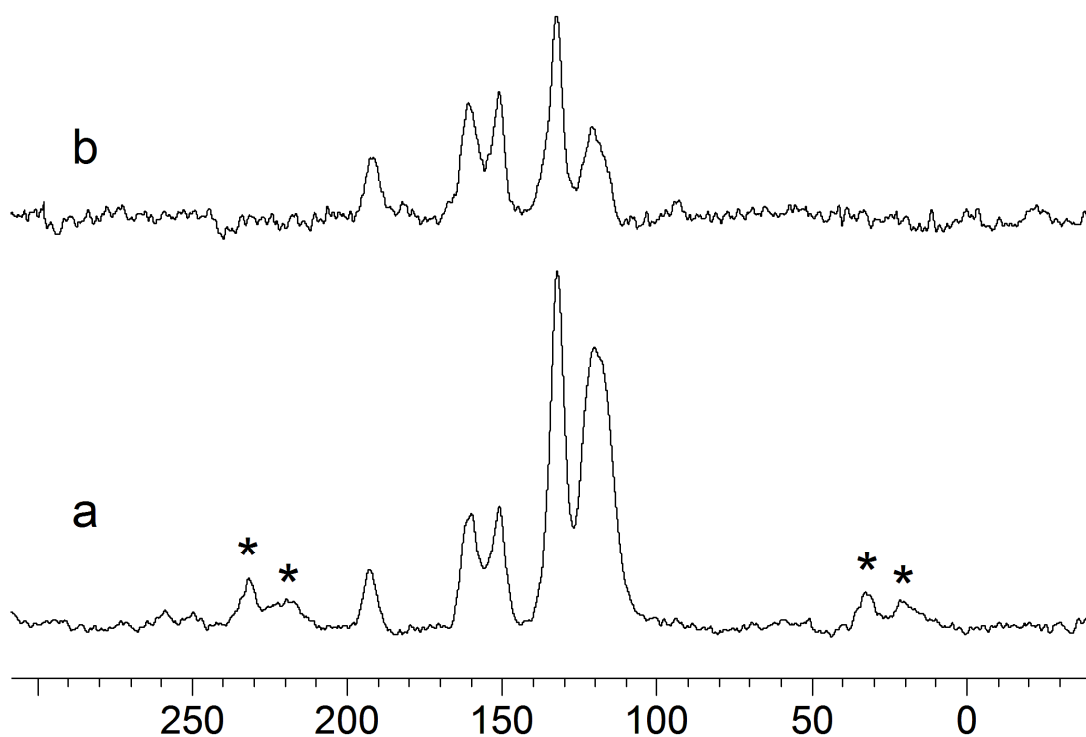


Figure 5.11. (a) ^{13}C CP/MAS and (b) ^{13}C Dipolar Dephasing ($40\ \mu\text{s}$ dephasing delay) NMR spectra of Victrex 450P. The asterisks denote rotational sidebands.

Next it was investigated, whether differences would be visible in the ^{13}C CP/MAS spectra of various PEEK polymers from different vendors. As the ^{13}C CP/MAS spectra in Figure 5.12 show, subtle differences are clearly visible. Most striking are the signal intensity differences for the quaternary carbons at 160.0 and 150.9 ppm. Taking the above signal assignment into account, this indicates different amounts of ketoether

versus etherether segments. The difference in appearance between the spectra of the PEEK brands shown in Figure 5.12 becomes even more striking, when the ^{13}C DD/MAS spectra are compared.

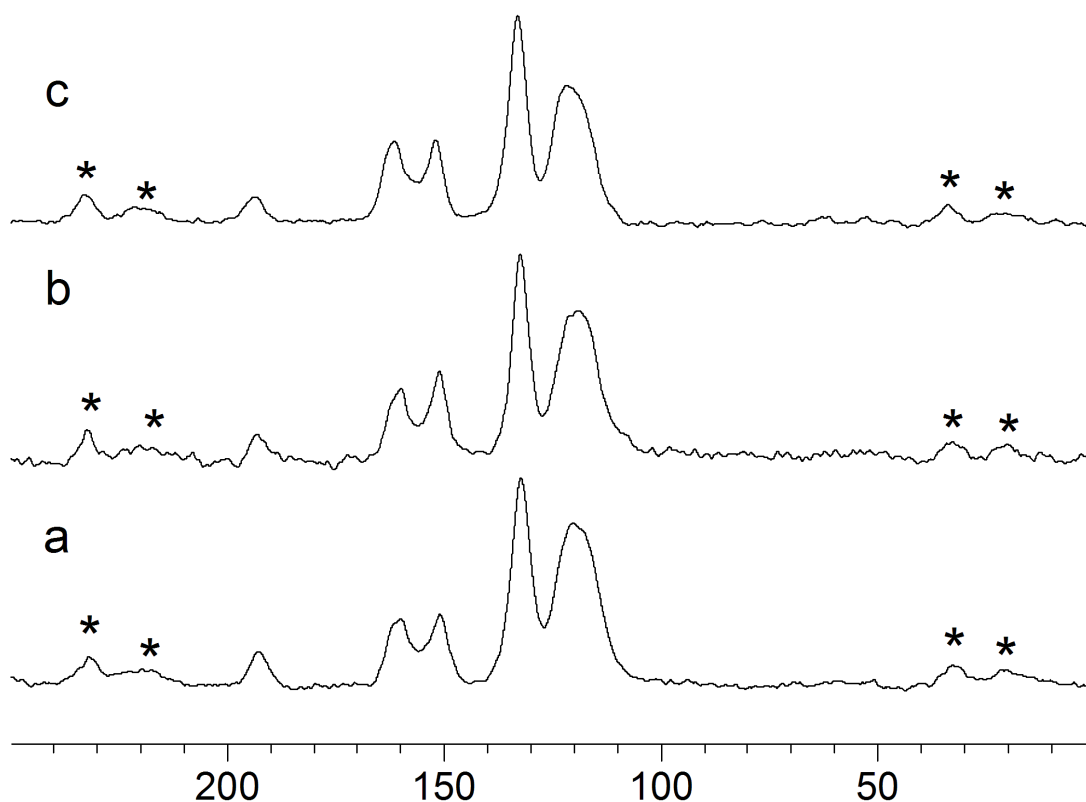


Figure 5.12. ^{13}C CP/MAS NMR spectra of Victrex 450P (a), Evonik 4000PF (b), and Evonik 5000G (c). The asterisks denote rotational sidebands.

Thus, it is possible to obtain all ^{13}C signals of PEEK polymers with reasonable linewidths, and to assign all signals unequivocally. Different PEEK brands can be distinguished, and some impurities in the polymer can be identified. The extension of this technique would be a differentiation of the various ether / keto ratios which exist in commercial products, coupled with spectroscopic measurements probing relaxation, in

order to assess relative molecular motion of these distinguishable species. This becomes important in the assessment of interactions between the bulk polymer and small molecules, which are expected to show very different diffusion into mobile domains compared to crystalline regions.

One key element in the characterization of polymers is the ratio between crystalline and amorphous domains in the material, as well as the dimensional scale of such domains in the bulk material. This ratio is one of the most important factors influencing the mechanical properties of PAEK polymers. Solid-state NMR analysis can provide valuable insights with respect to the mobility of these different domains. Crystalline sections of the polymers are always rigid in nature, as are amorphous domains in close proximity to the crystalline domains, in a region often referred to as the crystalline interphase. But the major part of the amorphous regions consists of a non-rigid phase that is rather mobile even in the solid state. The non-mobile and mobile domains can be distinguished and quantified by solid-state NMR spectroscopy via the different relaxation times T_1 of the ^{13}C nuclei. Typically, non-mobile, such as crystalline domains, feature much longer relaxation times than mobile domains.

Due to its large intensity, the signal of the non-quaternary carbons at 120.1 ppm was chosen to obtain the T_1 relaxation times (Fig. 5.7). For this purpose, the relative signal intensities are plotted versus the applied relaxation delays for the various PEEK samples (Figures 5.13, 5.14, 5.15). Then, assuming that the signal at 120.1 ppm stems from both mobile and rigid phases, a double-exponential fit is used to determine the shorter relaxation time of the mobile phase.¹³³ Hereby, the longest relaxation time for the purely crystalline and rigid domain had been determined to be 73 s. From the curve fitting process, the short T_1 time for the mobile amorphous domain, as well as the

percentages of mobile (A) versus non-mobile (B) phases, can be obtained. Table 5.1 summarizes all data for the indicated PEEK samples.

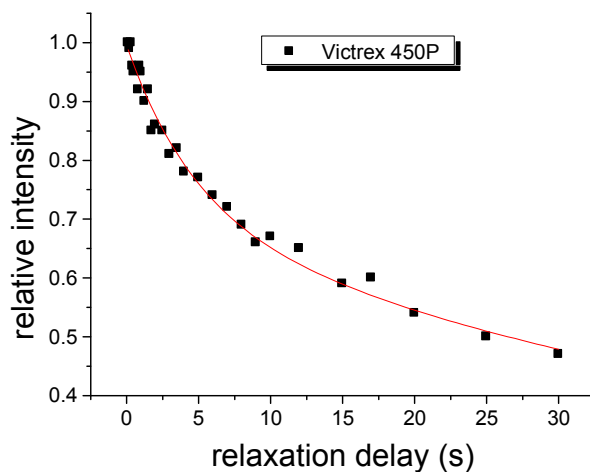


Figure 5.13. ^{13}C T_1 relaxation of PEEK Victrex 450P for the signal at 120.1 ppm.

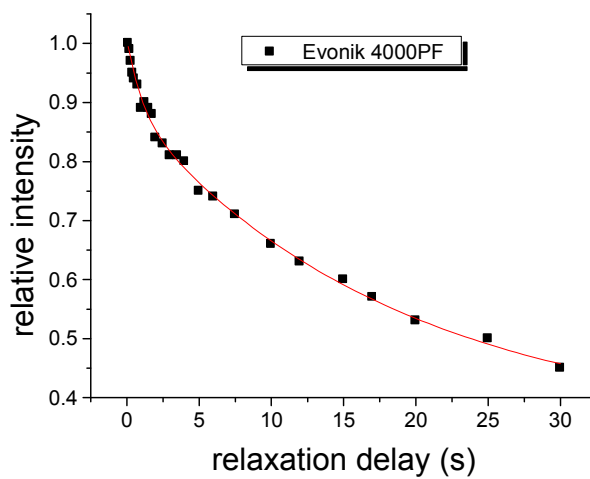


Figure 5.14. ^{13}C T_1 relaxation of PEEK Evonik 4000PF for the signal at 120.1 ppm.

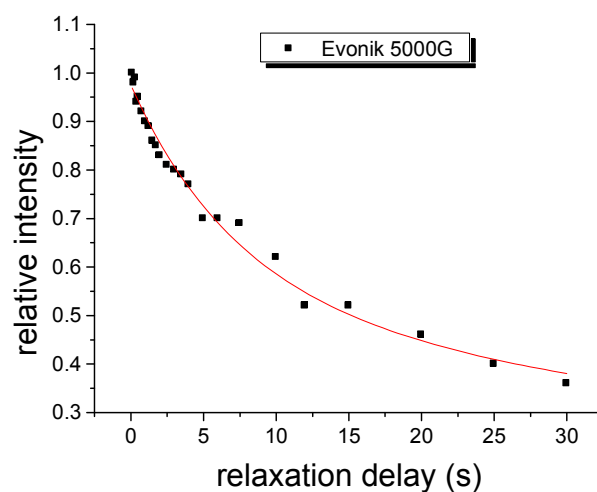


Figure 5.15. ^{13}C T_1 relaxation of PEEK Evonik 5000G for the signal at 120.1 ppm.

As Table 5.1 shows, the PEEK samples Victrex 450P and Evonik 4000PF are very similar. The T_1 times of the mobile region are in the same range from about 4.0 to 4.5 s, and the percent amount of amorphous domain is the same with 27% for both materials. The T_1 times are longer and the time differences are somewhat larger for the sample The amount of mobile matter A is, with 41 and 42%, more than 10% larger as compared to the previous two samples.

Table 5.1. ^{13}C T_1 relaxation times of the mobile domain **A** and the rigid domain **B** of the indicated samples. **A** and **B** are given in the percent amounts of the mobile and rigid domains after the curve fitting process with a goodness of fit r^2 .

Sample	A (%)	$T_1(\text{A})$ (s)	B (%)	$T_1(\text{B})$ (s)	r^2	Cryst. ^a	M_w
Victrex 450P	27	4.02	72	73	0.989	42	114362
Evonik 4000PF	27	4.54	71	73	0.987	32	119183
Evonik 5000G	41	6.69	56	73	0.992	32	118548

^a The degree of crystallinity was determined by DSC measurements. Data recorded by K. White.

These preliminary relaxation time measurements will be expanded to other grades and to samples with various processing histories. Combined with results from other techniques this will help to establish a sound structure–property relationship for this class of polymers.

Related to the structure–property relationship of the polymers, the influence of the material processing, which requires high temperatures, on the polymer structure is of interest. Also an understanding of changes to the molecular composition under service conditions is crucial to elucidate failure mechanisms and possibly avoid them altogether.

It is thought that cross-linking between polymer chains is the main reaction taking place at elevated temperatures (Figure 5.16). This has been suggested by Jonas *et al.* who observed an increase in molecular weight under processing conditions.¹³⁴

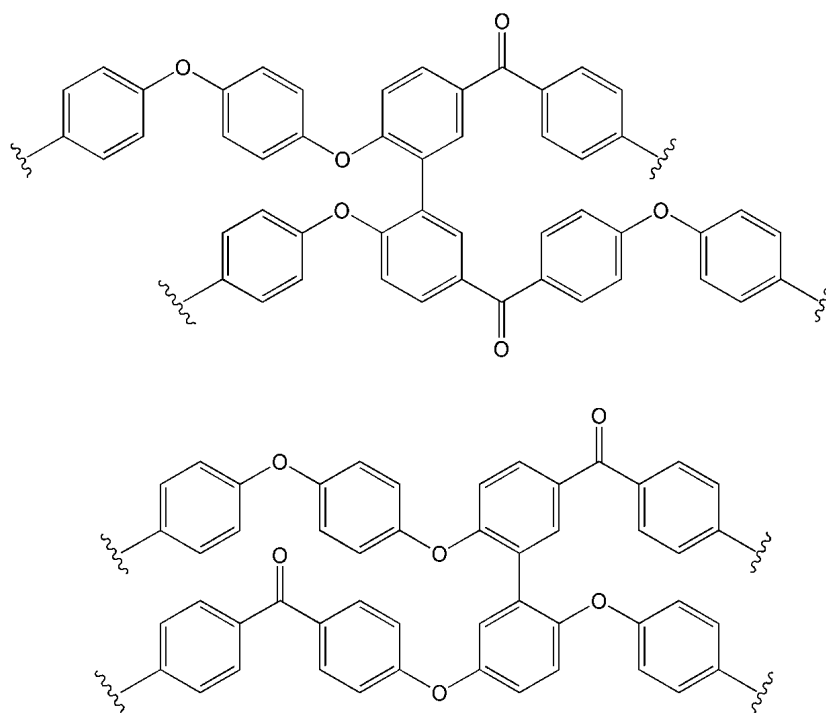


Figure 5.16. Possible structures of cross-linked PEEK.

The oxidative degradation of PEEK has been studied by Day and coworkers with spectroscopic methods including IR and solid-state NMR.¹³⁵ Based on a slight change in signal intensities in the ^{13}C CP/MAS NMR peaks at 160 ppm and 150 ppm they propose cross-linking as shown in Figure 5.16. Furthermore, they suggest reduction of the carbonyl group and cross-linking via ether formation based on changes in the IR spectrum.

PEEK 450 was thermally treated at 300 °C both in air and in a nitrogen atmosphere and at 420 °C in air. The samples were investigated by IR, ^{13}C CP/MAS NMR, and the ^{13}C T_1 relaxation times were determined.

As shown in Figure 5.17 the changes in ^{13}C CP/MAS are subtle. No additional peaks, an *ipso* carbon of a biphenyl linkage resonates at 140 ppm, are visible even in the sample treated at 420 °C. Also there is no significant decrease of any of the resonance intensities. The most striking observation is the change in linewidths. Heating to 300 °C for 4 h, which is well above the T_g of 160 °C, led to an increase in crystallinity and thus narrower lines due the well defined molecular environment within the crystalline domains. The sample heated to 420 °C led to melting of the polymer. Thus the polymer morphology depends very much on the cooling conditions which strongly influence the crystallization kinetics. The quick drop in temperature after exposure, the sample was removed from an oven and allowed to cool in an open atmosphere at RT, led to broad lines in ^{13}C CP/MAS indicating lower crystallinity as compared to the untreated polymer.

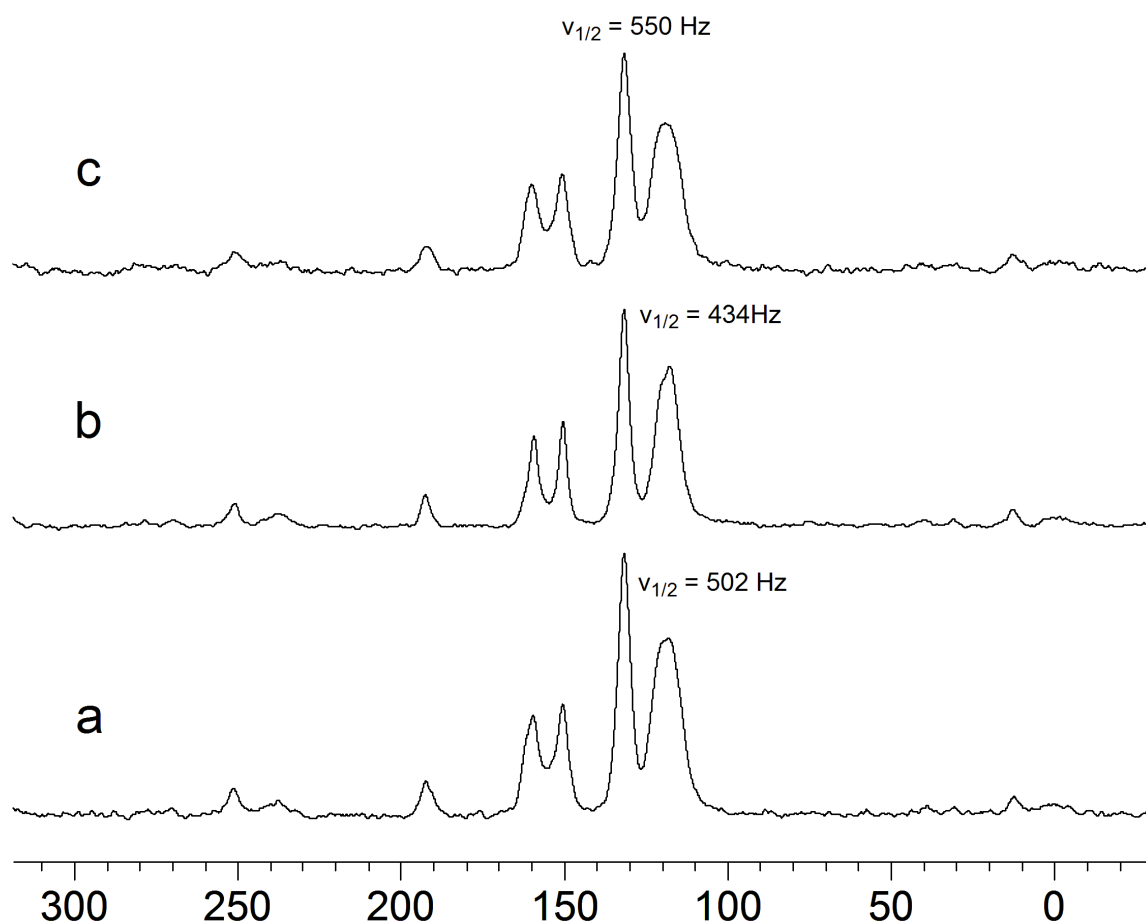


Figure 5.17. ^{13}C CP/MAS NMR of Victrex PEEK 450 (a) as received, (b) after heating to 300 °C for 4h, and (c) heating to 420 °C for 1.5 h.

These qualitative observations based on the linewidths are corroborated by the ^{13}C T_1 relaxation times given in Table 5.2. Figure 5.18 shows the relaxation curves of the original polymer and the heated samples. As can be seen for the sample heated to 300 °C, there is distinctly slower relaxation which is indicative of reduced molecular motion. This is most likely due to increased crystallinity. It is, however, difficult to distinguish between crystalline domains and regions of low molecular mobility due to other effects, such as chain entanglement, by NMR methods. The relaxation behavior of

the sample treated at 420 °C and the original sample do not differ that strongly and the slight difference might not solely be due to changes in crystallinity, but may also be influenced by potential cross-linking and changes in molecular weight, etc..

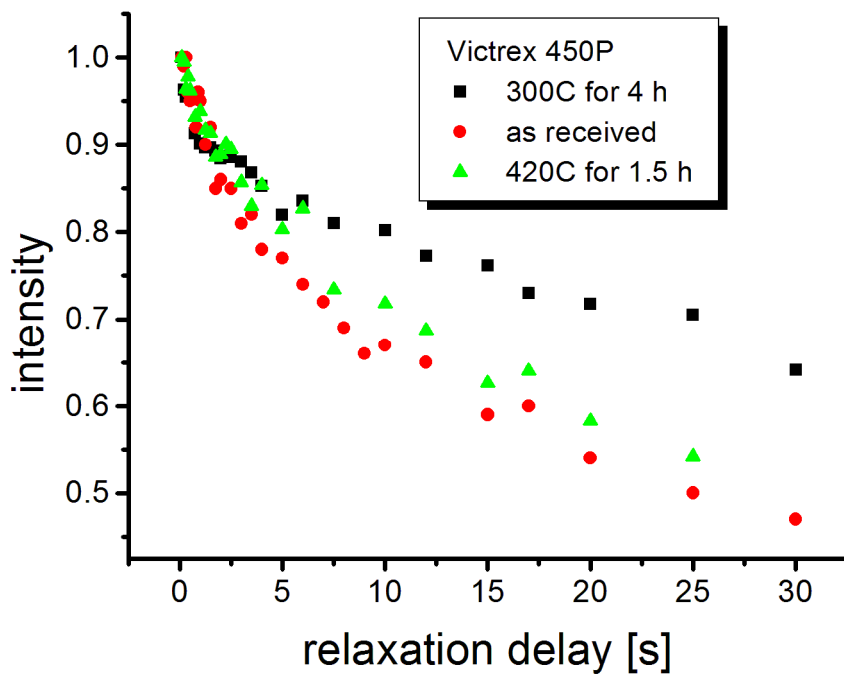


Figure 5.18. ^{13}C T_1 relaxation of a PEEK sample after the indicated thermal treatments.

Table 5.2. ^{13}C T_1 relaxation times of the mobile domain **A** and the rigid domain **B** of the indicated samples. **A** and **B** are given in the percent amounts of the mobile and rigid domains after the curve fitting process with a goodness of fit r^2 .

sample	A (%)	$T_1(\text{A})$ (s)	B (%)	$T_1(\text{B})$ (s)	r^2
untreated	27	4.02	72	73	0.989
300°C	21	5.56	77	73	0.985
420°C	11	0.75	89	92	0.984

IR spectroscopy also revealed no further insights regarding changes on the molecular level (Figure 5.19). The CO double bond stretch, which is observed at 1647 cm^{-1} does not shift and is also not diminished in intensity upon thermal treatment. Furthermore, the C-C stretching modes at 1595 cm^{-1} and 1489 cm^{-1} remain unchanged. A striking change is observed in the ratio of the peaks at 1305 cm^{-1} and 1276 cm^{-1} , as well as 1112 cm^{-1} and 1099 cm^{-1} . The ratio of these peaks is indicative of the crystallinity of the polymer.¹³⁶ The higher the ratio of the peak at 1305 cm^{-1} to the peak at 1276 cm^{-1} the higher the crystallinity. According to the peak ratio and crystallinity reported by Chalmers *et al.*^{136a} the crystallinity increased from 22% for the original polymer to 50% for the sample treated at 300 °C. Therefore, the conclusion from the IR measurements is in agreement with the ^{13}C T_1 relaxation data. It should be noted, however, that the crystallinities obtained by IR spectroscopy do not agree well with crystallinities determined via DSC measurements.

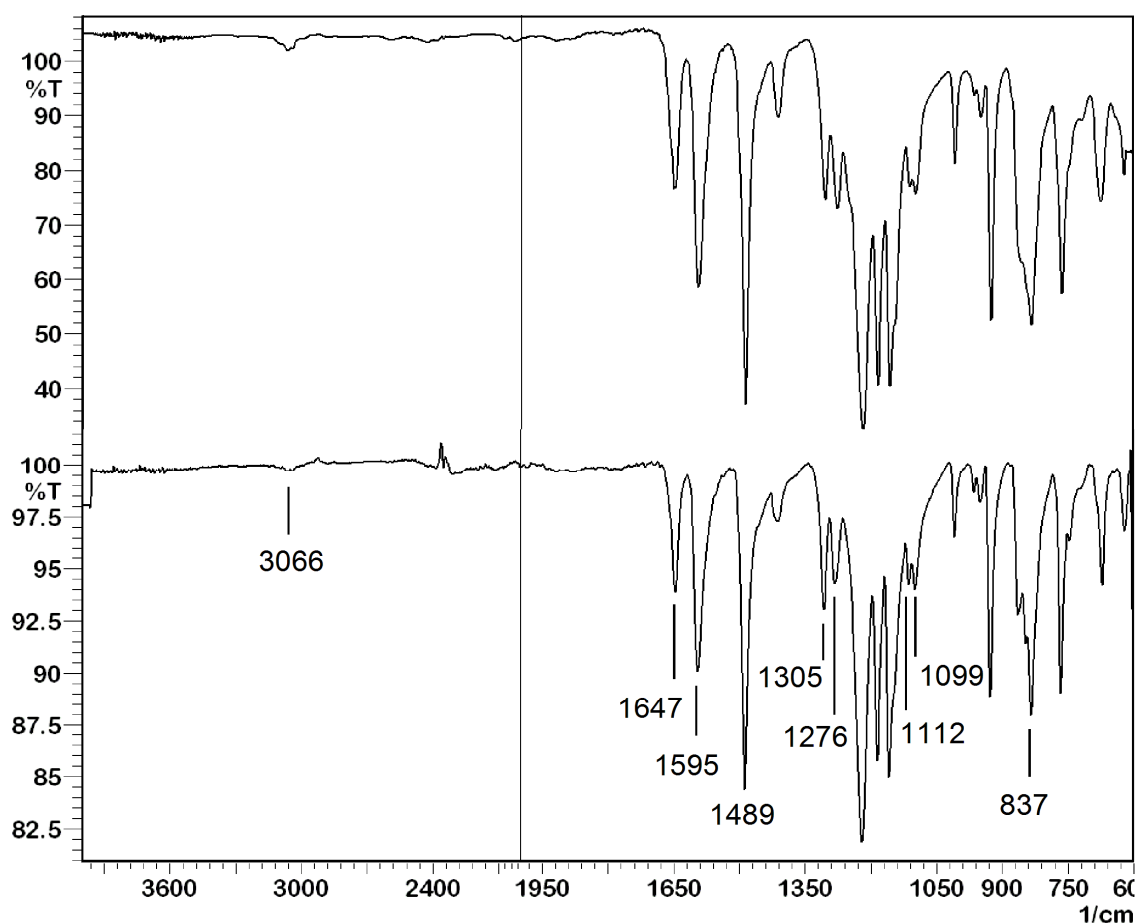


Figure 5.19. IR spectra of PEEK: original sample (*top*), and after thermal treatment at 300 °C (*bottom*).

It can be concluded that under the conditions tested the bulk material is not altered on a molecular level, but some cross-linking cannot be ruled out due to the detection limits of solid-state NMR and IR. Significant changes regarding the polymer morphology take place, which include, but are not limited to, changes in crystallinity.

More detailed information will be gained by high-temperature NMR studies above the T_g of PEEK polymers.

Polyphenylene Sulfide PPS

Polyphenylene Sulfide (PPS) polymers are another class of semicrystalline thermoplastics that are commonly used in high-temperature applications.¹²¹ Similar to the work on PEEK polymers it is of interest to further characterize these materials especially with respect to differences in the polymer structure on the molecular level and oxidative decomposition. Commercially available PPS is believed to consist predominately 1,4-disubstituted benzene rings linked to each other by thioether groups (Figure 5.20).

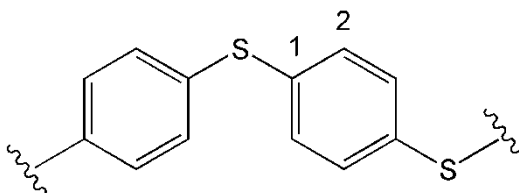


Figure 5.20. Structure of PPS (polyphenylene sulfide).

Figure 5.21 shows the ^{13}C CP/MAS NMR spectrum of PPS. The *ipso* carbon resonates at 134 ppm and the *ortho* carbon at 131 ppm.^{137,138} Both the crystalline domains and amorphous regions contribute to the spectrum, and they differ in the linewidths of the peaks associated with them.

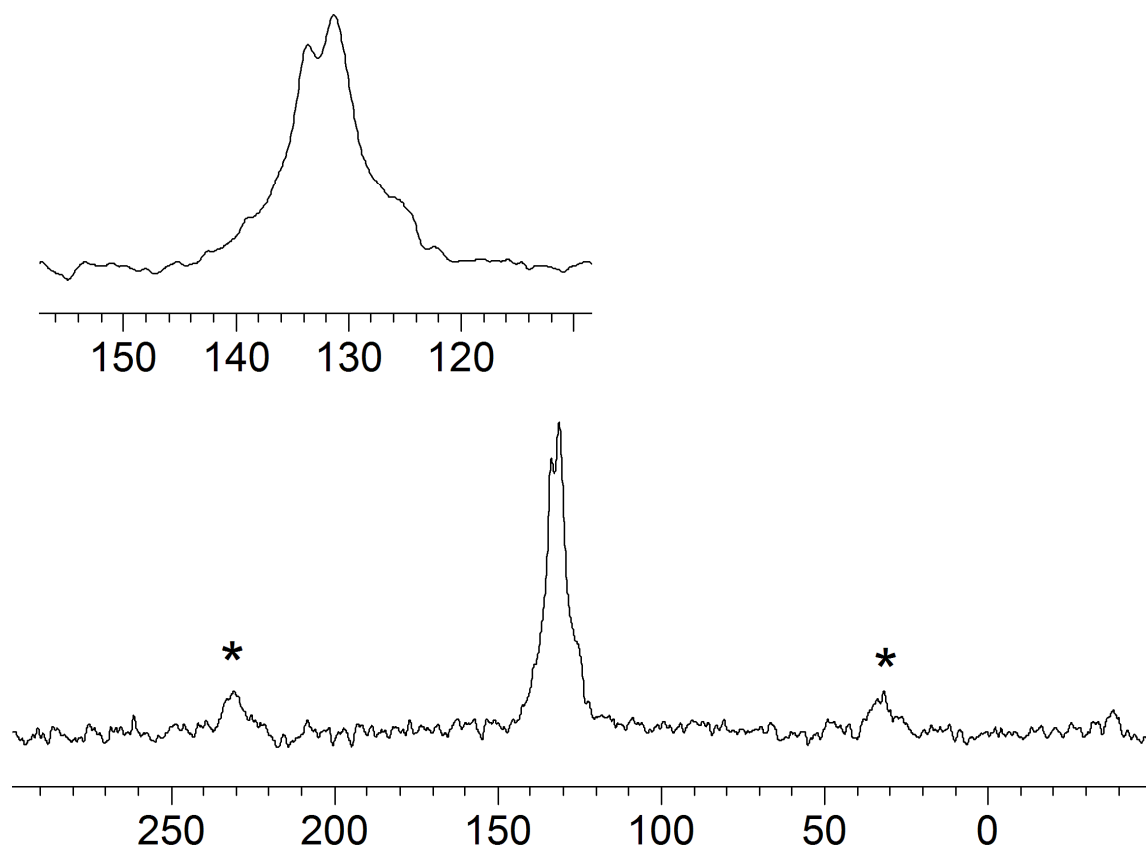


Figure 5.21. ^{13}C CP/MAS NMR spectrum of PPS. Asterisks denote spinning sidebands.

To confirm this signal assignment CP/MAS spectra with various dipolar dephasing delays were recorded (Figure 5.22). The resonance at 131 ppm, which is assigned to the carbons that are directly bound to a proton, decreases in intensity as compared to the peak at 134 ppm with increasing dephasing delay.

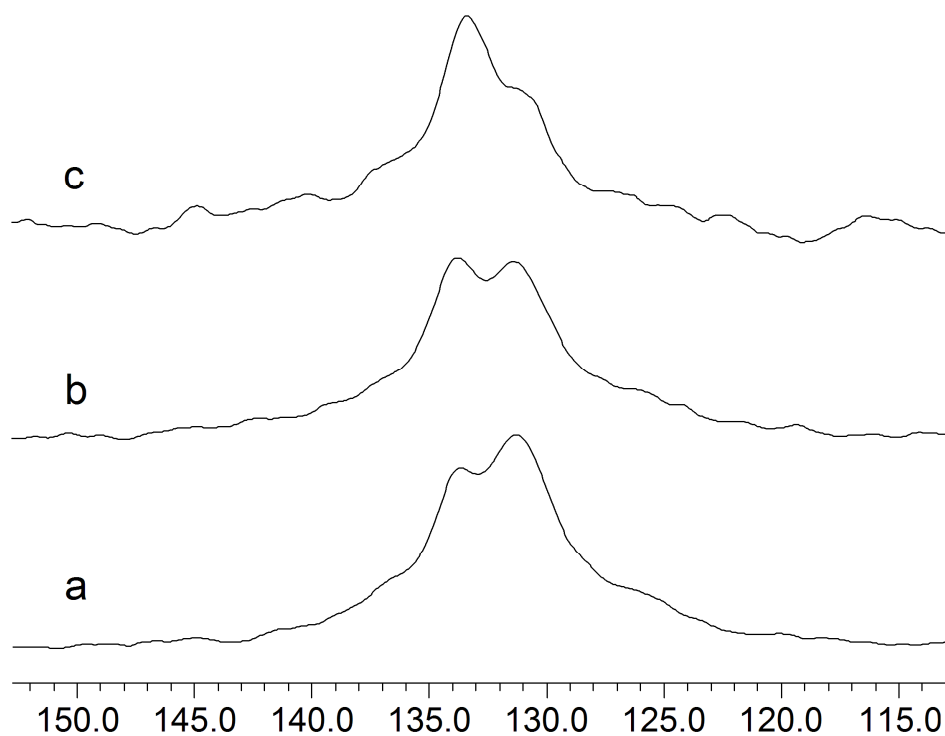


Figure 5.22. ^{13}C CP/MAS NMR spectra of PPS (10 kHz) obtained with dipolar dephasing delays of (a) 0 μs , (b) 10 μs , and (c) 40 μs .

Measuring CP/MAS with very short contact times, on the other hand, suppresses signals of quaternary carbons due to the less efficient magnetization transfer under cross-polarization conditions. This is shown for PPS in Figure 5.23 where the resonance at 134 ppm is almost vanished using a very short contact time of 0.2 ms. The difference between 1.5 ms and 6.0 ms is small, thus a contact time of 1.5 ms was used to equally efficiently detect both resonances while keeping the power input as low as possible.

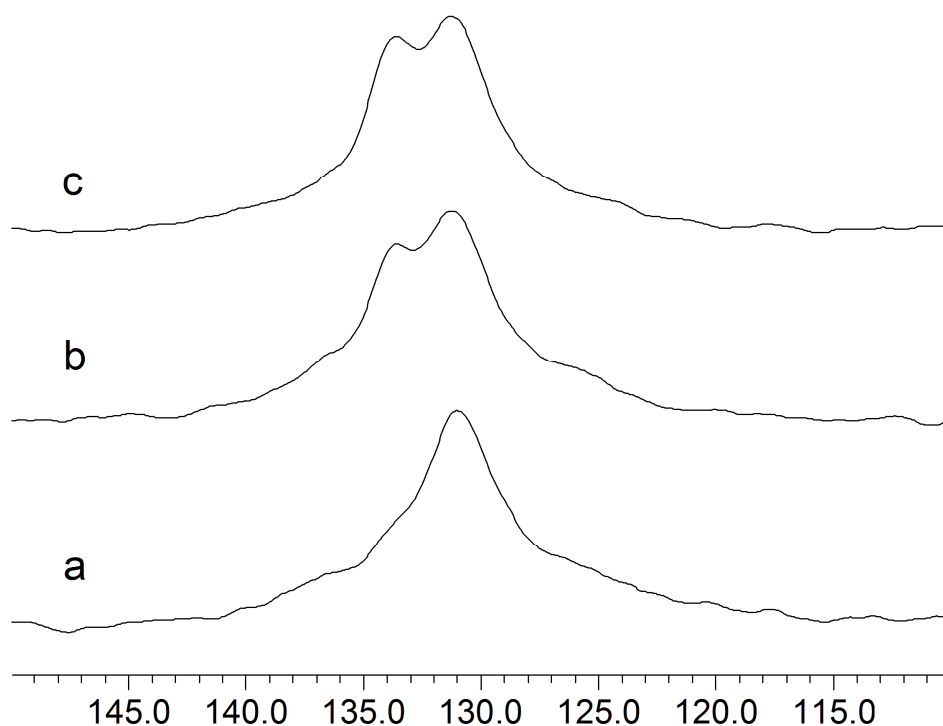


Figure 5.23. ^{13}C CP/MAS NMR spectra of PPS (10 kHz) obtained with variable contact times of (a) 0.2 ms, (b) 1.5 ms, and (c) 6.0 ms.

Different commercially available grades of PPS were studied by ^{13}C CP/MAS NMR (Figure 5.24). According to Mehl *et al.* the Fortron grade developed by Celanese is highly linear whereas Ryton grades contain various degrees of chain branching.¹³⁹ No difference in the ratio of the peaks at 134 ppm and 131 ppm can be detected. Apart from the broad signal base, which stems from amorphous domains, a shoulder on the low field side of the signals can be seen at about 137 ppm. This resonance is most pronounced in trace b for the sample R475. All three samples also display a resonance at 125 ppm.

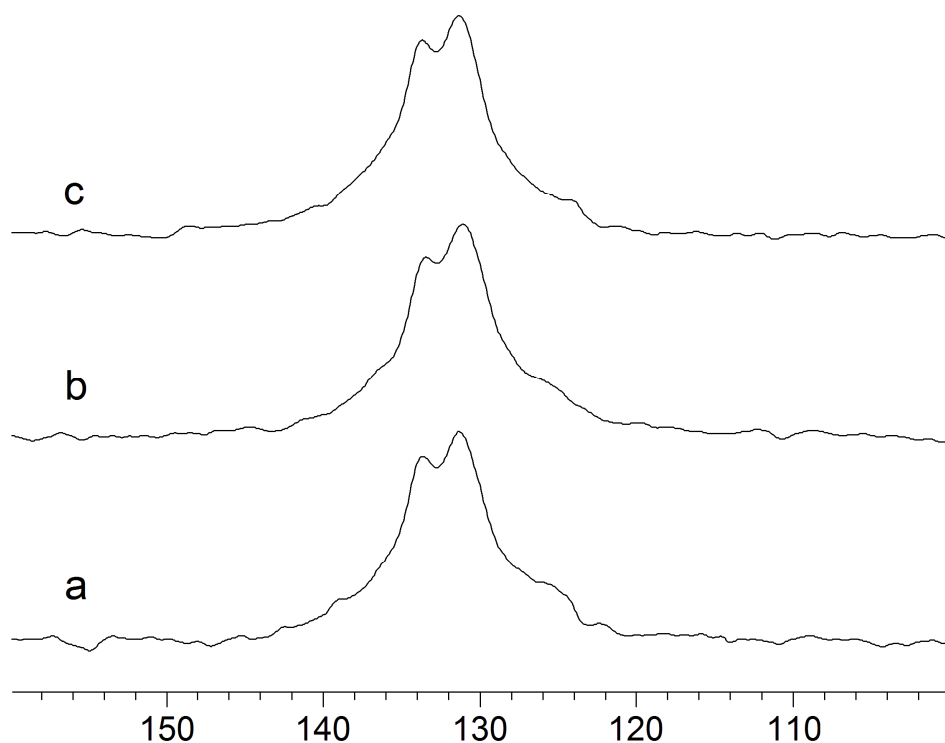


Figure 5.24. ^{13}C CP/MAS NMR spectra of PPS obtained from vendors Fortron (a) and ChevronPhillips, grades R475 (b) and R470 (c).

The differences in the commercially available PPS grades are closely related to the behavior of PPS under oxidative stress. It is known that PPS, despite being a thermoplastic, shows some curing characteristics of thermosets.¹³⁹ In earlier studies it was demonstrated that with each processing cycle in air the materials properties, such as T_g , T_m , and crystallization kinetics, change significantly.^{139,140,141} The underlying chemical and physical effects are still poorly understood, but chain scission, crosslinking, and chain branching are believed to each play a role.

Therefore, PPS was thermally treated at 250 °C and 350 °C and analyzed by ^{13}C CP/MAS and IR spectroscopy.

Figure 5. 25 shows possible oxidation products of PPS that would arise from oxidation of the thioether group. Oxidation to a sulfoxide would shift the resonance of the *ipso* carbon downfield to 144 ppm.¹⁴² Full oxidation to the sulfone would lead to smaller changes of 6 ppm and 3 ppm for the *ipso* and *ortho* carbon resonances, respectively (Figure 5.25).

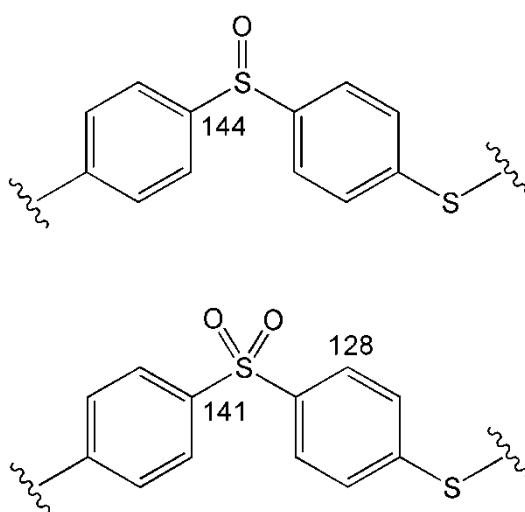


Figure 5.25. Possible oxidation products of the sulfide group of PPS with the expected ¹³C chemical shifts.¹⁴²

While oxidation of the sulfide is a likely scenario, it does not explain the significant changes in the mechanical properties upon thermal treatment. Branching, either due to cross-linking between the polymer chains or due to a chain scission-branching pathway, is a likely scenario suggested in the literature.^{141,143} Figure 5.26 shows molecular structures that would result from branching. The cross-links can form via C-C bonds, or ether and thioether linkages.

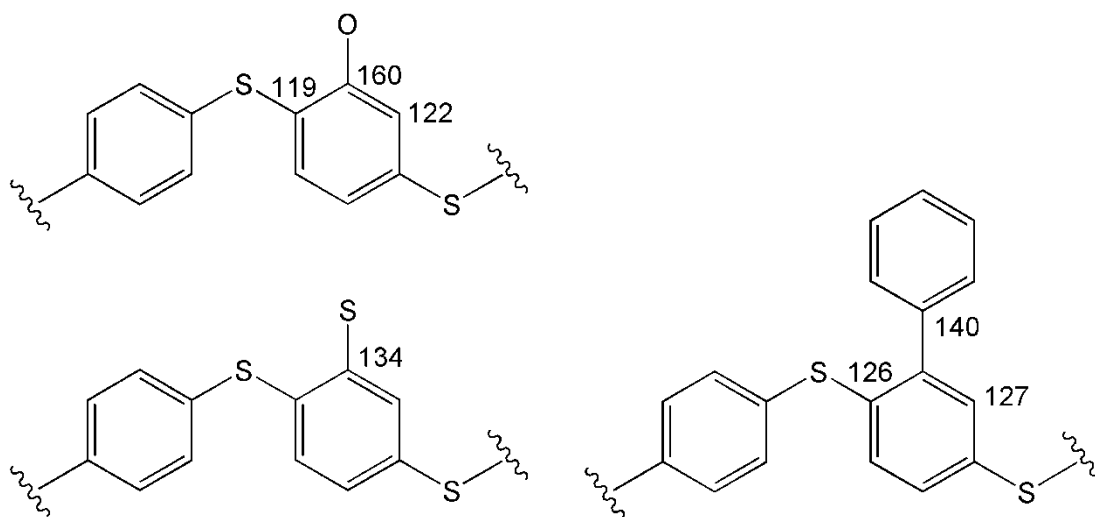


Figure 5.26. Possible branching of PPS with the expected ^{13}C chemical shifts.¹⁴²

Next, the Fortron grade PPS was thermally treated under four different conditions: in air at 250 °C for 4 h, under a nitrogen atmosphere at 250 °C for 4 h, in air at 350 °C for 4 h, and in air at 350 °C for 52 h. As can be seen from the ^{13}C CP/MAS spectra recorded after the treatments (Figure 5.27), heating to 250 °C leads to a decrease in linewidth, but no appearance of additional resonances. This is due to increased crystallinity and has been well documented by Cebé *et al.*¹³⁸ Additionally, it can be concluded that the changes are exclusively morphological and not due to changes of the polymer structure on a molecular level, because thermal treatment under oxygen exclusion led to identical results (Figure 5.28).

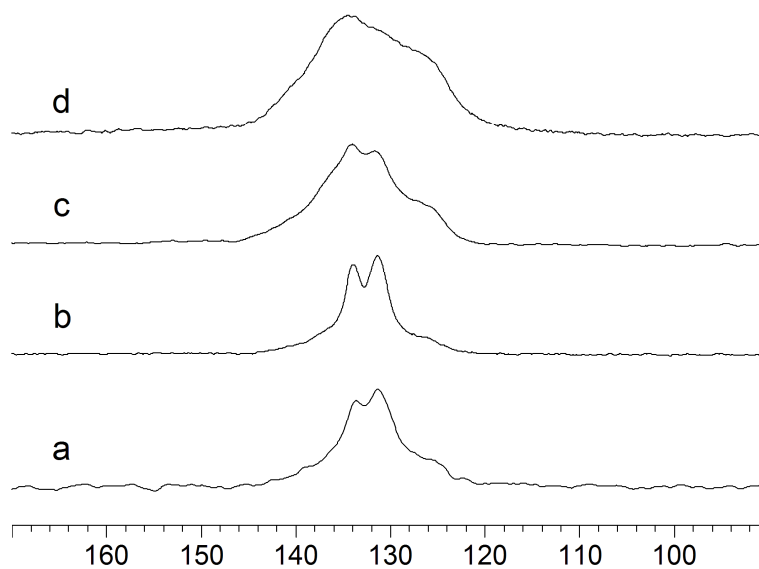


Figure 5.27. ^{13}C CP/MAS NMR spectra of PPS, (a) original sample, (b) heated to 250 °C for 4 h, (c) heated to 350 °C for 4 h, and (d) heated to 350 °C for 52 h.

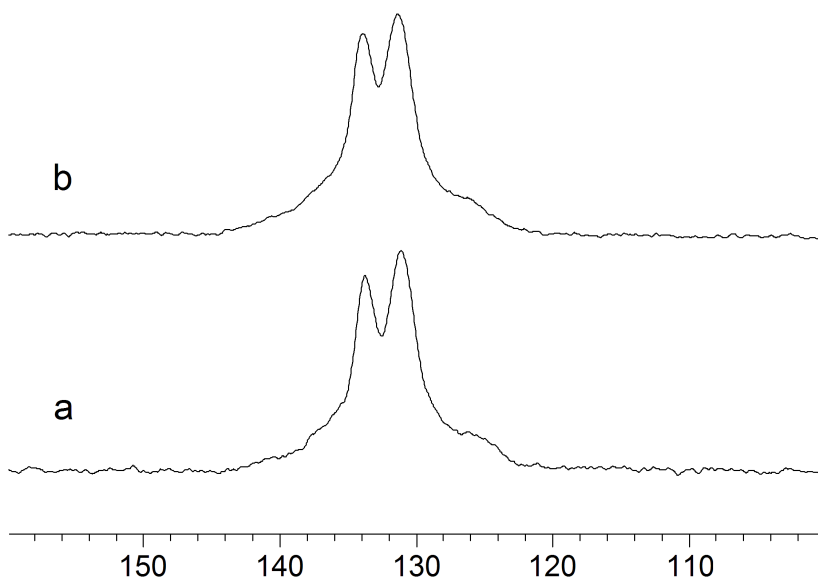


Figure 5.28. ^{13}C CP/MAS NMR spectra of PPS heated to 250 °C for 4 h (a) under a nitrogen atmosphere and (b) in air.

Thermal treatment at 350 °C (Figure 5.27, trace c), above the melting point (280 °C), leads to drastic changes in the ^{13}C CP/MAS spectrum even after the comparatively short time of 4 h. The shoulder at 137 ppm becomes more pronounced and an additional small peak is visible at 140 ppm. The ratio of the two main resonances at 134 ppm and 131 ppm changes, most probably due to a decrease of the peak corresponding to the CH carbon atoms. Furthermore, the height of the resonance at 125 ppm increases to nearly half the height of the peak at 131 ppm. Deconvolution leads to five resonances at 139.7, 135.6, 133.9, 131.5, and 127.1 ppm in a 2.6 : 3.3 : 1 : 3.7 : 3.3 ratio (Figure 5.29). The linewidths for the resonances at 139.4 ppm and at 127.2 ppm are 655 Hz and 566 Hz, and thus larger than the linewidths of the other resonances 400, 205, and 354 Hz.

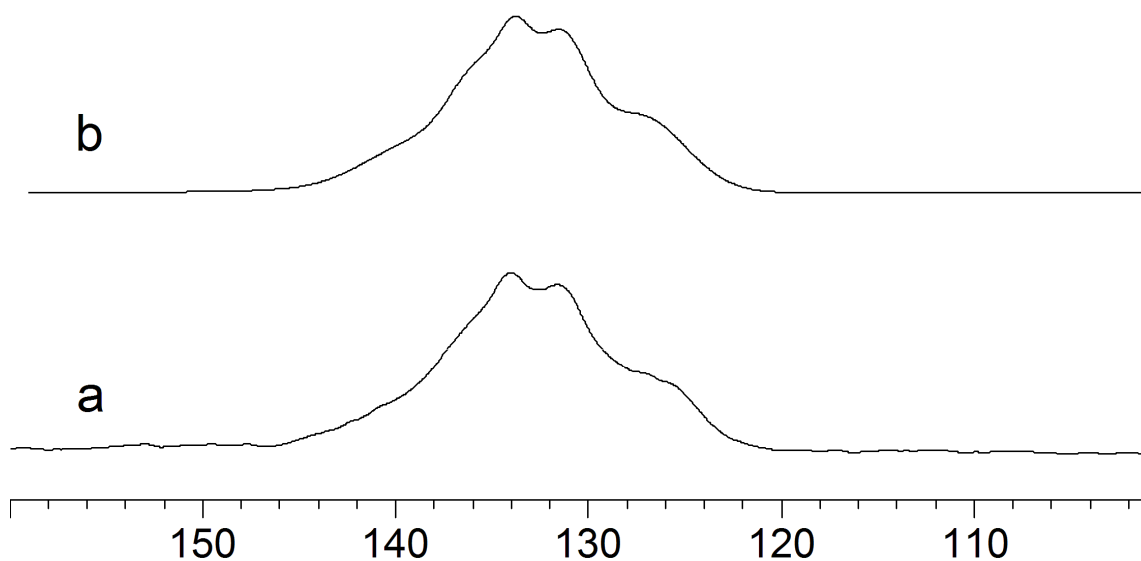


Figure 5.29. ^{13}C CP/MAS NMR spectrum of PPS heated to 350 °C for 4 h (a) and simulated spectrum (b).

The large linewidths of the new resonances suggest that they stem from amorphous domains. This is expected, since these regions are more accessible to species such as O₂. Measurements with DD CP/MAS NMR and CP/MAS with a short contact time reveal that the resonances at 139.7 ppm and at 127.2 ppm consist of both CH and quaternary carbons, whereas the resonance at 135.6 ppm stems predominantly from a carbon bound to hydrogen (Figure 5.30).

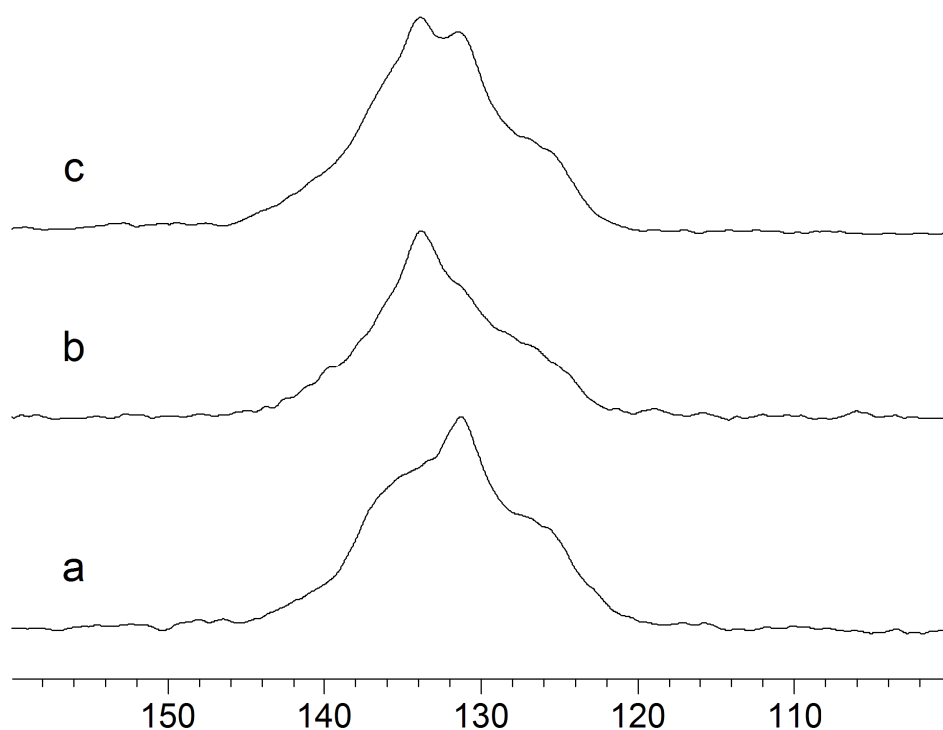


Figure 5.30. PPS heated to 350 °C for 4 h in air: (a) ¹³C CP/MAS NMR with a contact time of 0.2 ms, (b) ¹³C CP/MAS NMR with a 50 μs dipolar dephasing delay, and (c) routine ¹³C CP/MAS NMR.

Longer heat-treatment times led to a featureless ^{13}C CP/MAS spectrum with broad lines. It is noteworthy, however, that no resonances at 160 or 144 ppm which would be indicative of arylethers, are visible. The ^{13}C CP/MAS data therefore suggest that no sulfoxides or arylethers are formed in substantial amounts under thermal treatment. The formation of biphenyl linkages is in agreement with the data due to the quaternary carbon resonances at 139.7 and 127.2 ppm and the decrease of the intensity of the peak at 131 ppm. The formation of sulfones or thioether crosslinks is also in accord with the observed IR spectra.

The samples were also analyzed by IR spectroscopy (Figure 5.31).¹⁴⁴ No changes were seen in the samples treated at 250 °C either in air or in a nitrogen atmosphere. For the sample treated at 350 °C for 52 h significant changes occur, as can be seen in Figures 5.31 and 5.32.

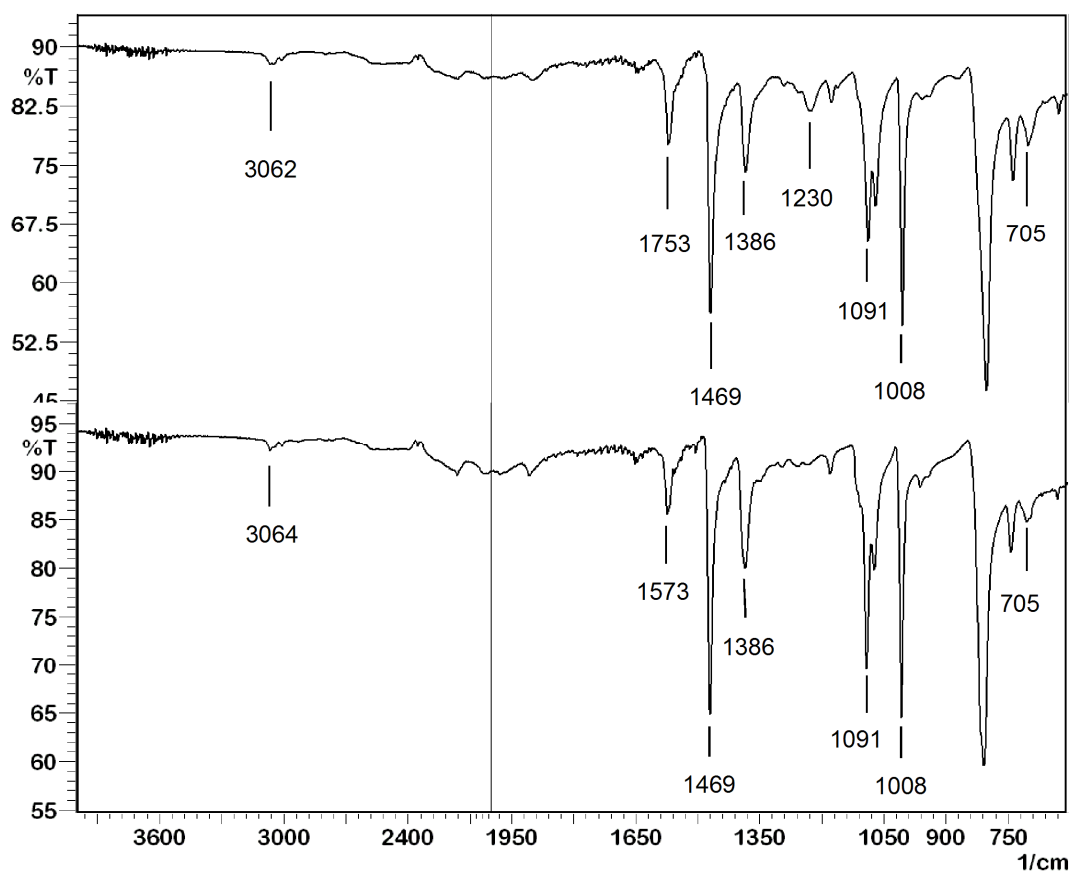


Figure 5.31. IR spectra of original PPS sample (*bottom*), and after heating it to 350 °C for 52 h (*top*).

The unsymmetric peak shape with the sharp slope on the high wavenumber side and the tailing on the low wavenumber side is due to the Christiansen effect and is often observed for samples that consist of large particles.¹⁴⁵ It arises from large differences of the refractive indices of the sample and the surrounding medium. That aside the spectrum of the original PPS sample is identical to the IR spectrum reported by Zhang *et al.*¹⁴⁴ The spectrum is dominated by skeletal vibrations of the benzene rings leading to the peaks at 1573, 1469, 1386, and 1008 cm^{-1} , as well as C-H bending modes giving rise to the peaks at 1091 and 818 cm^{-1} .

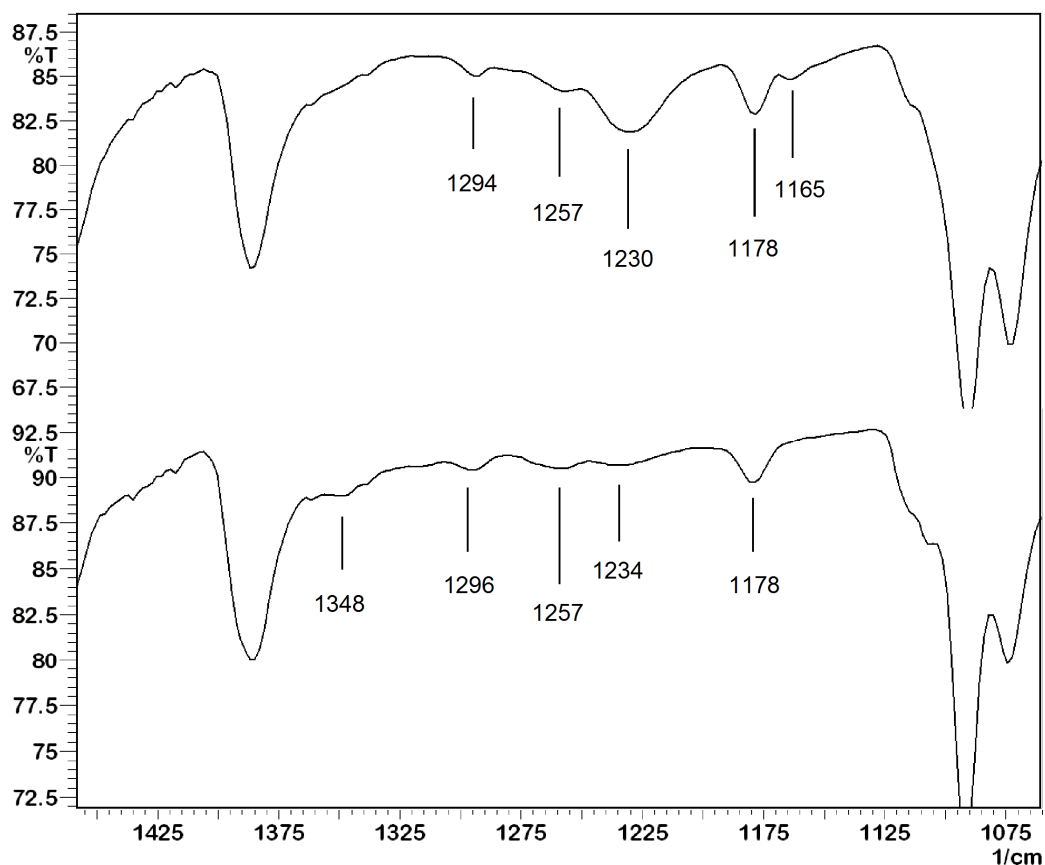


Figure 5.32. IR spectral region from 1500 to 1050 cm^{-1} of the original PPS sample (*bottom*), and after heating it to 350 °C for 52 h (*top*).

Differences between the original and the heated sample are most pronounced in the spectral region from 1400 to 1100 cm^{-1} (Figure 5.32). An additional, though weak, IR absorption at 1165 cm^{-1} can be assigned to one of the stretching bands associated with a sulfone group.^{145,146} The second sulfone stretching band is expected between 1290 and 1370 cm^{-1} and might be obscured by the shoulder of the strong peak at 1386 cm^{-1} . The most drastic change is the appearance of the peak at 1230 cm^{-1} . An absorption at this wavenumber is outside the range typically observed for either sulfones or sulfoxides. Ma *et al.* claim that this peak is associated with increased crystallinity of the sample.¹⁴¹ This

conclusion seems erroneous, since samples of high crystallinity, according to ^{13}C CP/MAS, showed no appearance of the peak at 1236 cm^{-1} . A more obvious explanation would be the formation of aryether linkages, which have been proposed by Hawkins.¹⁴³ Formation of ether cross-links also results in a weak absorption at 870 cm^{-1} indicative of 1,2,4-trisubstitution of a benzene ring which is indeed observed in the sample heated to $350\text{ }^{\circ}\text{C}$ for 52 h.

The fact that no resonance around 160 ppm, corresponding to the ether groups, was observed in ^{13}C CP/MAS NMR might be due to the low sensitivity of solid-state NMR.

In summary, it can be said that at $250\text{ }^{\circ}\text{C}$ the changes are not of a chemical nature but are due to changes in the polymer morphology, i.e. increases in crystallinity. At $350\text{ }^{\circ}\text{C}$, especially for extended heating times, it appears that multiple chemical transformations take place. Oxidation at sulfur to form sulfone groups seems plausible and can lead to the formation of biphenyl links accompanied with loss of SO_2 . Branching due to ether and possibly thioether linkages also takes place according to spectroscopic evidence.

PEKK-PBI Blend

PAEK (polyaryletherketone) polymers¹²¹ are of growing importance as performance polymers for the oil and gas industry. Their low weight and chemical inertness against corrosive environments make them ideal materials to replace analogous metal parts in drilling and fracking applications. PEKK-PBI blends are manufactured to combine the water resistance of PEKK (polyetherketoneketone) polymers with the high temperature stability of the PBI (polybenzimidazole, poly[2,2'-(*m*-phenylene)-5,5'-bibenzimidazole]) component.

In the work described in this chapter PEKK and PBI polymers, as well as their 60% : 40% PEKK-PBI blend are exposed to water at ambient temperature. Additionally, all pure components and the PEKK-PBI blend are exposed to steam at 300 F (148.9 °C) and 600 F (315.6 °C) for a prolonged time to simulate real-life conditions. It is shown that all changes are reversible and that any deterioration of the mechanical properties of the polymers and blend are not based on a chemical decomposition, but are due to changes of their morphology.

According to expectation, the pure PEKK and PBI components, as well as the PEKK-PBI blend give well-resolved ^{13}C CP/MAS NMR signals (Figure 5.33). The signal assignments have been made using dipolar dephasing techniques,^{122,132} and short contact times,¹²² and they are in accord with literature values for PEKK^{147,148} and PBI¹⁴⁹ polymers. The ^{13}C CP/MAS spectrum of the PEKK-PBI blend (Figure 5.33, bottom) represents approximately a weighted 60 : 40 sum of the spectra of pure PEKK and PBI.

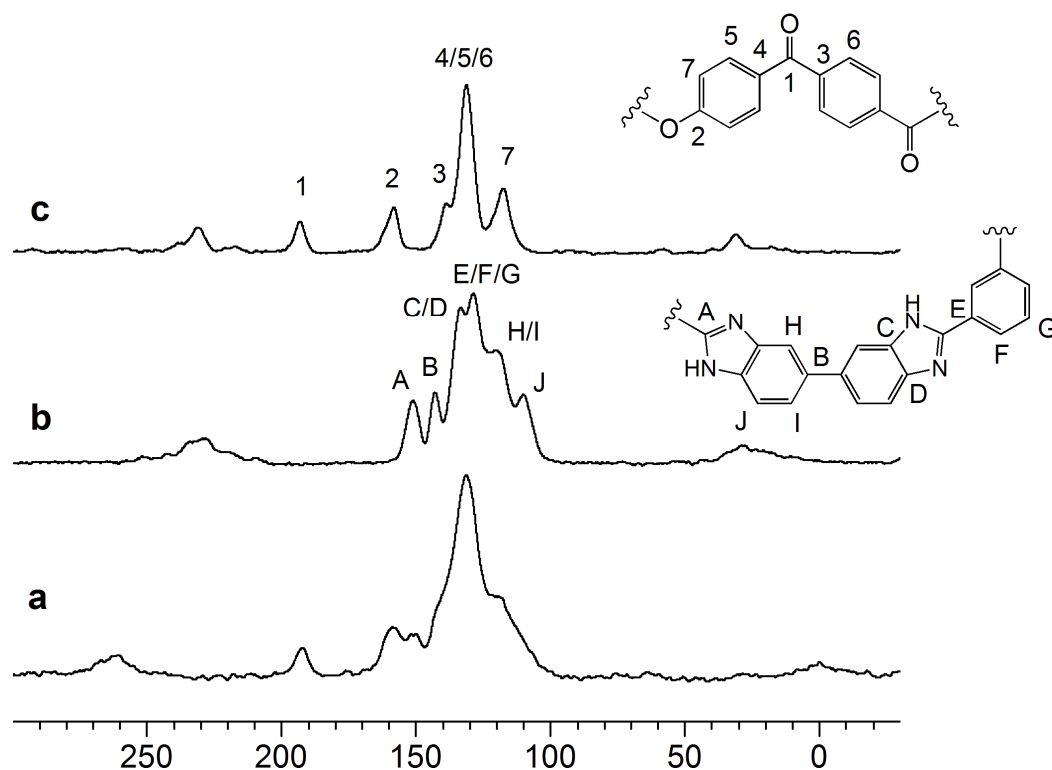


Figure 5.33. ^{13}C CP/MAS NMR spectra of the PEKK-PBI blend (*bottom*, $\nu_{\text{rot}} = 13$ kHz), neat PBI (*middle*, 10 kHz), and neat PEKK (*top*, 10 kHz). Peaks outside the region from 100 to 200 ppm are rotational sidebands.

Steam-treated PBI

Figure 5.34 compares the ^{13}C CP/MAS spectra of PBI (a) with those of PBI exposed to water at ambient temperature (b) and samples treated with steam at 300 F for 48 h (c) and 600 F for 72 h (d). According to expectation, an obvious change of the signals in the region from 110 to 135 ppm already takes place when PBI is allowed to take up water at room temperature. As it can best be seen in the expansion in Figure 5.34, the signal at 133.5 ppm loses intensity, while the resonance at 120.2 ppm splits into two signals at 122.0 and 117.1 ppm. Due to the overlap of multiple signals at 128.6 ppm it is not possible to judge on any intensity loss or gain. However, the CSA (chemical

shift anisotropy)^{132,150} of this signal changes. This can be deduced from the shape change of the rotational sideband at 28 ppm (Figure 5.34, traces a and b). Steam-treatment of PBI at 300 F enhances these effects. Interestingly, however, when treating the sample with steam at 600 F for a prolonged time, the ¹³C CP/MAS spectrum practically resumes its original appearance. Most probably, at this higher temperature, the water previously incorporated into the polymer matrix is expelled again from the material.

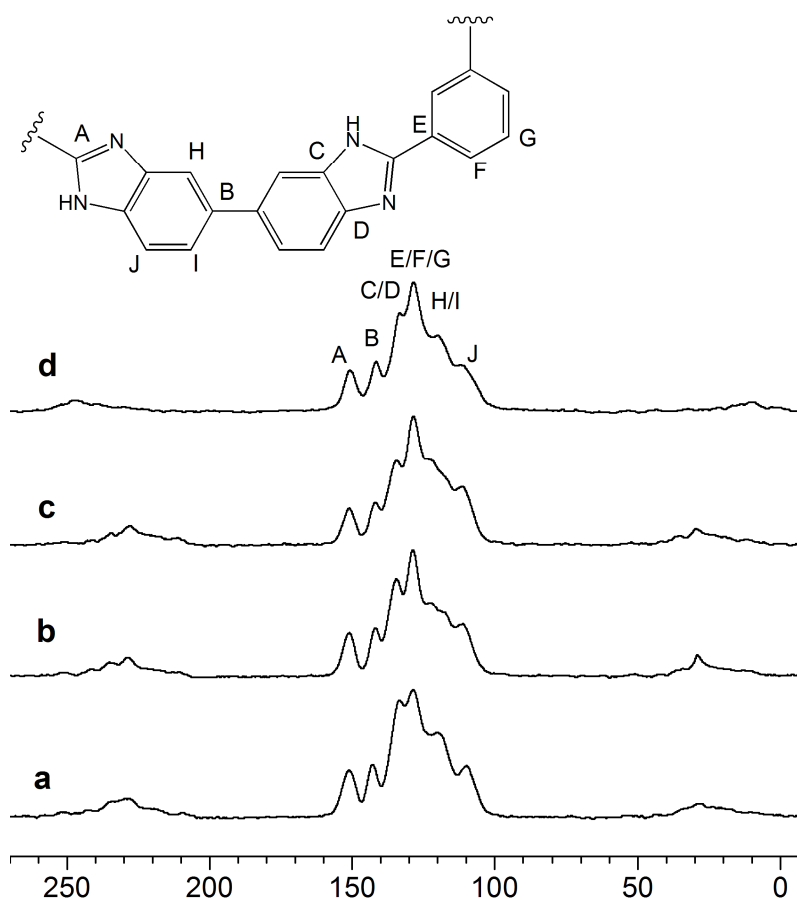


Figure 5.34. ¹³C CP/MAS NMR spectra of (a) PBI ($\nu_{\text{rot}} = 10$ kHz), (b) PBI exposed to water at RT (10 kHz), (c) PBI steam-treated at 300 F for 48 h (10 kHz), and (d) PBI

steam-treated at 600 F for 72 h (13 kHz). Signals outside the region from 100 to 200 ppm are rotational sidebands.^{150,151}

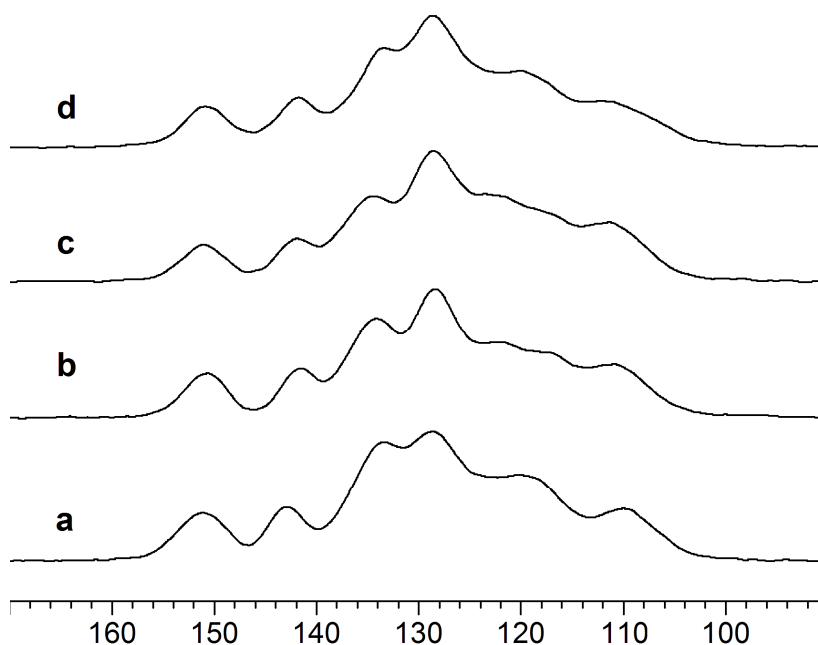


Figure 5.35. Expansion of the aryl signal region of the ^{13}C CP/MAS NMR spectra of (a) PBI ($\nu_{\text{rot}} = 10$ kHz), (b) PBI exposed to water at RT (10 kHz), (c) PBI steam-treated at 300 F for 48 h (10 kHz), and (d) PBI steam-treated at 600 F for 72 h (13 kHz).

Most importantly, the ^{13}C CP/MAS spectra in Figure 5.34 and Figure 5.35 do not indicate any chemical changes of the PBI on a molecular level. In particular, no carboxylic acid carbon signal in the region from 160 to 180 ppm, which would be expected in case the imidazole ring is hydrolyzed, can be detected.

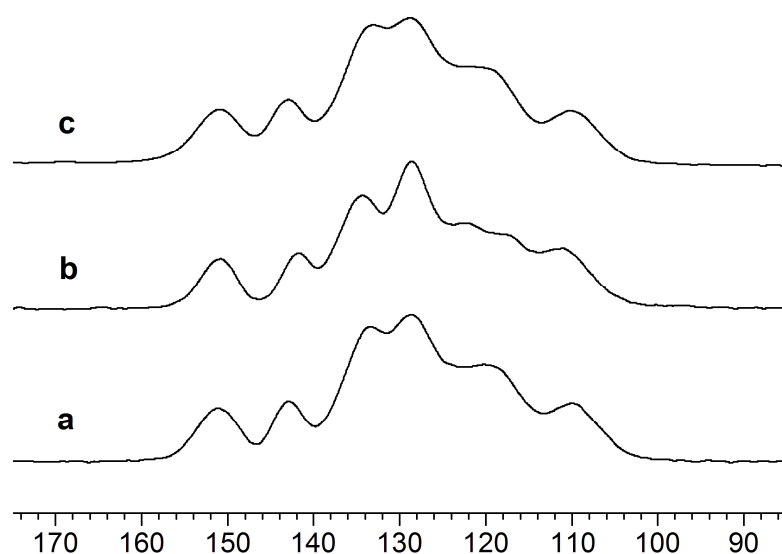


Figure 5.36. ^{13}C CP/MAS NMR spectra of (a) PBI ($v_{\text{rot}} = 10$ kHz), (b) PBI treated with water at RT (10 kHz), and (c) PBI after re-drying the wet sample *in vacuo* (10 kHz).

The assumption that there is no chemical transformation of PBI is further corroborated by the fact that the spectral changes visible after water- or steam-treatment at higher temperatures are fully reversible. Figure 5.36 shows from the bottom to the top the expansion of the ^{13}C CP/MAS spectra for the full cycle of original, water-treated, and re-dried material. The bottom and top trace are practically identical, and therefore we conclude that the water uptake of PBI under the conditions applied here is fully reversible.

The fact that PBI stays intact upon steam-treatment is not too surprising, considering the chemical inertia of the monomers, as imidazole rings are chemically very robust. Furthermore, potential protonation of the imidazole nitrogen is unlikely, because the $\text{p}K_{\text{a}}$ of imidazole is much lower (18.6) than the $\text{p}K_{\text{a}}$ of water (31.2) in dimethylsulfoxide as the solvent.

We interpret the reversible change of the aryl signal region in the spectra displayed in Figures 5.34 to 5.36 as conformational changes that can be the result of rotational reorientation of the aromatic ring segments. This effect can be quite large, as it has been shown earlier by Tonelli and Gomez¹³⁷ in the case of cyclic phenyl sulfides. Typical overall spreads of phenyl ¹³C signals of 8 and 18 ppm have been found. For PBI, the maximal chemical shift change, assuming, for example, that one resonance migrates from 134 to 124 ppm (Figures 5.34 to 5.36) would result in a signal spread of about 10 ppm, which is well within the described scenario.¹³⁷

¹H solid-state NMR spectroscopy of polycrystalline powders or polymers without MAS (wideline spectroscopy) is a very useful tool to study species with different mobilities.^{122,151,152,153} Mobile species typically result in comparatively narrow ¹H wideline signals, while protons bound to a rigid backbone yield signals with up to 100 kHz halfwidth. In the case of rigorously dried PBI, only the protons of the polymer backbone are present, which result in the broad signal with a halfwidth of about 27.4 kHz shown in Figure 5.37a (see also Table 5.3 below). When PBI is steam-treated at 300 F, a maximal amount of water is incorporated into the polymer network. Due to the mobility of the water molecules in the polymer, a comparatively narrow signal with a halfwidth of about 2.6 kHz is found on top of the polymer backbone signal (Figure 5.37c, Table 5.3). When this sample is exposed to the atmosphere for two months, it loses some of the water and the narrow signal shrinks again (Figure 5.36b).

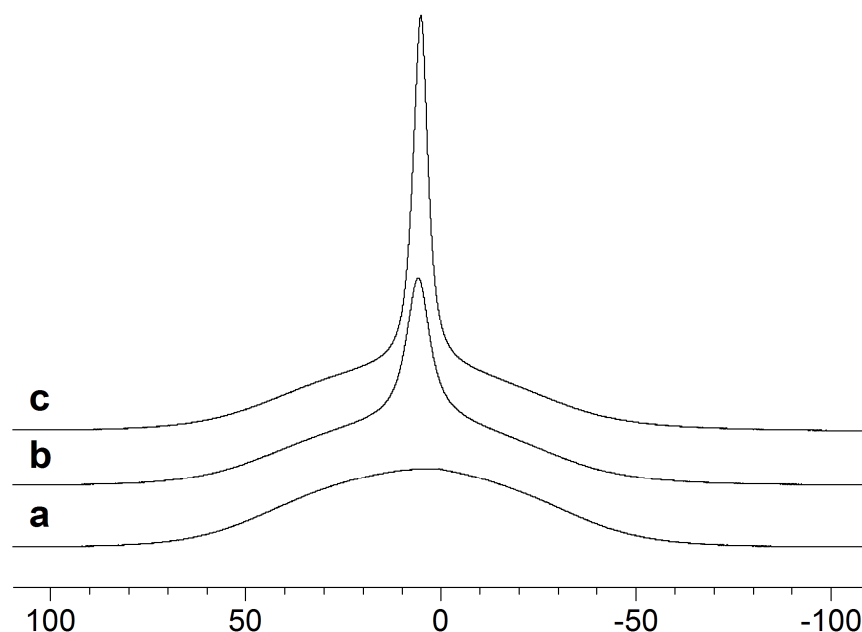


Figure 5.37. ^1H Wideline NMR spectra of (a) PBI that has been rigorously dried at $100\text{ }^\circ\text{C}$ *in vacuo* for 24 h, (b) PBI that has been steam-treated at 300 F for 48 h, and then left exposed to the atmosphere for two months, and (c) PBI after steam-treatment at 300 F for 48 h.

The amount of incorporated water after two months is about the same as the amount of water found in the polymer after treating the PBI with water at RT for a prolonged period (Figure 5.38a). This indicates that PBI takes up an equilibrium amount of water at a given temperature and does not eventually dissolve or decompose, in accordance to the findings described above using ^{13}C CP/MAS. This assumption is also corroborated by the fact that after steam-treatment at 600 F for a prolonged time (Figure 5.37c), a smaller amount of water is incorporated into the PBI than at 300 F (Figure 5.38b). Obviously, at this high temperature the water is expelled again from the polymer,

potentially due to the fact that at higher temperatures the more mobile polymer chains do not allow for a maximal amount of incorporated water any more.

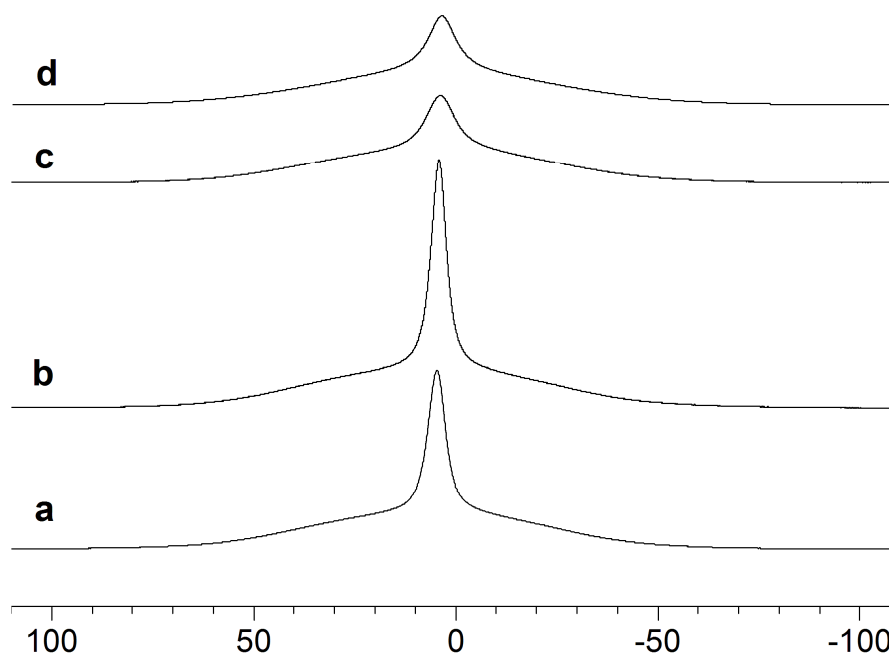


Figure 5.38. ^1H Wideline NMR spectra of (a) PBI after treatment with water at RT, (b) PBI after steam-treatment at 300 F for 48 h, (c) PBI after steam-treatment at 600 F for 72 h, (d) simulation of the spectrum (c). The spectra are normalized to the height of the broad signal of the polymer protons.

The ^1H wideline NMR spectra of all polymer samples investigated in this chapter have been subjected to a deconvolution to quantify the halfwidths. One example of a simulated spectrum is shown in Figure 5.38d, on top of the experimental spectrum (Figure 5.38c). Table 5.3 summarizes all obtained ^1H wideline NMR data, also for the pure PEKK and the PEKK-PBI blend samples (see below). Although the large

linewidths of the polymer backbone signals and the ensuing loss of signal intensity due to the probehead deadtime do not allow a precise quantitative analysis, a very useful qualitative estimate of the amount of water incorporated in the polymers can be obtained. The integrals of the individual signals after deconvolution are given as % contributions to the overall intensity of the overlapping two signals (Table 5.3). The highest amount of incorporated water, 34%, is found when PBI is exposed to it at room temperature. At the higher temperature of 300 F, which is already nearly 50 °C above the boiling point of water, a slightly smaller amount of 30% is found, and this amount is further diminished to 25% after letting the sample dry in the air for 2 months. The steam-treatment at 600 F leads to half the amount of incorporated water as compared to the same treatment at 300 F.

Table 5.3. ¹H chemical shifts δ , signal halfwidths $\Delta\nu_{1/2}$, and integrals of the two signals after deconvolution of the wideline NMR spectra of the respective materials.

Sample	δ [ppm]	$\nu_{1/2}$ [kHz]	integral ^d [%]	δ [ppm]	$\nu_{1/2}$ [kHz]	integral ^d [%]
PBI^a	e	e	e	5.4	27.4	100
PBI ^b	4.6	2.6	34	6.8	27.4	66
PBI 300 F	3.9	2.0	30	5.6	27.4	70
PBI 300 F ^c	4.3	3.0	25	5.5	27.4	75
PBI 600 F	3.4	3.3	15	4.4	27.4	85
PEKK	1.0	3.0	3	5.0	24.0	98
PEKK 300 F	e	e	e	3.2	24.4	100
PEKK 600 F	3.0	3.4	1	5.4	58.7	99
PEKK-PBI^a	e	e	e	4.7	23.2	100
PEKK-PBI ^b	3.5	5.0	13	3.5	23.2	87
PEKK-PBI 300 F	3.3	4.0	2	3.2	30.2	98
PEKK-PBI 600 F	3.3	3.0	1	3.0	38.0	99

^a Sample dried *in vacuo* at 100 °C for 24 h. ^b Samples exposed to water at RT (Experimental Section). ^c Same sample as in row above, after being exposed to the atmosphere for two months. ^d Intensity contribution to the overall intensity of the overlapping two signals. ^e No signal on top of the broad signal detectable.

The IR spectra of PBI corroborate the NMR spectroscopic results described above. When the spectra of dry PBI and PBI steam-treated at 300 and 600 F are compared (Figure 5.39), the most obvious changes are visible in the region of the OH stretching bands from 3060 to 3400 cm^{-1} . As in the ^1H wideline NMR spectra, the largest amount of incorporated water is found for the sample that has been steam-treated at 300 F. At 600 F the broad absorption in the OH stretching band region is significantly smaller again. Other changes in the IR spectra are visible for the absorptions between 1531 and 1625 cm^{-1} . This region corresponds to the aryl C=C stretching bands, and changes might again indicate a change in the conformation or crystallinity of PBI upon steam-treatment, as visible in the ^{13}C CP/MAS spectra. IR spectroscopy also corroborates the results obtained by ^{13}C and ^1H solid-state NMR with respect to the reversibility of the effects of steam-treatment. As shown in Figure 5.40, top, the spectrum of the re-dried material displays an absorption band in the OH stretching frequency range that is reduced in intensity as compared to the one of the sample steam-treated at 300 F (Figure 5.40, bottom), and it resembles the IR spectrum of the pristine PBI shown in Figure 5.39.

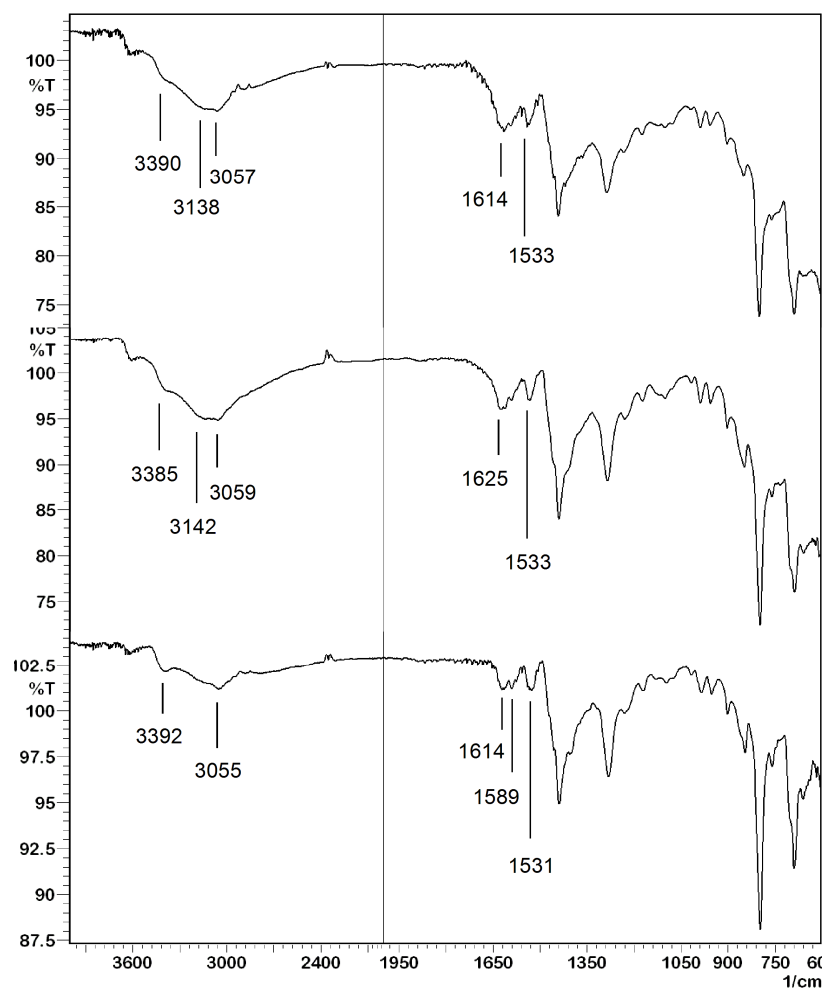


Figure 5.39. IR spectra of original PBI (*bottom*), and PBI after steam-treatment at 300 F for 48 h (*middle*) and 600 F for 72 h (*top*).

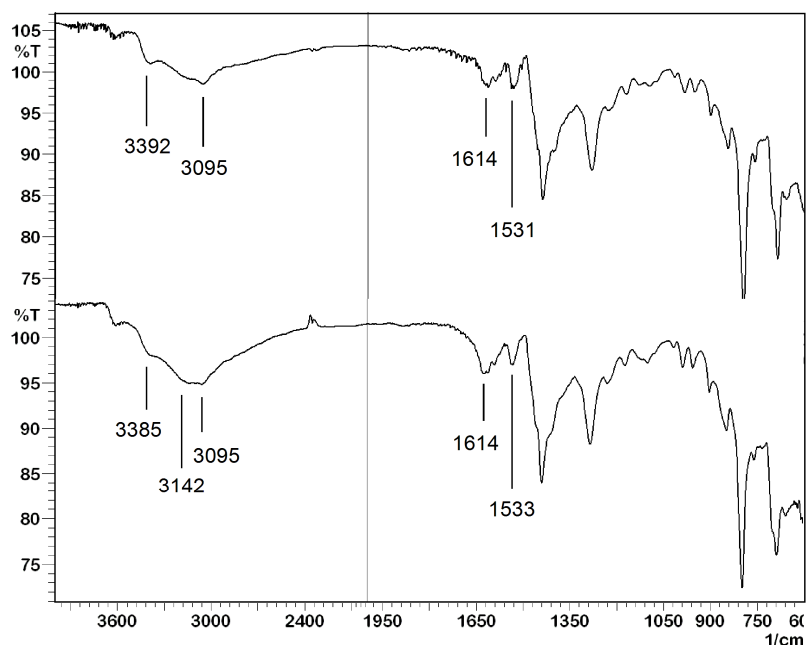


Figure 5.40. IR spectra of PBI after steam-treatment at 300 F for 48 h (*bottom*), and subsequent redrying *in vacuo* at 120 °C (*top*).

Steam-treated PEKK

The ^{13}C CP/MAS spectra shown in Figure 5.41 suggest that PEKK does not interact with water at RT. First changes in the spectra manifest themselves after steam-treatment of PEKK at 300 F (Figure 5.41c). All signals become broader, but especially in the region of the signals 3 to 7 some resonances also change their chemical shifts. As in the case of PBI, the spectrum of the sample steam-treated at 600 F resembles more the one of the original material. According to the ^1H wideline measurements, only a tiny amount of water, less than 3%, is incorporated into the PEKK polymer, no matter how it was treated (Table 5.3). As for PBI, no chemical changes of the polymer can be identified, so the different signal shapes must be solely based on conformational or crystallinity changes.

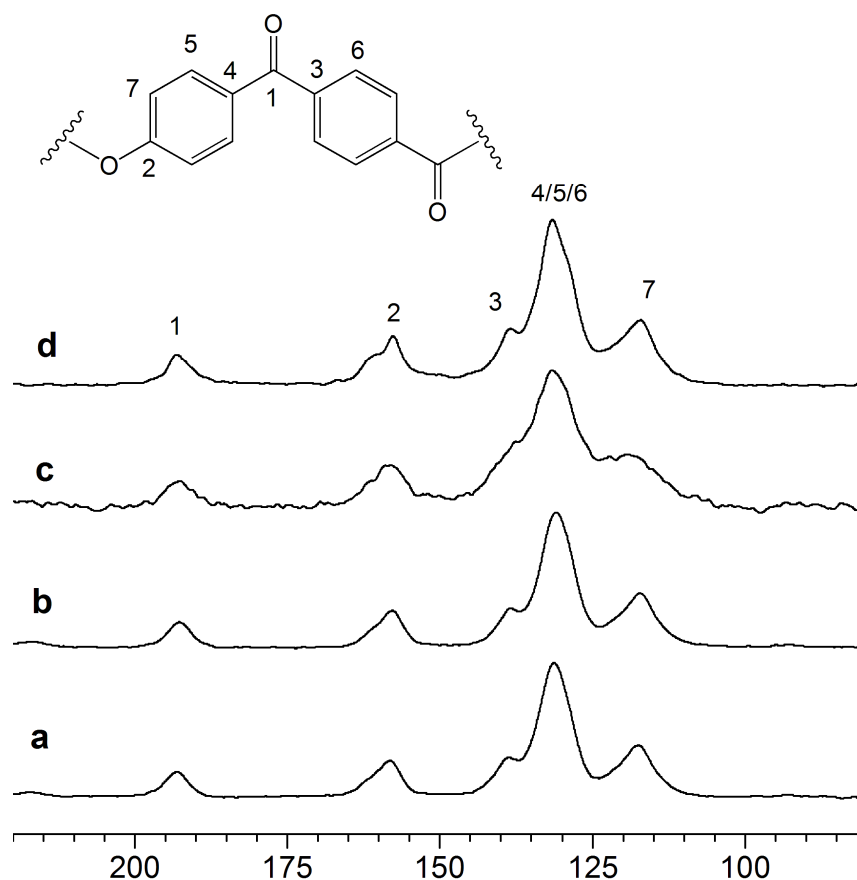


Figure 5.41. ^{13}C CP/MAS NMR spectra of (a) original PEKK ($v_{\text{rot}} = 10$ kHz), (b) PEKK treated with water at RT (10 kHz), (c) PEKK steam-treated at 300 F for 48 h (10 kHz), and (d) PEKK steam-treated at 600 F for 72 h (13 kHz).

The ^{13}C CP/MAS and ^1H wideline NMR results described above indicate that water is not incorporated in amounts larger than 3% into the PEKK polymer. This is confirmed by the IR spectra of the original and steam-treated samples. There is practically no change in the wavenumbers of the $\text{C}=\text{O}$ stretching band at 1651 cm^{-1} or the aryl $\text{C}-\text{H}$ absorption at 3064 cm^{-1} (Figure 5.42). Therefore, the slight changes visible in the ^{13}C CP/MAS spectra discussed above can only be due to changes in the conformation or crystallinity of the samples upon steam-treatment. In order to check this

assumption, the crystallinities of all samples have been determined by DSC and will be discussed in the next chapter.

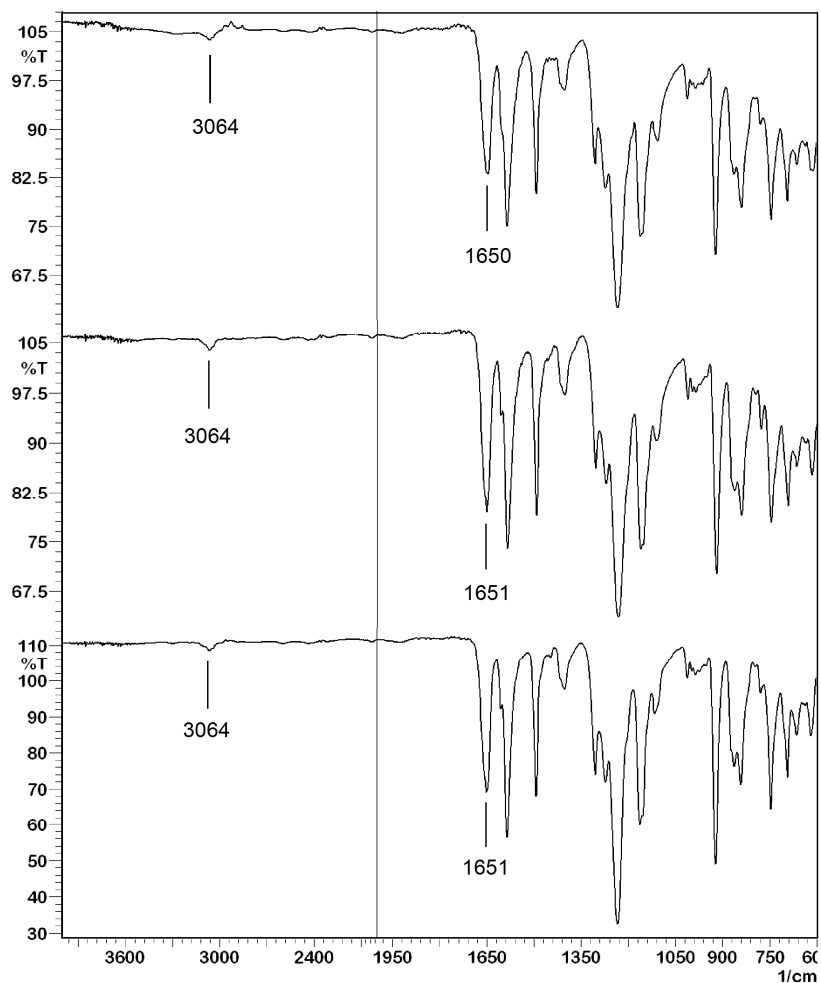


Figure 5.42. IR spectra of PEKK (*bottom*), PEKK after steam-treatment at 300 F for 48 h (*middle*) and at 600 F for 72 h (*top*).

The NMR and IR results presented above indicate that incorporating water into the PBI does not result in a chemical decomposition, but rather in a change in conformation or crystallinity of the polymer. In order to probe the latter possibility, DSC measurements^{154,155} of all samples discussed in this chapter have been performed (Figures 5.43, 5.44, and 5.45). Table 5.4 summarizes the data obtained from the DSC measurements.

PBI is known from the measurements described above and from the literature to have a relatively high moisture content at room temperature. Furthermore, it is an amorphous polymer that does not crystallize.¹⁵⁵ The DSC measurements show an endothermic peak in the first heating cycle which does not reappear in the second heating cycle (Figure 5.43). This indicates that an irreversible phase change has taken place which can be explained by the release of absorbed water from the polymer.

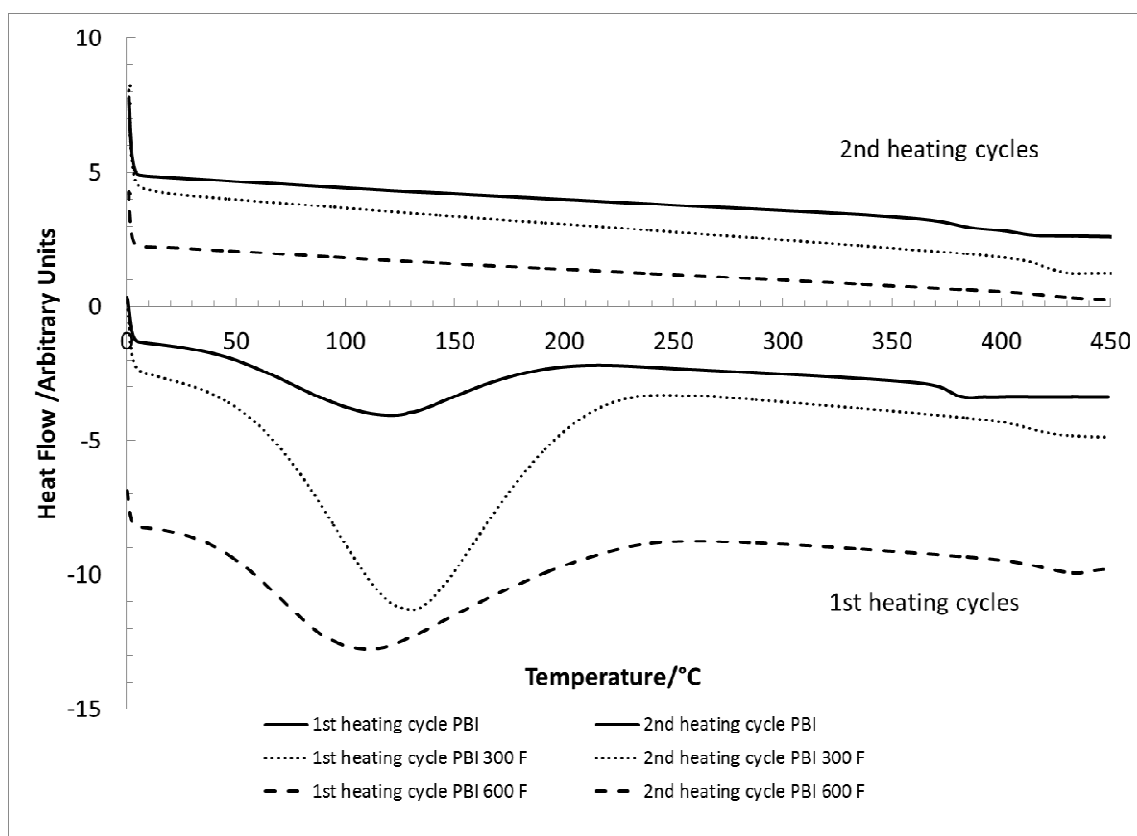


Figure 5.43. DSC curves of the indicated original and steam-treated PBI samples. Curves are offset vertically for clarity.

In general, the peak temperatures for samples containing PBI are much higher than those for pure PEKK (Table 5.4, Figure 5.44), which suggests that water binds more strongly to PBI than PEKK. This assumption is further corroborated by the energy absorbed by calculating the area under the peak. These specific enthalpies are highest for PBI samples, implying highest level of water absorption, followed by the PEKK-PBI blend samples, while they are lowest for pure PEKK materials.

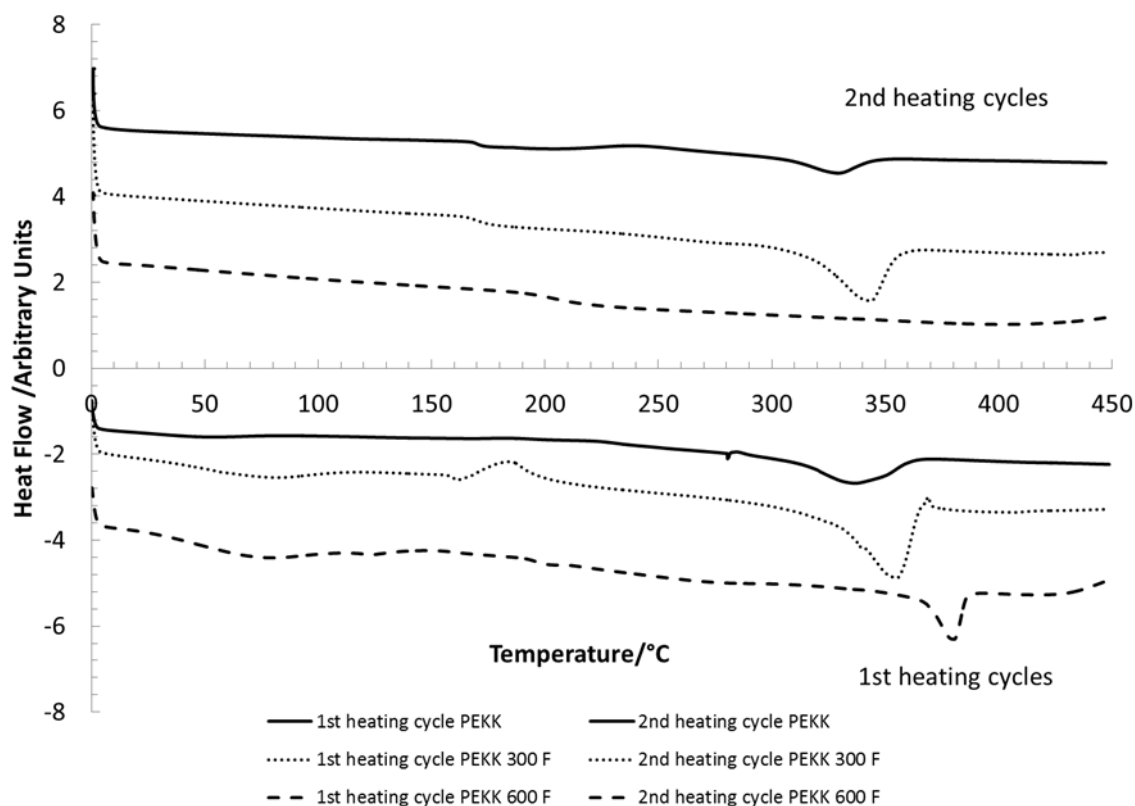


Figure 5.44. DSC curves of the indicated original and steam-treated PEKK samples. Curves are offset vertically for clarity.

It is obvious that PEKK absorbs a much smaller amount of water as compared to PBI, in accordance with the above ^1H wideline NMR measurements. The T_g values for PBI and PEKK increase after steam-treatment due to physical aging. PBI 300 F that was dried after exposure to steam showed a similar level of water absorption to the dry PBI, while T_g remains unaffected by the drying procedure. The dry PEKK-PBI blend shows two T_g values (Figure 5.45) which correspond to the individual components.

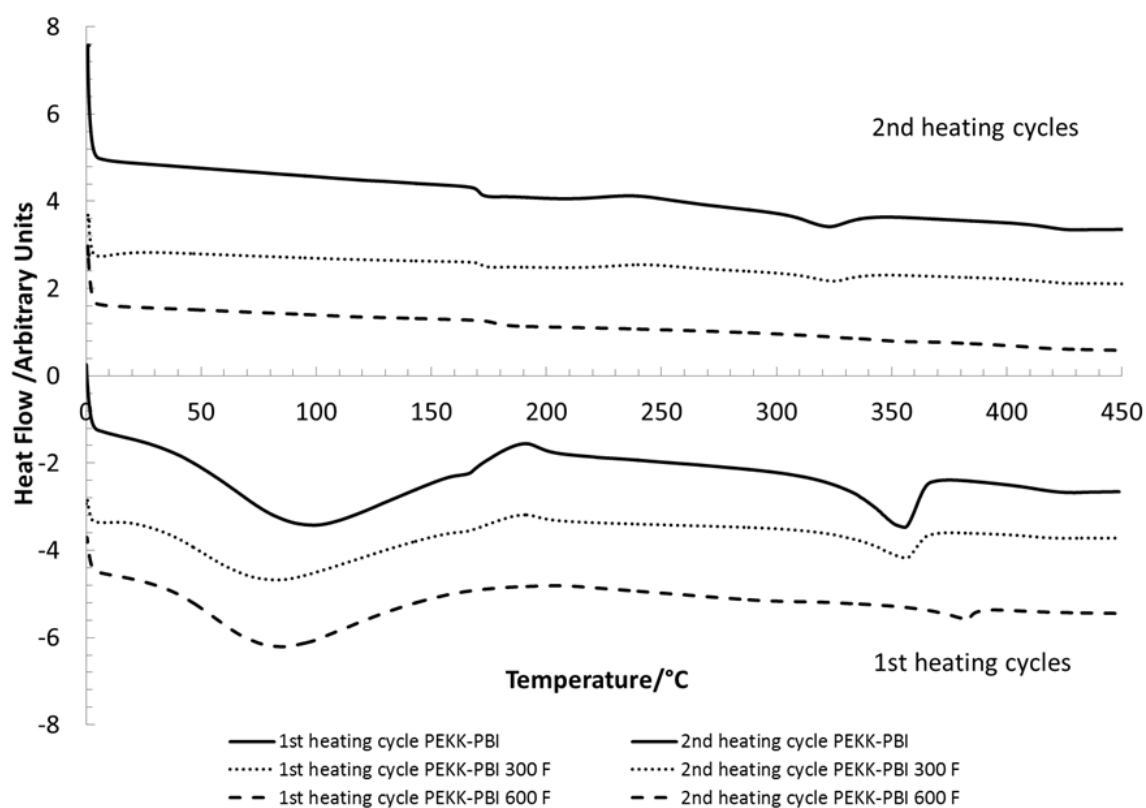


Figure 5.45. DSC curves of the indicated original and steam-treated PEKK-PBI blend samples. Curves are offset vertically for clarity.

In contrast to the pure polymers, the T_g values of the blend remain relatively stable even after steam-treatment. The melting points T_m of both polymers, pure PEKK and the PEKK-PBI blend, increase after steam-treatment with a corresponding decrease in crystallinity.

Table 5.4. DSC data of the indicated original and steam-treated samples.

Sample ^a	1 st peak T [°C]	Specific Enthalpy [J/g]	T _g [°C]	T _m [°C] ^d	Crystallinity [%] ^d
PBI	119.0	116.2	406.4	b	c
PBI 300 F	130.4	379.2	417.1	b	c
PBI 600 F	101.9	377.3	423.4	b	c
PEKK	48.5	9.5	169.9	336.3/328.9	39.0/19.8
PEKK 300 F	75.4	7.2	170.3	343.4/355.1	21.3/12.5
PEKK 600 F	75.3	29.33	203.3	380.3/-	13.2/0
PEKK-PBI	95.1	102.5	170.8 / 418.3	355.5/322.5	20.4/6.3
PEKK-PBI 300 F	83.7	171.7	171.5 / 418.6	356.1/324.4	17.1/4.6
PEKK-PBI 600 F	82.1	159.8	178.8/-	382.9/-	4.6/0

^a Samples untreated or exposed to steam at 300 F (148.9 °C) for 48 h or 600 F (315.6 °C) for 72 h. ^b Decomposition at temperatures higher than T_g. ^c PBI constitutes a fully amorphous material without any crystalline domains.¹¹ ^d First and second heating cycle (see also Experimental Section).

Steam-treated PEKK-PBI blend

The change in the ¹³C CP/MAS spectra of the PEKK-PBI blend after steam-treatment follows the trend observed for the pure components PEKK and PBI. Again, the largest change is visible for the sample steam-treated at 300 F for 48 h (Figure 5.46). Comparing the spectra in Figure 5.45 with those of the pure PBI component (Figure 5.34) confirms that the changes are mostly due to the PBI signals at about 120 and 134 ppm. Overall, at higher temperatures the PEKK component prevents water from being incorporated into the blend, while at room temperature, according to expectation, it is mostly the PBI part of the blend that interacts with the water.

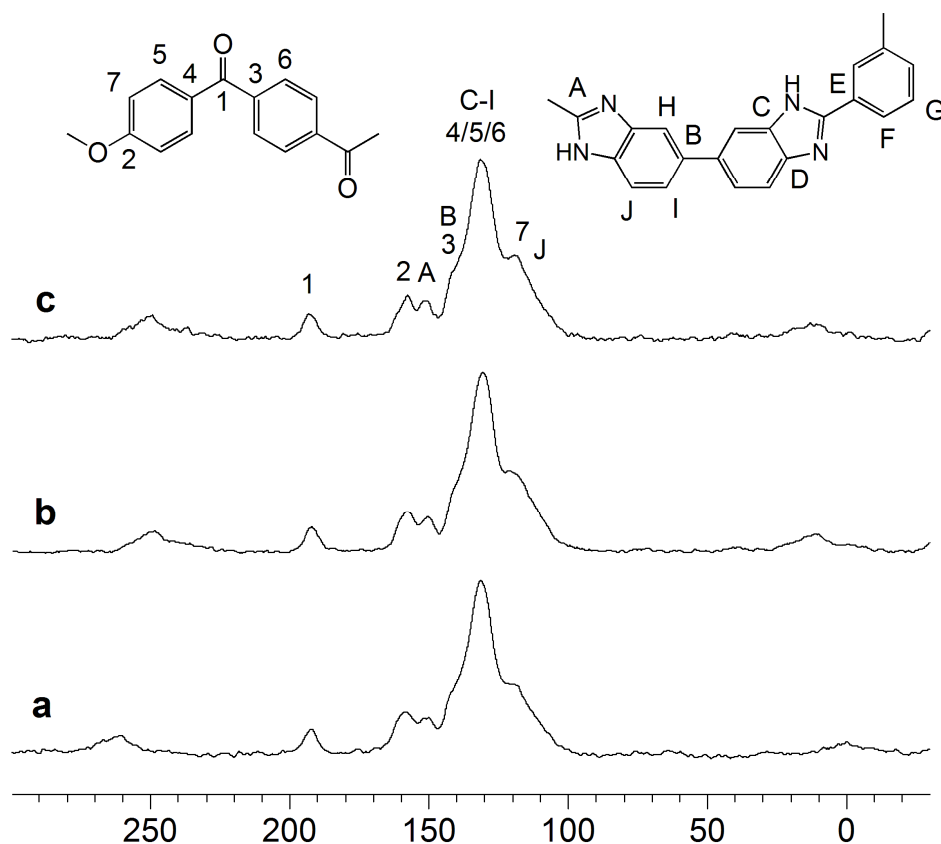


Figure 5.46. ^{13}C CP/MAS NMR spectra of (a) original PEKK-PBI blend ($\nu_{\text{rot}} = 13$ kHz), (b) PEKK-PBI blend steam-treated at 300 F for 48 h (12 kHz), and (c) PEKK-PBI blend steam-treated at 600 F for 72 h (12 kHz). Peaks outside the region from 100 to 200 ppm are rotational sidebands.

The ^1H wideline NMR spectra confirm the assumption that water is incorporated into the PEKK-PBI blend (Figure 5.47), as there is a signal with smaller halfwidth sitting on top of the broad polymer backbone proton resonance (see also Table 5.3 above). As in the case of pure PBI, the amount of water is largest, when the sample is exposed to water (moist atmosphere?) at room temperature (Figure 5.47a). At higher temperatures

the water is not incorporated as readily, again following the trend for pure PBI. However, overall the water contents of the PEKK-PBI blend is much lower with maximally 15% than the one of the pure PBI. Therefore, one can conclude that especially at high temperatures the PEKK component in the blend does what it is supposed to do, fend off intruding water.

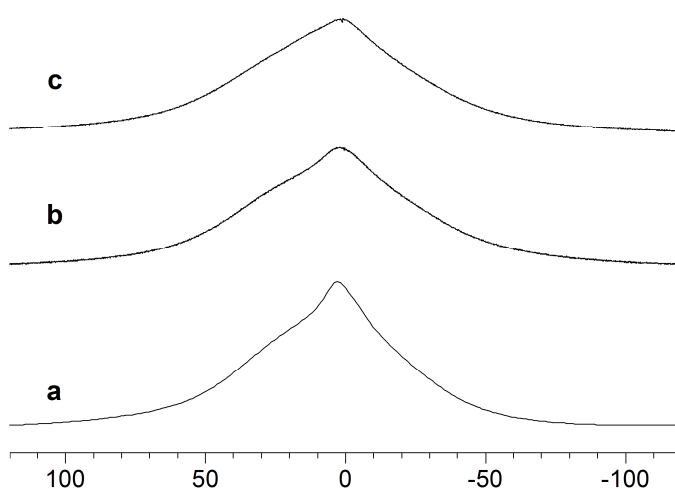


Figure 5.47. ^1H Wideline NMR spectra of PEKK-PBI blend after (a) treatment with water at RT, (b) steam-treatment at 300 F for 48 h, and (c) steam-treatment at 600 F for 72 h.

The IR spectra of the PEKK-PBI blend shown in Figure 5.48 corroborate the findings obtained by the ^1H wideline spectra (Table 5.3, Figure 5.47), namely that some water is incorporated into the polymer network at room temperature in spite of the presence of the PEKK component. Treatment of the PEKK-PBI blend with water at ambient temperature leads to a large $\nu(\text{O-H})$ stretching band between 3000 and 4000 cm^{-1} . The $\nu(\text{C=O})$ band of the PEKK component remains unchanged at 1651 cm^{-1} . It

should be pointed out that there was no free water attached to the surface of any of the polymer samples.

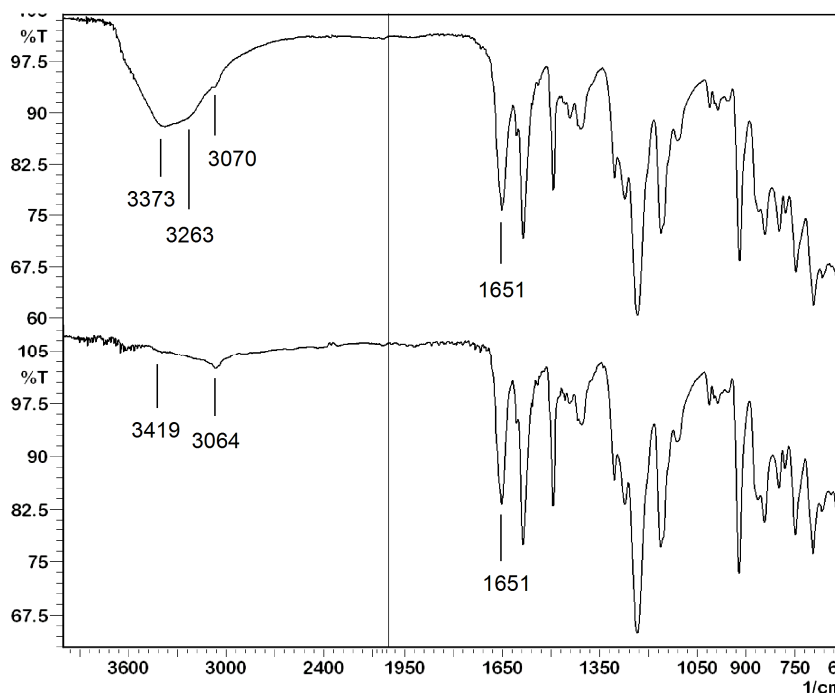


Figure 5.48. IR spectra of original PEKK-PBI blend (*bottom*), and after being exposed to water at RT for 48 h (*top*).

¹³C T₁ relaxation time measurements

T₁ relaxation times of the PBI, the PEKK, and the PEKK-PBI blend samples were determined by the measurement method developed by Torchia.¹³⁰ In the case of PEKK, due to its large intensity, we chose the signal of the non-quaternary carbons at 131 ppm for analyzing the spectra in order to obtain the T₁ relaxation times. For this purpose, the relative signal intensities are plotted versus the applied relaxation delays for the various polymer samples (Figure 5.49). Then, assuming that the signal at 120.1 ppm

stems from both mobile and rigid phases, a double-exponential fit¹³³ is used to determine the relaxation times of the rigid and mobile phases. From the curve fitting process, the short T_1 time for the mobile amorphous domain, and the percentages of mobile (**A**) versus non-mobile (**B**) phases, can be obtained. Table 5.5 summarizes all data for the indicated polymer samples.

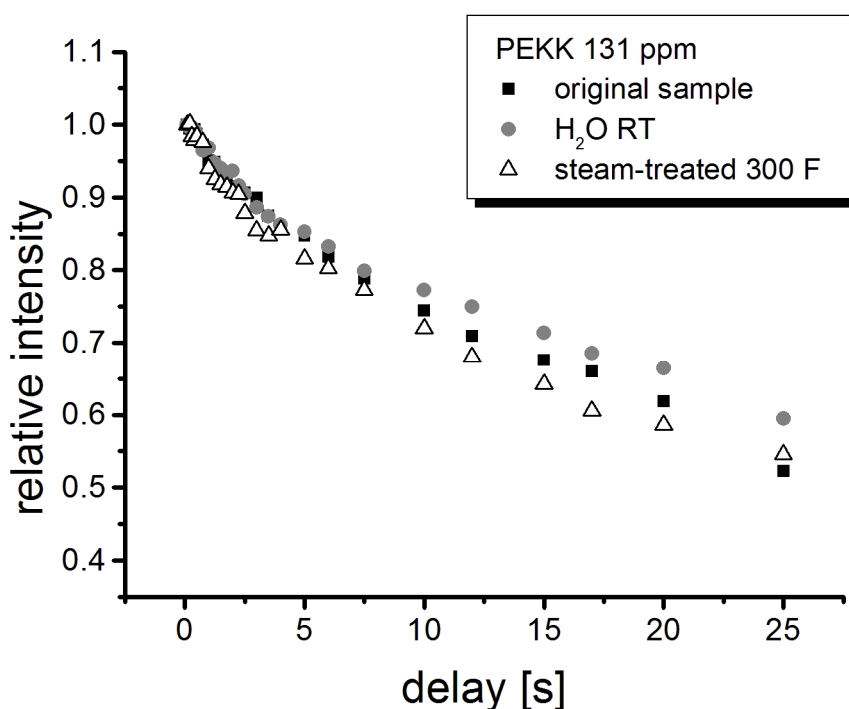


Figure 5.49. ^{13}C T_1 relaxation time characteristics of PEKK samples, treated as indicated.

Interestingly, the T_1 time for PEKK is longest, when it has been exposed to water at ambient temperature (Figure 5.49). The T_1 time characteristics for PEKK steam-treated at 300 F are similar to the original sample. This means that with water uptake the

polymer network becomes slightly more rigid in nature, as the rigid phase **B** increases to 87% (Table 5.5).

Table 5.5. ^{13}C T_1 relaxation times of the mobile domain **A** and the rigid domain **B** of the indicated water-containing and dry samples. **A** and **B** are given in the percent amounts of the mobile and rigid domains after the curve fitting process.

Sample		A [%]	$T_1(\text{A})$ [s]	B [%]	$T_1(\text{B})$ [s]
PBI	dry	25	2.50	76	39.6
	wet	6	2.98	91	41.2
PEKK	dry	19	3.96	79	81.8
	wet	12	3.39	87	79.8
PEKK-PBI Blend	dry	18	3.95	80	45.8
	wet	12	3.31	88	79.3

The same phenomenon, but much more pronounced, is observed for the T_1 characteristics of the resonance at 128 ppm of the PBI samples (Figure 5.50). The more water PBI incorporates, the longer the T_1 relaxation times become, and the % rigid domain of **B** increases from 76 to 91% (Table 5.5). In accordance with the previous ^{13}C CP/MAS, ^1H wideline NMR, and IR measurements there is practically no difference in the T_1 characteristics between the material treated with water at ambient temperature and

the steam-treated PBI (Figure 5.50). The original sample with significantly lower water content shows the fastest relaxation and is therefore most mobile. This effect might be due to the formation of hydrogen bridges between the imidazole nitrogen atoms and the water protons in the polymer network, which lead to an immobilization of the polymer chains and a more rigid structure. While this might at first sight seem counterintuitive, the structure-giving effect due to the relatively strong hydrogen bridges in biological material such as proteins is well-known. So, water could act as a "glue", holding the polymer chains of PBI together and in this way reducing their mobility.

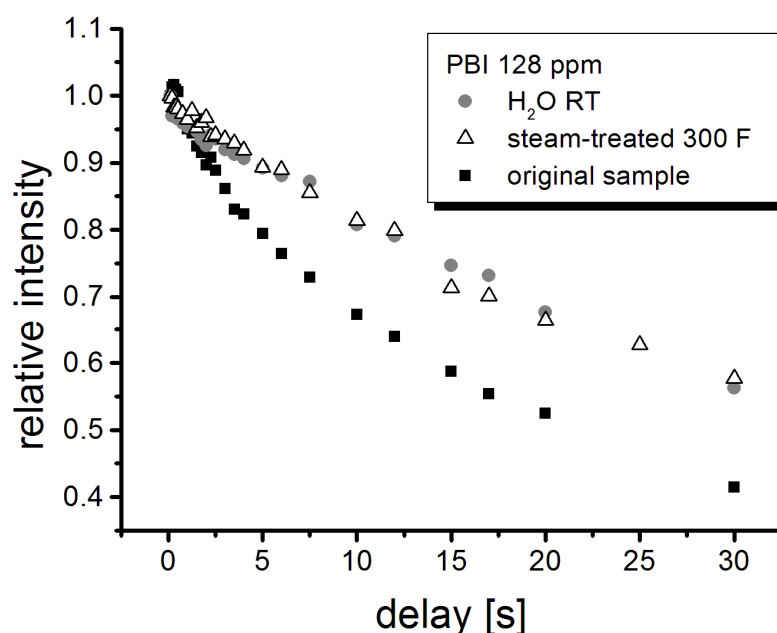


Figure 5.50. ^{13}C T_1 relaxation time characteristics of the indicated PBI samples.

According to the expectation based on the measurements in the previous chapters, the T_1 time characteristics of the PEKK-PBI blend show the reversibility of the water treatments (Figure 5.51). The original dry sample can be exposed to water at

ambient temperature over a prolonged time, and then re-dried *in vacuo*. The T_1 time curve for the original sample is practically identical to the one of the re-dried sample, while the signal intensities for the blends incorporating water are much higher, thus again indicating a more rigid polymer network.

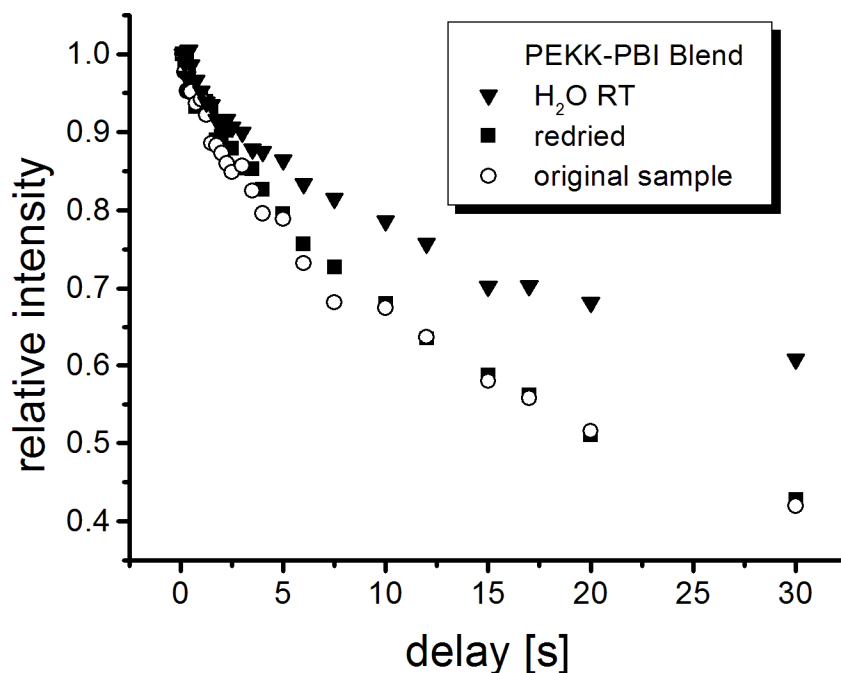


Figure 5.51. ^{13}C T_1 relaxation time characteristics of the indicated PEKK-PBI blend samples obtained from the ^{13}C NMR signal at 128 ppm.

For easy comparisons, Figure 5.52 summarizes all T_1 time characteristics of the studied samples. All dry samples display faster ^{13}C T_1 relaxation than water-containing polymers. While for the dry samples the PBI component of the blend seems to dominate the T_1 time characteristics, the water-treated blends resemble more the PEKK component. So, the T_1 time characteristics of the PEKK-PBI blend do not contradict the

general assumption that PEKK makes PBI more water resistant, while PBI improves the stability of PEKK.

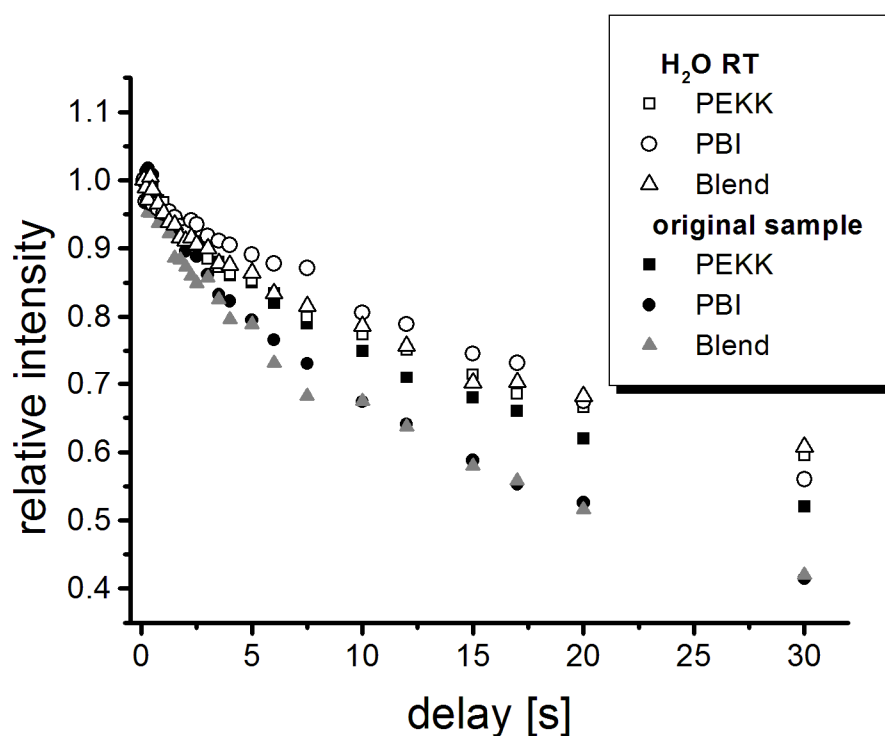


Figure 5.52. Overview of the ^{13}C T_1 relaxation time characteristics of water-treated and original pure components PEKK and PBI and PEKK-PBI blends.

Three materials, PEKK, PBI, and a PEKK-PBI blend (60% : 40%) have been exposed to water at room temperature and subjected to steam-treatment at 300 and 600 F. Using ^{13}C CP/MAS and ^1H solid-state NMR, as well as ^{13}C T_1 relaxation time, IR, and DSC measurements it could be concluded that all polymers take up a maximal amount of water at ambient temperature or 300 F, while at 600 F the water does not intrude or remain in the polymer network. Most importantly, no chemical changes on a

molecular basis have been detected. All changes are reversible and due to changes in conformation (PBI) or crystallinity (PEKK). For the PEKK-PBI blend it has been demonstrated that less water is incorporated than potentially possible, based on the 40 wt% amount of PBI in the blend. Therefore, it is concluded that the PEKK-PBI blend fulfills the promise of protecting the PBI component from excessive incorporation of water in the polymer network.

CONCLUSION

Regarding PEEK polymers it can be concluded that heating samples up to 400 °C leads predominantly to morphological changes, for example, changes in crystallinity. ^{13}C T_1 relaxation times are a suitable probe to detect these changes, yet NMR experiments carried out at higher temperatures, above T_g , are expected to yield further insights. Especially ^1H T_2 relaxation times are of interest in this regard.

Concerning the chemical decomposition the experiments suggest that no decomposition on a molecular level takes place, even though some cross-linking by biphenyl linkages up to 3% cannot be ruled out due to the sensitivity limitations of solid-state NMR and IR spectroscopy.

PPS polymers behave slightly differently. At 250 °C the changes are again mostly of a morphological nature, but treating the material at temperatures above 300 °C leads to both oxidation of the thioether group and to cross-linking in substantial amounts.

All materials, PEKK, PBI, and a PEKK-PBI blend (60% : 40%) take up some amount of water at ambient temperature or 300 F, while at 600 F the water does not intrude or remain in the polymer network. PEKK, however, was shown to be much less hydrophilic than PBI. In none of these cases have any chemical changes on a molecular

level been detected. All changes are reversible and due to changes in conformation (PBI) or crystallinity (PEKK). For the PEKK-PBI blend it has been demonstrated that less water is incorporated than potentially possible, based on the 40 wt% amount of PBI in the blend. Therefore, it is concluded that the PEKK-PBI blend fulfills the promise of protecting the PBI component from excessive incorporation of water in the polymer network.

EXPERIMENTAL

The solid-state NMR spectra were measured on a *Bruker* AVANCE 400 spectrometer operating at 400.1 MHz for ^1H and 100.6 MHz for ^{13}C . The ^{13}C CP/MAS (Cross Polarization with Magic Angle Spinning) experiments were carried out at MAS rates of 13, 12, and 10 kHz using densely packed powders of the polymers in 4 mm ZrO_2 rotors. The ^1H $\pi/2$ pulse was 2.5 μs and TPPM decoupling was used during the acquisition. The Hartmann-Hahn matching condition was optimized using the polymer Victrex P450 at a rotational speed of 10 kHz. Adamantane served as the external chemical shift standard. All spectra were measured with a contact time of 1.5 ms, unless stated otherwise, and a relaxation delay of 3.0 s, and typically 512 to 2048 FIDs were accumulated. Line-broadening factors of less than 100 Hz were applied for the processing of the FIDs. The dipolar dephasing delay for the spectra discussed was 40 μs . The ^1H wideline NMR spectra were recorded in the MAS probehead without sample spinning. H_2O was used as the external chemical shift standard, but it should be noted that with the obtained broad signals the chemical shifts determined are very sensitive to miniscule changes in the phase correction of the signals. A $\pi/2$ pulse of 2.7 μs and a pulse delay of 3 s were used and typically 32 FIDs were accumulated. The signals in the ^1H NMR spectra were deconvoluted using the program MestRe-C[®]. The broad signal of

the polymer backbone was fitted using mainly a Gaussian lineshape, while the narrower signal sitting on top of the broad one was best emulated by a Lorentzian fit.

The ^{13}C T_1 relaxation times were obtained by the method reported by Torchia [6]. Typically 30 increments with relaxation delays ranging from 100 ms to 30 s were recorded. The decay of the signal intensity over time was plotted and the curves were fitted to a double exponential decay using the program TableCurve 2D 4.0.

Exposing the dry materials to water at room temperature included an initial 30 min of sonication to achieve homogeneous suspension of the polymer powder in water prior to letting the mixture stand for 48 hours. Then the polymer powder was filtered off and dried in an air stream. The steam-treatment of all samples was undertaken using a Parr pressure reactor model 4913. Hereby, dogbone-shaped samples of the polymers were placed on a grid in the reactor together with 150 ml of distilled water and heated to 300 F (148.9 °C) and 600 F (315.6 °C). The resulting pressures in the closed vessels amounted to 5 bar (72 psi) and 110 bar (1600 psi), respectively. The re-drying procedure consisted of removing the water at 120 °C under vacuum for 3 days.

The IR spectra were recorded on the instrument Shimadzu IRAffinity-1 FTIR by placing the powdered polymers on top of a Pike Technologies MIRacle ATR diamond plate. 100 scans were typically recorded for optimal spectrum quality. Differential scanning calorimetry^{154,155} (DSC) (TA instruments Q-20) was conducted under nitrogen with a flow rate of 50 ml/min. The samples were heated from 30 °C to 450 °C with a heating rate of 10 °C per minute, and then cooled to 30 °C with a cooling rate fo 10 °C per minute. Subsequently, a second heating and cooling cycle identical to the first one was applied.

CHAPTER VI

CONCLUSION

After a brief overview of solid-state NMR and its relevance to the various areas of chemistry, chapters II and III detail the synthesis, immobilization, and characterization of tridentate phosphine ligands, $\text{EtOSi}((\text{CH}_2)_n\text{PPh}_2)_3$ ($n = 4, 7, 11$) and $[\text{MeP}^+((\text{CH}_2)_n\text{PPh}_2)_3]^+\text{I}^-$ ($n = 4, 7, 11$) on silica. Both, immobilization by electrostatic interactions and by a covalent siloxane bond to the support, is studied and compared. It is demonstrated that the mobility of immobilized phosphine ligands differ depending on the mode of binding. In the case of attachment via a phosphonium salt in the presence of an organic solvent, not only the phosphine moieties are mobile, but the entire ligand scaffold displays isotropic motion on the surface. This result is deduced both from ^{31}P HRMAS and ^2H NMR measurements.

Ligand exchange with Wilkinson's catalyst affords immobilized Rh complexes. These materials are applied to catalytic olefin hydrogenation. In either case active hydrogenation catalysts are obtained that can easily and efficiently be recycled up to 30 times. Various techniques, including NMR spectroscopy, TEM analysis, reaction kinetics, and various chemical tests reveal that irrespective of the linkage to the support the catalysts consist initially of well-defined molecular species that form supported Rh nanoparticles with a narrow size distribution in the course of the catalytic reaction. The nanoparticles are active hydrogenation catalysts as well, and no metal leaching into solution is detected. A future direction of study for these catalyst systems is the investigation of nanoparticle formation, including a more detailed TEM study. The results from this thesis indicate that the flexibility of the tether contribute to the

transformation of well defined Rh phosphine complexes into Rh nanoparticles. The use of more rigid linker systems might be beneficial to catalyst stability.

In the area of C(sp³)-Si bond activation it is shown that oxidative addition to Rh and Ir is feasible intramolecularly using the tridentate phosphine ligands EtOSi[(CH₂)₂PPh₂]₃ and MeSi[(CH₂)₂PPh₂]₃. This reaction leads selectively to cleavage of the C(sp³)-Si bond to yield octahedral Rh or Ir complexes with the metal in the +III oxidation state. These complexes are fully characterized by multinuclear NMR in solution and in the solid state. Preliminary density functional theory (DFT) calculations corroborate the preference for oxidative addition. The study of the complexes by X-ray diffraction techniques is a goal of further research. Modification of the complexes by halide abstraction and introduction of non-coordinating counter anions might be beneficial towards obtaining single crystals of sufficient quality.

Chapter V focuses on the study of performance thermoplastics which are important materials for the oil and gas industry. The polymer morphology is studied by solid-state NMR techniques. Especially potential decomposition pathways at elevated temperatures are investigated for polyetheretherketone (PEEK) and polyphenylene sulfide (PPS) polymers. ¹³C CP/MAS (cross polarization with magic angle spinning) NMR and IR spectroscopy reveal that PEEK polymers show no detectable chemical change on the molecular level, while PPS polymers display signs of oxidation of the thioether group and branching via formation of ether, thioether, and biphenyl linkages. These important results help guide further research regarding the change of mechanical properties upon melt processing.

The determination of ¹³C T₁ relaxation times for PEEK polymers will be expanded further to samples with varying processing histories, and will be complemented by ¹H T₂ relaxation times at elevated temperature to establish a firm

structure-property relationship for this class of polymers. The detection of chain branching will be a major focus.

Furthermore, the water absorption of polybenzimidazole (PBI), polyetherketoneketone (PEKK), and their blend PEKK-PBI is studied. It is demonstrated that steam-treatment even at high temperatures and pressures does not cause chemical decomposition and that the changes, which are morphological in nature, are fully reversible. Future research including ^2H NMR techniques are directed towards the question of the interaction of H_2O with the polymer backbone on a molecular level.

REFERENCES

- 1 Hagen, J. *Industrial Catalysis: A Practical Approach*; Wiley-VCH: Weinheim, Germany, **1999**; Rothenberg, G. *Catalysis: Concepts and Green Applications*; Wiley-VCH: Weinheim, Germany, **2008**; Nicolaou, K. C.; Hanks, R.; Hartwig, W.; Eds. *Handbook of Combinatorial Chemistry*; Wiley-VCH: Weinheim, Germany, **2002**; Bannworth, W.; Felder, E.; Eds. *Combinatorial Chemistry*; Wiley-VCH: Weinheim, Germany, **2000**; Gladysz, J. A.; Ed. *Recoverable Catalysts and Reagents*, Special Issue of *Chem. Rev.* **2002**, *102*.
- 2 Landis, C. R.; Halpern, J. *J. Am. Chem. Soc.* **1987**, *109*, 1746-1754; Brown, J. M.; Chaloner, P. A.; Morris, G. A. *J. Chem. Soc., Perkin Trans. 2* **1987**, *11*, 1583-1588.
- 3 Resconi, L.; Cavallo, L.; Fait, A.; Piemontesi, F. *Chem. Rev.* **2000**, *100*, 1253-1346; Coates, G. W.; Hustad, P. D.; Reinartz, S. *Angew. Chem. Int. Ed.* **2002**, *41*, 2236-2257.
- 4 Osborne, J. A.; Jardine, F. H.; Young, J. F.; Wilkinson, G. *J. Chem. Soc. A* **1966**, 1711-1732.
- 5 Trnka, T. M.; Grubbs, R. H. *Acc. Chem. Res.* **2001**, *34*, 18-29.
- 6 Schrock, R. R.; Hoveyda, A. H. *Angew. Chem. Int. Ed.* **2003**, *42*, 4592-4633.
- 7 a) Hartley, F. R. *Supported Metal Complexes*; D. Reidel Publishing Co.: Dordrecht, Netherlands, **1985**; b) Clark, J. H. *Supported Reagents in Organic Reactions*; Wiley-VCH: Weinheim, Germany, **1994**; c) DeVos, D. E.; Vankelecom, I. F. J.; Jacobs, P. A. *Chiral Catalyst Immobilization and Recycling*; Wiley-VCH: Weinheim, Germany, **2000**; d) Wight, A. P.; Davis, M. E. *Chem. Rev.* **2002**, *102*, 3589-3614; e) Barbaro, P.; Liguori, F. *Heterogenized*

Homogeneous Catalysts for Fine Chemicals Production: Materials and Processes, Springer: New York, **2010**.

- 8 Ertl, G. *Reactions at Solid Surfaces*; John Wiley & Sons: Hoboken, NY, **2009**.
- 9 Somorjai, G. A.; Li, Y. *Top. Catal.* **2010**, *53*, 311-325.
- 10 a) Song, C. E.; Lee, S. *Chem. Rev.* **2002**, *102*, 3495-3524; b) End, N.; Schoening, K. U. *Top. Curr. Chem.* **2004**, *242*, 241-271; c) Horn, J.; Michalek, F.; Tzschucke, C. C.; Banwarth, W. *Top. Curr. Chem.* **2004**, *242*, 43-75; d) McCorn, P.; Hutchings, G. J. *Chem. Soc. Rev.* **2004**, *33*, 108-122.
- 11 Bianchini, C.; Burnaby, D. G.; Evans, J.; Frerdiani, P.; Meli, A.; Oberhauser, W.; Psaro, R.; Sordelli, L.; Vizza, F. *J. Am. Chem. Soc.* **1999**, *121*, 5961-5971; Bianchini, C.; Dal Santo, V.; Meli, A.; Oberhauser, W.; Psaro, R.; Vizza, F. *Organometallics* **2000**, *19*, 2433-2444; Bianchini, C.; Barbaro, P.; Dal Santo, V.; Gobetto, R.; Meli, A.; Oberhauser, W.; Psaro, R.; Vizza, F. *Adv. Synth. Catal.* **2001**, *343*, 41-45.
- 12 Arhancet, J. P.; Davis, M. E.; Merola, J. S.; Hanson, B. E. *Nature* **1989**, *339*, 454-455; Davis, M. E. *Chemtech.* **1992**, *22*, 498-502.
- 13 Bhanage, B. M.; Shirai, M.; Arai, M. *J. Mol. Catal. A: Chem.* **1999**, *145*, 69-74; Fujita, S.; Yoshida, T.; Bhanage, B. M.; Shirai, M.; Arai, M. *J. Mol. Catal. A: Chem.* **2002**, *180*, 277-284.
- 14 Quignard, F.; Larbot, S.; Goutodier, S.; Choplin, A. *J. Chem. Soc., Dalton Trans.* **2002**, 1147-1152.
- 15 Wan, K. T.; Davis, M. E. *Nature* **1994**, *370*, 449-450.
- 16 Kalck, P.; Escaffre, P.; Serein-Spirau, F.; Thorez, A. *New J. Chem.* **1988**, *12*, 687-690; Monteil, F.; Queau, R.; Kalck, P. *J. Organomet. Chem.* **1994**, *480*, 177-184; Turov, V. V.; Leboda, R. *Adv. Colloid Interface Sci.* **1999**, *79*, 173-211.

- 17 Mirza, A. R.; Anson, M. S.; Hellgardt, K.; Leese, M. P.; Thompson, D. F.; Tonks, L.; Williams, J. M. *Org. Process Res. Dev.* **1998**, *2*, 325-331.
- 18 Arends, I. W. C. E.; Sheldon, R. A. *Appl. Catal., A* **2001**, *212*, 175-187.
- 19 a) Guillevic, M. A.; Rocaboy, C.; Arif, A. M.; Horvath, I. T.; Gladysz, J. A. *Organometallics* **1998**, *17*, 707-717; b) Rutherford, D.; Juliette, J. J. J.; Rocaboy, C.; Horvath, I. T.; Gladysz, J. A. *Catal. Today* **1998**, *42*, 381-388; c) Chechik, V.; Crooks, R. M. *J. Am. Chem. Soc.* **2000**, *122*, 1243-1244.
- 20 Tzschucke, C. C.; Markert, C.; Glatz, H.; Banwarth, W. *Angew. Chem. Int. Ed.* **2002**, *41*, 4500-4503.
- 21 Bremeyer, N.; Ley, S. V.; Ramarao, C.; Shirley, I. M.; Smith, S. C. *Synlett* **2002**, 1843-1845; Yu, J. Q.; Wu, H. C.; Ramarao, C.; Spennner, J. B.; Ley, S. V. *Chem. Commun.* **2003**, 678-679.
- 22 Ley, S. V.; Ramarao, C.; Gordon, R. S.; Holmes, A. B.; Morrison, A. J.; McConvey, I. F.; Shirley, I. M.; Smith, S. C.; Smith, M. D. *Chem. Commun.* **2002**, 1134-1135.
- 23 Jamis, J.; Anderson, J. R.; Dickson, R. S.; Campi, E. M.; Jackson, W. R. *J. Organomet. Chem.* **2001**, *627*, 37-43.
- 24 Sabatier, M. J.; Corma, A.; Domenech, A.; Fornes, V.; Garcia, H. *Chem. Commun.* **1997**, 1285-1286; Ogunwami, S. B.; Bein, T. *Chem. Commun.* **1997**, 901-902; DeVos, D. E.; Thibault-Starzky, F.; Knops-Gerrits, P. P.; Parton, R. F.; Jacobs, P. A. *Macromol. Symp.* **1994**, *80*, 157-184.
- 25 Vankelecom, I. F. J.; Jacobs, P. A. *Catalyst Immobilization on Inorganic Supports*; Wiley-VCH: Weinheim, Germany, **2000**.

- 26 Merrifield, B. *Science* **1986**, *232*, 341-347.
- 27 McNamara, C. A.; Dixon, M. J.; Bradley, M. *Chem. Rev.* **2002**, *102*, 3275-3300;
Benaglia, M.; Puglisi, A.; Cozzi, F. *Chem. Rev.* **2003**, *103*, 3401-3430.
- 28 Gravert, D. J.; Janda, K. D. *Chem. Rev.* **1997**, *97*, 489-510; Wentworth, J. P.;
Janda, K. D. *Chem. Commun.* **1999**, 1917-1924; Haag, R. *Chem. Eur. J.* **2001**, *7*,
327-335.
- 29 Collman, J. P.; Hegedus, L. S.; Cooke, M. P.; Norton, J. R.; Dolcetti, G.;
Marquardt, D. *J. Am. Chem. Soc.* **1972**, *94*, 1789-1790; Bayer, E.; Schurig, V.
Angew. Chem. Int. Ed. **1975**, *87*, 484-485.
- 30 Yao, Q. *Angew. Chem. Int. Ed.* **2000**, *39*, 3896-3898.
- 31 Bergbreiter, D. E. *Chem. Rev.* **2002**, *102*, 3345-3384.
- 32 Schlenk, C.; Kleij, A. W.; Frey, H.; Koten, G. *Angew. Chem. Int. Ed.* **2000**, *39*,
3445-3447.
- 33 Schwab, E.; Mecking, S. *Organometallics* **2001**, *20*, 5504-5506.
- 34 Buhleier, W.; Wehner, W.; Voegtle, F. *Synthesis* **1978**, 155-158.
- 35 Ulman, M.; Grubbs, R. H. *J. Org. Chem.* **1999**, *64*, 7202-7207.
- 36 Mukhopadhyah, S.; Rothenberg, G.; Gitis, D.; Sasson, Y. *J. Org. Chem.*, **2000**,
65, 3107-3110.
- 37 a) Iler, R. K. *The Chemistry of Silica*; John Wiley & Sons, Ltd.: New York, **1979**;
b) Vansant, E. F.; VanDer Voort, P.; Vrancken, K. C. *Characterization and
Chemical Modification of Silica*; Elsevier: Amsterdam, Netherlands, **1995**; c)

- Scott, R. P. W. *Silica Gel and Bonded Phases*; John Wiley & Sons: New York, **1993**.
- 38 Kinting, A.; Krause, H.; Čapka, M. *J. Mol. Catal.* **1985**, *33*, 215-223.
- 39 Pugin, B.; Mueller, M. *Stud. Surf. Sci. Catal.* **1993**, *78*, 107-111.
- 40 Blümel, J. *Coord. Chem. Rev.* **2008**, *252*, 2410-2423, and lit. cited therein.
- 41 a) Stejskal, E. O.; Memory, J. D. *High Resolution Solid-State NMR of Silicates and Zeolites*; John Wiley & Sons: Toronto, Canada, **1987**; b) Fyfe, C. A. *Solid-State NMR for Chemists*; C.F.C. Press: Guelph, Canada, **1983**; c) Duer, M. J. *Introduction to Solid-State NMR Spectroscopy*; Blackwell Publishing: Oxford, UK, **2004**; d) Reinhard, S.; Blümel, J. *Magn. Reson. Chem.* **2003**, *41*, 406-416.
- 42 a) Yang, Y.; Beele, B.; Blümel, J. *J. Am. Chem. Soc.* **2008**, *130*, 3771-3773; b) Beele, B.; Guenther, J.; Perera, M.; Stach, M.; Oeser, T.; Blümel, J. *New J. Chem.* **2010**, *34*, 2729-2731.
- 43 Mazzei, M. M.; Marconi, W.; Riocci, M. *J. Mol. Catal.* **1980**, *9*, 381-387.
- 44 Selke, R.; Čapka, M. *J. Mol. Catal.* **1990**, *63*, 319-334.
- 45 Guenther, J.; Reibenspies, J.; Blümel, J. *Adv. Synth. Catal.* **2011**, *353*, 443-460.
- 46 a) Shima, T.; Hampel, F.; Gladysz, J. A. *Angew. Chem. Int. Ed.* **2004**, *43*, 5537-5540; b) Nawara-Hultsch, A. J.; Skopek, K.; Shima, T.; Barbasiewicz, M.; Hess, G. D.; Skaper, D.; Gladysz, J. A. *Z. Naturforsch.* **2010**, *65b*, 414-424.
- 47 a) Clark, P. W.; Curtis, J. L. S.; Garrou, P. E.; Hartwell, G. E. *Can. J. Chem.* **1974**, *52*, 1714-1720; b) Clark, P. W.; Hartwell, G. E. *Inorg. Chem.* **1970**, *9*, 1948-1951; c) Clark, P. W.; Jones, A. J. *J. Organomet. Chem.* **1976**, *122*, C41-C48.

- 48 Hirai, T.; Han, L.-B. *Org. Lett.* **2007**, *9*, 53-55.
- 49 Bunlaksananurson, T.; Knochel, P. *Tetrahedron Lett.* **2002**, *43*, 5817-5819.
- 50 Shulyupin, M. O.; Kazankova, M. A.; Beletskaya, I. P. *Org. Lett.* **2002**, *4*, 761-763.
- 51 a) Mimeau, D.; Delacroix, O.; Gaumont, A.-C. *Chem. Commun.* **2003**, 2928-2929; b) Mimeau, D.; Delacroix, O.; Benoit, J.; Gaumont, A.-C. *C. R. Chimie* **2004**, *7*, 845-854.
- 52 a) Tsiavalieris, G.; Haubrich, S.; Merckle, C.; Blümel, J. *Synlett* **2001**, 391-393; b) Fetouaki, R.; Seifert, A.; Bogza, M.; Oeser, T.; Blümel, J. *Inorg. Chim. Acta* **2006**, *359*, 4865-4873.
- 53 Baacke, M.; Stelzer, O.; Wray, V. *Chem. Ber.* **1980**, *113*, 1356-1369.
- 54 Fraenkel, G.; Winchester, W. R.; Williard, P. G. *Organometallics* **1989**, *8*, 2308-2311.
- 55 Cámpora, J.; Maya, C. M.; Matas, I.; Claasen, B.; Palma, P.; Álvarez, E. *Inorg. Chim. Acta* **2006**, *359*, 3191-3196.
- 56 Bogza, M.; Oeser, T.; Blümel, J. *J. Organomet. Chem.* **2005**, *690*, 3383-3389.
- 57 Mitchell, H. L. U.S. Patent 4,522,932 A, June 11, **1985**.
- 58 Monkowius, U.; Nogai, S.; Schmidbaur, H. *Organometallics* **2003**, *22*, 145-152.
- 59 a) Herold, S.; Mezetti, A.; Venanzi, L. M.; Albinati, A.; Lianza, F.; Gerfin, T.; Gramlich, V. *Inorg. Chim. Acta* **1995**, *235*, 215-231; b) Baechechi, F.; Venanzi, L. M. *Acta Crystallogr.* **1989**, *C45*, 724.

- 60 Hauger, B. E.; Huffman, J. C.; Caulton, K. G. *Organometallics* **1996**, *15*, 1856-1864.
- 61 a) Scherer, J.; Huttner, G.; Walter, O.; Janssen, B. C.; Zsolnai, L. *Chem. Ber.* **1996**, *129*, 1603-1615; b) Bianchini, C.; Ghilardi, C. A.; Meli, A.; Midollini, S.; Orlandini, A. *Inorg. Chem.* **1985**, *24*, 924-931; c) Barney, A. A.; Heyduk, A. F.; Nocera, D. G. *Chem. Commun.* **1999**, 2379-2380; d) Peters, J. C.; Feldman, J. D.; Tilley, T. D. *J. Am. Chem. Soc.* **1999**, *121*, 9871-9872; e) Jiminéz, S.; López, J. A.; Ciriano, M. A.; Tejel, C.; Martínez, A.; Sánchez-Delgado, R. A. *Organometallics* **2009**, *28*, 3193-3202.
- 62 a) Merckle, C.; Blümel, J. *Chem. Mater.* **2001**, *13*, 3617-3623; b) Blümel, J. *J. Am. Chem. Soc.* **1995**, *117*, 2112-2113; c) Behringer, K. D.; Blümel, J. *J. Liq. Chromatogr.* **1996**, *19*, 2753-2765; d) Reinhard, S.; Soba, P.; Rominger, F.; Blümel, J. *Adv. Synth. Catal.* **2003**, *345*, 589-602; e) Behringer, K. D.; Blümel, J. *Chem. Commun.* **1996**, 653-654; f) Reinhard, S.; Behringer, K. D.; Blümel, J. *New J. Chem.* **2003**, *27*, 777-778; g) Merckle, C.; Blümel, J. *Adv. Synth. Catal.* **2003**, *345*, 584-588; h) Merckle, C.; Blümel, J. *Top. Catal.* **2005**, *34*, 5-15; i) Merckle, C.; Haubrich, S.; Blümel, J. *J. Organomet. Chem.* **2001**, *627*, 44-54; j) Posset, T.; Rominger, F.; Blümel, J. *Chem. Mater.* **2005**, *17*, 586-595; k) Piestert, F.; Fetouaki, R.; Bogza, M.; Oeser, T.; Blümel, J. *Chem. Commun.* **2005**, 1481-1483; l) Brenna, S.; Posset, T.; Furrer, J.; Blümel, J. *Chem. Eur. J.* **2006**, *12*, 2880-2888; m) Posset, T.; Blümel, J. *J. Am. Chem. Soc.* **2006**, *128*, 8394-8395; n) Posset, T.; Guenther, J.; Pope, J.; Oeser, T.; Blümel, J. *Chem. Commun.* **2011**, 47, 2059-2061.

- 63 a) Blümel, J. *Inorg. Chem.* **1994**, 33, 5050-5056; b) Sommer, J.; Yang, Y.; Rambow, D.; Blümel, J. *Inorg. Chem.* **2004**, 43, 7561-7563.
- 64 a) Nakazawa, J.; Smith, B. J.; Stack, T. D. P. *J. Am. Chem. Soc.* **2012**, 134, 2750-2759; b) Marras, F.; Kluwer, A. M.; Siekerzycka, J. R.; Voza, A.; Brouwer, A. M.; Reek, J. N. H. *Angew. Chem. Int. Ed.* **2010**, 49, 5480-5484.
- 65 Perera, M. I., M.S. Thesis, Texas A&M University, College Station, TX, August 2011.
- 66 Wiench, G. C.; Michon, C.; Ellern, A.; Hazendonk, P.; Iuga, A.; Angelici, J.; Pruski, M. *J. Am. Chem. Soc.* **2009**, 131, 11801-11810.
- 67 Casper, D. J.; Sklyarov, A. V.; Hardcastle, S.; Barr, T. L.; Försterling, F. H.; Surerus, K. F.; Hossain, M. M. *Inorg. Chim. Acta* **2006**, 359, 3129-3138.
- 68 a) Pellon, P. *Tetrahedron Lett.* **1992**, 33, 4451-4452; b) Sommer, T. Ph.D. Dissertation, University of Heidelberg, March 2007.
- 69 David, J. G.; Hallam, H. E. *J. Chem. Soc. A* **1966**, 1103-1106.
- 70 Williams, E. A. *Ann. Rep. NMR Spectrosc.* **1983**, 15, 235-289; Engelhardt, G. In *Encyclopedia of Nuclear Magnetic Resonance*; Grant, D. M., Harris, R. K., Becker, E. D., Eds.; John Wiley & Sons, Ltd.: Sussex, UK, **1996**, Vol. 7, p 4398.
- 71 Duncan, T. M. *A Compilation of Chemical Shift Anisotropies*; Farragut Press: Chicago, **1990**.
- 72 a) *The Handbook of Homogeneous Hydrogenation, 1st ed., Vols 1-3*; De Vries, J. G.; Elsevier, J. G., Eds.; Wiley-VCH: Weinheim, Germany, **2007**; b) Wende, M.; Meier, R.; Gladysz, J. A. *J. Am. Chem. Soc.* **2001**, 123, 11490-11491, and lit. cited therein; c) *Adv. Synth. Catal.* **2003**, 345, vols. 1+2, Special Issue on Hydrogenation, including e. g.: Knowles, W. S. *Adv. Synth. Catal.* **2003**, 345, 3-13; Noyori, R. *Adv. Synth. Catal.* **2003**, 345, 15-32; Imamoto, T. *Adv. Synth.*

- Catal.* **2003**, *345*, 79-101; d) Heinekey, D. M.; Lledós, A.; Llunch, J. M. *Chem. Soc. Rev.* **2004**, *33*, 175-182.
- 73 a) Renaud, E.; Baird, M. C. *J. Chem. Soc., Dalton Trans.* **1992**, *2*, 2905-2906; b) Buriak, J. M.; Klein, J. C.; Herrington, D. G.; Osborn, J. A. *Chem. Eur. J.* **2000**, *6*, 139-150.
- 74 Chang, J.-R.; Lin, H.-M.; Cheng, S.-W.; Tseng, C.-K.; Tzou, D.-L.; Shyu, S.-G. *J. Mol. Catal. A: Chem.* **2010**, *329*, 27-35.
- 75 Widegren, J. A.; Finke, R. G. *J. Mol. Catal. A: Chem.* **2003**, *198*, 317-341.
- 76 Collman, J. P.; Kosydar, K. M.; Bressan, M.; Lamanna, W.; Garret, T. *J. Am. Chem. Soc.* **1984**, *106*, 2569-2519.
- 77 Gao, H.; Angelici, R. J. *Organometallics* **1999**, *18*, 989-995.
- 78 Anton, D. R.; Crabtree, R. H. *Organometallics* **1983**, *2*, 855-859.
- 79 a) Čapka, M.; Hetflejš, J.; Vdovin, V. M.; Fedorov, V. E.; Pritula, N. A.; Fedorova, G. K. *React. Kinet. Catal. Lett.* **1986**, *31*, 41-46; b) Biellmann, J. F.; Jung, M. J. *J. Am. Chem. Soc.* **1980**, *90*, 1673-1674.
- 80 Stanger, K. J.; Tang, Y.; Anderegg, J.; Angelici, R. J. *J. Mol. Catal. A: Chem.* **2003**, *202*, 147-161.
- 81 a) Barthe, L.; Denicourt-Nowicki, A.; Roucoux, A.; Philippot, K.; Chaudret, B.; Hemati, M. *Catal. Commun.* **2009**, *10*, 1235-1239; b) Mévellec, V.; Nowicki, A.; Roucoux, A.; Dujardin, C.; Granger, P.; Payen, E.; Philippot, K. *New J. Chem.* **2006**, *30*, 1214-1219; c) Beyer, H.; Chatziapostolou, K.; Köhler, K. *Top. Catal.* **2009**, *52*, 1752-1756; d) Roucoux, A.; Nowicki, A.; Philippot, K. *Nanopart. Catal.* **2008**, 349-388; e) Starkey Ott, L.; Finke, R. G. *Coord. Chem. Rev.* **2007**, *251*, 1075-1100.

- 82 a) Raja, R.; Thomas, J. M.; Jones, M. D.; Johnson, B. F. G.; Vaughan, D. E. W. *J. Am. Chem. Soc.* **2003**, *125*, 14982-14983. b) Yu, C.; He, J. *Chem. Commun.* **2012**, *48*, 4933-4940.
- 83 Jones, C. W. *Top. Catal.* **2010**, *53*, 942-952.
- 84 Ananikov, V. P.; Beletskaya, I. P. *Organometallics* **2012**, *31*, 1595-1604; Bayram, E.; Linehan, J. C.; Fulton, J. L.; Roberts, J. S. A.; Szymczak, N. K.; Smurthwaite, T. D.; Özkar, S.; Balasubramanian, M.; Finke, R. G. *J. Am. Chem. Soc.* **2011**, *133*, 18889-18902. Richardson, J. M.; Jones, C. W. *J. Catal.* **2007**, *251*, 80-93. Gajan, D.; Coperet, C. *New J. Chem.* **2011**, *35*, 2403-2408.
- 85 Mondloch, J. E.; Finke, R. G. *ACS Catal.* **2012**, *2*, 298-305. Mondloch, J. E.; Finke, R. G. *J. Am. Chem. Soc.* **2011**, *133*, 7744-7756. Mondloch, J. E.; Bayram, E.; Finke, R. G. *J. Mol. Catal., A* **2012**, *355*, 1-38. Serna, P.; Gates, B. C. *J. Am. Chem. Soc.* **2011**, *133*, 4714-4717; Li, D.; Nielsen, M. H.; Lee, J. R. I.; Frandsen, C.; Banfield, J. F.; De Yoreo, J. J. *Science* **2012**, *336*, 1014-1018; Liao, H.-G.; Cui, L.; Whitelam, S.; Zheng, H. *Science* **2012**, *336*, 1011-1014.
- 86 Serna, P.; Gates, B. C. *Angew. Chem., Int. Ed.* **2011**, *50*, 5528-5531. Marciniec, B.; Szubert, K.; Potrzebowski, M. J.; Kownacki, I.; Łęszczak, K. *Angew. Chem.* **2008**, *120*, 551-554; *Angew. Chem., Int. Ed.* **2008**, *47*, 541-544.
- 87 Pinoie, V.; Biesemans, M.; Willem, R. *Organometallics* **2008**, *27*, 3633-3634. Polito, L.; Colombo, M.; Monti, D.; Melato, S.; Caneva, E.; Prosperi, D. *J. Am. Chem. Soc.* **2008**, *130*, 12712-12724. Gonzáles-Gálvez, D.; Nolis, P.; Philippot, K.; Chaudret, B.; van Leeuwen, P. V. N. M. *ACS Catal.* **2012**, *2*, 317-321.

- 88 Grünberg, A.; Yeping, X.; Breitzke, H.; Buntkowsky, G. *Chem. Eur. J.* **2010**, *16*, 6993-6998. Wang, L.; Jia, M.; Shylesh, S.; Philippi, T.; Seifert, A.; Ernst, S.; Singh, A. P.; Thiel, W. R. *ChemCatChem* **2010**, *2*, 1477-1482.
- 89 Beele, B., Dissertation Thesis, University of Heidelberg, July 2010.
- 90 a) Brodzki, D.; Pannetier, G. *J. Organomet. Chem.* **1973**, *63*, 431-440; b) Rajput, J.; Hutton, A. T.; Moss, J. R.; Su, H.; Imrie, C. *J. Organomet. Chem.* **2006**, *691*, 4573-4588.
- 91 Reddy, V. V. S.; Varshney, A.; Gray, G. M. *J. Organomet. Chem.* **1990**, *391*, 259-266.
- 92 Elschenbroich, C. *Organometallics. 3rd Ed.*; Wiley-VCH: Weinheim, Germany, **2006**.
- 93 Hilliard, C. R.; Bhuvanesh, N.; Gladysz, J. A.; Blümel, J. *Dalton Trans.* **2012**, *41*, 1742-1754.
- 94 Debouttière, P.-J.; Coppel, Y.; Denicourt-Nowicki, A.; Roucoux, A.; Chaudret, B.; Philippot, K. *Eur. J. Inorg. Chem.* **2012**, *8*, 1229-1236.
- 95 Aguilà, D.; Escribano, E.; Speed, S.; Talancón, D.; Yermán, L.; Alvarez, S. *Dalton Trans.* **2009**, 6610-6625.
- 96 Tejel, C.; Geer, A. M.; Jiménez, S.; Lopez, J. A.; Ciriano, M. A. *Organometallics* **2012**, *31*, 2895-2906.
- 97 Bogza, M. Ph.D. Dissertation, University of Heidelberg, Heidelberg, June 2007.
- 98 a) Horita, A.; Tsurugi, H.; Satoh, T.; Miura, M. *Org. Lett.* **2008**, *10*, 1751-1754.
- 99 a) Thomson, S. K.; Young, G. B. *Organometallics* **1989**, *8*, 2068-2070; b) Hofmann, P.; Heiss, H.; Neiteler, P.; Müller, G.; Lachmann, J. *Angew. Chem. Int. Ed.* **1990**, *29*, 880-882; c) Burger, P.; Bergman, R. G. *J. Am. Chem. Soc.* **1993**, *115*, 10462-10463; d) Heyduck, A. F.; Labinger, J. A.; Bercaw, J. E. *J. Am.*

- Chem. Soc.* **2003**, *125*, 6366-6367; e) Ong, C. M.; Burchell, T. J.; Puddephatt, R. *J. Organometallics* **2004**, *23*, 1493-1495; Muhiedinne, S.; Jennings, M. C.; Puddephatt, R. *J. Organometallics* **2012**, *31*, 3539-3550.
- 100 Lin, W.; Wilson, S. R.; Girolami, G. S. *J. Am. Chem. Soc.* **1993**, *115*, 3022-3023.
- 101 Mitton, S. J.; McDonald, R.; Turculet, L. *Angew. Chem., Int. Ed.* **2009**, *48*, 8568-8571.
- 102 a) He, T.; Tsvetkov, N. P.; Andino, J. G.; Gao, X.; Fullmer, B. C.; Caulton, K. G. *J. Am. Chem. Soc.* **2010**, *132*, 910-911; b) Fullmer, B. C.; Fan, H.; Pink, M.; Huffman, J. C.; Tsvetkov, N. P.; Caulton, K. G. *J. Am. Chem. Soc.* **2011**, *133*, 2571-2582.
- 103 Liang, Y.; Geng, W.; Wei, J.; Xi, Z. *Angew. Chem., Int. Ed.* **2012**, *51*, 1934-1937.
- 104 Hendriksen, D. E.; Oswald, A. A.; Ansell, G. B.; Leta, S.; Kastrup, R. V. *Organometallics* **1989**, *8*, 1153-1157.
- 105 a) Baird, N. C. *Inorg. Chim. Acta* **1989**, *164*, 93-97; b) Grubba, R.; Chojnaki, J.; Wojnowski, W.; Pikies, J. *Acta Cryst.* **2006**, *E62*, 5312-5314.
- 106 a) Mann, B. E.; Taylor, B. F. in *¹³C NMR Data for Organometallic Compounds*, Academic Press Inc, London, UK, **1981**, pp. 44-45; b) Goodfellow, R. J. in *Multinuclear NMR* (Ed.: Mason, J.), Plenum Press, New York, **1987**, pp. 551-554.
- 107 Nishihara, Y.; Takemura, M.; Osakada, K. *Organometallics* **2002**, *21*, 825-831.
- 108 Okazaki, M.; Ohshitanai, S.; Tobita, H.; Ogina, H. *J. Chem. Soc., Dalton Trans.* **2002**, 2061-2068.
- 109 Muller, G.; Sainz, D. *J. Organomet. Chem.* **1995**, *495*, 103-111.

- 110 a) Becke, A. D. *J. Chem. Phys.* **1993**, *98*, 5648-5652; b) Becke, A. D. *Phys. Rev. A* **1988**, *38*, 3098-3100; c) Lee, C.; Yang, W.; Parr, R. G. *Phys. Rev.* **1988**, *B37*, 785-789.
- 111 Kaupp, M.; Schleyer, P. V. R.; Stoll, H.; Preuss, H. *J. Chem. Phys.* **1991**, *94*, 1360-1366; Bergner, H.; Dolg, M.; Küchle, W.; Stoll, H.; Preuss, H. *Mol. Phys.* **1993**, *80*, 1431-1441; Dolg, M.; Stoll, H.; Preuss, H.; Pitzer, R. M. *J. Chem. Phys.* **1993**, *97*, 5852-5859.
- 112 Hariharan, P. C.; Pople, J. A. *Theor. Chim. Acta* **1973**, *28*, 213-222; Hehre, W. J.; Ditchfield, R.; Pople, J. A. *J. Chem. Phys.* **1972**, *56*, 2257-2261.
- 113 Cordero, B.; Gómez, V.; Platero-Prats, E. A.; Revés, M.; Echeverría, J.; Cremades, E.; Barragán, F.; Alvarez, S. *Dalton Trans.* **2008**, 2832-2838.
- 114 a) Reed, J.; Eisenberger, P.; Boon-Keng, T.; Kincaid, B. M. *J. Am. Chem. Soc.* **1977**, *99*, 5217-5218; b) Hitchcock, P. B.; McPartlin, M.; Mason, R. *Chem. Commun.* **1969**, 1367-1368; c) Bennett, M. J.; Donaldson, P. B. *Inorg. Chem.* **1977**, *16*, 655- 660.
- 115 Wilson, P. J.; Bradley, T. J.; Tozer, D. J. *J. Chem. Phys.* **2001**, *115*, 9233-9242.
- 116 Perdew, J. P.; Wang, Y. *Phys. Rev. B* **1992**, *45*, 13244–13249.
- 117 a) Poblador-Bahamonde, A. I.; Poteau, R.; Raynaud, C.; Eisenstein, O. *Dalton Trans.* **2011**, *40*, 11321-11326; b) Xu, X.; Fang, L.; Chen, Z.-X.; Yang, G.-C.; Sun, S.-L.; Su, Z.-M. *J. Organomet. Chem.* **2006**, *691*, 1927-1933; c) Ruiz-Morales, Y.; Ziegler, T. *J. Phys. Chem. A* **1998**, *102*, 3970-3976; d) Eichele, K.; Wasylishen, R. E.; Corrigan, J. F.; Taylor, N. J.; Carty, A. J.; Feindel, K. W.; Bernard, G. M. *J. Am. Chem. Soc.* **2002**, *124*, 1541-1552.
- 118 WSolids1, Eichele, K.; Wasylishen, R. E. Dalhousie University & Universität Tübingen, **2010**.

- 120 <http://www.ensinger-online.com/fi/materiaalit/>
- 121 Kemmish, D. *Update on the Technology and Applications of Polyaryletherketones*, iSmithers: Shropshire, UK, **2010**.
- 122 a) Schmidt-Rohr, K.; Spiess, H.-W. *Multidimensional Solid-State NMR and Polymers*, AP Inc.: CA, **1999**; b) Stejskal, E. O.; Memory, J. D. *High Resolution NMR in the Solid State; Fundamentals of CP/MAS*, Oxford University Press, Oxford: New York, **1994**.
- 123 Spiess, H. W. *Chem. Rev.* **1991**, *91*, 1321-1338.
- 124 Schmidt, C.; Blümich, B.; Spiess, H. W. *J. Magn. Reson.* **1988**, *79*, 269-290.
- 125 Maas, W. E. J. R.; Kentgens, A. P. M.; Veeman, W. S. *J. Chem. Phys.* **1987**, *87*, 6854-6858.
- 126 Schmidt-Rohr, K.; Spiess, H. W. *Macromolecules* **1991**, *24*, 5288-5293.
- 127 Nagaoka, N.; Ueda, T.; Nakamura, N. *Z. Naturforsch.* **2002**, *57*, 435-440.
- 128 VanderHart, D. L.; Garroway, A. N. *J. Chem. Phys.* **1979**, *71*, 2773-2787.
- 129 Kolodziejwski, W.; Klinowski, J. *Chem. Rev.* **2002**, *102*, 613-628.
- 130 Torchia, D. A. *J. Magn. Reson.* **1978**, *30*, 613-616.
- 131 Clark, J. N.; Jagannatan, N. R., Herring, F. G. *Polymer* **1988**, *29*, 341-345.
- 132 Blümel, J. *Inorg. Chem.* **1994**, *33*, 5050-5056.
- 133 Poliks, M. D.; Schaefer, J. *Macromolecules*, **1990**, *23*, 3426-3431
- 134 Jonas, A.; Legras, R. *Polymer* **1991**, *32*, 2691-2706.
- 135 Day, M.; Sally, D.; Wiles, D. M. *J. Appl. Polym. Sci.* **1990**, *40*, 1615-1625.
- 136 a) Chalmers, J. M.; Gaskin, W. F.; Mackenzie, M. W. *Polym. Bull.* **1984**, *11*, 433-435; b) Voice, A. M.; Bower, D. I.; Ward, I. M. *Polymer* **1993**, *34*, 1164-1173.
- 137 Gomez, M. A.; Tonelli, A. E. *Polymer* **1991**, *32*, 796-801.

- 138 Huo, P. P.; Cebe, P. *Polymer* **1992**, *33*, 4913-4919.
- 139 Mehl, N. A.; Rebenfeld, L. *Polym. Eng. Sci.* **1992**, *32*, 1451-1457.
- 140 Park, M.; Lee, K. H.; Choe, C. R. *Polym. Eng. Sci.* **1994**, *34*, 81-85.
- 141 Ma, C.-C. M.; Hsiue, L.-T.; Wu, W.-G.; Liu, W.-L. *J. Appl. Polym. Sci.* **1990**, *39*, 1399-1415.
- 142 Kalinowski, H.-O.; Braun, S.; Berger, S. *Carbon-13 NMR Spectroscopy*, Wiley-VCH: Weinheim, Germany, **1988**.
- 143 Hawkins, R. T. *Macromolecules* **1976**, *9*, 189-194.
- 144 Zhang, G.; Wang, Q.; Yu, X.; Su, D.; Li, Z.; Zhang, G. *Spectrochim. Acta* **1991**, *47*, 737-741.
- 145 a) Günzler, H.; Gremlich, H.-U. *IR-Spectroscopy*, Wiley-VCH: Weinheim, Germany, **2002**; b) Larkin, P. *Infrared and Raman Spectroscopy, Principles and Spectral Interpretation*; Academic Press: Elsevier, Netherlands, **2011**.
- 146 Dizman, C.; Ates, S.; Torun, L.; Yagci, Y. *Beilstein J. Org. Chem.* **2010**, *6*, doi:10.3762/bjoc.6.56.
- 147 Grobelny, J.; Rice, D. M.; Karasz, F. E.; MacKnight, W. J. *Macromolecules* **1990**, *23*, 2139-2144.
- 148 Musto, P.; Karasz, F. E.; McKnight, W. J. *Polymer* **1993**, *34*, 2934-2945.
- 149 Zolotukhin, M. G.; Rueda, D. R.; Bruix, M.; Cagiao, M. E.; Balta Calleja, F. J. *Polymer* **1997**, *38*, 3441-3453.
- 150 Fyfe, C. A. *Solid-State NMR for Chemists*; C.F.C. Press: Guelph, Canada: **1983**.
- 151 Akbey, Ü.; Graf, R.; Chu, P. P.; Spiess, H. W. *Austr. J. Chem.* **2009**, *62*, 848-856.

- 152 Herrmann, W. A.; Scherer, W.; Fischer, R. W.; Blümel, J.; Kleine, M.; Mertin, W.; Gruehn, R.; Mink, J.; Boysen, H.; Wilson, C. C.; Ibberson, R. M.; Bachmann, L.; Mattner, M. *J. Am. Chem. Soc.* **1995**, *117*, 3231-3243.
- 153 Oksanen, A.; Zografi, G. *Pharm. Res.* **1993**, *10*, 791-799.
- 154 Menczel, J. *J. Therm. Anal. Calorim.* **2000**, *59*, 1023-1027.
- 155 Vogel, H.; Marvel, C. S. *J. Polym. Sci.* **1961**, *50*, 511-539.

APPENDIX A

CRYSTALLOGRAPHIC DATA FOR STRUCTURES

A-1 X-ray structure of Ligand X

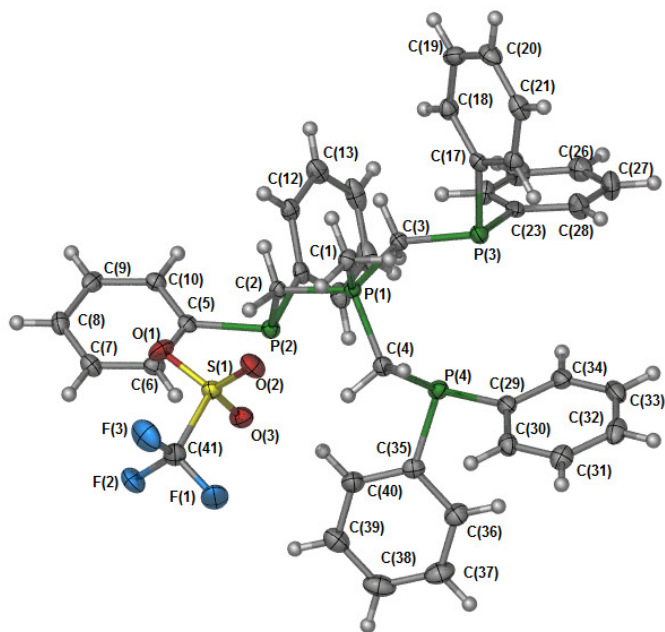


Table A-1. Crystal data and structure refinement for-XY.

Identification code	jb06	
Empirical formula	C41 H36 F3 O3 P4 S	
Formula weight	789.64	
Temperature	113(2) K	
Wavelength	0.71073 Å	
Crystal system	Monoclinic	
Space group	P2(1)/c	
Unit cell dimensions	a = 15.693(4) Å	$\alpha = 90^\circ$.
	b = 12.853(3) Å	$\beta = 94.480(3)^\circ$.
	c = 18.548(4) Å	$\gamma = 90^\circ$.
Volume	3730.0(15) Å ³	
Z	4	
Density (calculated)	1.406 Mg/m ³	

Absorption coefficient	0.313 mm ⁻¹
F(000)	1636
Crystal size	0.20 x 0.10 x 0.10 mm ³
Theta range for data collection	2.05 to 24.99°.
Index ranges	-18<=h<=18, -15<=k<=15, -21<=l<=21
Reflections collected	29704
Independent reflections	6455 [R(int) = 0.0708]
Completeness to theta = 24.99°	98.4 %
Absorption correction	Semi-empirical from equivalents
Max. and min. transmission	0.9694 and 0.9401
Refinement method	Full-matrix least-squares on F ²
Data / restraints / parameters	6455 / 0 / 469
Goodness-of-fit on F ²	1.009
Final R indices [I>2sigma(I)]	R1 = 0.0423, wR2 = 0.0907
R indices (all data)	R1 = 0.0716, wR2 = 0.1046
Largest diff. peak and hole	0.547 and -0.254 e.Å ⁻³

Table A-2. Bond lengths [Å] and angles [°] for jb06.

S(1)-O(2)	1.436(2)
S(1)-O(3)	1.437(2)
S(1)-O(1)	1.437(2)
S(1)-C(41)	1.824(3)
P(1)-C(3)	1.782(3)
P(1)-C(1)	1.788(3)
P(1)-C(2)	1.792(3)
P(1)-C(4)	1.806(3)
P(2)-C(5)	1.827(3)
P(2)-C(11)	1.829(3)
P(2)-C(2)	1.863(3)
P(3)-C(23)	1.834(3)
P(3)-C(17)	1.836(3)

P(3)-C(3)	1.851(3)
P(4)-C(29)	1.830(3)
P(4)-C(35)	1.840(3)
P(4)-C(4)	1.876(3)
F(1)-C(41)	1.317(3)
F(2)-C(41)	1.328(3)
F(3)-C(41)	1.331(3)
C(2)-H(2A)	0.9900
C(2)-H(2B)	0.9900
C(3)-H(3A)	0.9900
C(3)-H(3B)	0.9900
C(4)-H(4A)	0.9900
C(4)-H(4B)	0.9900
C(5)-C(10)	1.386(4)
C(5)-C(6)	1.404(4)
C(6)-C(7)	1.385(4)
C(6)-H(6)	0.9500
C(7)-C(8)	1.376(4)
C(7)-H(7)	0.9500
C(8)-C(9)	1.383(4)
C(8)-H(8)	0.9500
C(9)-C(10)	1.385(4)
C(9)-H(9)	0.9500
C(10)-H(10)	0.9500
C(11)-C(12)	1.390(4)
C(11)-C(16)	1.395(4)
C(12)-C(13)	1.385(4)
C(12)-H(12)	0.9500
C(13)-C(14)	1.382(4)
C(13)-H(13)	0.9500
C(14)-C(15)	1.379(5)
C(14)-H(14)	0.9500
C(15)-C(16)	1.379(4)
C(15)-H(15)	0.9500

C(16)-H(16)	0.9500
C(17)-C(22)	1.391(4)
C(17)-C(18)	1.391(4)
C(18)-C(19)	1.379(4)
C(18)-H(18)	0.9500
C(19)-C(20)	1.384(4)
C(19)-H(19)	0.9500
C(20)-C(21)	1.368(4)
C(20)-H(20)	0.9500
C(21)-C(22)	1.391(4)
C(21)-H(21)	0.9500
C(22)-H(22)	0.9500
C(23)-C(24)	1.382(4)
C(23)-C(28)	1.397(4)
C(24)-C(25)	1.389(4)
C(24)-H(24)	0.9500
C(25)-C(26)	1.368(4)
C(25)-H(25)	0.9500
C(26)-C(27)	1.378(4)
C(26)-H(26)	0.9500
C(27)-C(28)	1.377(4)
C(27)-H(27)	0.9500
C(28)-H(28)	0.9500
C(29)-C(30)	1.386(4)
C(29)-C(34)	1.391(4)
C(30)-C(31)	1.377(4)
C(30)-H(30)	0.9500
C(31)-C(32)	1.387(4)
C(31)-H(31)	0.9500
C(32)-C(33)	1.379(4)
C(32)-H(32)	0.9500
C(33)-C(34)	1.389(4)
C(33)-H(33)	0.9500
C(34)-H(34)	0.9500

C(35)-C(36)	1.388(4)
C(35)-C(40)	1.393(4)
C(36)-C(37)	1.384(4)
C(36)-H(36)	0.9500
C(37)-C(38)	1.374(5)
C(37)-H(37)	0.9500
C(38)-C(39)	1.374(4)
C(38)-H(38)	0.9500
C(39)-C(40)	1.379(4)
C(39)-H(39)	0.9500
C(40)-H(40)	0.9500

O(2)-S(1)-O(3)	114.75(12)
O(2)-S(1)-O(1)	114.38(13)
O(3)-S(1)-O(1)	115.11(13)
O(2)-S(1)-C(41)	103.81(13)
O(3)-S(1)-C(41)	103.65(13)
O(1)-S(1)-C(41)	102.95(13)
C(3)-P(1)-C(1)	110.24(13)
C(3)-P(1)-C(2)	106.98(13)
C(1)-P(1)-C(2)	109.17(13)
C(3)-P(1)-C(4)	112.10(13)
C(1)-P(1)-C(4)	107.43(13)
C(2)-P(1)-C(4)	110.92(13)
C(5)-P(2)-C(11)	105.37(12)
C(5)-P(2)-C(2)	97.15(12)
C(11)-P(2)-C(2)	102.89(12)
C(23)-P(3)-C(17)	100.58(12)
C(23)-P(3)-C(3)	100.04(13)
C(17)-P(3)-C(3)	103.05(13)
C(29)-P(4)-C(35)	100.27(13)
C(29)-P(4)-C(4)	101.17(13)
C(35)-P(4)-C(4)	101.99(13)
P(1)-C(2)-P(2)	115.94(14)

P(1)-C(2)-H(2A)	108.3
P(2)-C(2)-H(2A)	108.3
P(1)-C(2)-H(2B)	108.3
P(2)-C(2)-H(2B)	108.3
H(2A)-C(2)-H(2B)	107.4
P(1)-C(3)-P(3)	114.57(15)
P(1)-C(3)-H(3A)	108.6
P(3)-C(3)-H(3A)	108.6
P(1)-C(3)-H(3B)	108.6
P(3)-C(3)-H(3B)	108.6
H(3A)-C(3)-H(3B)	107.6
P(1)-C(4)-P(4)	116.55(15)
P(1)-C(4)-H(4A)	108.2
P(4)-C(4)-H(4A)	108.2
P(1)-C(4)-H(4B)	108.2
P(4)-C(4)-H(4B)	108.2
H(4A)-C(4)-H(4B)	107.3
C(10)-C(5)-C(6)	118.4(3)
C(10)-C(5)-P(2)	126.3(2)
C(6)-C(5)-P(2)	115.3(2)
C(7)-C(6)-C(5)	120.6(3)
C(7)-C(6)-H(6)	119.7
C(5)-C(6)-H(6)	119.7
C(8)-C(7)-C(6)	120.3(3)
C(8)-C(7)-H(7)	119.9
C(6)-C(7)-H(7)	119.9
C(7)-C(8)-C(9)	119.6(3)
C(7)-C(8)-H(8)	120.2
C(9)-C(8)-H(8)	120.2
C(8)-C(9)-C(10)	120.6(3)
C(8)-C(9)-H(9)	119.7
C(10)-C(9)-H(9)	119.7
C(9)-C(10)-C(5)	120.6(3)
C(9)-C(10)-H(10)	119.7

C(5)-C(10)-H(10)	119.7
C(12)-C(11)-C(16)	118.9(3)
C(12)-C(11)-P(2)	125.8(2)
C(16)-C(11)-P(2)	115.3(2)
C(13)-C(12)-C(11)	120.4(3)
C(13)-C(12)-H(12)	119.8
C(11)-C(12)-H(12)	119.8
C(14)-C(13)-C(12)	119.9(3)
C(14)-C(13)-H(13)	120.0
C(12)-C(13)-H(13)	120.0
C(15)-C(14)-C(13)	120.2(3)
C(15)-C(14)-H(14)	119.9
C(13)-C(14)-H(14)	119.9
C(14)-C(15)-C(16)	120.0(3)
C(14)-C(15)-H(15)	120.0
C(16)-C(15)-H(15)	120.0
C(15)-C(16)-C(11)	120.5(3)
C(15)-C(16)-H(16)	119.7
C(11)-C(16)-H(16)	119.7
C(22)-C(17)-C(18)	118.5(3)
C(22)-C(17)-P(3)	116.4(2)
C(18)-C(17)-P(3)	125.1(2)
C(19)-C(18)-C(17)	120.6(3)
C(19)-C(18)-H(18)	119.7
C(17)-C(18)-H(18)	119.7
C(18)-C(19)-C(20)	120.3(3)
C(18)-C(19)-H(19)	119.9
C(20)-C(19)-H(19)	119.9
C(21)-C(20)-C(19)	119.8(3)
C(21)-C(20)-H(20)	120.1
C(19)-C(20)-H(20)	120.1
C(20)-C(21)-C(22)	120.3(3)
C(20)-C(21)-H(21)	119.8
C(22)-C(21)-H(21)	119.8

C(17)-C(22)-C(21)	120.5(3)
C(17)-C(22)-H(22)	119.8
C(21)-C(22)-H(22)	119.8
C(24)-C(23)-C(28)	118.3(3)
C(24)-C(23)-P(3)	126.3(2)
C(28)-C(23)-P(3)	115.4(2)
C(23)-C(24)-C(25)	120.5(3)
C(23)-C(24)-H(24)	119.7
C(25)-C(24)-H(24)	119.7
C(26)-C(25)-C(24)	120.6(3)
C(26)-C(25)-H(25)	119.7
C(24)-C(25)-H(25)	119.7
C(25)-C(26)-C(27)	119.5(3)
C(25)-C(26)-H(26)	120.3
C(27)-C(26)-H(26)	120.3
C(28)-C(27)-C(26)	120.6(3)
C(28)-C(27)-H(27)	119.7
C(26)-C(27)-H(27)	119.7
C(27)-C(28)-C(23)	120.5(3)
C(27)-C(28)-H(28)	119.8
C(23)-C(28)-H(28)	119.8
C(30)-C(29)-C(34)	118.5(3)
C(30)-C(29)-P(4)	123.4(2)
C(34)-C(29)-P(4)	118.0(2)
C(31)-C(30)-C(29)	121.1(3)
C(31)-C(30)-H(30)	119.5
C(29)-C(30)-H(30)	119.5
C(30)-C(31)-C(32)	120.2(3)
C(30)-C(31)-H(31)	119.9
C(32)-C(31)-H(31)	119.9
C(33)-C(32)-C(31)	119.4(3)
C(33)-C(32)-H(32)	120.3
C(31)-C(32)-H(32)	120.3
C(32)-C(33)-C(34)	120.4(3)

C(32)-C(33)-H(33)	119.8
C(34)-C(33)-H(33)	119.8
C(33)-C(34)-C(29)	120.5(3)
C(33)-C(34)-H(34)	119.8
C(29)-C(34)-H(34)	119.8
C(36)-C(35)-C(40)	117.9(3)
C(36)-C(35)-P(4)	120.0(2)
C(40)-C(35)-P(4)	121.6(2)
C(37)-C(36)-C(35)	121.0(3)
C(37)-C(36)-H(36)	119.5
C(35)-C(36)-H(36)	119.5
C(38)-C(37)-C(36)	120.2(3)
C(38)-C(37)-H(37)	119.9
C(36)-C(37)-H(37)	119.9
C(37)-C(38)-C(39)	119.5(3)
C(37)-C(38)-H(38)	120.3
C(39)-C(38)-H(38)	120.3
C(38)-C(39)-C(40)	120.7(3)
C(38)-C(39)-H(39)	119.7
C(40)-C(39)-H(39)	119.7
C(39)-C(40)-C(35)	120.7(3)
C(39)-C(40)-H(40)	119.6
C(35)-C(40)-H(40)	119.6
F(1)-C(41)-F(2)	107.7(2)
F(1)-C(41)-F(3)	108.2(2)
F(2)-C(41)-F(3)	107.4(2)
F(1)-C(41)-S(1)	111.7(2)
F(2)-C(41)-S(1)	111.3(2)
F(3)-C(41)-S(1)	110.4(2)

A-2 X-ray structure of Rhodium complex X

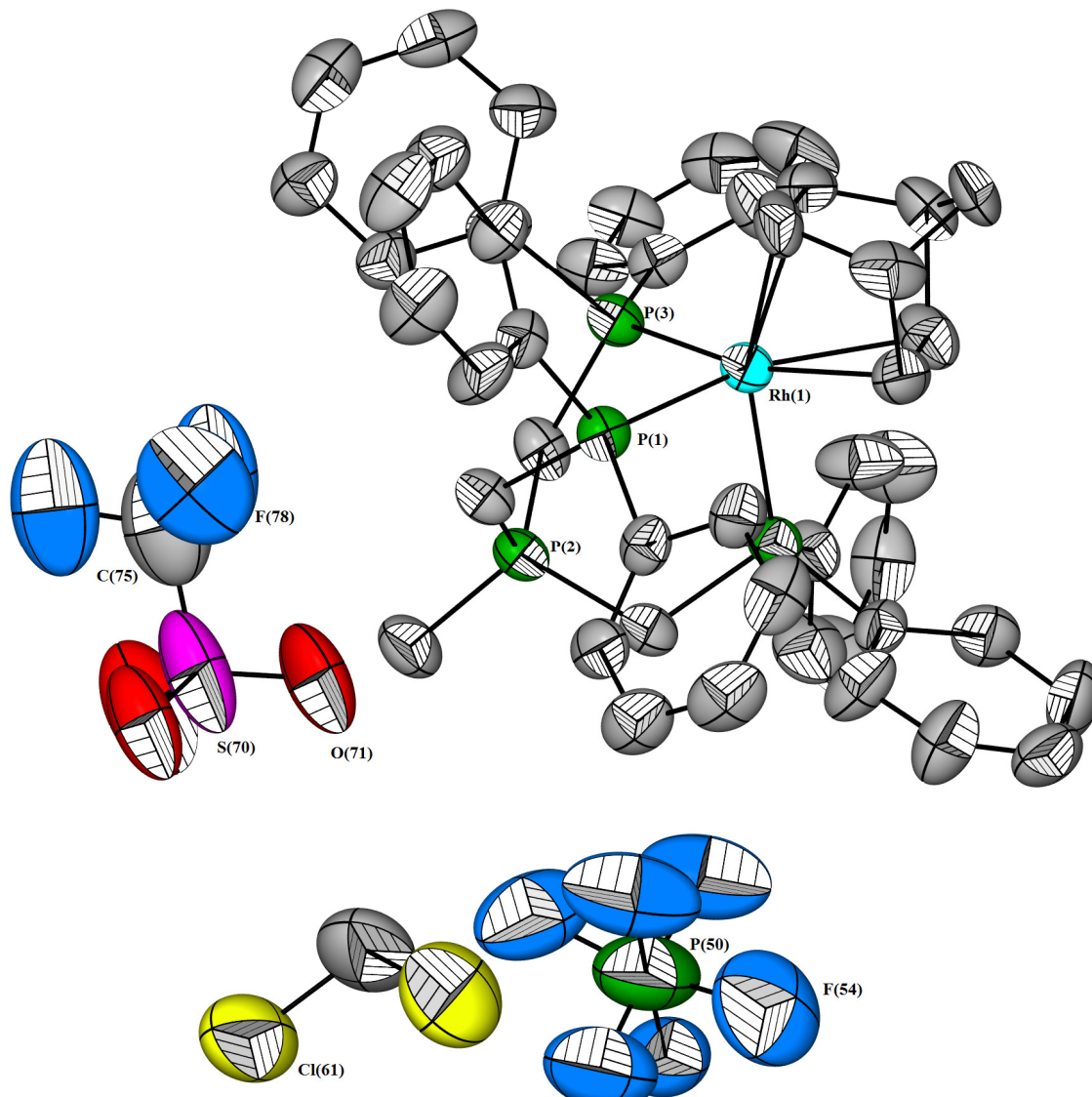


Table A-3. Crystal data and structure refinement for- JBB_JG_10429_A1_JG258.

Identification code	jbb	
Empirical formula	C ₄₉ H ₄₉ Cl ₂ F ₉ O ₃ P ₅ Rh S	
Formula weight	1217.60	
Temperature	296(2) K	
Wavelength	0.71073 Å	
Crystal system	Monoclinic	
Space group	P2(1)/c	
Unit cell dimensions	a = 16.005(4) Å	α = 90°.
	b = 19.384(5) Å	β = 113.121(3)°.
	c = 19.312(5) Å	γ = 90°.
Volume	5510(3) Å ³	
Z	4	
Density (calculated)	1.468 Mg/m ³	
Absorption coefficient	0.659 mm ⁻¹	
F(000)	2472	
Crystal size	0.18 x 0.04 x 0.03 mm ³	
Theta range for data collection	1.38 to 25.00°.	
Index ranges	-19 ≤ h ≤ 19, -23 ≤ k ≤ 23, -22 ≤ l ≤ 22	
Reflections collected	50109	
Independent reflections	9680 [R(int) = 0.1197]	
Completeness to theta = 25.00°	99.9 %	
Absorption correction	Semi-empirical from equivalents	
Max. and min. transmission	0.9805 and 0.8905	
Refinement method	Full-matrix least-squares on F ²	
Data / restraints / parameters	9680 / 131 / 631	
Goodness-of-fit on F ²	1.116	
Final R indices [I > 2σ(I)]	R1 = 0.1096, wR2 = 0.3039	
R indices (all data)	R1 = 0.1495, wR2 = 0.3368	
Largest diff. peak and hole	2.125 and -1.997 e.Å ⁻³	

Table A-4. Bond lengths [\AA] and angles [$^\circ$] for **JBB_JG_10429_A1_JG258**.

Rh(1)-C(2)	2.151(11)
Rh(1)-C(1)	2.185(11)
Rh(1)-C(5)	2.265(10)
Rh(1)-C(4)	2.266(10)
Rh(1)-P(4)	2.304(3)
Rh(1)-P(3)	2.381(3)
Rh(1)-P(1)	2.389(3)
P(1)-C(14)	1.838(9)
P(1)-C(8)	1.843(10)
P(1)-C(20)	1.847(9)
P(2)-C(47)	1.770(10)
P(2)-C(20)	1.787(10)
P(2)-C(22)	1.796(10)
P(2)-C(21)	1.805(10)
P(3)-C(29)	1.798(9)
P(3)-C(23)	1.835(10)
P(3)-C(22)	1.852(10)
P(4)-C(35)	1.798(10)
P(4)-C(41)	1.801(10)
P(4)-C(47)	1.833(9)
C(1)-C(2)	1.390(16)
C(1)-C(6)	1.530(16)
C(1)-H(1A)	0.9800
C(2)-C(3)	1.525(15)
C(2)-H(2A)	0.9800
C(3)-C(4)	1.501(15)
C(3)-C(7)	1.518(16)
C(3)-H(3A)	0.9800
C(4)-C(5)	1.423(16)
C(4)-H(4A)	0.9800
C(5)-C(6)	1.458(15)
C(5)-H(5A)	0.9800

C(6)-C(7)	1.519(17)
C(6)-H(6A)	0.9800
C(7)-H(7A)	0.9700
C(7)-H(7B)	0.9700
C(8)-C(13)	1.349(14)
C(8)-C(9)	1.422(14)
C(9)-C(10)	1.407(16)
C(9)-H(9A)	0.9300
C(10)-C(11)	1.338(18)
C(10)-H(10A)	0.9300
C(11)-C(12)	1.377(19)
C(11)-H(11A)	0.9300
C(12)-C(13)	1.349(15)
C(12)-H(12A)	0.9300
C(13)-H(13A)	0.9300
C(14)-C(19)	1.354(14)
C(14)-C(15)	1.391(14)
C(15)-C(16)	1.347(16)
C(15)-H(15A)	0.9300
C(16)-C(17)	1.453(18)
C(16)-H(16A)	0.9300
C(17)-C(18)	1.330(17)
C(17)-H(17A)	0.9300
C(18)-C(19)	1.392(14)
C(18)-H(18A)	0.9300
C(19)-H(19A)	0.9300
C(20)-H(20A)	0.9700
C(20)-H(20B)	0.9700
C(21)-H(21A)	0.9600
C(21)-H(21B)	0.9600
C(21)-H(21C)	0.9600
C(22)-H(22A)	0.9700
C(22)-H(22B)	0.9700
C(23)-C(28)	1.407(14)

C(23)-C(24)	1.407(14)
C(24)-C(25)	1.388(15)
C(24)-H(24A)	0.9300
C(25)-C(26)	1.336(17)
C(25)-H(25A)	0.9300
C(26)-C(27)	1.400(18)
C(26)-H(26A)	0.9300
C(27)-C(28)	1.385(16)
C(27)-H(27A)	0.9300
C(28)-H(28A)	0.9300
C(29)-C(30)	1.366(14)
C(29)-C(34)	1.411(15)
C(30)-C(31)	1.397(14)
C(30)-H(30A)	0.9300
C(31)-C(32)	1.303(16)
C(31)-H(31A)	0.9300
C(32)-C(33)	1.462(19)
C(32)-H(32A)	0.9300
C(33)-C(34)	1.408(17)
C(33)-H(33A)	0.9300
C(34)-H(34A)	0.9300
C(35)-C(36)	1.377(15)
C(35)-C(40)	1.387(16)
C(36)-C(37)	1.328(17)
C(36)-H(36A)	0.9300
C(37)-C(38)	1.331(19)
C(37)-H(37A)	0.9300
C(38)-C(39)	1.40(2)
C(38)-H(38A)	0.9300
C(39)-C(40)	1.356(18)
C(39)-H(39A)	0.9300
C(40)-H(40A)	0.9300
C(41)-C(42)	1.375(15)
C(41)-C(46)	1.387(15)

C(42)-C(43)	1.463(17)
C(42)-H(42A)	0.9300
C(43)-C(44)	1.370(18)
C(43)-H(43A)	0.9300
C(44)-C(45)	1.329(18)
C(44)-H(44A)	0.9300
C(45)-C(46)	1.374(16)
C(45)-H(45A)	0.9300
C(46)-H(46A)	0.9300
C(47)-H(47A)	0.9700
C(47)-H(47B)	0.9700
P(50)-F(53)	1.559(5)
P(50)-F(55)	1.563(5)
P(50)-F(51)	1.566(5)
P(50)-F(56)	1.577(5)
P(50)-F(54)	1.582(5)
P(50)-F(52)	1.583(5)
C(60)-Cl(62)	1.71(2)
C(60)-Cl(61)	1.74(2)
C(60)-H(60A)	0.9700
C(60)-H(60B)	0.9700
S(70)-O(73)	1.411(5)
S(70)-O(71)	1.426(5)
S(70)-O(72)	1.426(5)
S(70)-C(75)	1.786(5)
C(75)-F(78)	1.334(5)
C(75)-F(77)	1.335(5)
C(75)-F(76)	1.341(5)
C(2)-Rh(1)-C(1)	37.4(4)
C(2)-Rh(1)-C(5)	75.4(4)
C(1)-Rh(1)-C(5)	62.4(4)
C(2)-Rh(1)-C(4)	64.0(4)
C(1)-Rh(1)-C(4)	75.6(4)

C(5)-Rh(1)-C(4)	36.6(4)
C(2)-Rh(1)-P(4)	93.0(3)
C(1)-Rh(1)-P(4)	88.9(3)
C(5)-Rh(1)-P(4)	146.1(3)
C(4)-Rh(1)-P(4)	156.4(3)
C(2)-Rh(1)-P(3)	160.7(3)
C(1)-Rh(1)-P(3)	123.8(4)
C(5)-Rh(1)-P(3)	91.3(3)
C(4)-Rh(1)-P(3)	112.8(3)
P(4)-Rh(1)-P(3)	90.53(9)
C(2)-Rh(1)-P(1)	105.1(3)
C(1)-Rh(1)-P(1)	142.4(3)
C(5)-Rh(1)-P(1)	119.6(3)
C(4)-Rh(1)-P(1)	87.9(3)
P(4)-Rh(1)-P(1)	94.03(9)
P(3)-Rh(1)-P(1)	93.60(9)
C(14)-P(1)-C(8)	101.3(4)
C(14)-P(1)-C(20)	98.4(4)
C(8)-P(1)-C(20)	103.9(5)
C(14)-P(1)-Rh(1)	123.1(3)
C(8)-P(1)-Rh(1)	116.4(3)
C(20)-P(1)-Rh(1)	110.9(3)
C(47)-P(2)-C(20)	108.2(5)
C(47)-P(2)-C(22)	107.9(5)
C(20)-P(2)-C(22)	112.5(5)
C(47)-P(2)-C(21)	110.4(5)
C(20)-P(2)-C(21)	109.7(5)
C(22)-P(2)-C(21)	108.2(5)
C(29)-P(3)-C(23)	99.3(4)
C(29)-P(3)-C(22)	100.5(5)
C(23)-P(3)-C(22)	102.5(5)
C(29)-P(3)-Rh(1)	122.8(3)
C(23)-P(3)-Rh(1)	118.8(3)
C(22)-P(3)-Rh(1)	109.8(3)

C(35)-P(4)-C(41)	102.5(5)
C(35)-P(4)-C(47)	102.9(5)
C(41)-P(4)-C(47)	102.8(5)
C(35)-P(4)-Rh(1)	119.5(4)
C(41)-P(4)-Rh(1)	115.3(3)
C(47)-P(4)-Rh(1)	111.9(3)
C(2)-C(1)-C(6)	106.2(10)
C(2)-C(1)-Rh(1)	70.0(6)
C(6)-C(1)-Rh(1)	98.9(7)
C(2)-C(1)-H(1A)	122.9
C(6)-C(1)-H(1A)	122.9
Rh(1)-C(1)-H(1A)	122.9
C(1)-C(2)-C(3)	104.9(10)
C(1)-C(2)-Rh(1)	72.6(7)
C(3)-C(2)-Rh(1)	99.3(7)
C(1)-C(2)-H(2A)	122.7
C(3)-C(2)-H(2A)	122.7
Rh(1)-C(2)-H(2A)	122.7
C(4)-C(3)-C(7)	102.5(10)
C(4)-C(3)-C(2)	101.4(8)
C(7)-C(3)-C(2)	101.0(10)
C(4)-C(3)-H(3A)	116.5
C(7)-C(3)-H(3A)	116.5
C(2)-C(3)-H(3A)	116.5
C(5)-C(4)-C(3)	103.9(9)
C(5)-C(4)-Rh(1)	71.6(6)
C(3)-C(4)-Rh(1)	95.3(6)
C(5)-C(4)-H(4A)	124.1
C(3)-C(4)-H(4A)	124.1
Rh(1)-C(4)-H(4A)	124.1
C(4)-C(5)-C(6)	106.9(10)
C(4)-C(5)-Rh(1)	71.8(6)
C(6)-C(5)-Rh(1)	97.8(7)
C(4)-C(5)-H(5A)	122.6

C(6)-C(5)-H(5A)	122.6
Rh(1)-C(5)-H(5A)	122.6
C(5)-C(6)-C(7)	103.3(10)
C(5)-C(6)-C(1)	100.9(9)
C(7)-C(6)-C(1)	99.6(10)
C(5)-C(6)-H(6A)	116.8
C(7)-C(6)-H(6A)	116.8
C(1)-C(6)-H(6A)	116.8
C(3)-C(7)-C(6)	93.3(8)
C(3)-C(7)-H(7A)	113.0
C(6)-C(7)-H(7A)	113.0
C(3)-C(7)-H(7B)	113.0
C(6)-C(7)-H(7B)	113.0
H(7A)-C(7)-H(7B)	110.4
C(13)-C(8)-C(9)	118.5(10)
C(13)-C(8)-P(1)	127.2(8)
C(9)-C(8)-P(1)	114.3(8)
C(10)-C(9)-C(8)	119.0(11)
C(10)-C(9)-H(9A)	120.5
C(8)-C(9)-H(9A)	120.5
C(11)-C(10)-C(9)	120.3(12)
C(11)-C(10)-H(10A)	119.9
C(9)-C(10)-H(10A)	119.9
C(10)-C(11)-C(12)	119.2(11)
C(10)-C(11)-H(11A)	120.4
C(12)-C(11)-H(11A)	120.4
C(13)-C(12)-C(11)	122.2(13)
C(13)-C(12)-H(12A)	118.9
C(11)-C(12)-H(12A)	118.9
C(12)-C(13)-C(8)	120.8(12)
C(12)-C(13)-H(13A)	119.6
C(8)-C(13)-H(13A)	119.6
C(19)-C(14)-C(15)	118.0(9)
C(19)-C(14)-P(1)	119.9(8)

C(15)-C(14)-P(1)	122.1(8)
C(16)-C(15)-C(14)	123.1(11)
C(16)-C(15)-H(15A)	118.5
C(14)-C(15)-H(15A)	118.5
C(15)-C(16)-C(17)	117.3(12)
C(15)-C(16)-H(16A)	121.4
C(17)-C(16)-H(16A)	121.4
C(18)-C(17)-C(16)	119.6(12)
C(18)-C(17)-H(17A)	120.2
C(16)-C(17)-H(17A)	120.2
C(17)-C(18)-C(19)	120.8(12)
C(17)-C(18)-H(18A)	119.6
C(19)-C(18)-H(18A)	119.6
C(14)-C(19)-C(18)	121.2(11)
C(14)-C(19)-H(19A)	119.4
C(18)-C(19)-H(19A)	119.4
P(2)-C(20)-P(1)	115.3(5)
P(2)-C(20)-H(20A)	108.5
P(1)-C(20)-H(20A)	108.5
P(2)-C(20)-H(20B)	108.5
P(1)-C(20)-H(20B)	108.5
H(20A)-C(20)-H(20B)	107.5
P(2)-C(21)-H(21A)	109.5
P(2)-C(21)-H(21B)	109.5
H(21A)-C(21)-H(21B)	109.5
P(2)-C(21)-H(21C)	109.5
H(21A)-C(21)-H(21C)	109.5
H(21B)-C(21)-H(21C)	109.5
P(2)-C(22)-P(3)	115.1(5)
P(2)-C(22)-H(22A)	108.5
P(3)-C(22)-H(22A)	108.5
P(2)-C(22)-H(22B)	108.5
P(3)-C(22)-H(22B)	108.5
H(22A)-C(22)-H(22B)	107.5

C(28)-C(23)-C(24)	117.7(10)
C(28)-C(23)-P(3)	118.1(8)
C(24)-C(23)-P(3)	124.2(8)
C(25)-C(24)-C(23)	120.1(11)
C(25)-C(24)-H(24A)	120.0
C(23)-C(24)-H(24A)	120.0
C(26)-C(25)-C(24)	122.9(12)
C(26)-C(25)-H(25A)	118.5
C(24)-C(25)-H(25A)	118.5
C(25)-C(26)-C(27)	117.4(12)
C(25)-C(26)-H(26A)	121.3
C(27)-C(26)-H(26A)	121.3
C(28)-C(27)-C(26)	122.3(12)
C(28)-C(27)-H(27A)	118.8
C(26)-C(27)-H(27A)	118.8
C(27)-C(28)-C(23)	119.3(11)
C(27)-C(28)-H(28A)	120.4
C(23)-C(28)-H(28A)	120.4
C(30)-C(29)-C(34)	117.8(9)
C(30)-C(29)-P(3)	123.1(8)
C(34)-C(29)-P(3)	119.1(8)
C(29)-C(30)-C(31)	121.6(11)
C(29)-C(30)-H(30A)	119.2
C(31)-C(30)-H(30A)	119.2
C(32)-C(31)-C(30)	122.0(12)
C(32)-C(31)-H(31A)	119.0
C(30)-C(31)-H(31A)	119.0
C(31)-C(32)-C(33)	120.4(11)
C(31)-C(32)-H(32A)	119.8
C(33)-C(32)-H(32A)	119.8
C(34)-C(33)-C(32)	116.7(12)
C(34)-C(33)-H(33A)	121.6
C(32)-C(33)-H(33A)	121.6
C(33)-C(34)-C(29)	121.5(12)

C(33)-C(34)-H(34A)	119.3
C(29)-C(34)-H(34A)	119.3
C(36)-C(35)-C(40)	113.3(10)
C(36)-C(35)-P(4)	122.3(8)
C(40)-C(35)-P(4)	124.0(9)
C(37)-C(36)-C(35)	124.0(12)
C(37)-C(36)-H(36A)	118.0
C(35)-C(36)-H(36A)	118.0
C(36)-C(37)-C(38)	121.0(14)
C(36)-C(37)-H(37A)	119.5
C(38)-C(37)-H(37A)	119.5
C(37)-C(38)-C(39)	119.6(12)
C(37)-C(38)-H(38A)	120.2
C(39)-C(38)-H(38A)	120.2
C(40)-C(39)-C(38)	117.0(13)
C(40)-C(39)-H(39A)	121.5
C(38)-C(39)-H(39A)	121.5
C(39)-C(40)-C(35)	124.7(14)
C(39)-C(40)-H(40A)	117.6
C(35)-C(40)-H(40A)	117.6
C(42)-C(41)-C(46)	118.6(10)
C(42)-C(41)-P(4)	119.5(8)
C(46)-C(41)-P(4)	122.0(8)
C(41)-C(42)-C(43)	119.0(11)
C(41)-C(42)-H(42A)	120.5
C(43)-C(42)-H(42A)	120.5
C(44)-C(43)-C(42)	119.1(11)
C(44)-C(43)-H(43A)	120.5
C(42)-C(43)-H(43A)	120.5
C(45)-C(44)-C(43)	120.0(12)
C(45)-C(44)-H(44A)	120.0
C(43)-C(44)-H(44A)	120.0
C(44)-C(45)-C(46)	122.1(13)
C(44)-C(45)-H(45A)	119.0

C(46)-C(45)-H(45A)	119.0
C(45)-C(46)-C(41)	120.8(12)
C(45)-C(46)-H(46A)	119.6
C(41)-C(46)-H(46A)	119.6
P(2)-C(47)-P(4)	113.9(5)
P(2)-C(47)-H(47A)	108.8
P(4)-C(47)-H(47A)	108.8
P(2)-C(47)-H(47B)	108.8
P(4)-C(47)-H(47B)	108.8
H(47A)-C(47)-H(47B)	107.7
F(53)-P(50)-F(55)	102.9(7)
F(53)-P(50)-F(51)	86.1(8)
F(55)-P(50)-F(51)	89.9(7)
F(53)-P(50)-F(56)	99.4(8)
F(55)-P(50)-F(56)	93.0(7)
F(51)-P(50)-F(56)	173.0(9)
F(53)-P(50)-F(54)	168.0(8)
F(55)-P(50)-F(54)	88.2(7)
F(51)-P(50)-F(54)	89.3(9)
F(56)-P(50)-F(54)	84.4(8)
F(53)-P(50)-F(52)	81.0(8)
F(55)-P(50)-F(52)	175.1(8)
F(51)-P(50)-F(52)	93.3(7)
F(56)-P(50)-F(52)	83.3(7)
F(54)-P(50)-F(52)	88.1(9)
Cl(62)-C(60)-Cl(61)	108.9(11)
Cl(62)-C(60)-H(60A)	109.9
Cl(61)-C(60)-H(60A)	109.9
Cl(62)-C(60)-H(60B)	109.9
Cl(61)-C(60)-H(60B)	109.9
H(60A)-C(60)-H(60B)	108.3
O(73)-S(70)-O(71)	112.4(7)
O(73)-S(70)-O(72)	111.6(7)
O(71)-S(70)-O(72)	115.5(8)

O(73)-S(70)-C(75)	106.3(4)
O(71)-S(70)-C(75)	104.9(4)
O(72)-S(70)-C(75)	105.2(4)
F(78)-C(75)-F(77)	102.9(11)
F(78)-C(75)-F(76)	114.6(10)
F(77)-C(75)-F(76)	109.1(9)
F(78)-C(75)-S(70)	110.0(5)
F(77)-C(75)-S(70)	110.5(5)
F(76)-C(75)-S(70)	109.6(5)

A-3 X-ray structure of Ligand X

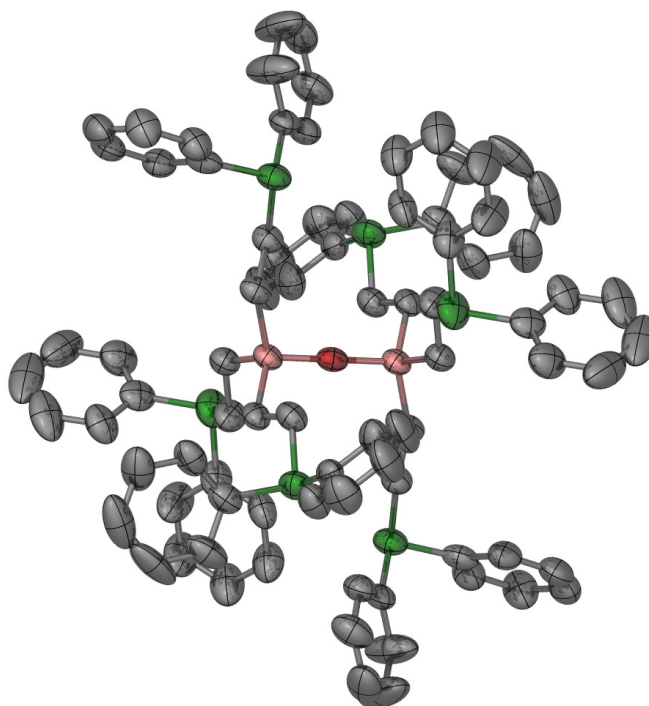


Table A-5. Crystal data and structure refinement for- jb08.

Identification code	jb08	
Empirical formula	C101.50 H104 O2.50 P6 Si2	
Formula weight	1605.85	
Temperature	110(2) K	
Wavelength	1.54178 Å	
Crystal system	Monoclinic	
Space group	C2/c	
Unit cell dimensions	a = 29.936(6) Å	$\alpha = 90^\circ$.
	b = 8.832(2) Å	$\beta = 93.540(7)^\circ$.
	c = 32.871(7) Å	$\gamma = 90^\circ$.
Volume	8674(3) Å ³	
Z	4	
Density (calculated)	1.230 Mg/m ³	
Absorption coefficient	1.806 mm ⁻¹	
F(000)	3404	
Crystal size	0.20 x 0.10 x 0.01 mm ³	
Theta range for data collection	2.69 to 60.00°.	
Index ranges	-33 ≤ h ≤ 33, -9 ≤ k ≤ 9, -36 ≤ l ≤ 36	
Reflections collected	45841	
Independent reflections	6410 [R(int) = 0.1193]	
Completeness to theta = 60.00°	99.5 %	
Absorption correction	Semi-empirical from equivalents	
Max. and min. transmission	0.9822 and 0.7140	
Refinement method	Full-matrix least-squares on F ²	
Data / restraints / parameters	6410 / 0 / 433	
Goodness-of-fit on F ²	1.031	
Final R indices [I > 2σ(I)]	R1 = 0.0605, wR2 = 0.1124	
R indices (all data)	R1 = 0.1209, wR2 = 0.1237	
Largest diff. peak and hole	0.240 and -0.196 e.Å ⁻³	

Table A-6. Bond lengths [Å] and angles [°] for jb08.

O(2)-P(1)	1.178(13)
O(3)-P(2)	1.240(10)
O(4)-P(3)	1.23(2)
Si(1)-O(1)	1.6321(12)
Si(1)-C(18)	1.866(4)
Si(1)-C(6)	1.868(4)
Si(1)-C(7)	1.871(4)
P(1)-C(4)	1.825(5)
P(1)-C(29)	1.840(5)
P(1)-C(5)	1.848(4)
P(2)-C(9)	1.821(5)
P(2)-C(21)	1.824(5)
P(2)-C(8)	1.851(4)
P(3)-C(35)	1.823(5)
P(3)-C(16)	1.829(5)
P(3)-C(17)	1.839(4)
O(1)-Si(1)#1	1.6321(12)
C(1)-C(2)	1.358(7)
C(1)-C(28)	1.380(6)
C(1)-H(1)	0.9500
C(2)-C(3)	1.382(7)
C(2)-H(2)	0.9500
C(3)-C(4)	1.391(6)
C(3)-H(3)	0.9500
C(4)-C(27)	1.374(6)
C(5)-C(6)	1.540(5)
C(5)-H(5A)	0.9900
C(5)-H(5B)	0.9900
C(6)-H(6A)	0.9900
C(6)-H(6B)	0.9900
C(7)-C(8)	1.536(5)
C(7)-H(7A)	0.9900

C(7)-H(7B)	0.9900
C(8)-H(8A)	0.9900
C(8)-H(8B)	0.9900
C(9)-C(20)	1.378(5)
C(9)-C(10)	1.392(6)
C(10)-C(11)	1.374(6)
C(10)-H(10)	0.9500
C(11)-C(12)	1.379(6)
C(11)-H(11)	0.9500
C(12)-C(19)	1.381(6)
C(12)-H(12)	0.9500
C(13)-C(14)	1.362(7)
C(13)-C(42)	1.362(7)
C(13)-H(13)	0.9500
C(14)-C(15)	1.414(6)
C(14)-H(14)	0.9500
C(15)-C(16)	1.374(6)
C(15)-H(15)	0.9500
C(16)-C(41)	1.381(6)
C(17)-C(18)	1.531(5)
C(17)-H(17A)	0.9900
C(17)-H(17B)	0.9900
C(18)-H(18A)	0.9900
C(18)-H(18B)	0.9900
C(19)-C(20)	1.384(6)
C(19)-H(19)	0.9500
C(20)-H(20)	0.9500
C(21)-C(26)	1.355(6)
C(21)-C(22)	1.357(6)
C(22)-C(23)	1.386(7)
C(22)-H(22)	0.9500
C(23)-C(24)	1.370(8)
C(23)-H(23)	0.9500
C(24)-C(25)	1.357(7)

C(24)-H(24)	0.9500
C(25)-C(26)	1.388(6)
C(25)-H(25)	0.9500
C(26)-H(26)	0.9500
C(27)-C(28)	1.386(6)
C(27)-H(27)	0.9500
C(28)-H(28)	0.9500
C(29)-C(34)	1.367(6)
C(29)-C(30)	1.382(6)
C(30)-C(31)	1.408(8)
C(30)-H(30)	0.9500
C(31)-C(32)	1.390(9)
C(31)-H(31)	0.9500
C(32)-C(33)	1.357(9)
C(32)-H(32)	0.9500
C(33)-C(34)	1.358(7)
C(33)-H(33)	0.9500
C(34)-H(34)	0.9500
C(35)-C(36)	1.377(6)
C(35)-C(40)	1.386(6)
C(36)-C(37)	1.373(6)
C(36)-H(36)	0.9500
C(37)-C(38)	1.368(8)
C(37)-H(37)	0.9500
C(38)-C(39)	1.389(8)
C(38)-H(38)	0.9500
C(39)-C(40)	1.411(8)
C(39)-H(39)	0.9500
C(40)-H(40)	0.9500
C(41)-C(42)	1.392(6)
C(41)-H(41)	0.9500
C(42)-H(42)	0.9500
O(1)-Si(1)-C(18)	106.91(14)

O(1)-Si(1)-C(6)	107.88(14)
C(18)-Si(1)-C(6)	111.84(18)
O(1)-Si(1)-C(7)	108.53(14)
C(18)-Si(1)-C(7)	110.78(18)
C(6)-Si(1)-C(7)	110.72(19)
O(2)-P(1)-C(4)	111.7(6)
O(2)-P(1)-C(29)	121.9(6)
C(4)-P(1)-C(29)	102.5(2)
O(2)-P(1)-C(5)	111.5(6)
C(4)-P(1)-C(5)	102.7(2)
C(29)-P(1)-C(5)	104.6(2)
O(3)-P(2)-C(9)	111.5(5)
O(3)-P(2)-C(21)	117.2(5)
C(9)-P(2)-C(21)	99.8(2)
O(3)-P(2)-C(8)	117.6(5)
C(9)-P(2)-C(8)	105.33(19)
C(21)-P(2)-C(8)	103.25(19)
O(4)-P(3)-C(35)	116.8(9)
O(4)-P(3)-C(16)	113.1(10)
C(35)-P(3)-C(16)	101.1(2)
O(4)-P(3)-C(17)	116.6(10)
C(35)-P(3)-C(17)	103.3(2)
C(16)-P(3)-C(17)	103.9(2)
Si(1)#1-O(1)-Si(1)	180.00(7)
C(2)-C(1)-C(28)	119.1(5)
C(2)-C(1)-H(1)	120.5
C(28)-C(1)-H(1)	120.5
C(1)-C(2)-C(3)	121.6(5)
C(1)-C(2)-H(2)	119.2
C(3)-C(2)-H(2)	119.2
C(2)-C(3)-C(4)	120.7(5)
C(2)-C(3)-H(3)	119.6
C(4)-C(3)-H(3)	119.6
C(27)-C(4)-C(3)	116.7(4)

C(27)-C(4)-P(1)	120.8(4)
C(3)-C(4)-P(1)	122.5(4)
C(6)-C(5)-P(1)	112.2(3)
C(6)-C(5)-H(5A)	109.2
P(1)-C(5)-H(5A)	109.2
C(6)-C(5)-H(5B)	109.2
P(1)-C(5)-H(5B)	109.2
H(5A)-C(5)-H(5B)	107.9
C(5)-C(6)-Si(1)	114.7(3)
C(5)-C(6)-H(6A)	108.6
Si(1)-C(6)-H(6A)	108.6
C(5)-C(6)-H(6B)	108.6
Si(1)-C(6)-H(6B)	108.6
H(6A)-C(6)-H(6B)	107.6
C(8)-C(7)-Si(1)	114.9(3)
C(8)-C(7)-H(7A)	108.5
Si(1)-C(7)-H(7A)	108.5
C(8)-C(7)-H(7B)	108.5
Si(1)-C(7)-H(7B)	108.5
H(7A)-C(7)-H(7B)	107.5
C(7)-C(8)-P(2)	111.9(3)
C(7)-C(8)-H(8A)	109.2
P(2)-C(8)-H(8A)	109.2
C(7)-C(8)-H(8B)	109.2
P(2)-C(8)-H(8B)	109.2
H(8A)-C(8)-H(8B)	107.9
C(20)-C(9)-C(10)	118.0(4)
C(20)-C(9)-P(2)	119.2(4)
C(10)-C(9)-P(2)	122.8(3)
C(11)-C(10)-C(9)	121.0(4)
C(11)-C(10)-H(10)	119.5
C(9)-C(10)-H(10)	119.5
C(10)-C(11)-C(12)	121.0(5)
C(10)-C(11)-H(11)	119.5

C(12)-C(11)-H(11)	119.5
C(11)-C(12)-C(19)	118.3(5)
C(11)-C(12)-H(12)	120.8
C(19)-C(12)-H(12)	120.8
C(14)-C(13)-C(42)	120.6(5)
C(14)-C(13)-H(13)	119.7
C(42)-C(13)-H(13)	119.7
C(13)-C(14)-C(15)	119.3(5)
C(13)-C(14)-H(14)	120.4
C(15)-C(14)-H(14)	120.4
C(16)-C(15)-C(14)	121.2(4)
C(16)-C(15)-H(15)	119.4
C(14)-C(15)-H(15)	119.4
C(15)-C(16)-C(41)	117.4(4)
C(15)-C(16)-P(3)	120.7(3)
C(41)-C(16)-P(3)	121.7(4)
C(18)-C(17)-P(3)	112.3(3)
C(18)-C(17)-H(17A)	109.1
P(3)-C(17)-H(17A)	109.1
C(18)-C(17)-H(17B)	109.1
P(3)-C(17)-H(17B)	109.1
H(17A)-C(17)-H(17B)	107.9
C(17)-C(18)-Si(1)	115.1(3)
C(17)-C(18)-H(18A)	108.5
Si(1)-C(18)-H(18A)	108.5
C(17)-C(18)-H(18B)	108.5
Si(1)-C(18)-H(18B)	108.5
H(18A)-C(18)-H(18B)	107.5
C(12)-C(19)-C(20)	120.8(4)
C(12)-C(19)-H(19)	119.6
C(20)-C(19)-H(19)	119.6
C(9)-C(20)-C(19)	120.8(5)
C(9)-C(20)-H(20)	119.6
C(19)-C(20)-H(20)	119.6

C(26)-C(21)-C(22)	117.9(5)
C(26)-C(21)-P(2)	122.8(3)
C(22)-C(21)-P(2)	119.2(4)
C(21)-C(22)-C(23)	121.0(5)
C(21)-C(22)-H(22)	119.5
C(23)-C(22)-H(22)	119.5
C(24)-C(23)-C(22)	121.2(6)
C(24)-C(23)-H(23)	119.4
C(22)-C(23)-H(23)	119.4
C(25)-C(24)-C(23)	117.3(5)
C(25)-C(24)-H(24)	121.4
C(23)-C(24)-H(24)	121.4
C(24)-C(25)-C(26)	121.3(5)
C(24)-C(25)-H(25)	119.3
C(26)-C(25)-H(25)	119.3
C(21)-C(26)-C(25)	121.2(4)
C(21)-C(26)-H(26)	119.4
C(25)-C(26)-H(26)	119.4
C(4)-C(27)-C(28)	122.9(4)
C(4)-C(27)-H(27)	118.6
C(28)-C(27)-H(27)	118.6
C(1)-C(28)-C(27)	119.1(5)
C(1)-C(28)-H(28)	120.4
C(27)-C(28)-H(28)	120.4
C(34)-C(29)-C(30)	120.2(5)
C(34)-C(29)-P(1)	123.2(4)
C(30)-C(29)-P(1)	116.4(4)
C(29)-C(30)-C(31)	118.7(6)
C(29)-C(30)-H(30)	120.6
C(31)-C(30)-H(30)	120.6
C(32)-C(31)-C(30)	119.1(7)
C(32)-C(31)-H(31)	120.5
C(30)-C(31)-H(31)	120.5
C(33)-C(32)-C(31)	120.7(8)

C(33)-C(32)-H(32)	119.7
C(31)-C(32)-H(32)	119.7
C(32)-C(33)-C(34)	120.1(7)
C(32)-C(33)-H(33)	119.9
C(34)-C(33)-H(33)	119.9
C(33)-C(34)-C(29)	121.2(6)
C(33)-C(34)-H(34)	119.4
C(29)-C(34)-H(34)	119.4
C(36)-C(35)-C(40)	118.3(5)
C(36)-C(35)-P(3)	124.0(4)
C(40)-C(35)-P(3)	117.7(4)
C(37)-C(36)-C(35)	123.1(5)
C(37)-C(36)-H(36)	118.5
C(35)-C(36)-H(36)	118.5
C(38)-C(37)-C(36)	119.2(6)
C(38)-C(37)-H(37)	120.4
C(36)-C(37)-H(37)	120.4
C(37)-C(38)-C(39)	119.8(6)
C(37)-C(38)-H(38)	120.1
C(39)-C(38)-H(38)	120.1
C(38)-C(39)-C(40)	120.4(6)
C(38)-C(39)-H(39)	119.8
C(40)-C(39)-H(39)	119.8
C(35)-C(40)-C(39)	119.3(6)
C(35)-C(40)-H(40)	120.4
C(39)-C(40)-H(40)	120.4
C(16)-C(41)-C(42)	121.8(5)
C(16)-C(41)-H(41)	119.1
C(42)-C(41)-H(41)	119.1
C(13)-C(42)-C(41)	119.6(5)
C(13)-C(42)-H(42)	120.2
C(41)-C(42)-H(42)	120.2

A-4 X-ray structure of Rhodium complex X

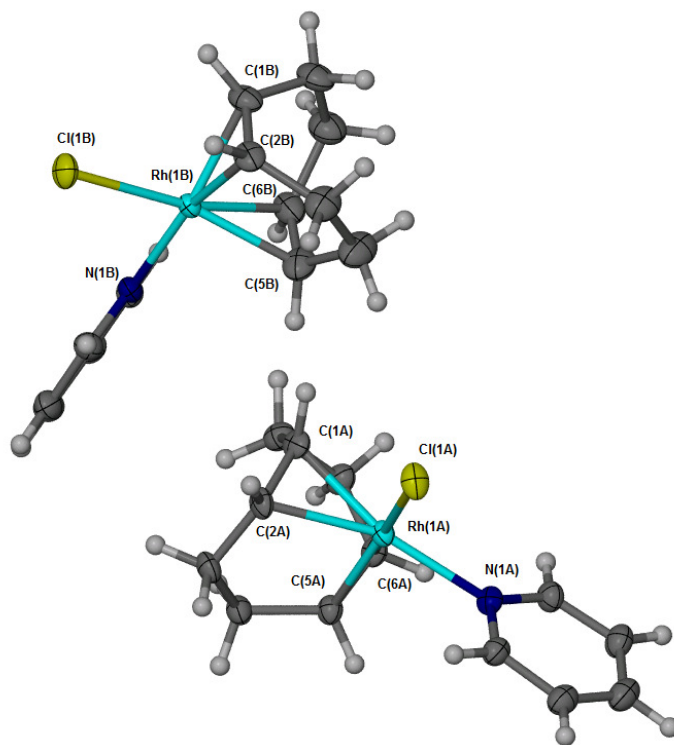


Table A-7. Crystal data and structure refinement for- JB03A.

Identification code	jb03a	
Empirical formula	C ₁₃ H ₁₇ Cl N Rh	
Formula weight	325.64	
Temperature	150(2) K	
Wavelength	0.71073 Å	
Crystal system	Monoclinic	
Space group	P2(1)/c	
Unit cell dimensions	a = 17.177(5) Å	α = 90°.
	b = 11.143(3) Å	β = 113.714(4)°.
	c = 13.994(4) Å	γ = 90°.
Volume	2452.2(12) Å ³	
Z	8	
Density (calculated)	1.764 Mg/m ³	
Absorption coefficient	1.581 mm ⁻¹	
F(000)	1312	

Crystal size	0.32 x 0.22 x 0.13 mm ³
Theta range for data collection	2.24 to 24.99°.
Index ranges	-20<=h<=20, -13<=k<=13, -16<=l<=16
Reflections collected	31006
Independent reflections	3929 [R(int) = 0.0277]
Completeness to theta = 24.99°	90.9 %
Absorption correction	Semi-empirical from equivalents
Max. and min. transmission	0.8208 and 0.6316
Refinement method	Full-matrix least-squares on F ²
Data / restraints / parameters	3929 / 144 / 290
Goodness-of-fit on F ²	1.012
Final R indices [I>2sigma(I)]	R1 = 0.0686, wR2 = 0.1495
R indices (all data)	R1 = 0.0701, wR2 = 0.1503
Extinction coefficient	0.00026(13)
Largest diff. peak and hole	3.754 and -1.914 e.Å ⁻³

Table A-8. Bond lengths [Å] and angles [°] for JB03A.

Rh(1A)-C(6A)	2.102(9)
Rh(1A)-C(5A)	2.107(10)
Rh(1A)-N(1A)	2.125(8)
Rh(1A)-C(2A)	2.133(9)
Rh(1A)-C(1A)	2.137(10)
Rh(1A)-Cl(1A)	2.377(2)
N(1A)-C(13A)	1.340(12)
N(1A)-C(9A)	1.348(13)
C(1A)-C(2A)	1.408(14)
C(1A)-C(8A)	1.503(14)
C(1A)-H(1A)	1.0000
C(2A)-C(3A)	1.477(14)
C(2A)-H(2A)	1.0000
C(3A)-C(4A)	1.526(13)

C(3A)-H(3A1)	0.9900
C(3A)-H(3A2)	0.9900
C(4A)-C(5A)	1.529(13)
C(4A)-H(4A1)	0.9900
C(4A)-H(4A2)	0.9900
C(5A)-C(6A)	1.398(14)
C(5A)-H(5A)	1.0000
C(6A)-C(7A)	1.522(14)
C(6A)-H(6A)	1.0000
C(7A)-C(8A)	1.533(13)
C(7A)-H(7A1)	0.9900
C(7A)-H(7A2)	0.9900
C(8A)-H(8A1)	0.9900
C(8A)-H(8A2)	0.9900
C(9A)-C(10A)	1.395(14)
C(9A)-H(9A)	0.9500
C(10A)-C(11A)	1.354(15)
C(10A)-H(10A)	0.9500
C(11A)-C(12A)	1.397(16)
C(11A)-H(11A)	0.9500
C(12A)-C(13A)	1.383(14)
C(12A)-H(12A)	0.9500
C(13A)-H(13A)	0.9500
Rh(1B)-C(5B)	2.102(11)
Rh(1B)-N(1B)	2.114(8)
Rh(1B)-C(6B)	2.119(10)
Rh(1B)-C(1B)	2.131(10)
Rh(1B)-C(2B)	2.131(10)
Rh(1B)-Cl(1B)	2.387(2)
N(1B)-C(13B)	1.340(12)
N(1B)-C(9B)	1.345(13)
C(1B)-C(2B)	1.413(15)
C(1B)-C(8B)	1.500(14)
C(1B)-H(1B)	1.0000

C(2B)-C(3B)	1.501(15)
C(2B)-H(2B)	1.0000
C(3B)-C(4B)	1.507(15)
C(3B)-H(3B1)	0.9900
C(3B)-H(3B2)	0.9900
C(4B)-C(5B)	1.522(15)
C(4B)-H(4B1)	0.9900
C(4B)-H(4B2)	0.9900
C(5B)-C(6B)	1.398(17)
C(5B)-H(5B)	1.0000
C(6B)-C(7B)	1.503(16)
C(6B)-H(6B)	1.0000
C(7B)-C(8B)	1.491(15)
C(7B)-H(7B1)	0.9900
C(7B)-H(7B2)	0.9900
C(8B)-H(8B1)	0.9900
C(8B)-H(8B2)	0.9900
C(9B)-C(10B)	1.364(14)
C(9B)-H(9B)	0.9500
C(10B)-C(11B)	1.382(15)
C(10B)-H(10B)	0.9500
C(11B)-C(12B)	1.397(16)
C(11B)-H(11B)	0.9500
C(12B)-C(13B)	1.354(14)
C(12B)-H(12B)	0.9500
C(13B)-H(13B)	0.9500
C(6A)-Rh(1A)-C(5A)	38.8(4)
C(6A)-Rh(1A)-N(1A)	91.9(3)
C(5A)-Rh(1A)-N(1A)	93.8(3)
C(6A)-Rh(1A)-C(2A)	98.0(4)
C(5A)-Rh(1A)-C(2A)	81.9(4)
N(1A)-Rh(1A)-C(2A)	157.8(4)
C(6A)-Rh(1A)-C(1A)	81.5(4)

C(5A)-Rh(1A)-C(1A)	90.4(4)
N(1A)-Rh(1A)-C(1A)	163.7(3)
C(2A)-Rh(1A)-C(1A)	38.5(4)
C(6A)-Rh(1A)-Cl(1A)	163.6(3)
C(5A)-Rh(1A)-Cl(1A)	157.7(3)
N(1A)-Rh(1A)-Cl(1A)	87.5(2)
C(2A)-Rh(1A)-Cl(1A)	88.4(3)
C(1A)-Rh(1A)-Cl(1A)	94.6(3)
C(13A)-N(1A)-C(9A)	117.9(9)
C(13A)-N(1A)-Rh(1A)	125.6(7)
C(9A)-N(1A)-Rh(1A)	116.5(6)
C(2A)-C(1A)-C(8A)	122.7(9)
C(2A)-C(1A)-Rh(1A)	70.6(6)
C(8A)-C(1A)-Rh(1A)	113.4(6)
C(2A)-C(1A)-H(1A)	114.3
C(8A)-C(1A)-H(1A)	114.3
Rh(1A)-C(1A)-H(1A)	114.3
C(1A)-C(2A)-C(3A)	126.1(9)
C(1A)-C(2A)-Rh(1A)	70.9(5)
C(3A)-C(2A)-Rh(1A)	110.1(7)
C(1A)-C(2A)-H(2A)	113.8
C(3A)-C(2A)-H(2A)	113.8
Rh(1A)-C(2A)-H(2A)	113.8
C(2A)-C(3A)-C(4A)	113.7(8)
C(2A)-C(3A)-H(3A1)	108.8
C(4A)-C(3A)-H(3A1)	108.8
C(2A)-C(3A)-H(3A2)	108.8
C(4A)-C(3A)-H(3A2)	108.8
H(3A1)-C(3A)-H(3A2)	107.7
C(3A)-C(4A)-C(5A)	111.7(8)
C(3A)-C(4A)-H(4A1)	109.3
C(5A)-C(4A)-H(4A1)	109.3
C(3A)-C(4A)-H(4A2)	109.3
C(5A)-C(4A)-H(4A2)	109.3

H(4A1)-C(4A)-H(4A2)	107.9
C(6A)-C(5A)-C(4A)	123.7(9)
C(6A)-C(5A)-Rh(1A)	70.4(6)
C(4A)-C(5A)-Rh(1A)	113.1(6)
C(6A)-C(5A)-H(5A)	114.0
C(4A)-C(5A)-H(5A)	114.0
Rh(1A)-C(5A)-H(5A)	114.0
C(5A)-C(6A)-C(7A)	125.8(9)
C(5A)-C(6A)-Rh(1A)	70.8(5)
C(7A)-C(6A)-Rh(1A)	111.4(6)
C(5A)-C(6A)-H(6A)	113.6
C(7A)-C(6A)-H(6A)	113.6
Rh(1A)-C(6A)-H(6A)	113.6
C(6A)-C(7A)-C(8A)	111.5(8)
C(6A)-C(7A)-H(7A1)	109.3
C(8A)-C(7A)-H(7A1)	109.3
C(6A)-C(7A)-H(7A2)	109.3
C(8A)-C(7A)-H(7A2)	109.3
H(7A1)-C(7A)-H(7A2)	108.0
C(1A)-C(8A)-C(7A)	112.4(8)
C(1A)-C(8A)-H(8A1)	109.1
C(7A)-C(8A)-H(8A1)	109.1
C(1A)-C(8A)-H(8A2)	109.1
C(7A)-C(8A)-H(8A2)	109.1
H(8A1)-C(8A)-H(8A2)	107.9
N(1A)-C(9A)-C(10A)	122.2(9)
N(1A)-C(9A)-H(9A)	118.9
C(10A)-C(9A)-H(9A)	118.9
C(11A)-C(10A)-C(9A)	119.1(10)
C(11A)-C(10A)-H(10A)	120.4
C(9A)-C(10A)-H(10A)	120.4
C(10A)-C(11A)-C(12A)	119.6(10)
C(10A)-C(11A)-H(11A)	120.2
C(12A)-C(11A)-H(11A)	120.2

C(11A)-C(12A)-C(13A)	118.2(10)
C(11A)-C(12A)-H(12A)	120.9
C(13A)-C(12A)-H(12A)	120.9
N(1A)-C(13A)-C(12A)	122.9(10)
N(1A)-C(13A)-H(13A)	118.6
C(12A)-C(13A)-H(13A)	118.6
C(5B)-Rh(1B)-N(1B)	91.4(4)
C(5B)-Rh(1B)-C(6B)	38.7(4)
N(1B)-Rh(1B)-C(6B)	90.2(4)
C(5B)-Rh(1B)-C(1B)	92.9(4)
N(1B)-Rh(1B)-C(1B)	161.7(4)
C(6B)-Rh(1B)-C(1B)	82.1(4)
C(5B)-Rh(1B)-C(2B)	82.8(4)
N(1B)-Rh(1B)-C(2B)	159.5(4)
C(6B)-Rh(1B)-C(2B)	97.1(4)
C(1B)-Rh(1B)-C(2B)	38.7(4)
C(5B)-Rh(1B)-Cl(1B)	159.0(3)
N(1B)-Rh(1B)-Cl(1B)	89.6(2)
C(6B)-Rh(1B)-Cl(1B)	162.4(3)
C(1B)-Rh(1B)-Cl(1B)	92.7(3)
C(2B)-Rh(1B)-Cl(1B)	89.1(3)
C(13B)-N(1B)-C(9B)	116.9(9)
C(13B)-N(1B)-Rh(1B)	126.9(7)
C(9B)-N(1B)-Rh(1B)	116.2(6)
C(2B)-C(1B)-C(8B)	122.9(10)
C(2B)-C(1B)-Rh(1B)	70.6(6)
C(8B)-C(1B)-Rh(1B)	112.0(7)
C(2B)-C(1B)-H(1B)	114.5
C(8B)-C(1B)-H(1B)	114.5
Rh(1B)-C(1B)-H(1B)	114.5
C(1B)-C(2B)-C(3B)	124.3(10)
C(1B)-C(2B)-Rh(1B)	70.6(6)
C(3B)-C(2B)-Rh(1B)	110.7(7)
C(1B)-C(2B)-H(2B)	114.4

C(3B)-C(2B)-H(2B)	114.4
Rh(1B)-C(2B)-H(2B)	114.4
C(2B)-C(3B)-C(4B)	114.8(9)
C(2B)-C(3B)-H(3B1)	108.6
C(4B)-C(3B)-H(3B1)	108.6
C(2B)-C(3B)-H(3B2)	108.6
C(4B)-C(3B)-H(3B2)	108.6
H(3B1)-C(3B)-H(3B2)	107.5
C(3B)-C(4B)-C(5B)	114.0(10)
C(3B)-C(4B)-H(4B1)	108.7
C(5B)-C(4B)-H(4B1)	108.7
C(3B)-C(4B)-H(4B2)	108.7
C(5B)-C(4B)-H(4B2)	108.7
H(4B1)-C(4B)-H(4B2)	107.6
C(6B)-C(5B)-C(4B)	121.4(11)
C(6B)-C(5B)-Rh(1B)	71.3(6)
C(4B)-C(5B)-Rh(1B)	112.9(7)
C(6B)-C(5B)-H(5B)	114.7
C(4B)-C(5B)-H(5B)	114.7
Rh(1B)-C(5B)-H(5B)	114.7
C(5B)-C(6B)-C(7B)	126.8(11)
C(5B)-C(6B)-Rh(1B)	70.0(6)
C(7B)-C(6B)-Rh(1B)	110.8(7)
C(5B)-C(6B)-H(6B)	113.6
C(7B)-C(6B)-H(6B)	113.6
Rh(1B)-C(6B)-H(6B)	113.6
C(8B)-C(7B)-C(6B)	114.1(10)
C(8B)-C(7B)-H(7B1)	108.7
C(6B)-C(7B)-H(7B1)	108.7
C(8B)-C(7B)-H(7B2)	108.7
C(6B)-C(7B)-H(7B2)	108.7
H(7B1)-C(7B)-H(7B2)	107.6
C(7B)-C(8B)-C(1B)	115.1(9)
C(7B)-C(8B)-H(8B1)	108.5

C(1B)-C(8B)-H(8B1)	108.5
C(7B)-C(8B)-H(8B2)	108.5
C(1B)-C(8B)-H(8B2)	108.5
H(8B1)-C(8B)-H(8B2)	107.5
N(1B)-C(9B)-C(10B)	122.8(9)
N(1B)-C(9B)-H(9B)	118.6
C(10B)-C(9B)-H(9B)	118.6
C(9B)-C(10B)-C(11B)	119.6(10)
C(9B)-C(10B)-H(10B)	120.2
C(11B)-C(10B)-H(10B)	120.2
C(10B)-C(11B)-C(12B)	117.9(10)
C(10B)-C(11B)-H(11B)	121.0
C(12B)-C(11B)-H(11B)	121.0
C(13B)-C(12B)-C(11B)	118.5(10)
C(13B)-C(12B)-H(12B)	120.8
C(11B)-C(12B)-H(12B)	120.7
N(1B)-C(13B)-C(12B)	124.2(10)
N(1B)-C(13B)-H(13B)	117.9
C(12B)-C(13B)-H(13B)	117.9

APPENDIX B

DFT CALCULATIONS

A-1 Computaional Details

Calculations were performed with the Gaussian 03^I suite of programs, using the density functional method. The hybrid exchange functional B3LYP¹¹⁰ set was used in combination with the 6-31G(d)¹¹² basis set for C, H, Si, P, O, and Cl. The Stuttgart/Dresden (sdd)¹¹¹ quasi-relativistic effective core potentials were used for Rh and Ir. B3LYP is a three parameter functional developed by Becke which combines the Becke gradient-corrected exchange functional and the Lee-Yang-Parr and Vosko-Wilk-Nusair correlation functionals with part of exact HF exchange energy. Geometry optimisations were carried out without any symmetry restrictions; the nature of the extrema (minimum) was verified with analytical frequency calculations. All free Gibbs energies have been zero-point energy (ZPE) and temperature corrected using unscaled density functional frequencies. Molecular structures were generated with Mercury 3.0.

^IGaussian 03, Revision B.04, M. J. Frisch, G. W. Trucks, H. B. Schlegel, G. E. Scuseria, M. A. Robb, J. R. Cheeseman, J. A. Montgomery, Jr. T. Vreven, K. N. Kudin, J. C. Burant, J. M. Millam, S. S. Iyengar, J. Tomasi, V. Barone, B. Mennucci, M. Cossi, G. Scalmani, N. Rega, G. A. Petersson, H. Nakatsuji, M. Hada, M. Ehara, K. Toyota, R. Fukuda, J. Hasegawa, M. Ishida, T. Nakajima, Y. Honda, O. Kitao, H. Nakai, M. X. Klene, X. Li, J. E. Knox, H. P. Hratchian, J. B. Cross, C. Adamo, J. Jaramillo, R. Gomperts, R. E. Stratmann, O. Yazyev, A. J. Austin, R. Cammi, C. Pomelli, J. W. Ochterski, P. Y. Ayala, K. Morokuma, G. A. Voth, P. Salvador, J. J. Dannenberg, V. G. Zakrzewski, S. Dapprich, A. D. Daniels, M. C. Strain, O. Farkas, D. K. Malick, A. D. Rabuck, K. Raghavachari, J. B. Foresman, J. V. Ortiz, Q. Cui, A. G. Baboul, S. Clifford, J. Cioslowski, B. B. Stefanov, G. Liu, A. Liashenko, P. Piskorz, I. Komaromi, R. L. Martin, D. J. Fox, T. Keith, M. A. Al-Laham, C. Y. Peng, A. Nanayakkara, M. Challacombe, P. M. W. Gill, B. Johnson, W. Chen, M. W. Wong, C. Gonzalez, J. A. Pople, Gaussian, Inc., Pittsburgh PA, **2003**.

A-2 Optimized Geometries

complex 48

Sum of electronic and thermal free energies = -3549.433630 ua

Number		Label	SybylType	Xfrac + ESD	Yfrac + ESD	Zfrac + ESD
1	Rh	Rh	0.0208	-0.0135	0.0706	
2	Cl	Cl	-0.0685	0.1301	2.6809	
3	Si	Si	0.1557	0.1041	-2.2897	
4	P	P.3	1.2646	-2.1402	-0.1733	
5	P	P.3	1.8760	1.4739	0.0327	
6	P	P.3	-2.2743	-0.8055	0.1991	
7	C	C.3	-1.3543	1.6280	0.0712	
8	H	H	-1.4891	2.0896	-0.9109	
9	H	H	-1.0030	2.3842	0.7714	
10	C	C.3	-2.6541	0.9697	0.5690	
11	H	H	-3.5834	1.3541	0.1319	
12	H	H	-2.7337	1.0590	1.6545	
13	C	C.3	1.0043	-1.5161	-2.9362	
14	H	H	0.5489	-1.8286	-3.8862	
15	H	H	2.0469	-1.2640	-3.1746	
16	C	C.3	1.3869	1.5249	-2.7072	
17	H	H	1.7760	1.4087	-3.7292	
18	H	H	0.8393	2.4763	-2.6905	
19	C	C.3	-1.3349	0.4575	-3.4285	
20	H	H	-1.9484	1.2905	-3.0672	
21	H	H	-0.9494	0.7397	-4.4185	
22	H	H	-1.9908	-0.4061	-3.5625	
23	C	C.3	0.9634	-2.6879	-1.9399	
24	H	H	1.6524	-3.4947	-2.2180	
25	H	H	-0.0394	-3.1268	-1.9270	
26	C	C.3	2.5447	1.5578	-1.7027	
27	H	H	3.2053	2.4231	-1.8314	
28	H	H	3.1696	0.6625	-1.8147	
29	C	C.3	1.4796	3.2317	0.4693	
30	C	C.2	1.0673	3.5248	1.7813	
31	C	C.2	1.5853	4.2821	-0.4532	
32	C	C.2	0.7845	4.8370	2.1580	
33	H	H	0.9455	2.7205	2.5006	
34	C	C.2	1.2969	5.5960	-0.0729	
35	H	H	1.8923	4.0929	-1.4761	
36	C	C.2	0.8996	5.8780	1.2332	
37	H	H	0.4680	5.0439	3.1769	
38	H	H	1.3873	6.3967	-0.8026	
39	H	H	0.6779	6.9001	1.5288	
40	C	C.3	3.3908	1.2212	1.0785	
41	C	C.2	4.6714	1.4708	0.5578	
42	C	C.2	3.2718	0.8729	2.4336	
43	C	C.2	5.8019	1.3816	1.3717	

44	H	H	4.8032	1.7444	-0.4831
45	C	C.2	4.4045	0.7965	3.2459
46	H	H	2.2934	0.6519	2.8478
47	C	C.2	5.6719	1.0513	2.7210
48	H	H	6.7834	1.5781	0.9477
49	H	H	4.2902	0.5314	4.2940
50	H	H	6.5520	0.9919	3.3564
51	C	C.3	-3.0278	-1.8520	1.5370
52	C	C.2	-3.5780	-3.1123	1.2486
53	C	C.2	-3.0553	-1.4003	2.8680
54	C	C.2	-4.1438	-3.8943	2.2557
55	H	H	-3.5829	-3.4902	0.2325
56	C	C.2	-3.6260	-2.1846	3.8720
57	H	H	-2.6024	-0.4534	3.1323
58	C	C.2	-4.1730	-3.4328	3.5722
59	H	H	-4.5659	-4.8640	2.0052
60	H	H	-3.6376	-1.8132	4.8934
61	H	H	-4.6187	-4.0395	4.3563
62	C	C.3	-3.2957	-1.3139	-1.2565
63	C	C.2	-4.4655	-0.6310	-1.6195
64	C	C.2	-2.9314	-2.4488	-1.9993
65	C	C.2	-5.2362	-1.0586	-2.7025
66	H	H	-4.7884	0.2399	-1.0591
67	C	C.2	-3.7058	-2.8852	-3.0751
68	H	H	-2.0367	-3.0027	-1.7322
69	C	C.2	-4.8591	-2.1850	-3.4349
70	H	H	-6.1353	-0.5101	-2.9705
71	H	H	-3.4043	-3.7672	-3.6339
72	H	H	-5.4598	-2.5162	-4.2775
73	C	C.3	0.7263	-3.6125	0.8096
74	C	C.2	0.9540	-4.9243	0.3561
75	C	C.2	0.1071	-3.4206	2.0529
76	C	C.2	0.5590	-6.0180	1.1250
77	H	H	1.4516	-5.0989	-0.5937
78	C	C.2	-0.2798	-4.5208	2.8247
79	H	H	-0.0689	-2.4119	2.4157
80	C	C.2	-0.0592	-5.8176	2.3630
81	H	H	0.7397	-7.0265	0.7613
82	H	H	-0.7664	-4.3545	3.7816
83	H	H	-0.3648	-6.6714	2.9626
84	C	C.3	3.1071	-2.2980	-0.0046
85	C	C.2	3.9718	-2.3415	-1.1095
86	C	C.2	3.6651	-2.3751	1.2826
87	C	C.2	5.3528	-2.4648	-0.9332
88	H	H	3.5795	-2.2929	-2.1199
89	C	C.2	5.0418	-2.5022	1.4573
90	H	H	3.0174	-2.3443	2.1538
91	C	C.2	5.8920	-2.5473	0.3498
92	H	H	6.0032	-2.5035	-1.8036
93	H	H	5.4510	-2.5615	2.4619
94	H	H	6.9654	-2.6464	0.4874

complex 49

Sum of electronic and thermal free energies = -3549.430825 ua

Number		Label	SybylType	Xfrac + ESD	Yfrac + ESD	Zfrac + ESD
1	Rh	Rh	-0.0113	-0.0300	0.0480	
2	Cl	Cl	-0.2424	-0.0298	2.6715	
3	Si	Si	0.1171	-0.0540	-2.2597	
4	P	P.3	-0.8534	2.2004	-0.2938	
5	P	P.3	2.4042	0.6023	-0.0366	
6	P	P.3	0.3287	-2.3867	-0.1038	
7	C	C.3	-2.0850	-0.5403	-0.1834	
8	H	H	-2.4194	-0.7593	0.8329	
9	H	H	-2.7070	0.2621	-0.5849	
10	H	H	-2.2545	-1.4210	-0.8078	
11	C	C.3	2.5943	1.4043	-1.7172	
12	C	C.3	1.8416	0.6283	-2.8215	
13	C	C.3	-1.1749	1.1821	-2.9358	
14	C	C.3	-0.9529	2.4916	-2.1498	
15	C	C.3	-0.0213	-1.8730	-2.8593	
16	H	H	-1.0761	-2.1760	-2.8767	
17	H	H	0.3643	-2.0085	-3.8792	
18	C	C.3	0.7741	-2.7670	-1.8807	
19	H	H	1.8464	-2.5447	-1.9565	
20	H	H	0.6620	-3.8342	-2.1033	
21	H	H	1.7247	1.2744	-3.7033	
22	H	H	2.4434	-0.2240	-3.1605	
23	H	H	2.1652	2.4065	-1.6008	
24	H	H	3.6534	1.5430	-1.9654	
25	H	H	-1.6918	3.2612	-2.3942	
26	H	H	0.0224	2.9088	-2.4271	
27	H	H	-1.0557	1.3777	-4.0104	
28	H	H	-2.1932	0.8070	-2.7858	
29	C	C.3	3.7917	-0.6481	-0.0459	
30	C	C.2	4.2563	-1.1692	1.1732	
31	C	C.2	4.4292	-1.0650	-1.2254	
32	C	C.2	5.3212	-2.0672	1.2116	
33	H	H	3.7939	-0.8614	2.1045	
34	C	C.2	5.4936	-1.9707	-1.1881	
35	H	H	4.1215	-0.6754	-2.1884	
36	C	C.2	5.9452	-2.4738	0.0304	
37	H	H	5.6600	-2.4522	2.1691	
38	H	H	5.9737	-2.2700	-2.1165	
39	H	H	6.7764	-3.1731	0.0614	
40	C	C.3	3.1589	1.8141	1.1432	
41	C	C.2	4.0604	2.8075	0.7308	
42	C	C.2	2.8849	1.6714	2.5134	
43	C	C.2	4.6777	3.6375	1.6677	
44	H	H	4.2950	2.9376	-0.3210	
45	C	C.2	3.5204	2.4910	3.4488	
46	H	H	2.1498	0.9415	2.8422	

47	C	C.2	4.4168	3.4753	3.0299
48	H	H	5.3704	4.4050	1.3318
49	H	H	3.3017	2.3646	4.5062
50	H	H	4.9075	4.1156	3.7586
51	C	C.3	0.0241	3.7033	0.3377
52	C	C.2	0.3616	3.7359	1.7008
53	C	C.2	0.2872	4.8321	-0.4537
54	C	C.2	0.9450	4.8743	2.2557
55	H	H	0.1718	2.8655	2.3232
56	C	C.2	0.8803	5.9670	0.1045
57	H	H	0.0181	4.8480	-1.5050
58	C	C.2	1.2083	5.9913	1.4600
59	H	H	1.2062	4.8812	3.3098
60	H	H	1.0768	6.8335	-0.5219
61	H	H	1.6664	6.8760	1.8945
62	C	C.3	-2.5522	2.5664	0.3680
63	C	C.2	-3.4836	3.3480	-0.3310
64	C	C.2	-2.8817	2.1086	1.6543
65	C	C.2	-4.7197	3.6611	0.2390
66	H	H	-3.2625	3.7272	-1.3229
67	C	C.2	-4.1144	2.4314	2.2227
68	H	H	-2.1798	1.4859	2.2021
69	C	C.2	-5.0382	3.2055	1.5183
70	H	H	-5.4302	4.2645	-0.3203
71	H	H	-4.3528	2.0663	3.2182
72	H	H	-5.9999	3.4508	1.9616
73	C	C.3	1.5774	-3.3039	0.9079
74	C	C.2	1.6740	-3.0168	2.2794
75	C	C.2	2.3367	-4.3572	0.3770
76	C	C.2	2.5002	-3.7848	3.1014
77	H	H	1.1077	-2.1875	2.6960
78	C	C.2	3.1716	-5.1135	1.2015
79	H	H	2.2796	-4.6035	-0.6785
80	C	C.2	3.2493	-4.8350	2.5669
81	H	H	2.5589	-3.5568	4.1627
82	H	H	3.7548	-5.9255	0.7748
83	H	H	3.8903	-5.4332	3.2097
84	C	C.3	-1.1481	-3.4444	0.2710
85	C	C.2	-1.6914	-4.3538	-0.6460
86	C	C.2	-1.7231	-3.3446	1.5496
87	C	C.2	-2.7802	-5.1558	-0.2917
88	H	H	-1.2801	-4.4472	-1.6458
89	C	C.2	-2.8049	-4.1502	1.9011
90	H	H	-1.3368	-2.6194	2.2607
91	C	C.2	-3.3367	-5.0595	0.9829
92	H	H	-3.1892	-5.8554	-1.0163
93	H	H	-3.2383	-4.0600	2.8936
94	H	H	-4.1821	-5.6844	1.2586

complex 50

Sum of electronic and thermal free energies = -3549.420378 ua

Number		Label	SybylType	Xfrac + ESD	Yfrac + ESD	Zfrac + ESD
1	Si	Si	0.0827	-0.0279	0.0743	
2	Cl	Cl	-0.0089	-0.1720	4.7065	
3	P	P.3	2.5680	0.0762	2.9298	
4	P	P.3	1.9309	-2.9842	1.4868	
5	P	P.3	-1.2327	-2.5578	2.6957	
6	C	C.3	-1.7300	-2.3734	0.9118	
7	H	H	-2.7625	-2.7237	0.7841	
8	C	C.3	1.6488	1.5650	2.2568	
9	C	C.3	2.4472	-2.0896	-0.0658	
10	H	H	3.3058	-1.4954	0.2484	
11	H	H	2.8272	-2.8151	-0.7961	
12	H	H	-1.1017	-3.0758	0.3566	
13	C	C.3	0.3449	1.2562	1.4894	
14	H	H	0.0044	2.2086	1.0528	
15	H	H	-0.4039	0.9853	2.2407	
16	C	C.3	-1.5912	-0.9483	0.3309	
17	H	H	-2.2196	-0.2513	0.9019	
18	H	H	-2.0392	-0.9751	-0.6741	
19	C	C.3	1.4171	-1.1619	-0.7420	
20	H	H	0.7888	-1.7501	-1.4296	
21	H	H	1.9831	-0.4938	-1.4073	
22	C	C.3	-0.3322	1.0825	-1.4325	
23	H	H	0.4921	1.7711	-1.6616	
24	H	H	-0.5319	0.4965	-2.3389	
25	H	H	-1.2203	1.6978	-1.2381	
26	H	H	2.3323	2.1777	1.6615	
27	H	H	1.3902	2.1533	3.1432	
28	Rh	Rh	0.8824	-1.6226	2.9710	
29	C	C.3	4.1573	0.0929	1.9452	
30	C	C.2	5.2824	-0.5722	2.4628	
31	C	C.2	4.2874	0.7357	0.7028	
32	C	C.2	6.4904	-0.5921	1.7669	
33	H	H	5.2182	-1.0720	3.4238	
34	C	C.2	5.4979	0.7179	0.0046	
35	H	H	3.4414	1.2494	0.2576	
36	C	C.2	6.6046	0.0547	0.5344	
37	H	H	7.3438	-1.1134	2.1921	
38	H	H	5.5720	1.2273	-0.9528	
39	H	H	7.5473	0.0434	-0.0062	
40	C	C.3	-1.4875	-4.3564	3.0755	
41	C	C.2	-0.7957	-4.8946	4.1723	
42	C	C.2	-2.3959	-5.1729	2.3872	
43	C	C.2	-1.0138	-6.2121	4.5779	
44	H	H	-0.0792	-4.2731	4.7043	
45	C	C.2	-2.6013	-6.4962	2.7814	
46	H	H	-2.9535	-4.7832	1.5411	

47	C	C.2	-1.9157	-7.0180	3.8802
48	H	H	-0.4748	-6.6099	5.4342
49	H	H	-3.3048	-7.1176	2.2330
50	H	H	-2.0848	-8.0457	4.1912
51	C	C.3	1.2581	-4.5882	0.8140
52	C	C.2	1.2767	-5.7381	1.6201
53	C	C.2	0.7675	-4.7075	-0.4958
54	C	C.2	0.8187	-6.9625	1.1361
55	H	H	1.6629	-5.6800	2.6324
56	C	C.2	0.3048	-5.9334	-0.9822
57	H	H	0.7506	-3.8476	-1.1570
58	C	C.2	0.3294	-7.0650	-0.1680
59	H	H	0.8436	-7.8365	1.7806
60	H	H	-0.0655	-6.0008	-2.0021
61	H	H	-0.0254	-8.0199	-0.5465
62	C	C.3	-2.6879	-1.8823	3.6320
63	C	C.2	-3.8236	-1.3546	3.0019
64	C	C.2	-2.6781	-1.9608	5.0345
65	C	C.2	-4.9191	-0.9156	3.7515
66	H	H	-3.8752	-1.2803	1.9215
67	C	C.2	-3.7738	-1.5330	5.7806
68	H	H	-1.8037	-2.3469	5.5462
69	C	C.2	-4.8985	-1.0050	5.1420
70	H	H	-5.7885	-0.5086	3.2413
71	H	H	-3.7430	-1.6009	6.8648
72	H	H	-5.7505	-0.6653	5.7252
73	C	C.3	3.2702	0.6658	4.5401
74	C	C.2	3.9324	1.9008	4.6214
75	C	C.2	3.1898	-0.1362	5.6852
76	C	C.2	4.4923	2.3287	5.8253
77	H	H	4.0207	2.5310	3.7403
78	C	C.2	3.7621	0.2859	6.8871
79	H	H	2.6488	-1.0751	5.6386
80	C	C.2	4.4107	1.5193	6.9609
81	H	H	4.9954	3.2910	5.8747
82	H	H	3.6861	-0.3442	7.7695
83	H	H	4.8488	1.8509	7.8988
84	C	C.3	3.5423	-3.6331	2.1462
85	C	C.2	4.5611	-4.1136	1.3090
86	C	C.2	3.7298	-3.6900	3.5352
87	C	C.2	5.7440	-4.6208	1.8480
88	H	H	4.4367	-4.0978	0.2301
89	C	C.2	4.9090	-4.2088	4.0766
90	H	H	2.9440	-3.3137	4.1862
91	C	C.2	5.9208	-4.6707	3.2333
92	H	H	6.5265	-4.9815	1.1854
93	H	H	5.0372	-4.2457	5.1554
94	H	H	6.8410	-5.0705	3.6514

complex 52

Sum of electronic and thermal free energies = -3543.265097 ua

Number	Label	Sybyl	Xfrac + ESD	Yfrac + ESD	Zfrac +
ESD					
1	Cl	Cl	-0.1252	-0.0134	-0.1448
2	Si	Si	-0.1232	0.0139	4.8599
3	P	P.3	2.3967	-0.0091	2.7961
4	P	P.3	-0.4876	-2.2386	2.6141
5	P	P.3	-0.3961	2.4695	2.2223
6	C	C.3	-2.1328	0.5490	2.3668
7	H	H	-2.6480	0.4748	3.3298
8	H	H	-2.6320	-0.1158	1.6617
9	C	C.3	-2.1470	2.0031	1.8426
10	H	H	-2.9146	2.6608	2.2665
11	H	H	-2.2594	2.0207	0.7560
12	C	C.3	1.6871	0.0267	5.5590
13	H	H	1.7399	0.6234	6.4800
14	H	H	1.9307	-1.0024	5.8579
15	C	C.3	-0.8286	-1.7153	5.3333
16	H	H	-0.5687	-1.9710	6.3705
17	H	H	-1.9248	-1.6683	5.2911
18	C	C.3	-1.1578	1.2189	5.9176
19	H	H	-2.1697	1.3523	5.5181
20	H	H	-1.2576	0.7973	6.9278
21	H	H	-0.7049	2.2088	6.0156
22	C	C.3	2.7347	0.5427	4.5574
23	H	H	3.7574	0.2754	4.8491
24	H	H	2.6995	1.6359	4.5184
25	C	C.3	-0.3051	-2.7972	4.3806
26	H	H	-0.7796	-3.7737	4.5321
27	H	H	0.7727	-2.9433	4.5269
28	C	C.3	-2.2208	-2.7069	2.1502
29	C	C.2	-2.6310	-2.5447	0.8153
30	C	C.2	-3.1340	-3.2322	3.0751
31	C	C.2	-3.9160	-2.9128	0.4193
32	H	H	-1.9499	-2.1084	0.0911
33	C	C.2	-4.4234	-3.5962	2.6756
34	H	H	-2.8560	-3.3644	4.1150
35	C	C.2	-4.8169	-3.4413	1.3473
36	H	H	-4.2142	-2.7804	-0.6174
37	H	H	-5.1159	-4.0034	3.4078
38	H	H	-5.8185	-3.7271	1.0367
39	C	C.3	0.4496	-3.5176	1.6460
40	C	C.2	0.7835	-4.7525	2.2261
41	C	C.2	0.7430	-3.3116	0.2882
42	C	C.2	1.3881	-5.7566	1.4680
43	H	H	0.5707	-4.9497	3.2708
44	C	C.2	1.3367	-4.3232	-0.4683
45	H	H	0.5137	-2.3565	-0.1728

46	C	C.2	1.6600	-5.5485	0.1156
47	H	H	1.6390	-6.7043	1.9378
48	H	H	1.5497	-4.1458	-1.5196
49	H	H	2.1216	-6.3347	-0.4765
50	C	C.3	0.2318	3.5554	0.8513
51	C	C.2	1.1036	4.6261	1.1111
52	C	C.2	-0.1638	3.3242	-0.4778
53	C	C.2	1.5625	5.4431	0.0776
54	H	H	1.4225	4.8414	2.1245
55	C	C.2	0.2948	4.1464	-1.5086
56	H	H	-0.8039	2.4853	-0.7184
57	C	C.2	1.1581	5.2085	-1.2371
58	H	H	2.2338	6.2667	0.3059
59	H	H	-0.0263	3.9491	-2.5280
60	H	H	1.5109	5.8484	-2.0418
61	C	C.3	-0.4019	3.6619	3.6339
62	C	C.2	-1.5363	4.4207	3.9556
63	C	C.2	0.7701	3.8673	4.3796
64	C	C.2	-1.5053	5.3420	5.0044
65	H	H	-2.4541	4.3015	3.3898
66	C	C.2	0.8070	4.7954	5.4210
67	H	H	1.6652	3.3021	4.1406
68	C	C.2	-0.3357	5.5313	5.7415
69	H	H	-2.3981	5.9142	5.2421
70	H	H	1.7258	4.9385	5.9835
71	H	H	-0.3135	6.2484	6.5576
72	C	C.3	3.4758	1.1200	1.8026
73	C	C.2	4.7139	1.5744	2.2914
74	C	C.2	3.0751	1.4990	0.5132
75	C	C.2	5.5257	2.3967	1.5110
76	H	H	5.0571	1.2807	3.2791
77	C	C.2	3.8969	2.3156	-0.2698
78	H	H	2.1211	1.1552	0.1241
79	C	C.2	5.1188	2.7681	0.2263
80	H	H	6.4791	2.7417	1.9034
81	H	H	3.5668	2.6060	-1.2632
82	H	H	5.7539	3.4069	-0.3822
83	C	C.3	3.3839	-1.5781	2.6694
84	C	C.2	3.7670	-2.3208	3.7972
85	C	C.2	3.7681	-2.0447	1.4014
86	C	C.2	4.5179	-3.4916	3.6623
87	H	H	3.4954	-1.9892	4.7940
88	C	C.2	4.5204	-3.2105	1.2679
89	H	H	3.4863	-1.4873	0.5130
90	C	C.2	4.8988	-3.9389	2.3979
91	H	H	4.8098	-4.0472	4.5501
92	H	H	4.8085	-3.5515	0.2774
93	H	H	5.4862	-4.8471	2.2922
94	Ir	Ir	-0.0208	0.0875	2.4858

complex 54

Sum of electronic and thermal free energies = -3543.231559 ua

Number		Label	SybylType	Xfrac + ESD	Yfrac + ESD	Zfrac + ESD
1	Si	Si	0.0894	-0.0279	0.0713	
2	Cl	Cl	-0.0532	-0.1087	4.6513	
3	P	P.3	2.5508	0.0919	2.9147	
4	P	P.3	1.9408	-2.9651	1.4820	
5	P	P.3	-1.2273	-2.5593	2.6807	
6	C	C.3	-1.7422	-2.3593	0.9062	
7	H	H	-2.7788	-2.7005	0.7879	
8	C	C.3	1.6657	1.5934	2.2288	
9	C	C.3	2.4476	-2.0924	-0.0856	
10	H	H	3.3138	-1.5006	0.2123	
11	H	H	2.8144	-2.8287	-0.8116	
12	H	H	-1.1253	-3.0613	0.3379	
13	C	C.3	0.3707	1.3114	1.4348	
14	H	H	0.0860	2.2598	0.9528	
15	H	H	-0.4112	1.1007	2.1720	
16	C	C.3	-1.5949	-0.9291	0.3420	
17	H	H	-2.2049	-0.2313	0.9316	
18	H	H	-2.0584	-0.9372	-0.6562	
19	C	C.3	1.4147	-1.1653	-0.7569	
20	H	H	0.7785	-1.7543	-1.4365	
21	H	H	1.9745	-0.5004	-1.4305	
22	C	C.3	-0.3411	1.0572	-1.4551	
23	H	H	0.4839	1.7363	-1.7094	
24	H	H	-0.5576	0.4556	-2.3476	
25	H	H	-1.2226	1.6822	-1.2607	
26	H	H	2.3714	2.1922	1.6453	
27	H	H	1.4053	2.1883	3.1103	
28	C	C.3	4.1506	0.0771	1.9501	
29	C	C.2	5.2681	-0.5795	2.4928	
30	C	C.2	4.2969	0.7051	0.7020	
31	C	C.2	6.4859	-0.6071	1.8139	
32	H	H	5.1910	-1.0664	3.4593	
33	C	C.2	5.5170	0.6799	0.0213	
34	H	H	3.4561	1.2114	0.2389	
35	C	C.2	6.6165	0.0245	0.5753	
36	H	H	7.3336	-1.1222	2.2575	
37	H	H	5.6042	1.1771	-0.9413	
38	H	H	7.5669	0.0077	0.0484	
39	C	C.3	-1.4776	-4.3581	3.0601	
40	C	C.2	-0.7825	-4.8985	4.1537	
41	C	C.2	-2.3941	-5.1698	2.3771	
42	C	C.2	-1.0062	-6.2143	4.5616	
43	H	H	-0.0584	-4.2804	4.6793	
44	C	C.2	-2.6046	-6.4917	2.7736	
45	H	H	-2.9539	-4.7774	1.5337	
46	C	C.2	-1.9164	-7.0158	3.8696	

47	H	H	-0.4646	-6.6145	5.4151
48	H	H	-3.3141	-7.1098	2.2294
49	H	H	-2.0897	-8.0422	4.1827
50	C	C.3	1.2536	-4.5736	0.8313
51	C	C.2	1.2925	-5.7222	1.6381
52	C	C.2	0.7440	-4.6981	-0.4707
53	C	C.2	0.8331	-6.9498	1.1634
54	H	H	1.6967	-5.6609	2.6430
55	C	C.2	0.2802	-5.9270	-0.9481
56	H	H	0.7141	-3.8395	-1.1331
57	C	C.2	0.3235	-7.0569	-0.1324
58	H	H	0.8735	-7.8229	1.8085
59	H	H	-0.1052	-5.9981	-1.9621
60	H	H	-0.0316	-8.0145	-0.5038
61	C	C.3	-2.6679	-1.8893	3.6436
62	C	C.2	-3.8085	-1.3510	3.0326
63	C	C.2	-2.6441	-1.9879	5.0446
64	C	C.2	-4.8959	-0.9214	3.7994
65	H	H	-3.8697	-1.2595	1.9541
66	C	C.2	-3.7310	-1.5689	5.8080
67	H	H	-1.7657	-2.3839	5.5421
68	C	C.2	-4.8615	-1.0307	5.1881
69	H	H	-5.7695	-0.5057	3.3038
70	H	H	-3.6894	-1.6519	6.8907
71	H	H	-5.7071	-0.6985	5.7846
72	C	C.3	3.2384	0.6685	4.5355
73	C	C.2	3.9099	1.8974	4.6296
74	C	C.2	3.1363	-0.1378	5.6759
75	C	C.2	4.4580	2.3155	5.8423
76	H	H	4.0146	2.5307	3.7525
77	C	C.2	3.6963	0.2751	6.8868
78	H	H	2.5893	-1.0726	5.6159
79	C	C.2	4.3545	1.5025	6.9736
80	H	H	4.9687	3.2732	5.9023
81	H	H	3.6038	-0.3578	7.7656
82	H	H	4.7832	1.8269	7.9183
83	C	C.3	3.5546	-3.6205	2.1320
84	C	C.2	4.5734	-4.0893	1.2884
85	C	C.2	3.7418	-3.6973	3.5202
86	C	C.2	5.7562	-4.6043	1.8204
87	H	H	4.4504	-4.0574	0.2098
88	C	C.2	4.9209	-4.2237	4.0542
89	H	H	2.9538	-3.3298	4.1738
90	C	C.2	5.9330	-4.6738	3.2046
91	H	H	6.5390	-4.9554	1.1528
92	H	H	5.0488	-4.2763	5.1324
93	H	H	6.8531	-5.0796	3.6173
94	Ir	Ir	0.8797	-1.6014	2.9414

complex 56

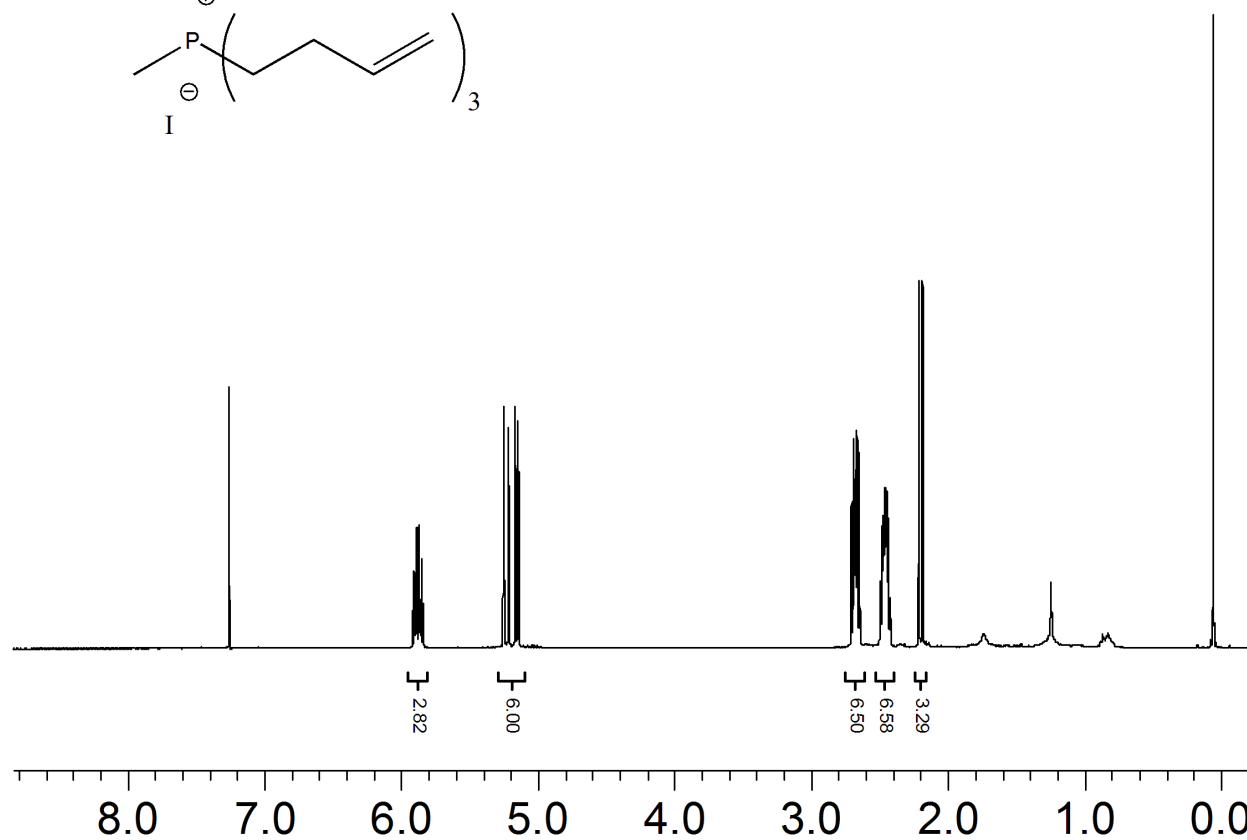
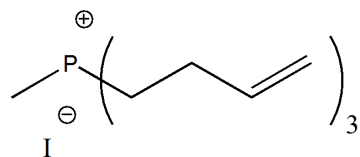
Sum of electronic and thermal free energies = -3543.260855 ua

Number	Label	SybylType	Xfrac + ESD	Yfrac + ESD	Zfrac + ESD
1	Cl	Cl	0.0534	-0.2401	-0.1416
2	Si	Si	-0.0406	-0.0272	4.8275
3	P	P.3	2.3833	-0.0838	2.8069
4	P	P.3	-0.2516	2.3667	2.6559
5	P	P.3	-2.3204	-0.5935	2.6620
6	C	C.3	0.2641	-2.2259	2.6166
7	H	H	0.1717	-2.6072	1.5959
8	H	H	1.2366	-2.5415	3.0022
9	H	H	-0.4901	-2.7214	3.2343
10	C	C.3	0.4285	2.8123	4.3447
11	C	C.3	0.0003	1.8107	5.4420
12	C	C.3	1.5836	-0.8215	5.4476
13	C	C.3	2.7115	-0.1214	4.6589
14	C	C.3	-1.6896	-0.8185	5.4135
15	H	H	-1.5989	-1.9124	5.3946
16	H	H	-1.9538	-0.5401	6.4429
17	C	C.3	-2.8122	-0.3617	4.4524
18	H	H	-2.9847	0.7168	4.5617
19	H	H	-3.7693	-0.8510	4.6654
20	H	H	0.6717	1.9135	6.3063
21	H	H	-0.9987	2.0653	5.8171
22	H	H	1.5181	2.7946	4.2230
23	H	H	0.1599	3.8429	4.6050
24	H	H	3.6998	-0.5391	4.8749
25	H	H	2.7549	0.9308	4.9644
26	H	H	1.7537	-0.6805	6.5238
27	H	H	1.5887	-1.9004	5.2561
28	C	C.3	-1.9189	3.2107	2.6851
29	C	C.2	-2.5628	3.5172	1.4749
30	C	C.2	-2.5453	3.5999	3.8801
31	C	C.2	-3.7819	4.1924	1.4601
32	H	H	-2.1031	3.2415	0.5324
33	C	C.2	-3.7713	4.2713	3.8664
34	H	H	-2.0785	3.4050	4.8381
35	C	C.2	-4.3933	4.5725	2.6564
36	H	H	-4.2554	4.4177	0.5089
37	H	H	-4.2293	4.5676	4.8069
38	H	H	-5.3430	5.1007	2.6437
39	C	C.3	0.6011	3.5343	1.4979
40	C	C.2	1.2078	4.7214	1.9370
41	C	C.2	0.5538	3.2661	0.1200
42	C	C.2	1.7519	5.6213	1.0194
43	H	H	1.2549	4.9585	2.9950
44	C	C.2	1.0811	4.1791	-0.7957
45	H	H	0.1321	2.3281	-0.2309
46	C	C.2	1.6816	5.3575	-0.3499

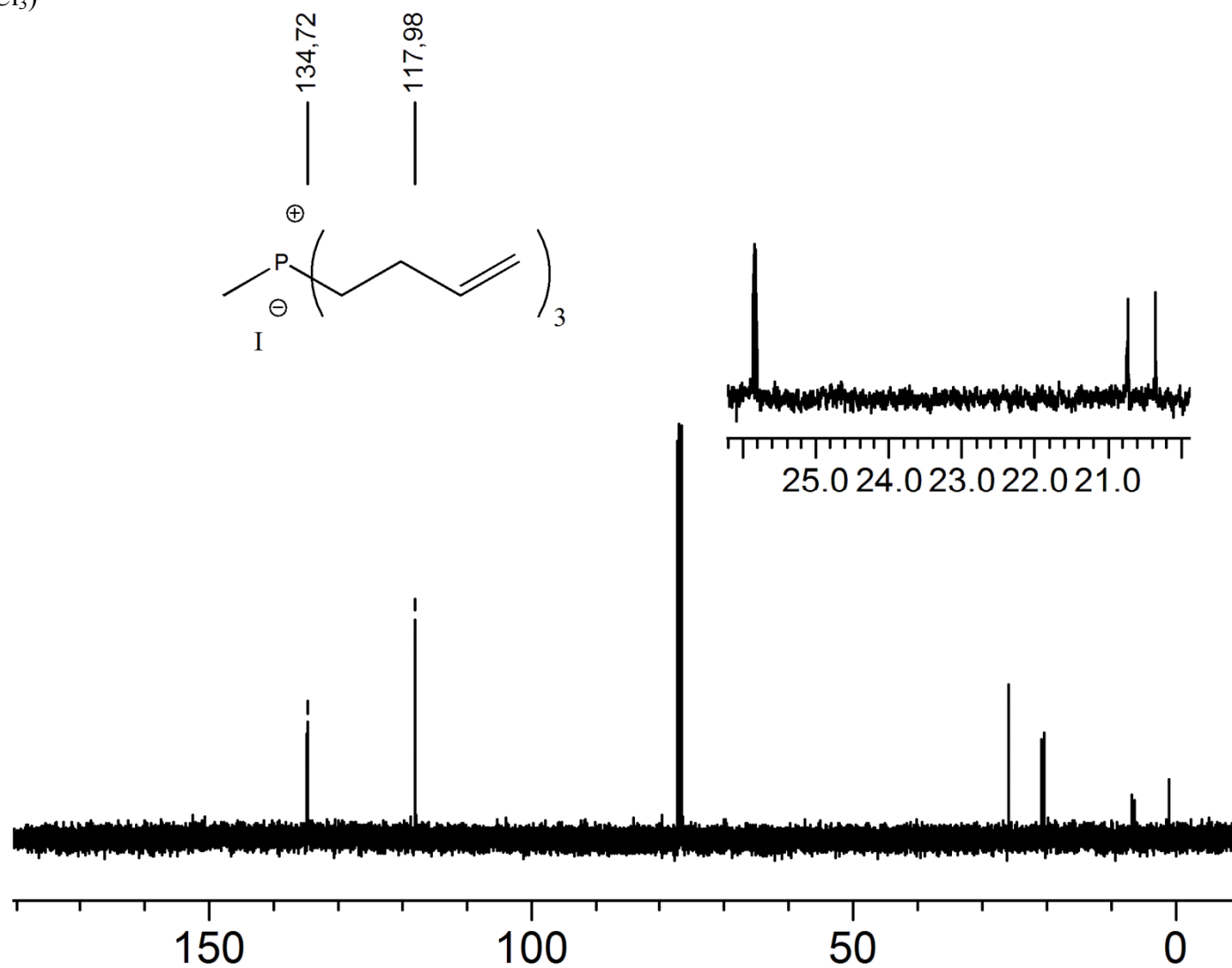
47	H	H	2.2225	6.5339	1.3764
48	H	H	1.0312	3.9590	-1.8592
49	H	H	2.0958	6.0655	-1.0633
50	C	C.3	3.4747	1.2829	2.2001
51	C	C.2	3.3816	1.6403	0.8449
52	C	C.2	4.4437	1.9070	3.0007
53	C	C.2	4.2411	2.5973	0.3068
54	H	H	2.6313	1.1709	0.2147
55	C	C.2	5.2965	2.8723	2.4599
56	H	H	4.5577	1.6377	4.0457
57	C	C.2	5.1985	3.2178	1.1122
58	H	H	4.1517	2.8670	-0.7414
59	H	H	6.0419	3.3460	3.0936
60	H	H	5.8649	3.9659	0.6910
61	C	C.3	3.3225	-1.5233	2.0971
62	C	C.2	4.3862	-2.1380	2.7736
63	C	C.2	3.0100	-1.9519	0.7966
64	C	C.2	5.1178	-3.1622	2.1682
65	H	H	4.6632	-1.8305	3.7762
66	C	C.2	3.7495	-2.9692	0.1927
67	H	H	2.1760	-1.5023	0.2655
68	C	C.2	4.8035	-3.5795	0.8750
69	H	H	5.9353	-3.6296	2.7111
70	H	H	3.4908	-3.2893	-0.8132
71	H	H	5.3743	-4.3756	0.4040
72	C	C.3	-3.6328	0.2735	1.6875
73	C	C.2	-3.4175	0.4935	0.3170
74	C	C.2	-4.8803	0.5961	2.2414
75	C	C.2	-4.4404	1.0066	-0.4817
76	H	H	-2.4470	0.2686	-0.1176
77	C	C.2	-5.8956	1.1221	1.4403
78	H	H	-5.0757	0.4351	3.2967
79	C	C.2	-5.6817	1.3205	0.0756
80	H	H	-4.2625	1.1636	-1.5426
81	H	H	-6.8564	1.3689	1.8848
82	H	H	-6.4778	1.7179	-0.5490
83	C	C.3	-2.7938	-2.3378	2.2439
84	C	C.2	-3.4472	-3.1893	3.1444
85	C	C.2	-2.5171	-2.8050	0.9477
86	C	C.2	-3.8252	-4.4784	2.7574
87	H	H	-3.6650	-2.8658	4.1569
88	C	C.2	-2.9012	-4.0885	0.5634
89	H	H	-1.9799	-2.1709	0.2481
90	C	C.2	-3.5576	-4.9296	1.4658
91	H	H	-4.3298	-5.1259	3.4700
92	H	H	-2.6784	-4.4344	-0.4425
93	H	H	-3.8533	-5.9311	1.1646
94	Ir	Ir	0.0005	-0.0752	2.5008

APPENDIX C
NMR SPECTRA

$^1\text{H}(\text{CDCl}_3)$

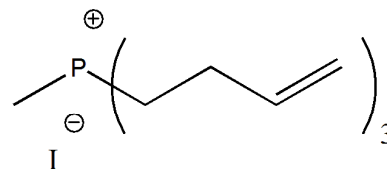


$^{13}\text{C}(\text{CDCl}_3)$



$^{31}\text{P}(\text{CDCl}_3)$

32,28

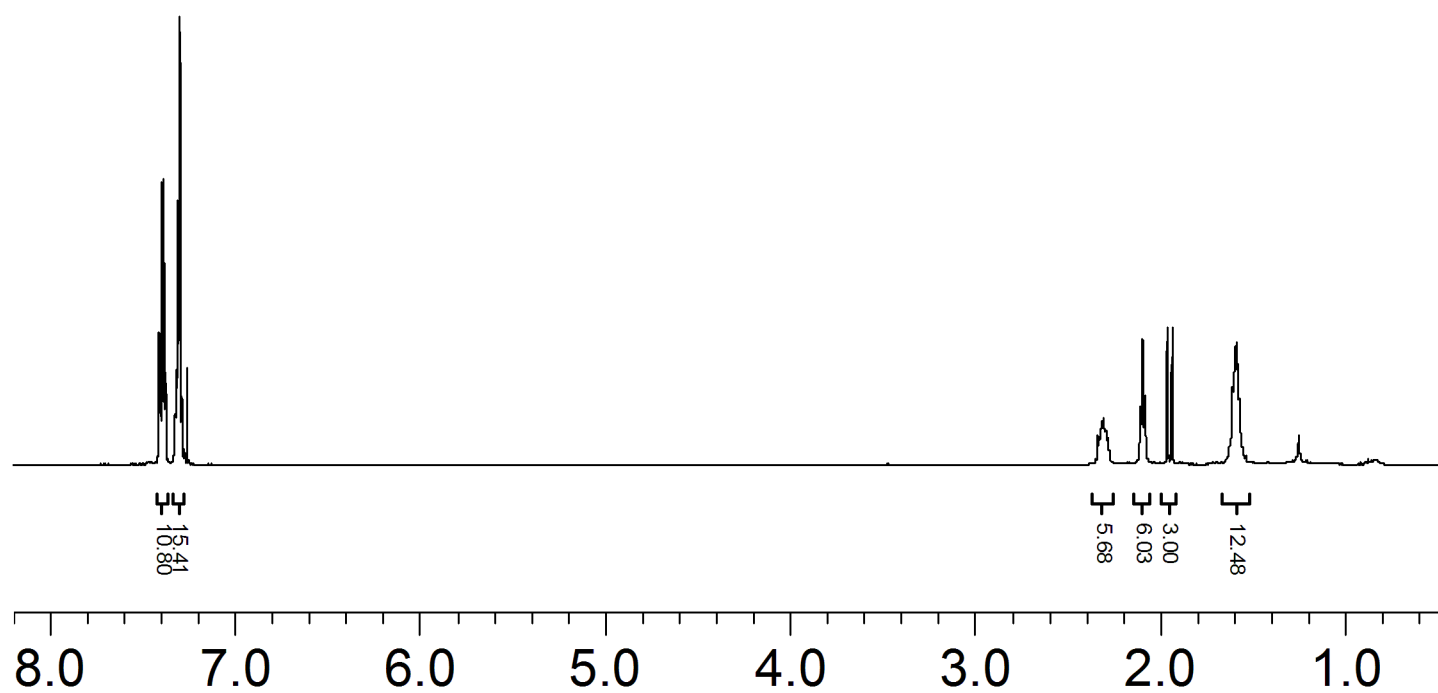
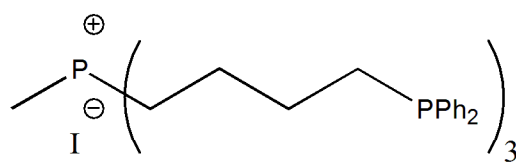


50

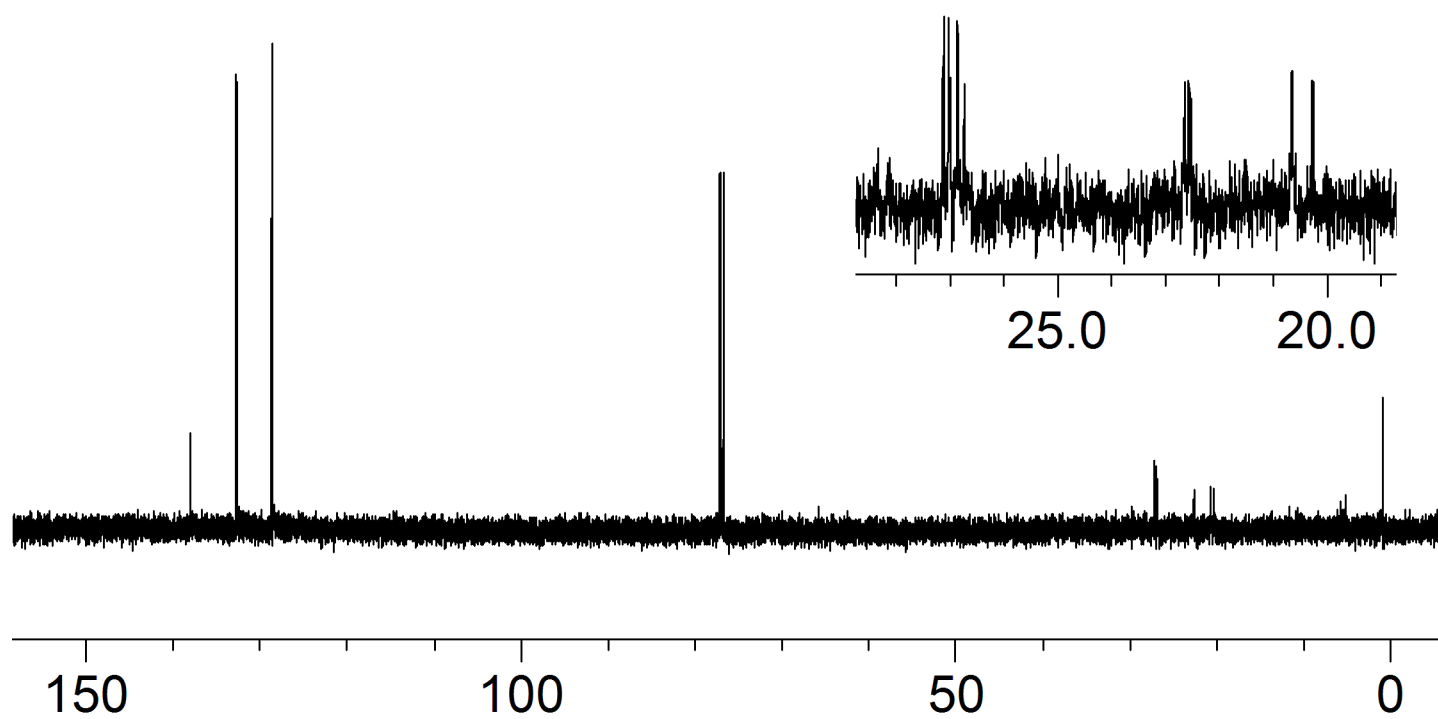
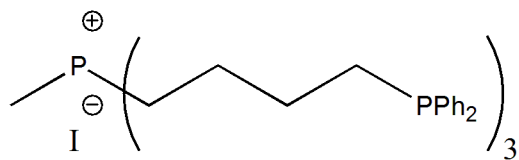
0

-50

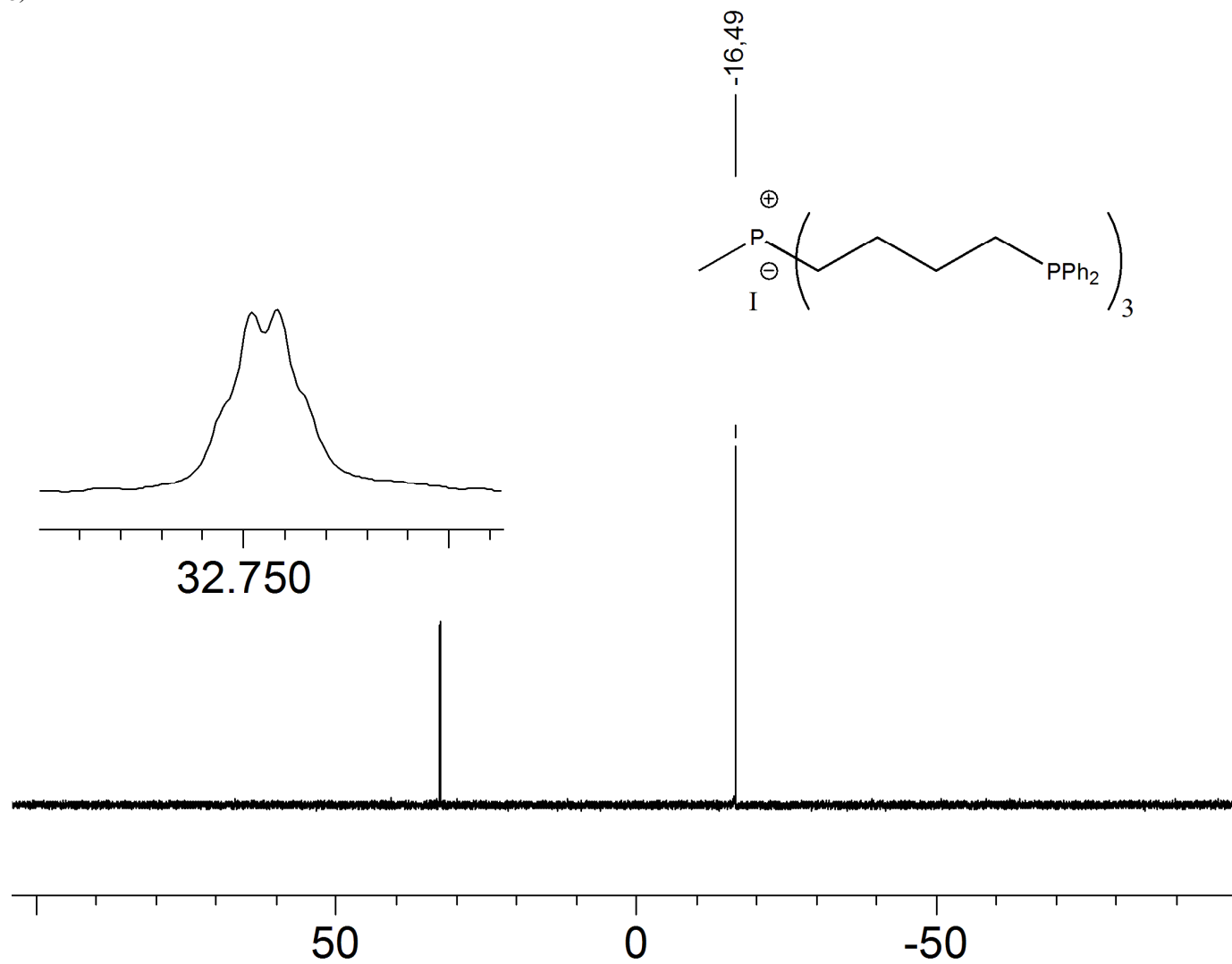
$^1\text{H}(\text{CDCl}_3)$



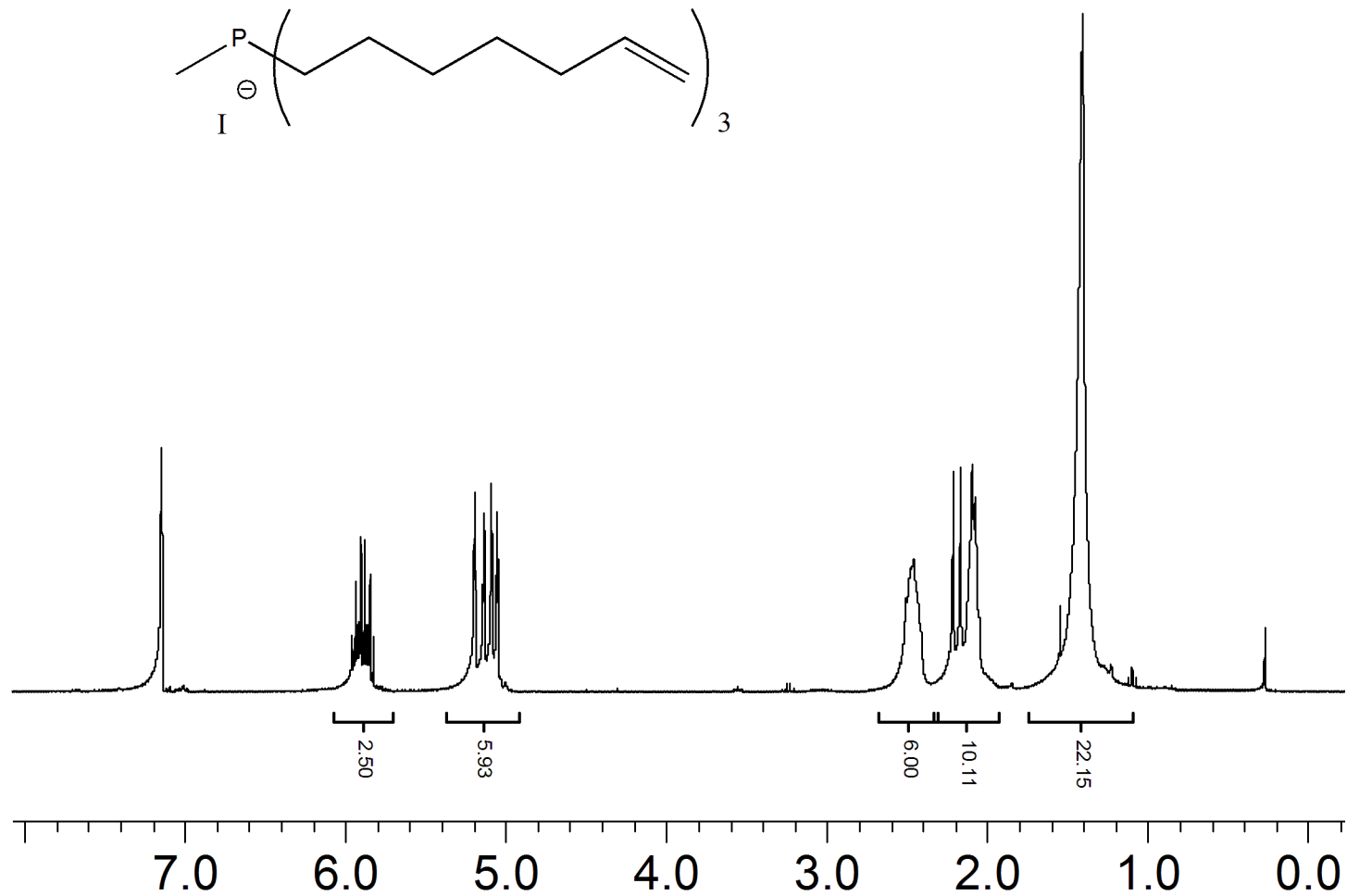
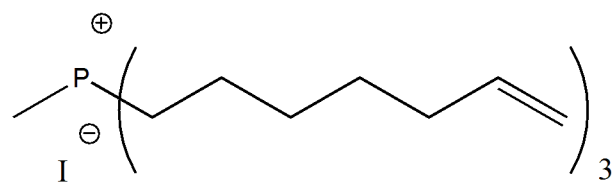
$^{13}\text{C}(\text{CDCl}_3)$



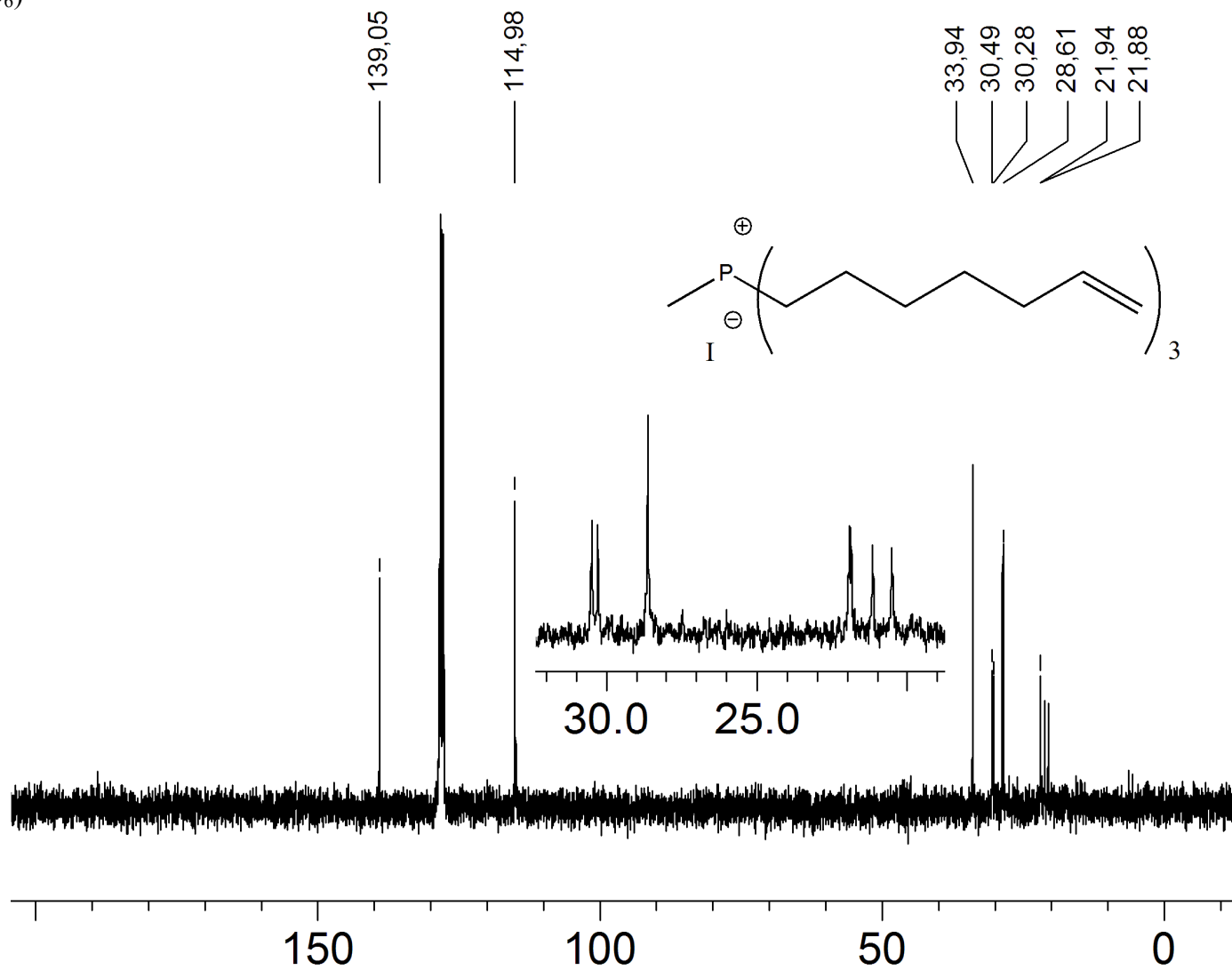
$^{31}\text{P}(\text{CDCl}_3)$



^1H (C_6D_6)

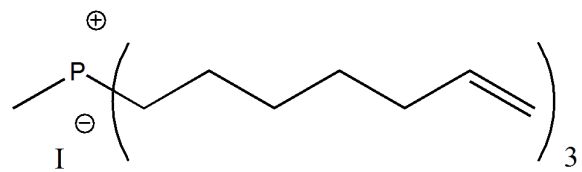


^{13}C (C_6D_6)



$^{31}\text{P}(\text{C}_6\text{D}_6)$

29,69



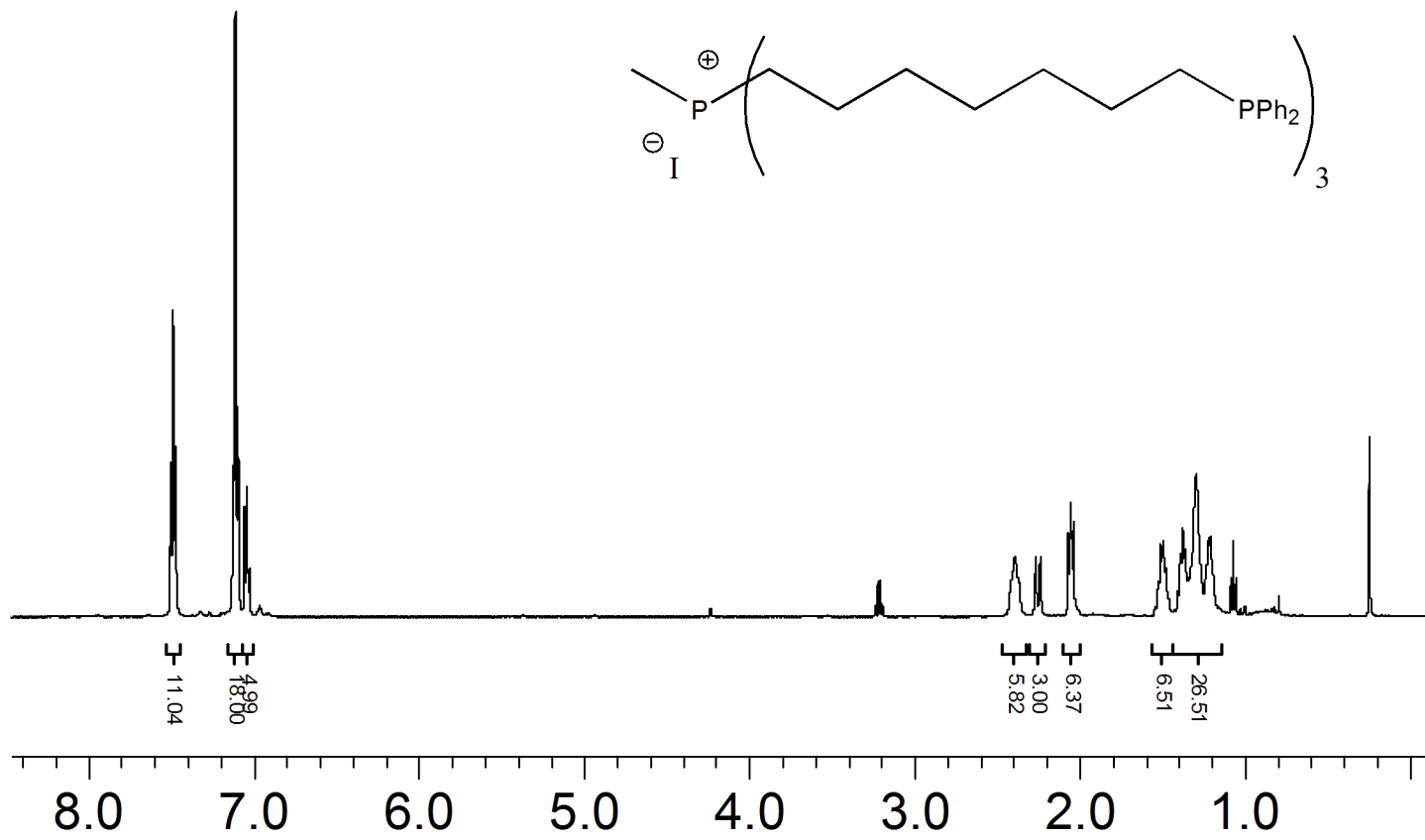
100

50

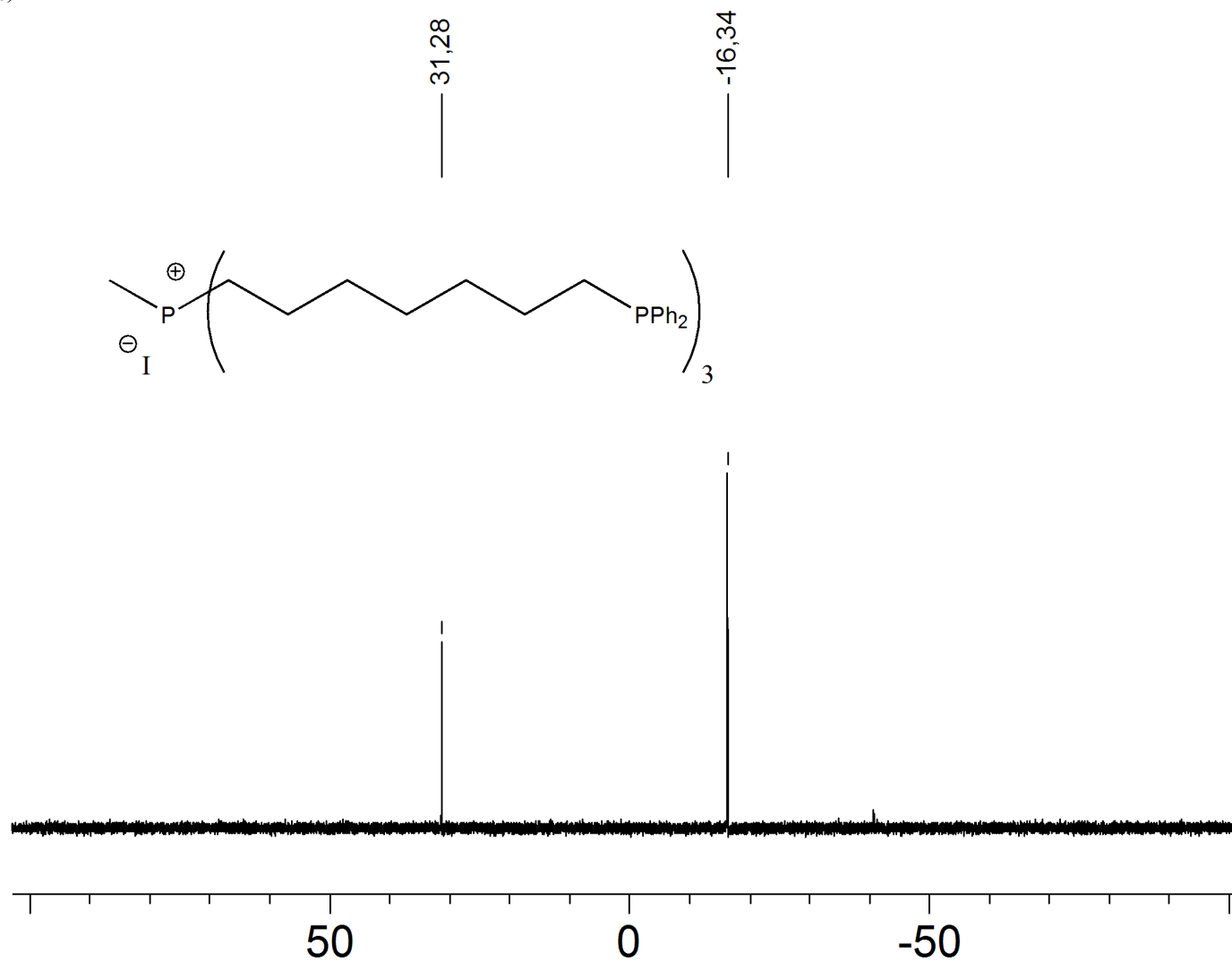
0

-50

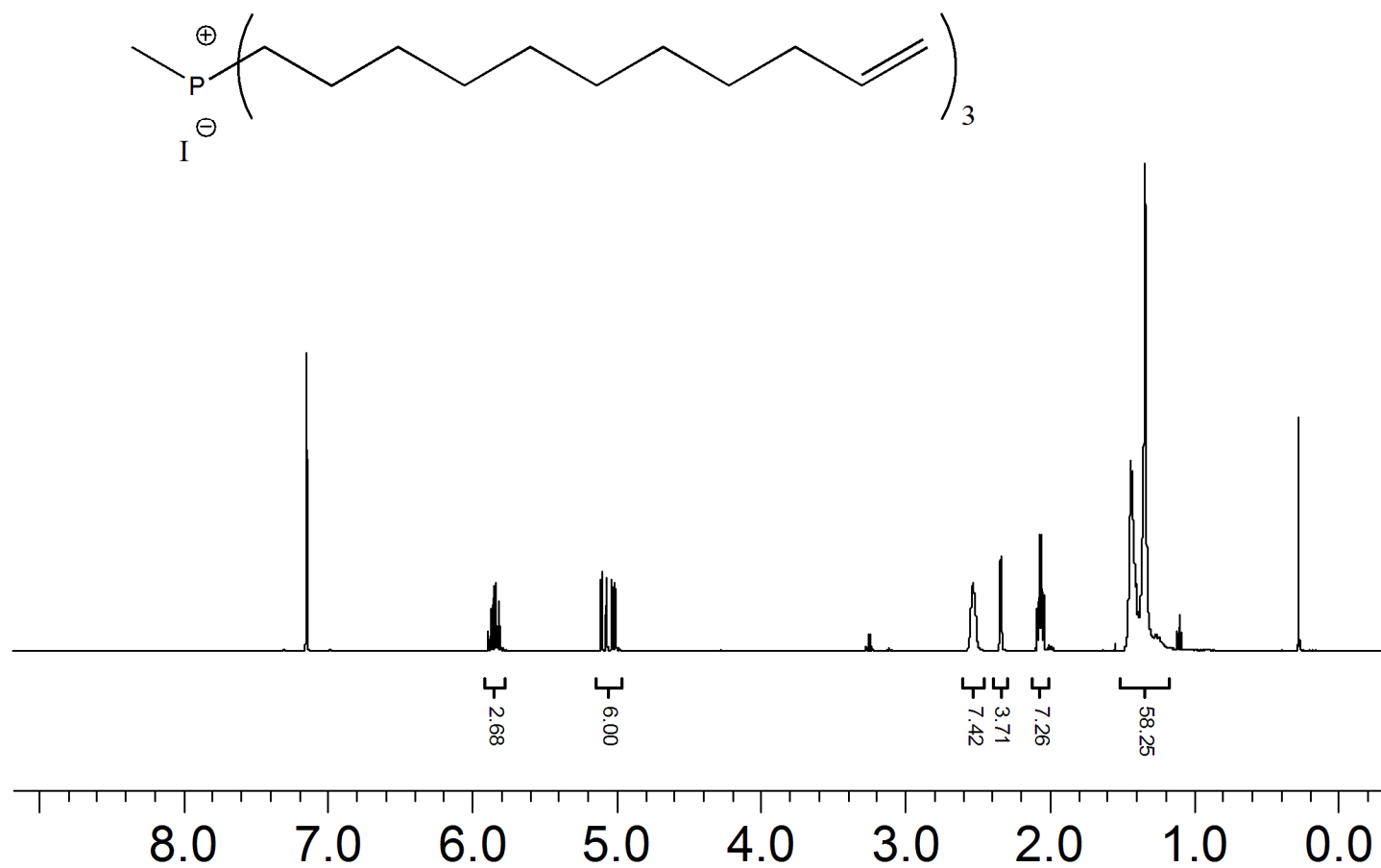
-100

¹H (C₆D₆)

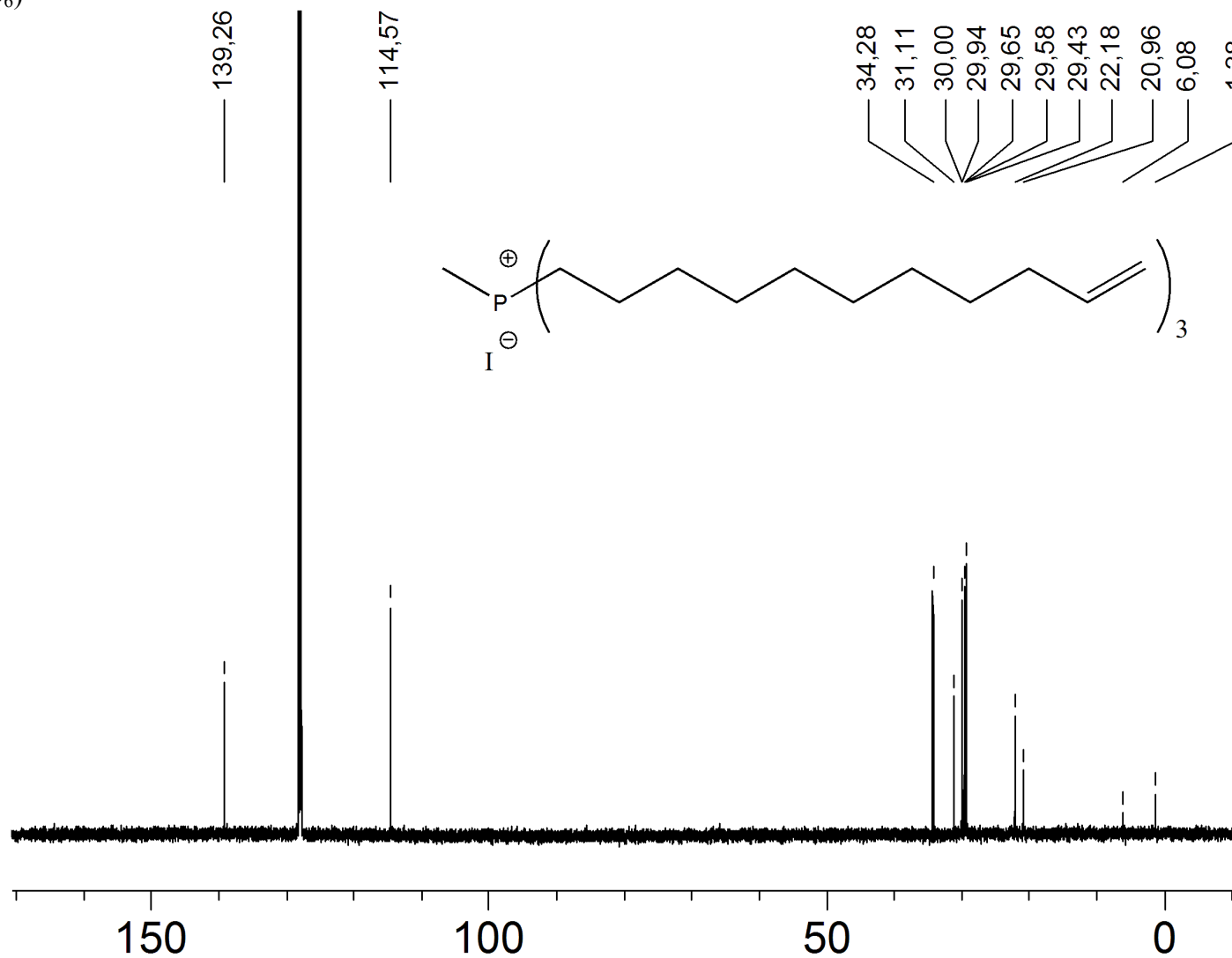
^{31}P (C_6D_6)



^1H (C_6D_6)

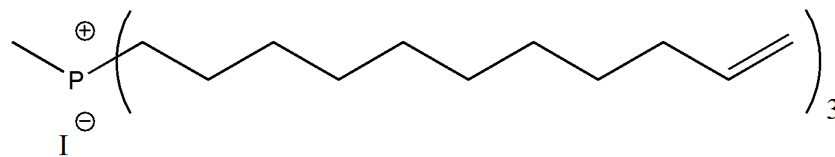


^{13}C (C_6D_6)



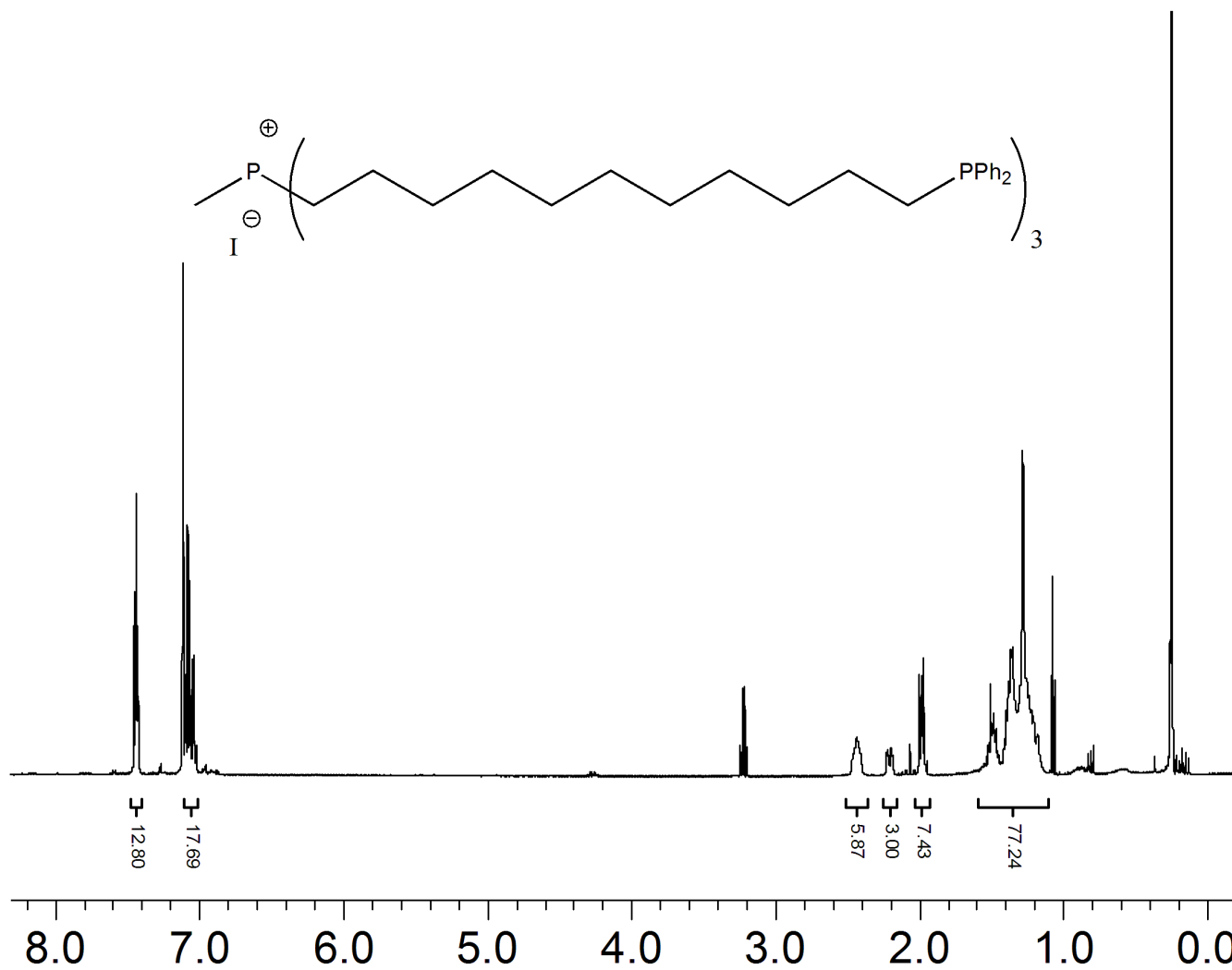
^{31}P (C_6D_6)

31,11

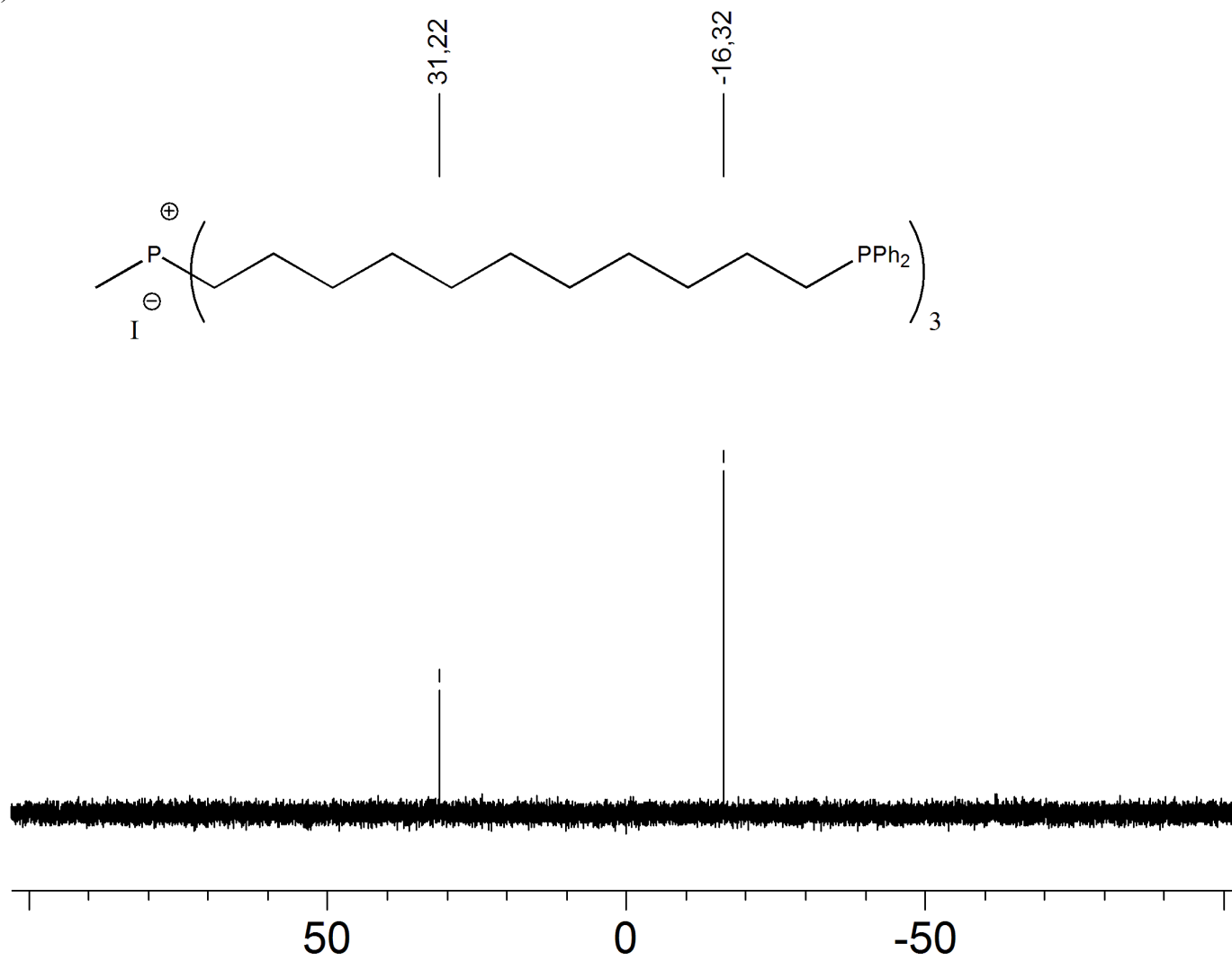


40 30 20 10 0 -10 -20 -30 -40

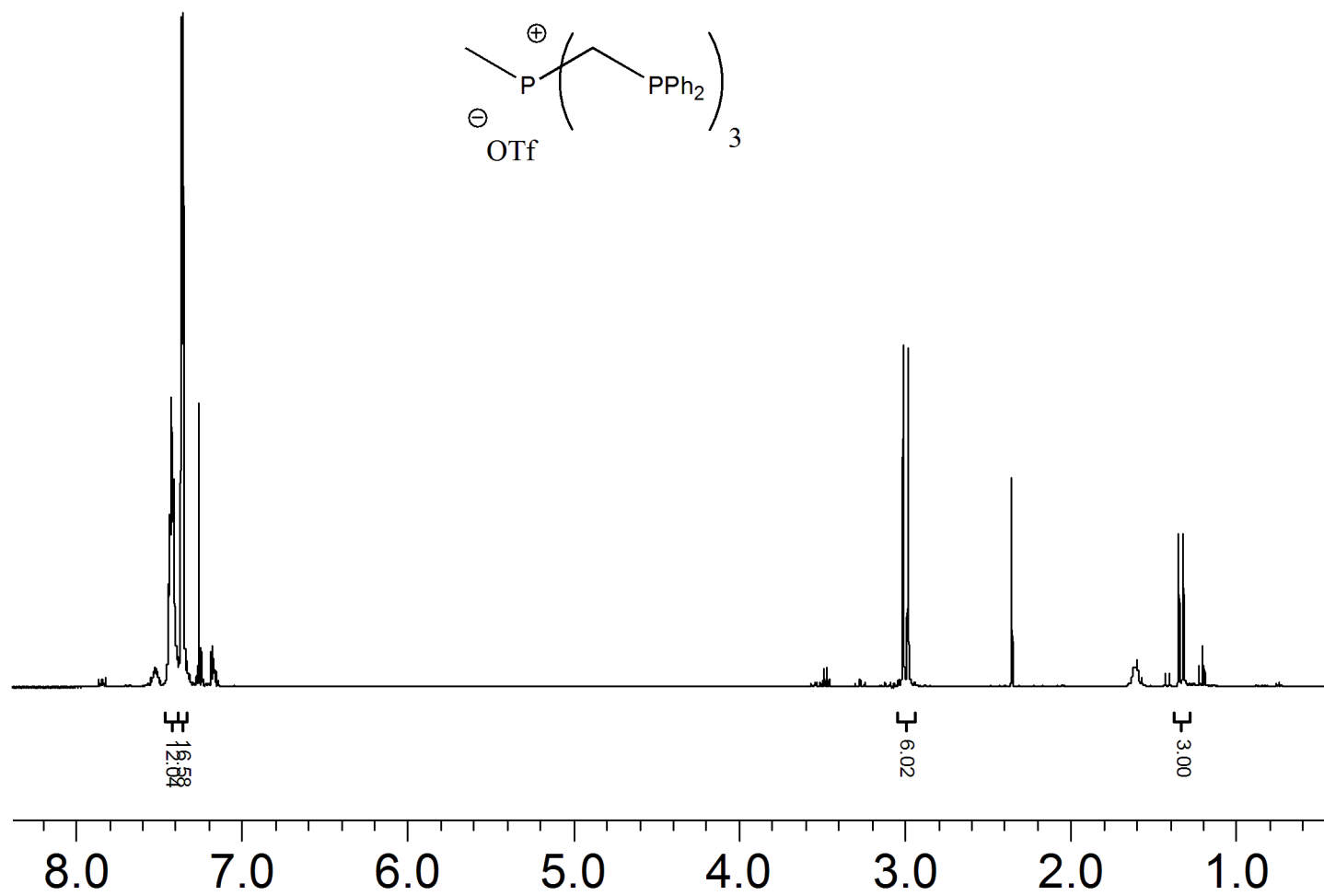
$^1\text{H}(\text{C}_6\text{D}_6)$



^{31}P (C_6D_6)



^1H (CDCl_3)

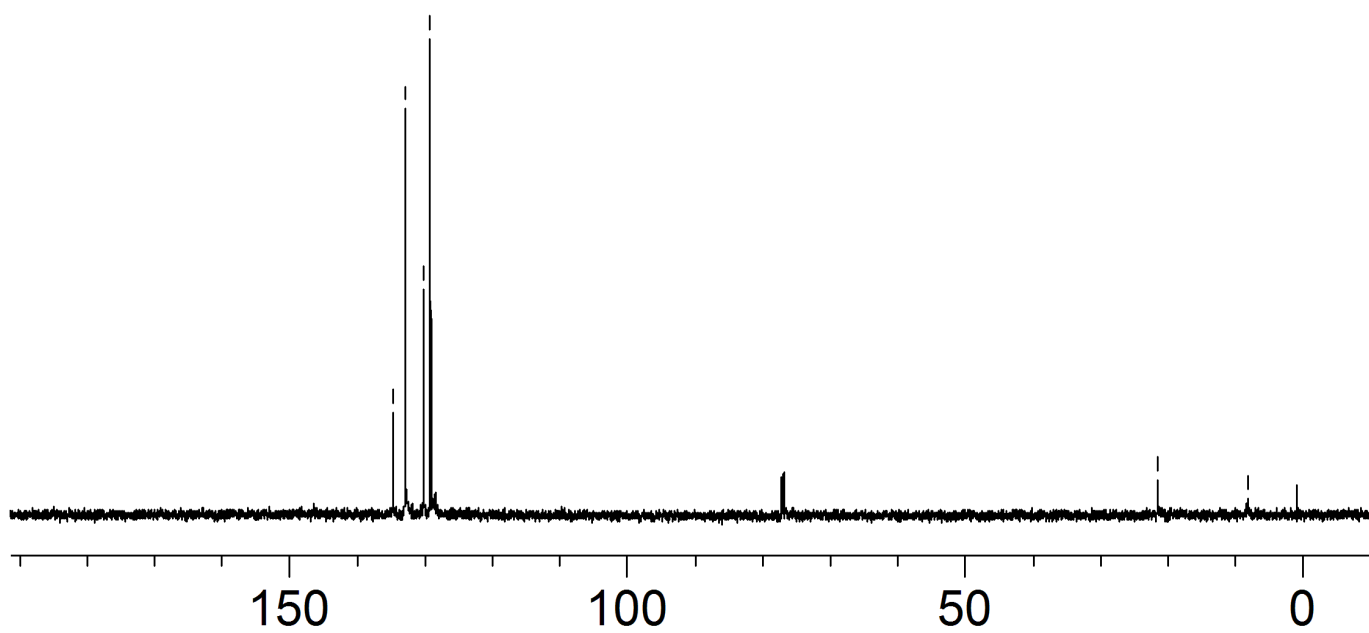
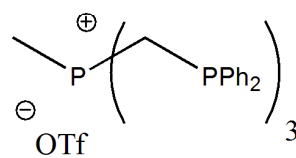


^{13}C (CDCl_3)

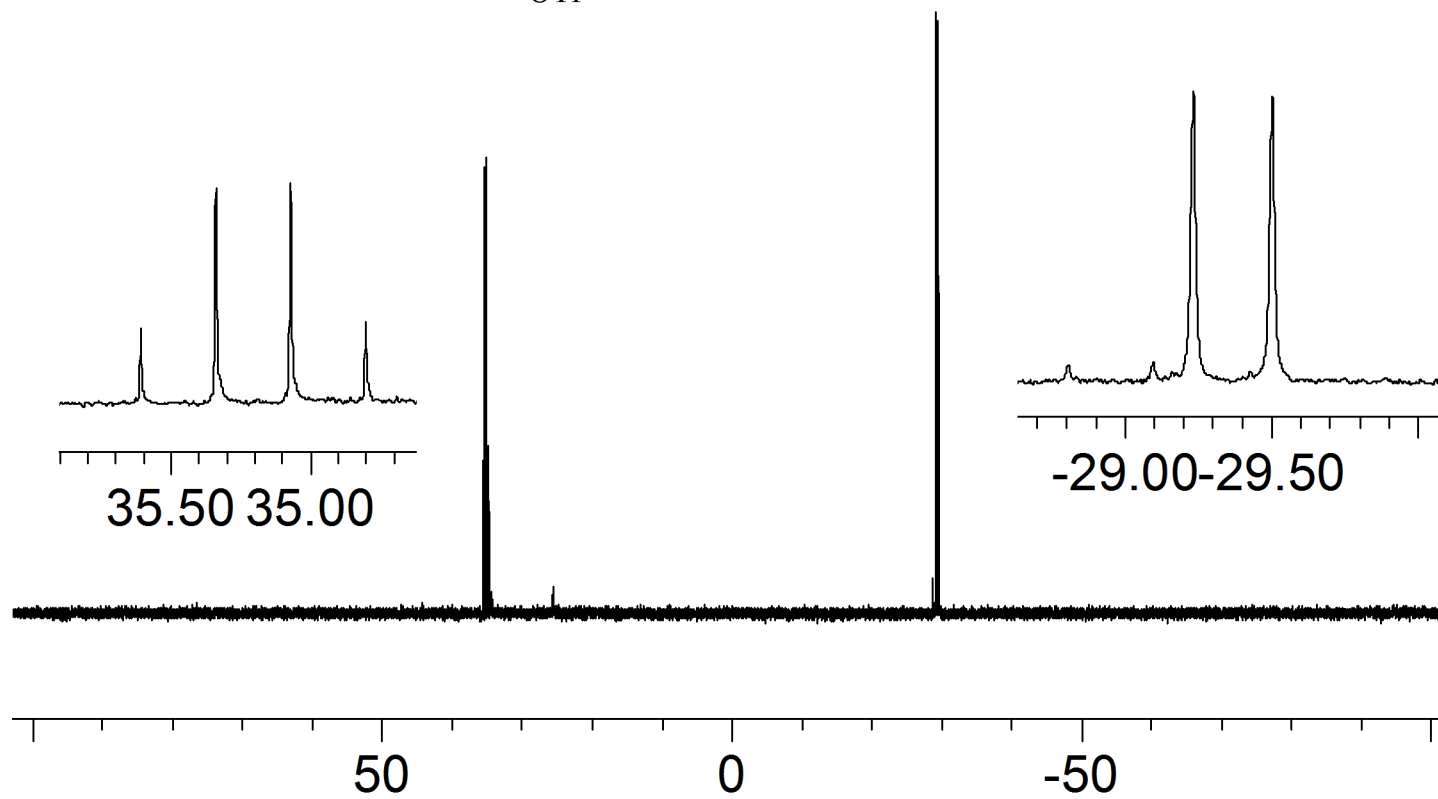
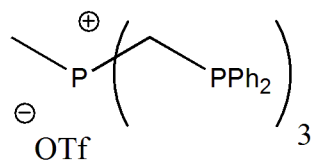
134,69
132,84
130,21
129,16

21,57

8,32

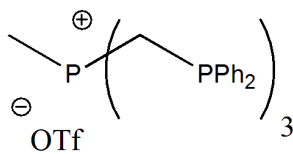


^{31}P (CDCl_3)



^{19}F (CDCl_3)

-78,13



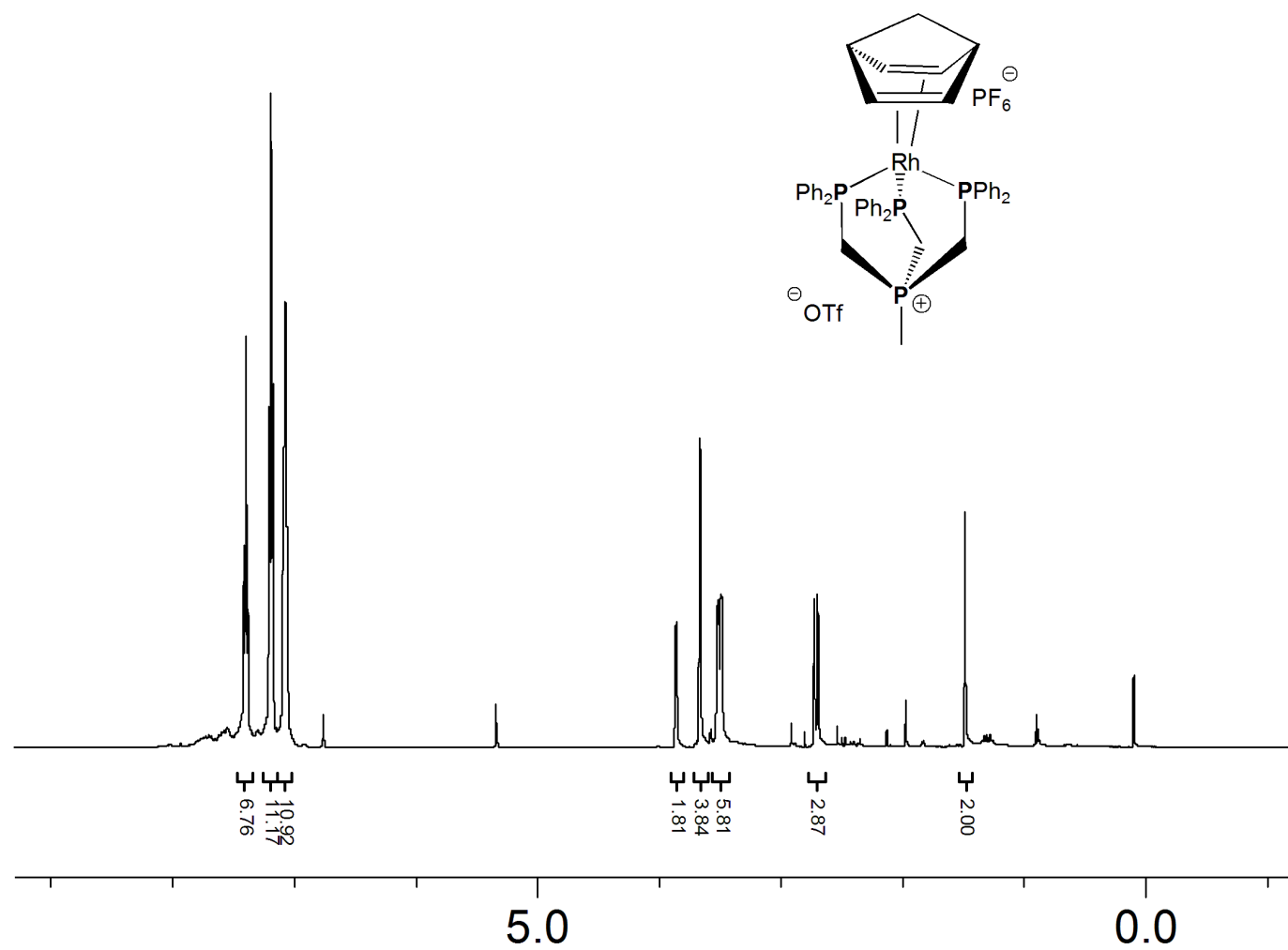
-50

-100

-150

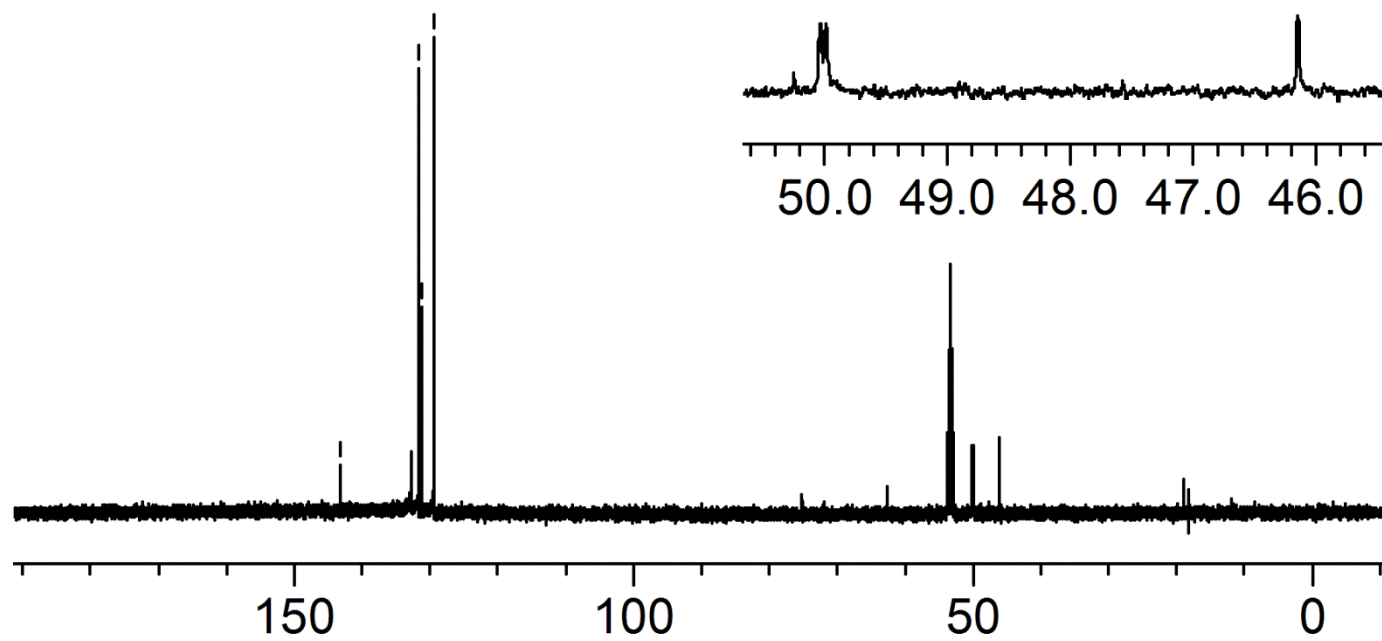
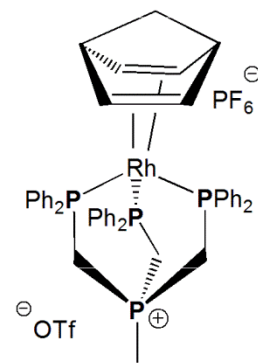
-200

^1H (CD_2Cl_2)

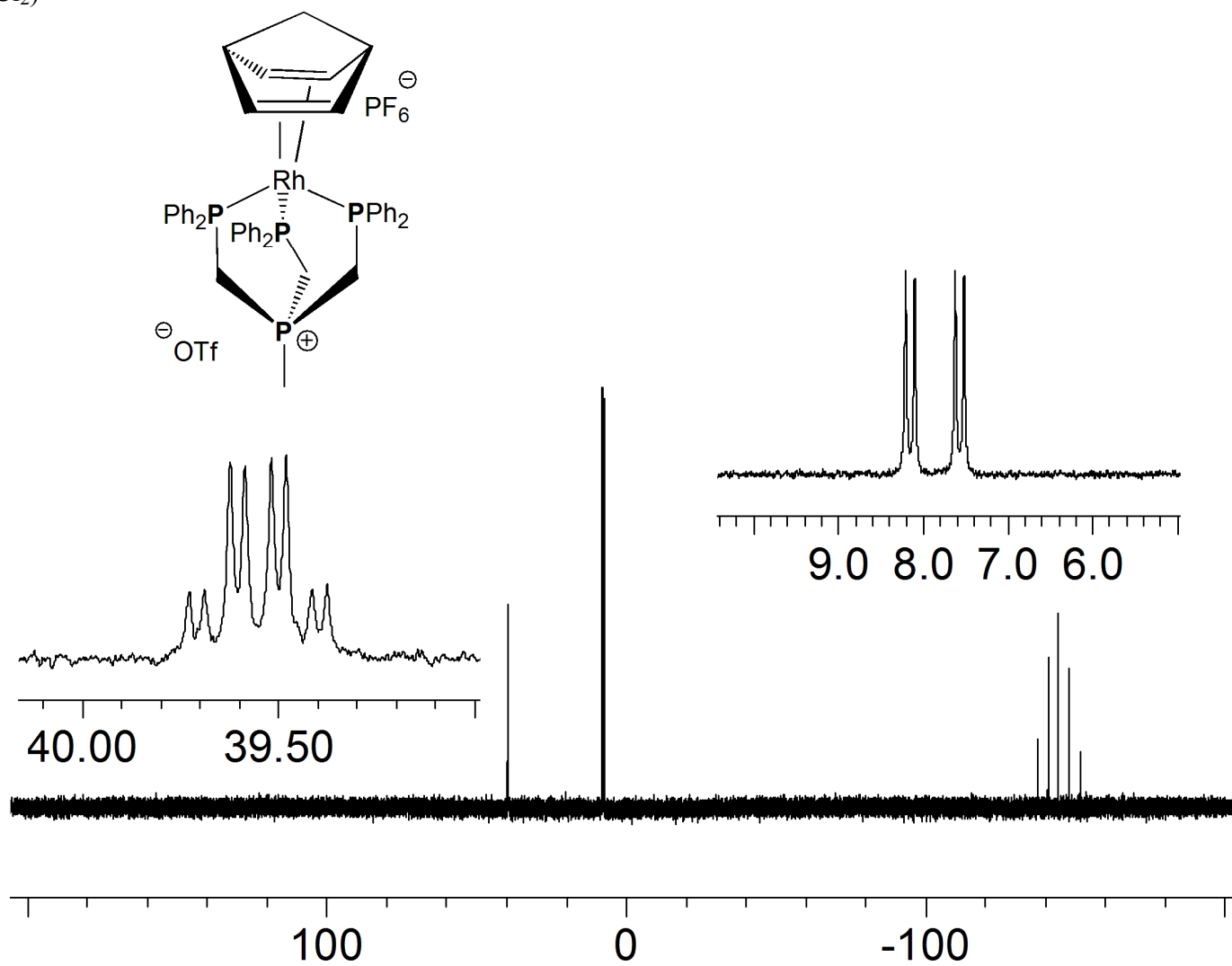


$^{13}\text{C} \{^3\text{P}\}(\text{CD}_2\text{Cl}_2)$

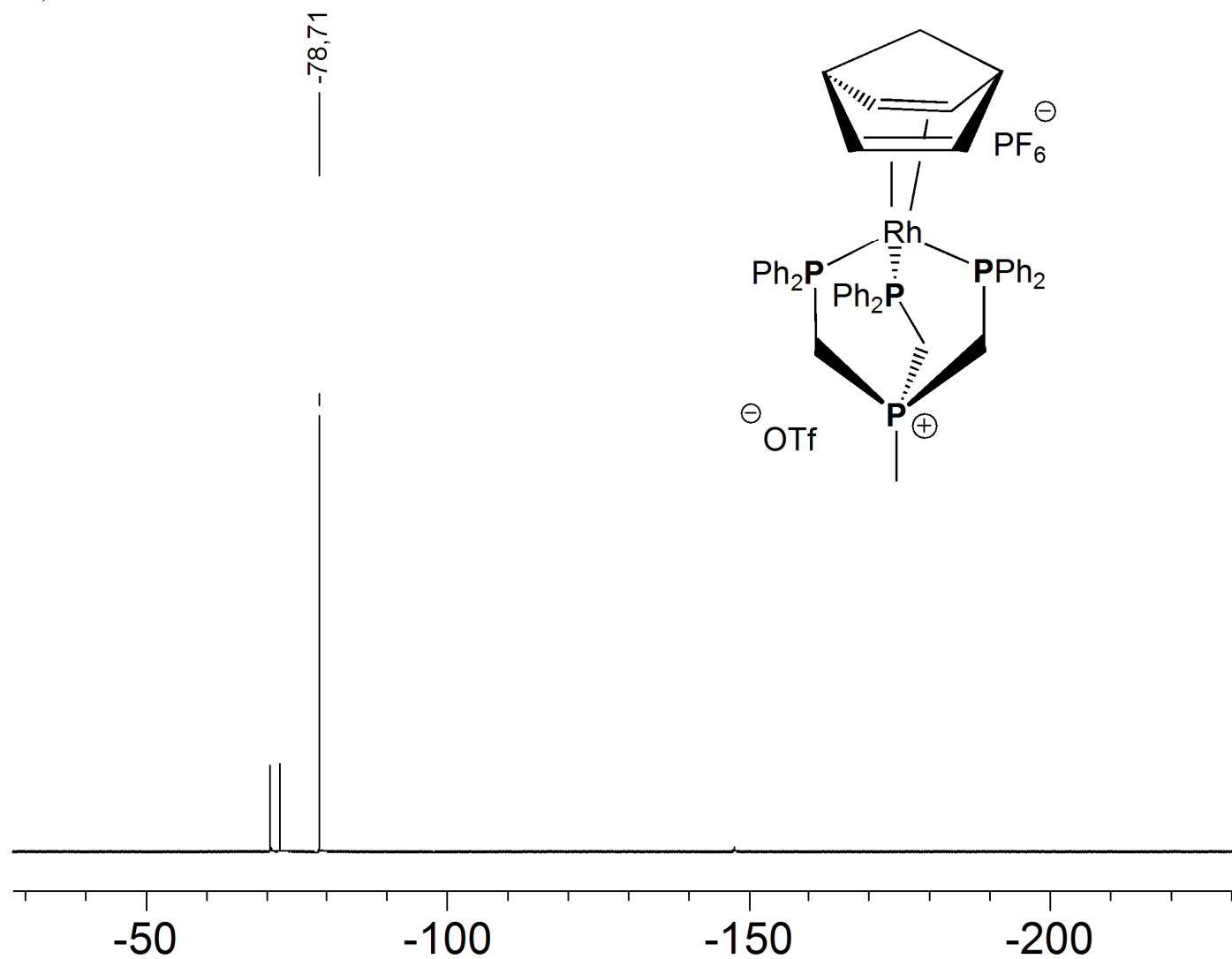
143,24
131,60
131,18
129,39



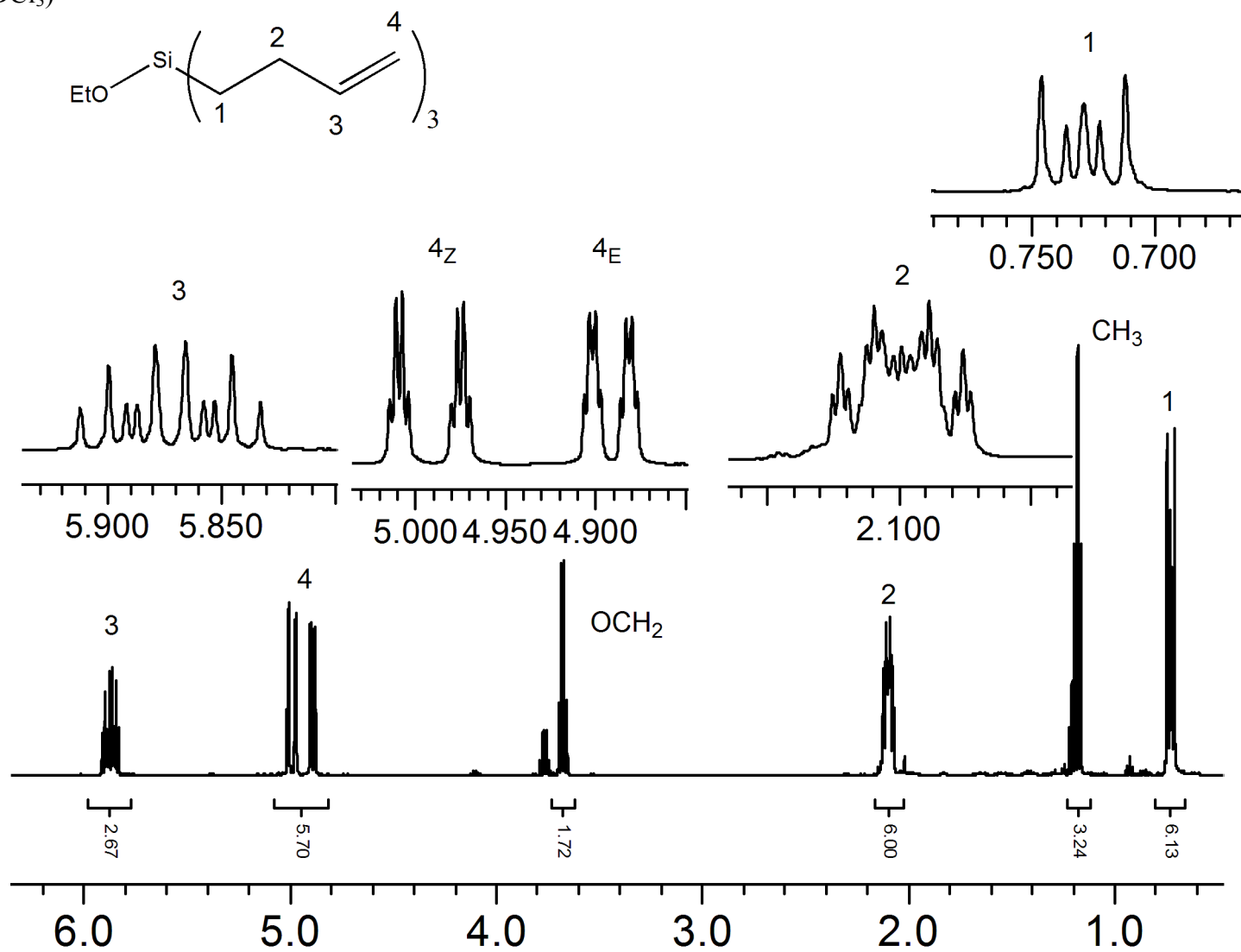
^{31}P (CD_2Cl_2)



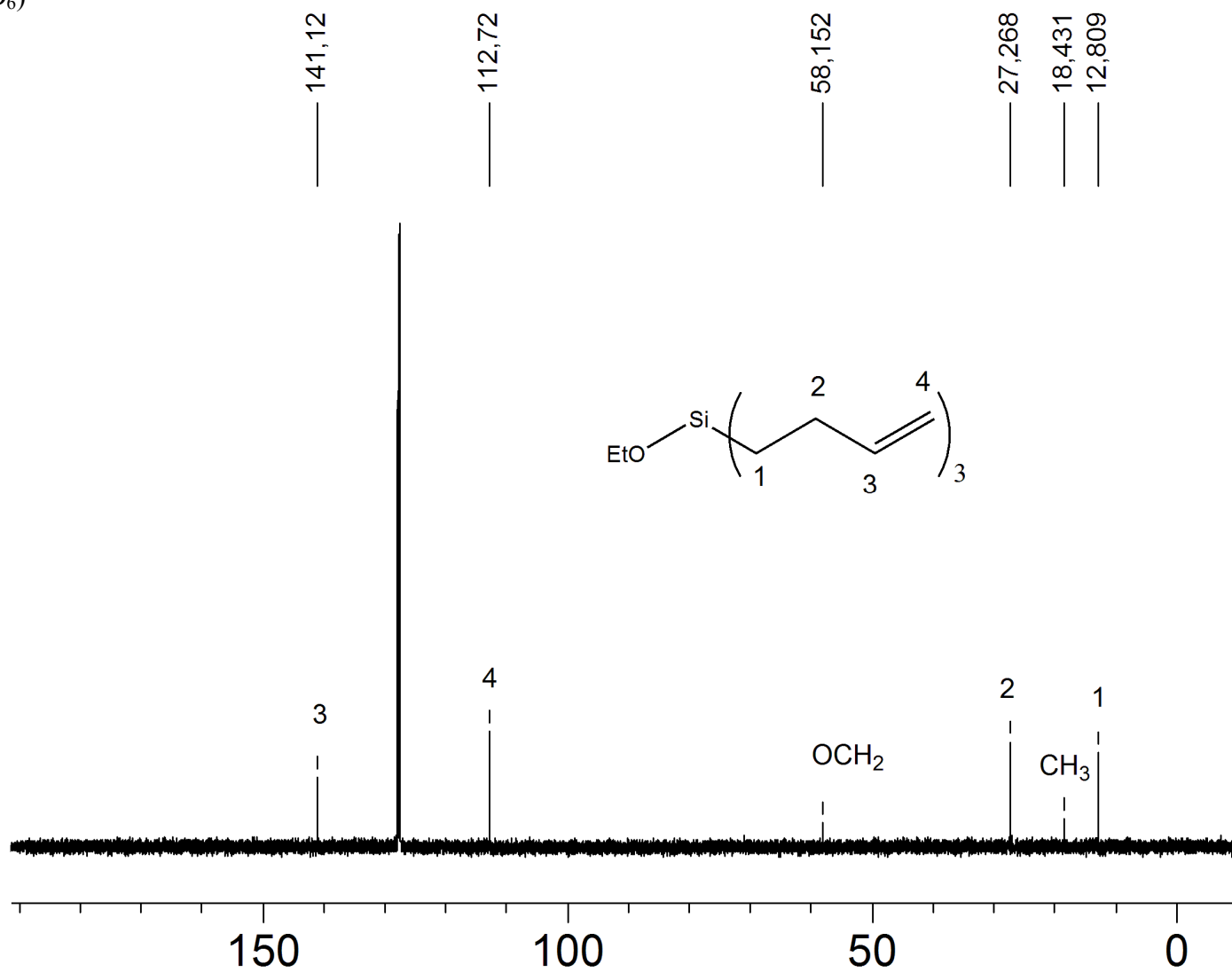
^{19}F (CD_2Cl_2)



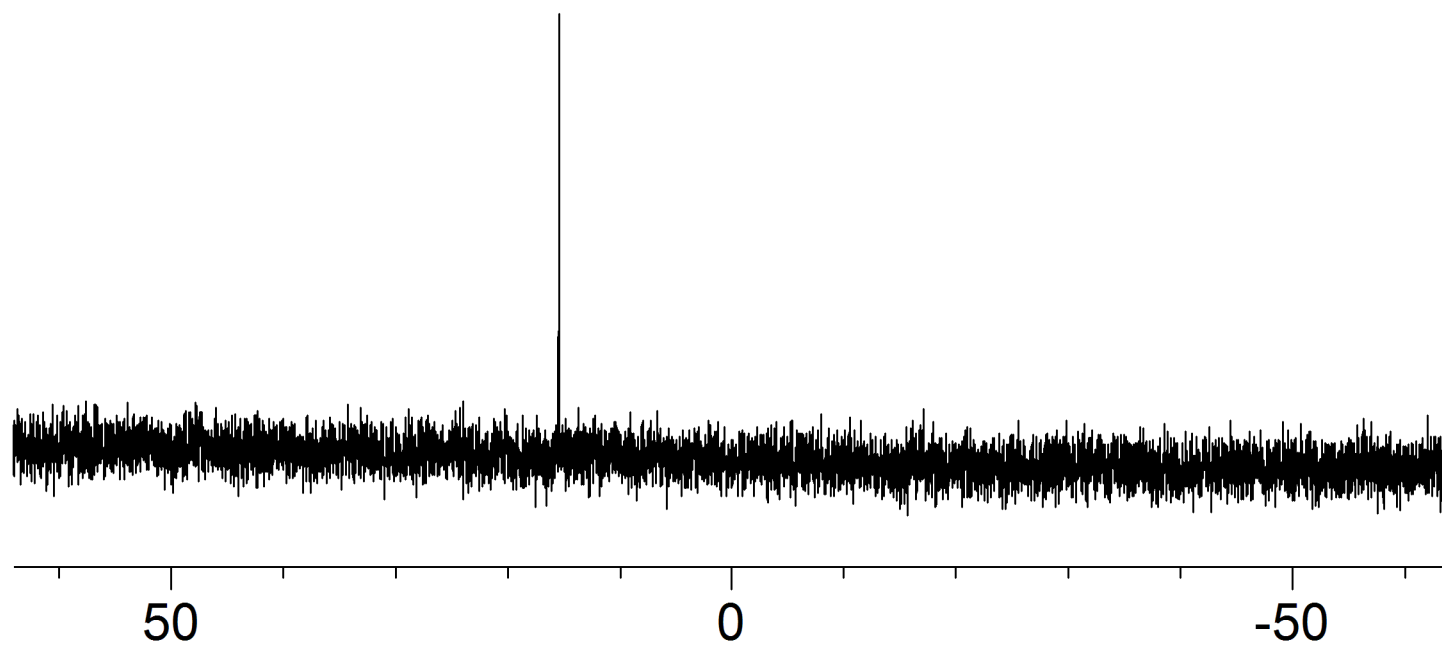
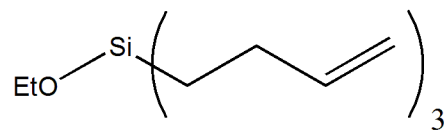
^1H (CDCl_3)



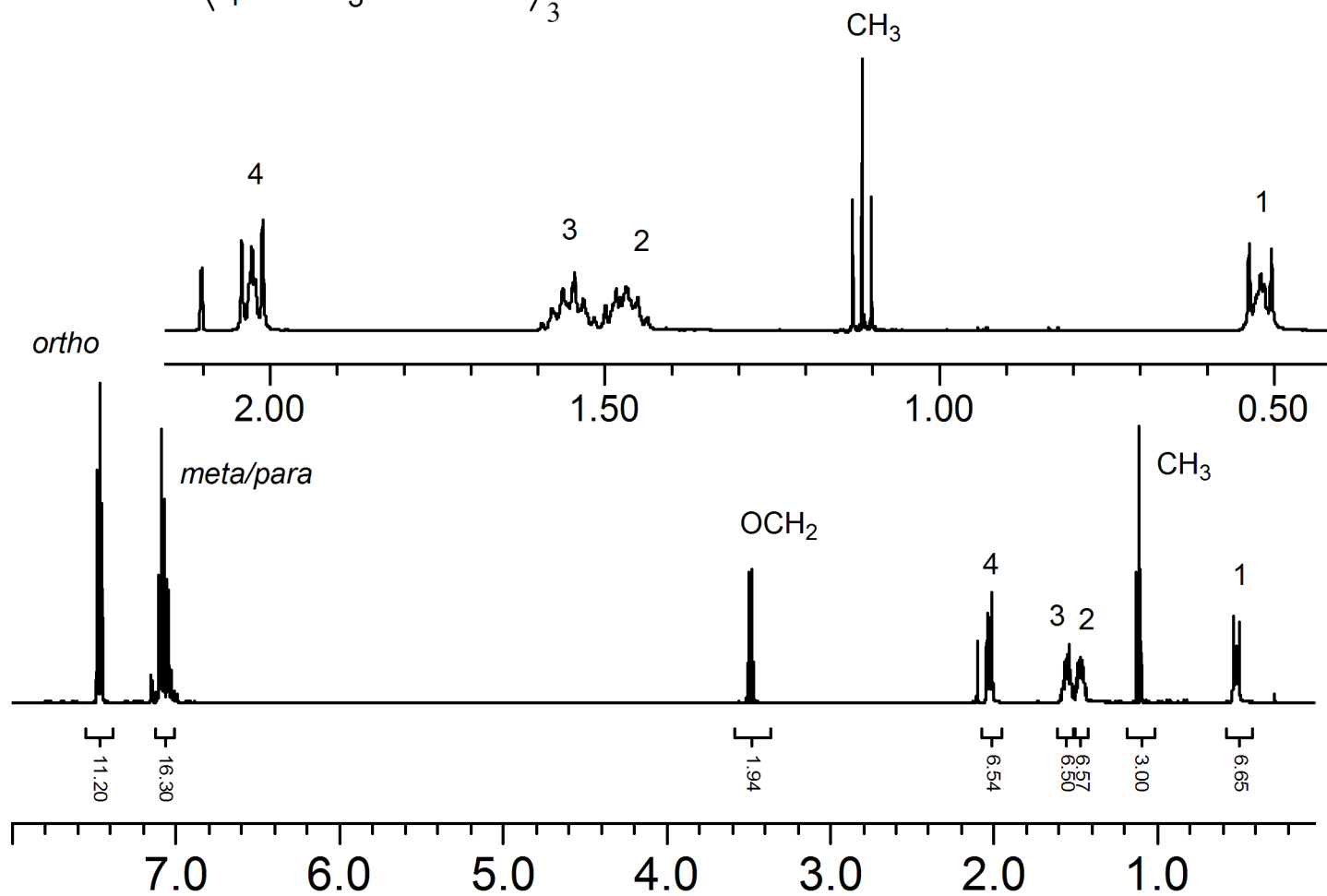
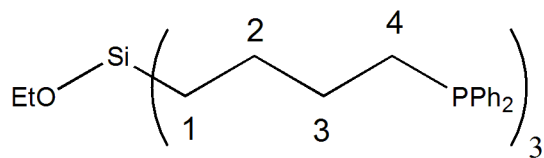
^{13}C (C_6D_6)



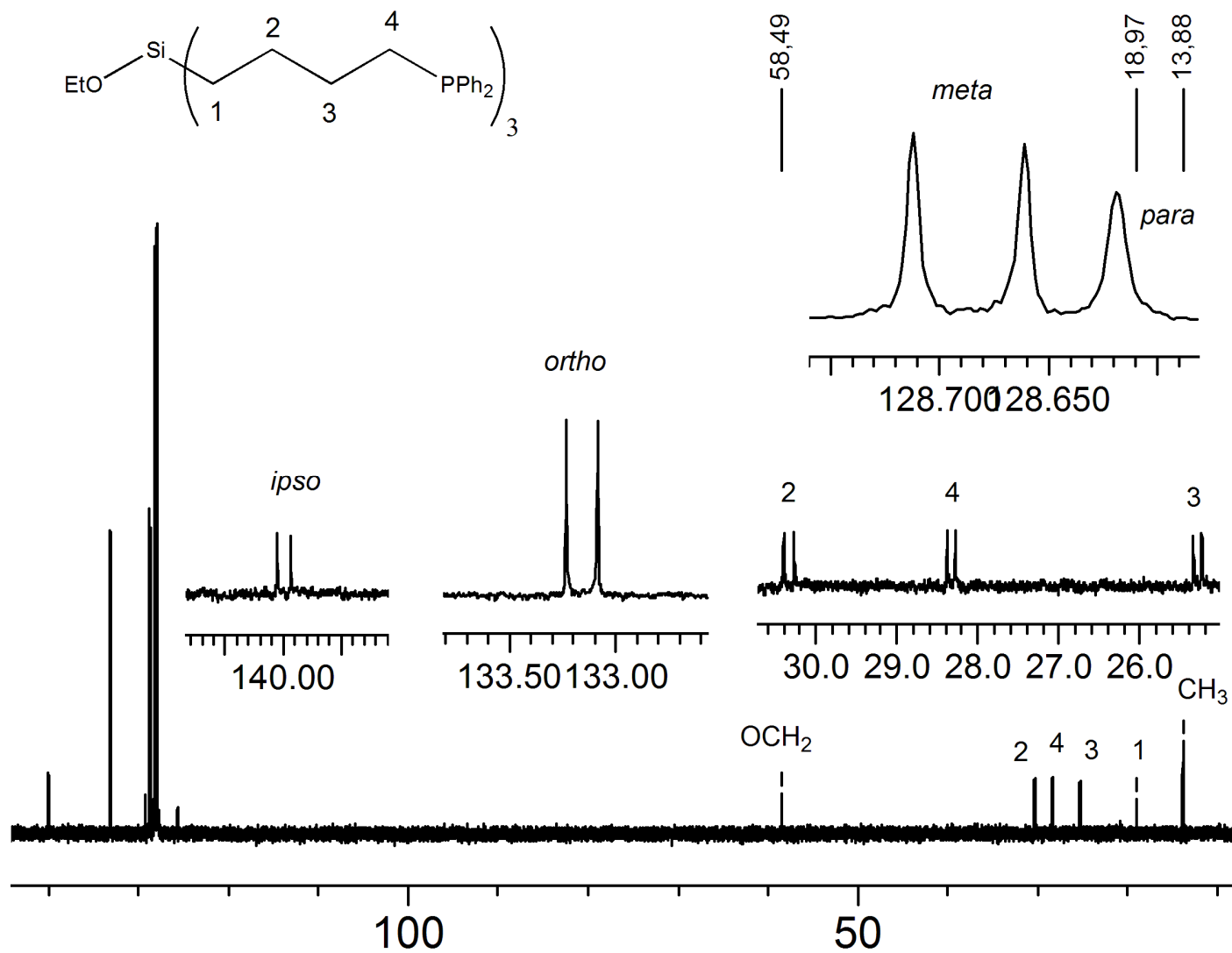
^{29}Si (C_6D_6)



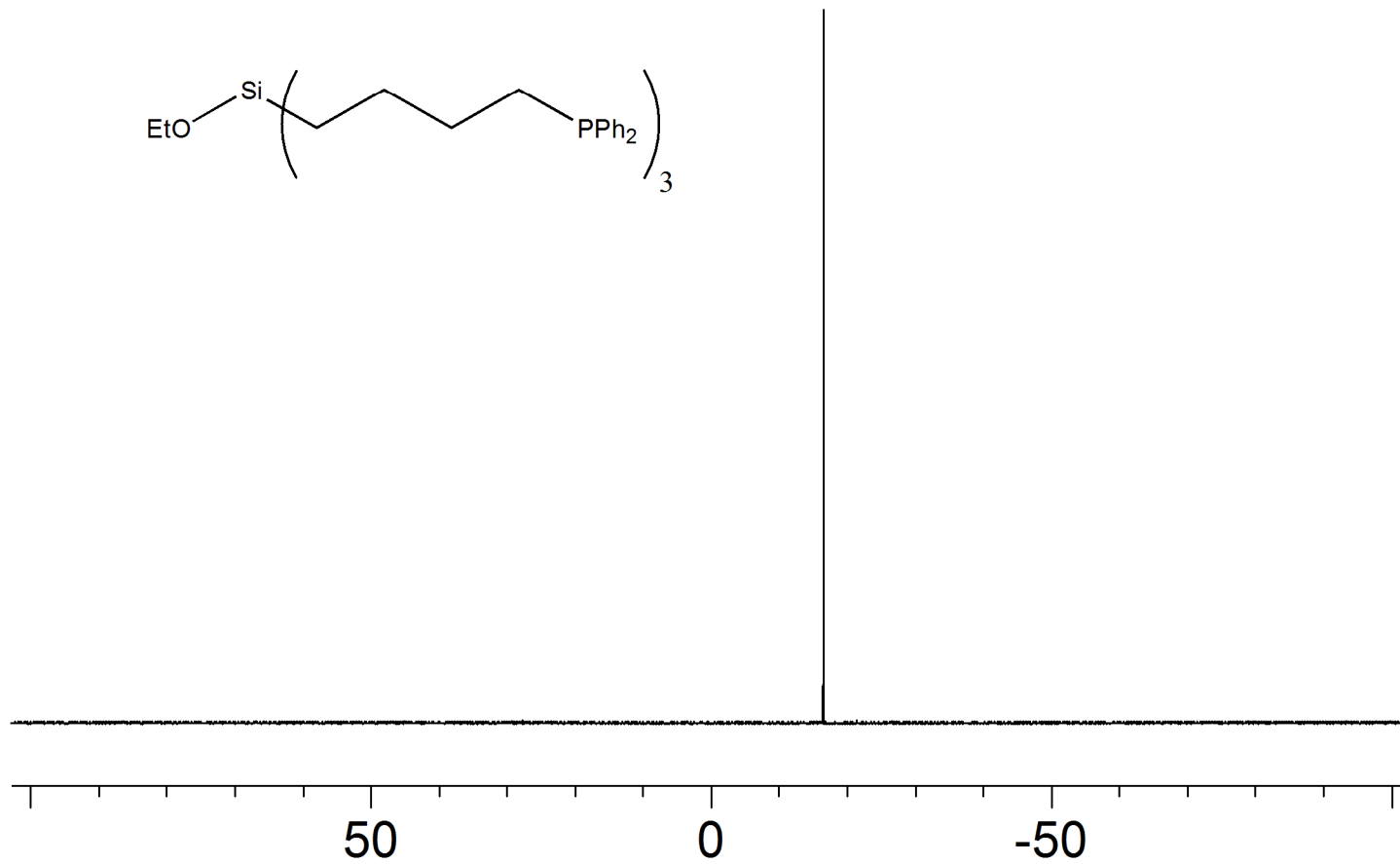
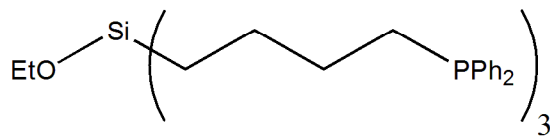
^1H (C_6D_6)



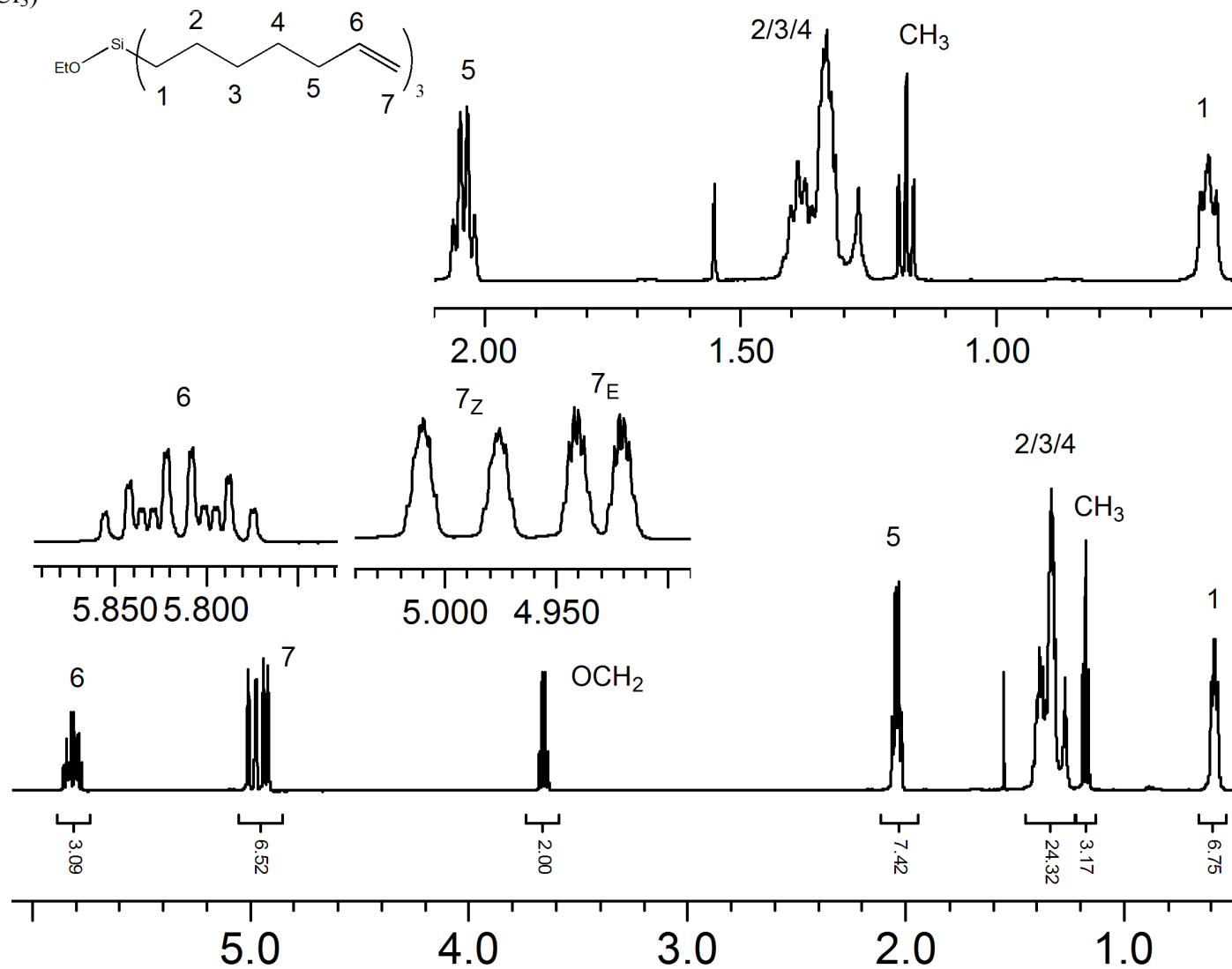
^{13}C (C_6D_6)



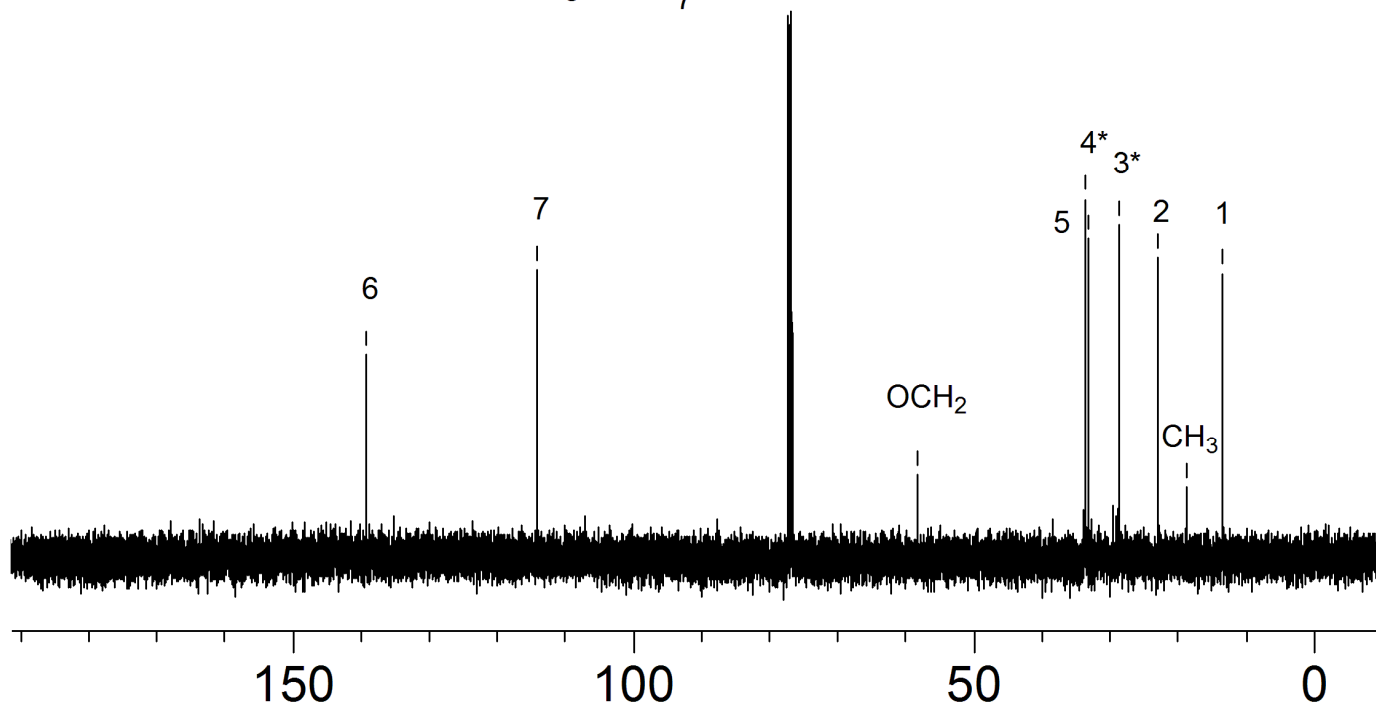
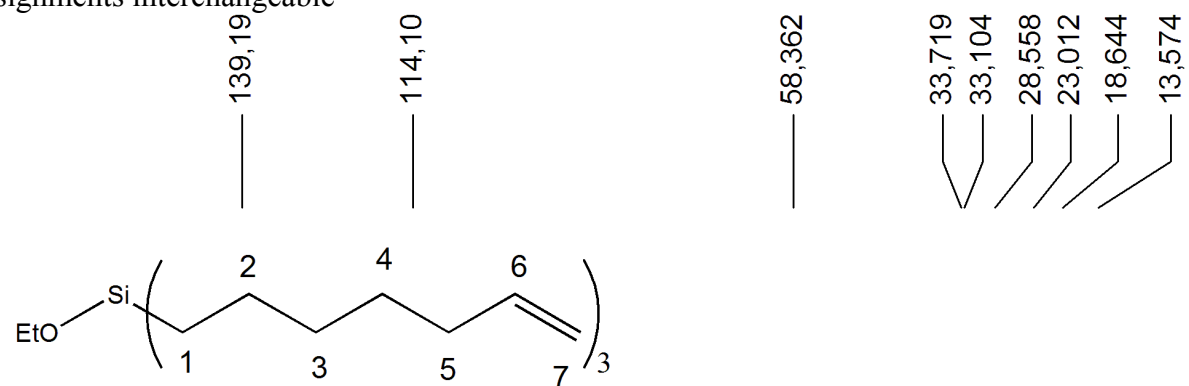
^{31}P (C_6D_6)



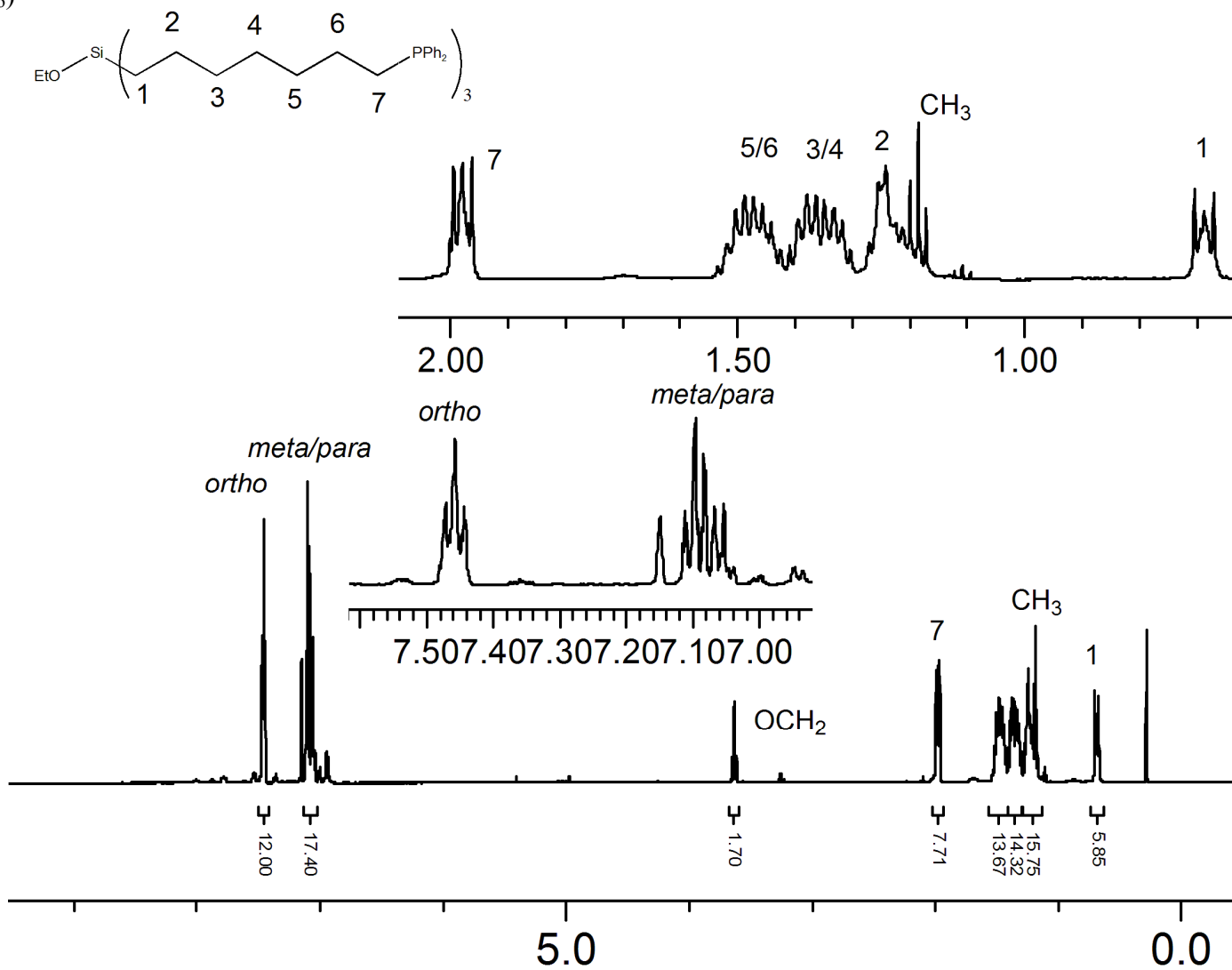
^1H (CDCl_3)



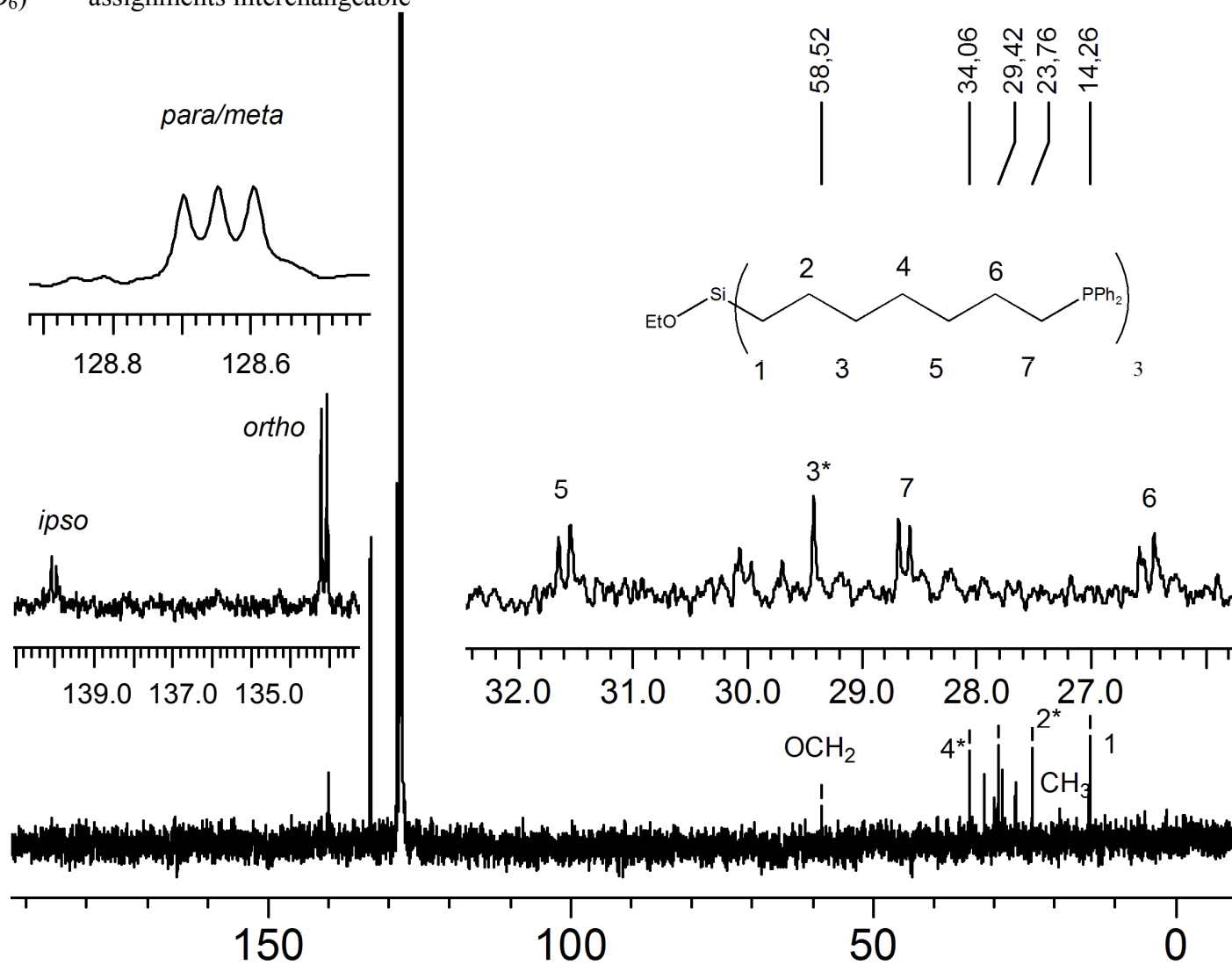
^{13}C (CDCl_3) *assignments interchangeable

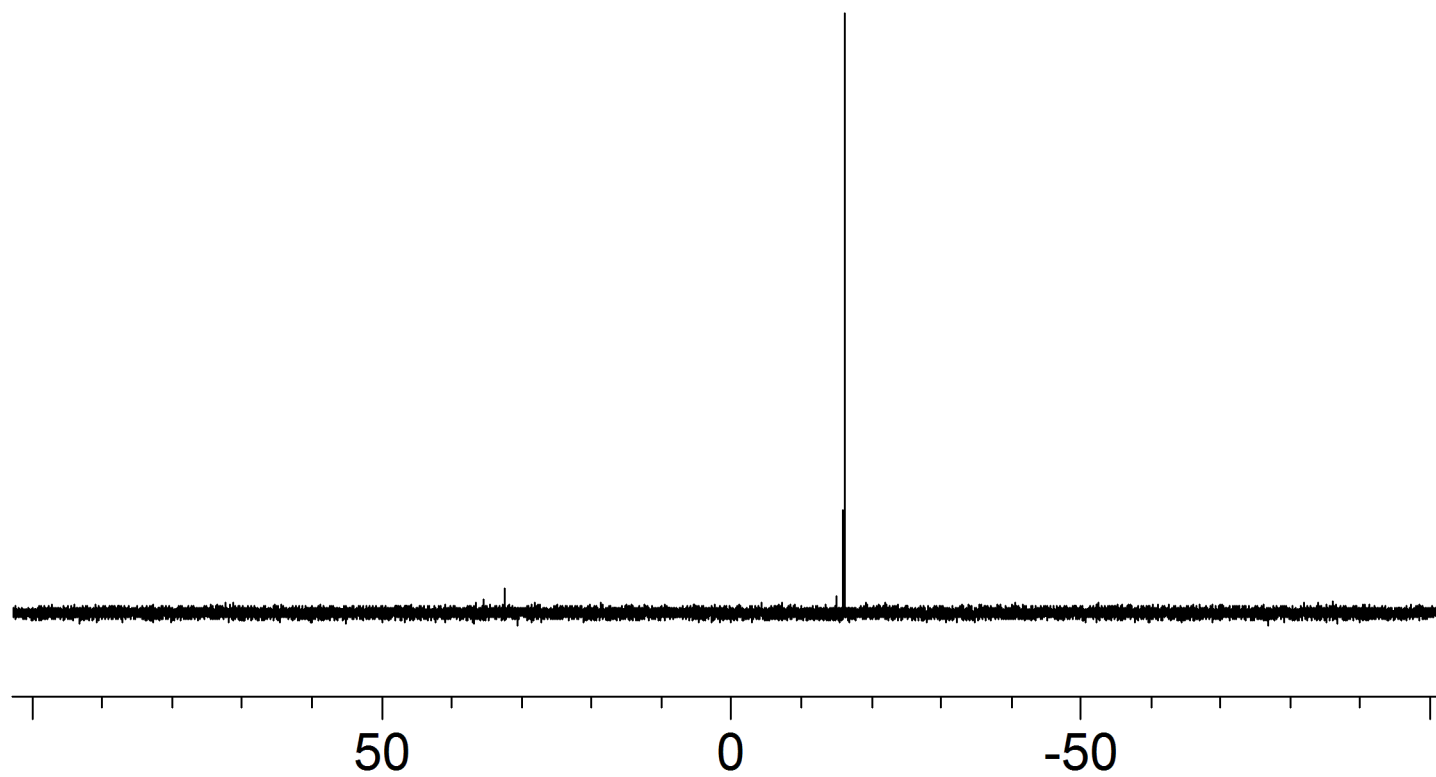
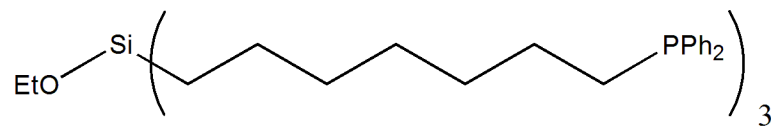


^1H (C_6D_6)

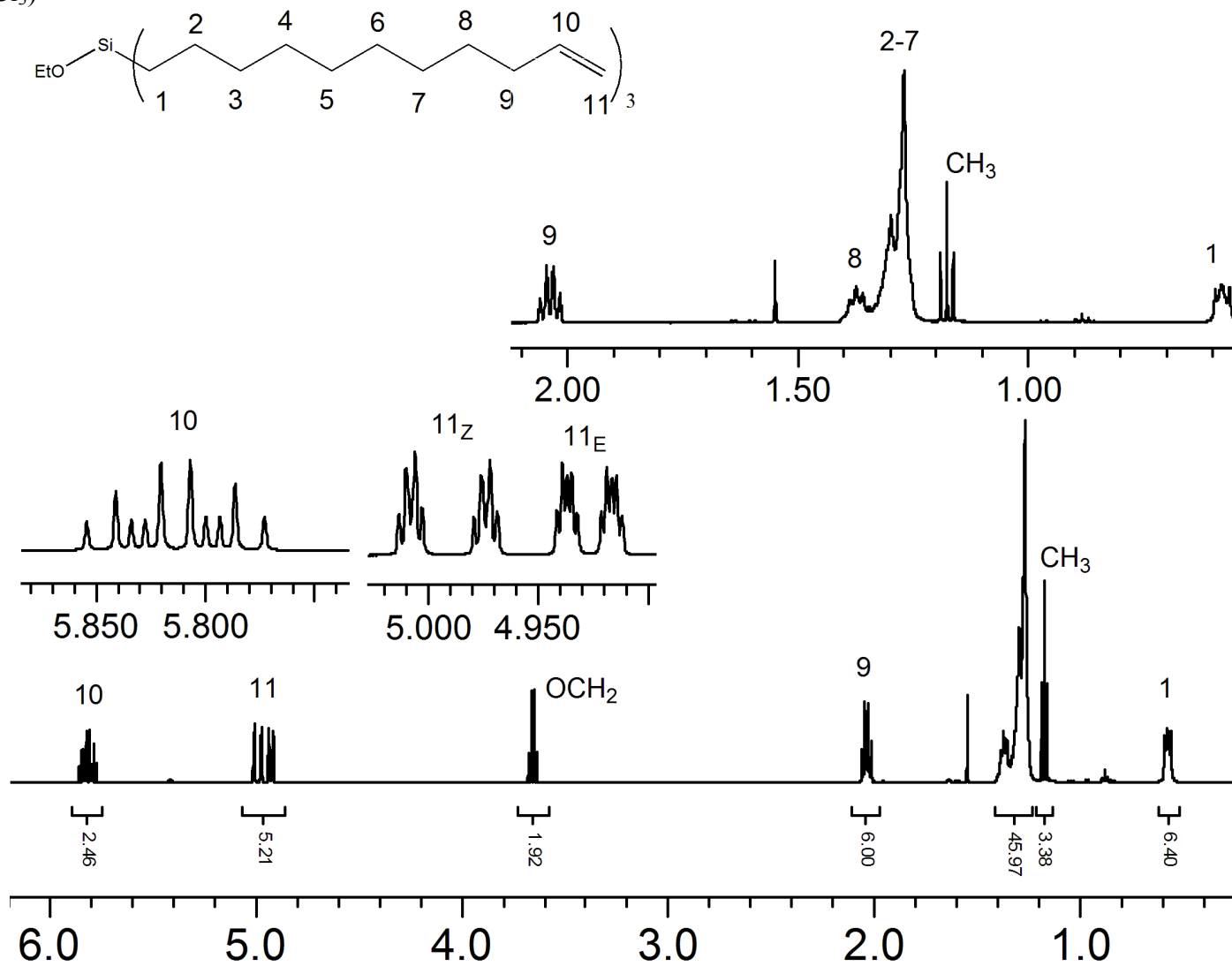


^{13}C (C_6D_6) *assignments interchangeable

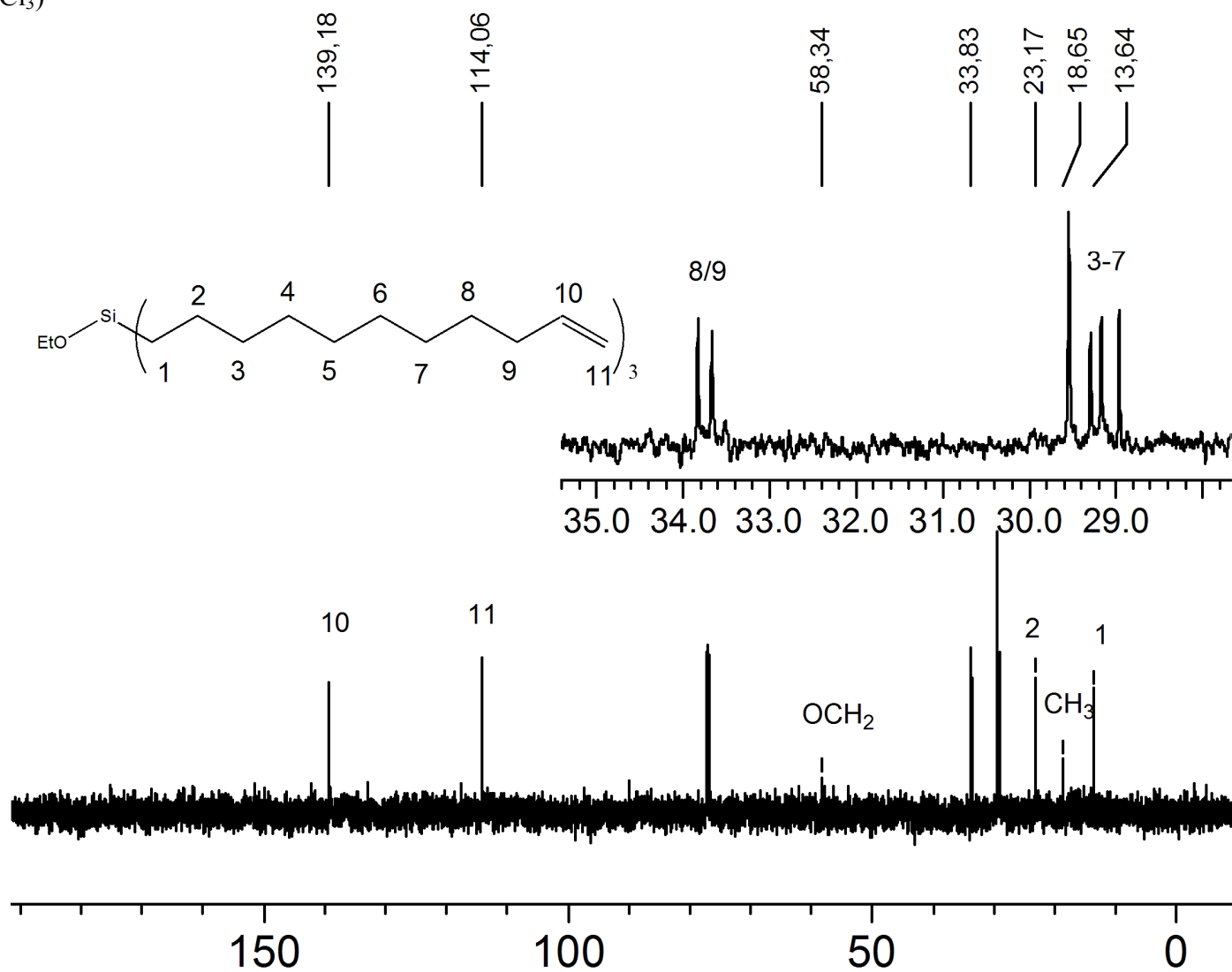


^{31}P (C_6D_6)

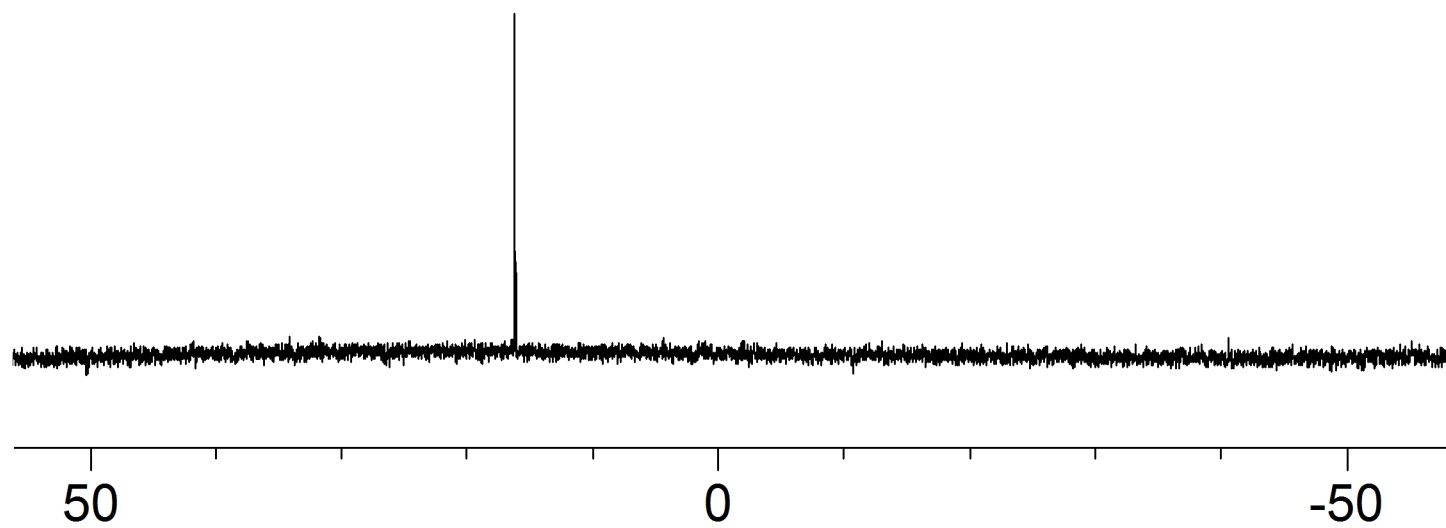
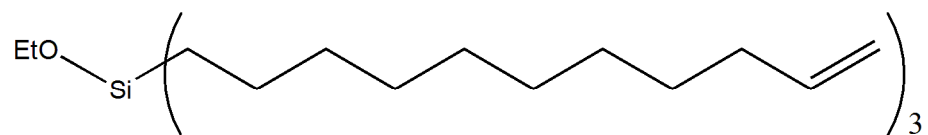
^1H (CDCl_3)



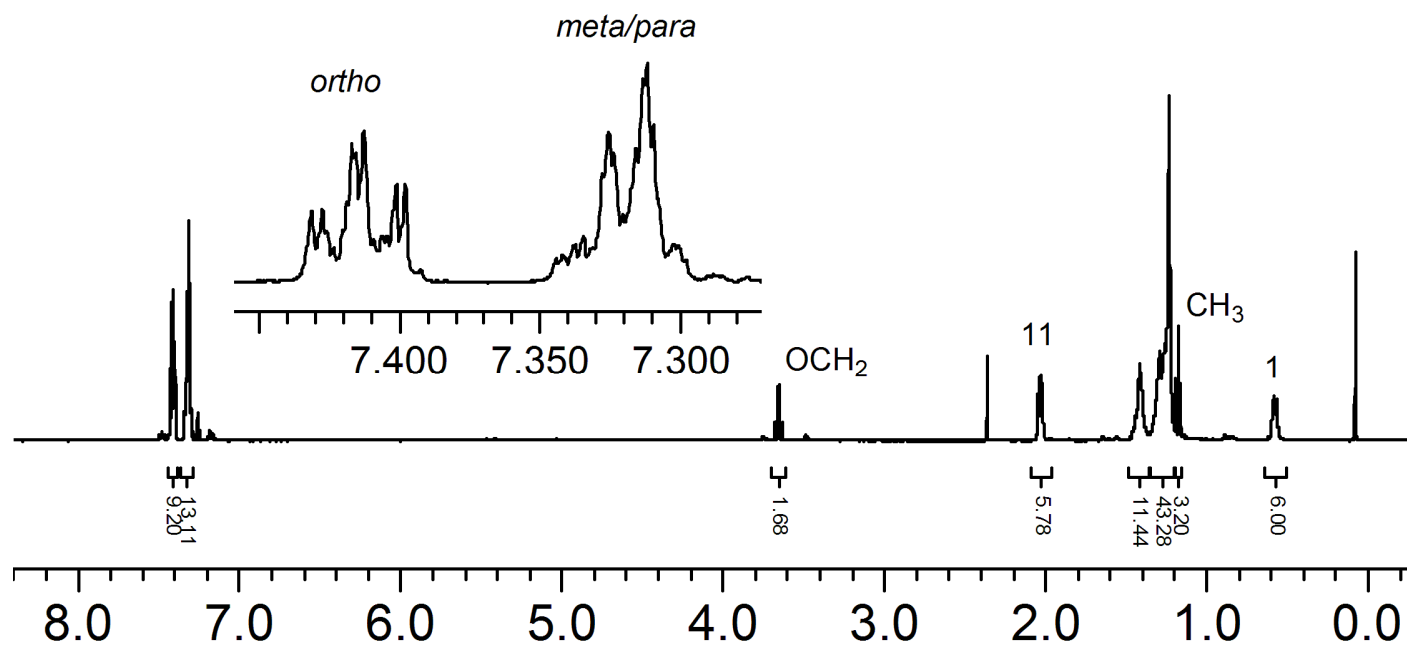
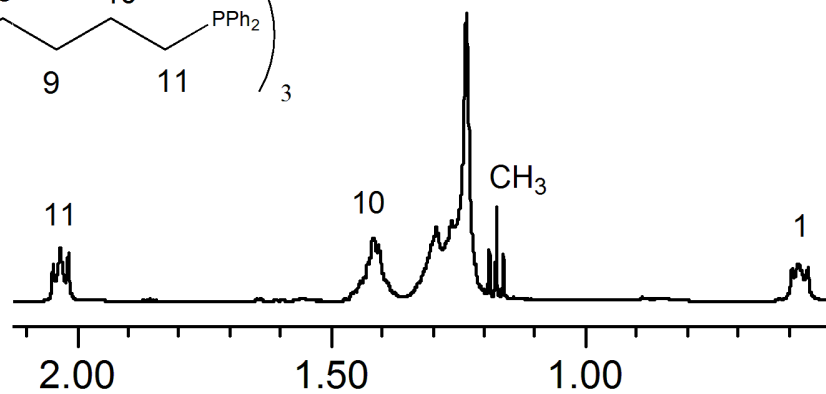
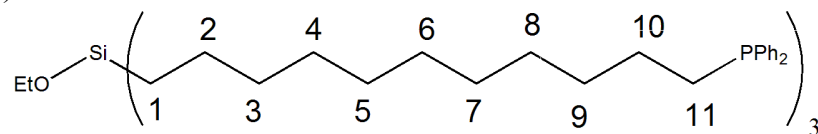
^{13}C (CDCl_3)



^{29}Si (CDCl₃)



^1H (CDCl_3)



$^{13}\text{C}\{^{31}\text{P}\}$ (CDCl_3)

*assignments interchangeable

139,05
132,68

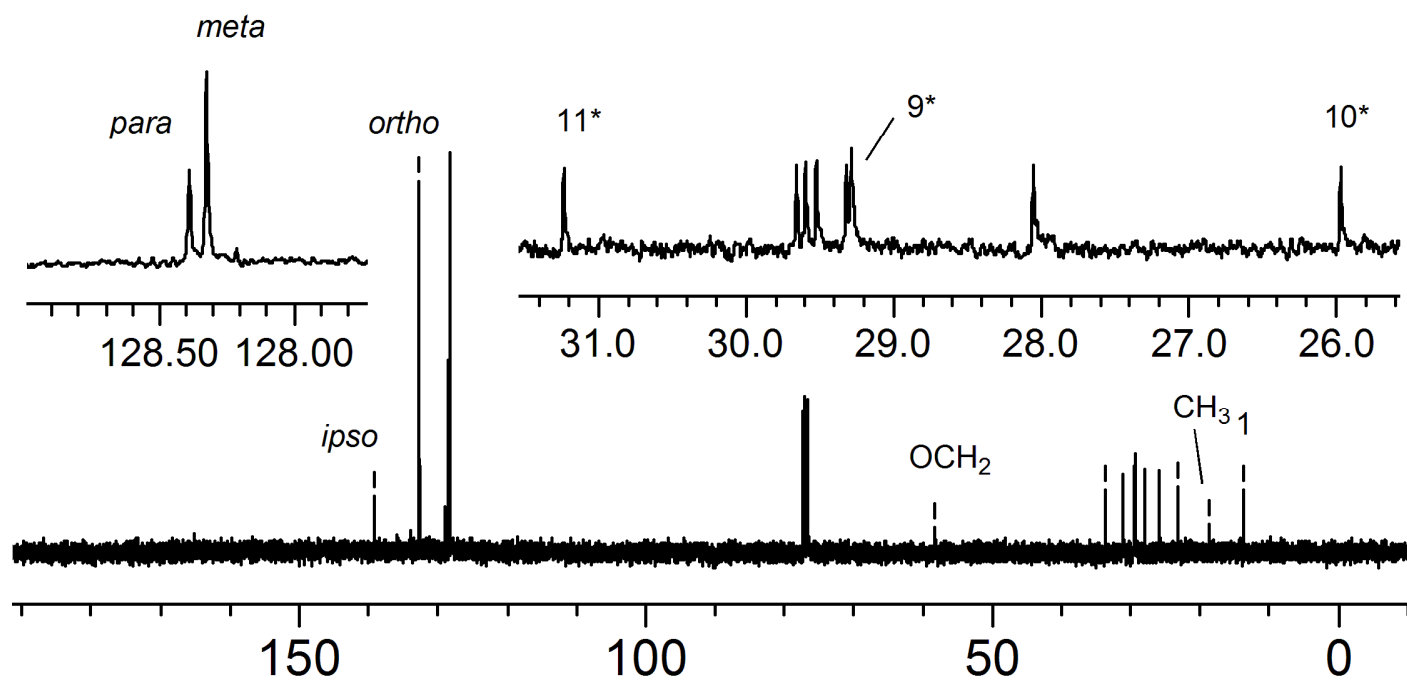
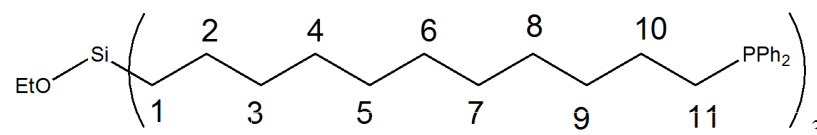
58,35

33,70

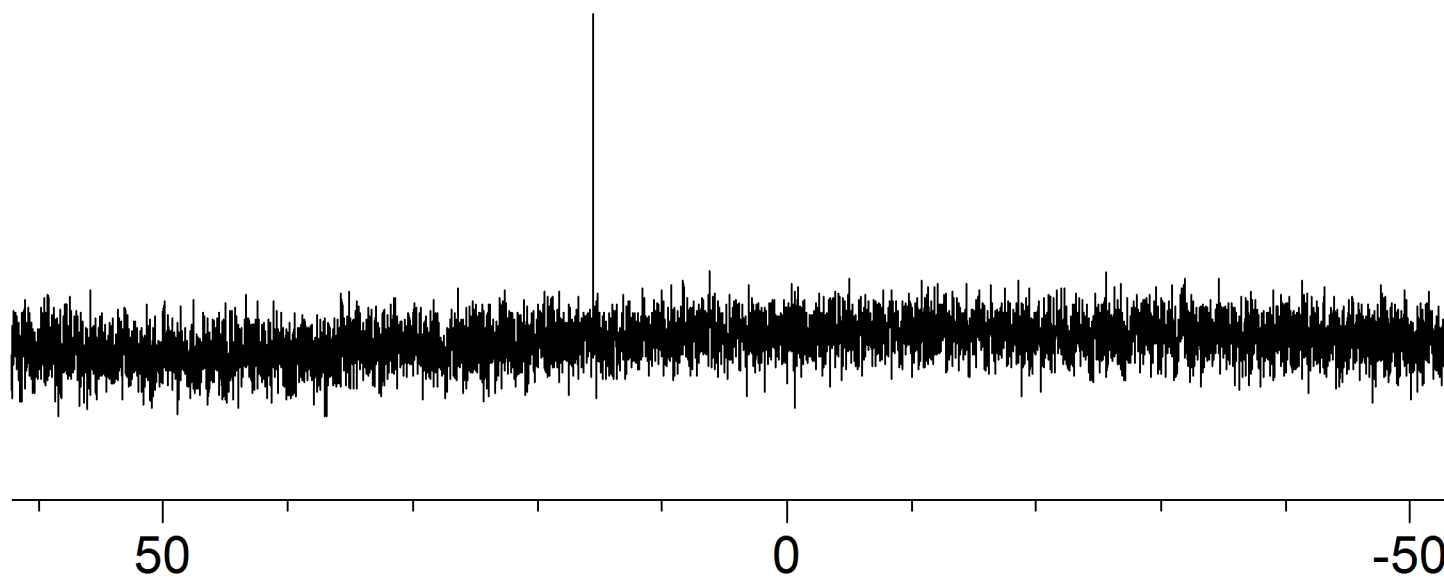
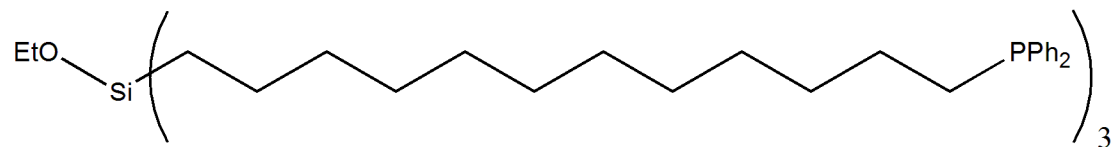
23,19

18,67

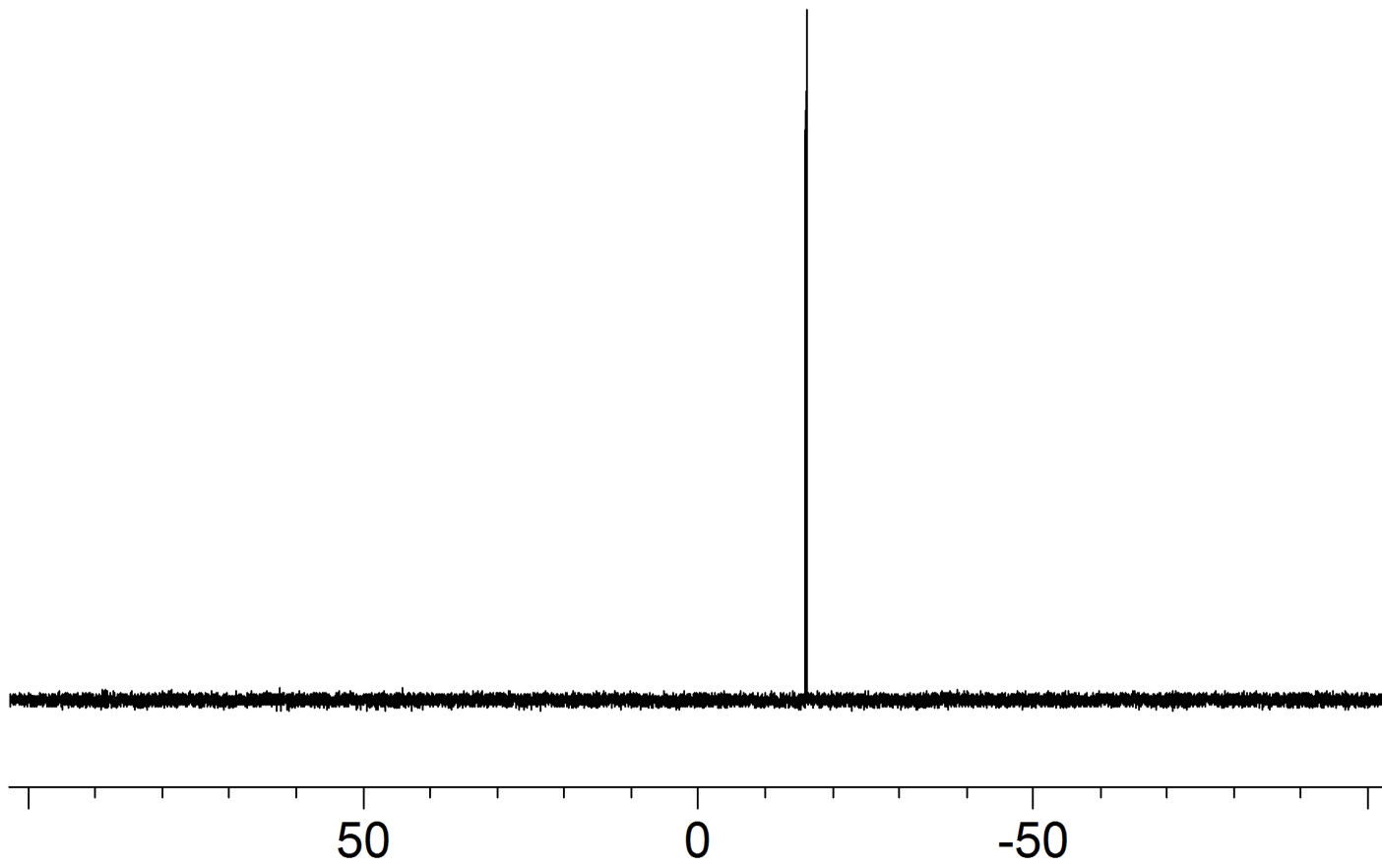
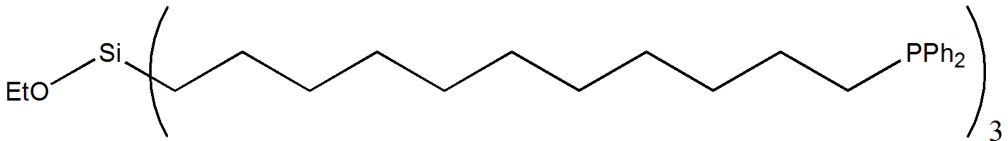
13,66



^{29}Si (CDCl_3)

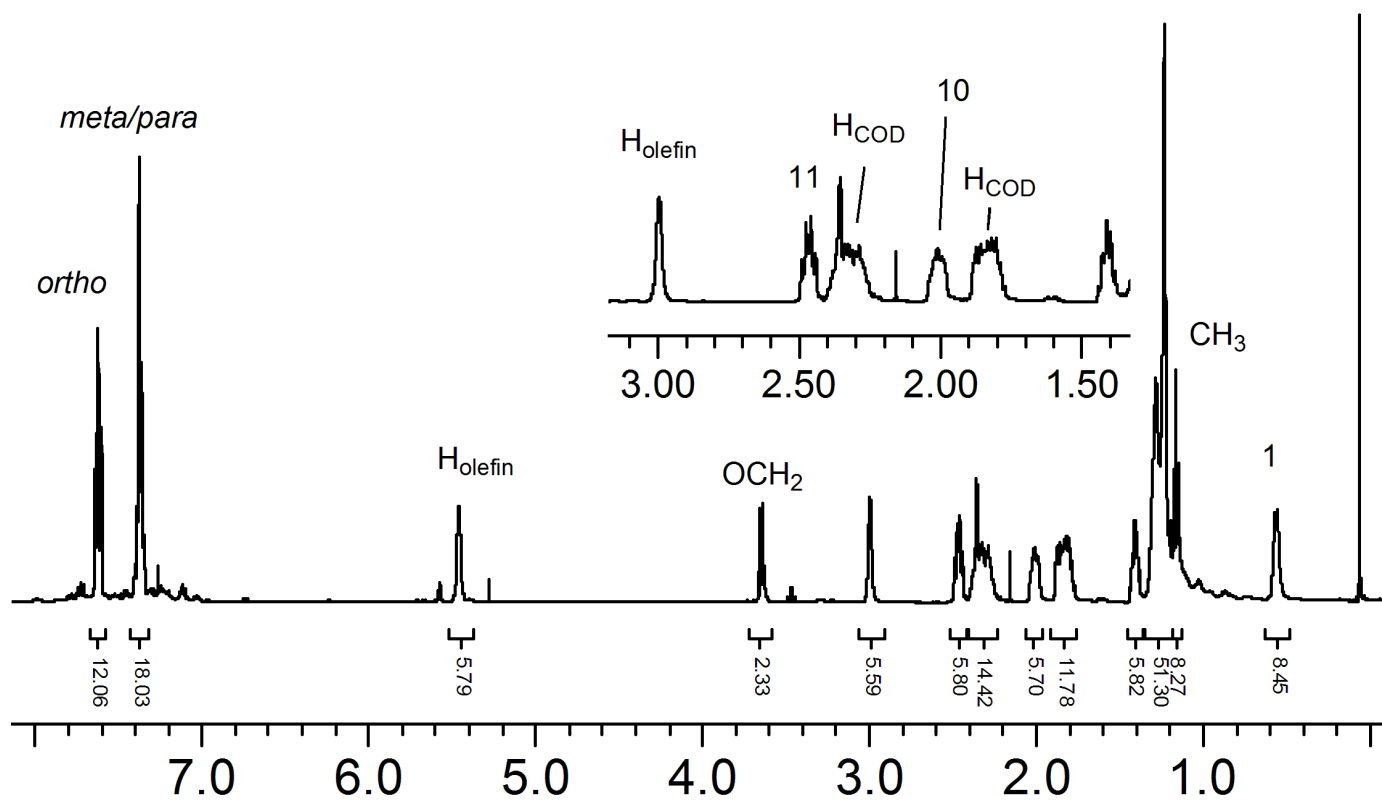
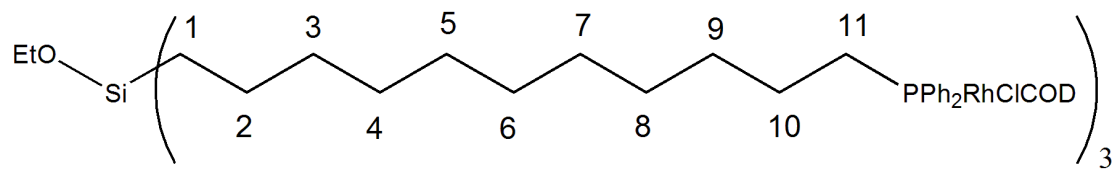


370

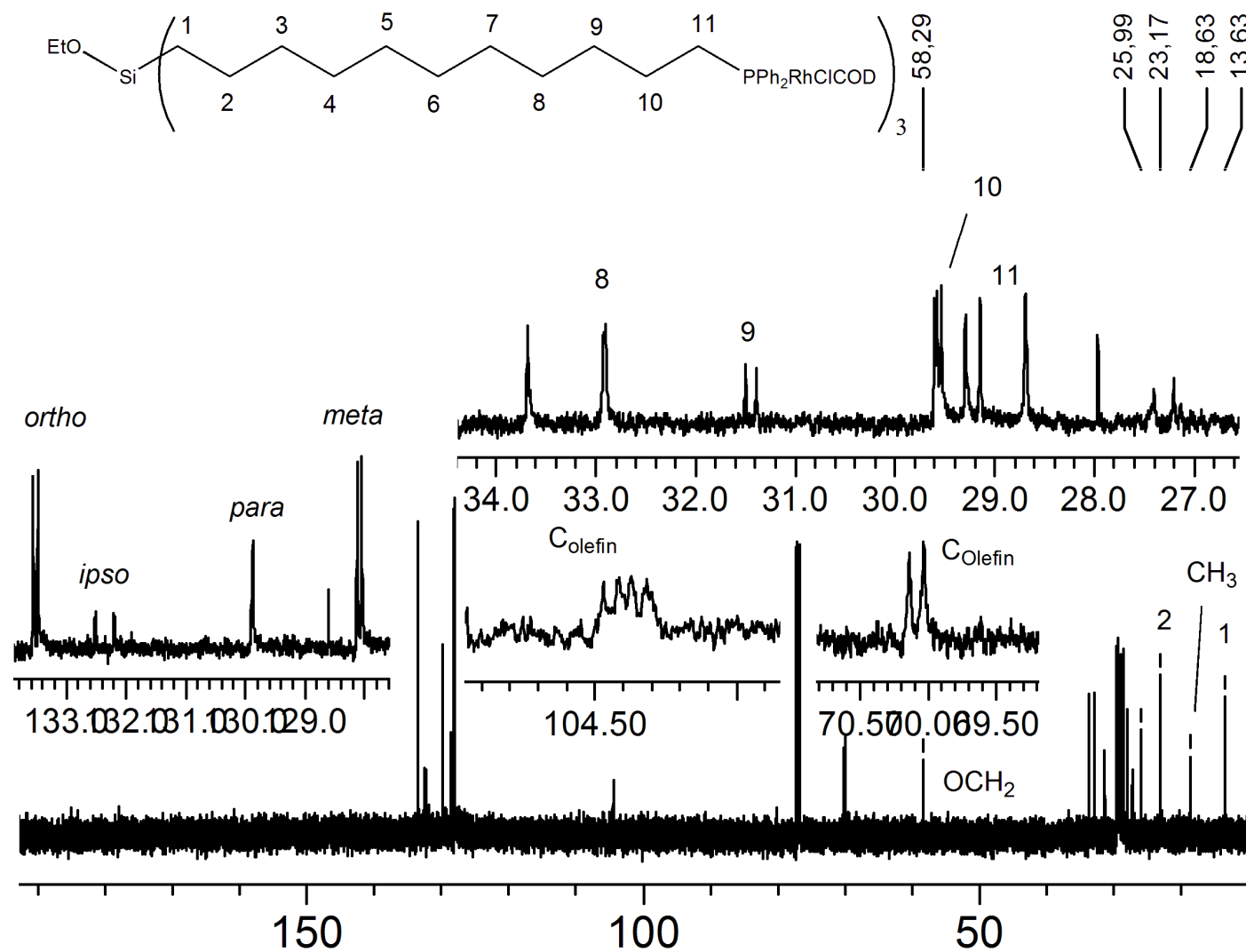
^{31}P (CDCl_3)

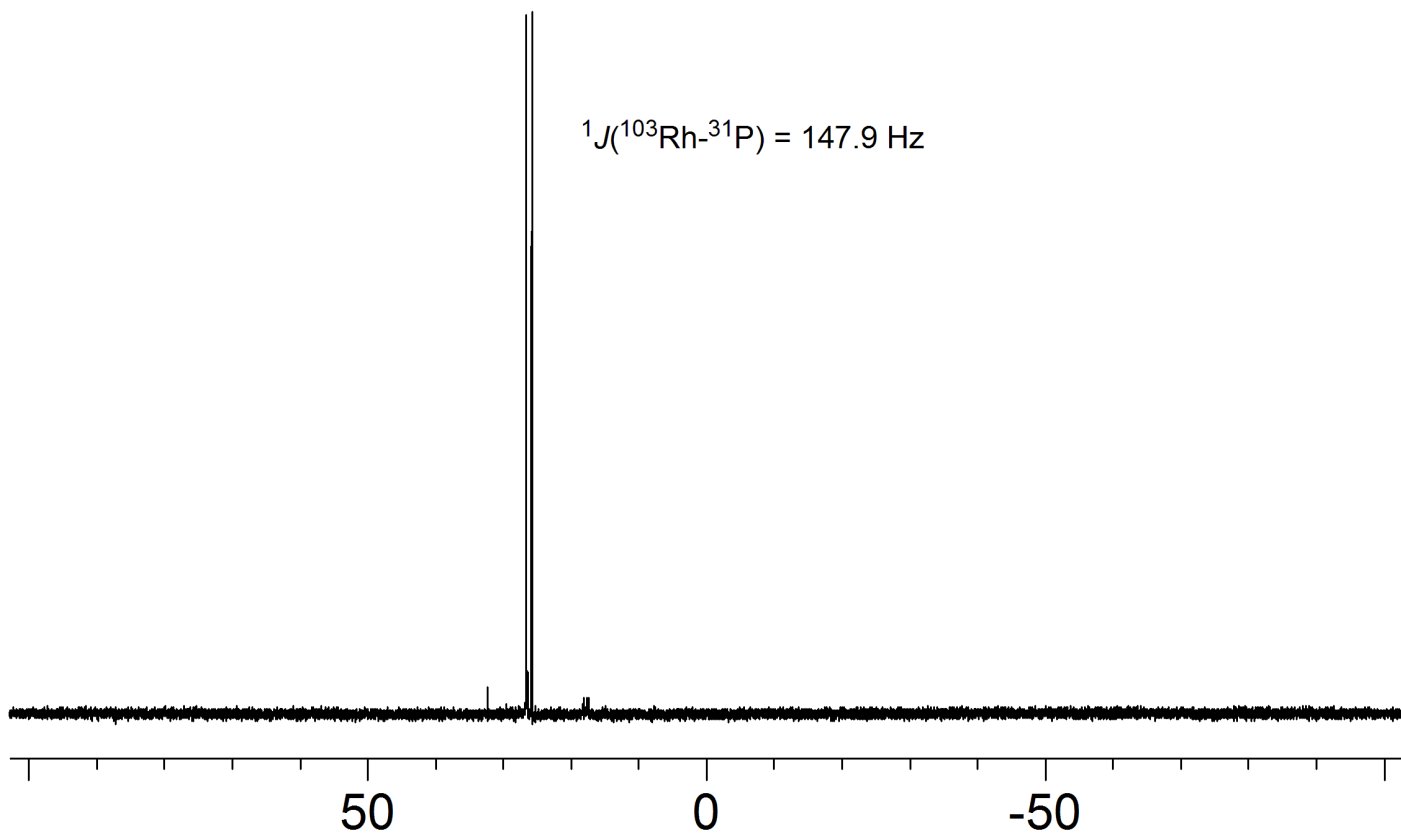
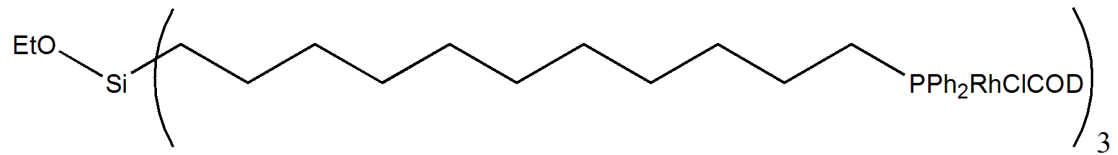
371

^1H (CDCl_3)

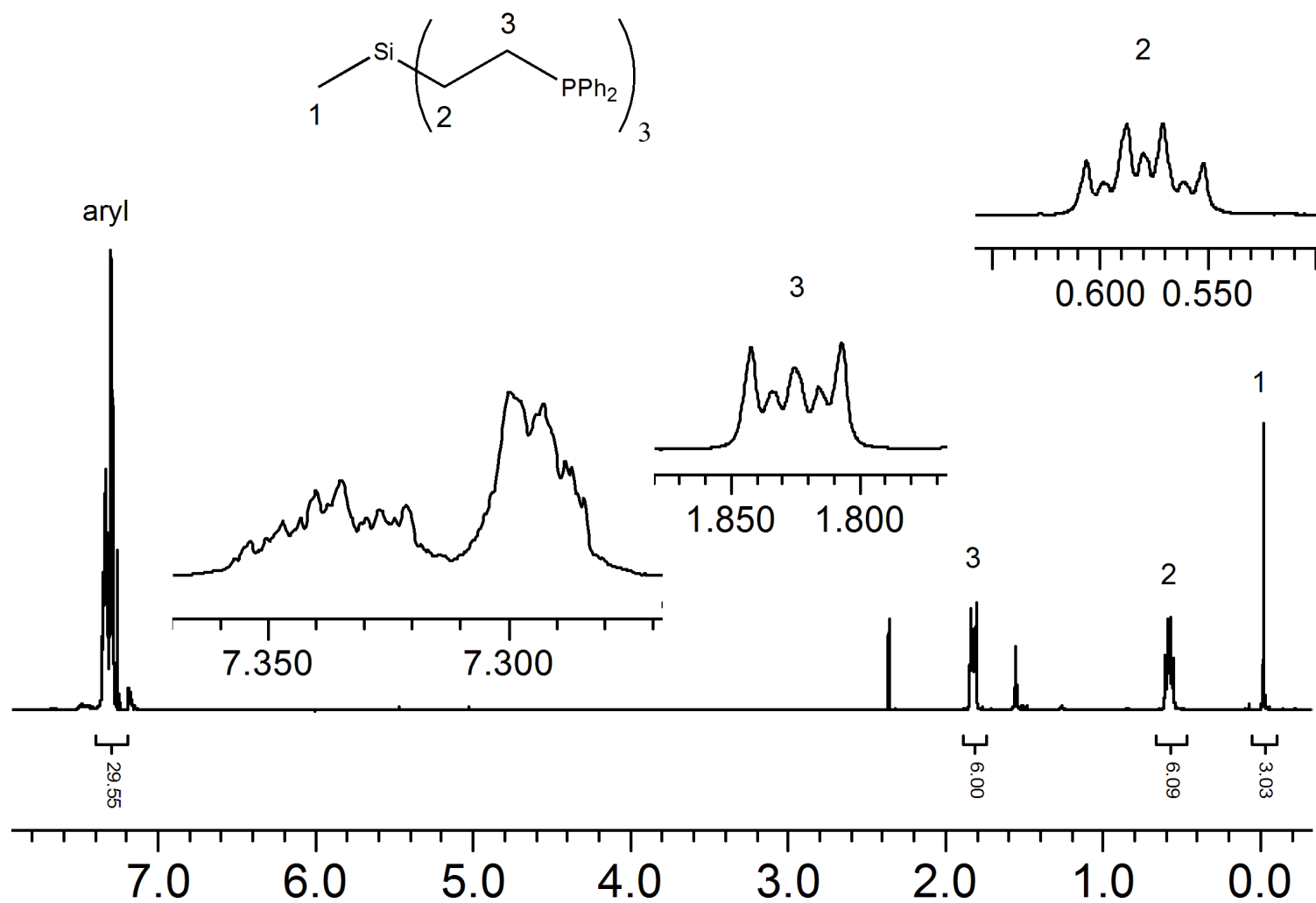


^{13}C (CDCl_3)

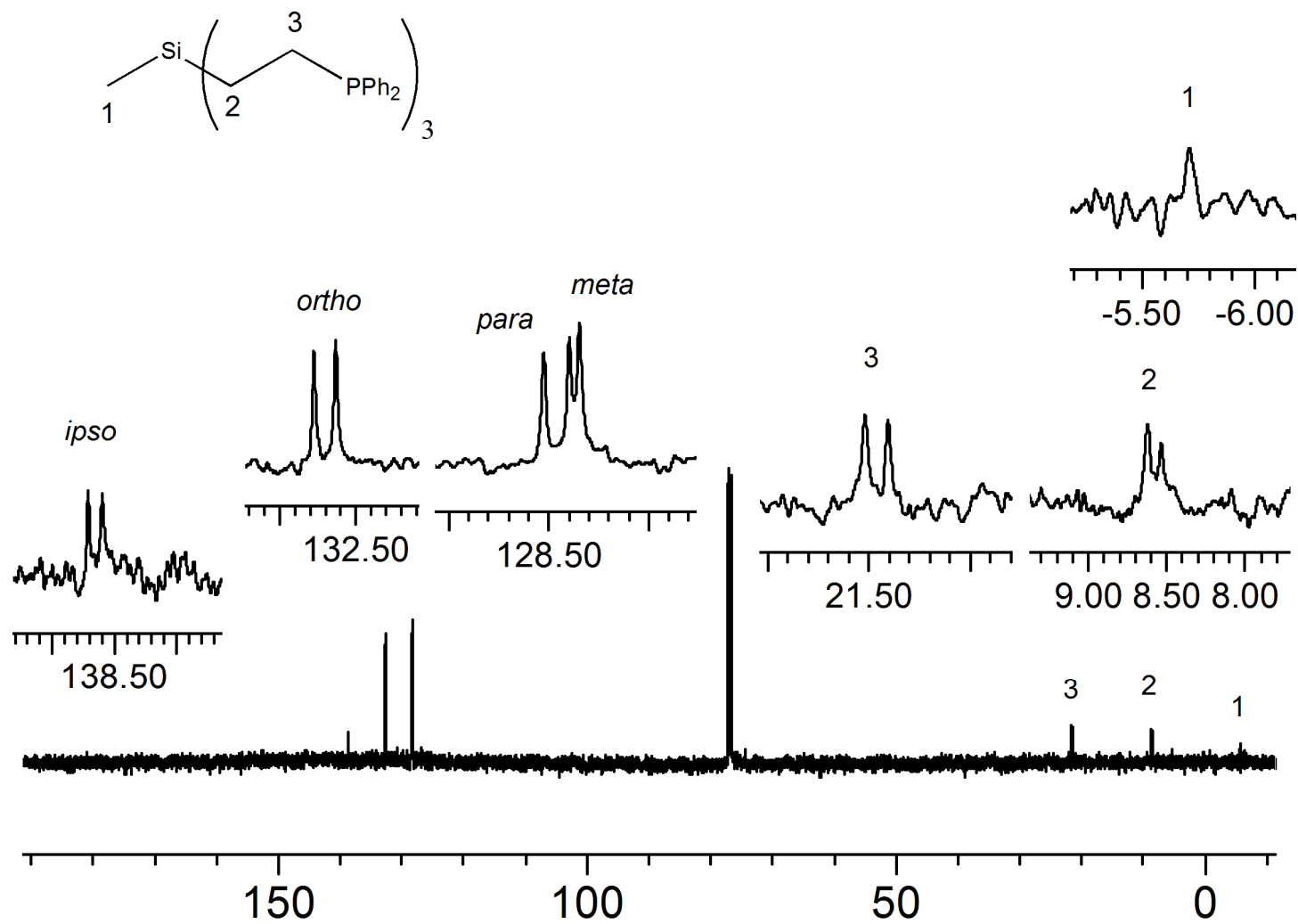


^{31}P (CDCl_3)

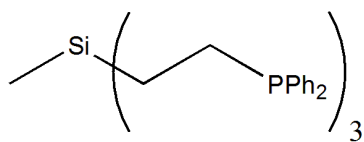
^1H (CDCl_3)



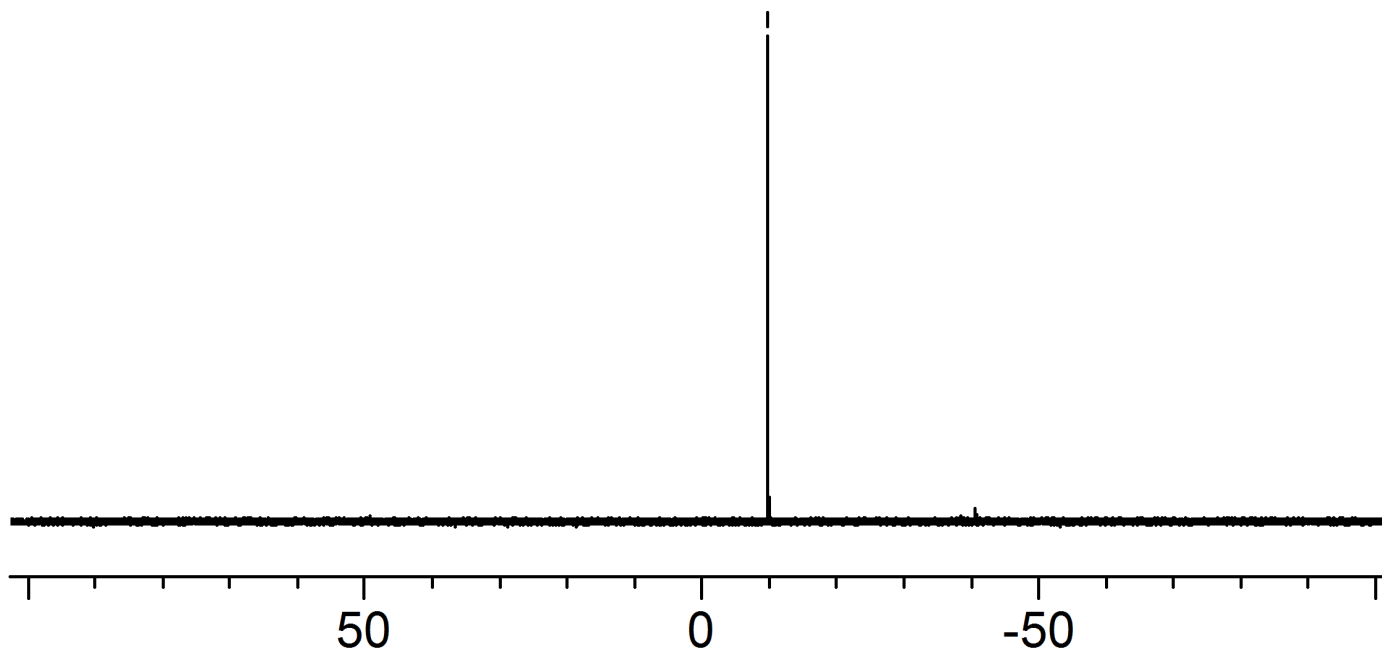
^{13}C (CDCl_3)



^{31}P (CDCl_3)



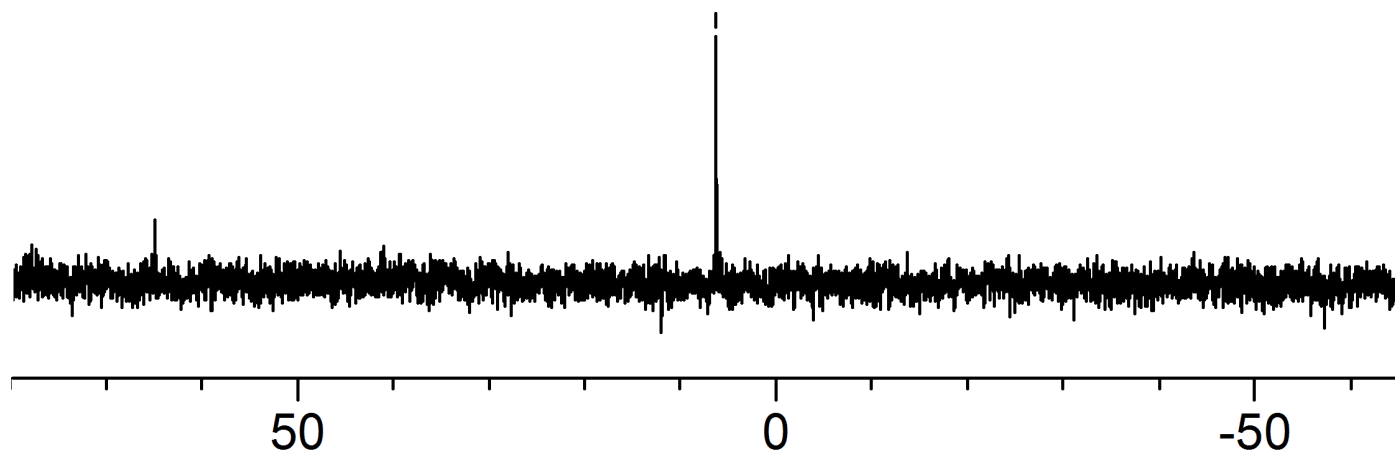
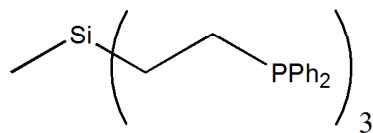
-9.88



377

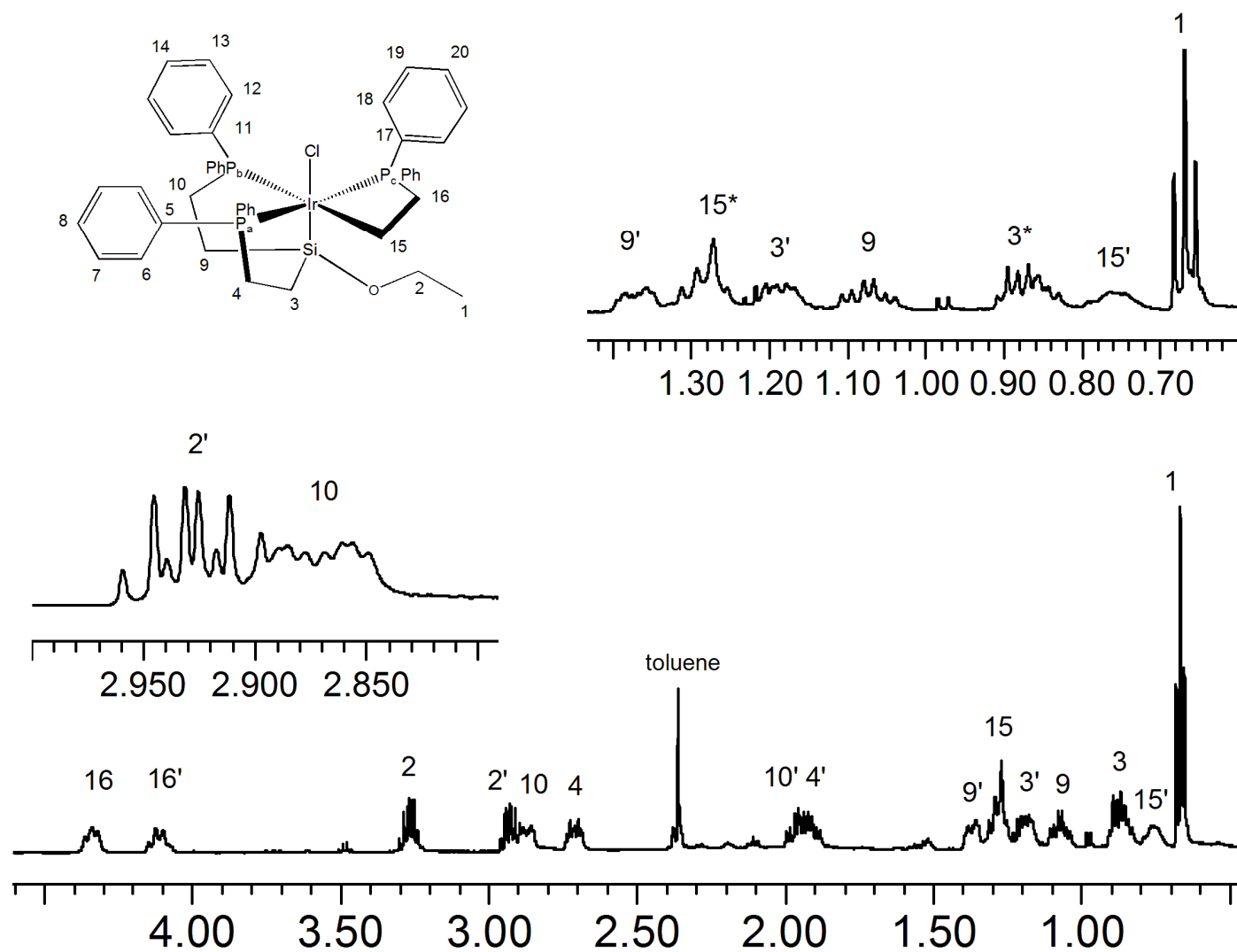
^{29}Si (CDCl₃)

6,27

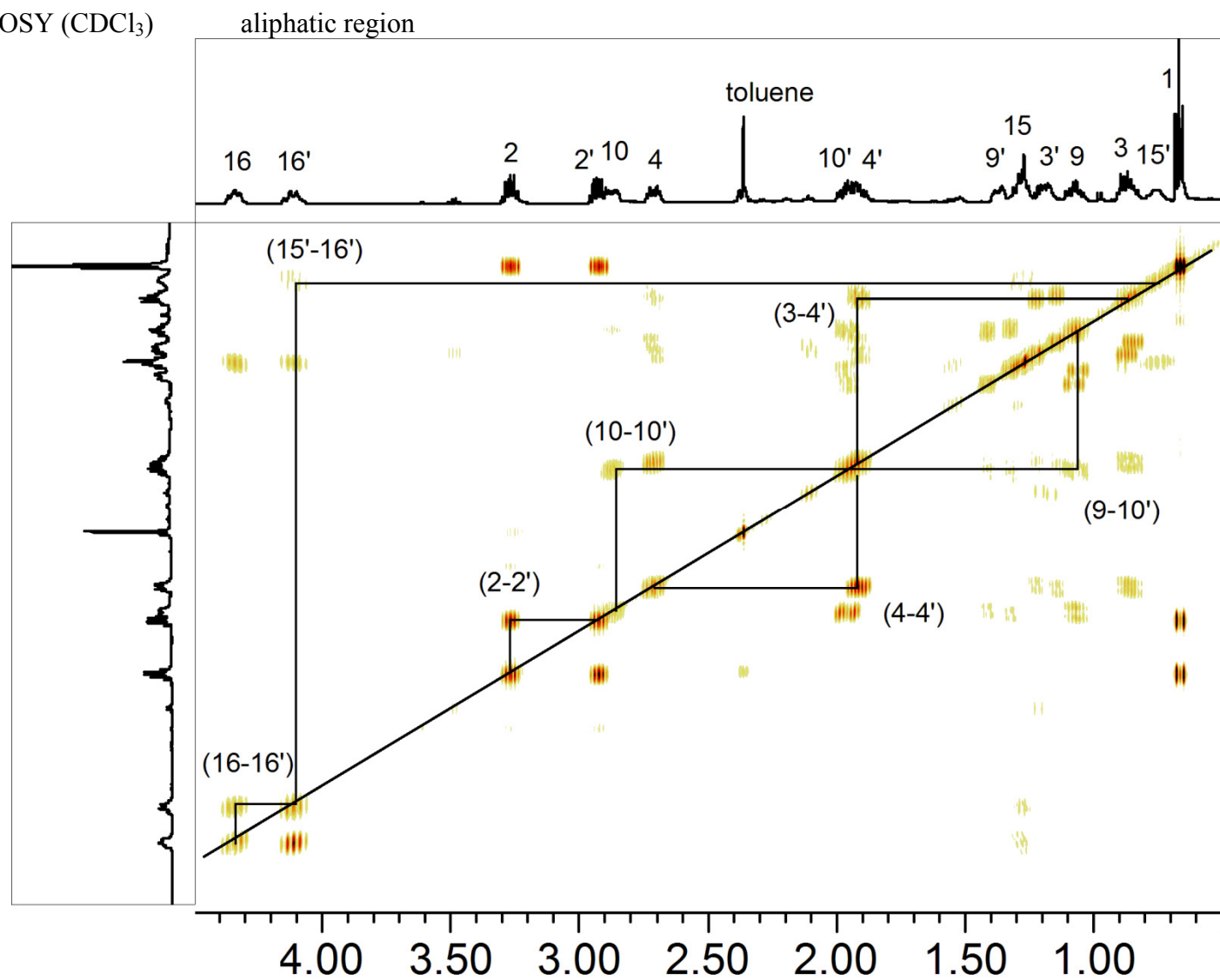


378

^1H (CDCl_3) aliphatic region *hexanes

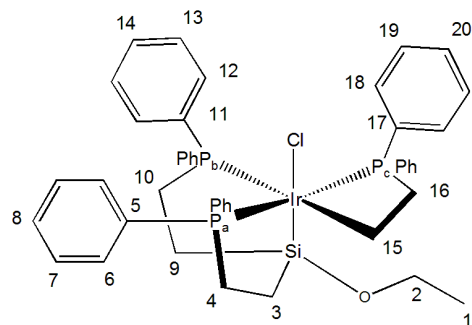


$^1\text{H}, ^1\text{H}$ COSY (CDCl_3)



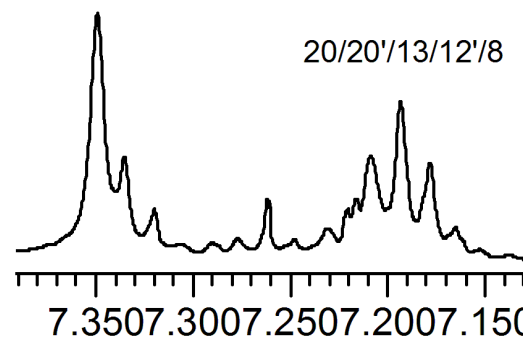
$^1\text{H}\{^{31}\text{P}\}$ (CDCl_3)

aromatic region



19/18/14/7

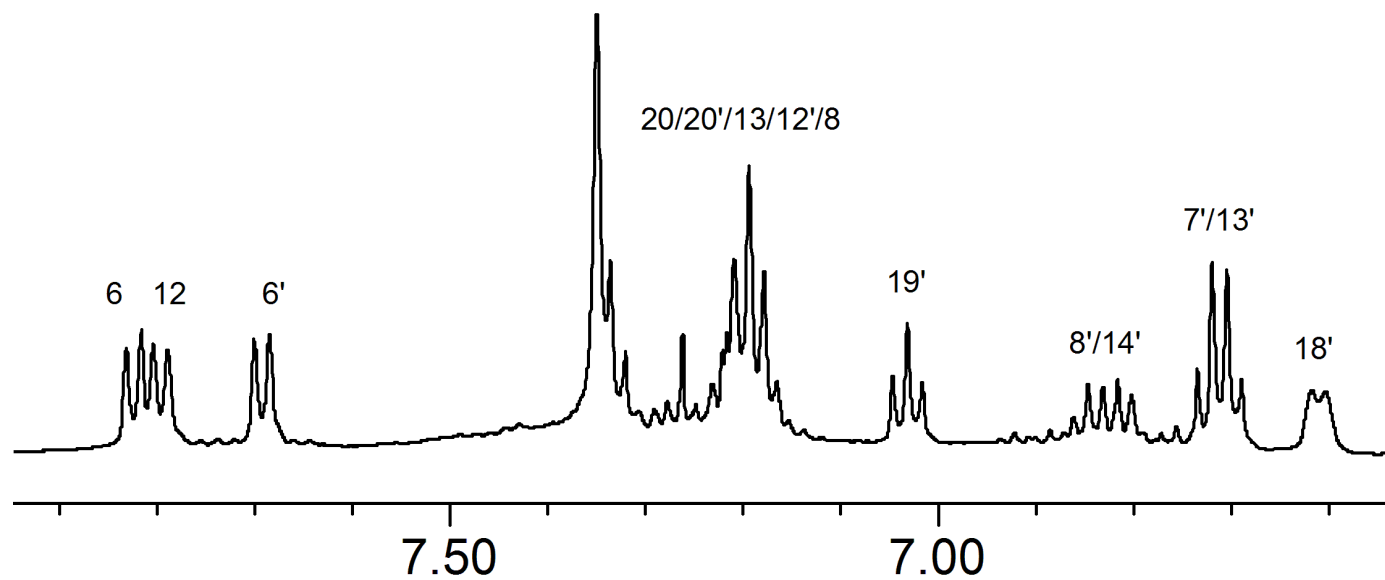
20/20'/13/12'/8



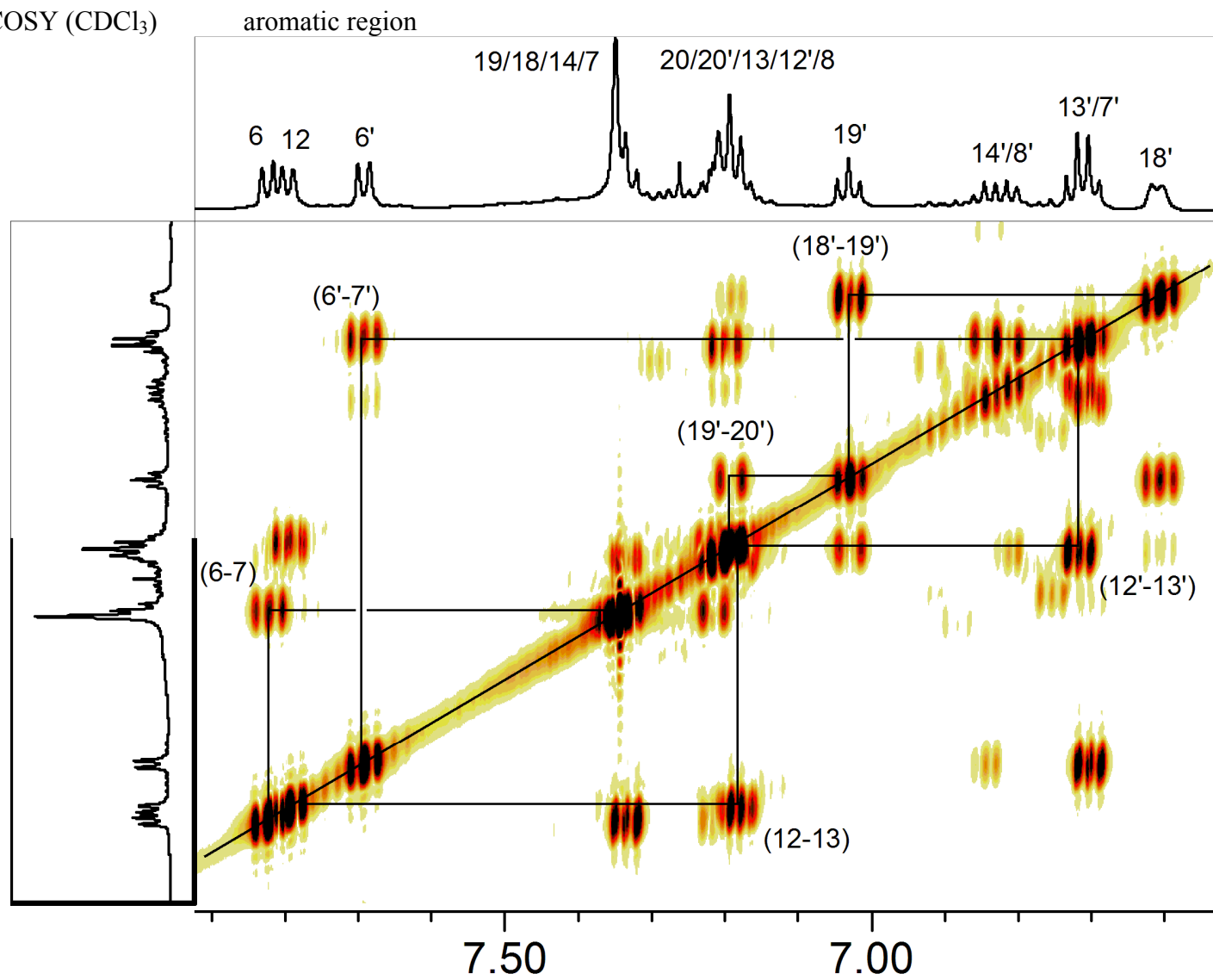
19/18/14/7

20/20'/13/12'/8

7'/13'



$^1\text{H}, ^1\text{H}$ COSY (CDCl_3)



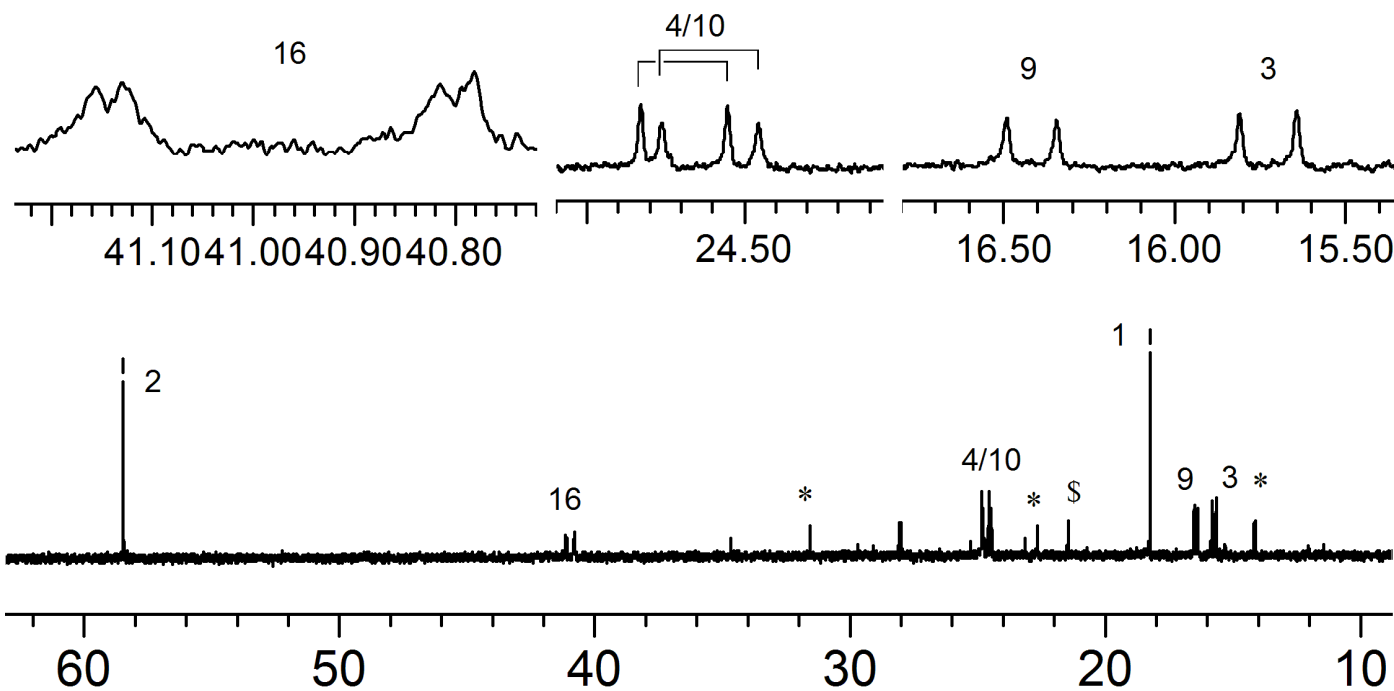
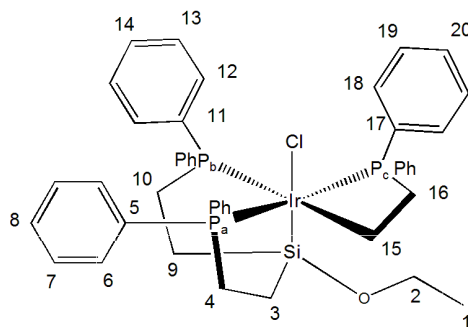
^{13}C (CDCl_3) aliphatic region

*hexane

δ_{toluene}

58,49

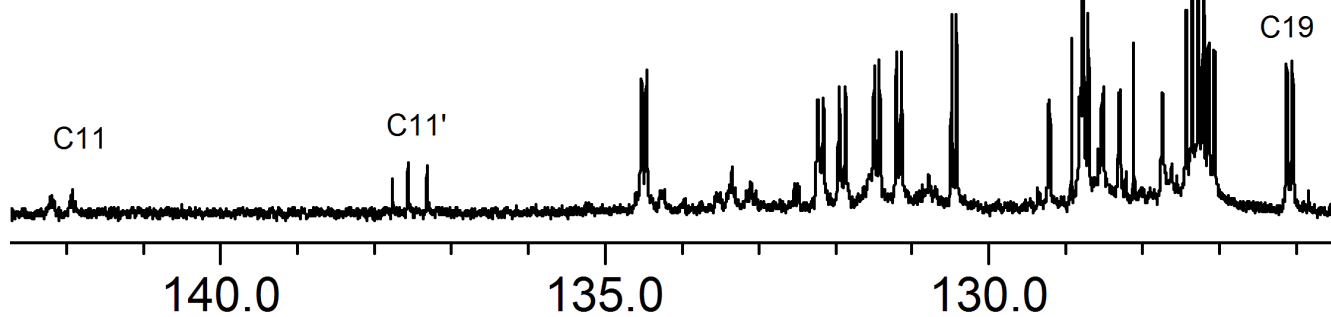
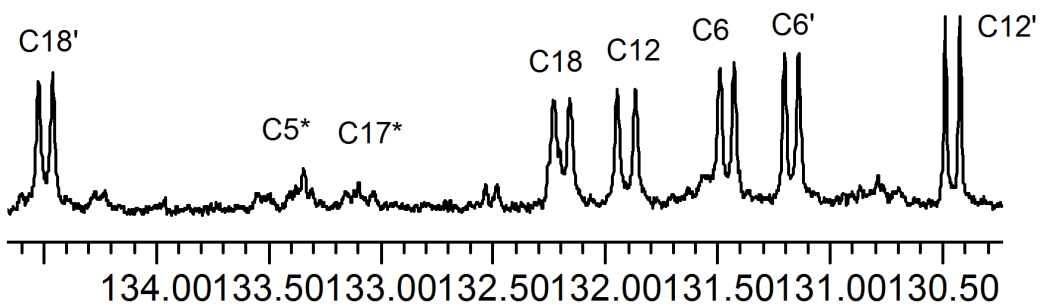
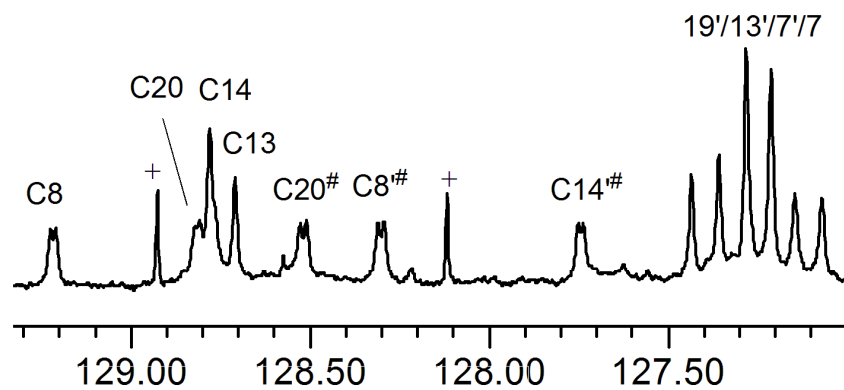
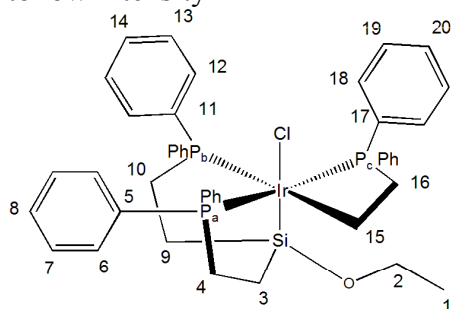
18,23



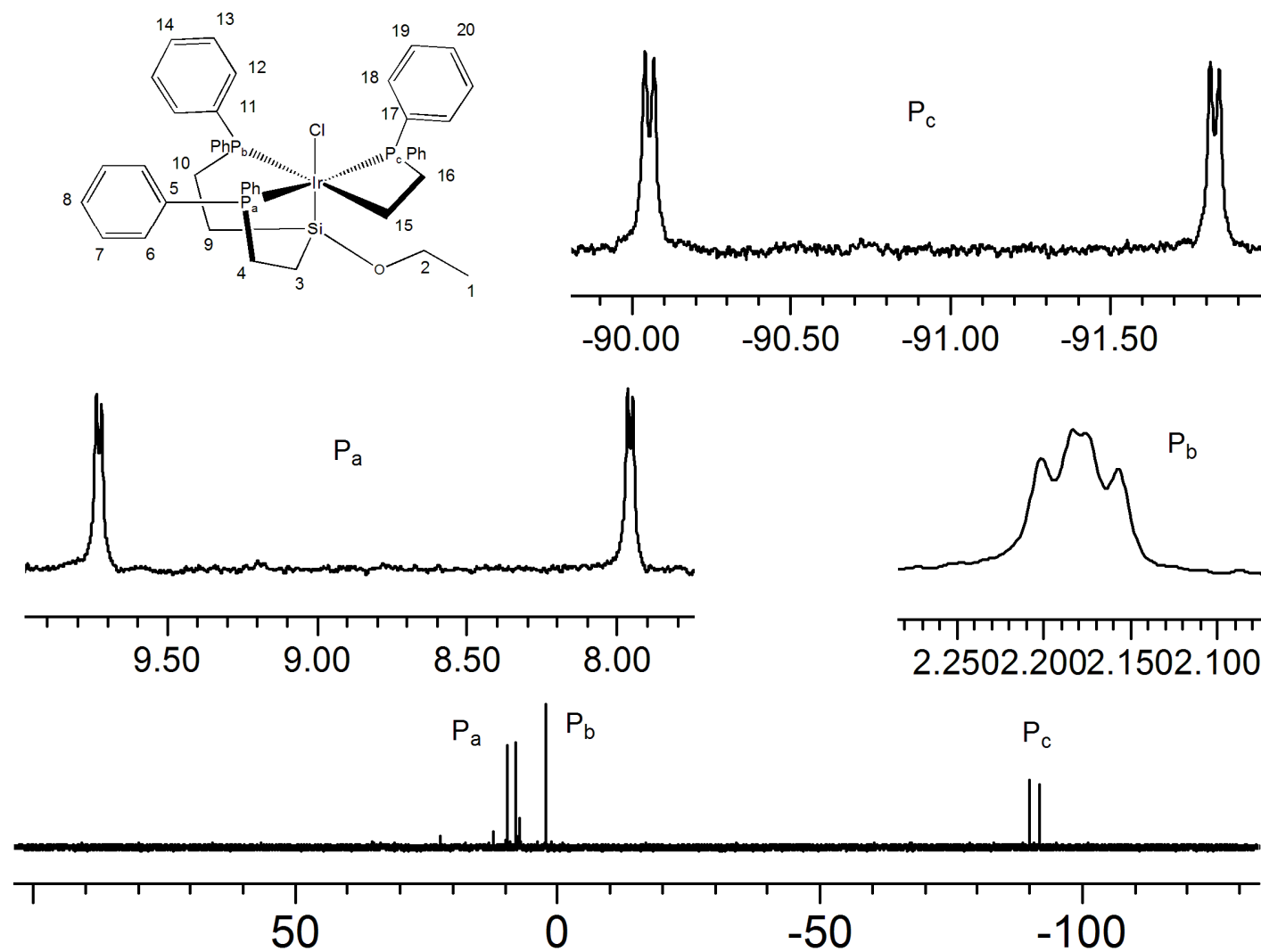
^{13}C (CDCl_3) aromatic region
missing due to low intensity

+toluene

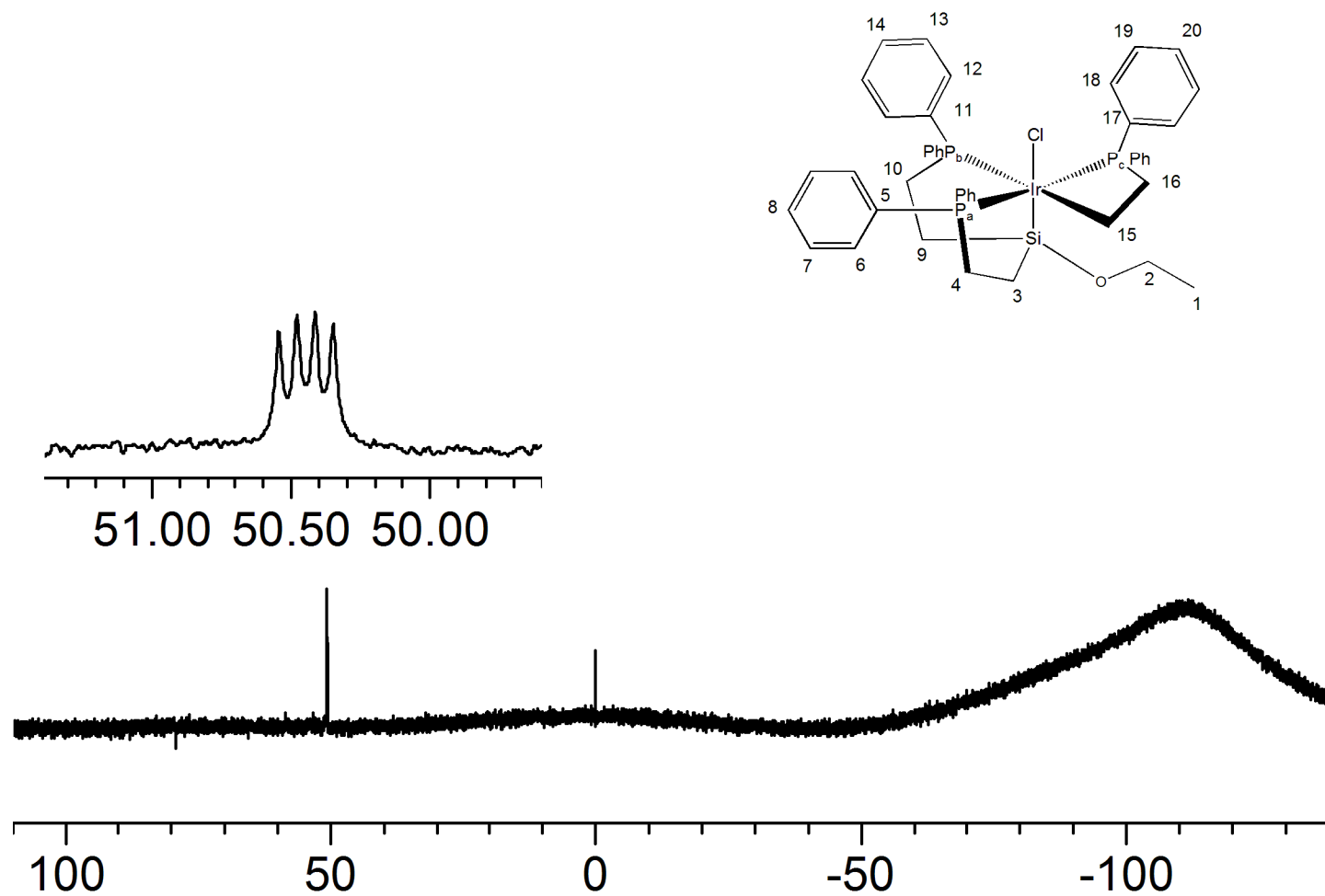
*,# assignments interchangeable; the signals for C15, C5' and C17' are

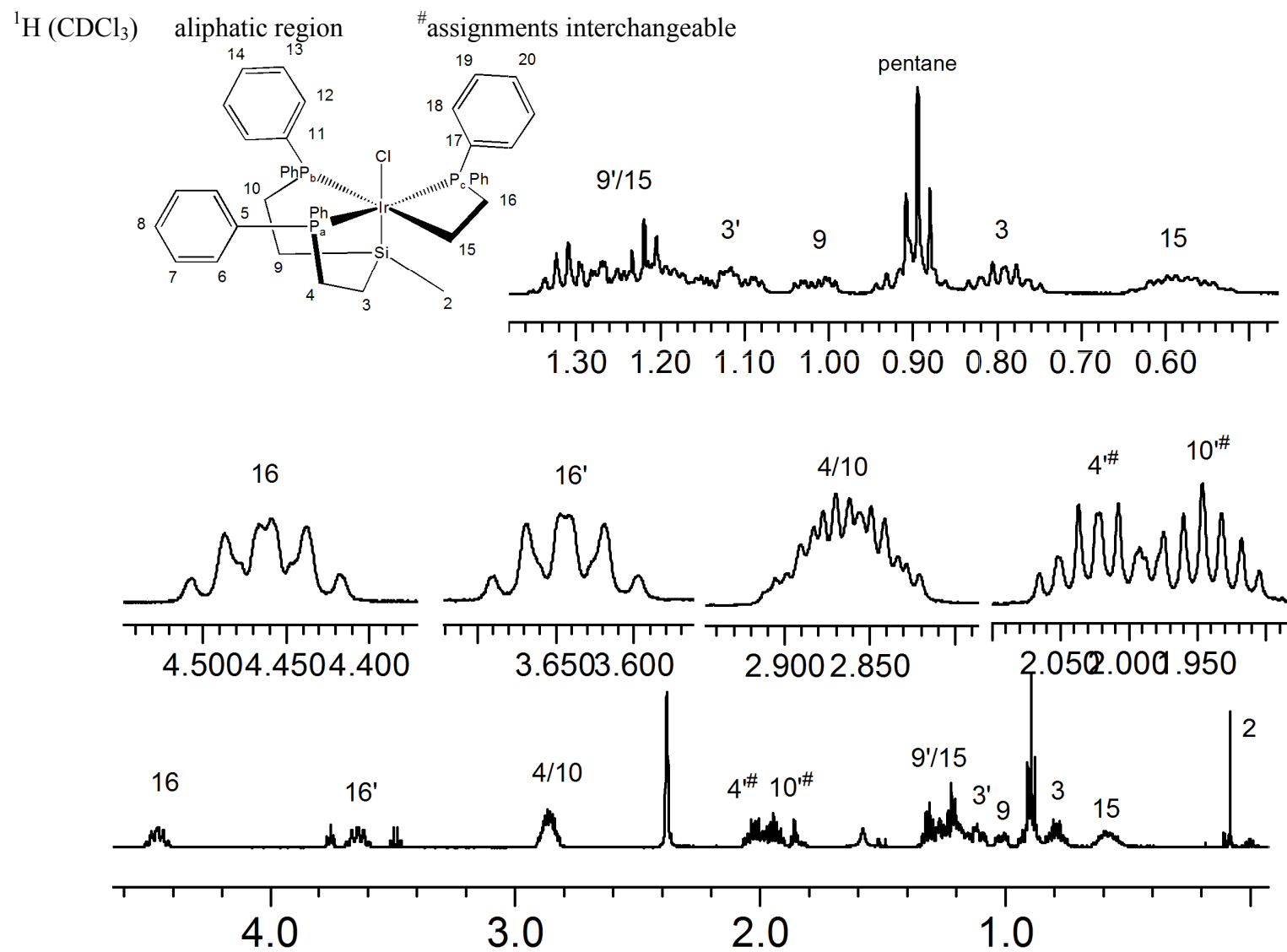


^{31}P (CDCl_3)

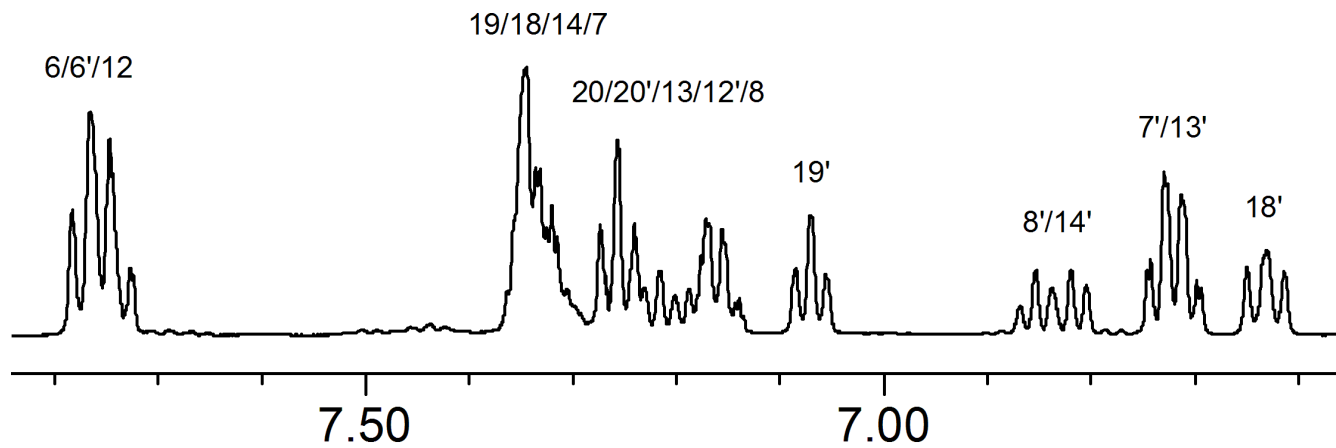
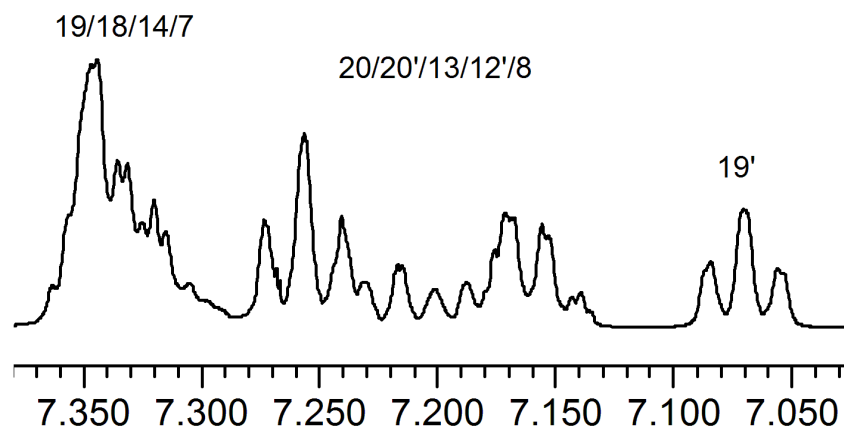
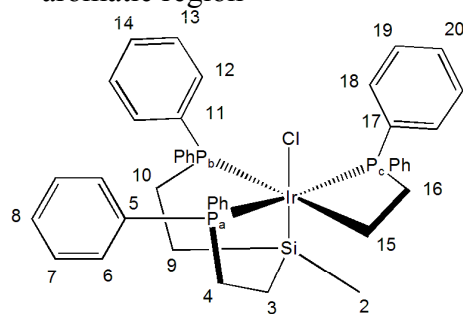


^{29}Si (CDCl_3)

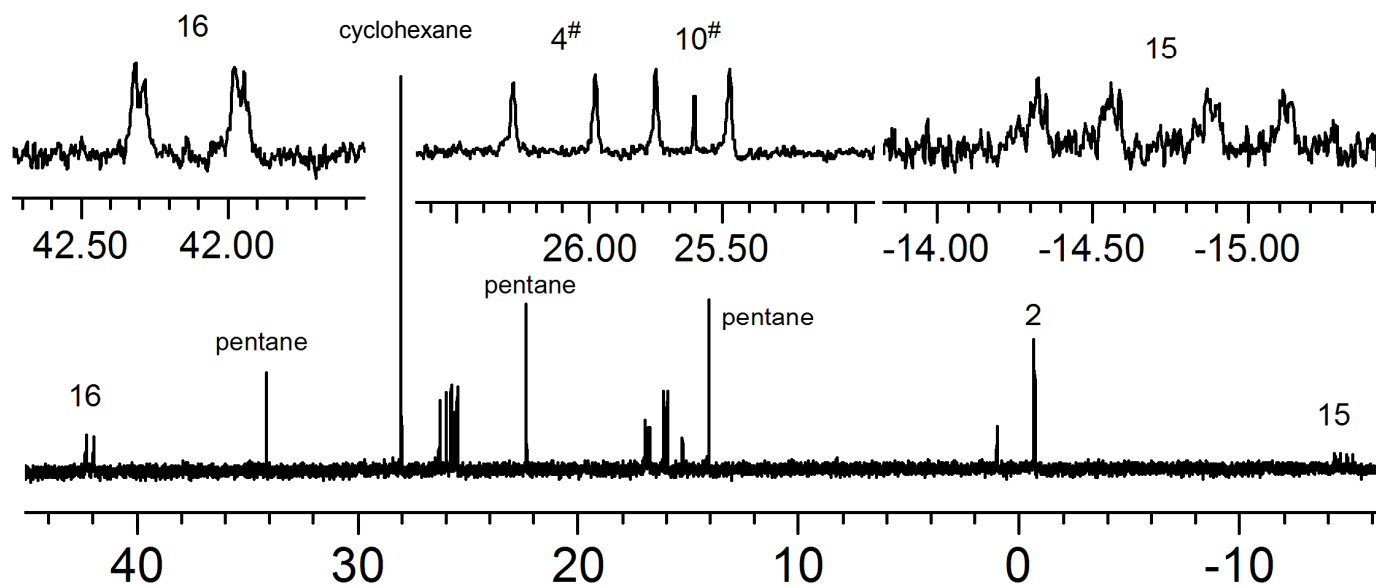
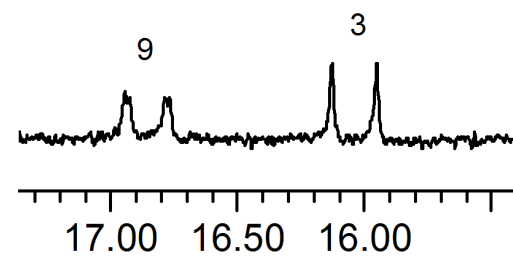
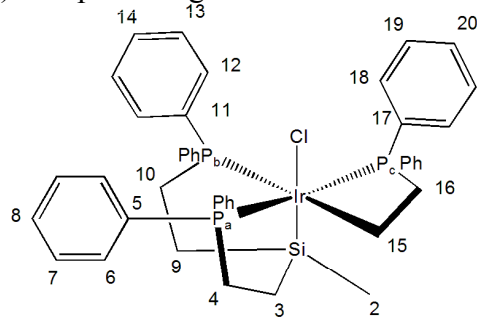


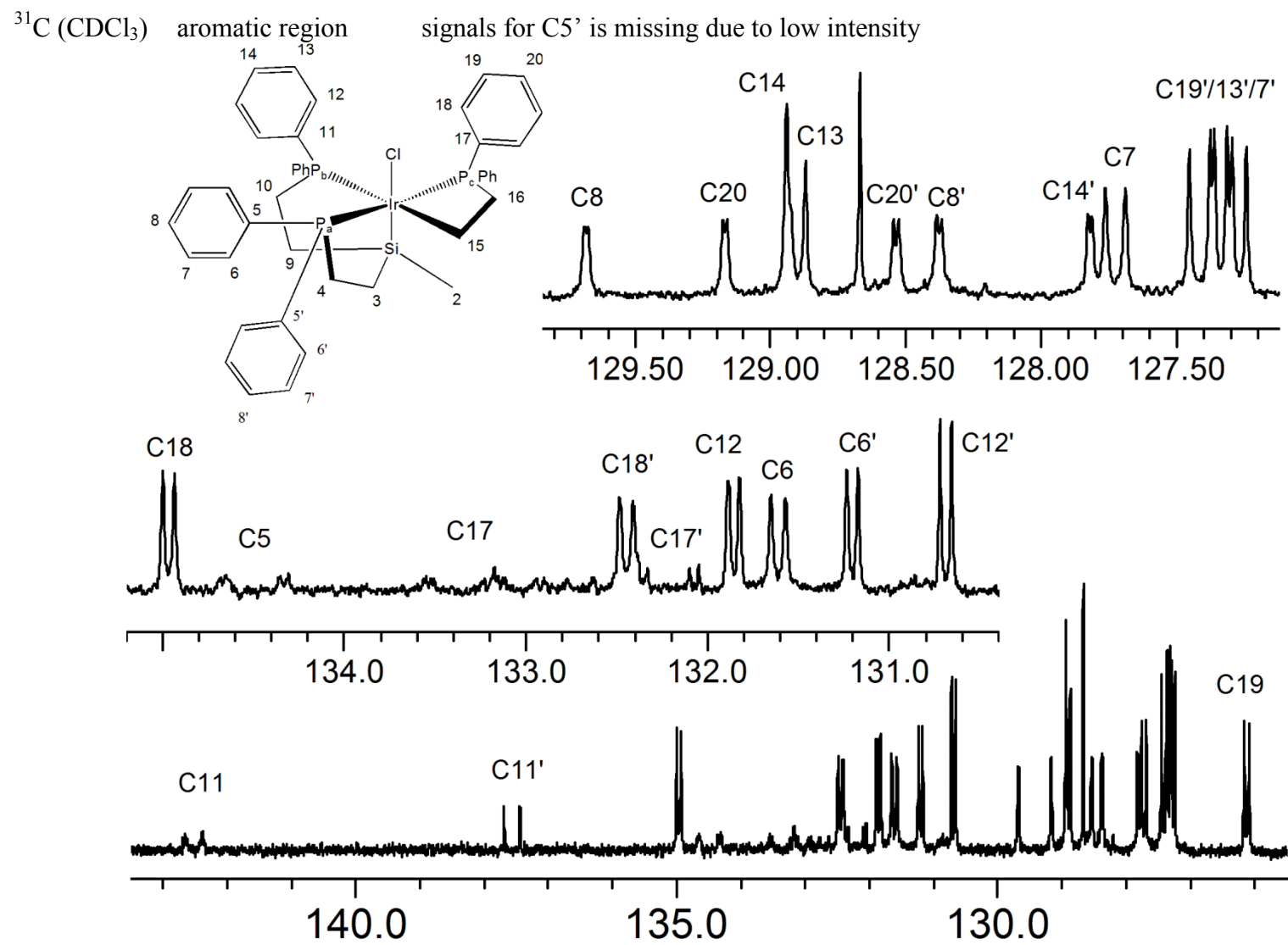


^1H (CDCl_3) aromatic region

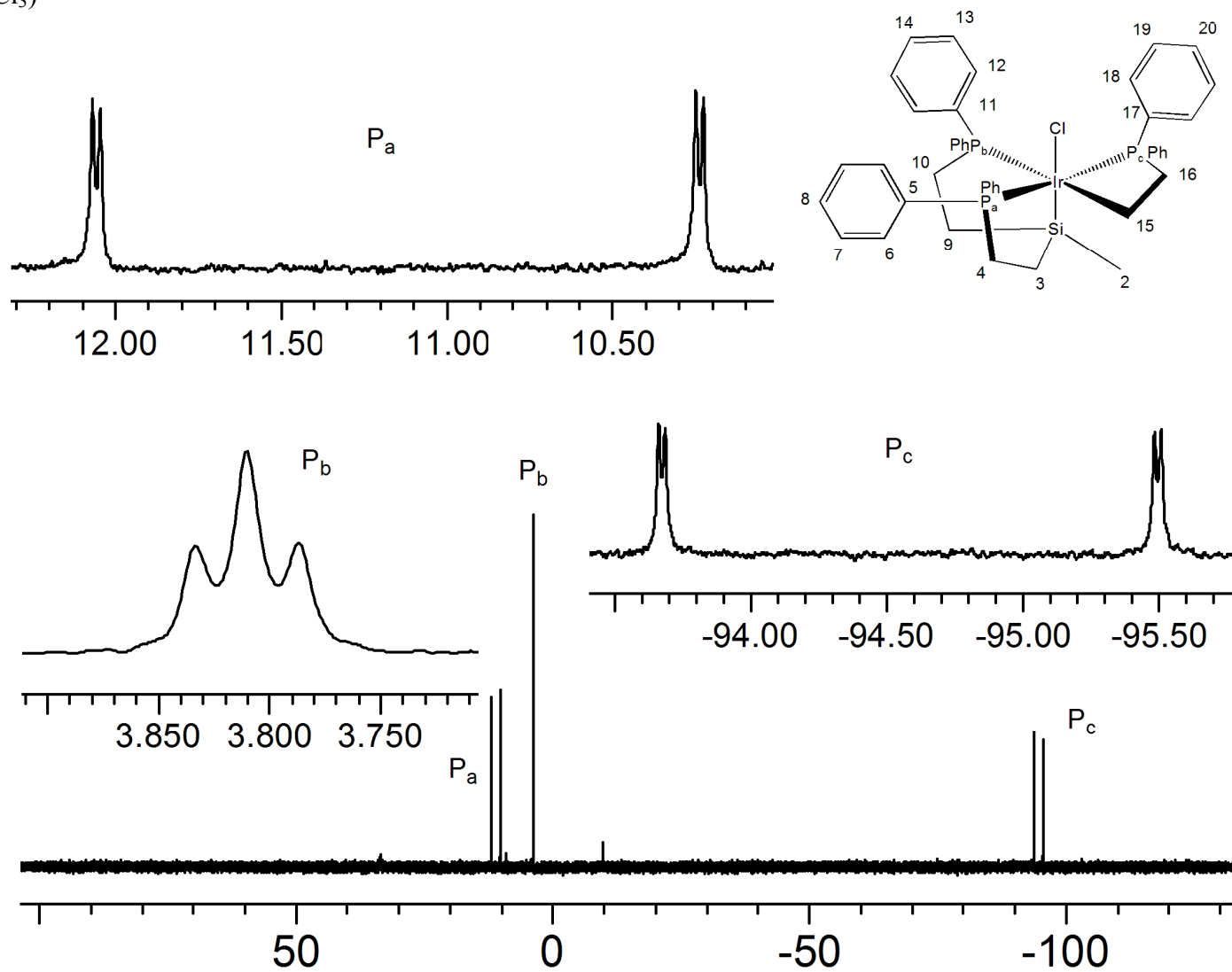


^{13}C (CDCl_3) aliphatic region

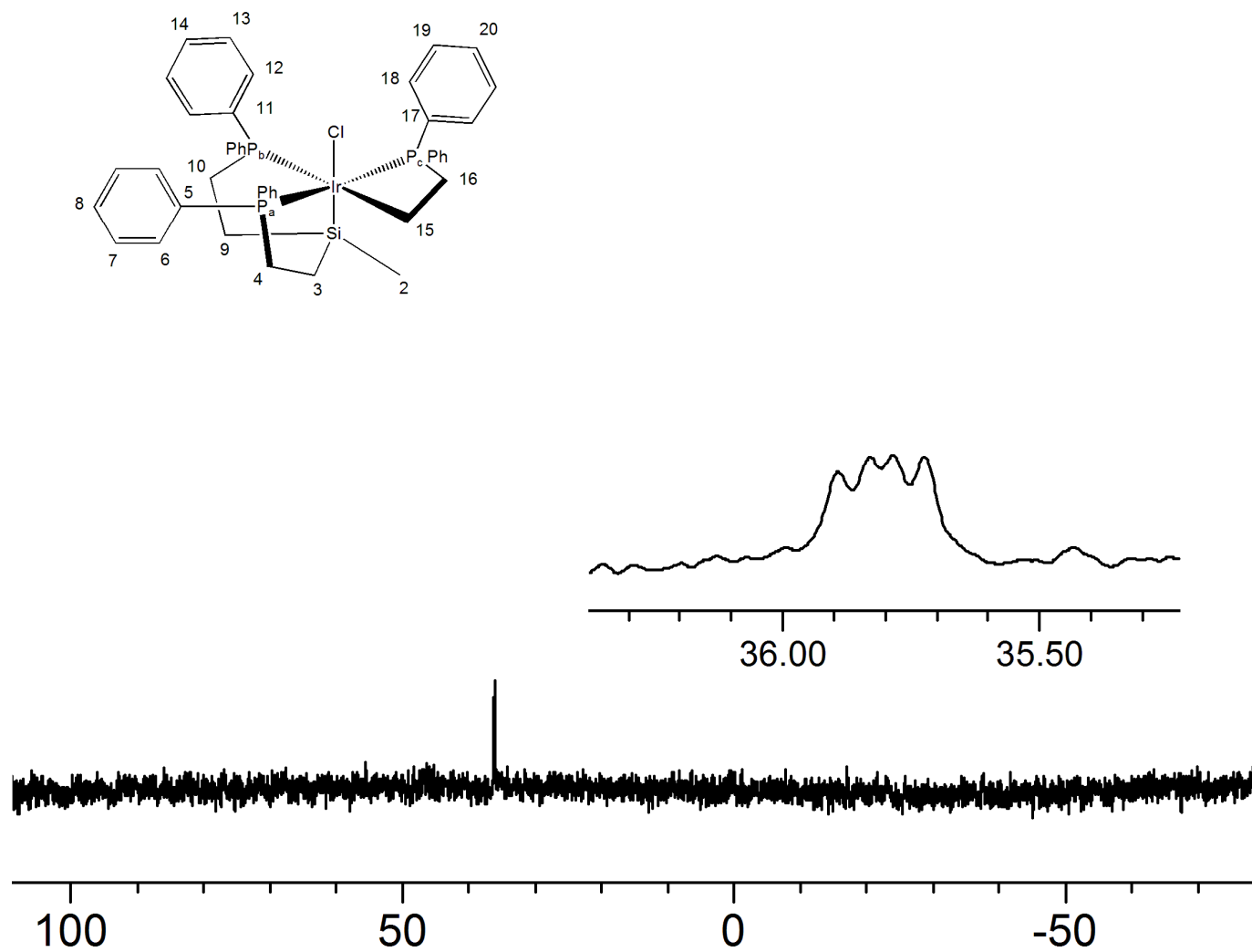




^{31}P (CDCl_3)

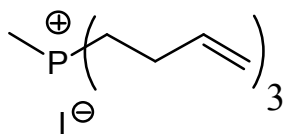


^{29}Si (CDCl_3)

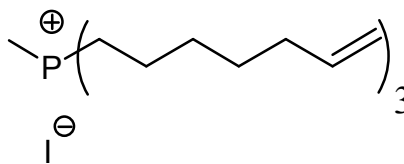


APPENDIX D
CATALOG OF COMPOUNDS

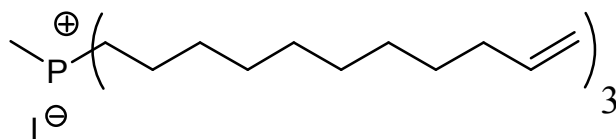
D.1 Molecular Compounds



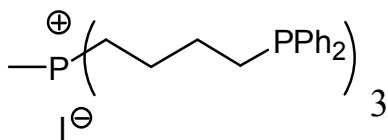
4



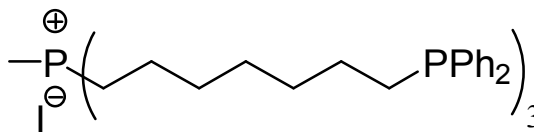
5



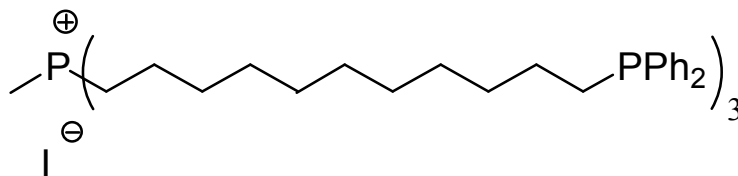
6



13

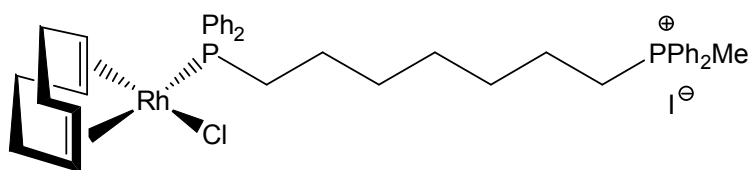


14

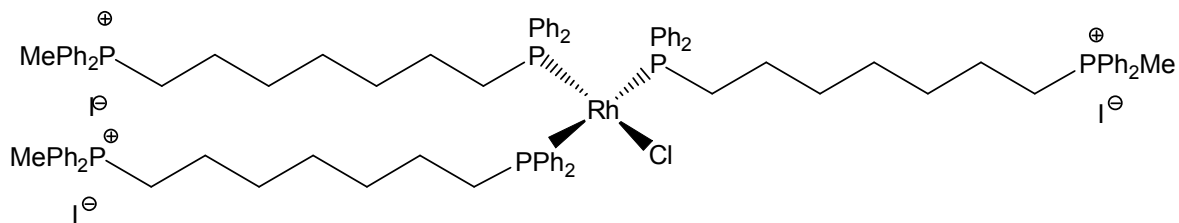


15

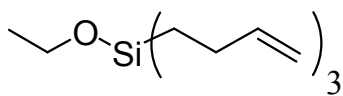




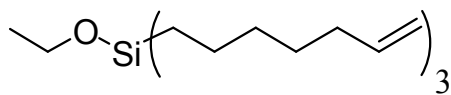
25



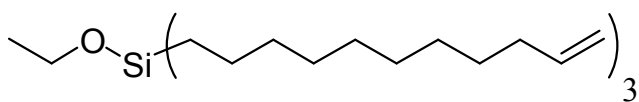
26



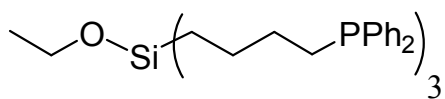
30



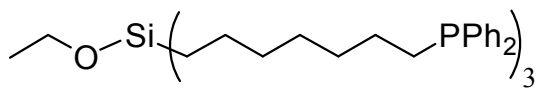
31



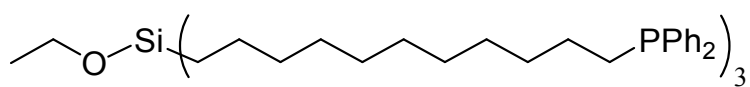
32



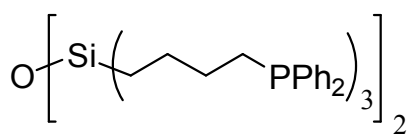
33



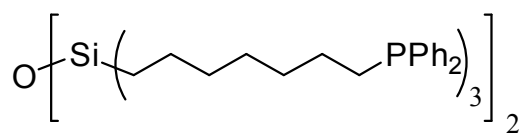
34



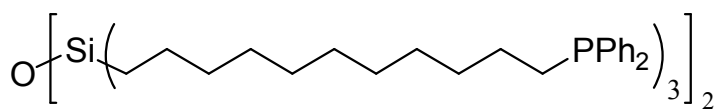
35



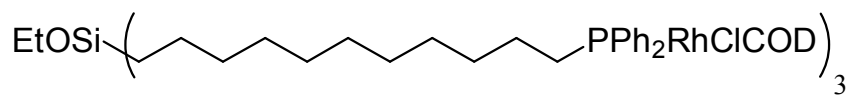
33b



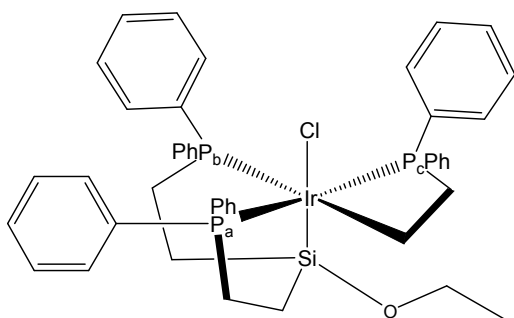
34b



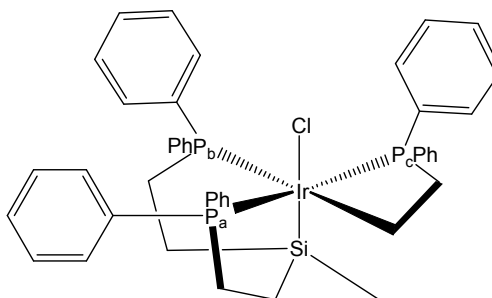
35b



43



47



48